# Thermal and Mechanical Design and Simulation for the first High Precision Quantum Optics Experiment on a Sounding Rocket

Vom Fachbereich Produktionstechnik
der
UNIVERSITÄT BREMEN

zur Erlangung des Grades
*Doktor-Ingenieur*
genehmigte

Dissertation
von
Dipl.-Ing. Jens Grosse

Gutachter: Prof. Dr. H.-J. Dittus
Prof. Dr. C. Braxmaier

Tag der mündlichen Prüfung: 07.10.2016

*Additional information and materials related to this thesis and the author are available through*

*www.jensgrosse.de*

# Contents

# Abstract

The MAIUS-1 scientific payload is a high precision quantum optics experiment about to fly on a VSB-30 sounding rocket with the scientific objective to demonstrate the feasibility of creating the first Bose-Einstein condensates in Space. To achieve this goal the experiment is using various sensitive instruments imposing strong requirements on the thermal and mechanical design.
This thesis is divided into four major parts. The first part will introduce the reader without physics background into the field of atom interferometry and identify the necessary methods and instruments to successfully generate a Bose-Einstein condensate and perform atom interferometry. Furthermore the advantages of performing these experiments in microgravity environment are elaborated and possible platforms to access this environment are compared. Finally some ground-based and microgravity experiments are described to report the state-of-the-art and emphasize the level of miniaturization carried out to fit the experimental setup into a sounding rocket.
The second part introduces the Brazilian-German VSB30 sounding rocket and the German recovery system, service module and attitude control system. The mechanical, thermal and magnetic environment aboard the sounding rocket are characterized by evaluating flight data from former TEXUS and MASER flights. Moreover the requirements of the scientific payload and its instruments regarding attitude, accelerations, vibration, operating temperatures and magnetic environment are summarized and compared with the environment. The hard thermal and mechanical requirements are a priori incompatible with the environment aboard the sounding rocket. The laser modules for example have to be temperature stabilized with an accuracy of $\pm 0.1$K, while the rocket hull temperature increases by 80 K during the flight. Some of the vacuum components are know to be very sensitive to vibrations, while passing a test with a vibration level of 8.1 g RMS is mandatory to qualify those components for the use on a sounding rocket.
The third part will present the mechanical design of the MAIUS-1 scientific payload, which ensures a reliable operation of the instruments in the harsh environment of the sounding rocket. A universal low-cost suspension of the instruments platforms has been developed and tested, which reduces the vibrational loads significantly. Because the optics require an ambient pressure of at least 800 hPa, a sealing method to maintain this pressure level in the entire scientific payload has been elaborated and tested. This includes sealing of the standard RADAX connections, which were slightly modified for this purpose.
While the instrument selection or design, as well as the functional design of the four MAIUS-1 systems has been elaborated by the project partners, the mechanical and thermal design of an system housing suitable for the use on a sounding rocket has also been in the scope of this thesis. All system housings have been minimized in size and mass and have been designed according to requirements of the sheltered instruments. The laser system for example houses 8 laser modules,

a Zerodur spectroscopy board, a Zerodur splitting and distribution board as well as multiple fibre splitters and sensors in only 0.021 $m^3$ at a mass of 23 kg. The laser system and all other system housing designs and the housed instruments are described in detail in this thesis.
As an additional topic of this thesis all of these systems have been successfully vibration tested according to a especially developed test methodology at vibration levels between 2.0g RMS and 8.1g RMS. The results of these tests are presented herein as well.
Vacuum components appeared to be very sensitive to vibrational loads during component and subsystem level tests. To perform the quantum optics experiments a vacuum chamber with a pressure below $5 \times 10^{-10}$ hPa is essential. Thus intensive vibrational and static load tests on indium and con-flat seals, as well as on ion-getter and titanium sublimation pumps have been performed. The results of these tests helped to find a suitable vacuum system design. The innovative design and the components of the MAIUS vacuum system will be presented in detail in this thesis. This design and the used components have been qualified for operation under vibrational loads of up to 8.1g RMS. A pressure rise has been observed in all test runs, which is caused by temporary leaks at the seals. It was proven that the pressure rise is depending on the level of vibrations applied. The design presented herein is capable of regaining a pressure of $5 \times 10^{-10}$ hPa in less than 40 s. To the author's knowledge the presented system is the first vacuum system at this pressure level qualified for the use on a sounding rocket.
In the last part of the thesis the thermal design of the scientific payload is described. The payload systems are thermally controlled with fans and two water cooling circuits, which cool the systems until lift-off. For this purpose a water-cooling umbilical has been developed and tested. The water cooling ensures a thermally stable environment in the lab operation and at the launch pad until lift-off. During the flight the heat is passively stored in the system heat sinks.
For the sizing of the heat sinks the heat input due to aerodynamic heating has to be known. A code has been developed, which approximates the heat flux and the wall temperatures based on the free stream conditions. Furthermore the code is capable of approximating the heat transfer coefficient of natural convection during the boost (hyper-g) phase of the flight based on the wall temperatures and acceleration profile. Additionally the code allows to estimate the air temperature inside a capsuled payload.
The heat input to the payload systems by convection is estimated using the parameters obtained from this code. The thermal conductivity of the rubber dampers has been determined experimentally to simulate the heat input to the payload systems through the instrument platform suspension by conduction. In addition to the heat input through aerodynamic heating, the internally dissipated heat from each system is specified and included into a detailed finite element simulation to verify the heat sink mass. Ultimately the thermal control system for ground and flight mode was tested during a payload bench test. The thesis closes with recommendations and possible improvements for future space-born quantum optics experiments.

# Zusammenfassung

Die wissenschaftliche Nutzlast von MAIUS-1 ist ein hochpräzises quanten-optisches Experiment, was das Ziel der Erzeugung des ersten Bose-Einstein Kondensats im Weltraum verfolgt. Um diese Ziel zu erreichen nutzt das Experiment eine Vielzahl von empfindlichen Komponenten und Instrumenten, die herausfordernde Anforderungen an das mechanische und thermische Design stellen.
Diese Arbeit teilt sich in vier Abschnitte auf. Der erste Abschnitt ist eine Einführung in das Feld der Atominterferometrie, der sich hauptsächlich an Leser richtet, die nicht aus diesem Feld kommen. Es werden die nötigen Techniken und Instrumente vorgestellt um ein Bose-Einstein Kondensat zu erzeugen. Zudem wird der Vorteil erörtert, diese Experimente unter Schwerelosigkeit durchzuführen. Weiterhin werden die verschiedenen Plattformen, die Zugang zu dieser Umgebung bieten vorgestellt und verglichen. Zum Abschluss wird der Stand der Technik von quanten-optischen Experimenten unter Schwerelosigkeit und in sogenannten Fontänen beleuchtet um den erforderlichen Grad der Miniaturisierung des Experimentes herauszustellen.
Der zweite Teil dieser Arbeit stellt die brasilianisch-deutsche Höhenforschungsrakete VSB-30 und das deutsche Bergungs-, Service- und Lagerregelungssystem vor, welches mit der MAIUS-1 Nutzlast genutzt wird. Anhand von Messdaten aus vergangenen TEXUS und MASER Flügen wird das thermische, mechanische und magnetische Umfeld an Bord der Rakete charakterisiert. Dieses Umfeld wird den Anforderungen der Vielzahl von Instrumenten in der wissenschaftlichen Nutzlast gegenübergestellt. Dabei ist zu beobachten, dass die Anforderungen teilweise deutlich von der zu erwartenden Umgebung abweichen. Die Lasermodule beispielsweise erfordern eine thermische Stabilisierung auf $\pm 0.1\,\mathrm{K}$ wohingegen die die Außenhülle der Rakete sich um fast $80\,\mathrm{K}$ erwärmt. Weiterhin sind ultra-hoch Vakuumkomponenten bekannt dafür empfindlich auf Vibrationen zu reagieren. Trotzdem müssen die Komponenten ein Vibrationstest mit einen Lastlevel von $8.1\,\mathrm{g\,RMS}$ bestehen um auf der Rakete eingesetzt werden zu können.
Der dritte Teil der Arbeit widmet sich diesem Widerspruch und präsentiert ein mechanisches Design, welches einen verlässlichen Betrieb der sensitiven Komponenten in diesem harschen Umfeld ermöglicht. Es wurde beispielsweise eine universell einsetzbare, effektive und kostengünstige Vibrationsdämpfung für die Montage der Systeme an der Raketenaußenhülle entwickelt und getestet. Weiterhin wurde eine hermetische Dichtung der gesamten Nutzlast entwickelt und getestet um einen Druck von mindestens $800\,\mathrm{hPa}$ während des gesamten Flug aufrecht zu erhalten, wie es von den optischen Komponenten gefordert wurde. Während die Auswahl und Konstruktion der Komponenten, sowie das funktionelle System-Design der vier MAIUS Systeme bei den Projektpartnern lag, ist das mechanische und thermische Design der Systemgehäuse Bestandteil dieser Arbeit. Hierbei wurden die Gehäuse weitestgehend in Masse und Volumen optimiert ohne die thermischen und mechanischen Anforderungen der beherbergten Instrumente außer Acht zu lassen. Ein gutes

Beispiel liefert hier das Lasersystem, welches acht leistungsstarke Lasermodule, zwei Zerodurboards mit Freistrahloptiken, sowie eine Vielzahl von Photodioden, Elektronikkomponenten und Fasern auf einem Volumen von nur $0.021\,\mathrm{m}^3$ beherbergt. Das System hat dabei eine Masse von nur 23 kg. Das Lasersystem und seine Komponenten wurde, genau wie alle anderen MAIUS-1 Systeme, erfolgreich in einer Vibrationstestkampagne für die Nutzung auf einer VSB-30 Höhenforschungsrakete qualifiziert. Die genaue Beschreibung der erarbeiteten Methodologie zur Qualifizierung der Systeme bei Lasten zwischen 2.0 g RMS und 8.1 g RMS, sowie die Ergebnisse dieser Tests sind ebenfalls Bestandteil dieser Arbeit.
Besonders ausführlich wird die Konstruktion und Auslegung des Ultrahochvakuumsystems behandelt. Für die Erzeugung von Bose-Einstein Kondensaten ist ein niedriger Hintergrunddruck unabdingbar. Dieser Druck sollte während der Experimente $5 \times 10^{-8}$ Pa nicht überschreiten um das Erreichen der wissenschaftlichen Ziele nicht zu gefährden. In Rahmen dieser Arbeit wurde der Gaseintrag durch Desorption und Permeation der Kammerwände und der Einbauten abgeschätzt und einige Möglichkeiten vorgestellt diesen in zukünftigen Experimenten zu reduzieren. Vor allem aber wurde eine Vielzahl von Vibrationstests im Bereich von 2.0 g RMS und 8.1 g RMS und statischen Lasttests bis zu 1200 N durchgeführt, um die Leckrate von Indium und ConFlat (CF) Dichtungen unter Last zu bestimmen. Die Ergebnisse dieser Tests flossen in das innovative Design des MAIUS Vakuumsystem ein. Bei allen Vibrationstests wurde ein Druckanstieg beobachtet. Das hier präsentierte System ist in der Lage innerhalb von 40 s nach einem Vibrationstest bei 5.4 g RMS den geforderten maximal Druck von $5 \times 10^{-8}$ Pa wiederherzustellen. Nach Kenntnis des Autors ist dieses System das erste Vakuumsystem für einen solchen Druckbereich das für den Einsatz auf einer Höhenforschungsrakete qualifiziert wurde.
Der letzte Teil der Arbeit betrachtet das thermische Design der wissenschaftlichen Nutzlast. Die verschiedenen Systeme der Nutzlast nutzen im Bodenbetrieb Lüfter und Wasserkühlungen um die Temperaturen in den geforderten Bereichen zu halten. Die zwei Wasserkühlungskreisläufe kühlen die System bis zum Start der Rakete. Zu diesem Zweck wurde ein Umbilical zur Wasserkühlung entwickelt und getestet, welches beim Start getrennt wird. Von diesem Zeitpunkt an wird die dissipierte Wärme passiv in den System Wärmesenken gespeichert. Zur Auslegung dieser Wärmesenke ist es erforderlich den Wärmeeintrag durch die aerodynamische Erwärmung der Raketenhülle zu kennen. Im Rahmen dieser Arbeit wurde daher ein Code entwickelt der den Wärmestrom durch aerodynamische Erwärmung und die resultierenden Hüllentemperaturen basierend auf den Parametern der freien Anströmung abschätzt. Außerdem ist der Code in der Lage die Wärmeübergangskoeffizienten der freien Konvektion in der Beschleunigungsphase der Rakete aus den Beschleunigungswerten und den Wandtemperaturen zu approximieren. Dies erlaubt auch die Abschätzung der Erwärmung der eingeschlossenen Luft. Die Temperatur der in der Nutzlast eingeschlossenem Luft und der berechnete Wärmeübergangskoeffizient werden genutzt um den Wärmeeintrag durch freie Konvektion in die Nutzlastsysteme zu bestimmen. Außerdem wurde die thermische Leitfähigkeit der Vibrationsdämpfer experimentell bestimmt um auch den Wärmeeintrag durch Wärmeleitung in die Systeme simulieren zu können. Schließlich wurde auch die dissipierte Energie der Systeminstrumente ausführlich charakterisiert und in einer detaillierten FEM Simulation integriert um die Wärmesenkenmasse zu verifizieren. Die Ergebnisse der Simulation wurden mit Messwerten von thermischen Tests verglichen. Diese Arbeit schließt mit einigen Verbesserungsvorschlägen und Empfehlungen für das mechanische und thermische Design zukünftiger quanten-optischer Experimente für Weltraumanwendungen.

# Part I

# Introduction

# 1
# Scientific Background

To propose a suitable design for a scientific payload, one will have to understand the principle, architecture and specialties of its experiment. Since the scientific objective of the MAIUS mission is to demonstrate the feasibility of performing atom interferometry in space, the principle of the creation of Bose Einstein Condensates (BECs) and atom interferometry shall be presented in the following to the reader without. Moreover a typical experimental setup as well as the general requirements and constraints for the generation of a BEC shall be stated.

## 1.1 General Definition and Atomic Species Selection

In 1924 the existence of BECs was proposed by Satyendranath Bose [Bos24] and Albert Einstein [Ein24]. Einstein postulates that cooling bosonic gases to a temperature very close to absolute zero will cause the atoms to condense to the lowest possible quantum state. At this point quantum effects become apparent on a macroscopic scale. Since the atoms are in the same state, they can be described using one single wave function. This characteristic behavior can be used to perform atom interferometry.

To create a BEC a dilute gas of bosons needs to be cooled to a critical temperatures $T_c$. This is achieved using laser light, magnetic fields and radiofrequencies as described in the following section. The critical temperature is defined in [Pet02] as

$$T_c \approx 3.3125 \, \frac{\hbar^2 n^{2/3}}{m k_B} \tag{1.1}$$

It is depending on the particle density $n$, the mass per boson $m$, the reduced Planck constant $\hbar$ and the Boltzmann constant $k_B$. Therefore the temperature is only depending on the atom species and particle density $n$.

The latter factor is strongly depending on the experiment configuration (trap geometry and particle number). Therefore it can not be calculated from literature values and is only valid for a certain experiment configuration. For Rubidium 87 in the QUANTUS-2 setup the critical temperature has been measured as $T_c = 313\,\mathrm{nK}$ [Her13a].

BECs have been demonstrated for a large number of other isotopes such as $^{7}$Li, $^{23}$Na, $^{39}$K, $^{41}$K, $^{85}$Rb, $^{133}$Cs, $^{52}$Cr, $^{40}$Ca, $^{84}$Sr, $^{86}$Sr, $^{88}$Sr, $^{174}$Yb, $^{164}$Dy and $^{168}$Er. In the MAIUS experiment the alkaline atom isotope $^{87}$Rb is used, because the heritage and knowledge in the QUANTUS-3 consortium gained with the predecessor experiments, which are also using Rubidium 87.

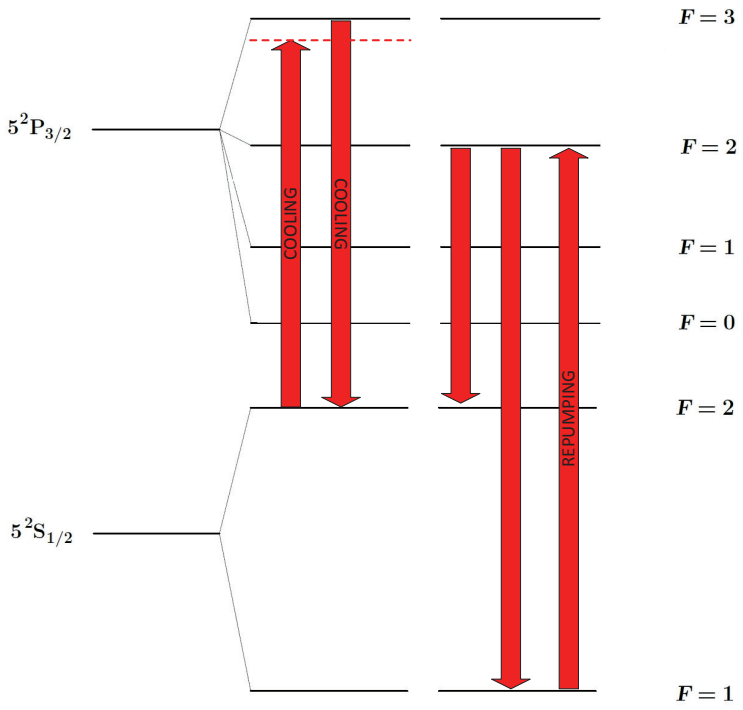


**Figure 1.1:** Hyperfine structure $^{87}Rb$ with transitions for cooling and Repumping. Detuning to red indicated by dotted line.

Rubidium 87 has one valence electron on the outer shell, which is advantageous in laser cooling. Figure 1.1 shows the energy level structure of $^{87}$Rb naming the different hyperfine states and important allowed transitions. In presence of a magnetic field the hyperfine states (F) will split into 2F+1 Zeeman sublevels $m_f$. Thus the F=1 level will split into 3 sublevels $m_f = [-1,0,1]$, the F=2 state splits into the 5 sublevels $m_f = [-2,-1,0,1,2]$ and the F=3 state into 7 sublevels $m_f = [-3,-2,-1,0,1,2,3]$.

How the energy level structure and the different transitions can be used to cool Rubidium-87 shall be described in the next section.

## 1.2 Cooling Procedures

There are different procedures to cool (Rubidium 87) atoms to the desired temperature. These techniques should be described briefly in the following. This should explain the necessity of the different technical instruments and underline the complexity of the experiment.

### 1.2.1 Doppler Cooling & Magneto-Optical Trap

A basic principle used for laser cooling is the stimulated absorption and spontaneous emission of photons from a laser beam. If the laser wavelength equals the transition frequency in the specific hyperfine structure, the atom will absorb a photon from the laser beam and cause the atom to be transfered in the excited state. The absorption process causes a loss in the momentum of the atom. After a short period of time the electron is emitted spontaneously in a random direction transferring the atom to its initial state again. This process can be repeated infinitely thus it is a spontaneous emission cycle as indicated in 1.1.

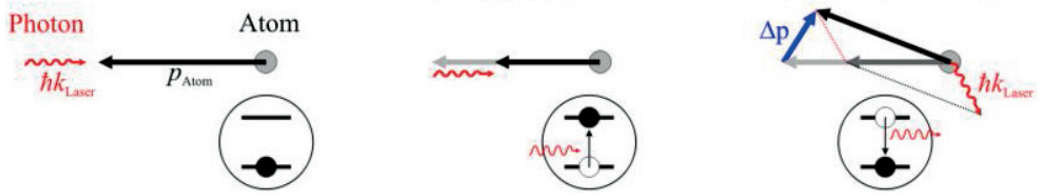


**Figure 1.2:** Illustration of slowing of atoms by stimulated absorption and spontaneous re-emission (adapted from [Kri08])

If the wavelength of the lasers is tuned slightly below an transition of the atom (red detuned) as illustrated by the dotted line in figure 1.1 this process will become velocity selective. Atoms which do not move or are traveling in the same direction as the laser beam will not perform a transition, because the transfered energy is to low. However atoms with a velocity vector opposing the laser beam will see the wavelength of the laser light blue detuned to match the transition wavelength due to the Doppler effect. Therefore only atoms moving towards the laser light will absorb a photon as illustrated in figure 1.2.

For this method of cooling only three orthogonal pairs of counter-propagating lasers beams are needed to shine in light from all directions in space. The frequency of the laser diode for cooling of Rubidium is typically set to 780 nm and can be controlled (for de-tuning) by current modulation of the master oscillator.

Rubidium 87 is excited by laser light from the $5^2S_{1/2}$ F=2 state to the $5^2P_{3/2}$ F=3 state and vice-versa. However it is also possible that the atom is transferred into the $5^2P_{3/2}$ F=2 state. From this state the electron can perform two allowed transitions either into the $5^2S_{1/2}$ F=2 or F=1 state as illustrated at the right side of figure 1.1. Therefore it is possible that those atoms exits the spontaneous emission cycle.

Atoms in the $5^2S_{1/2}$ F=1 state would not be cooled by the incident laser light. To avoid loosing those atoms, an additional re-pump laser at a different frequency is used to bring the atoms back into the cycle.

The Doppler cooling procedure mentioned above is only velocity selective. The atoms are slowed and thus cooled, but they are not trapped at a certain position as desired. This can be achieved by adding a quadro-pole magnetic field to the setup. This setup and method is called magneto-optical trap (MOT).

The magnetic field is generated with an anti-helmholtz configuration of magnetic coils with zero-crossing in the center of the field. Contrary to the Doppler laser cooling the laser light needs to have a circular polarization, otherwise it would not interact with the magnetic sublevels of the atoms. The counter-propagating laser beams will have different polarizations ( $\sigma^+$-$\sigma^-$-configuration).

A exemplary one-dimensional MOT setup is illustrated in figure 1.3 for a fictitious transition from a ground state F=0 (without magnetic sublevels) to an excited state F=1 (with three sublevels $m_f = [+1, 0, -1]$). In the MAIUS-1 setup the transition used for magneto-optical trapping will be $5^2S_{1/2}$ F=2 to $5^2P_{3/2}$ F=3 as shown in figure 1.1 resulting in more sublevels.

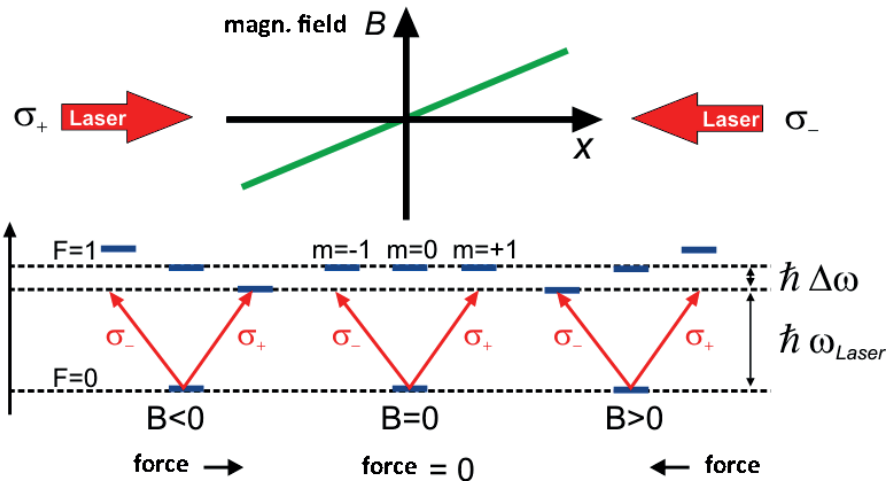


**Figure 1.3:** Principle of MOT cooling for a fictitious transition from a ground state F=0 to an excited state F=1 (adapted from [Kri08])

As illustrated in figure 1.3 the magnetic field causes a Zeeman shift to the magnetic sensitive $m_f$ states of the rubidium atoms (in this example $m = +1$ and $m = -1$). The shift increases with the intensity of the magnetic field and therefore with the distance of the atoms to the trap center. With an increase in the Zeeman shift the transition frequency changes towards the frequency of the detuned lasers and a transition becomes possible.

Laser beams with $\sigma_+$ polarization can only interact with the $m = +1$ state, while the laser with $\sigma_-$-polarization will only interact with the $m = -1$ state. If the $\sigma_+$ laser is pointing at

the MOT from the left, the $\sigma_-$ laser from the right and the frequency of the laser is detuned by the sum of Doppler shift and Zeeman shift the atoms will be cooled and pushed towards the trap center simultaneously.

This cooling method is limited by a minimum (Doppler) temperature. This temperature can be calculated from

$$T_{Doppler} = \frac{\hbar\Gamma}{2k_b} \tag{1.2}$$

as given in [Met99]. With given values of the reduced Boltzmann constant $k_b$, Planck constant $\hbar$ and line width $\Gamma$ for Rubidium 87 D2 transition, the Doppler limit temperature for Rubidium 87 can be determined as $T_{Doppler}\left({}^{87}Rb\right) \approx 145\mu K$.

### 1.2.2 Sub-Doppler Cooling

It was demonstrated that the laser setup described above can be used to cool the atoms below the Doppler limit [Ada97]. The red-detuned counter-propagating $\sigma^+$- and $\sigma^-$-polarized laser beams, described in the MOT setup above, will result into a light field, whose polarization remains linear ($\Pi$) and rotates around the beam axis forming an helix as shown in figure 1.4. When progressing one wavelength $\lambda$ along the beam the polarization vector will rotate by 360°.

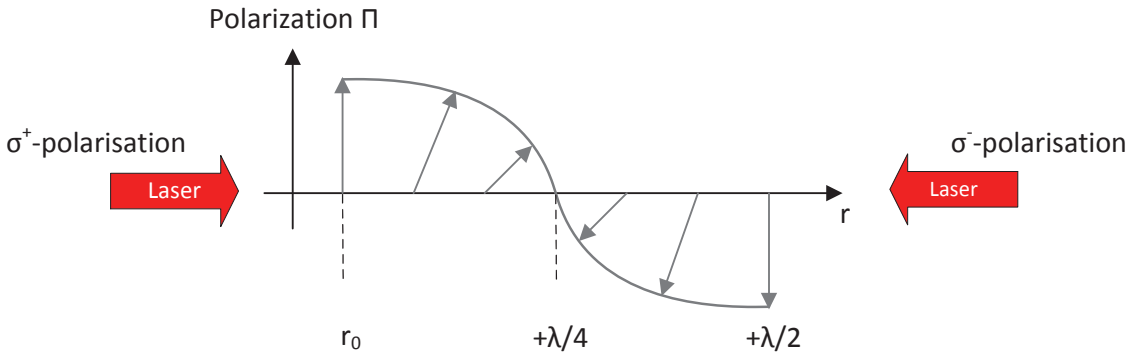


**Figure 1.4:** Polarization resulting from two counter-propagating $\sigma^+$- and $\sigma^-$-polarized laser beams. The polarization is linear $\Pi$ and oscillates around the light axis forming a helix.

If an atom moves within this field, the polarization vector will rotate within the fixed coordinate system of the atom. The rotation speed is depending on the velocity of the atom. This rotation is basically imposing a virtual magnetic field oscillating with the rotation of the vector. This field results in velocity depending coupling between the sub-states $m_f$ of the hyperfine structure. As a matter of fact the population distribution in the different $m_f$-states changes for an moving atom.

If an atom moves towards a $\sigma^-$-polarized laser beam (in direction $r > 0$) as illustrated in figure 1.5, the changing polarization described above will result in a higher population in the $m_f = -1$, than in the $m_f = +1$ sub level.

Due to the fact that the probability is higher for an $m_f = -1$-atom to absorb a photon from a $\sigma^-$-polarized than from a $\sigma^+$-polarized laser beam, there is an unbalance between the force of both beams for a moving atom. Thus the atom will more likely absorb an photon from the opposing laser beam, as from the co-propagating beam [Dal89].

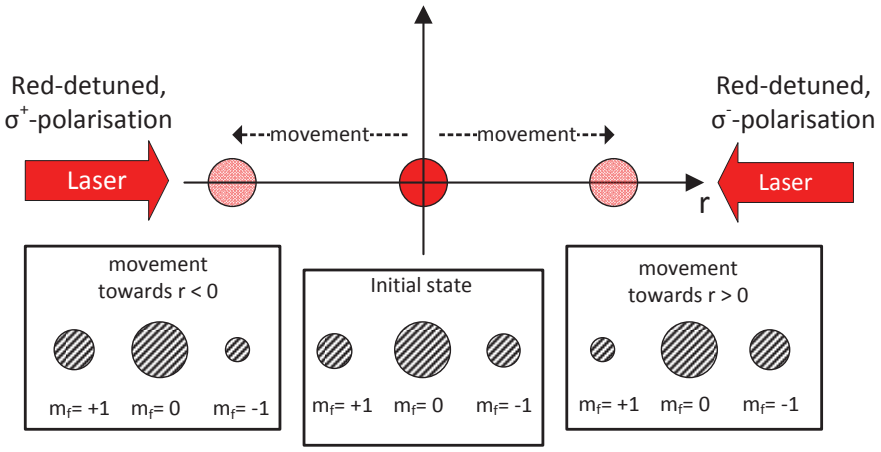


**Figure 1.5:** Influence of the atom movement on the population distribution in the different sublevels ($m_f$) of the ground state

This results in a velocity selective cooling as described for the Doppler cooling in the previous section. However this cooling is not induced by the Doppler Effect, but by the velocity depending population distribution in the sub-states, thus it will also effect slower atoms . For this reason it is possible to cool the ensemble below the Doppler temperature, without additional hardware but with demanding requirements to the polarization stability of the lasers.

The sub-doppler cooling procedure is limited by the recoil temperature, defined by the energy deposited transfered to an atom by the spontaneous emission of a single photon

$$T_{recoil} = \frac{\hbar^2 k^2}{2mk_b} \tag{1.3}$$

The theoretical minimum temperature for the sub-doppler cooling of Rubidium-87 is given as $T_{recoil}\left({}^{87}Rb\right) \approx 362nK$.

### 1.2.3 Magnetic Trap and Evaporative Cooling

Evaporative cooling is the last step in the cooling process selectively removing fast atoms from the ensemble. For evaporative cooling the atoms are transfered into a harmonic magnetic trap, with a field minimum at a value larger than zero as exemplary shown in figure 1.6a. This is important to prevent the loss of atoms due to unwanted transitions into non trappable states (spin-flips).

In MAIUS this trap is created by superposition of the field generated by the magnetic coils and an inhomogenous field generated by planar circuits on an (atom) chip [Sei14]. This chip consists of different layers which reduce in conductor diameter. The size of the trap is reduced stepwise by switching to smaller circuits on the chip. This will lead to a compression of the atomic ensemble in the trap.

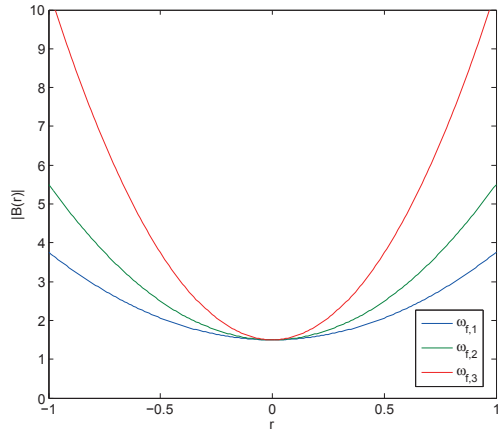


**(a)** Trap frequency for different trap geometries on exemplary square trap potential ($\omega_{f,1} < \omega_{f,2} < \omega_{f,3}$). Units are arbitrary.

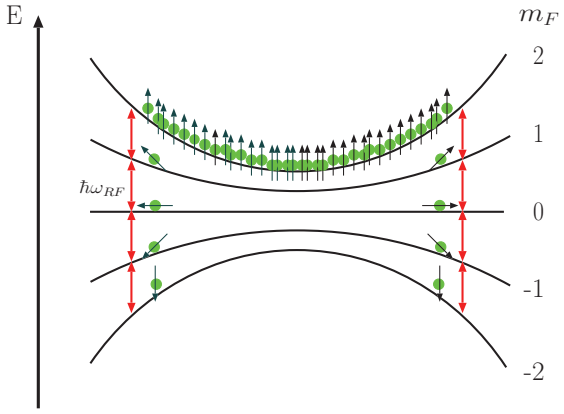


**(b)** RF-evaportation scheme [Din04]

**Figure 1.6:** Principle of evaporation cooling

During the evaporative cooling process hot atoms are removed from the trapped ensemble by applying a RF-field emitted by an RF antenna. The RF signal will remove atoms with a certain energy and coordinate in the magnetic field of the trap selectively. If the energy of the RF field is equal to the potential difference between two $m_f$-states as illustrated in figure 1.6b, a spin-flip will be induced. This will transfer the atoms in a magnetic state, which is not trappable and remove them from the trap.

Stepwise reduction of the RF frequency will remove the hottest atoms in each step. Thus the mean temperature of the ensemble will be lowered with every step and finally cool the atoms below the critical temperature $T_c$ and create the BEC.

## 1.3 Atom Interferometry

Before atom interferometry is performed, it is desirable to reduce the expansion rate of the BEC. This is achieved with a method called delta-kick cooling. The atoms are released from the magnetic trap, an re-trapped after a short time. This procedure will reduce the expansion rate significantly giving access to longer interferometer times.

Additionally, the atoms are transferred into a non magnetic state by applying a laser pulse to reduce the influence of residual magnetic fields which effect the measurements despite magnetic shielding. This procedure is named adiabatic rapid passage. Finally, the prepared atoms are used to perform atom interferometry.

In an atom interferometer setup the BEC is used as matter wave source, while laser light pulses are used as mirror or beam splitter. Since interferometers are inherently depending on the wave nature, cold atoms can be used to establish interferometers with ultra high sensitivity due to the short de Broglie wavelength.

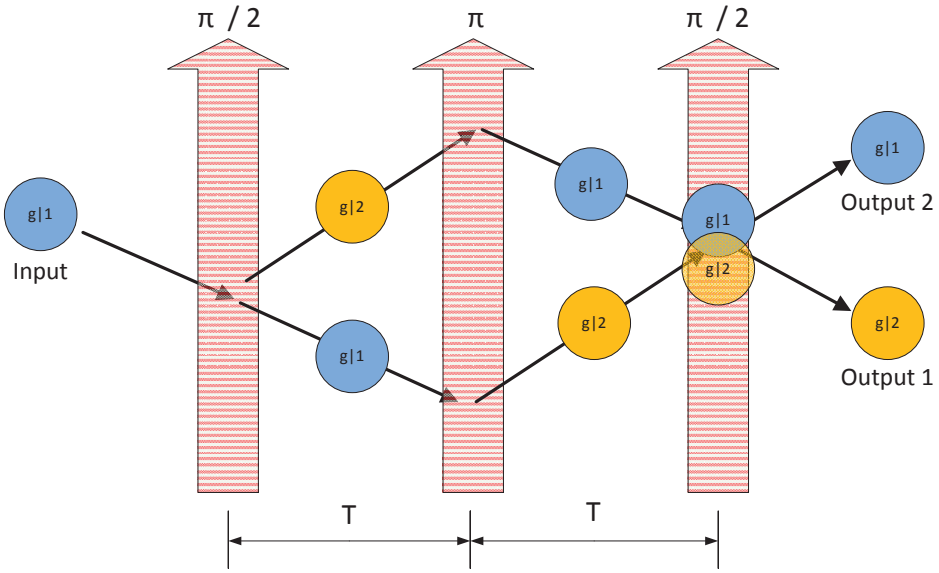


**Figure 1.7:** Mach Zehnder atom interferometer schematic with a spacing between the pulses of $T$ and an interferometer time of $2T$. The output of the interferometer is the population in the two states $g|1$ and $g|2$.

Figure 1.7 shows the schematic of a typical Mach-Zehnder atom interferometer. The mirror is realized by applying a $\pi/2$-pulse of laser light. The probability of the atoms to absorb two photons from the light pulse is 50%. Thus the pulse will cause a superposition of the two states $g_1$ and $g_2$. Moreover the atoms receive a recoil impulse from the absorbed photons and separate from the atoms that are left in the ground state.

The $\pi$-pulse shown in after a time T, will mirror the states as indicated in the figure. When a period of 2T has passed a second $\pi/2$-pulse recombines the clouds again.

Depending on the phase difference that has accumulated between the two paths, some atoms will remain in the manipulated state and most of them will fall back to the initial state. The atoms in each state are detected by absorption imaging. The ratio of the atom number of the two states represent the interferometer signal and will allow to calculate the phase difference.

This phase difference is depending on the external acceleration and rotation. If the light pulses are not only separated in time but are also in space and the atoms are moving with a velocity perpendicular to the light pulse the atom interferometer is sensitive to rotations and can thus be used as gyroscope. Atom interferometer gyroscopes offer high precision combined with ultra long time stability. Other than laser gyroscopes they do not need a GPS link to compensate their drift. This is why these gyroscopes are used e.g. on nuclear powered submarines giving opportunity of long under water operation [Ric08].

In an accelerometer setup the light pulses are only separated in time. Thus the atoms will only receive a recoil impulse along the interferometer axis and will not posses a velocity component perpendicular to the light pulse. In an accelerometer configuration atom interferometers can be used to measure the local gravitational field of the earth with an accuracy of $10^{-6}$ to $10^{-9}$ g in ground based devices. With this accuracy it is possible to detect natural resources such as metals, oil or water [Pet01].

Moreover an atom interferometer offers the possibility to test the university of free fall (UFF) or the weak equivalence principle (WEP) postulated by Einstein. The university of free fall states, that two bodies with different masses $m_1$ and $m_2$ will be accelerated equally by an gravitational field if there are no disturbances (such as air friction) present [Ein07]. This can be tested by using two clouds of different isotopes (e.g. $^{40}K$ and $^{87}Rb$) as test masses.

The difference between the acceleration of the test masses is defined as Eötvös factor:

$$\eta = 2\frac{|a_{m1} - a_{m2}|}{|a_{m1} + a_{m2}|} \tag{1.4}$$

This factor has been measured to be smaller than $10^{-13}$ using lunar laser ranging [Wil04] and a rotating torsion balance instrument [Sch08]. A setup with two atom interferometer would allow a precise measurement of the acceleration of both clouds and therefore of the Eötvos factor. Hereby the sensitivity is strongly depending on the environment and the platform used. The satellite mission study STE-QUEST proposed an accuracy in the order of $10^{-15}$ after 5 years of operation in [Lei13], which would be a significant improvement to current measurements.

## 1.4 Typical Experimental Setup

In the following the different subsystems and interfaces of an atom interferometer apparatus as described above shall be summarized. Figure 1.8 shows a functional diagram of a typical atom interferometer, illustrating the different subsystems and their interfaces.

The vacuum chamber is the centerpiece of the atom interferometer. For cooling and performing atom interferometry at least three pairs of coils in anti-helmholtz configuration and three orthogonal pairs of laser beams are needed as described above. An atom chip will reduce the size of the apparatus and the needed power to operate it. While the atom chip needs to be placed close to the atoms and is typically mounted inside the vacuum chamber, the coils are directly attached to the chamber.

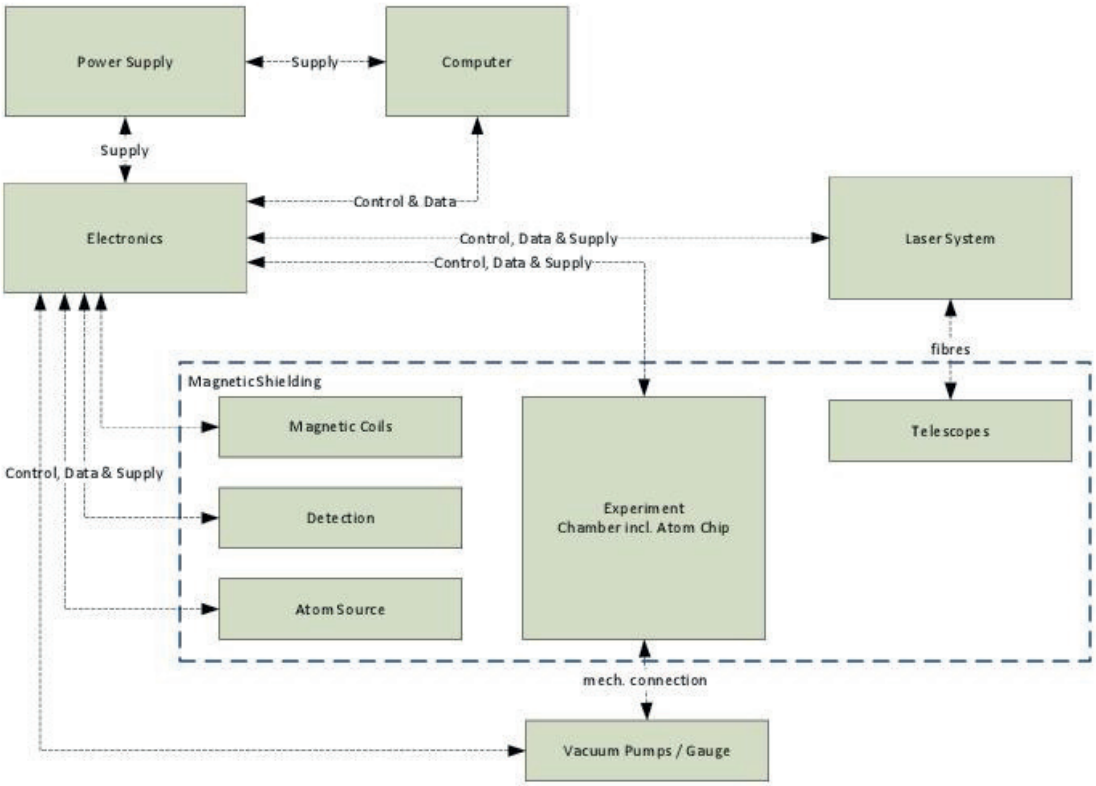


**Figure 1.8:** Components of a typical atom interferometer setup arranged in a functional diagram

The laser system provides the light with the needed power, frequency and polarization for trapping, re-pumping, detection and atom interferometry. Aside from the laser modules a high number of optics and modulators might be needed to achieve this. The produced light is often guided to the vacuum chamber by optical fibers. Collimators will couple the laser light from the optical fiber into the vacuum chamber through a viewport. A collimator offers the possibility to adjust the angle of the laser beams and ensures its coherence. Moreover waveplates allow to change the polarization of the beam.

Aside from light and magnetic fields, a trappable atom species is needed to perform atom interferometry. Either dispensers or ovens are used to provide the atoms. In general the atom source is situated close to the chamber, to ensure a stable vapor pressure of the atomic species.

To measure the temperature of a cold atoms or to evaluate the atom interferometer, a detection device is essential. Typically the detection is performed by a CCD camera detecting the fluorescence of the atoms or by taking an absorption image of the cloud. The used device has to be situated close to the experiment chamber to keep the optical path short and improve accuracy.

In order to achieve measurements of high accuracy disturbances have to be minimized. One disturbance is the collision of the trapped atoms with the residual gas in the vacuum chamber. For this reason a vacuum pressure of less than $5 \times 10^{-10}$ hPa has to be maintain ed in the chamber. This is achieved by a suitable combination of vacuum pumps.

Moreover external magnetic fields can disturb the experiment. A magnetic shielding made from MUMETALL, which is of high magnetic permeability protects the atoms from these fields as illustrated by the dotted line in figure 1.8.

For control, power supply and data acquisition of/from the different components mentioned above, a significant amount of electronics will be needed. The computer will manage and process all data from the electronics and the detection and display it for the operating personnel.

A detailed description of the configuration of different ground-based and microgravity experiments as well as of the MAIUS payload will be given in chapter 3 and 7.

## 1.5 Advantages and Approaches of Atom Interferometry under Microgravity

Within this section the advantages of performing atom interferometry under microgravity shall be pointed out. As mentioned above atom interferometry is used to measure accelerations and/or rotations from an accumulated phase difference between the two interferometer paths. This phase difference is not only depending on the acceleration $a$ or rotation $\Omega$ but also quadratically depending on the time $T$ between the applied light pulses as given in equation 1.5 and 1.6 [Bar13].

$$\Delta\phi_{acc} = k_{eff} a T^2 \tag{1.5}$$

$$\Delta\phi_{rot} = \left(\frac{4\pi}{\lambda_{dB}}\right) \Omega \left(L^2 \frac{v_t}{v_l^2}\right) \tag{1.6}$$

While the dependency is obvious in the accelerometer equation, it is not that intuitive in the gyroscope setup. However with the distance between two light pulses $L$ and the longitudinal velocity $v_l$ perpendicular to those light pulses and along $L$, the pulse separation time becomes $T = L/v_l$. Thus $\Delta\phi_{rot}$ is proportional to $T^2$.

Thus longer interrogation times will directly result in higher accuracy of the atom interferometer. To perform atom interferometry the atoms have to be released from the magnetic trap. Without the trap the atoms will be accelerated by gravity towards the bottom of the vacuum chamber. Thus the interferometer interrogation time is limited by the time of free fall of the atomic ensemble.

There are several approaches to extend the time of free fall. The simplest way is to enlarge the vacuum chamber and drop the atoms. A second option to enlarge the time of free fall in ground-based experiments is the use of atomic fountains. Hereby the atoms themselves are accelerated against gravity inside the vacuum chamber and will return to the bottom of the vacuum chamber performing a parabolic flight. This will double the time of free fall of the cold atoms compared to a drop of the atoms. The achievable time of free fall (and pulse separation time) is depending directly on the geometry of the chamber. Obviously building large vacuum chambers and magnetic shielding with meters of height is challenging. Moreover it is difficult to keep the environmental conditions stable along the drop/fountain tube and to isolate the tube from external disturbances.

In ground-based experiments gravity could also be compensated by a magnetic force acting in the opposite direction as the vector of gravity. This procedure is called (electromagnetic) levitation. However there are a few drawbacks to levitation. Most importantly levitated atoms can not be used for atom interferometry as proposed in section 1.3, because the atoms need to be in a magnetic sensitive state ($m_f \neq 0$) to be levitated. Moreover it is impossible to use this technique for tests of the equivalence principle, since the necessary levitation force is depending on the atomic mass of the atom species. Therefore different atomic species would require different magnetic fields.

Another possibility to enlarge the time of free fall of the atoms is to provide microgravity for the atom ensemble by using a free falling laboratory as e.g. a satellite or a drop capsule.

The time of free fall $t_{ff}$ of the atomic cloud for a given length $s_{max}$, in which the atomic cloud can been detected can been calculated for a given gravitational acceleration from

$$t_{ff} = \sqrt{\frac{2s_{max}}{g}} \tag{1.7}$$

neglecting all disturbances. For a microgravity level of $10^{-6}\mathrm{g}_0$ the time of flight would increased from to 0.078 s at earth gravity to 78 s with $g_0 = 9.81\ \mathrm{m/s^2}$.

Aside from the time of free fall the expansion rate of the atomic cloud influences the time of free evolution. As described in section 1.3 the expansion rate itself can be influenced by the trap geometry before release and by advanced methods as the delta-kick-cooling.

The geometry of the magnetic trap before release of the atoms is limited by the gravitational field, since the potential of the trap must feature a gradient that is larger than the gravitational force on the trapped atoms. This does not allow the use of shallow traps without a significant loss of atoms.

Performing atom interferometry in microgravity will allow to access lower trap frequencies and reduce the rate of expansion. Simultaneously the time of flight is increased due to the lower residual acceleration of the atomic cloud. This allows to stick with compact vacuum chambers and magnetic shielding. Lastly disturbances such as vibrations and accelerations, which are the dominant noise source in lab experiments, are avoided or minimized on some microgravity platforms.

Therefore it is possible to achieve similar or even better sensitivity on microgravity platforms than on fountain experiments [Lei13]. The sensitivity is depending on the available time of microgravity and the environmental conditions (as e.g. disturbances). Thus the choice of the microgravity platform is important. A trade off between available microgravity time, repeatability rate, engineering afford and costs has to be performed. Some possible candidates for providing micro gravity to an atom interferometer experiment shall be introduced in the following chapter.

# 2
# Microgravity Platforms

Several platforms are available to perform experiments under microgravity. There are advantages and disadvantages associated with each platform, which shall be discussed in this section focusing on platforms supported by the European Space Agency (ESA).

## 2.1 Parabolic Flights

Multiple providers worldwide offer parabolic flights for scientific purposes. The NASA is using a Boeing KC-135 for parabolic flights, while the russian space agency is using a Iljuschin 76. The German Space Agency (DLR) and the European Space Agency (ESA) are both using an Airbus A300 "ZERO-G", which is operated by the French company NOVESPACE and based in Bordeaux-Mérignac, France. The A300 "ZERO-G" offers

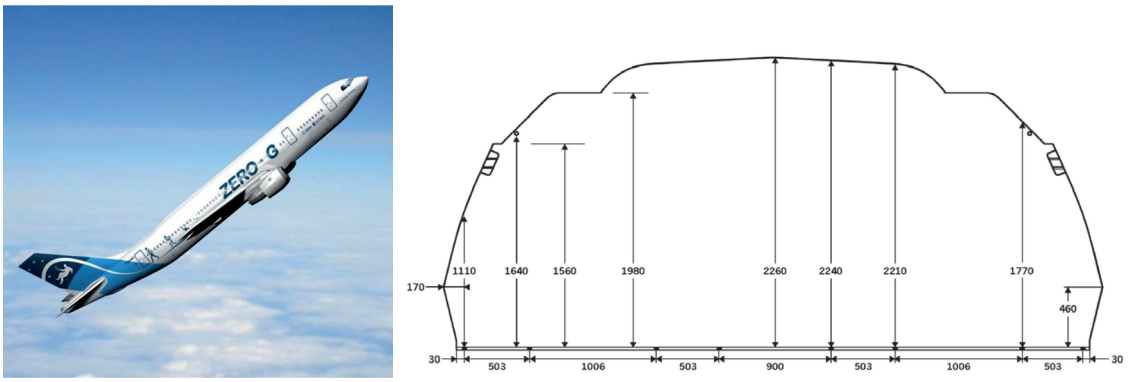


**Figure 2.1:** A300 Zero G (left) and cross section of experiment area (right) [Ros09]

100 $m^2$ (5 m $\times$ 20 m) of experimental area, which is usually divided between up to 15 experiments. The maximum height of an experiment is approximately 2.5 m as shown in figure 2.1. There is almost no limitation in mass. The Airbus A300 Zero-G is Based on the A300B2, which is capable of carrying an estimated payload of 35 t [Air09]. A total of 40 passengers can be accommodate within the aircraft.

Electrical power is provided by the plane as 220 V AC or 28 V DC in energy panels with standard sockets [Ros09]. Thus the plane offers almost laboratory conditions regarding space and power supply.

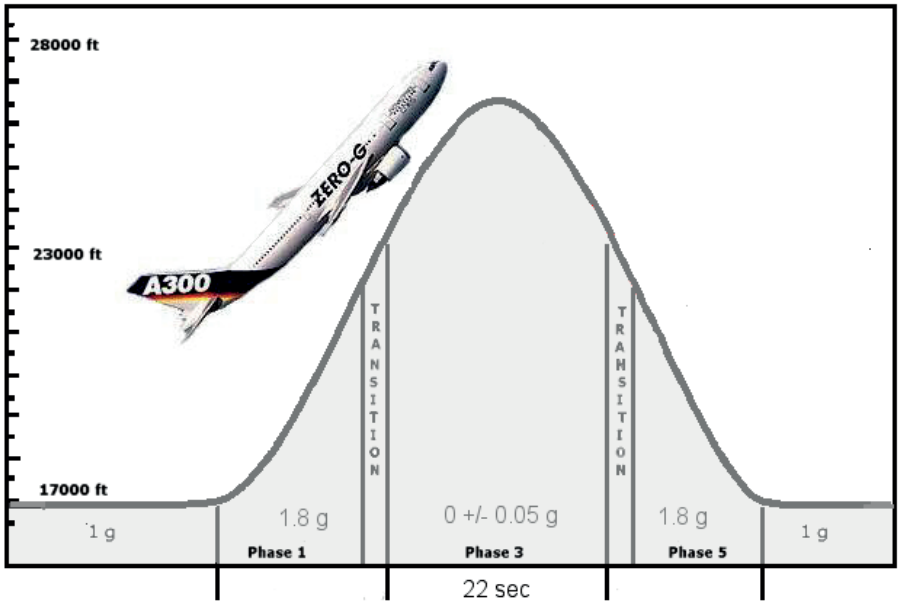


**Figure 2.2:** Flight profile for microgravity experiments

As shown in figure 2.2, the plane provides microgravity for roughly 22 s in every parabola. Typically a plane will perform around 100 parabolas in one campaign. Thus a high repeatability can be performed on very low costs. However the quality of microgravity on parabola flights is limited to $\pm 0.05$ g.

The loads on the experiment are moderate compared to the other platforms. During ascent and decent phase accelerations of 1.8 g appeal to the payload as shown in figure 2.2. In the worst case scenario of a “hard landing” the loads will not exceed 9 g [Ros09]. Another important advantage is that the plane can accommodate the scientists as well. Therefore the payload can be accessed and influenced at any time if the experiment requires input/decisions of humans.

The Airbus A300 "Zero-G" was replaced by an Airbus A310 "Zero-G" mid 2015. This plane offers the same possibilities as its predecessor.

## 2.2 Drop Tower Bremen

The drop tower in Bremen is one of the most prominent drop towers for scientific experiments in the world. The facility is situated at the University of Bremen and operated by the Center of Applied Space Technology and Microgravity (ZARM). During operation the whole tower will be evacuated in order to improve microgravity quality. The tower will provide a microgravity level as low as $10^{-6}$ g.

The tower can be used in a drop mode, whereby the capsule is lifted 120 m to the top of the tower and released. This will result in 4.74 s of microgravity time. The second operation mode is the catapult launch. For a catapult launch the capsule is pneumatically accelerated from the basement of the tower, which will almost double the time of microgravity to approximately 9.3 s.

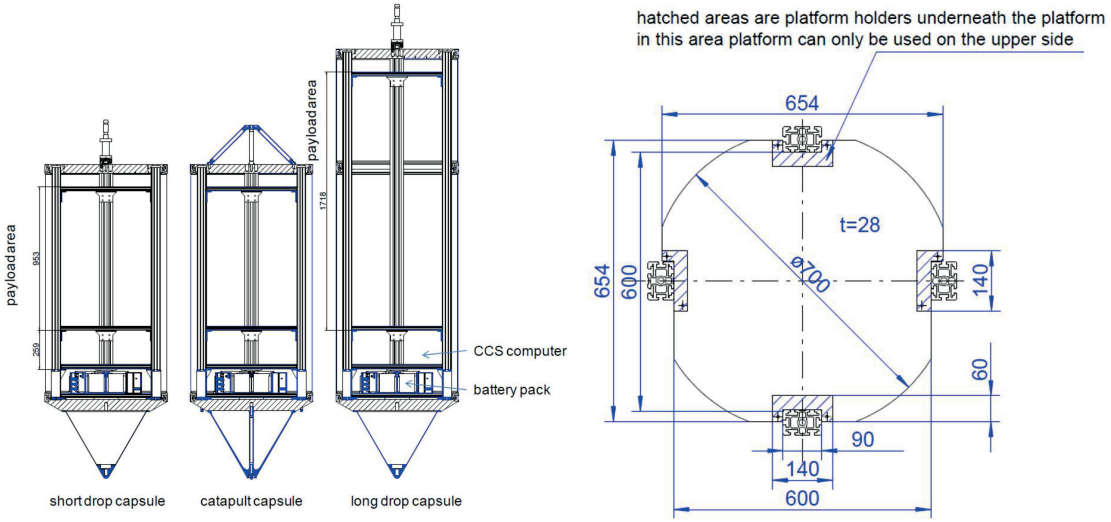


**Figure 2.3:** Different drop capsules sizes and dimension drawing of experiment platform of ZARM Drop Tower [Dro12]

As shown in figure 2.3 there are two sizes of capsules used in the drop tower. The choice of the capsule size is depending on the operation mode. In the drop mode either the large or the short capsule can be used. The available volume for experiment within the large capsule is defined by the capsule length of 1.72 m and the diameter of the experiment platforms of 0.7 m [Dro12]. The usable length of the payload area decreases to 0.95 m when using the catapult mode or the short capsule. The mass of the payload should not exceed 264.4 kg (short capsule) or 221.2 kg (long capsule) in drop mode. The maximum mass of the payload for the catapult operation is given as 161.5 kg.

The capsule is supplied with power until short before the drop or launch. After release the electrical power is provided by batteries situated at the bottom of the capsule (ref. figure 2.3). The nominal voltage of these batteries is 24 V DC. Their nominal capacity is 25 A h. For thermal control of the payload, water cooling can be provided until drop / launch.

Figure 2.4 shows a typical acceleration profile inside a capsule in catapult operation. The average acceleration of the catapult system is about 18 g for 280 ms.

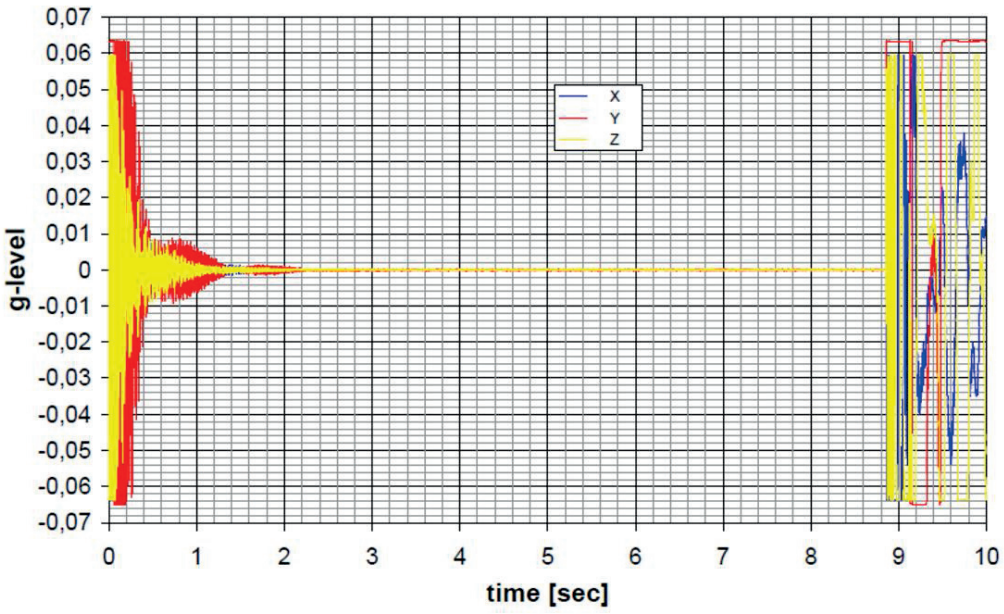


**Figure 2.4:** Accelerations during catapult launch and landing of drop capsule. The acceleration in these phases exceeds the range of the accelerometer. In between during the microgravity phase the accelerations are in the order of $10^{-6}$ g. [Dro12]

The peak value in the acceleration phase has been recorded with 30 g. The deceleration at the end of any drop is 25 g in average for about 200 ms, which also applies for drop operation. The peak value in both types of operation is given as 50 g for approximately 11 ms [Dro12].

Although the presence of vibrations and accelerations is limited to a short period of time, the environment is challenging for sensitive instruments and has to be considered in the design phase of the experiments.

Since the whole tower has to be evacuated before each drop, a maximum of three drops or catapult launches per day can be performed within the drop tower Bremen. This still allows to make e.g. parameter studies at moderate costs.

## 2.3 Sounding Rockets

Worldwide, a lot of sounding rocket types are in service and launched from various sites around the globe. The sounding rocket community in Europe is dominated by the German and Swedish space companies. Therefore most sounding rockets are launched from Esrange in northern Sweden. Figure 2.5 shows some sounding rockets used in Europe. At Esrange mainly four types of sounding rockets are launched, which shall be described in the following.

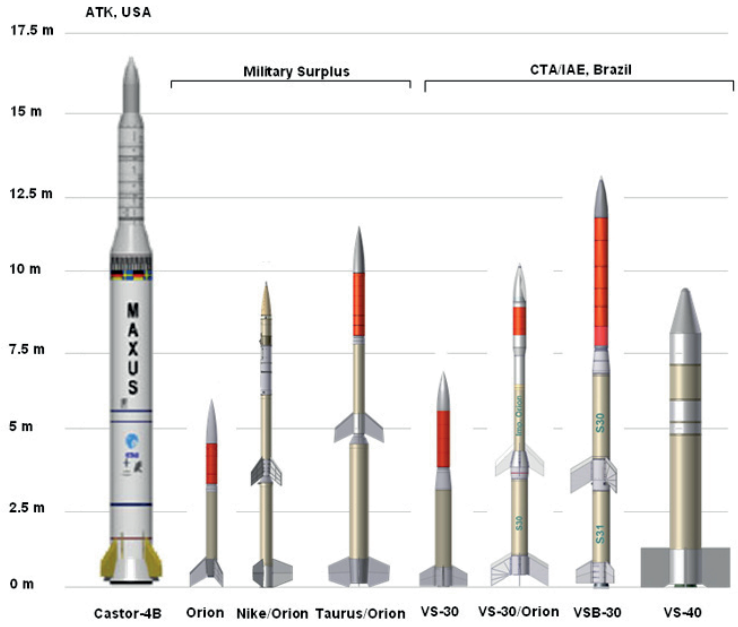


**Figure 2.5:** Some sounding rockets operated in Europe with suppliers of motors (adapted from [Sta13])

The smallest and cheapest launcher is the Improved Orion, which is used by the Mobile Rocket Base (MORABA) as part of the German Aerospace Center (DLR) for the REXUS student sounding rocket program. The Orion motor is combined with the Nike motor to the Nike/Orion launcher, used for the Mini-Texus program operated by Airbus Defense and Space. This launcher might be replaced by the Brazilian VS-30 in the near future. The VS-30 is already launched by the MORABA with smaller scientific payloads. The S-30 motor of the VS-30 vehicle is also used as an upper stage within the Brazilian VSB-30 launcher. The S31 motor is providing the lower stage for this launcher. The European Space Agency (ESA) in cooperation with Airbus DS uses the launcher for the TEXUS program, while the ESA cooperates with the Swedish Space Corporation (SSC) within the MASER missions using the same launcher. For heavier payloads and access to longer microgravity times, the MORABA is providing the Brazilian VS-40 motor consisting of the S40TM lower stage and the S44M upper stage. Airbus DS is using the Castor-4B motor in the MAXUS program offering similar performance.

In table 2.1 the different launchers are compared regarding usable experiments time ($t$), the residual acceleration or quality of the reduced gravity environment ($a_{res}$), the maximum payload mass for given experiment time ($m_{max}$), module diameter ($d_{module}$), maximum scientific payload length ($l_{max}$), the maximal acceleration during ascent ($a_{max}$) and the recommended qualification test level ($a_{qual}$).

| Motor (Launcher) | $t$ [s] | $a_{res}$ [g] | $m_{max}$ [kg] | $d_{max}$ [m] | $l_{max}$ [m] | $a_{max}$ [g] | $a_{qual}$ [$g_{rms}$] |
|---|---|---|---|---|---|---|---|
| Imp. Orion (Rexus) | 180 | $\leq 10^{-4}$ | 95 | 0.356 | 0.6 | 20 | 12.7 |
| Nike/Orion (MiniTexus) | 240 | $\leq 10^{-4}$ | 180 | 0.438 | 1.00 | 21 | N/A |
| VS-30 | 240 | $\leq 10^{-4}$ | 260 | 0.5 | N/A | 8 | 8.1 |
| VSB-30 (Texus/Maser) | 360 | $\approx 10^{-6}(*)$ | 400 | 0.5 | 3m | 12 | 8.1 |
| VS-40 | 720 | $\leq 10^{-5}$ | 500 | N/A | N/A | N/A | N/A |
| Castor-4B (Maxus) | 750 | $\leq 4 \times 10^{-5}$ | 800 | 0.64 | 3.8m | 13 | 5.9 |

**Table 2.1:** Comparison of major rockets launched in Europe [Maw14] [Ceg05] [Hof14] [Sta12] [Bar12] (* predicted $\mu g$-level with attitude and rate control supported by DMARS inertial platform)

As illustrated in table 2.1 sounding rockets offer good microgravity quality for long continuous periods of time. This allows to perform longer experiment cycles as e.g. on parabolic flights or in the drop tower. The Castor-4B motor used in the MAXUS program is offering the highest payload volume and mass. Moreover the long microgravity time of about 12 minutes is attractive to scientists. However a MAXUS launch is also the most expensive launch opportunity in Europe.

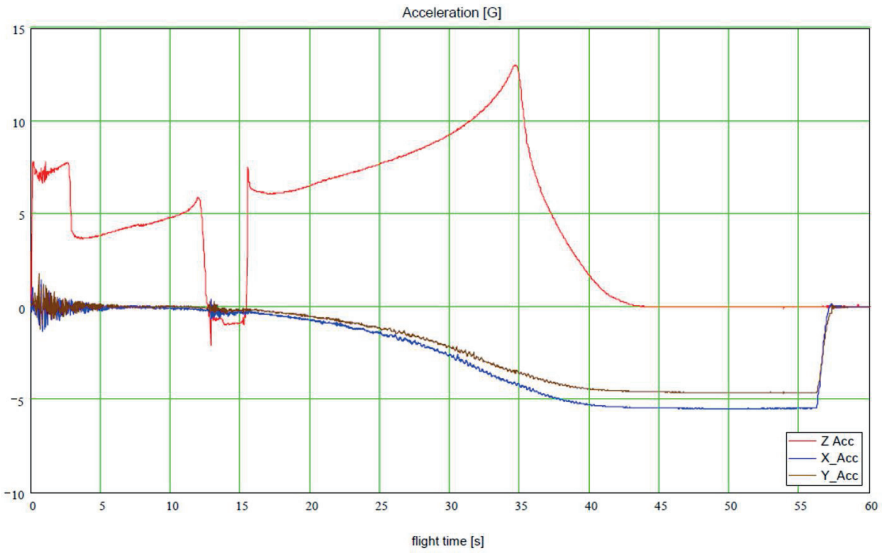


**Figure 2.6:** DC accelerations during flight of TEXUS 42 (VSB-30 launcher) [Ett06a]

Due to the high mechanical loads and vibration caused by the motor burn, the experiment has to be designed and tested to withstand these loads, although they will only occur in the first seconds of the flight. A typical distribution of the accelerations during a sounding rocket flight is shown in figure 2.6. The actual loads may vary depending on the mass of the payload, but the distribution over time is characteristic for the launcher. The vibrational loads for qualification are given in table 2.1 for every launcher. During the re-entry in the earth atmosphere even higher loads of up to 25 g could be recorded on former missions [Ett06b]. However the payload might be reused for future flights, if the experiment is designed to withstand both launch and re-entry loads.

The loads affecting the experiment and its instruments on a sounding rocket are comparable to those of some larger launchers. Moreover the qualification procedures (as vibration and/or thermal testing) are similar, this is why an experiment or instrument is often tested on sounding rockets first before it is being chosen for an satellite or ISS mission.

## 2.4 Foton Capsule

Several reentry capsules have been developed worldwide. Foton capsules have been developed by the Russian Space Agency and are used in a cooperation with the European Space Agency for European microgravity experiments.

The capsule is launched with the Soyuz-U rocket into a circular near earth orbit with a maximum apogee of 305 km. The capsules will remain in orbit for 12 to 18 days and the re-entry capsule will return the experiment(s) to earth after this period. Within Fonton 1.6 $m^3$ are available for experiment hardware, which shall not exceed 650 kg in mass. This volume can be pressurized at 1 atm if required by the payload. During flight the temperatures in the payload compartment are stabilized between 19 °C to 26 °C [Ceg05].

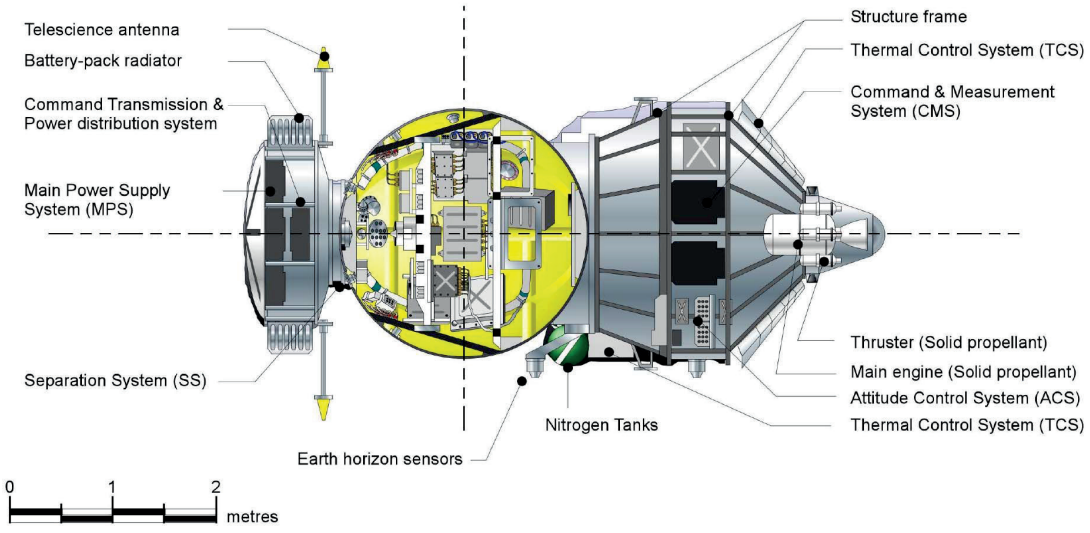


**Figure 2.7:** Foton capsule layout with payload accommodation (highlighted in yellow) [Ceg05]

The orbit altitude and the low level of perturbations result in a microgravity quality of $1 \times 10^{-5}$ g or better. Therefore Foton offers an opportunity to perform experiments with longer durations and prepare future experiments on the international space station (ISS) or on a satellite.

The Soyuz launcher causes linear accelerations at the payload mounts of up to $\pm 10$ g for about 600 s during launch. During re-entry the measured peak accelerations are $\pm 16$ g for a duration of 20 s. The landing shock is demanding as well with 40 g for 40 ms to 50 ms. Moreover the hardware has to be vibration tested at a maximum level of 7.5 $g_{rms}$ for 120 s in each axis [Ari12]. In addition sine vibration with up to 1.3 g ($10 - 30$ Hz) and shock tests have to be performed. Because of the long time in orbit, the instruments inside Foton have to withstand ionizing background radiation of 0.055 rad/day. During solar flares the instruments can be subject to a radiation of up to 50 rad.

## 2.5 International Space Station

The International Space Station (ISS) offers the possibility to perform microgravity experiments aboard. Experiments can either be placed inside the station in racks or outside on the truss. Inside the station the experiments are accommodated in international standard payload racks (ISPRs). There are overall 35 ISPRs station-wide. In addition there are 18 external and unpressurized accommodations for microgravity experiments.

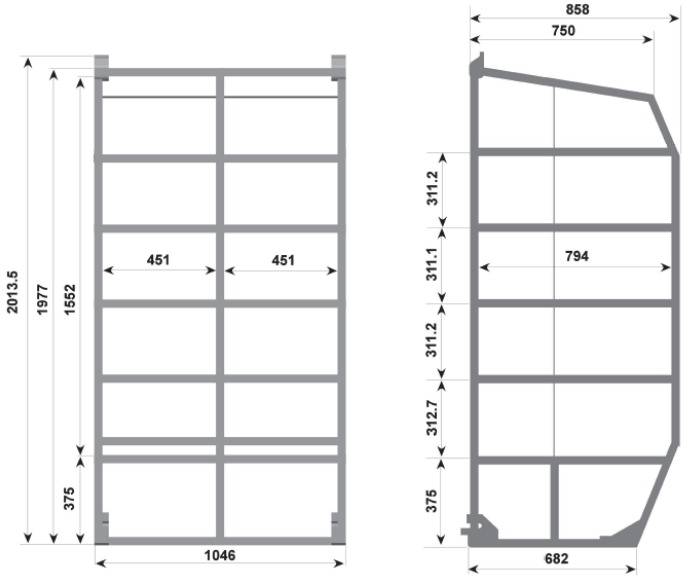


**Figure 2.8:** International Standard Payload Rack (ISPR) dimensions [Ceg05]

Internal payloads are exposed to the artificial atmosphere of the ISS. This atmosphere consists of 78% nitrogen and 21% oxygen and is kept in the pressure range between 97.9 kPa to 102.7 kPa. A water cooling loop can be provided for thermal management capable of dissipating up to 1200 W [Ceg05].

The payload envelope in each ISPR measures 1.2 $m^3$ as illustrated in figure 2.8 with a maximum mass of the payload hardware of 704 kg (excluding rack structure). The power supply varies between 3 kW and 12 kW depending on the ISPR. Therefore the ISS offers almost laboratory conditions in space with reduced gravity and most important the possibility of human interaction.

External space exposed payload accommodations differ in size. At the Columbus module operated by ESA, the payloads are mounted to a standardized Columbus External Payload adapter (CEPA) offering a envelope of 1.39 $m^3$ as shown in figure 2.9. The payload mass including CEPA shall not exceed 290 kg. External payloads at Columbus module are supplied with 1.25 kW. There is no active temperature control implemented.

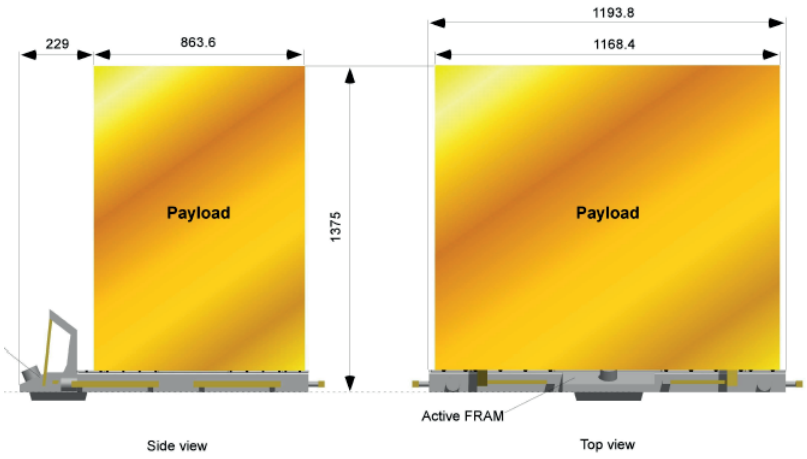


**Figure 2.9:** Columbus External Payload Adapter (CEPA) dimensions [Ceg05]

The station is set to "microgravity mode" six times a year. This mode is defined to last for 30 days. Within this period of time scheduled activities, that might influence the microgravity quality (such as steering maneuvers or sports activities of the crew) are minimized.

The microgravity level within this time should therefore only influenced by two types of acceleration, the quasi-steady acceleration and vibrations. Accelerations are considered quasi-steady if at least 95% of their power lies below 0.01 Hz as measured over one orbit, which lasts 5400 s [NAS]. The aerodynamic drag, which slows the station down, limits the microgravity level to $1 \times 10^{-6}$ g. The gravitation gradient of structural parts not in line with the stations center of mass will reduce the microgravity level depending on the payload location to a maximum of $3 \times 10^{-6}$ g as presented in figure 2.10.

Vibrations above 0.01 Hz and up to 300 Hz are not considered within these levels, since they are damped by the active rack isolation system (ARIS). The ISS will allow continuous measurements of 30 days in microgravity with the quality of $3 \times 10^{-6}$ g or better. However normal crew activity and vibrations might have a significant impact on measurements.

Crew activities will exceed the usual acceleration level by orders of magnitude. Skylab T-013 recorded the effect of several crew activities. It was proven that crew activity can have a significant effect on the spacecraft and the microgravity level [Ols81]. Although the ISS mass is significantly higher than the one of the Spaceshuttle and isolation methods have been improved this effect needs to be considered.

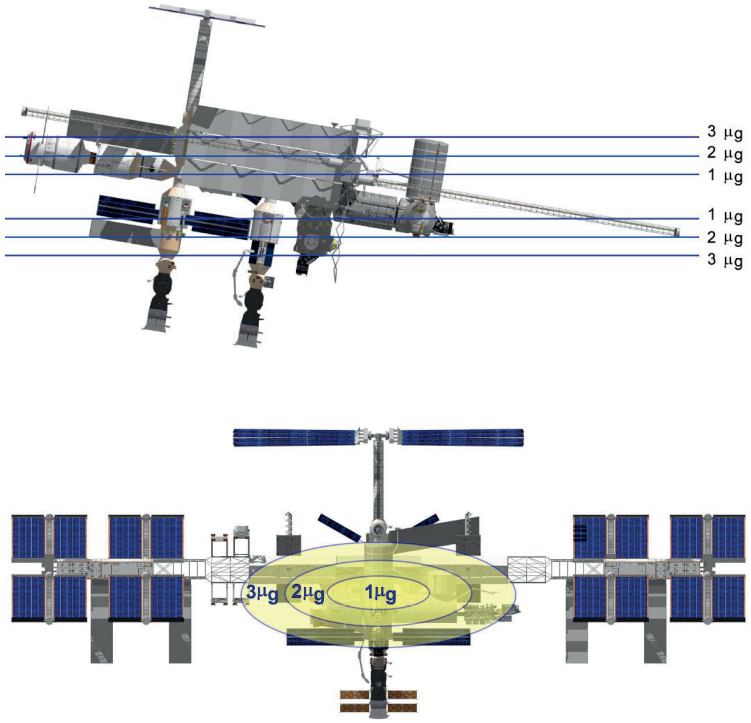


**Figure 2.10:** At the ISS the $\mu g$ quality is depending on the location of the experiment. With increasing distance from the stations center of gravity the quality can reduce to $3 \times 10^{-6}$ g [Ceg05]

All payloads have to fulfill the strict ESA safety requirements. Requirements differ for internal and external payloads. Payloads inside ISS have to meet requirements regarding astronaut safety and payloads outside the station require radiation hardness. Regardless their position all payloads need to pass several tests and need to be well documented to grant access to the ISS.

Once a payload is accepted it has to be transported to the ISS. This is usually done with the European automated transfer vehicle (ATV), the American DRAGON carrier or the Russian PROGRESS capsule. These are typically launched with an Ariane 5, Falcon 9 or Soyuz rocket. Therefore the payload has to be tested to fulfill the requirements of the launcher as well. Mechanically the requirements of the launcher are the most demanding.

Exemplary Ariane 5 requires a random vibration test with $11 g_{rms}$ for qualification of hardware. Moreover a sine vibration test with maximum loads of 5g (5-150Hz) and a test with shocks up to 2820g have to be passed for successful qualification. [Bra97] [Ari11]. Soyuz qualification levels have been summarized in section 2.4 [Ari12].

## 2.6 Satellite Missions

Satellite missions are usually launched with the same vessels as the ISS cargo (including payloads). Therefore some of the tests performed in the qualification process are similar to the ones for ISS payloads. However there are several tests, which have to be passed additionally. One of the most challenging might be the qualification for radiation hardness, which is mandatory since the instruments might be exposed to radiation of multiple kinds for the duration of the mission.

Moreover thermal requirements have to be considered, which depend on the orbit of the satellite. Near earth orbits will always have to consider direct sun, Earth albedo and Earth infrared heat flux aside from heat dissipation of internal instruments. Exemplary direct solar flux density on a plane perpendicular to the solar rays is given by the solar constant with $1367\,\mathrm{W/m^2}$. Although the actual thermal loads will be smaller than this, high thermal fluxes will require well designed thermal control systems, which will be tested by thermal cycling tests simulating hot and cold cases during the mission and orbit.

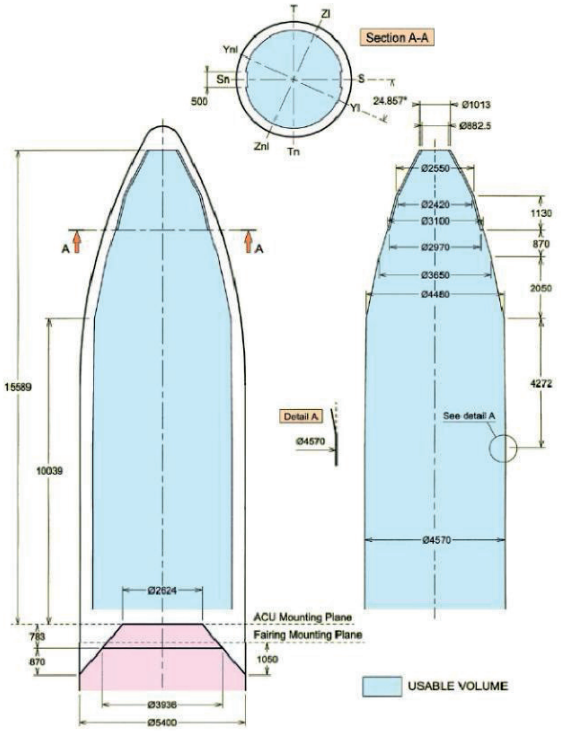


**Figure 2.11:** Useable volume beneath Ariane 5 fairing [Ari11]

The most powerful launcher available in Europe, the Ariane 5, is capable of carrying a maximum of 20 t into low earth orbit. Payload mass will reduce for higher orbits. The usable volume for payloads underneath the fairing is approximately $180\,\mathrm{m^3}$ as illustrated in figure 2.11.

Launch costs for Ariane 5 are estimated with 90 Million Euro. This results in a approximated price of 4500 Euro per kilogram. For this reason weight and size of the payload should be decreased as far as possible. A shared launch with multiple satellites will reduce costs for a mission significantly.

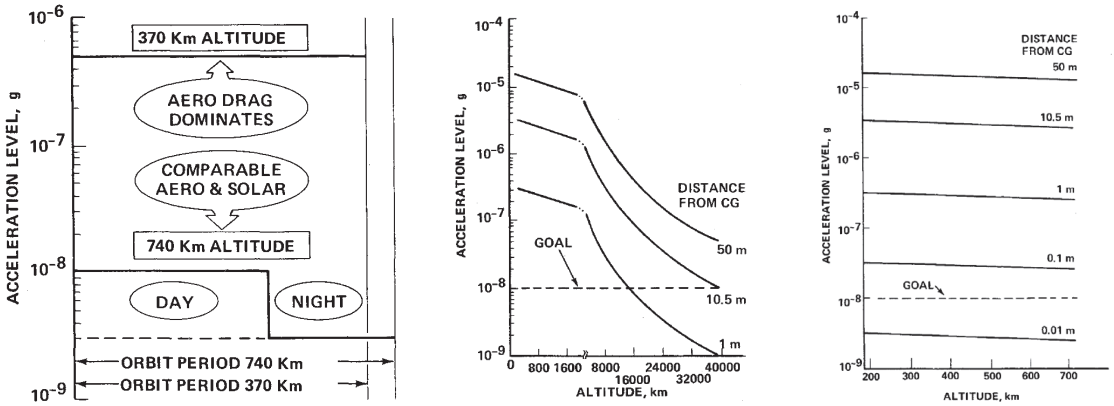


**(a)** Environmental effects and their impact on the acceleration level aboard a satellite for a 370 km and 740 km orbit

**(b)** Induced accelerations by center of gravity (CG) displacement for high altitude orbit

**(c)** Induced accelerations by center of gravity (CG) displacement for low altitude orbit

**Figure 2.12:** Induced accelerations aboard satellites with an drag area of $60\,\mathrm{m}^2$, moment of inertia of $1 \times 10^7\,\mathrm{kg\,m}^2$ and a mass of $3270\,\mathrm{kg}$ [Ols81]

The quality of microgravity on an unmanned spacecraft is depending on multiple factors influenced by the orbit height. These are environmental conditions (such as aerodynamic drag or solar pressure) and center of gravity misalignment (resulting in accelerations due to laws of orbital dynamics). The impact of these effects is illustrated in figure 2.12 for a spacecraft with an drag area of $60\,\mathrm{m}^2$, moment of inertia of $1 \times 10^7\,\mathrm{kg\,m}^2$ and a mass of 3270 kg on a circular orbit [Ols81].

As pictured in figure 2.12a aerodynamic drag will be dominant in low earth orbit. At an attitude of roughly 740 km solar pressure effects will be dominant at day time. This results in a cycling effect over one orbit as illustrated. Although the absolute drag is depending on the geometry of the individual spacecraft the impact of the orbit altitude on the microgravity level can be estimated from the numbers given in [Ols81]

If the satellite is not spin stabilized and the orbit is perfectly circular, only objects aligned along the orbital path of the center of gravity will experience zero gravity conditions. Misalignment of e.g. experiments will lead to a reduced microgravity level. Figure 2.12b and 2.12c demonstrates the influence of a center of mass misalignment for different circular orbits with the given satellite configuration. Technically a alignment of the area of interest for the scientist (e.g. detection zone of experiment) in the order of a centimeter to the spacecraft center of gravity is reasonable. In this case it is possible to achieve a microgravity level better than $10^{-8}$ g at an orbit altitude of approximately 740 km.

## 2.7 Comparison of Microgravity Platforms

Although there are several other possibilities to perform experiments in microgravity, the platforms mentioned above are capable of carrying complex high precision experiments such as an atom interferometry experiment with all payload subsystems needed. Therefore only these platforms are compared in this section.

As shown in table 2.2 the different platforms offer different advantages and disadvantages. The best microgravity quality and longest experiment duration is offered on satellites. Aboard the satellite a constant level of microgravity is obtained for the lifetime of the satellite mission, which is typically 5-10 years. This allows long integration times for measurements and therefore high accuracy. However satellite missions require intensive testing, long time of preparation, investments in the order of hundreds of million Euro and they do not allow to return the experiment to earth.

| Platform | $t$ [s] | $a_{res}$ [$g_0$] | $m_{max}$ [kg] | $V_{max}$ [$m^3$] | $a_{max}$ [$g_0$] | Remark |
|---|---|---|---|---|---|---|
| Parab. Flights | 20 | $\leq 10^{-3}$ | »1000 | 250 | 2.5 | Lab-like environment |
| Drop Tower | 9.3 | $\approx 10^{-6}$ | 161.5 | 1.54 | 18 | High Repeatability |
| Sound. rocket | 750 | $\leq 10^{-5}$ | 800 | 4.9 | 13 | Intermediate costs |
| Foton capsule | 12-18d | $\leq 10^{-5}$ | 650 | 1.6 | 10 | |
| ISS | 30d | $\leq 3 * 10^{-6}$ | 704 | 1.2 | 10 | human spaceflight restr. |
| Satellite | 5-10y | $\leq 10^{-7}$ | »1000 | 180 | 10 | High costs |

**Table 2.2:** Comparison of microgravity platforms

Parabolic flights and drop tower experiments allow high repetition rates, but only short experiment cycles. The access to these platforms is relatively easy and fast. Moreover the operation cost for both platforms are small compared to the other platforms. Sounding rockets can significantly increase the time of microgravity. Motor vibrations before the measurement phase require a accurate qualification process to ensure reliable operation of all instruments. This will increase development cost and time for the experiment hardware. Moreover the cost for a launch campaign are higher.

ISS and Foton capsule close the gap between the largest sounding rocket MAXUS and a satellite payload. ISS and Foton offer very good microgravity quality, with less risk of disturbances on the Fonton capsule then aboard the ISS. The qualification process gets more complicated and challenging for advanced platforms such as ISS or satellites and most often a certain technology readiness level (TRL) is demanded from space agencies in order to provide funding for such complex and expensive missions.

The platforms with easy access (parabolic flights,drop tower and sounding rockets) can be used to test the instruments under microgravity and prove the concept of the experiment. Qualification for these platforms will increase the TRL and the chance of selection for more advanced platforms.

# 3
# State of the Art

Since the first BEC has been produced by Cornell and Weiman in 1995 a lot of investigations have been performed in lab-based experiments. Bose-Einstein Condensates helped to study many questions of fundamental physics, such as matter wave interferometry, superfluidity or even the slowing of light pulses. Hereby the quality of the BECs (atom number, temperature, etc.) has improved a lot over time and the accuracy of measurements was increased significantly. Simultaneously the size of the experimental setup has been decreased further and further.

With access to new technologies atom interferometry became a large field of interest in physics allowing e.g. for an improved test of the weak equivalence principle (WEP). As described above large times of expansion and respectively large times of (free) flight (TOF) of the atomic ensemble is essential for atom interferometry measurements with high accuracy. In the following some ground-based fountain and microgravity experiments on different platforms shall be introduced.

## 3.1 Atomic Fountain Interferometer

As described in section 1.5 it is possible to increase the time of free flight of the atomic ensemble by launching the atoms vertically and performing a parabola. This principle is called atomic fountain. There are several atomic fountain interferometer operated worldwide, three of which are to be presented here. These apparatuses represent the state of the art of ground based experiments and shall be characterized and compared in this section. The basic parameters are summarized in table 3.1.

| | GAIN | Stanford | Wuhan |
|---|---|---|---|
| Volume | $3.68\text{m}^3$ | $> 10\text{m}^3$ | $> 13\text{m}^3$ |
| Weight | N/A | N/A | N/A |
| Atomic species | $^{87}$Rb | $^{87}$Rb & $^{85}$Rb | $^{87}$Rb, $^{85}$Rb, $^{6}$Li & $^{133}$Cs |
| Platform | ground-based | ground-based | ground-based |
| Microgravity time | ground-based | ground-based | ground-based |
| Interferometer time (2T) | 460 ms | 2300 ms | $\geq$ 2600 ms (*) |
| Sensitivity ($\Delta g/g$) | $2.5 \times 10^{-8}$ | $6.7 \times 10^{-12}$ | N/A |

**Table 3.1:** Comparison of characteristics of atomic fountain interferometers (*targeted values) [Hau13] [Dic13b] [Kas13] [Hog14]

The only mobile and very compact atom interferometer described in this section is the Gravimetric Atom Interferometer (GAIN) developed by the Humbold University Berlin, which should be described here for comparison. The whole experiment setup consists of two standard racks, sheltering the laser system, electronics and optics, and a mobile trolley carrying the physics package. In total the complete apparatus occupies 3.68 $\text{m}^3$.

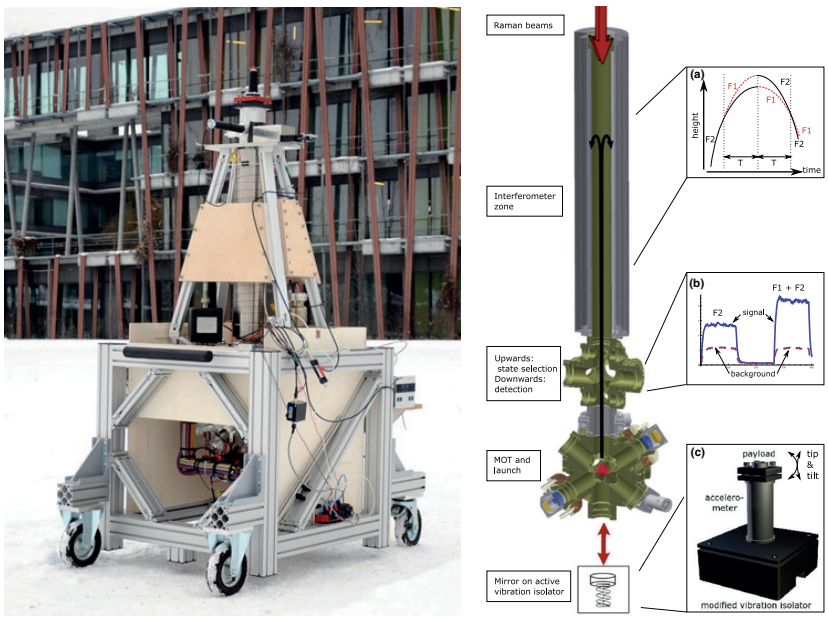


**Figure 3.1:** Photo of GAIN physics package outside of Humboldt University and drawing of interferometer set-up [Hau13]

As illustrated in figure 3.1 the physics package consists of a 3D MOT vacuum chamber and a large vacuum tube representing the interferometer zone. Within the vacuum chamber $^{87}$Rb atoms are loaded into a 3D MOT directly from dispensers connected to the chamber. After loading the atoms is completed the optical molasses is launched upwards and is cooled to a final temperature of about 13 nK by state and velocity selection [Hau13]. These selections are performed by applying laser light and RF signals (evaporation cooling).

Since the Raman beams and the third MOT beam enter the chamber only at the top they need to be retro reflected at the bottom of the chamber to cover all three axes in space. By passing a $\lambda/4$ waveplate twice the polarization is rotated by 90° to perform subdoppler cooling as described in section 1.2.2.

After state and velocity selection the atomic cloud enters the interferometer zone, which is protected by a three layer magnetic shield. When entering the interferometer tube, a Raman pulse sequence as described in section 1.3 is applied. The first pulse separates the atoms in the F1 and F2 states. The different states perform a different parabola and are first mirrored by a second pulse after time T and finally recombined by a third pulse at the end of their flight (after 2T) (fig. 3.1a.). When exiting the interferometer zone the atoms in each state are measured with fluorescence detection (fig. 3.1b.). From the population in both states the phase difference and the local gravitation can be calculated. Hereby sensitivity is enlarged with the pulse separation time T between two Raman pulses.

The maximal time T is limited by the geometry of the interferometer zone and external disturbances. For instance, vibrations have a significant and direct influence on the interferometer signal. In the GAIN setup vibrations are compensated by active vibration isolation of the retro reflection mirror (fig. 3.1c.). This reduced the vibrations and therewith the noise in the interferometer signal significantly. The active vibration isolator enabled to enlarge the pulse seperation time T from 40 ms to 230 ms, which increased the sensitivity in $\Delta g/g$ from $7 \times 10^{-6}$ to $2.5 \times 10^{-8}$ [Hau13]. Moreover the Earth rotation is compensated during interferometer phase by a piezo driven tip/tilt mount for the mirror. This minimizes the effect of the Coriolis force due to earth rotation on the measurement. These two techniques are also used by the 10 m fountains in Stanford and Wuhan.

The setup of those two 10 m towers is similar, although there are some smaller differences. The techniques for launching and trapping are the same as used in the smaller fountains. Both towers use a 3-layer magnetic shielding, which has been assembled and annealed afterwards. Moreover both shields are stabilized by a tower of aluminum profiles as illustrated in figure 3.2 and 3.3.

The Stanford fountain is operated with Rubidium 87 and Rubidium 85, which are prepared at the bottom of the fountain and launched upwards. Hereby the atoms are pre-cooled in a 2D MOT from which the 3D MOT is loaded. This increases the atomic flux and therefore shortens the loading time of the 3D MOT.

The interferometer zone is 8.2 m high, which allows a time $T$ between the Raman pulses of the interferometer of 1150 ms. This equals 2300 ms of interferometer time (2T) [Dic13b]. The long interferometer time results in a a single shot precision of $6.7 \times 10^{-12}$. For integration over several shots in one hour a resolution of $5 \times 10^{-13}$ $g$ has been demonstrated and a resolution in the order of $10^{-15}$ $g$ is theoretically possible.

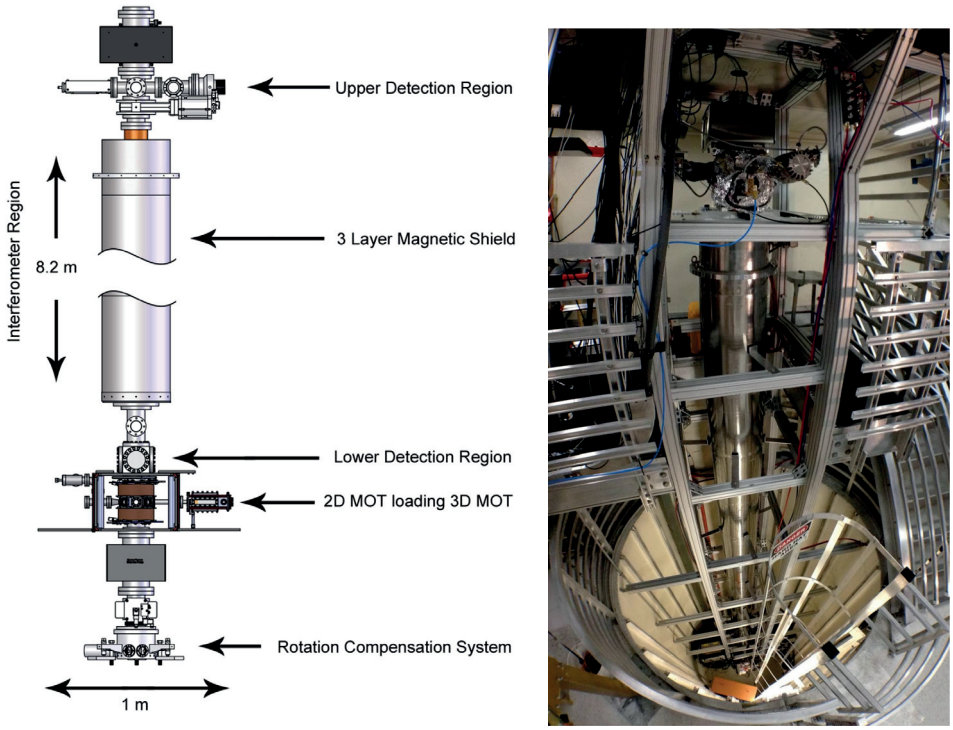


**Figure 3.2:** Principle and photo of 10m atomic fountain experiment in Stanford [Kas13]

Due to its high sensitivity the apparatus can not only be used as a sensitive gravimeter, but also to perform tests of general relativity and quantum mechanics with a much higher resolution, than in common experiments. As mentioned above the Stanford 10m atomic fountain uses two atomic species, which offers the opportunity to test the weak equivalence principle (WEP) by trapping and launching Rubidium 87 and Rubidium 85 atoms simultaneously.

The atomic fountain situated in Wuhan (China) has been developed and built after the Stanford apparatus and thus provides some additional features. It includes two magneto-optical traps (MOT). One at the bottom of a 10 m interferometer zone and one at the top. The top MOT is designed to trap Lithium 6 and Rubidium 85 simultaneously. These atoms are dropped instead of launched to perform atom interferometry and e.g. test the WEP. The second MOT situated at the bottom is capable of trapping Rubidium 87, Rubidium 85 and Caesium 133. While Rubidium 85 will be used in an atomic fountain gravimeter for precise measurements, Rubidium 87 and Caesium 133 will be used for implementation of a dual fountain clock.

Other than in the Stanford experiment Zeeman slowers are used to pre-cool the atomic beam generated directly from the atom source. These tube-shaped devices will slow and cool the atoms of the beam by applying a magnetic field with a intensity decreasing towards the exit of the slower and a laser beam pointing opposite to the atomic beam, which is red detuned to the transition wavelength of the atoms.

Due to the combined shift of the atomic transition by the Zeeman effect and Doppler effect of the moving atoms, fast atoms will be slowed already at the beginning of the device by the laser light (as explained in section 1.2.1), while slower atoms will be cooled later on. The exit temperature can be adjusted by the field gradient along the atomic beam path. As shown in figure 3.3 there are two Zeeman slowers attached to each 3D MOT chamber. These will slow the atoms down to some 10 m/s before they will enter the actual MOT from which they will be either launched or dropped into the interferometer zone.

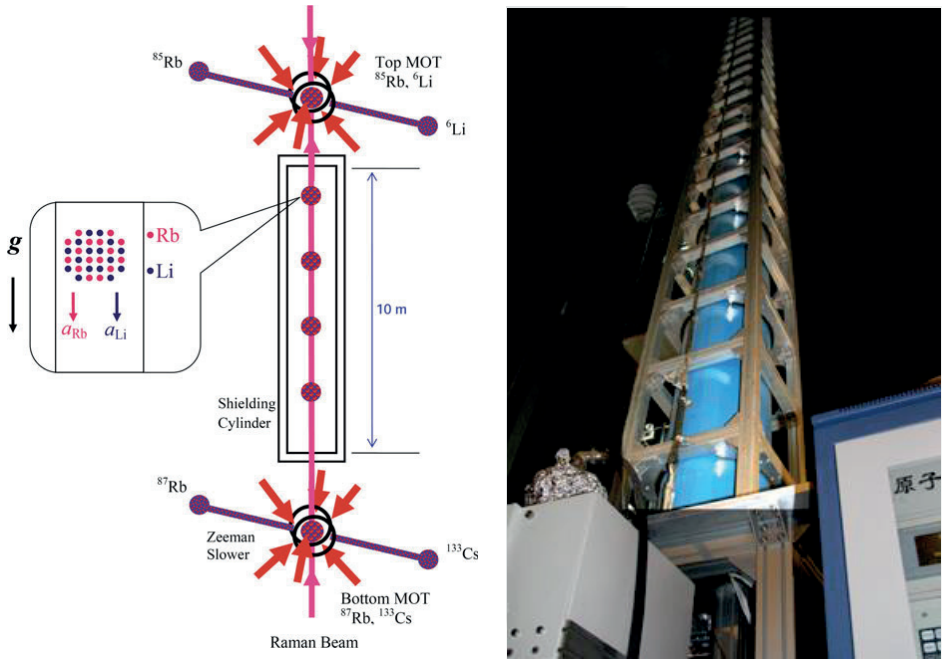


**Figure 3.3:** Principle and photo of 10m atomic fountain experiment in Wuhan [Zho11]

Unfortunately, no data of the performance of the Wuhan fountain have been published so far. However, measurements of the tidal phenomena and gravity measurements with a resolution of $4.5 \times 10^{-9}$ $g$ for integration over 1.8 s have been demonstrated in [Zho11]. The slightly larger interferometer zone might enable interferometer times of up to 2.6 s ($T = 1300\,ms$) as proposed in [Zho11] and therefore might also exceed the accuracy of the Stanford fountain.

Although the performance of the lab-based fountains is outstanding and they have the advantage of their high repeatability, they occupy whole buildings. The vacuum chamber and shielding of the Stanford apparatus for example has a volume of more than 10 $m^3$. Due to the large volume and the material needed the cost are comparable to space missions, but still limited by systematic effects (as e.g. magnetic field inhomogeneities and gravity anomalies) as given in [Kas13]. These limits might be overcome by future space missions in absence of gravity and vibrations as proposed in [Lei13].

## 3.2 I.C.E

The I.C.E. (Interférométrie Cohérente pour l'Espace) collaboration is performing experiments and measurements with atom interferometry under microgravity on parabolic flights. The consortium has designed an atom interferometer for inertial sensing aboard a A300 Zero-G [Nym06]. The apparatus is operated with a mixture of $^{40}K$ and $^{87}Rb$.

| | I.C.E |
|---|---|
| Volume | $\approx 6\,\mathrm{m}^3$ |
| Weight | 800 kg |
| Atomic species | $^{87}$Rb & $^{40}$K |
| Platform | Airbus A300 Zero-G |
| Microgravity time | 20 s |
| Interferometer time (2T) | 150 ms |
| Sensitivity ($\Delta g/g$) | $8 \times 10^{-8}$ (*) |

**Table 3.2:** Key parameters of I.C.E. experiment aboard the Airbus A300 Zero-G (*targeted values for upgrade to MEMS capacitive accelerometer) [Ste09] [Gei11] [Nym06]

As described in 2.1 the plane offers up to 20 s of microgravity resulting in a maximum Raman pulse separation of $T = 75\ ms$ [Ste09] due to the challenging environment on the plane. Typically the microgravity quality on the plane is $10^{-2}$ g. This enlarges the maximal T from 20 ms on ground to 75 ms on the plane, because of the slowed fall of the atoms.

The accelerations aboard the plane vary by up to $1\,\mathrm{m\,s}^{-2}$ during the microgravity phase [Gei11], which influences the signal output. Instead of isolating the interferometer from vibrations, the I.C.E team measures the vibrations on the reference retro reflection mirror with mechanical accelerometers and correlates them with the interferometer data. The sensitivity of the atom interferometer is therefore limited by the accuracy of the mechanical accelerometers in a usual Mach-Zehnder interferometer configuration.

In the setup published in [Gei11] the accelerations have been measured with two accelerometers. The capacitive accelerometer Sensorex SX46020 for frequencies between up to 1 $Hz$ and the piezoelectric IMI626A03 for vibrations in range of 1 - 500 $Hz$. With this setup the atom interferometer is limited to a sensitivity of $2 \times 10^{-4}\ \mathrm{ms}^{-2}/\sqrt{Hz}$. The use of a MEMS advanced capacitive accelerometer is proposed to increase the resolution to $8 \times 10^{-8}$ $g$ per shot [Gei11].

The experiment setup consists of four racks with a total volume of about $6\,\mathrm{m}^3$ and a weight of 800 kg consuming 1 kW of power. There are three racks (marked 1 to 3 in figure 3.4a) with support equipment such as lasers and electronics. The centerpiece of the experiment is the physics package (marked with 3) which shelters the vacuum chamber, vacuum pumps, optics and atomic source as presented in figure 3.4b.

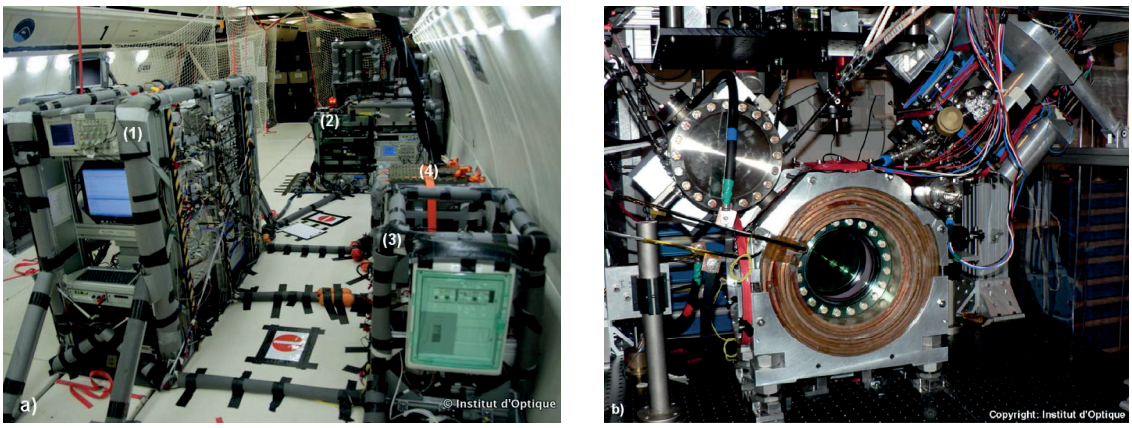


**(a)** Overview on ICE atom interferometer mounted in A300 Zero-G

**(b)** View inside the magnetic shield onto the vacuum chamber with optics

**Figure 3.4:** I.C.E. experimental setup aboard an Airbus Zero-G (Copyright: Institut d' Optique)

The physics package measures 1.2 m $\times$ 0.6 m $\times$ 0.9 m and is protected from external fields by a single layer magnetic shielding. The scientific chamber consists of a stainless steal trapping chamber (3D MOT) and a collection chamber (2D+ MOT for pre-cooling). The trapping chamber is offering eight 40 mm ports and two 63 mm view ports. Six of the eight ports are equipped with windows to shine in laser light. The other two connect to the pumping system and the collection chamber. As pictured in figure 3.5 the laser light is sent into the trapping and collection chamber without telescopes. Optics such as mirrors and beam splitters are included in the physics package envelope. The MOT and compensation coils are directly wound onto the chamber.

The collection chamber is mounted under an angle of 45° to the trapping chamber. Both chambers are divided by an orifice and a getter pump to achieve a high differential pressure between both chambers. This will allow high vapor pressure of Rubidium and/or Potassium in the $2D^+$ MOT to rapidly capture high numbers of atoms but only a low vapor pressure in the 3D MOT to prevent atom losses because of collisions of the trapped atoms with the background gas.

Potassium and Rubidium is provided by enriched dispensers directly attached to the collection chamber. The $2D^+$ MOT uses two pairs of coils to trap and pre-cool these atoms. Because one direction in space is not blocked, an atomic beam will be generated transporting the pre-cooled atoms into the trapping chamber. The flux of atoms can be increased by a push beam which will enter the collection chamber in the free axis pointing towards the trapping chamber.

Within the trapping chamber the atoms will be caught in a 3D MOT and subsequently transferred in a far-off-resonance trap (FORT) as preparation for the evaporative cooling. Finally the atoms are cooled below the critical temperature by evaporation.

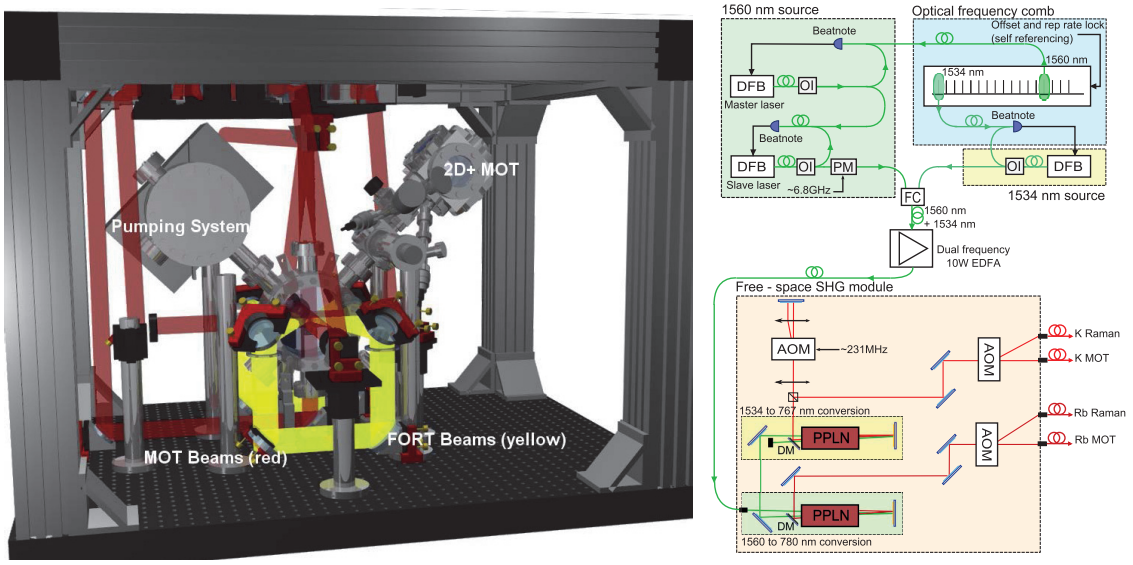


**Figure 3.5:** 3D MOT laser beams and setup of the I.C.E. physics package (left); Diagram of the complete I.C.E laser system: DFB, distributed feedback laser diode; OI, optical isolator; PM,phase modulator; FC, fiber combiner; SHG, second harmonic generation; DM, dichroic mirror; PPLN, periodically poled lithium niobate crystal; AOM, acousto-optic modulator (right) [Men11]

The pumping system to maintain the pressure within the trapping chamber is attached to the last remaining port as shown in figure 3.5. The pumping system is positioned with an angle of 45° to the floor and suspended to the aluminum profiles surrounding the physics package. The sufficient pumping rates are achieved by a combination of a powerful ion pump and a passive titanium sublimation pump.

The light for the magneto optical traps is provided by a robust and stable laser setup of two telecom lasers operating at 1560 nm and 1534 nm. The output of these lasers is amplified and frequency-doubled to generate light at 780 nm and 767 nm, which is needed to cool Rubidium and Potassium. The two lasers are frequency-stabilized on a self-referenced optical frequency comb designed by MenloSystems [Men11]. The laser system as shown in figure 3.5 will provide 200 mW of power in each of the four output ports (Raman $^{40}K$, Raman $^{87}Rb$, MOT $^{40}K$ and MOT $^{87}Rb$) supplying the optics of the physics package. The laser system has been operated during flight under vibrations of 0.5 g, accelerations of 1.8 g and temperature fluctuations between 17 °C and 30 °C without problems.

Interferometry has been performed with this setup with $10^6$ atoms at a temperature of 300 nK for Rubidium [Gei11]. Additionally a dual-species magneto optical trap of Potassium 40 and Rubidium 87 a has been demonstrated during a parabola flight in [Men11]. The I.C.E team managed to trap $10^9$ Rubidium atoms simultaneously with $5 \times 10^7$ Potassium atoms. The temperature of the Rubidium atoms in the MOT have been measured to be 8 µK, while the Potassium atom temperature was 200 µK.

## 3.3 QUANTUS-1

Motivated by potentially larger times of free evolution of BECs in microgravity the QUANTUS (Quantengase unter Schwerelosigkeit) project was started in 2004 with the objective to create a BEC in a drop tower [vZ10].

| | QUANTUS-1 |
|---|---|
| Volume | $< 0.66\,\mathrm{m}^3$ |
| Weight | 221 kg |
| Atomic species | $^{87}$Rb |
| Platform | Drop Tower Bremen |
| Microgravity time | 4.7 s |
| Interferometer time (2T) | 677 ms |
| Sensitivity ($\Delta g/g$) | N/A (*) |

**Table 3.3:** Key parameters of QUANTUS-I experiment (* N/A because of missing phaselock of laser) [Rud11] [Mun13] [vZ10]

To achieve this goal the instruments needed for the creation of a BEC had to be shrunk to fit into a volume of $0.66\,\mathrm{m}^3$. Although the space is limited and the mass shall not exceed 221 kg, the drop tower at the Center of Applied Space Technology and Microgravity (ZARM) offers not only good microgravity conditions with a quality of better than $10^{-5}\,g$ but also good accessibility with up to 3 drops per day.

As shown in figure 3.6 the experiment is mounted into a capsule measuring 0.82 m in diameter and 2.15 m in length. The experiment hardware can fill 0.7 m of the diameter and 1.72 m of the total capsule length. The remaining space is occupied by a data handling system for housekeeping data such as pressure or temperature of the capsule and a self-contained power supply for in-flight operation of the experiment.

When the experiment is set up, the capsule is closed and lifted to 120 m height by a crane. In this position it is supplied with energy and water cooling, while the tower is evacuated to reduce aerodynamic drag and improve microgravity conditions. After evacuation of the tower has been completed, the capsule is released by the scientists experiencing 4.7 s of free fall. Finally the capsule will be recaptured in in a pool of polystyrene balls at the bottom of the tower.

During deceleration at the end of the microgravity phase the experiment receives decelerations of up to 50 $g$. If all instruments inside the capsule are designed and mounted properly and survive the impact, the capsule can be used again without any modifications.

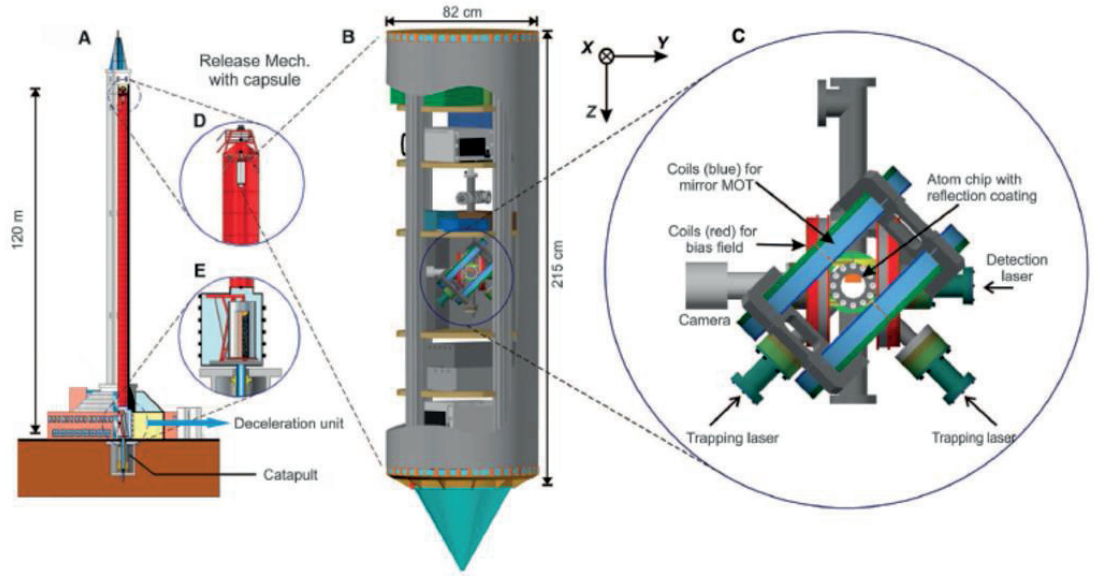


**Figure 3.6:** CAD drawing of the drop tower facility in Bremen (A), the QUANTUS-I drop capsule (B) and the scientific chamber (C) [vZ10]

QUANTUS-1 is the first apparatus, which has been designed and built by the QUANTUS consortium. It is basically a proof of principle for BEC generation in the harsh environment of the drop tower. Within this first experiment the team managed to minimize all the components necessary to create a BEC in a way that they fit into a drop capsule. This includes all support instruments such as lasers, vacuum pumps and electronics. An upgrade of a Bragg laser module in 2011 enabled atom interferometry as well.

Control and data handling of the QUANTUS-1 experiment is performed by a commercial real-time National Instruments PXI computer system. The same system is used for handling of the house keeping data. Both computer systems communicate via WLAN with the control room on ground during the drop.

The laser system and electronics have been customized for the experiment to suit the environment in the capsule. The laser system provides light for cooling from three distributed feedback diode (DFB) lasers. Aside from a master laser stabilized on Rubidium 85 transition ($^2S_{1/2}; F = 3 \rightarrow ^2P_{3/2}; F = 4$), the system consists of two additional lasers for cooling, re-pumping and detection which are stabilized with respect to the master laser. The cooling light is switched and distributed in a encapsulated module connected to the lasers with fibers.

A fourth DFB laser is used to provide light for Bragg interferometry. This laser is red de-tuned by 2 GHz to the $^2S_{1/2}; F = 2 \rightarrow ^2P_{3/2}; F = 3$ transition of Rubidium 87. The light of the Bragg module is switched and distributed by a separate switching module. Subsequently the laser light of both switching modules is guided to the main chamber using optical fibers, which are directly mounted to telescopes collimating and widening the beam to 21 mm in diameter.

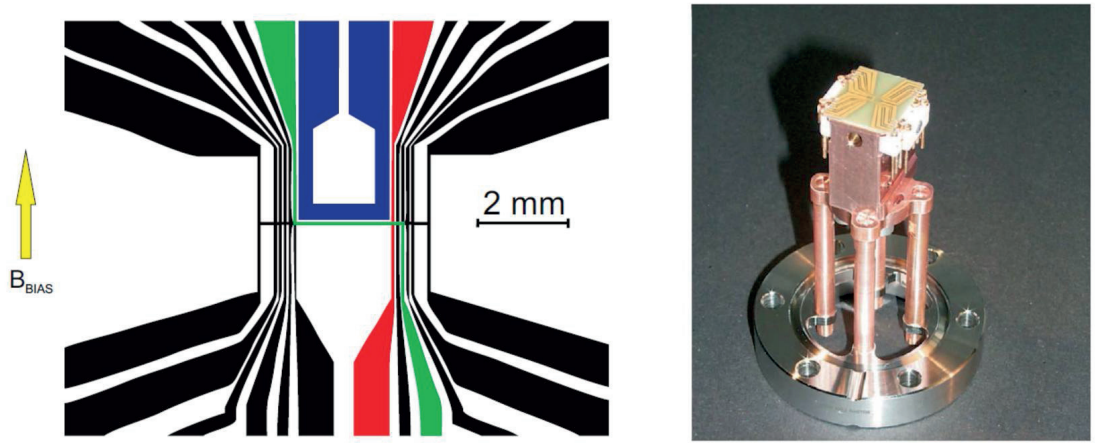


**Figure 3.7:** Atomchip schematic drawing with different geometries I,Z & U marked with red, green and yellow color and photo of the atom chip on its copper mount before installation in apparatus

As shown in figure 3.6 C. QUANTUS-1 is equipped with only one experimental chamber loading the atoms from the background gas. The chamber is equipped with 8 con-flat sealed ports. The magnetic coils for the bias field and the magnetic trap are mounted directly to the experiment chamber. Inside the chamber an atom chip (shown in figure 3.7) is completing the setup for the magneto optical trap. The atom chip wires act as "coils", capable of creating different trap geometries to control and manipulate the atoms. The use of atom chips significantly reduces the volume of the apparatus, since they offer the possibility to create high magnetic fields gradients while they consume only little energy.

The laser light for the MOT is shone in by two telescopes mounted under an angle of 45° to the chip surface and two additional telescopes aligned along the x-axis of the capsule parallel to the chip surface (figure 3.6 C.). The light of the telescopes mounted under 45° is mirrored from the atom chip. Therefore no third pair of telescopes is needed to cover all axis in space.

The telescopes in x-axis are used for interferometry light pulses as well. The two ports in the y-axis are used for detection of the BEC or interferometer fringes. A light pulse is shone in by a telescope attached to one of these ports and an image will be created on the CCD of the camera attached to the opposing port.

The pumping system is connected to the main chamber. It consists of an ion pump, which has been modified by the supplier to survive the high mechanical loads during deceleration. Beside the ion pump a titanium sublimation pump and a SAES getter pump are used to passively getter all atoms but noble gases and methane. All pumps maintain a pressure below $10^{-10}$ hPa in the chamber. This chamber and its magnetic coils, as described above, have to be shielded from outside magnetic fields, which vary during the flight. This is achieved by a single layer $\mu$-metal shield.

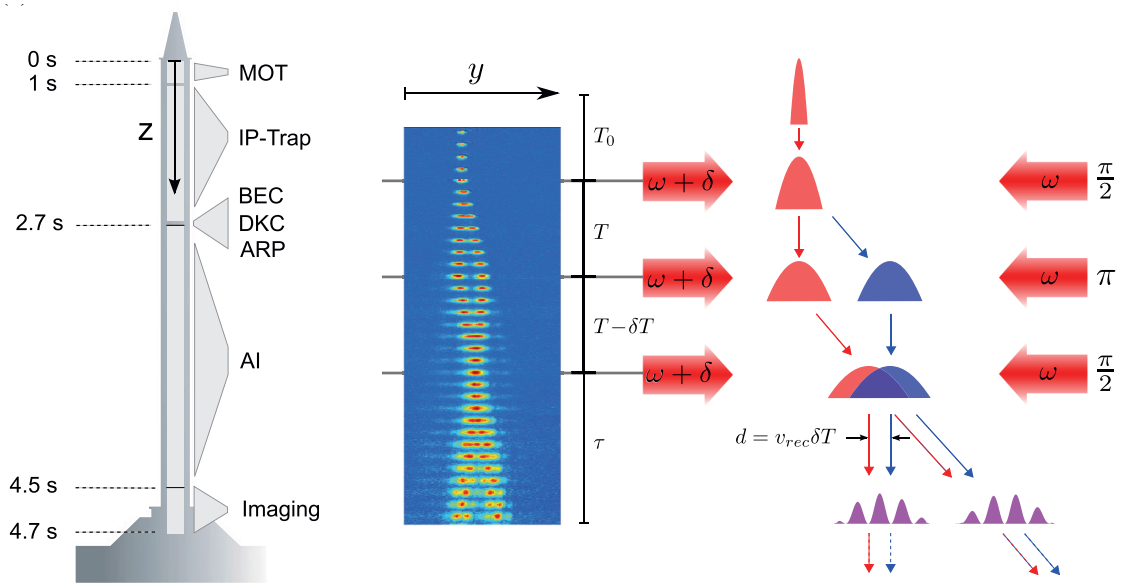


**Figure 3.8:** Optimized sequence of the QUANTUS-1 atom interferometer and asymmetric Mach-Zehnder interferometer sequence with asymmetry of $\delta T$ [Mun13]

Within 6 years of operation the parameters for BEC creation and the sequence for atom interferometry have been optimized by the QUANTUS-I team. The resulting sequence is shown in figure 3.8.

The atoms are captured from the background gas into a MOT using the external fields. These atoms are then transferred to a Chip-MOT, which uses the U-structure on the atom chip. Within this MOT $10^7$ atoms are trapped at a temperature of 200 µK [Bro10]. These atoms are the transferred into an Ioffe-Pritchard trap whereby the Z-structure of the chip is used. Within this step the atom number reduces furthermore to $4 \times 10^6$ and the atoms will cool to 50 µK. By evaporation the temperatures will be brought below the critical temperature to approximately 100 nK [Bro10]. The BEC will consist of roughly $1 \times 10^4$ atoms.

A novel method called delta-kick cooling (DKC) has been implemented within the experiment sequence. To achieve DKC the chip based trap is switched on for 2 ms approximately 30 ms after the release of the BEC from the MOT. This procedure will reduce the remaining thermal energy within the BEC. Thus a temperature of about 1 nK [Mun13] is achieved and the expansion rate is lowered significantly giving access to longer interferometer times.

Additionally the atoms are transferred into a non magnetic state to reduce the influence of residual magnetic fields which affect the measurements despite magnetic shielding. This procedure is named adiabatic rapid passage (ARP).

This preparation of the atoms for interferometry as described in [Mun13] takes approximately 2.7 s. Subsequently interferometer measurements will start at time $T_0$. As illustrated in figure 3.8 an asymmetric Mach-Zender interferometer (AMZI) sequence is applied using bragg scattering (ref. section 1.3). Interferometer times of 677 ms have been demonstrated with this apparatus at maximum pulse separation times $T$ of 340 ms.

## 3.4 QUANTUS-2

QUANTUS-2 has been redesigned in many aspects compared to the first generation apparatus with the objective to reduce the volume and increase the performance of the experiment. Most importantly the device will be capable of performing atom interferometry with two atomic species (Rubidium 87 and Potassium 40) simultaneously giving access to tests of the weak equivalence principle (WEP) and investigations on the behavior of quantum gas mixtures in chip-based traps under microgravity.

| | QUANTUS-2 |
|---|---|
| Volume | 0.38 $m^3$ |
| Weight | 162 kg |
| Atomic species | $^{87}$Rb & $^{40}$K |
| Platform | Drop Tower Bremen |
| Microgravity time | 9.2 s |
| Interferometer time (2T) | 2000 ms (*) |
| Resolution ($\Delta g/g$) | $5.6 \times 10^{-11}$ (*) |

**Table 3.4:** Key parameters of QUANTUS-2 experiment (* targeted values) [Mun13] [Rud11] [Her13a]

Further reduction of the experiment volume will allow usage of the catapult mode of the drop tower. This nearly doubles the time of microgravity and thus the time for experiments. A short capsule offers 0.98 m in length and 0.7 m in diameter for payload hardware. Obviously the increase in hardware due to the upgrade to dual species operation is contrary to the aim of reducing the size of the whole apparatus. Moreover operation in catapult mode requires the instruments to operate reliably even during the 30 g shock at launch.

Despite those limitations the design of QUANTUS-2 meets all objectives for catapult mode operation. As illustrated in figure 3.9 the apparatus can be divided into four sections each one mounted on an individual aluminum board with a wood core, which is attached to the stringers of the capsule. The laser system is placed on the top board. On the two boards below, all electronics necessary for operation of the experiment is arranged around the vacuum pumps. These pumps need to be situated outside of the magnetic shielding, because of its strong magnets. Protected by a two-layered magnetic shielding the experiment chambers are mounted onto the last experiment board. At the very bottom of the capsule default drop tower interface systems are stored. These are the PXI system for data handling of the housekeeping data as well as DC-DC converter and customized lithium iron phosphate ($LiFePO_4$) light-weight batteries. These batteries have replace the standard lead-acid batteries and save weight and space, which will add to the weight and volume available for the experiment.

The vacuum and experiment chamber has been redesigned completely. Contrary to the QUANTUS-1 experiment, a $2D^+$ MOT is used in its successor to pre-cool the atoms as it has already been described in section 3.2.

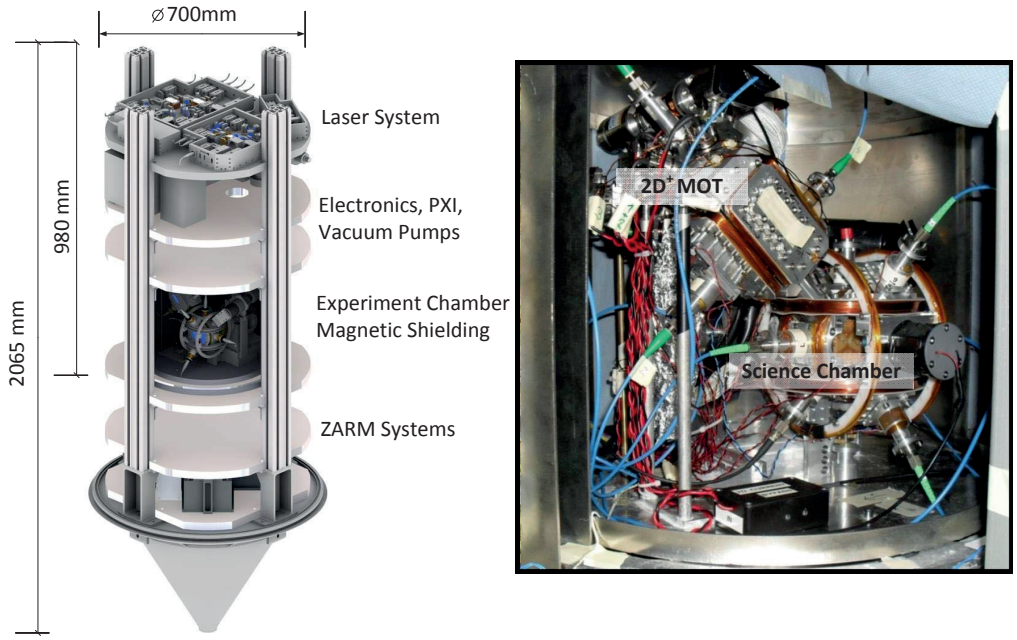


**Figure 3.9:** CAD Drawing of the QUANTUS-2 experiment with different subsystems and a foto of the science chamber within the $\mu$-metal magnetic shielding (adapted from [Her13a])

Both chambers are manufactured from grade 5 (Ti6Al4V) titanium, which is considered highly nonmagnetic and of low magnetic susceptibility. This will reduce time varying residual magnetic fields within the shielding.

As illustrated in figure 3.10 the $2D^+$ MOT offers four rectangular optical ports for 2D MOT beams distributed over the four sides of the chamber. One of these ports is slightly larger to shine in the retarder beam. An additional circular port at the back of the chamber provides access to the pusher beam.

The $2D^+$ MOT is connected to the science chamber by an aluminum tube, which should absorb loads, which will apply during launch and deceleration by elastic deformation. At the exit of the $2D^+$ MOT chamber a differential pumping stage will ensure that only the concentrated atomic beam will leave the pre-cooling chamber and the background pressure in the science chamber will remain at a low level. The principle of the differential pumping stage will be described in section 7.3.

Aside from the mechanical port for access to the $2D^+$ MOT, the science chamber uses a second mechanical port behind the atom chip to connect to the pumping system. This is achieved using commercial con-flat (CF) sealed components made from stainless steel. Moreover the science chamber is equipped with seven 30 mm and one 86 mm view ports.

In both the main chamber and the 2D chamber a different sealing technology has been used to reduce the size of both chambers. Adhesive indium wire is used to mount the windows directly into the associated pockets in the chamber by applying pressure to the window and compressing the indium wire.

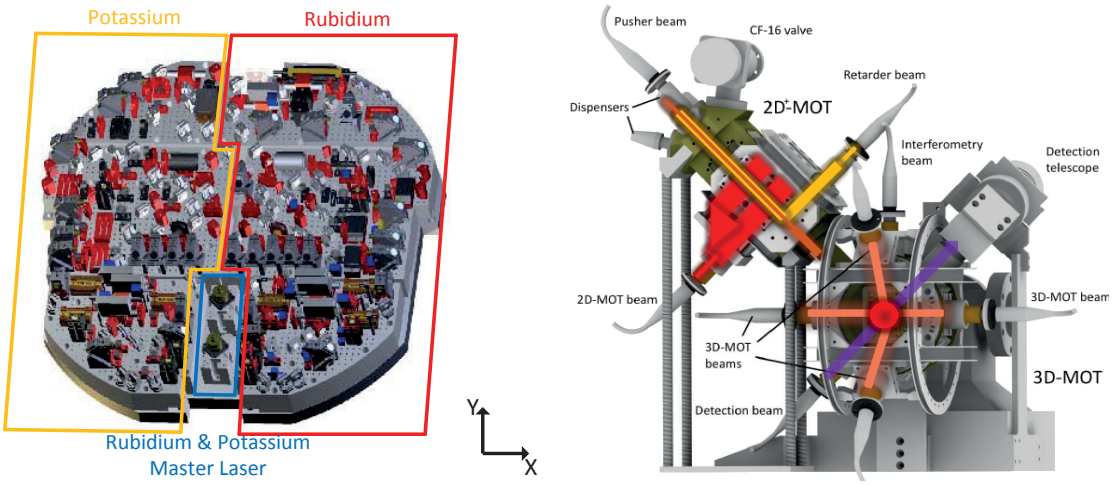


**Figure 3.10:** CAD drawing of QUANTUS-2 laser system for Potassium and Rubidium and experiment chamber with different laser beam paths (adapted from [Her13b])

The use of the different ports is presented in figure 3.10. The laser light for 3D trapping is shone in through the 86 mm view port in front of the atom chip under an angle of 45° and through the two smaller ports on the side of the chamber along the x-axis. Similar to the setup in QUANTUS-1 the light is mirrored at the chip surface to complete the 3D MOT setup. Orthogonally to the beams from the side the interferometer beams are directed along the y-axis. The seventh port is used for the absorption detection and will create a shadow image in a CCD camera connected to the opposite view port. Additionally a second camera is mounted between the coils facing the chip surface. This camera will take fluorescence images of the atoms.

The associated three pairs of coils are set up in Helmholtz configuration. The pair of coils creating a field in z-direction are wound directly onto the titanium chamber, while the coils for y- and x-fields are mounted to the chamber. The rectangular coils of the $2D^+$ MOT are wound onto aluminum bodies screwed to the $2D^+$ MOT chamber. These coils form the magneto optical trap in combination with the atom chip inside the experiment chamber. The chip is mounted onto a solid copper mount to ensure that the produced heat is conducted properly. The chip consists of three different structures as shown in figure 3.11 which decrease in conductor diameter and are mounted to each other with UHV suitable glue. While the lowest layer consist of mesoscopic structures (1 mm copper wire), the science and the base chip are fabricated from aluminum nitrate substrate with printed circuits made of gold. The chip layers are capable of forming various trap geometries with different distances of the trap bottom to the chip surface. Additionally a RF antenna is included in the chip setup to apply RF signals during evaporation.

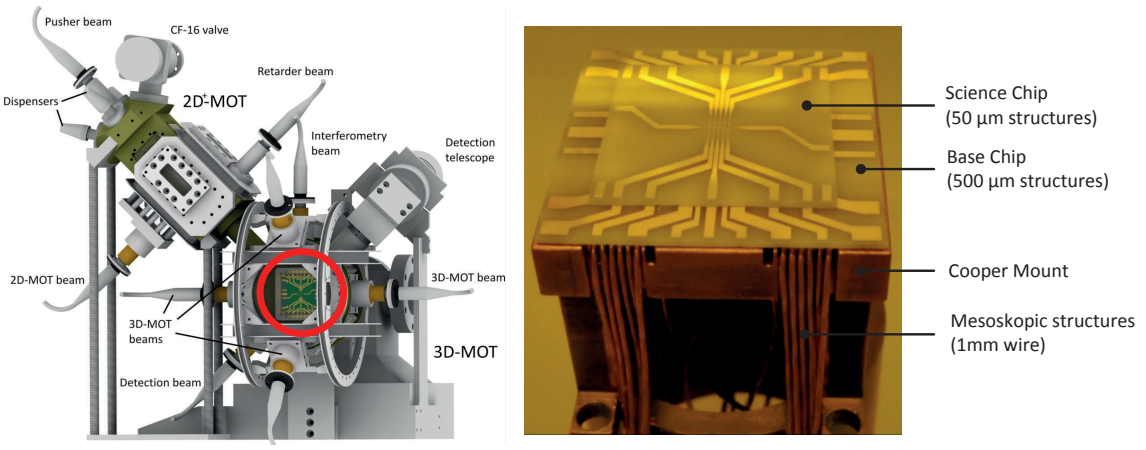


**Figure 3.11:** QUANTUS-2 science chamber with atom chip (adapted from [Her13b])

The laser system is especially designed by the Humboldt University of Berlin to withstand the loads of the catapult launch. It provides light with a wavelength of 767 nm and 780 nm for trapping and manipulation of Rubidium and Potassium. As illustrated in figure 3.10 the hardware itself consists of three parts: two master lasers stabilized on Rubidium and on Potassium transitions and a mixing and switching module for each species. The mixing module includes three master oscillator powered amplifier (MOPA) lasers, which are stabilized on the associated master laser. These modules will provide light for trapping and interferometry of both atomic species.

The vacuum pressure is maintained by two pumps. An active ion getter pump custom-made by VinciTech and a passive getter pump from SAES. These pumps maintain a pressure of $6 \times 10^{-10}$ hPa, which is sufficient for BEC experiments. The pressure is monitored by a cold cathode gauge (Pfeiffer IKR270).

The current drivers for coils, atom chip and laser as well as the temperature and vacuum pump controllers are an ultra-compact customized PCB design developed by the University of Hanover. Since these components are a lot smaller than commercial parts, this saves a lot in space and weight.

QUANTUS-2 is able to load its Rubidium 3D-MOT with an atomic flux of $1.4 \times 10^9$ atoms per second. The atoms are then held in a 3D MOT using the mesoscopic U-structure of the atomchip and the external coils. A 3D-chip MOT with $2.5 \times 10^9$ atoms has been demonstrated in this apparatus [Her13a]. Subsequently the atoms are transfered in a compressed MOT (cMOT) and prepared for evaporation. The largest BEC observed after evaporation had a size of $4 \times 10^5$ atoms at a temperature of 330 nK [Her13b]. As illustrated in figure 3.12 a typical BEC with $1 \times 10^5$ atoms can be produced within 1.1 s. Therefore the experiment is faster and provides more atoms in the BEC than its predecessor.

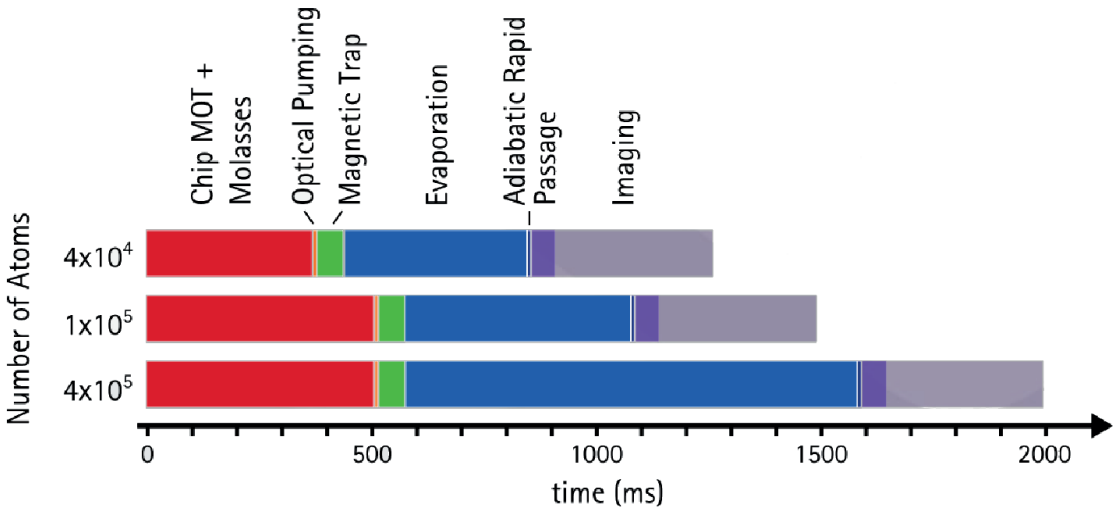


**Figure 3.12:** Sequence for BEC creation in QUANTUS-2 [Her13b]

As a final step of preparation the BEC is transferred into a non magnetic state (ARP) to reduce the influence of residual magnetic fields, as it is done in QUANTUS-1. Unfortunately optimization of the procedures within preparation of the atoms is still ongoing. Therefore there is no data for the performance of the QUANTUS-2 atom interferometer and Potassium MOT available so far. However with the planned implementation of delta kick cooling the apparatus shall allow interferometer times 2T of up to 2 seconds and reach a resolution ($\Delta g/g$) of $5.6 \times 10^{-11}$ [Mun13].

# Part II

# Payload Environment and Requirements

# 4
# Scientific Objective

The QUANTUS project was initiated in 2004 to prove the feasibility of atom interferometry in space-like environments and to develop and test the necessary technologies.

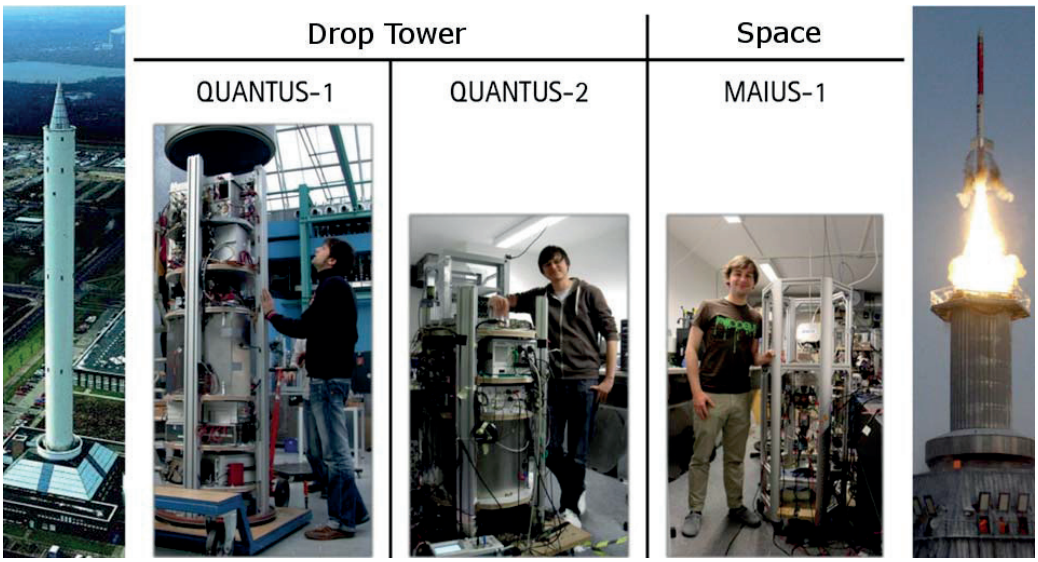


**Figure 4.1:** Three generations of QUANTUS experiments (Figure: IQO Hanover)

The project is led by the University of Hanover in cooperation with the University of Bremen, University of Hamburg, Humboldt-University Berlin, Ferdinand-Braun Institute Berlin (FBH), the University of Darmstadt and the University of Ulm. Moreover there are some universities and institutes involved as subcontractors, one of which is the German Aerospace Center's Institute of Space Systems in Bremen.

The QUANTUS projects have the aim to produce outstanding results in the field of atom interferometry and prepare future missions on satellite platforms, which offer the best environmental conditions for atom interferometers (refer chapter 2) and enable a test of the weak equivalence principle with accuracies not reached before [Lei13].

During the first project phase (QUANTUS-I) the first Rubidium-87 BEC was created in the microgravity environment of the drop tower Bremen [vZ10]. In the course of the project the sequences for BEC creation and atom interferometry under microgravity have been improved significantly revealing new techniques such as delta-kick cooling (refer section 3.3).

Subsequently in the project QUANTUS-II a new apparatus QUANTUS-2 was built, which was designed for the use with the catapult of the drop tower. The second generation of the experiment uses an improved setup (refer 3.4) to achieve higher atom numbers in the BEC and aims at longer interferometer times. Moreover dual species atom interferometry will be investigated and optimized within this experiment. Because of the high accessibility and repeatability in the drop tower, parameter studies can be performed, which prepare mission in space and on sounding rockets.

Within the third phase of the project (QUANTUS-III) not only optimization of atom interferometry in the QUANTUS-2 apparatus is addressed, but a new platform of microgravity is accessed - the sounding rocket. The qualification of an atom interferometer experiment for the use on a sounding rocket is a milestone on the way to access orbital platforms such as satellites or the international space station.

The MAIUS-1 scientific payload is a technology demonstrator and aims at generating the first generation of BECs in space. As an atomic species Rubidium-87 was chosen in order to benefit from the heritage of the QUANTUS-experiments. The payload is designed to create BECs with performance comparable to the QUANTUS-2 apparatus. In addition to the generation of BECs in space atom interferometry with Rubidium atoms will be performed. This would mark the first BEC-based atom interferometer in space and reach interferometer times of $2T > 2.3\,\mathrm{s}$. The BEC itself is aimed to have temperatures in the pK-regime. These low temperatures would allow for evolution times of multiple seconds. Even more sophisticated experiment sequences with two species and the possibility of testing the Einstein equivalence principle shall be carried out on following missions.

For a successful mission the environment during the sounding rocket flight needs to be characterized and the instruments aboard adapted and qualified accordingly. This includes the optimization of the experimental parameters and sequences of the atom interferometer, which might differ from those used on ground or in the drop tower. Additionally an autonomous experiment control has to be implemented and tested, because the experiment has to operate without a continuous tele-command link. An exemplary experimental sequence and the associated requirements for the payload design are given in chapter 6.

Within QUANTUS-III the German Aerospace Center's Institute of Space Systems is responsible for the thermal and mechanical design of the scientific payload and the qualification of the experimental hardware for the use on a sounding rocket. The results of this contribution are presented in this thesis.

# 5
# Launch Vehicle and Flight Environment

The MAIUS-I vehicle consists of the payload and the two-staged rocket motor assembly. By definition the payload includes not only the scientific payload(s), but also multiple support systems as shown in figure 5.1. The motor adapter is mounted above the two-staged VSB-30 motor combination, which measures 0.559 m in diameter and 7.4 m in length. The conical adapter will reduce the hull diameter to 500 mm on a length of 378 mm. The adapter is mounted to the de-spin and payload separation system. It will guarantee the separation of motor and payload and will remove rotations. The de-spin system is connected to the scientific payload by a manacle ring and a manacle adapter.

| Item | Mass [kg] | Length [m] | Diameter [m] |
|---|---|---|---|
| VSB30 Motor Assembly | 2265.1 | 6.638 | 0.559 |
| Motor adapter | 8.7 | 0.378 | conical |
| De-spin and separation | 25.2 | 0.123 | 0.500 |
| Manacle Adapter | 7.3 | 0.187 | 0.500 |
| Scientific Payload | 280 | 2.790 | 0.500 |
| Service Module | 53.5 | 0.500 | conical |
| ACS | 31.2 | 0.125 | 0.438 |
| Recovery system | 55.5 | 1.102 | conical |

**Table 5.1:** MAIUS-1 mass and geometry overview

The scientific payload itself consists of 5 hull segments with a diameter of 500 mm. The mass of the payload is approximated with 280 kg. The service system is situated above the payload. The service system hull is of conical shape and is reducing the diameter from 500 mm to 438 mm on a length of 500 mm. At the top the European Recovery System (ERS) and its parachute is situated below the nose cone. The total vehicle as shown in figure 5.1 has a length of 11.843 m and a mass of 2726.5 kg.The support systems are designed and operated by DLR's Mobile Rocket Base (MORABA) and will be described briefly in the following sections.

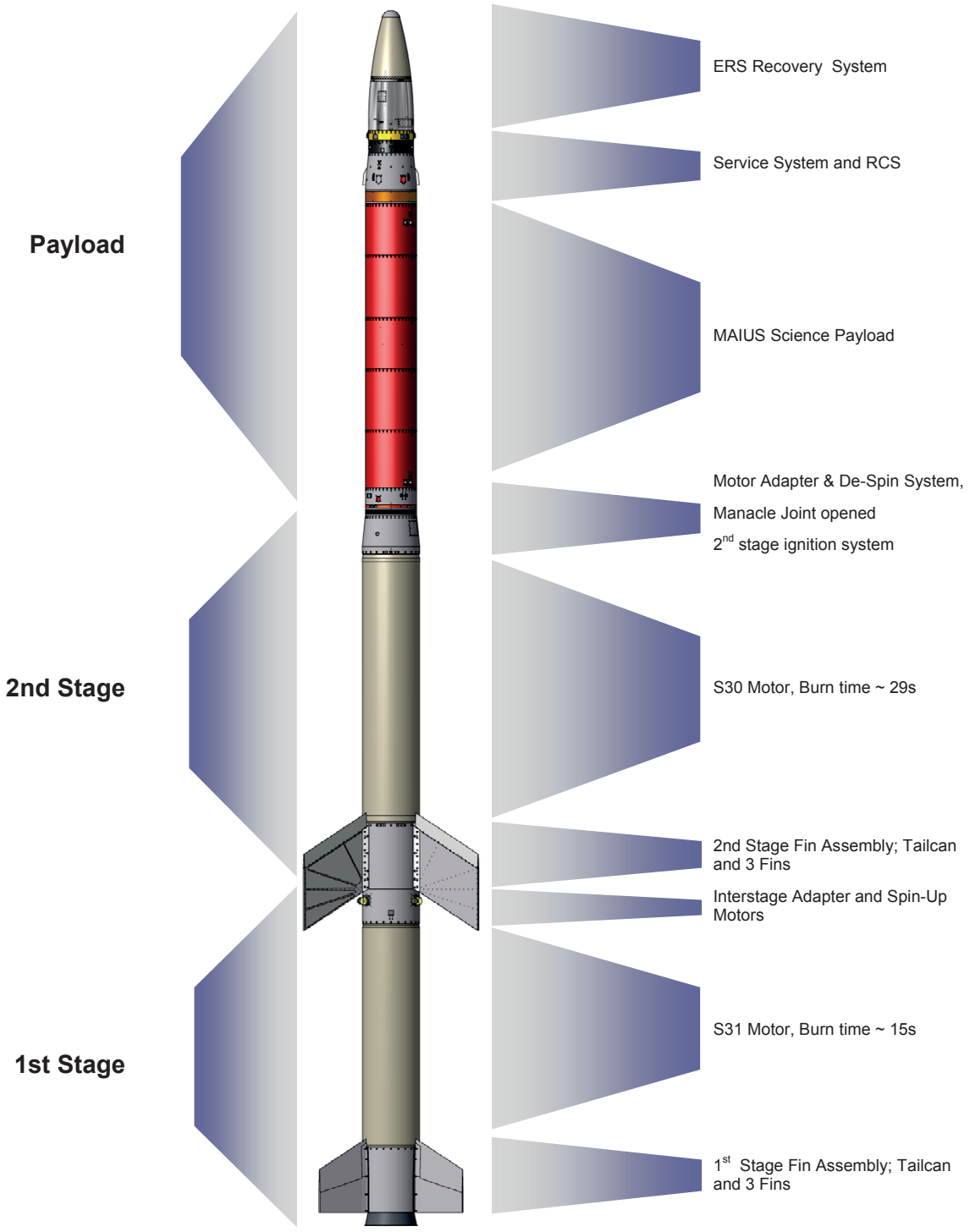


**Figure 5.1:** Overview of MAIUS-I vehicle [Sta12]

## 5.1 Motors and Spin-Up Motors

MAIUS-I will be launched with the two-staged Brazilian VSB-30 vehicle. The VSB-30 is a combination of a S31 Motor as first stage and a S30 motor as second stage as shown in figure 5.2. Both motors are filled with solid ammonium perchlorate composite propellant using aluminum as high energy fuel and HTPB as binder fuel.

**Figure 5.2:** VSB 30 motors in integration hall at Esrange [Sta12]

The first stage motor will create a total impulse of 1.741 MNs and an average thrust of 136.3 kN for 14.6 s. After burn-out the first stage will be separated and the second stage will be initiated by an independent ignition system. It will create an additional total impulse of 2.332 MNs and an average thrust of 103.7 kN for 29.5 s [Sch].

The vehicle is spin-stabilized during the entire propelled flight to compensate possible misalignment of the motor nozzle. The fins will be arranged in the standard canted 3-fin configuration with a nominally angle of 18’ (S31) and 24’ (S30). This will cause the vehicle to spin from lift-off through burnout. This "passive" spin up will be supported by three spin up motors situated at the interstage between the motors, which will be ignited 0.7 s after the vehicle has left the rail of the launch facility. Altogether fins and spin up motors will cause the vehicle to spin with a nominal rate of 2.71 Hz around its longitudinal axis.

## 5.2 Motor Adapter and De-Spin System

The payload is connected with the motors by the motor adapter, which is a conical shaped mechanical part reducing the diameter from 557 mm to 500 mm. Above this adapter the de-spin and separation module is mounted. Figure 5.3a shows the module of MASER-12, which is similar to the one which will be used on MAIUS.

For de-spin a yo-yo system is used, consisting of two masses which are placed opposite to each other on the hull of the module. These masses are attached to the payload by steel cables wound onto the hull as indicated in figure 5.3a. At de-spin the masses are released and the cable will unwind from the hull decreasing the angular velocity of the payload. If the cable is unwound completely the masses will be detached from the payload. By adjustment of the de-spin weights at a given length of the cable, the angular velocity will be decrease to $\pm 30\,^{\circ}/s$ within one second [Sta12].

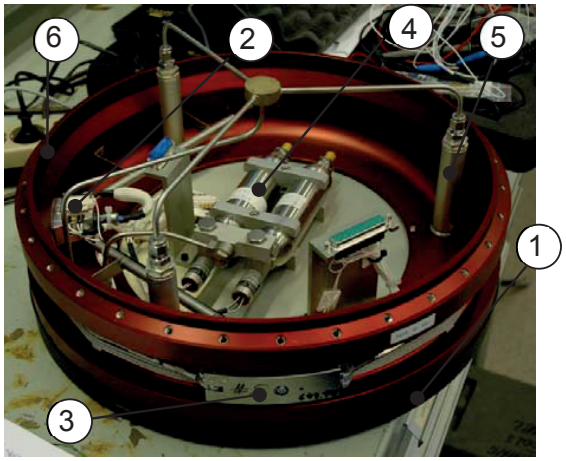


**(a)** MASER-12 de-spin module with interface to payload by manacle flange (1), pneumatic manacle ring opener plunge (2), Tungsten de-spin weight (3), 2 nitrogen gas bottles for plunge operation (4), three pneumatic payload separation plunges (5) and interface to motor adapter (6). [Sta12]

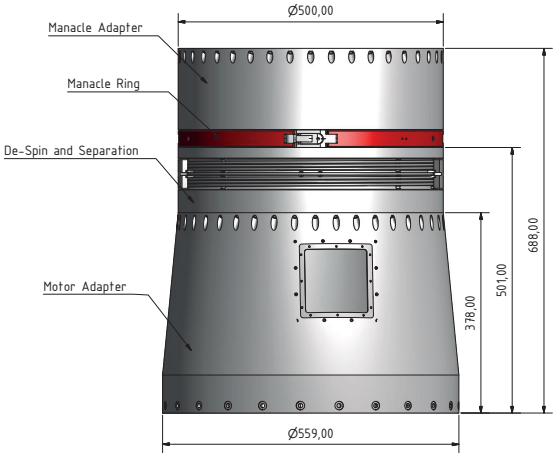


**(b)** De-spin system, motor and manacle adapter assembled with manacle ring in MAIUS configuration. The scientific payload will be mounted to the manacle adapter.

**Figure 5.3:** De-spin and separation system

After de-spin the second stage motor has to be separated from the payload. This is done by opening a manacle ring, which connects the manacle adapter and the de-spin module. Subsequently the motor and the de-spin system is pushed away by actuation of pneumatic separation plunges.

## 5.3 Service System and ACS

The service module will manage and monitor the housekeeping and flight performance data of the rocket such as position, speed or acceleration. Furthermore it will establish bidirectional communication between the sounding rocket and the ground station to transmit flight parameters or experiment data.

For this purpose the service system is equipped with several antennas and a telemetry system, which will obtain a data connection during flight with a downlink data rate of 5 Mbit/s and an uplink data rate of 38.4 kbit/s. Due to the fact that the uplink might be interrupted during flight the experiment has to operate autonomously as already mentioned above.

The service system provided for MAIUS-1 is a prototype, developed by DLR MORABA especially for this payload. The housing was re-designed to be a conical adapter between the 500 mm hull segments of the payload and the 438 mm structure of the attitude control system (ACS) and the European recovery system (ERS) as shown in figure 5.4. Moreover the experiment interfaces has been extended by four 100 Mbit/s Ethernet ports. These will add to four bi-directional RS-422 interfaces.

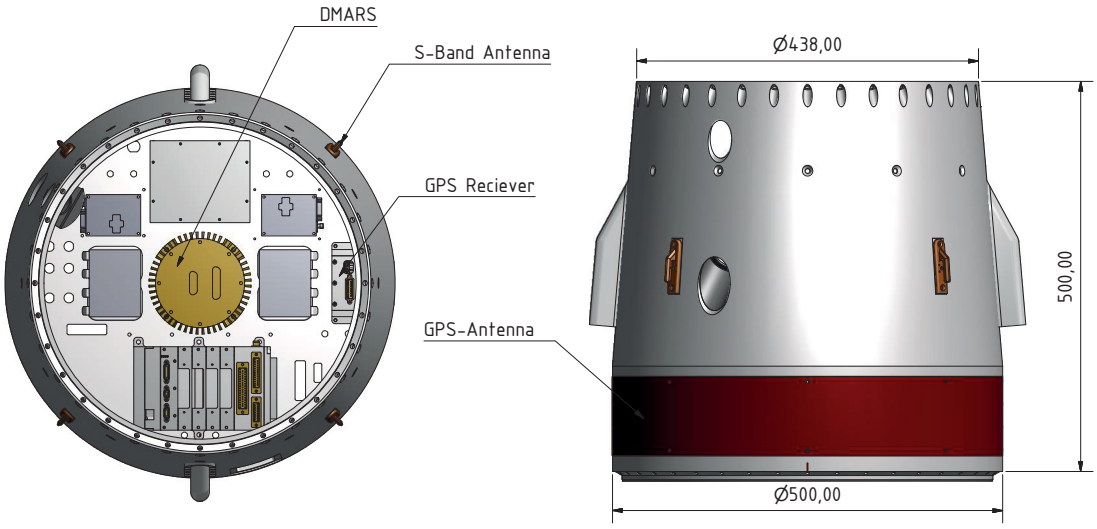


**Figure 5.4:** MAIUS-1 service system equipped with a DMARS inertial platform, GPS receiver, 6 antennas for communication and a GPS wrap-around antenna

Most importantly the service module has been equipped with a DMARS inertial navigation and flight control System and a GPS module to determine not only the rates of the rocket but also the position with high accuracy. This is necessary to align the interferometer measurement axis to the local gravity vector of earth as required in future MAIUS experiments (refer section 6.3).

Adjustments of the attitude and rates will be commanded from the service module to the two-staged cold gas steering system of the attitude control system. As shown in figure 5.5 the steering system comprises 8 nozzles, which are aligned to provide thrust either in roll, yaw or pitch direction.

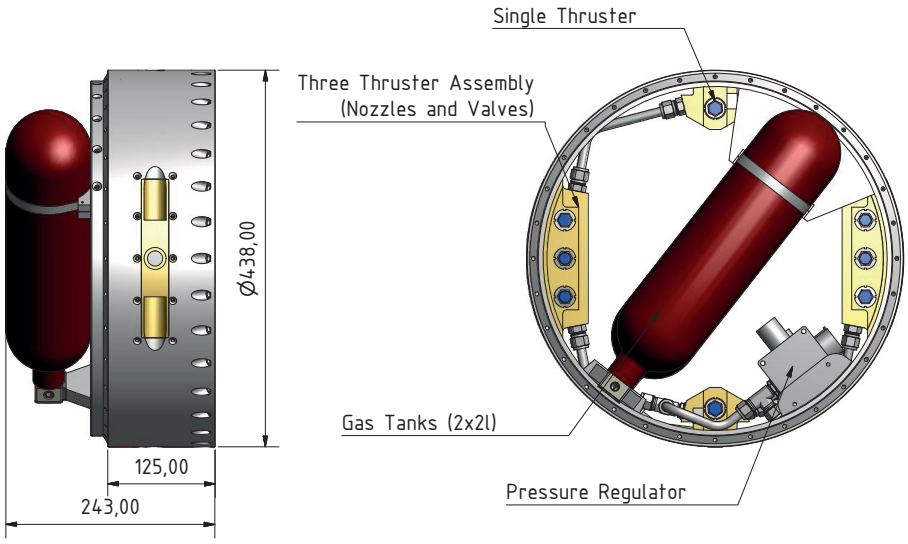


**Figure 5.5:** Attitude and rate control system

The nozzles will be supplied with gaseous Nitrogen by valves. The movement of the payload is controlled by the length of the thrust pulses. Overall the advanced ACS will be able to reduce the angular rates to $0.03\,^{\circ}/\mathrm{s}$ during microgravity phase and control the attitude with an accuracy of $0.1^{\circ}$.

## 5.4 European Recovery System (ERS)

The European Recovery System (ERS) is mounted to the upper end of the MAIUS vehicle. It consists of two parts: the upper and the lower nose cone as shown in figure 5.6.

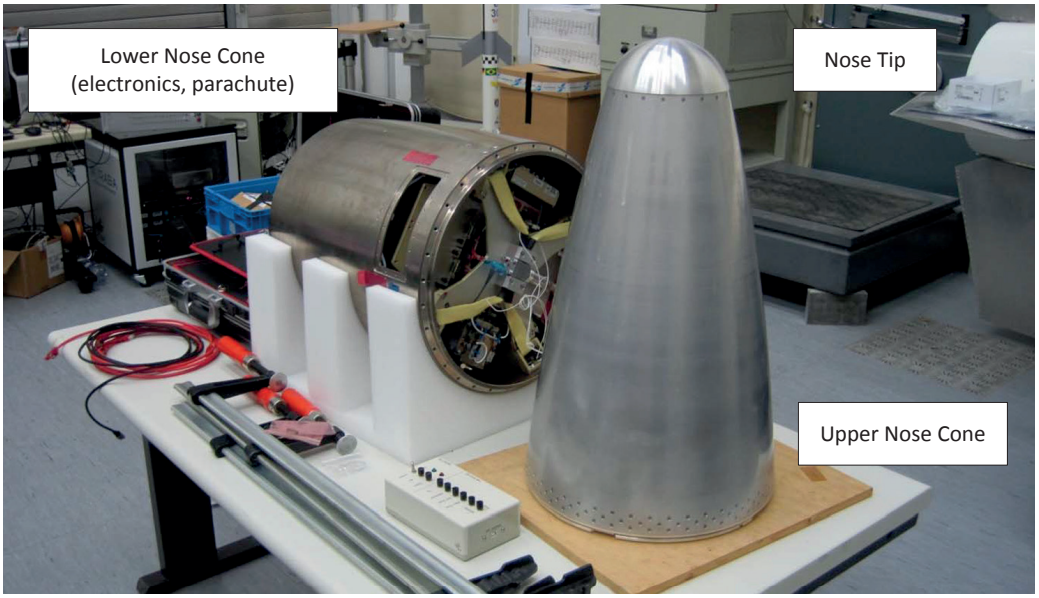


**Figure 5.6:** European Recovery System (ERS) [Sta12]

The outer structure of the upper nosecone is made of AlMg1 aluminium alloy with an average wall thickness of 2.25 mm. The cone radius is 3922 mm and the nose tip radius 110 mm. For heat protection the complete upper nosecone is coated with a cork heat shield Airbus Defence and Space NORCOAT HPK, which is protecting the structure from the high thermal loads during ascent.

At an altitude of 70 km, when the ascent through the lower atmosphere has been completed, the upper nose cone is detached from the vehicle by releasing the manacle ring. After release the upper nose cone is ejected from the vehicle by pyrotechnically actuated plungers.

Below the upper nose cone at the top of the lower part of the recovery system a second heat shield will protect the parachute from hot gases during re-entry. The hull of the lower nose cone is made of an 6 mm nickle-coated aluminum alloy. It accommodates the parachute recovery system, two redundant battery packs to supply the ERS and a set of electronics in the back of the lower nose cone. This electronic includes a barometric system for determination of the vehicle altitude, the ignition unit for the pyro actuators and acceleration sensitive g-switches as well as a lift-off switch for system initialization. The parachute will be activated at an altitude of about 4.6 km and will decrease the descent velocity to about $8\,\mathrm{m\,s^{-1}}$ to $10\,\mathrm{m\,s^{-1}}$.

## 5.5 Time Event List of MAIUS-1

The time event list given in table 5.2 is summarizing all major flight events during the MAIUS-1 mission. For simplicity some of those are also visualized in figure 5.7

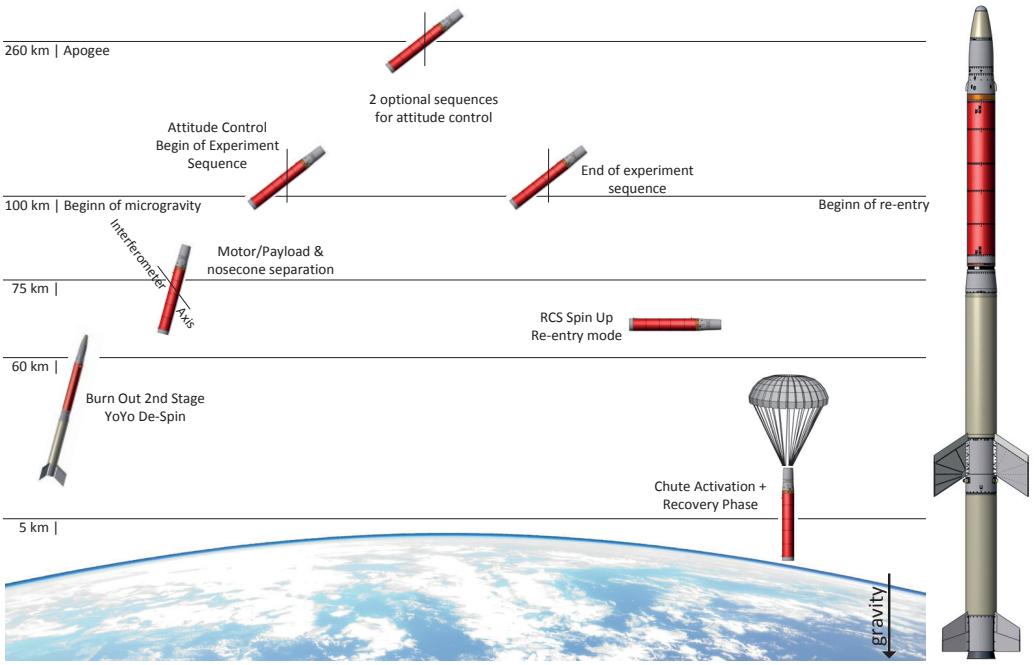


**Figure 5.7:** Illustration of flight events during MAIUS-1 mission. The payload is orientated along earth's gravity vector during the microgravity phase.

On the right hand side of figure 5.7 the launch configuration with the systems described in the section above is shown. This configuration will be maintained until the vehicle reaches an altitude of 4.3 km. At this time the first stage S30 motor will burn-out. Since there is no axial connection between the two stages (pin connection), the first stage will separate passively from the second stage and the payload due to the aerodynamic drag.

1.5 s after the burn out off the first stage second stage will be ignited. The second stage will lift the payload to 43.4 km in altitude. While the motor is still attached to the payload, the YoYo-despin will be carried out at an predicted altitude of 64.9 km. The nosecone will be separated from the payload shortly after the de-spin is completed. Subsequently the burned-out motor will be separated from the payload, which will continue its ballistic trajectory as shown in figure 5.7.

Next the attitude control system (ACS) will minimize the remaining spin of the rocket to $0.03\,^{\circ}\,\mathrm{s}^{-1}$. Simultaneousley the ACS will acquire the desired attitude of the vehicle. To be able to perform measurements for testing the weak equivalence principle or measurements of earth gravity field, the interferometer axis will be aligned to the gravity vector of the earth. Although this is not mandatory for the first flight, the attitude control should demonstrate its accuracy in MAIUS-1.

| No. | Time | Altitude [km] | Event |
|---|---|---|---|
| 1 | T-120 min | 0.33 | P/L Checkout |
| 2 | T-25 min | 0.33 | Possible Hold |
| 3 | T-25 min | 0.33 | Switch from Hardline to RF |
| 4 | T- 5 min | 0.33 | Switch to internal power supply |
| 5 | T- 5 min | 0.33 | Quantus Switch to internal power |
| 6 | T+ 0.0 | 0.33 | Lift-Off |
| 7 | T+ 0.0 | 0.33 | Quantus LO (Signal and Bit) |
| 8 | T+ 13.5 | 4.30 | Burnout 1st Stage (S31) |
| 9 | T+ 15.0 | 5.00 | Ignition 2nd Stage (S30) |
| 10 | T+ 44.0 | 43.40 | Burnout 2nd Stage (S30) |
| 11 | T+ 55.0 | 64.90 | YoYo De-spin |
| 12 | T+ 56.0 | 66.79 | GPS Antenna Switch |
| 13 | T+ 58.0 | 70.56 | Nosecone Separation |
| 14 | T+ 60.0 | 74.29 | Motor/PL Separation |
| 15 | T+ 61.0 | | MAIUS ACS On (Bit) |
| 16 | T+ 75.0 | 101.02 | Begin of microgravity phase |
| 17 | T+ 91.0 | | MAIUS ACS Off (Bit) |
| 18 | T+ 180.0 | | MAIUS ACS On (Bit) |
| 19 | T+ 190.0 | | MAIUS ACS Off (Bit) |
| 20 | T+ 260.0 | 258.30 | Apogee |
| 21 | T+ 300.0 | | MAIUS ACS On (Bit) |
| 22 | T+ 310.0 | | MAIUS ACS Off (Bit) |
| 23 | T+ 446.0 | 100.00 | Begin of Atmospheric Re-entry |
| 24 | T+ 448.0 | 97.40 | RCS Re-Entry Detection Mode |
| 25 | T+ 468.0 | 60.93 | Re-Entry Mode, Spin-Up by RCS |
| 26 | T+ 487.0 | 27.00 | Maximum Deceleration |
| 27 | | 4.70 | Heat shield, Stab Chute & Beacon Activation |
| 28 | | 3.9 | Stab Chute De-Reefing |
| 29 | | 2.9 | Main Chute Activation |
| 30 | | 1.7 | Main Chute De-Reefing |
| 31 | T+ 900.0 | | Power Off for Experiments |
| 32 | T+1000.0 | | Power Off TM/TV |

**Table 5.2:** MAIUS-1 time event list

For the following 355 s different experiment sequences will be run autonomous as described in section 6.3. In between there are two time frames of 10 s foreseen to correct the attitude and the rates of the payload if necessary. One of which is before the apogee at the ascent and one at the descent. At an altitude of 100 km, the experiment and microgravity phase will end and the payload will be aligned with the vertical axis parallel to the atmosphere.

Afterwards the payload will switch into re-entry mode. The rate control system will spin up the payload to distribute the thermal loads during re-entry equally over the hull surface. At an altitude of approximately 5 km the stab parachute will be activated. The stab chute activation will be followed by the main parachute activation at an altitude of roughly 3 km. The main parachute will return the payload safely to the ground. This last phase of the flight is called recovery phase.

The mechanical, thermal and magnetic environment related to the flight events described above will be discussed in the following section. This will characterize the environment aboard the sounding rocket. In combination with the requirements given in section 6 these represent the necessary information for the design of the payload.

## 5.6 Mechanical Environment

The vibrations and accelerations acting on the payload are the major factor of influence on the mechanical design. Unfortunately the mass of the payload will influence the actual mechanical environment. In the following predictions and estimates of the rates, vibrations and accelerations for a payload of 400 kg shall be discussed.

### 5.6.1 Ascent

It is important that the instruments will have full functionality after the occurrence of accelerations, otherwise no scientific output will be generated and the mission has to be considered a failure. In the following the expected mechanical loads due to motor burn or spin are summarized.

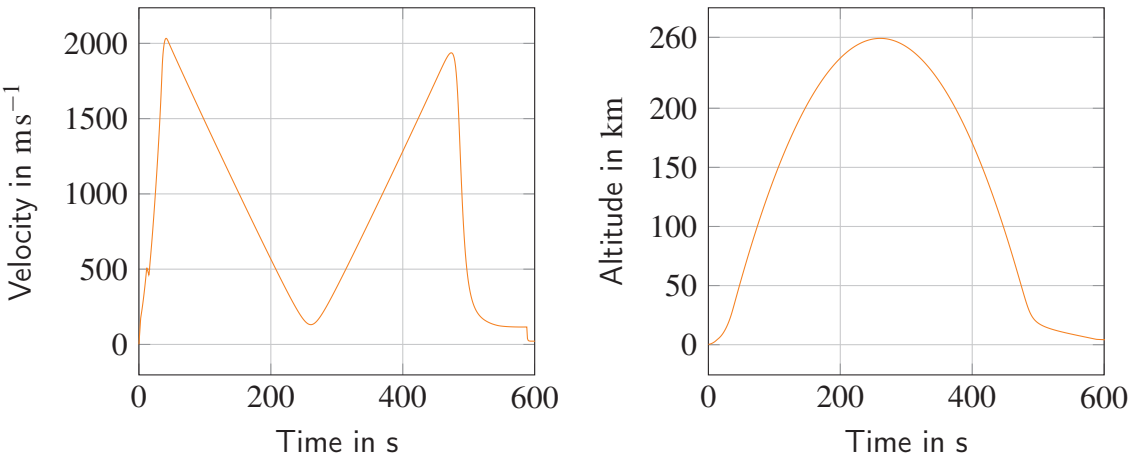


**(a)** Predicted velocity of MAIUS-1. The peak velocity is going to be 2033 m s$^{-1}$ at 41 s after launch.

**(b)** Predicted altitude of MAIUS-1. The apogee is expected to be 260 km and is reached 260 s after lift-off.

**Figure 5.8:** Predicted trajectory and velocity of MAIUS-1

Figure 5.8a shows the nominal trajectory for the MAIUS-1 flight. At a mass of 400 kg the vehicle is predicted to achieve an altitude of 260 km, which equates to a microgravity time of 355 s above 100 km.

The velocities and accelerations on this trajectory are presented in figure 5.8b and 5.9. Motor ignition will generate shock loads of approximately 20 g acting on the payload for 15 ms [Sch]. The rocket will accelerate from zero to MACH 1 within 7.9 s. The maximal velocity of 2033 m s$^{-1}$ will be reached after just 41 s in an altitude of 38.3 km. Respectively the accelerations caused by the rocket motor are strong. The gap after 10 s of flight represents the separation of first and second stage. The peak acceleration is marked in figure 5.9b with 12.4 g. It will be reached after 35 s and represents a critical phase, since the loads acting on the payload will reach its maximum before experiment operation.

While figure 5.9b shows the predicted steady accelerations, figure 5.9a presents the vibrations recorded during the test flight of the VSB-30. The vibration loads inside the payload were measured by a hard mounted 3 axis accelerometer, with a measurement range from 15 Hz to 10000 Hz. The accelerometer was attached to the deck of the instrumentation module used in the test flight.

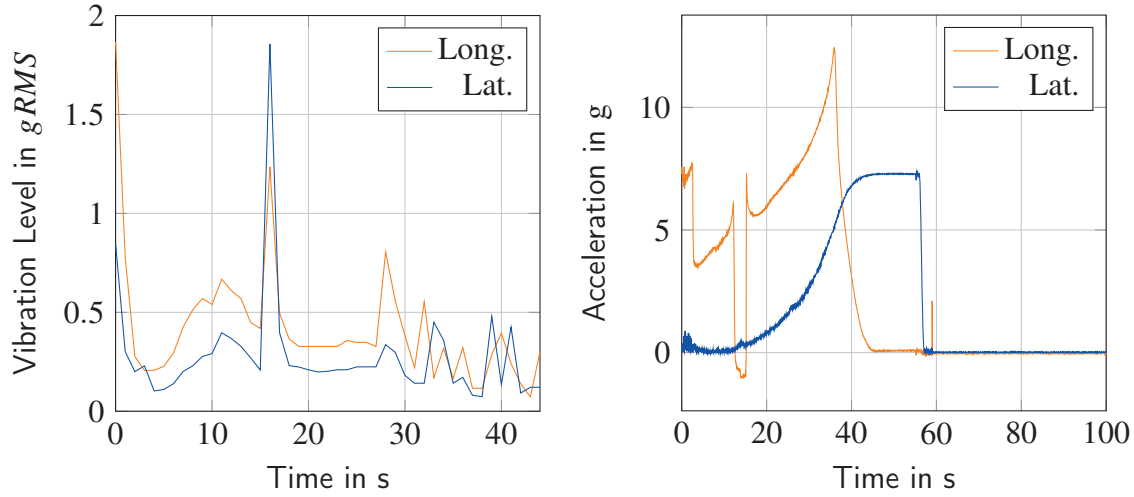


**(a)** Longitudinal and lateral vibrations measured on VSB30 test flight [Sch]. Peak accelerations in both direction is 1.8 $g_{rms}$ (longitudinal at lift off and lateral at 16 s respectively

**(b)** Measured longitudinal and lateral accelerations of TEXUS-44 during ascent. The peak acceleration along the long. z-axis is 12.4 g at 36 s

**Figure 5.9:** Measured vibrations accelerations during ascent

The data has been evaluated for 15 Hz and 2000 Hz, calculating the root mean square (RMS) in this frequency range in slices of 1 second. The maintained data points for the vibration root mean square are plotted over the flight time in figure 5.9a. The results show that the integrated RMS value does not exceed 2 $g_{rms}$, which is significantly below the test parameters as presented in section 8.

Aside from vibrations and accelerations, the rotation of the payload, which is induced by the fins and the spin up motors will add up to the total loads during ascent. As illustrated in figure 5.9b the maximum lateral acceleration is caused by the rotation around the z-axis. The rate will be 2.71 Hz and will be reached roughly 40 s after lift-off.

The rocket hull has a diameter of 500 mm and a wall thickness of 5 mm. Thus the maximum centrifugal acceleration inside the payload can be calculated from

$$a_{cent} = \omega^2 r \tag{5.1}$$

With a given radius from 0.245 m and a spin rate of 2.71 Hz the maximum acceleration is 71.05 $\mathrm{m\,s^{-2}}$ or 7.24 g. Other than the accelerations caused by the motor, these loads act radial to the payload, which has to be considered in the design phase of the payload. Table 5.3 summarizes all loads applicable for the design and qualification of the experiment and the structural parts. The loads are given for the ascent as well as for the descent loads described in the following chapter.

| Event | Begin | Duration | level |
|---|---|---|---|
| Motor ignition | 0 | Shock ( 15ms) | 20g |
| Motor acceleration (DC) | 0 | < 44s | max. 12.4g |
| Motor acceleration (AC) | 0 | < 44s | < 2g RMS |
| Spin | 0 | < 55s | max. 7.24g |
| Re-entry | 480 | < 40s | 20-25g |
| Touch down | 0 | Shock ( 15ms) | 100-200g |

**Table 5.3:** Overview on loads during ascent and descent

### 5.6.2 Descent

Most experiments want to use their hardware for multiple missions. So does the MAIUS experiment. Although the mission might be considered successful when the experiments have been carried out and the data has been sent to the ground, a safe return of the instruments is desirable. Therefore the experiment and especially the mounting has to be designed to withstands loads of the re-entry as well.

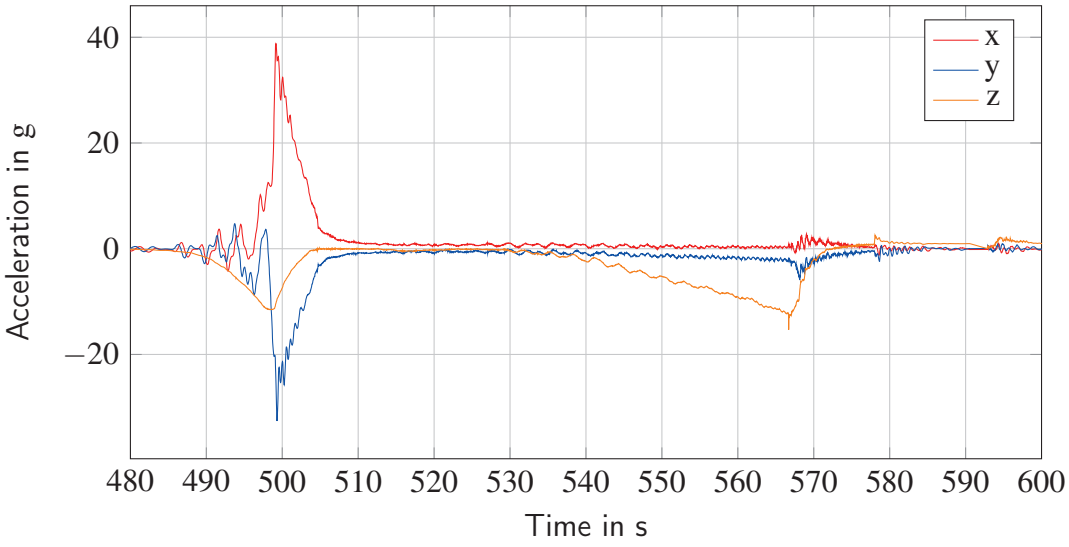


**Figure 5.10:** Deceleration during Re-entry of TEXUS 44

Unfortunately there is no prediction of the loads for the MAIUS vehicle during re-entry available. Figure 5.10 displays the loads of the re-entry of the TEXUS 42 mission. The mission had a similar mass as the MAIUS payload. The accelerations have been recorded by the service module of the payload. As shown in the figure the loads are a factor 2 above those at ascent. Especially within the first seconds of re-entry the atmospheric friction will generate decelerations of 20 g to 25 g. Those occur along the lateral x-axis, since the payload will be aligned to enter the atmosphere with the roll axis perpendicular to the flight direction. Otherwise the aerodynamic drag would be significantly stronger. Shortly before re-entry the payload is spun up to distribute the thermal loads equally on the cylinder walls.

As shown in the graph the payload went into a rotation around the x-axis during re-entry. This phenomena is called flat spin. Between T+550s and T+590s, the flat spin rate in the lateral axes reached its peak value of 1.4 Hz. This flat spin caused a maximum centrifugal acceleration of 8 g in the roll axis. In an altitude of roughly 4 km to 5 km at the time T+590s the recovery phase was initiated by stab chute activation which is indicated by 2 strong deceleration peaks in z- and x-axis. During main chute activation two more peaks are recorded. Subsequently the measured accelerations stabilize at 1 g during descent at the main chute. At touch down a strong shock load of 50 g to 100 g [Sch] has to be expected.

## 5.7 Thermal Environment

### 5.7.1 Pre-flight

The integration of the modules and payload is done in an integration room at normal room temperature $20 \pm 5$ °C. When the integration is completed the payload transported to the Skylark launch tower. Inside the tower the payload will be mounted to the motors. The temperature in the launcher building is controlled to $17 \pm 7$ °C. The tower is a closed heated building, which protects the payload from the rough outside temperatures which can drop below $-40$ °C in winter. Shortly before launch the roof and the blast doors are opened and the ambient temperatures might decrease for a short period of time.

### 5.7.2 Flight

The service module of TEXUS 44 was equipped with four PT100 sensors installed on the inner side of the outer hull with an angular separation of 90°. The sensors accuracy is given by $\pm 1$ °C in the data-sheet. The measured data is shown in figure 5.11. Two of the sensors failed after 55 s and no more data was recorded.

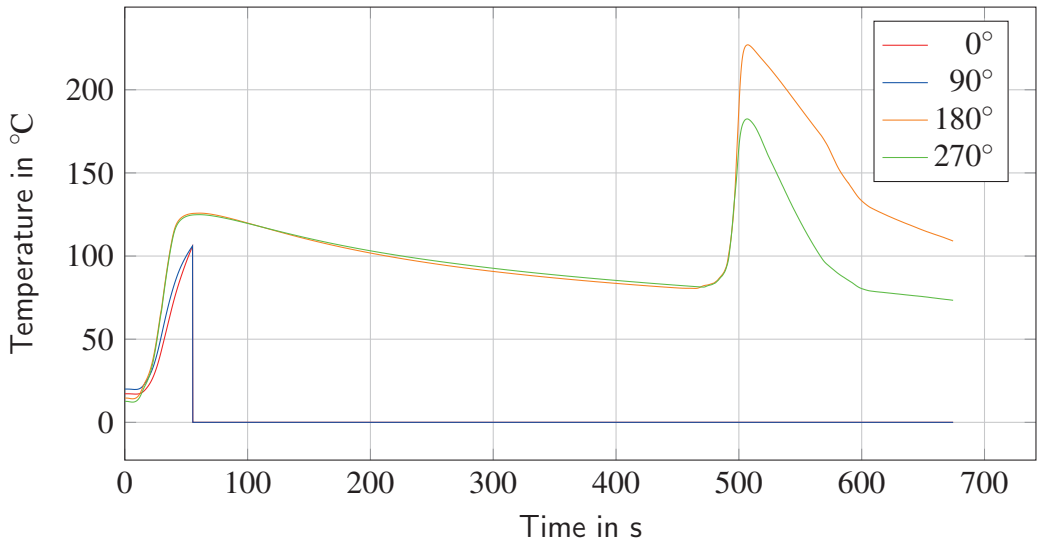


**Figure 5.11:** Temperatures during flight of TEXUS 44

The TEXUS 44 payload was heated during ascent by aerodynamic friction to roughly 100 °C. In chapter 10 the impact and prediction of aerothermal heating during ascent will be studied in more detail.

Within the microgravity phase the temperatures decreased due to radiation into space. During re-entry the hull elements were affected by aerothermal heating once more. Due to the new angle of attack and the absence of an ablative layer, the hull of the TEXUS service module was heated to more than 200 °C.

## 5.8 Magnetical Environment

### 5.8.1 Pre-flight

EGiS is an information service for data from Esrange's scientific instruments. This includes a magnetometer measuring the deviation of the earth magnetic field in North/South, East/West and Z directions.

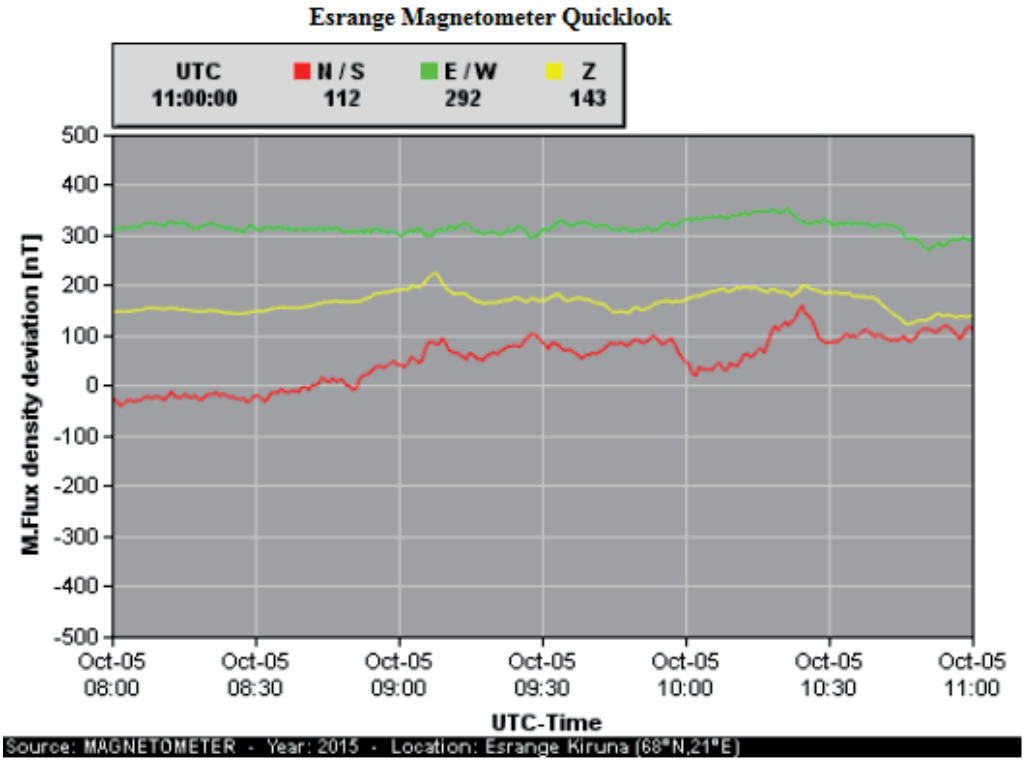


**Figure 5.12:** Magnetic field at Esrange obtained from EGiS database (http://egis.esrange.ssc.se/)

Figure 5.12 shows recorded data of the magnetic field at Esrange on October, 5th 2015 between 0800 and 1100 hours UTC. As depicted the magnetic environment only deviates in small amounts during a typical launch window (three hours). The deviations might be caused by the large iron ore deposits around the launch site. The strongest deviation recorded in this dataset 350 nT which equals 3.5 mG.

### 5.8.2 Flight

Aside from an accelerometer a three-axis magnetometer was mounted inside the TEXUS 42 service module. The data recorded by the magnetometer is shown in figure 5.13.

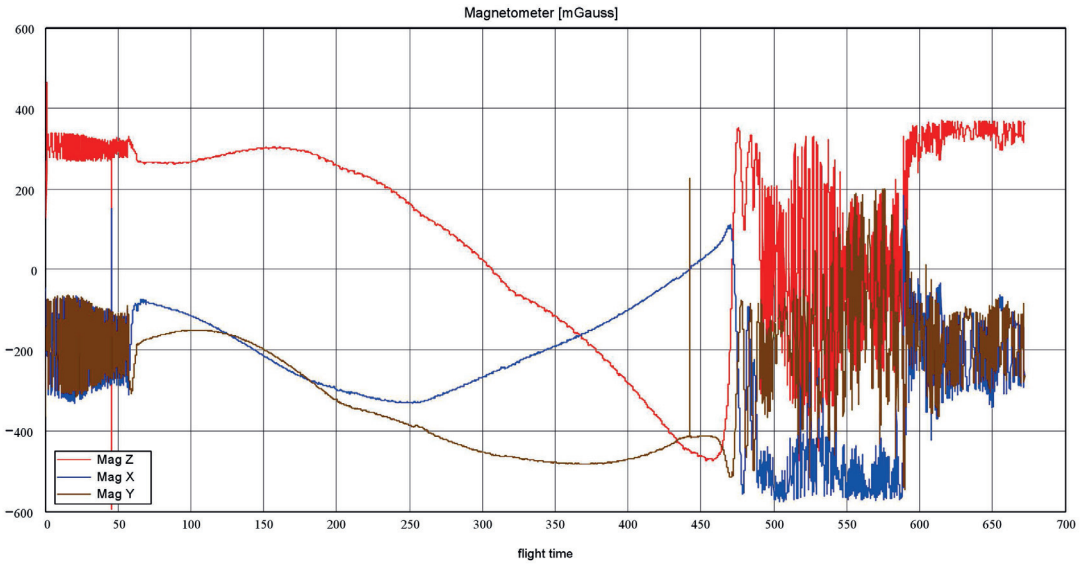


**Figure 5.13:** Magnetic fields during the flight of TEXUS-42 [Ett06b]

Since the orientation of the magnetometer inside the payload is fixed and the earth magnetic field vector does not vary, the spin between T0s and T+50s (ascent) and between T+480s and T670s (re-entry) of the vessel is recorded as pseudo high-frequency deviations. In reality the payload is moving (rotating) in an almost constant field.

During the microgravity phase (T+70s to T+480s) the payload performs a parabola as predicted in figure 5.8a, which influence the measurement of the local magnetic field. The field in z-direction will change its sign at the trajectory apogee. The lateral magnetic field deviations might be caused by slow rotations of the vehicle.

The maximum magnetic field variation of roughly 750mG has been recorded in z-direction (from 300 mG to $-450$ mG). Although the deviations represents the movement of the vehicle within earths magnetic field and no change of the field itself, the external fields at the BEC location will vary over time during flight. Since the MAIUS experiment is especially sensitive to such time varying magnetic fields, the shielding needs to be designed to protect the MOT chamber by minimizing residual fields in the surrounding of the atoms as presented in section 7.3.1.

# 6
# Payload Requirements

While chapter 1 presented how a BEC is achieved and what instruments are necessary to do so, this chapter will summarize the known requirements of the different (sub)systems of the scientific payload. Aside from mechanical, thermal and magnetic requirements, requirements addressing the payload orientation and thus the launcher are given herein.

Comparing these requirements with the given environment aboard the VSB30 sounding rocket as described in chapter 5, will give an estimate on the engineering effort necessary in design and characterization of the environment.

## 6.1 Coordinate Systems

There are only few requirements with respect to the operation or attitude control. The most important requirement on the attitude control is the right alignment of the interferometry axis to the gravitational field of Earth. To define these requirements the coordinate system of the launcher (body frame coordinate system) and of the atom interferometer should be introduced in the following.

### 6.1.1 Body Frame Coordinate System

The body frame coordinate system (BF) is used to define the orientation of rocket components of the entire payload (including the MORABA systems) with respect to each other and to their environment (e.g. the launch tower). Thus this coordinate system is important to guarantee a proper assembly of all payload components.

Moreover it is the coordinate system used by the attitude control and service system. Thus flight parameters like acceleration and rotation rates are given with respect to this axis definition. However the measurements of the MAIUS atom interferometer are performed in a different coordinate system as described in section 6.1.2.

The coordinate system is defined by certain components of the rocket. The origin of the system is located at the interface between the motor adapter and the payload on the cylinder axis of the vehicle. The cylinder (longitudinal) axis is the roll-axis $z_{BF}$ pointing towards the rocket nose cone. The position of the rocket motor fins dictate the pointing of the pitch-axis $x_{BF}$. This axis is aligned to the 0°-fin as shown in figure 6.1b.

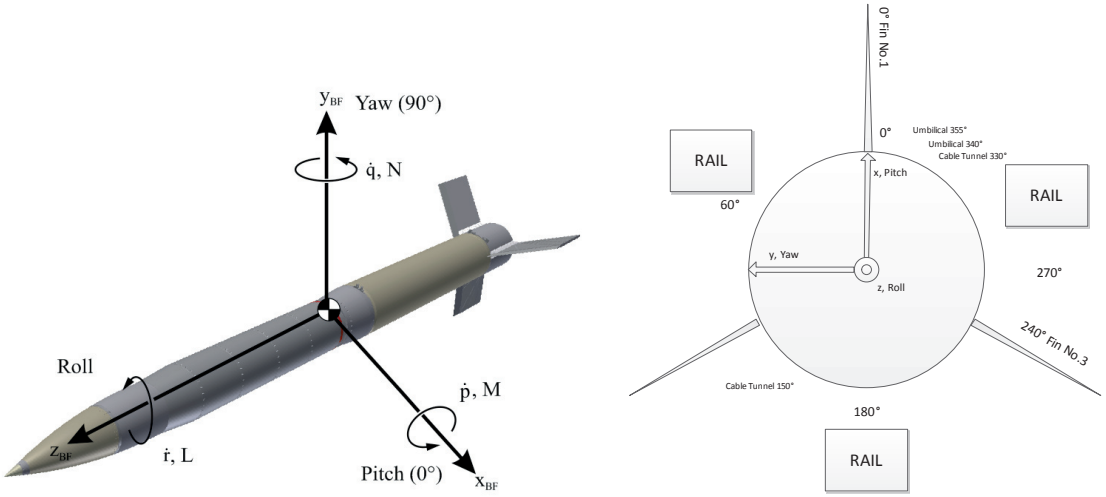


**(a)** Nomenclature of axes, angular velocities and roll-momentums

**(b)** Coordinate system orientation with respect to fins and launch tower rails

**Figure 6.1:** MAIUS bodyframe coordinate system

The yaw-axis $y_{BF}$ is completing a right-hand coordinate system. The associated angle velocities in the BF-system are named $\dot{p}$, $\dot{q}$ , $\dot{r}$ as shown in figure 6.1a. The same applies to the roll-momentum $L$, the pitch-momentum $M$ and the yaw-momentum $N$.

All drawings of the MAIUS systems and components respect these axis definition and are clearly indicating the position or orientation of each component. Thus also the orientation of external components as umbilical ports or hatches is defined and it is ensured that these can be accessed once payload and motor are assembled in the launch tower.

The umbilical ports of the MAIUS payload are located at 355° and 340°, while the hatch has been placed on the opposite site, with its symmetric line at 120°. All features help to identify the axis orientation. In addition to this a "0°-mark" has been engraved on each structure elements of the MAIUS payload indicating the x-axis alignment.

### 6.1.2 Experiment Coordinate System

As previously mentioned the measurements of the atom interferometer are performed in a different coordinate system. This system is defined by the atom chip and the magneto-optical setup of the MAIUS payload.

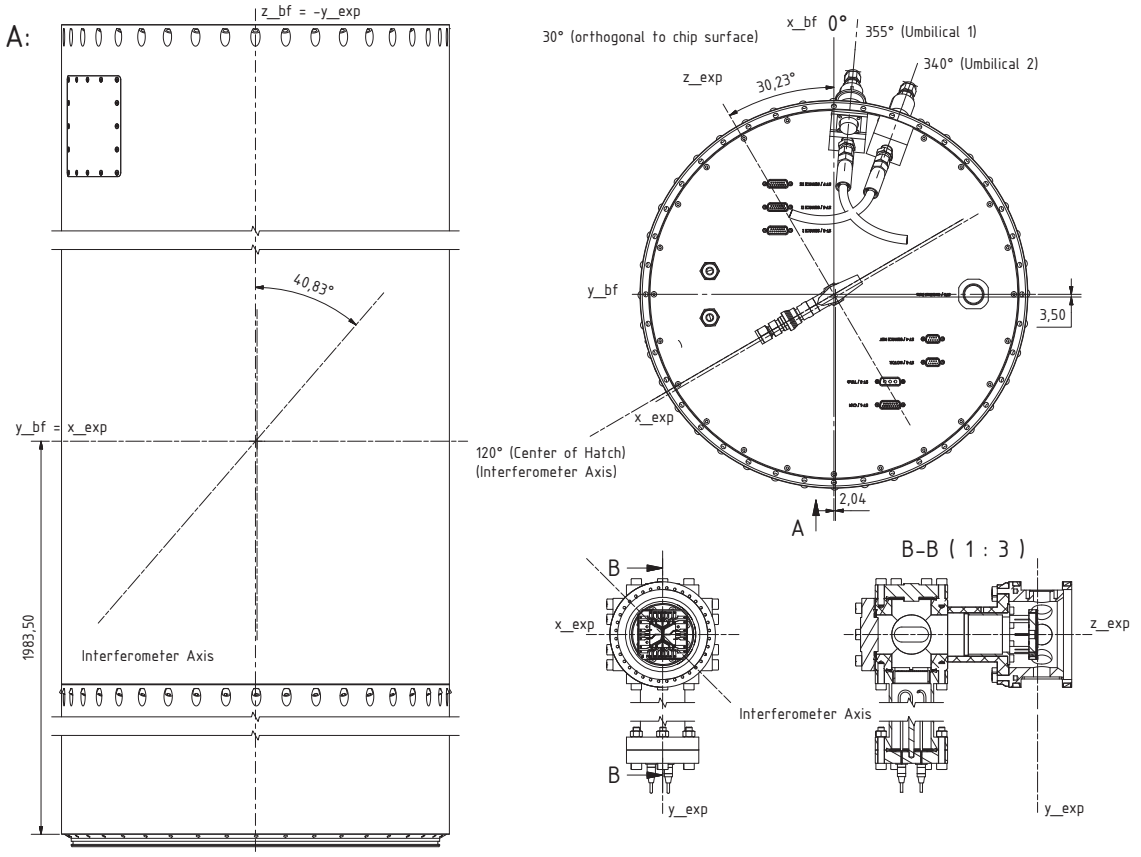


**Figure 6.2:** Drawing of the MAIUS-1 scientific payload and atom chip with bodyframe and experiment coordinate system axes and orientation of interferometry axis

The origin of the experiment coordinate system is defined to be in the center of the atom chip on the surface of the upper (mirror) layer. As illustrated in drawing 6.2 the $z_{exp}$-axis is pointing away from the chip surface. This axis is rotated by 30.23° to the $x_{bf}$-axis as defined in section 6.1.1. The $y_{exp}$-axis is pointing towards the rocket motor. Thus it is opposing the $z_{bf}$-axis. The $x_{exp}$-axis is completing a right-hand coordinate system.

Although the experiment chamber is aligned to have its center in the cylinder axis of the payload, the atom chip surface is not positioned in the center of the chamber, since this is the place were the atom ensemble should be. Thus the origin of the experiment system is shifted with respect to the origin of the bodyframe system in all three dimensions. The position of the origin of the experiment system in body frame coordinates is $x_0^{bf} = -3.50$, $y_0^{bf} = -2.04$ and $z_0^{bf} = 2153.50$.

## 6.2 Operational Requirements

The MAIUS mission is expecting 360 s of micro gravity, if the scientific payload mass will not exceed 280 kg. Although the MAIUS-1 mission is considered a technology demonstrator and no measurement campaign, it is essential to proof the feasibility of a precise alignment of the interferometer axis to the local gravity vector of Earth.

Figure 6.2 does not only show the different coordinate system axis, but also the interferometer axis as it is aligned in MAIUS-1. With the given angles the vector of the interferometer axis is defined to be

$$\vec{M} = \begin{pmatrix} \sin(40.83)\cos(59.77) \\ \sin(40.83)\sin(59.77) \\ \cos(40.83) \end{pmatrix} = \begin{pmatrix} 0.3292 \\ 0.5649 \\ 0.7567 \end{pmatrix} \tag{6.1}$$

in body frame coordinates. With a known position of the payload an alignment of this vector can be achieved with the attitude control system.

The required accuracy of the axis alignment and residual angular rates strongly depending on the interferometer scheme. A five-pulse-interferometer scheme will allow to perform long-time interferometry at rotation rates as high as $0.3°/s$ ($0.005\ rad/s$) [Sei14]. Unfortunately this scheme is insensitive to acceleration. Thus it is not suitable to measure earth gravitational field or carry out investigations on the universality of free fall. For this reason the alignment accuracy is not a limiting factor for performance of the experiment.

Measurements to e.g. determine the local gravitation acceleration would require a Mach-Zehnder interferometer scheme, which is not only sensitive to accelerations, but also to rotations. Thus the rotation rates of the payload would need to be reduced to $1 \times 10^{-5}\ rad/s$ for a pules separation time $T$ of 5 s [Sei14]. This is hard to achieve on a sounding rocket, thus MAIUS-1 will only be able to achieve significantly smaller pulse separation times in the order of $T = 50$ ms.

According to MORABA the alignment of this vector to the local gravity vector can be achieved with an accuracy of $\pm 1°$., which is sufficient for experiments planned in MAIUS-1. The alignment should be demonstrated in the first flight of the MAIUS payload by performing one attitude acquisition at T+61s. The attitude will not be controlled during microgravity phase.

As stated above residual angular rates are required to be below $0.3°/s$. Thus the threshold of the rate control system is set accordingly. In former flights the cold gas system had to be activated at least once to correct the rates. Thus two slots for correction of the angular rates are foreseen in the MAIUS-1 experiment sequence as listed in table 6.1.

## 6.3 Experimental Sequence of MAIUS-1

Within the MAIUS-1 mission a complex set of experiments has to be performed. Due to the lack of gravity the optimal experiment or sequence parameters (e.g. the evaporation end-frequency), which have been determined on ground might change. To produce good and reliable results these parameters have to be optimized for microgravity in flight. For this purpose the complexity of the sequences will be increased step-wise as listed in table 6.1.

This table serves as a guideline, in order to estimate the repetitions and time necessary to optimize the parameters starting from the lab-optima. A sequence player developed by the German Aerospace Center Brunswick will run the sequences and decide autonomously from the measured data how to proceed. Thus the actual duration and repetitions of some steps might differ from what is stated here.

| Time | Duration | Rep. | Event |
|---|---|---|---|
| T+ 0.0 | | | Lift-Off |
| T+ 55.0 | | | YoYo De-spin |
| T+ 60.0 | | | Motor/PL Separation |
| T+ 61.0 | | | MAIUS ACS On (Bit) |
| T+ 75.0 | | | Begin of microgravity phase |
| T+ 91.0 | | | MAIUS ACS Off (Bit) |
| T+ 92.0 | 1.06 | 15 | Optimization molasses |
| T+ 107.9 | 1.11 | 5 | Optimization transfer to magn. trap |
| T+ 113.5 | 3.11 | 5 | Optimization evaporation |
| T+ 129.0 | 3.15 | 5 | Optimization decompr. of trap / DKC |
| T+ 144.8 | 3.15 | 5 | Determine trap frequencies |
| T+ 160.5 | 3.11 | 5 | Optimization ARP |
| T+ 180.0 | | | MAIUS ACS On (Bit) |
| T+ 190.0 | | | MAIUS ACS Off (Bit) |
| T+ 191.0 | 3.11 - 3.6 | 17 | BEC TOF 10 ms to 500 ms |
| T+ 260.0 | | | Apogee |
| T+ 191.0 | 3.7 - 4.1 | 17 | BEC TOF 600 ms to 1000 ms |
| T+ 300.0 | | | MAIUS ACS On (Bit) |
| T+ 310.0 | | | MAIUS ACS Off (Bit) |
| T+ 311.0 | 3.11 - 4.6 | 34 | Atom Interferometry T 10 ms to 1500 ms |
| T+ 446.0 | | | Begin of Atmospheric Re-entry |

**Table 6.1:** MAIUS-1 proposed experiment sequence

Nevertheless the optimization steps remain the same. At the beginning the atom number in the magneto-optical trap and the temperature of the optical molasses (sub-doppler cooling) described in section 1.2.1 and 1.2.2 has to be optimized.

Once a certain threshold is achieved the algorithm will proceed to optimize the transfer into the magnetic trap to prepare the atoms for evaporation. Subsequently the evaporation itself will be optimized to achieve an optimal number of atoms in the BEC.

The evaporation is followed by a the decompression of the trap to reduce the expansion rates of the BEC. The optimization of this process will ensure that the expansion rate of the produced BEC is minimized and the reduction of the atom losses in this phase. This will allow long times of flight (TOF). Delta kick cooling as described in section 1.3 will also be applied to reduce the expansion rate furthermore.

The optimization of the adiabatic rapid passage (ARP) will result in BECs with high number of atoms in a magnetically insensitive state. This is important to supress the influence of residual magnetic fields on the experiment. This is the last step before the BEC observation or atom interferometry will be performed.

Within the experiment sequence two rate and attitude control (ACS) slots are foreseen. Within this 10 s interval the ACS will check whether the payload rates exceed the control threshold. If this applies the ACS will reduce the rates with the cold gas steering system. Otherwise the experiment sequence will be continued immediately. The experiment sequence aims at completing the preparation steps towards an optimized BEC before the first ACS-slot, which will start at T+180s.

After this slot the BEC will be observed for a time of free expansion which is increased in small steps from 10 ms to 1000 ms. This will allow to study the impact of the environment on the BEC and its behavior. This is important to validate simulations and to identify possible sources of disturbances. Both will help to optimize the performance in future missions.

Finally atom interferometry will be performed in a five-pulse-scheme, which will allow long interferometer times and in a Mach-Zehnder scheme to measure e.g the residual rotation of the sounding rocket. For both interferometer schemes the pulse separation times will be increased stepwise aiming at times of up to 2000 ms. However it is the objective to gain knowledge on the behavior of an atom interferometer in space and on the influence of this environment on experimental parameters. This will help to prepare future missions in Space.

## 6.4 Mechanical Requirements

In the following the mechanical requirements of the different (sub)systems are summarized. Most of the components used within this payload are customized or designed for laboratory use. These components have not been qualified for the use under vibrational load and no requirements with respect to vibrational loads or static accelerations are given.

For this reason the general approach is to qualify every critical component of the MAIUS-1 payload with an individual vibration test. The component level tests have been performed at frequencies between 20 Hz to 2000 Hz with an intensity of 8.1 $g_{rms}$ hard-mounted to the shaker as described in section 8. Moreover, a vibration test at 5.4 $g_{rms}$ has been carried out with each subsystem of the scientific payload. Thus all components are tested to at least 5.4 $g_{rms}$, which is already above the expected levels of $< 3$ $g_{rms}$ given in section 5.6.

Aside from vibrations, strong acceleration are expected during the sounding rocket flight. Thus all parts of the experiment should be designed to withstand accelerations of at least 13 g. This is the expected level of accelerations during ascent of the rocket (refer section 5.6.1).

| Component | Vibrational loads | Acceleration level |
|---|---|---|
| Critical components | 8.1 $g_{rms}$ | 13 g |
| Structure and housing elements | 8.1 $g_{rms}$ | 50 g |
| Suspension and hull segments | 8.1 $g_{rms}$ | 100 g |
| All other components | 5.4 $g_{rms}$ | 13 g |

**Table 6.2:** MAIUS-1 mechanical requirements of components

Moreover all structural components are designed to withstand at least 50 g, which is a load that the payload is exposed to in a typical touch-down scenario. The suspension connecting the hardware of scientific payload with the rocket hull and the segments themselves shall withstand accelerations of up to 100 g. This load is expected if the payload lands on rocky ground.

A design meeting the requirements above allows to re-use most of the hardware, even in the worst case scenario of landing on rocky ground. The design of the critical components is validated with detailed FEM simulations. The design of structure elements and system housing parts as well as the FEM analysis and tests of those parts is an important part of this thesis.

## 6.5 Thermal Requirements

Thermal requirements can be obtained from the data sheets or manuals of commercial components. Commonly an operating temperature range and a temperature range for storage is given in the operating conditions section of a manual. For the customized components the temperature requirements are discussed below. Aside from a required temperature range, a maximum temperature gradient during operation may be given as requirement.

| System / Component | Operating Temperature Min [°C] | Operating Temperature Max [°C] | Storage Temperature Min [°C] | Storage Temperature Max [°C] | ΔT [°C] |
|---|---|---|---|---|---|
| Physics Package | | | | | |
| Electronic Boards | 15 | 80 | -40 | 80 | - |
| Vacuum Chamber | 15 | 100 | 15 | 100 | 5 |
| Indium Seals | 10 | 100 | 10 | 100 | - |
| Laser System | | | | | |
| Laser Module DFB | ≈36 | | 15 | 70 | 0.1 |
| Laser Module ECDL | ≈36 | | 15 | 70 | 0.01 |
| Heat Sink | 26 | | - | - | 5 |
| Electronic System | | | | | |
| Electronic Boards | 15 | 80 | -40 | 80 | - |
| Coil Current Driver | 15 | 80 | -40 | 80 | 10 |
| LiFePO4 Cells | -30 | 55 | -40 | 60 | - |
| IDAN OBC | 15 | 80 | -55 | 125 | - |
| Batteries | | | | | |
| Electronic Boards | 15 | 80 | -40 | 80 | - |
| LiFePO4 Cells | -30 | 55 | -40 | 60 | - |

**Table 6.3:** MAIUS-1 thermal requirements of different payload systems and of some critical components. The exact laser module temperature varies for each laser module.

Table 6.3 summarizes the known requirements for some critical systems and their components. The operation and storage temperature of the electronic boards is limited by the melting point of the solder. The only exception is the chip and coil current driver. To avoid a thermal drift the card temperature shall not rise by more than 10 °C. The temperature requirements from the battery cells has been extracted from the cell data sheet.

The vacuum chamber temperature shall change by more than 5 °C during operation. This guarantees reproducible results of the experiment. Moreover the chamber temperature shall not exceed 100 °C to ensure the integrity of the indium seals, which melt at 156 °C.

The most sensitive components of the scientific payload are the laser modules. They have to be temperature stabilized to a temperature around 36 °C with an accuracy of 0.1 °C (DFB) or 0.01 °C (ECDL). The exact temperature differs from module to module due to temperature dependencies of the components of the laser. To allow the precise control of the laser module temperature, the laser heat sink has to be kept on a temperature of 26 °C and shall not rise by more than 5 °C.

To ensure a reliable operation of these components a thermal control system for the different systems of the MAIUS-1 payload is developed in this thesis. This system shall allow continuous operation on ground and autonomous operation for roughly 500 s during flight.

## 6.6 Other Requirements

Aside from operational, thermal and mechanical requirements, some other restrictions and requirements of the MAIUS-1 payload are given in this section.

### 6.6.1 Experiment Chamber Geometry

As stated in chapter 1 teh experimental performance is strongly depending on the geometry of the trap and thus also on the setup of coils and laser beams. Due to the limited time for design, production and optimization of the MAIUS-1 experiment it was determined that there should be no major changes in the chamber geometry of the 2D and 3D MOT compared to QUANTUS-2. Moreover the spacing between the different coils and their setup, as well as the beam setup should be adopted from QUANTUS-2. This will allow to benefit from the heritage of QUANTUS-2 in troubleshooting and also during optimization of the apparatus.

### 6.6.2 Magnetic Fields

As mentioned in chapter 1 the atoms are sensitive to magnetic fields if they are in a sublevel $m_f \neq 0$. In this case variations of the field of the magnetic trap may cause a loss of atoms or restrict the BEC quality. For this reason the intensity of the magnetic field variations should be $\Delta B(t) \leq 1\ mG$ [KL16]. With the given environmental conditions aboard the sounding rocket as defined in section 5.8 a maximum variation of $\Delta B(t)$ of 750 mg has to be expected. For this reason a magnetic shield with a shielding factor of at least 1000 is required [KL16] to provide some margin to the desired field strength of 1 mG.

For measurements of accelerations with an atom interferometer magnetic field gradients cause acceleration noise. For high precision measurement these gradients have to be reduced to values below $3\,\mu G/m$ [Agu14]. This does not apply for MAIUS, since no high-precision measurements are performed.

### 6.6.3 Payload Pressure

The laser system and the physics package require a stable and dry atmosphere inside the payload. The pressure should be kept between 0.8 bar and 1.1 bar during the entire flight. This prevents a change of the properties of the optical components and the chamber windows. Such a change might lead to lower optical power and thus a decrease in performance of the atom interferometer. Moreover this will allow to operate all lab equipment without qualification for the use in vacuum. Especially the laser modules would need to be qualified since they are very sensitive to changes in temperature and pressure.

# Part III

# Mechanical Design, Simulation and Testing

# 7
# Payload Setup and Mechanical Design

The MAIUS scientific payload outer hull consists of in five segments with an overall length of 2790 mm and a total weight of 280 kg. As shown in figure 7.1 the hull segments shelter five (sub)systems needed to perform atom interferometry. Each subsystem is mounted to an aluminum instrument platform, which is screwed to the rocket structure by mounting brackets equipped with rubber vibration dampers.

During flight the scientific payload will be sealed at the bottom and top and pressurized with artificial air at 1100 hPa to guarantee a stable pressure and defined atmosphere as required by the laser system and optics to maintain the optical properties of the components used in those systems during flight.

Inside the sealed area the physics package with the UHV pumping system and experiment chamber is situated at the top close to the center of gravity of the complete payload. The physics package consists of two platforms, which are suspended at the top and bottom as one unit. The pumping system is mounted to the upper side of the first platform. Between both platforms the experiment chamber, optics, two cameras and coils are placed inside a three layer magnetic shielding. Below the lower platform the laser system is mounted to ease the connection and routing of the optical fibers.

The electronics such as current drivers or temperature controllers are mounted to both sides of an individual platform below the laser system. The onboard computer is attached to the lower cover of the electronic housing. The platform at the bottom of the sealed area carries the batteries on the one side and the power distribution on the other. Both systems, as well as the laser system and electronics are suited into an individual housing and have been equipped with a thermal control system to meet the requirements listed above.

For transport the payload can be divided into two parts above the electronics section. The separation flange is marked with "S" in figure 7.1. The two parts of the scientific payload are stored and transported in custom-made flight cases in an upright position.

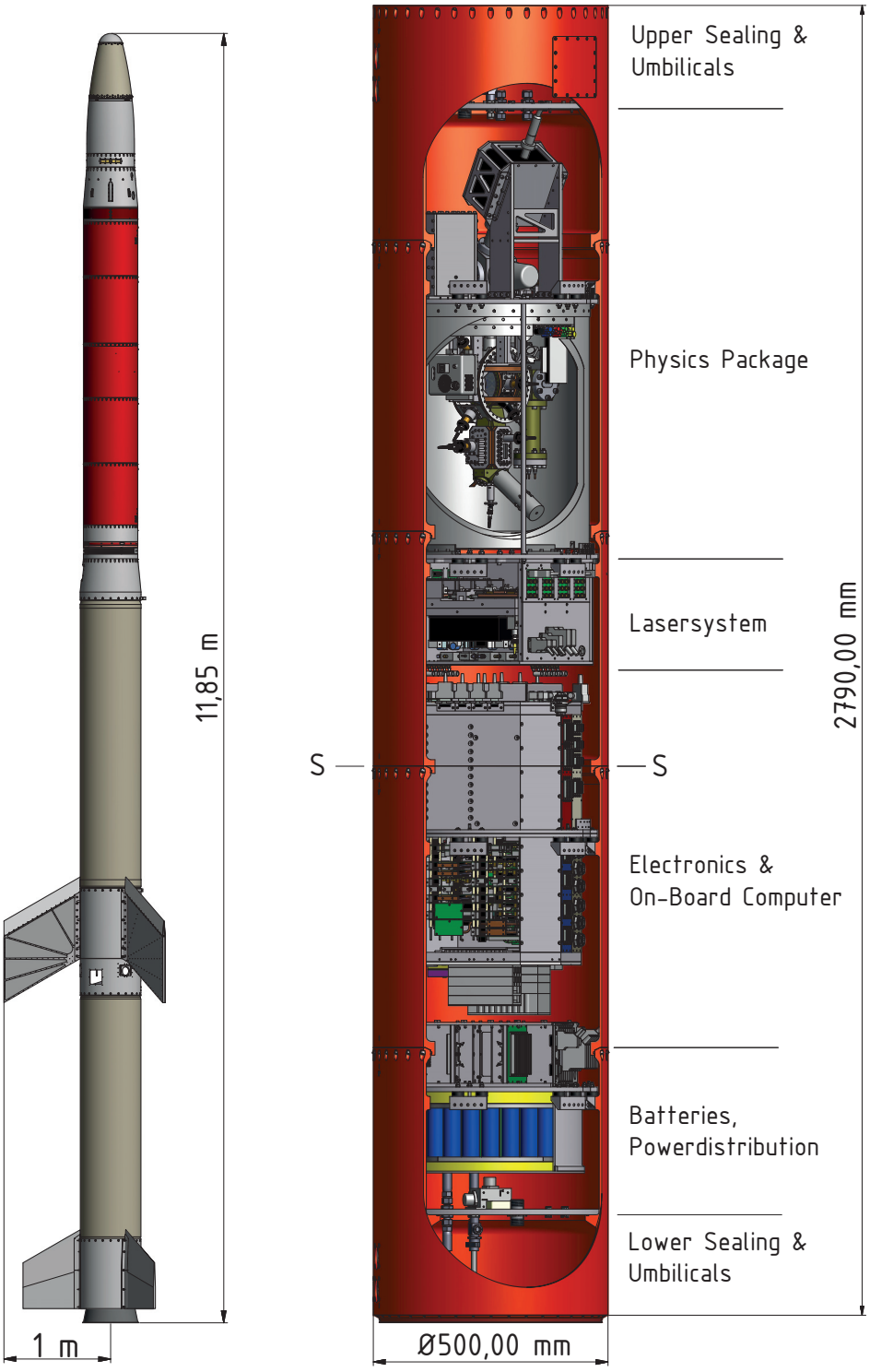


**Figure 7.1:** MAIUS-I vehicle consisting of VSB-30 motor, scientific payload and MORABA systems **(left)** and overview of scientific payload showing the (sub)systems described in the following sections and the separation flange marked with "S" **(right)**

The transport in an upright position should prevent sheer stress on the rubber vibrational dampers. The payload has been split into two parts, because this will allow using standard trucks as well as passing most doors in buildings, due to a package height below 2 m. Moreover the integration effort at Esrange and the risk of delays due to problems during integration is minimized by having just a few electric and only one mechanical connection to be re-assembled.

The mechanic and thermal design of the systems mentioned above, as well as the design of the MAIUS payload structure, sealing and harness is an essential part of this thesis and is described in the following pages.

Additional investigations have been carried out on testing, design and simulation of ultra high vacuum components and a low-cost vibration damping system. These systems, the developed simulation tools and the results of tests and simulations are presented in part III of this thesis. Moreover the characterization and simulation of the thermal environment aboard the payload during flight and the design of a suitable thermal control system for flight and laboratory operation will be discussed in part IV of the thesis.

## 7.1 Payload Structure and Sealing

As mentioned above, the payload consists of five segments which are meant to be kept under pressure during flight. In the following section the connection between the different hull segments, the sealing concept and the mounting of the different system platforms to the outer hull is described in detail. Moreover the concept for harness routing and the structural interface of the umbilicals shall be presented.

### 7.1.1 Outer Structure and RADAX Joints

The modules of the MAIUS scientific payload are 500 mm in diameter with a wall thickness of 5 mm. The increase of the wall thickness from standard 3 mm to 5 mm minimizes the impact of aerodynamic heating on the inside of the payload by increasing the thermal capacity of the outer structure. The impact of the wall thickness on the thermal behavior of the system is discussed in chapter 10 in more detail.

The length of the modules varies from 500 mm to 620 mm driven by the systems they are sheltering. All modules are made from aluminum EN AW 7020 (AlZn4,5Mg1) with a minimal yield strength of 275 $N/mm^2$ and a minimum specified tensile strength of 340 $N/mm^2$. Thus the material combines a low specific weight with a comparable high tensile strength.

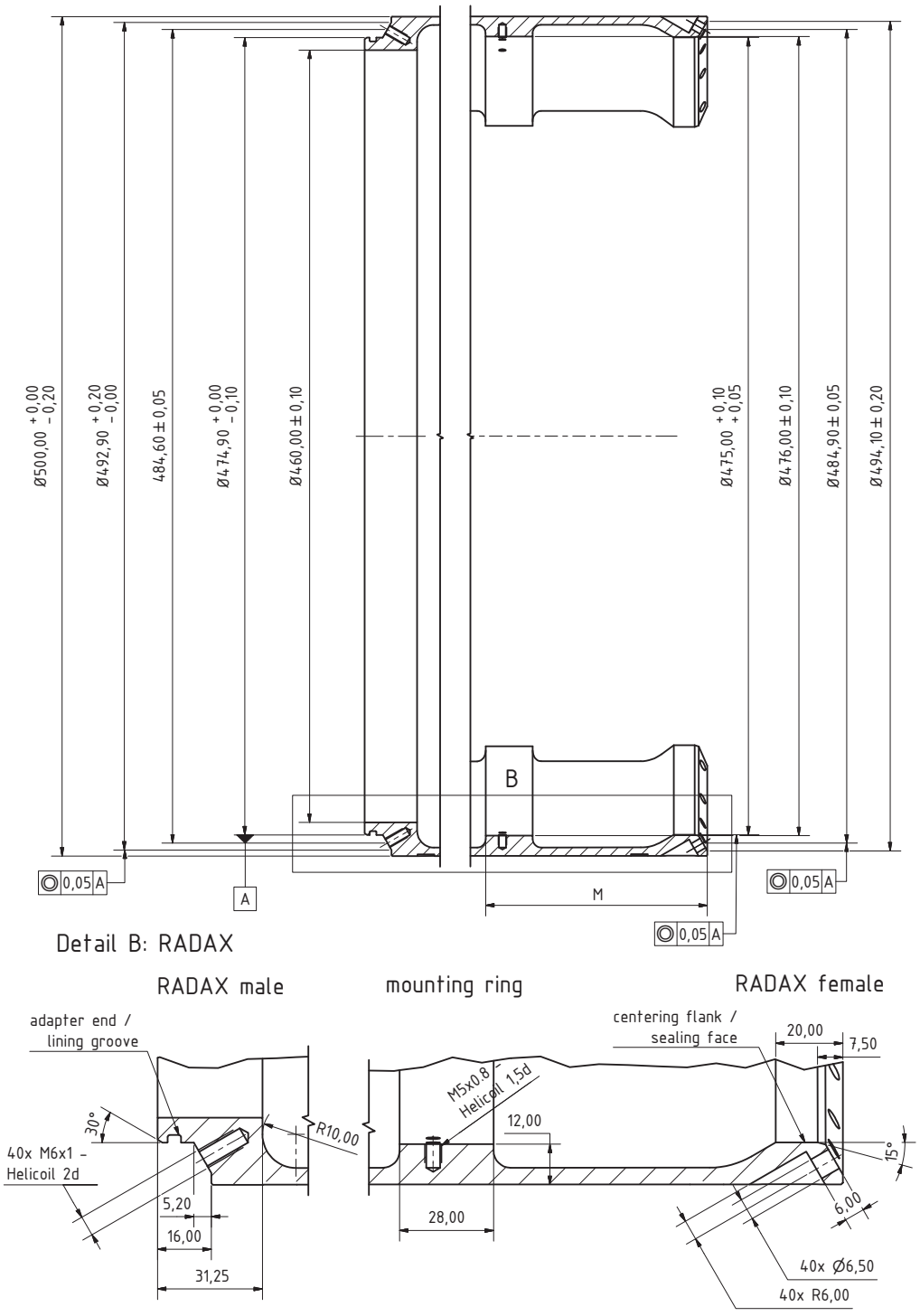


**Figure 7.2:** RADAX flange specifications for the MAIUS payload. A lining groove has been added for sealing purposes. Moreover the tolerances have been reduced to guarantee a proper sealing between the modules as discussed in the text.

The different hull segments are connected to each other by standardized RADAX-Flanges, which are used within several sounding rocket programs. *RADAX* is an abbreviation for *rad*ial-*ax*ial. The name derives from the screwing which is established by M6 screws applied radial under an angle of 60° to the module front edge as illustrated in detail B of figure 7.2.

Each hull segment is equipped with male and a female RADAX flange. The male flange provides M6x1 threads reinforced with steel Helicoils with a length of 2 x d (two times the diameter of the thread / 12 mm). The Helicoils strengthen the thread flanks in this connection, which is subject to high loads.

The female flange is equipped with countersink through holes according to DIN974-1 with a diameter of 6.5 mm. The number of screws is depending on the diameter of the modules. For 500 mm modules, as used in MAIUS, 40 screws are used. The threads have to be positioned with small tolerances as defined in drawing 7.2, to ensure a proper assembly of the hull segments.

The modules are assembled using screws made of stainless steel A2-80 with a tensile strength of 800 $N/mm^2$. These screws have to be torqued with 10 N m each. The modules are mounted from below with the female side facing upwards as shown in figure 7.1 to prevent the holes from pointing in flight direction for aerodynamic reasons.

The modules are centered with the cylindrical adapter end at the male flange as shown at the lower left in figure 7.2. For this reason the flank of the adapter end has to be concentric to 0.05 mm with the screwing circles and the associated centering flank of the female flange.

Since the modules have to be sealed and pressurized a lining groove is integrated into the adapter end. An O-ring will be used for sealing the gap between adapter end and the centering flank of the female flange of the next module. To ensure a proper sealing the dimensions and tolerances have been changed in comparison to the standard RADAX flanges. More details on the dimensioning of the lining grooves and the tolerances will be presented in section 7.1.3.

The instrument platforms carrying the (sub)systems are mounted to the hull segments by six mounting brackets, which will be described in subsection 7.1.2. Each hull module offers a mounting ring to attach these brackets to the hull segments. The dimension "M" defines the position of the platform within the module and is depending on the dimensions of the components mounted on the platforms.

At the ring the wall thickness has been increased to 12 mm as illustrated in figure 7.2, which allows applying radial threaded holes without breaking the sealing. The ring is equipped with a total of 36 (6 x 6) radial tapped blind holes, whose threads are strengthened by using Helicoils with a length of 1.5 x d (7.5 mm). Each bracket is mounted to this ring with five M5 screws. The sixth hole placed aside of each bracket, is a grounding point for electrical grounding of the instruments platform, which is isolated from the hull by the rubber mounts.

### 7.1.2 Suspension and Vibration Damping

As mentioned above the different (sub)systems are mounted to instrument platforms which are connected to the hull by brackets and a passive vibration damping to reduce (especially) vibrational loads with high frequencies. Each plate is mounted to the hull segment by a total of six brackets, each one equipped with two vibration dampers and a safety bolt as shown in figure 7.3.

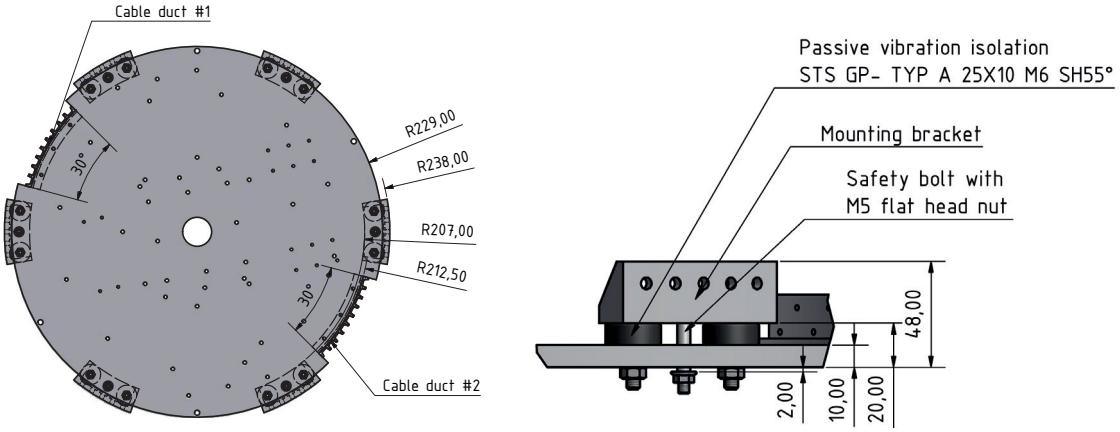


**(a)** System platform with vibration dampers and safety bolts

**(b)** Detail view on a mounting bracket with vibration damper and safety bolt

**Figure 7.3:** Component mounting concept for MAIUS payload

The vibration dampers GP-TYPA-25X10-M6-SH55 are provided by the company STS (Schwingungstechnik Schuster). The type "A" dampers are of cylindrical shape. They are made of natural rubber with a hardness of 55 Shore. The rubber cylinder has a diameter of 25 mm and a height of 10 mm. Two M6 bolts with a length of 20 mm are vulcanized into the cylinder for mounting. Each rubber damper is capable of carrying 80 kg and will allow a stretching of 3 mm before failing. The devices will in particular reduce high frequency vibrations. The damping features are essential for the reliable operation of the payload components. Thus these will be investigated in more detail in section 8.2.

The safety bolt will limit the stretch of the rubber dampers to 2 mm to prevent them from damage. After a stretch of 2 mm the safety bolts will carry all loads applied to the platforms without vibration damping. The safety bolts are designed to be capable of carrying the loads of launch and re-entry (of up to 30 g as given in section 5.6).

The brackets themselves are mounted to the hull with five DIN 912 M5 x 12 mm screws (class 8.8.) torqued with 5.9 Nm. Each bracket is manufactured from aluminum EN AW 7075, which has been provided by the company AMCO. The supplier specifies the typical yield strength to be 462 $N/mm^2$ and the typical tensile strength to be 533 $N/mm^2$. The ANSYS material properties have been set accordingly.

As defined in section 5.6 a maximum acceleration of 13 g is expected during ascent and a deceleration maximum of 25 g during re-entry. Moreover the shock at touchdown is assumed to range from 50 g to 100 g. In rare cases (e.g. landing on a rock) it might even reach 200 g and more. Accordingly the expected loads on the brackets are depending on the actual weights of the platforms mounted. Table 7.1 summarizes the resulting loads on the brackets and screws.

| | Accel. [g] | Load [N] | Load/bracket [N] | Load/screw [N] |
|---|---|---|---|---|
| Batteries Platform (32 kg/6 brackets) | | | | |
| Ascent | 15 | 4708.80 | 784.80 | 156.96 |
| Re-Entry | 30 | 9417.60 | 1569.60 | 313.92 |
| Touch Down min | 50 | 15696.00 | 2616.00 | 523.20 |
| Touch Down max | 100 | 31392.00 | 5232.00 | 1046.40 |
| Electronics Platform (65 kg/6 brackets) | | | | |
| Ascent | 15 | 9564.75 | 1594.13 | 318.83 |
| Re-Entry | 30 | 19129.50 | 3188.25 | 637.65 |
| Touch Down min | 50 | 31882.50 | 5313.75 | 1062.75 |
| Touch Down max | 100 | 63765.00 | 10627.50 | 2125.50 |
| Experiment Platform (120 kg/12 brackets) | | | | |
| Ascent | 15 | 17658.00 | 2943.00 | 588.60 |
| Re-Entry | 30 | 35316.00 | 5886.00 | 1177.20 |
| Touch Down min | 50 | 58860.00 | 9810.00 | 1962.00 |
| Touch Down max | 100 | 117720.00 | 19620.00 | 3924.00 |

**Table 7.1:** Bracket loads for all MAIUS systems

These calculations have been performed under the assumption, that the load of the platform is distributed equally between the six brackets. This is a reasonable assumption, since the center of gravity of the system setups mounted to the platforms is designed to be close to the center of the platform. For accelerations along the cylindrical axis, as expected during ascent and touch down, this will result in an equally distributed load.

Although the experiment platform is supported by a total of twelve brackets, calculations have been performed for six brackets carrying the total load to do a worst case analysis. Moreover the loads per bracket would be almost identical to those of the electronics platform if all twelve brackets would be loaded. All loads listed in table 7.1 have been included in an ANSYS FEM simulation with a total of 13 load steps. In step 1 the pretension of the screws is set to 6.4 kN. In the following load steps the loads listed in table 7.1 are applied sorted by their size.

The safety factor is defined as the quotient between the yield strength and the maximum van-Miese comparison stress computed for the bracket. At at maximum load of 19.6 kN per bracket the minimum factor of safety is 1.028 as illustrated in figure 7.4a.

Figure 7.4b shows the dependency of the factor of safety on the external loads applied on each bracket. As illustrated by the plot the pretension load of the five screws already results in a minimum safety factor of 1.89 due to the high contact pressure between the screw head and the bracket.

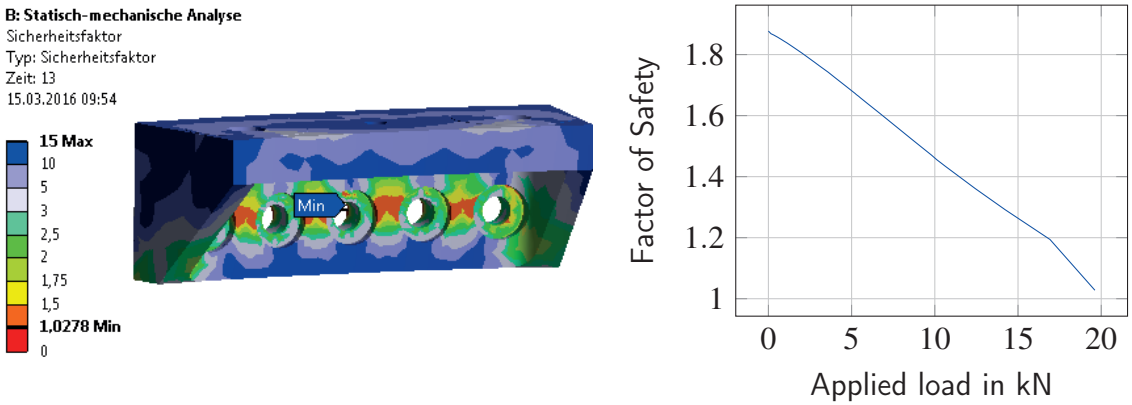


**(a)** Local distribution of factor of safety at maximum load 19.6 kN

**(b)** Minimum factor of safety for different loads

**Figure 7.4:** FEM simulation results for the brackets under different loads

Assuming that loads are distributed equally between all twelve brackets at the experiment platform, a maximum load of 10 kN per bracket is expected for a touch down shock of 100 g at the electronics platform and brackets. These loads result in a minimum factor of safety of 1.46 which is reasonable to guarantee a safe recovery of all equipment. Additionally the factor of safety against slipping of the brackets has to be calculated for the bracket screwing, which is given as

$$S_S = \frac{F_p \mu_s n}{F} \tag{7.1}$$

with $F_p$ being the pretension force in the radial screw, $\mu_s$ the coefficient of friction between the bracket and the hull, $n$ the number of screws per bracket and $F$ the load per bracket. The results for the worst case loads at payload touch-down are summarized in table 7.2.

| | Accel. [g] | Load [N] | Load/bracket [N] | $S_s$ |
|---|---|---|---|---|
| Batteries Platform | 100 | 31392.00 | 5232.00 | 6.42 |
| Electronics Platform | 100 | 63765.00 | 10627.50 | 3.16 |
| Experiment Platform | 100 | 117720.00 | 19620.00 | 1.71 |

**Table 7.2:** Factor of safety against slipping of brackets at different instrument platforms

Thus the mounting is capable of carrying accelerations or shocks of more than 100 g.

Higher loads are possible but not very likely. This is why a design to withstand higher loads is not considered reasonable.

### 7.1.3 Sealing and Feed Throughs

The scientific payload should be pressurized at 1100 hPa using artificial air during flight and on ground. To achieve this a hermetic sealing of the payload with a total of six seals is necessary. Four of those at the RADAX joints and one each at the bottom and the top. All of this seals will be established with rubber O-rings made of HNBR (hydrogenated nitrile rubber) with a hardness of 70 Shore. This material has a temperature range of use from 30 °C to 150 °C. Moreover the elastomer features high mechanical stability and abrasion resistance.

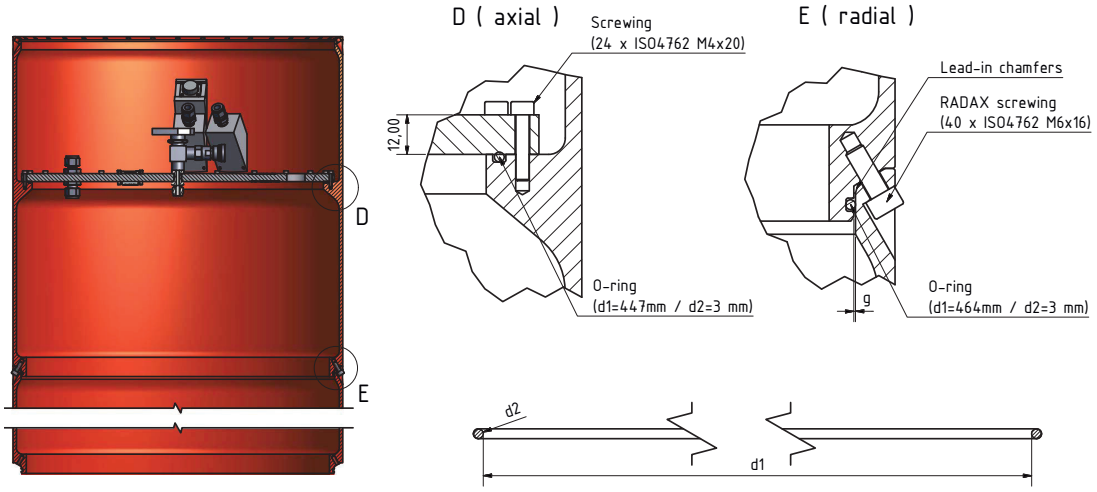


**Figure 7.5:** Different sealing type in MAIUS payload. The radial seal will provide a hermetic sealing between the hull segments. The axial seals are used at the top and bottom to close the pressurized volume of the payload.

As shown in figure 7.5 there are two different types of seals within the MAIUS payload. The seals at the top and bottom are axial, while the seals at the RADAX flanges of the modules are radial. For both types the lining groove and the gap has to be dimensioned individually. Design guidelines giving requirements for the geometry and the surface properties is provided by the O-ring manufacturer DICHTOMATIK [Dic13a].

As given in figure 7.5 both the axial and the radial O-ring have a diameter $d_2$ of 3 mm. Since this is a static application with the high pressure at the inside and low-pressure (Space) at the outside, the lining groove depth and width can be determined from the design guidelines.

The geometry of the groove is chosen to be rectangular. Therefore the depth of the groove of the radial sealing should be 2.3 mm and the width 3.9 mm. The lead-in chamfer has a size of 2.5 mm. The depth of the groove of the axial sealing is identical, while the width

shall be slightly larger (4.1 mm). Moreover the transition between the groove flank and base and between the groove flank and the adapter end surface must be slightly rounded to protect the o-ring from damages. The radii are related to the cross section of the O-ring. For a 3 mm cross section the radii are 0.2 mm and 0.5 mm as shown in figure 7.6.

For static applications the required surface qualities for the groove flank and groove base are also defined in the design guidelines. As shown in figure 7.6 the surface quality of the groove flank and bottom are chosen to be identically for the MAIUS payload. Moreover the dimensions of the lining groove and their tolerances have been adapted slightly to ensure that the sealing gap $g$, groove filling $N$ and deformation $D$ are within the limits given in the design guidelines.

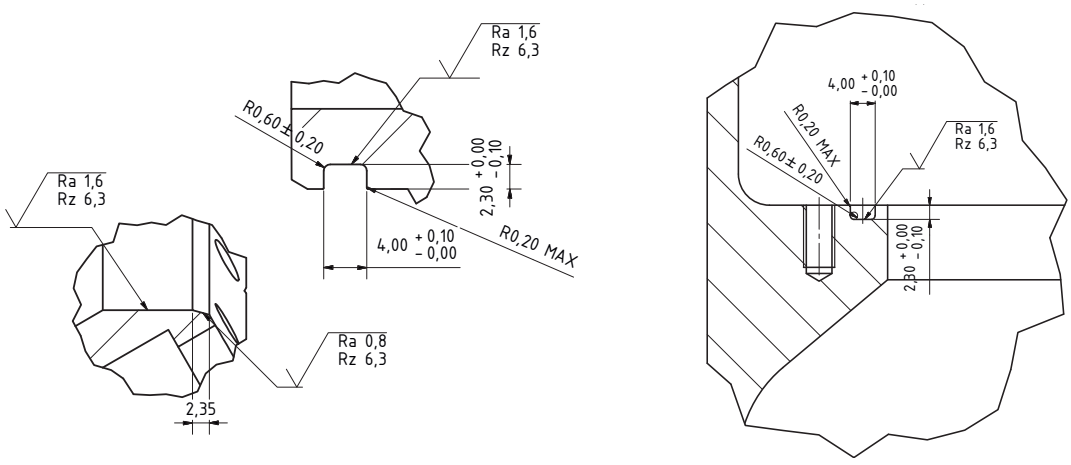


**(a)** Radial sealing **(b)** Axial sealing

**Figure 7.6:** MAIUS lining groove dimension of o-ring sealing

Especially the groove filling and the sealing gap size are depending on the tolerances given in the drawings and on the deformation of the parts involved in the sealing. For this reason these parameters have to be calculated for a maximum and minimum dimension value.

The groove filling is defined to be the ratio between the cross section of the O-ring $A_{OR}$ and the cross section of the lining groove $A_{groove}$

$$N_{fill} = \frac{A_{OR}}{A_{groove}} \times 100\% \tag{7.2}$$

It should be between 70% and 85% according to the design guidelines. With the cross sections of groove and O-ring

$$A_{OR} = d_2^2 \times \frac{\pi}{4} \tag{7.3}$$

$$A_{groove} = t_{groove} \times b_{groove} \tag{7.4}$$

and the tolerances given in figure 7.6 for the groove dimension, the minimum groove filling for axial and radial sealing is found to be $N_{max} = 85.17\%$ and the minimum $N_{min} = 70.49\%$.

The sealing effect of the o-ring is ensured by radial or axial deformation. According to the guidelines the deformation should be between 15% and 30% for static applications and is calculated from

$$D = \frac{d_2 - (g + t_{groove})}{d_2} \times 100\% \tag{7.5}$$

Obviously the size of the gap $g$ has a significant influence on the deformation and the sealing effect. The required values for this dimension are given in the design guidelines. For static applications with an operating pressure below 60 000 hPa and a material hardness of 70 Shore the gap dimension should not exceed 0.2 mm. This value is increased to 0.25 mm for a material hardness of 80 Shore.

The tolerances of the radial lining groove in figure 7.6 and for the adapter end of the RADAX connections in figure 7.2 will result in a minimal radial gap of $g_{rad,min} = 0.15$ mm and a maximum radial gap of $g_{rad,max} = 0.25$ mm. This should be reasonable due to the low operating pressure. For standard RADAX connection tolerances these values would be significantly higher ($g_{rad,min} = 0.2$ mm and $g_{rad,max} = 0.5$) mm. For this reason the tolerances have been reduced for MAIUS RADAX flanges.

While no deformations are expected at the radial seals, the gap size of the axial seals is depending on the deformation of the sealing plate due to the pressure difference and external loads.

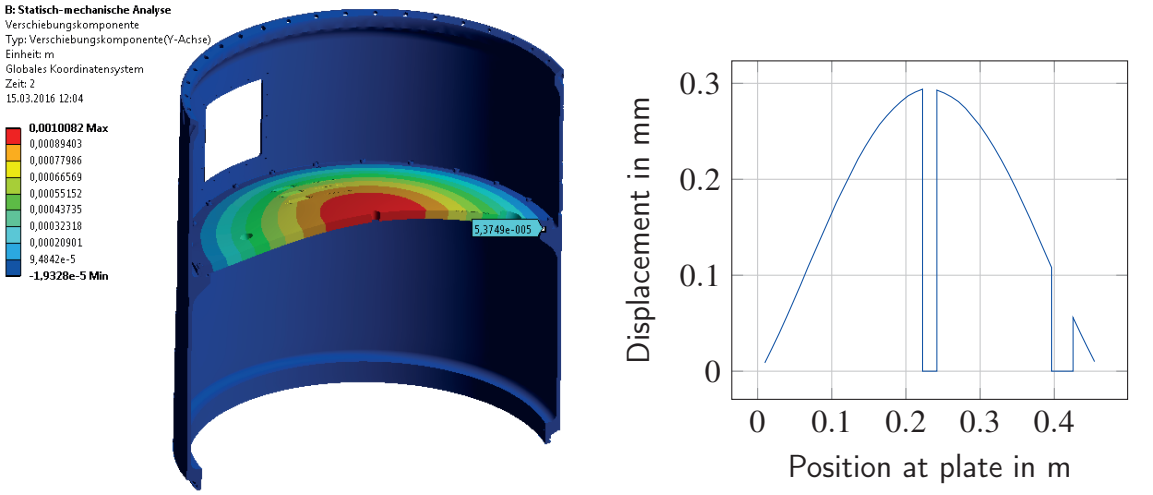


**(a)** Overview of displacements at bottom sealing

**(b)** Path plot of displacements in y-direction along the sealing plate. At bor holes the displacement is 0.

**Figure 7.7:** FEM simulation results for sealing plate deformation

The plate is made of aluminum EN AW 7075 and is fixed with 24 M4 steel screws (property class 8.8.). The screws are tightened with a torque of 3 Nm which results in a pretensioning force of 3.9 kN, which is included in the FEM simulation. Moreover a pressure difference of 1000 hPa and ascent accelerations of 15 g in positive y-direction have been assumed and

modeled. This is representative for the worst case at the bottom sealing plate, where those loads will add up, because they point in the same direction.

Figure 7.7 displays the results of a FEM simulations performed for the sealing plate with these parameters. It shows a maximum bending and lifting of the plate of 0.05 mm at the lining groove position (14 mm from the plate edge). The maximum deformation in y-direction at the center of the plate is about 1 mm.

With these results the deformation can be calculated from equation 7.5 resulting in a maximum deformation of the radial seal of $D_{rad,max} = 21.6\%$ and a minimum of $D_{rad,min} = 15$ %. The gap is significantly smaller in the axial sealing. This results in larger deformation $D_{ax,max} = 26.67\%$ and $D_{ax,min} = 21.66\%$ considering the deformations of the plate and the tolerances of the lining groove dimension. All of these values are within the requirements although often at the edge. However no leaks are expected at the O-ring seals, because of the low operation pressure.

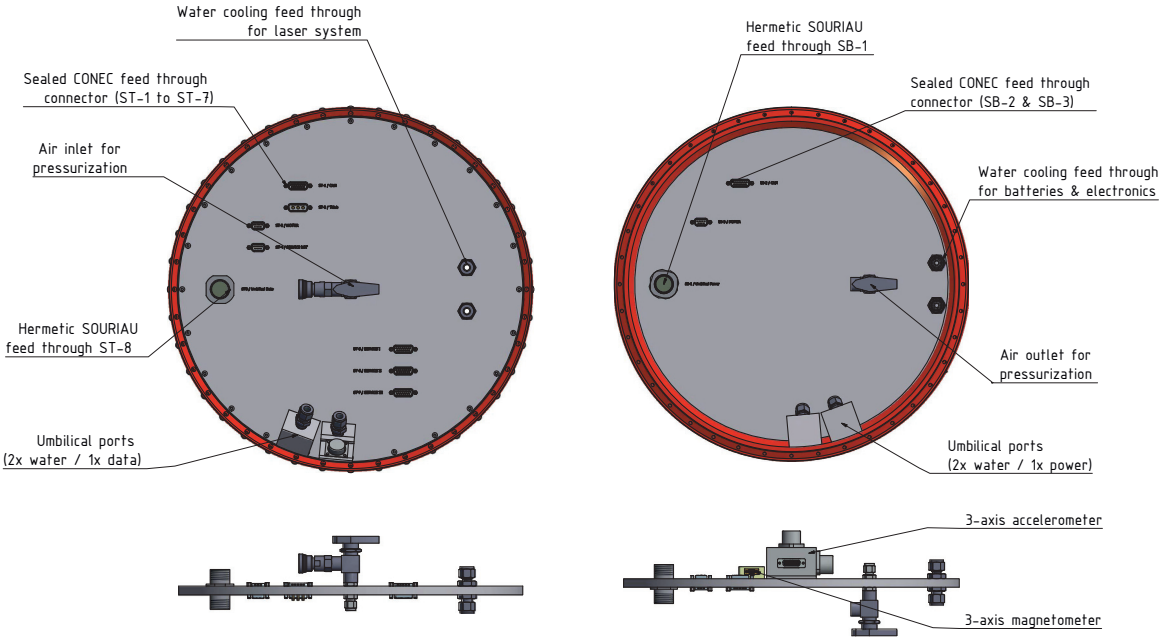


**(a)** Sealing Top **(b)** Sealing Bottom

**Figure 7.8:** MAIUS sealing plates with multiple feedthroughs for water-cooling, data and power supply.

The experiment requires multiple connections to the outside for power and water supply and data connection to the ground and the service module. Moreover the control and sensor data from and to the motor has to be passed through the sealed payload enclosure. All of these have to be fed through the sealing plates at the bottom and top without violating the sealing.

The ethernet and RS422 interfaces to the service module (connector #ST-4 to ST-7) as well as the interface from the service module to the motor (#ST-1 and ST-2) are connected

with rubber sealed IP67 graded feedthroughs manufactured by CONEC. These connectors consist of a female D-Sub connector on the atmospheric side and a male connector at the vacuum side as shown in figure 7.9a. The current for activation of the titanium sublimation pump is supplied over a similar connector (#ST-3) with high current contacts rated for a maximum of 30 A as shown in figure 7.9b.

**(a)** D-Sub 15 feedthrough **(b)** D-Sub 3W3 connector

**Figure 7.9:** Rubber sealed CONEC feedthroughs

The data and power umbilical ports are situated outside the pressurized enclosure, because a sealing of the umbilical port to the cylinder wall would be difficult to achieve. Thus the signals of the power and data umbilical will be fed through the sealing plate first. This is achieved by a SOURIAU bulkhead feedthrough with standard reinforcement sealing achieved by a silicone elastomer. A 37 pin layout 8DB-7-15F35-PS-N equipped with 5 A rated contacts at the top for the data and low current applications. For the charging of the main batteries a 12 pin layout 8DB-7-15F97-PS-N equipped with 4 contacts rated for 13 A and 8 contacts rated for 7.5 A has been chosen.

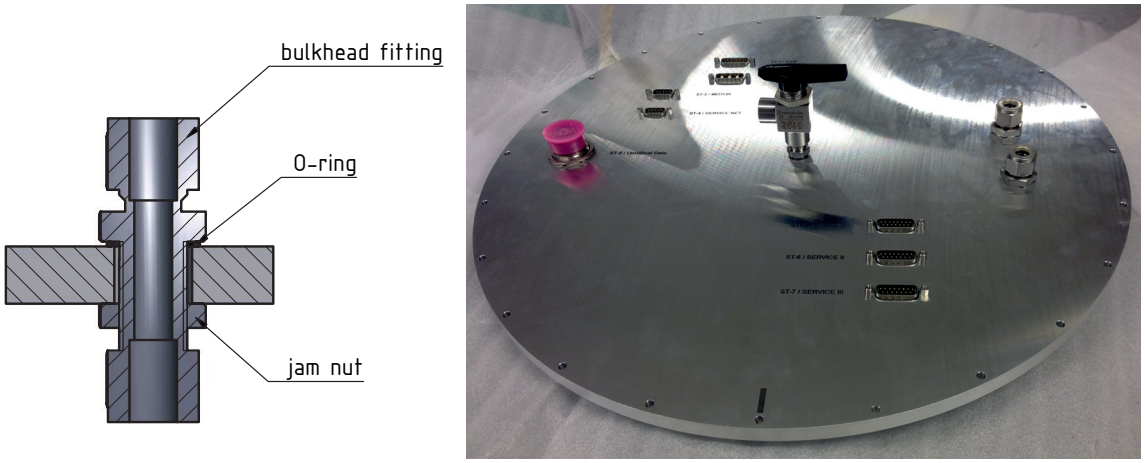


**(a)** Drawing of bulkhead fitting with sealing concept **(b)** Photo of the sealing plate with connectors, ball tap and bulkhead fitting

**Figure 7.10:** MAIUS sealing plate feedthrough concepts

The water for both the laser and the electronics cooling is provided by an umbilical as well.

The umbilical port has also been placed outside the pressurized volume. The feedthrough is realized with a bulkhead fitting, which has been equipped with a rubber O-ring at the body side of the fitting. From the other side the fitting is fixed with a jam nut as illustrated in figure 7.10a. This will provide the necessary deformation of the O-ring and establish a reliable sealing. Since the fitting itself is sealed and the cooling circles have no open end to the atmosphere in the enclosure this will ensure a reliable sealing.

For operation the enclosure should be filled with artificial air without carbon hydrates as required by the lasers and optics. The gas used for pressurization is a mixture of 20 % oxide (purity grade 5.0) and 80 % nitrogen (purity grade 5.0). For pressurization of the enclosure one ball tap is installed in the top and one in the bottom sealing plate. This will allow a flushing of the interior with the gas to ensure that the atmosphere will meet the requirements. After flushing the bottom ball tap is closed and the pressure is set to 1100 hPa absolute pressure, which will be measured at the bottom of the electronics section by a absolute pressure sensor. The slight overpressure inside the enclosure will allow to detect leaks during flight and on ground.

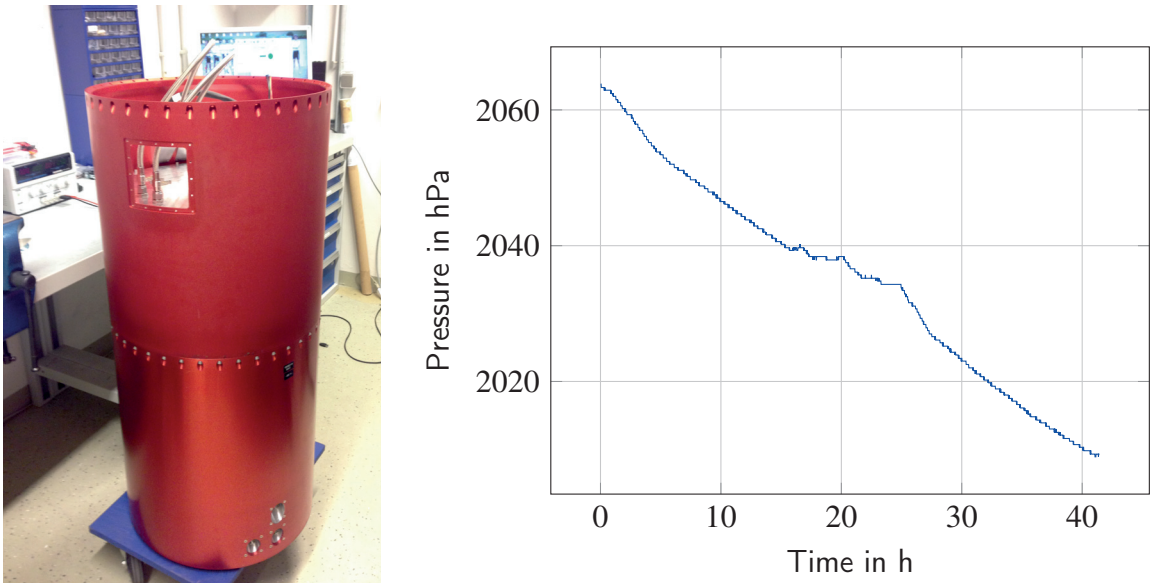


**(a)** Test setup of upper and lower MAIUS hull segments

**(b)** Full 40 hour pressure reading during the pressure test showing only 55 hPa reduction in pressure.

**Figure 7.11:** Pressure test of hull sealing performed with 2000 hPa absolute pressure

For verification of the design and the sealing methods, the upper and lower hull segments including the sealing plates and feedthroughs have been tested for leaks before integration of the components. The water in- and outlet fittings in the sealing plates have been connected to each other for this purpose.

For representative testing the absolute pressure has been set to 2000 hPa assuming that the outside pressure during flight will be close to absolute zero. Thus the pressure difference between the enclosure and the outside in both scenarios is approximately 1000 hPa.

After pressurization the setup has been observed for 40 hours recording the absolute inside pressure using an absolute pressure sensor with an external power supply and a simple voltage data logger. The test setup and the pressure reading are shown in figure 7.11.

Within a period of 40 hours the pressure within the hull segments dropped by 55 hPa. The slope of the pressure plot is almost constant, thus the leakage rate should be constant as well. For this reason the sealing concept is considered qualified. However the assembly of the entire structure will increase the number of seals, which will influence the leakage rate. For this reason a pressure test of the entire payload will be carried out in combination with a thermal test during the first flight simulation campaign in Hanover. Moreover a test of the sealing under vibrational loads will be performed during the final environmental tests in Ottobrunn.

## 7.2 Harness and Umbilicals

For operation of the MAIUS payload a significant number of cables and hose pipes is required to provide the experiment with water for cooling, power for charging the internal batteries and for communication.

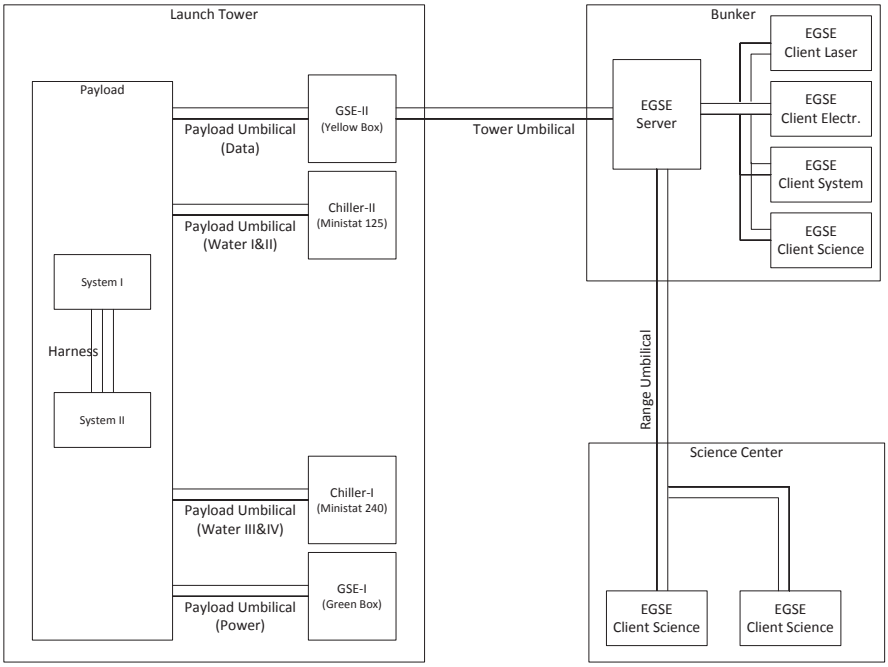


**Figure 7.12:** Concept of MAIUS ground support equipment (GSE) and its connections and locations at Esrange

As illustrated in figure 7.12 it has to be differentiated between internal cables and hoses connecting different systems within the payload and external cables connecting the rocket with the ground support equipment (GSE) or the electronic ground support equipment.

At Esrange the launch site composes of three buildings used during the MAIUS mission as illustrated. The integration hall, where the payload is integrated for final tests and launch, the Skylark launch tower, where the payload is attached to the motors and from where the rocket is launched and the main building. During launch the payload will be controlled from a bunker within the integration hall close to the skylark tower. Due to the limited space within the bunker some of the scientists are accommodated at a science center in the main building, where they also have access to the scientific data.

The launch tower at Esrange offers standard 230 V power sockets to supply the GSE with power. Moreover an Ethernet connection between the launch tower and the bunker is provided by the tower umbilical. The range umbilical will allow to connect the science center with the server in the bunker. All additional wiring has to be managed by the payload team. The internal wiring (harness) and the wiring between the payload and the ground support equipment (umbilicals) will be described in the following.

### 7.2.1 Cable Ducts and Harness

MAIUS is equipped with two cable ducts to route all internal cables situated between 135° and 165° as well as between 315° and 345° in the MAIUS coordinate system. The cable ducts span over 30° with an inner radius of 212.5 mm and an outer radius of minimum 230 mm limited by the rocket hull structure as illustrated in figure 7.13. While cable duct II will only shelter cables, cable duct II will also house the Swagelok hoses of the water cooling as described in section 12.1, which reduces the space available for cables.

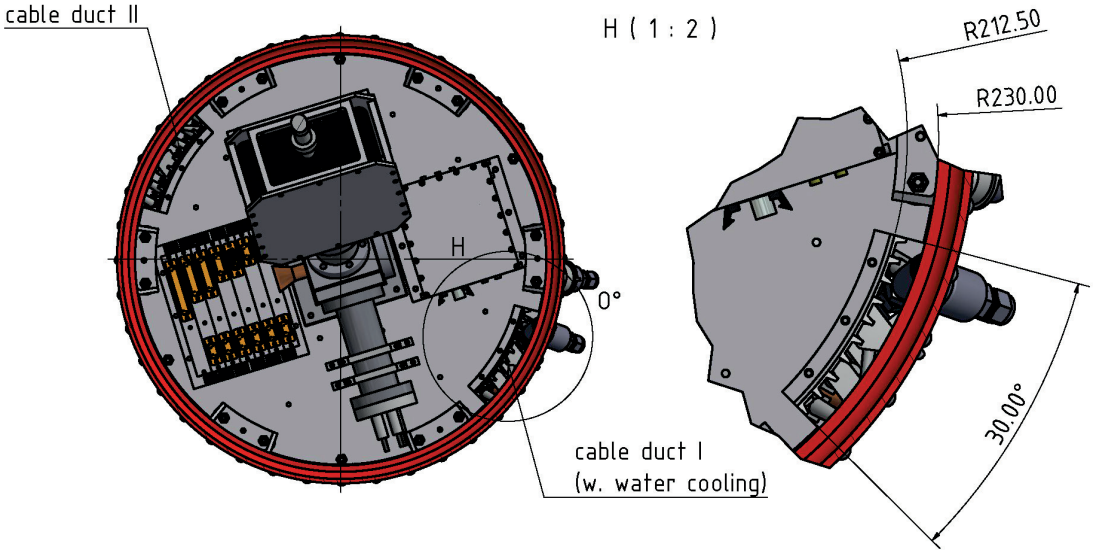


**Figure 7.13:** Cable duct geometries in MAIUS-1 for internal wiring between the different systems

In total 96 cables with a weight of approximately 18 kg connect the different subsystems within the payload. The cables between the subsystems have been dimensioned in length and diameter according to VDE standards depending on the geometry of payload and the

use of the cable. The length has been determined using the high detail CAD model of the payload which is also a result of this thesis. Additional 100 mm in cable length have been considered for every RADAX flange a cable will pass. This should allow to open the RADAX connection for inspection of the interior and minor repairs.

The conductor diameters vary from AWG10 to AWG26 depending on the power consumption of the appliance. Most cables are equipped with standard or combination subminiature (DSUB) connectors. The number of conductors or pins varies from 2 to 37. All internal cables are protected by rubber insulation rated for temperatures of at least 105 °C, which is sufficient since the temperatures at the surface of the outer rocket structure should not exceed these values (refer chapter 10).

The cables are fixed with tie raps to a bracket mounted at each instrument platform shown at the right hand side of figure 7.13. This will reduce the free length of the cables and prohibit uncontrolled movement of the harness.

### 7.2.2 Umbilical Ports

The MAIUS payload is equipped with six umbilicals. Two MIL-38999 push-pull connector umbilicals provide the power supply and communication with the payload. Moreover four custom umbilicals made of Swagelok components will allow a constant water cooling of the payload until lift off.

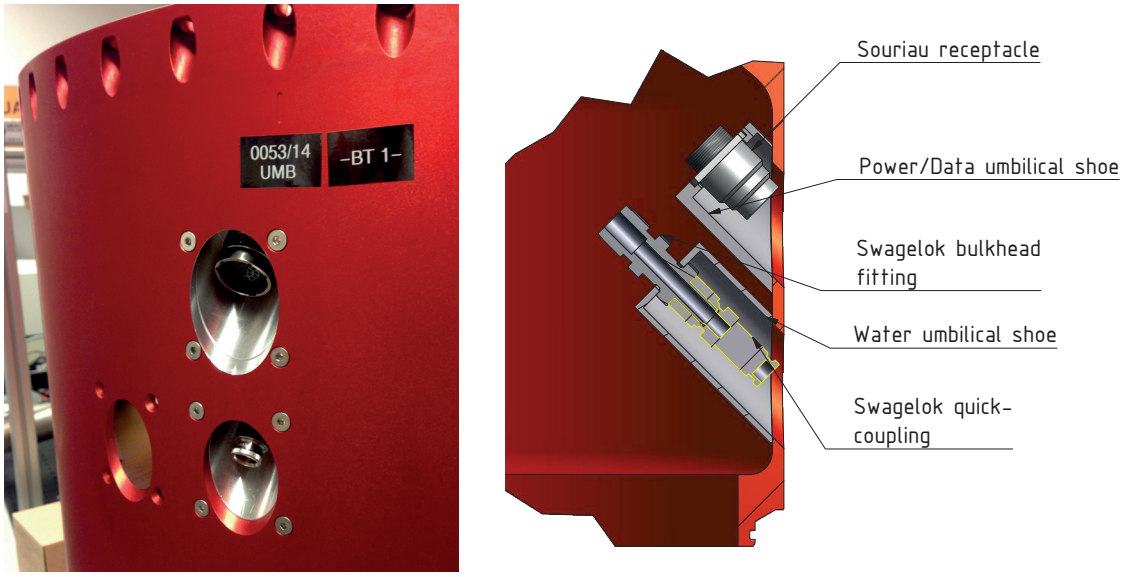


**(a)** Picture of data and water umbilical ports

**(b)** Cut through umbilical ports showing different components

**Figure 7.14:** Umbilical ports of MAIUS-1 payload

An umbilical connection is generally established by two parts. The receptacle at the payload side, which feeds the lines through the outer hull outside of the sealed area and the

push-pull lanyard connector at the ground side attached to the launch facility.

The umbilical receptacle is integrated into a umbilical shoe, which is mounted to the rocket structure feeding the lines through the rocket hull as shown in figure 7.14b. The umbilical cable itself is provided with a push-and-pull quick connect connector, which is attached to the launch rail by an laynard steel cable. Thus the plug will be unlocked automatically by the pull when the rocket lifts off.

The MAIUS power and data umbilical shoes are identical, since the SOURIAU receptacles have the same housing size. The connectors are mounted to the umbilical shoe by four M3 screws, while the umbilical shoe is attached to the structure by four M4 ISO 10476 screws as shown in figure 7.14a. The MAIUS umbilical cables are equipped with an additional mechanical and thermal protection, made from glass fibre meshwork increasing the temperature rating to 250 °C, which might allow reusing the umbilical for future missions.

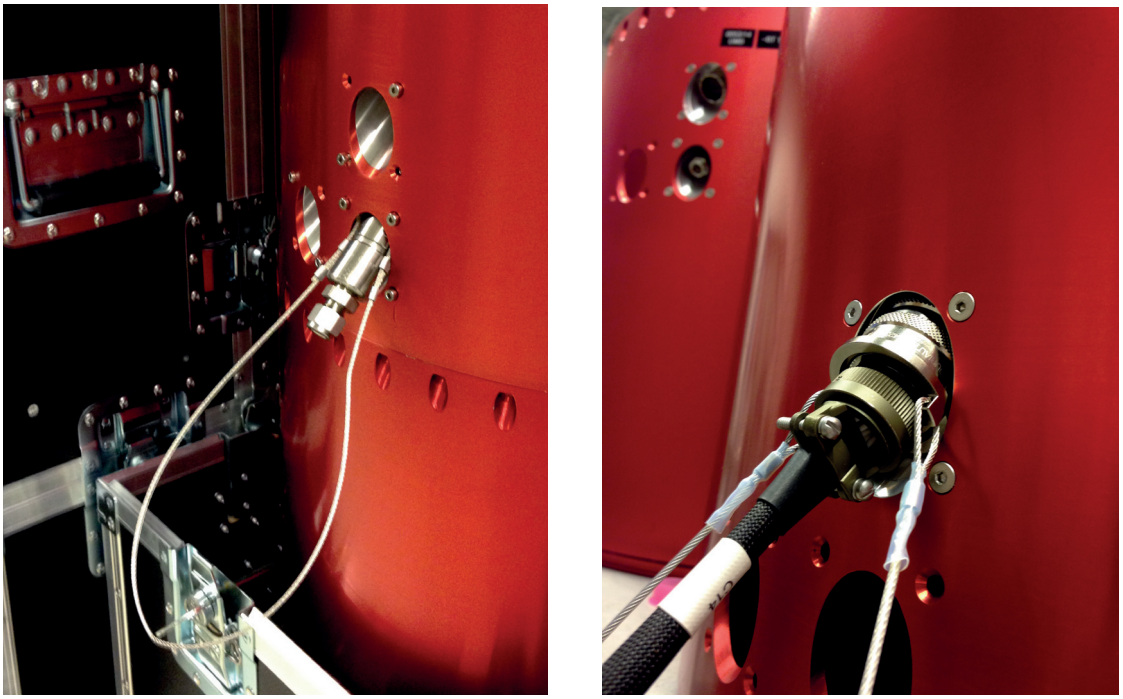

(a) Water umbilical (b) Power umbilical

**Figure 7.15:** MAIUS-1 umbilicals

The upper umbilical will provide power to the backup batteries of the pump controller and will establish an ethernet connection to the ground support computer for data handling and control of the experiment from the ground support computers at the bunker. Moreover the signal of two temperature sensors placed at the electronics and laser heat sink is provided through the umbilical as input for the temperature controller of the chillers. In total 37 pins rated for a maximum of 2A are connected via a Souriau 8D9P-15F35-P-N-L lanyard plug until lift off. The counter part at the payload side is the Souriau receptacle push-pull connector 8D8R-S-15F35-SN.

The lower umbilical supplies the main batteries of the payload with charging power. The lanyard plug 8D9P-15F97-P-N-L is used to connect the power supplies of the ground support equipment (GSE) with the payload. At the payload the receptacle push-pull connector 8D8R-S-15F97-SN is mounted to an umbilical shoe.

As mentioned above in addition to the data and power umbilical, four umbilical ports are used for providing cooling water until lift off. The two ports at the top supply the cooling cycle of the laser system and the two at the bottom supply the cycle of the electronics and batteries. All four umbilical ports are designed identically as shown in figure 7.14b.

A water cooling umbilical connector is not available commercially. For this reason one had to be developed within this mission based on industrial quick coupling connectors. These connectors have to be small in size and should be equipped with seals at the body and the stem to prevent water from spilling out when the connectors are disconnected. For simplicity of the design the connection should allow bidirectional flow and the connectors should be disconnected by pulling to allow a passive decoupling by a lanyard as it is done with regular power or data umbilicals.

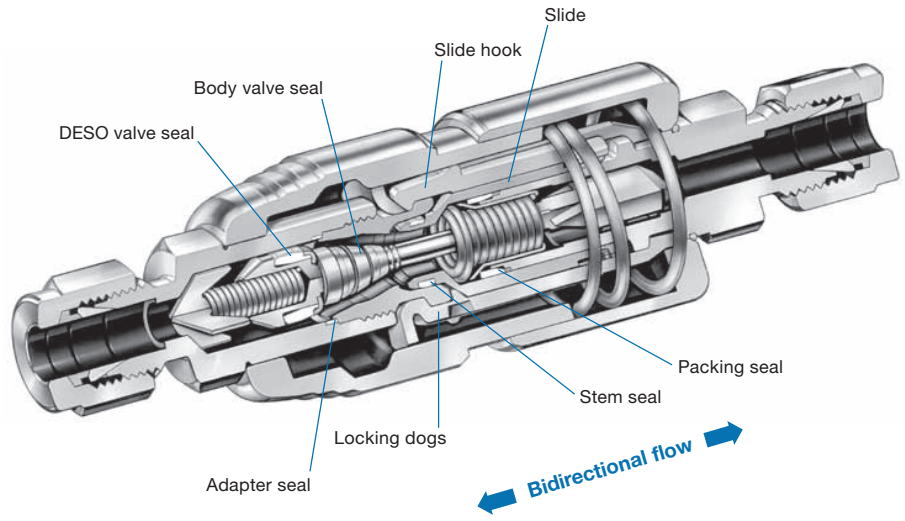


**Figure 7.16:** Concept of Swagelok QTM quick coupling. This coupling is rated for 30 MPa and suitable for bidirectional flow [Swa11].

Review of different concepts and suppliers revealed the stainless steel PTFE-sealed quick-connector series (QTM) from Swagelok to be most suitable for this application. Due to the limited space the smallest QTM2 connector with a 3/8" Swagelok tube fitting has been chosen. This connector is capable of handling a maximum flow of 56 l/min and will allow a maximum pressure of 6.89 MPa uncoupled and 31 MPa coupled. This is significantly above the requirements for the thermal control systems as calculated in chapter IV.

The Swagelok bulkhead fitting SS-600-R1-6 is directly mounted to the umbilical shoe by the bulkhead jam nut providing a 3/8" tube fitting at the inside and a 3/8" tube at the outside. The quick coupling stem SS-QTM2-D-600 is directly mounted to the short 3/8" tube to the outside. This quick coupling stem is the actual interface of the payload.

Its counterpart, the SS-QTM2A-B-600 quick coupling body is connecting the payload to the chiller, which are part of the ground support equipment as illustrated in figure 7.12. The water is transported with a Swagelok series W thermally insulated PTFE hose. The hose is protected by a fire jacket made of woven fiberglass with specially compounded aerospace-grade silicone rubber. The fire jacket withstands short-term flame exposure even at temperatures of more than 1000 °C. Thus the water umbilical hoses will survive the harsh environment in the launch tower and can be used again.

For separation of the connectors a small plate made of aluminum is placed between coupling stem and body. As shown in figure 7.17 plate is only 2.5 mm thick, thus the locking of the coupling will not be affected. As described above the lanyard will be attached to the tower, for this reason the connector will be unlocked during lift off. The seals in the stem and the body will prevent the water from flowing out at both, the rocket segment and the ground segment.

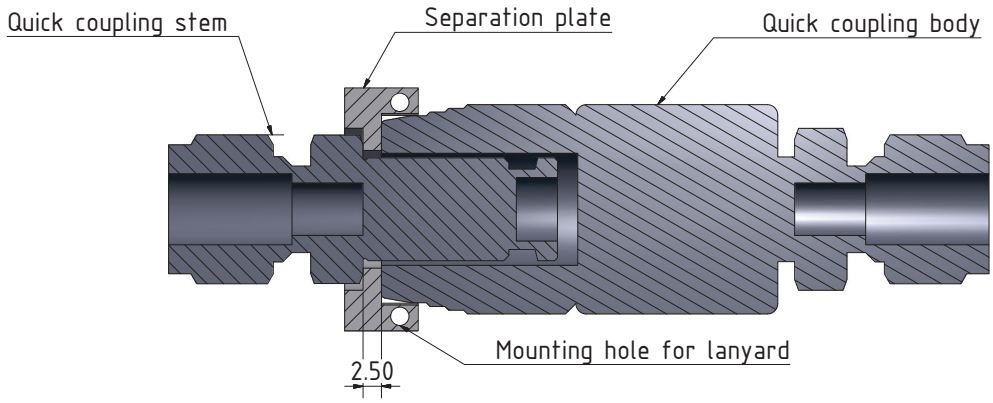


**Figure 7.17:** Water umbilical connectors with separation plate installed. The separation plate will automatically decouple the connection at lift-off.

The unlocking was tested on ground, to ensure that the force for separation of the connectors will not exceed the design loads of the umbilical shoe and the separation plate. For this purpose a force sensor has been attached to the lanyard of the umbilical and was separated manually as shown in figure 7.18b. For comparison the same test has been performed with the commercial MIL-38999 connector, which has been qualified for sounding rocket or missile applications.

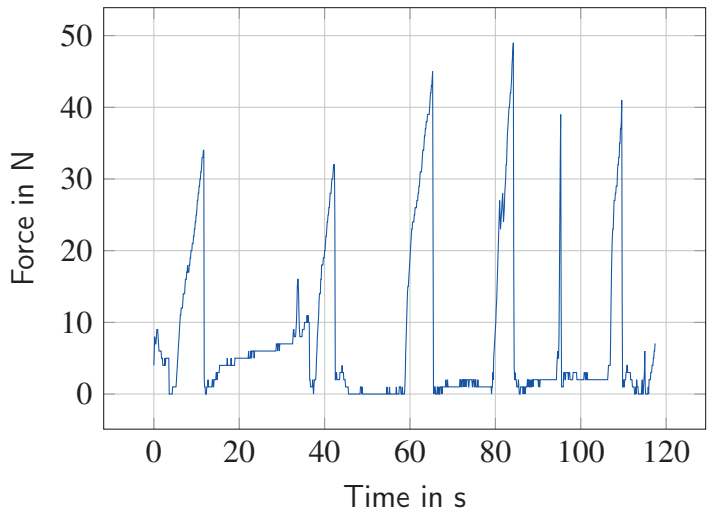


**(a)** Separation force for six separation tests with the water umbilical connector

**(b)** Test setup for water umbilical

**Figure 7.18:** MAIUS-1 water umbilical separation test

Figure 7.18a shows the results of the tests. In total six (manual) separation tests have been performed with constant data logging. In all tests the separation force was below 50 N. The MIL-38999 connector needs 80 N to 120 N for separation. In particular no blocking or other decoupling problems have been observed at the water umbilical. Thus the concept for separation is considered qualified.

## 7.3 Physics Package

The compact physics package consists of three main parts as named in figure 7.19. The pumping system, which is located outside of the magnetic shielding, the experiment chamber inside the shielding and the three layer magnetic shielding itself. Moreover the laser system is directly attached to the lower instruments platform of the physics package.

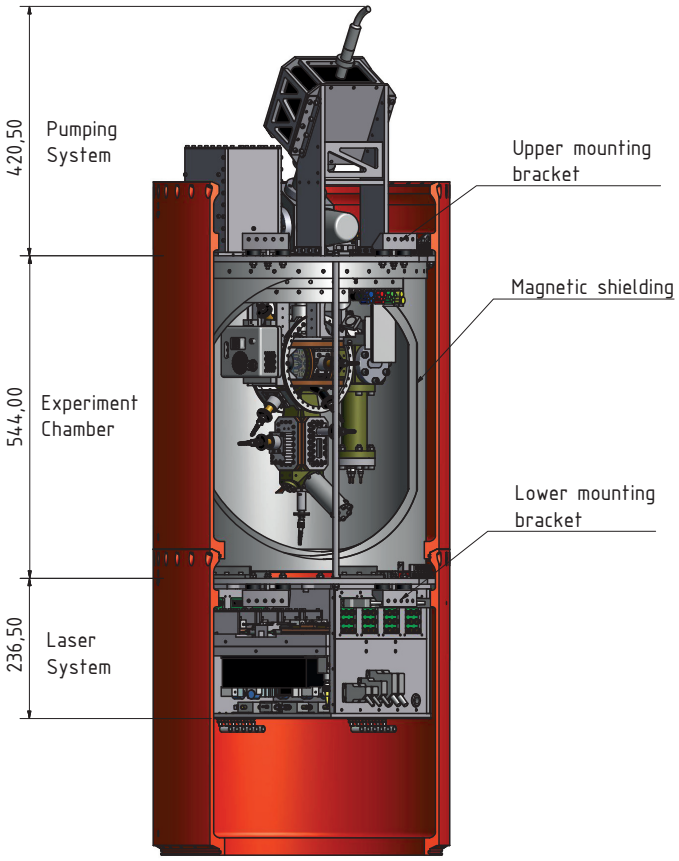


**Figure 7.19:** Overview of physics package integrated in hull segments

The physics package is the only system in the MAIUS payload mounted to two platforms. This is because of the magnetic shielding, which should be suspended at the top and the bottom to avoid any plastic deformation of the shield. Such deformations would decrease the shielding factor by changing the crystalline structure of the metal. Moreover the laser system should be situated close to the experiment chamber, since it is permanently connected to the chamber by sensitive single-mode optical fibers.

As shown in figure 7.20 the magnetic shielding and the experiment chamber are located between the two instrument platforms. The magnetic shielding, the experiment chamber and the pumping system are mounted to the upper platform, while the laser system is attached to the lower platform.

Both platforms are attached to the rocket structure by 6 mounting brackets each as described in section 7.1.2. The rubber dampers allow a maximum movement of 2 mm before the safety bolts will carry the loads. Bracket and safety bolts are mounted mirrored. Thus the assembly of both platforms might travel 2 mm upwards before the lower safety bolts will limit the deflection or 2 mm downwards before the upper bolts will do the same.

The two platforms are connected by four stand-offs with a diameter of 10 mm and a M6 thread at both ends. The stand offs will prohibit a movement of the platforms towards each other. The length of the stand-offs is 534 mm, which provides 10 mm of space between the lower platform and the bottom of the magnetic shielding. This should avoid any loads on the shielding to maintain the shielding factor. The stand-offs are made of stainless steel 1.4404/316L (DIN X2CrNiMo17-13-2) with a yield strength of 320 MPa, a tensile strength of 530 MPa and an elastic modulus of 210 GPa [Deu08].

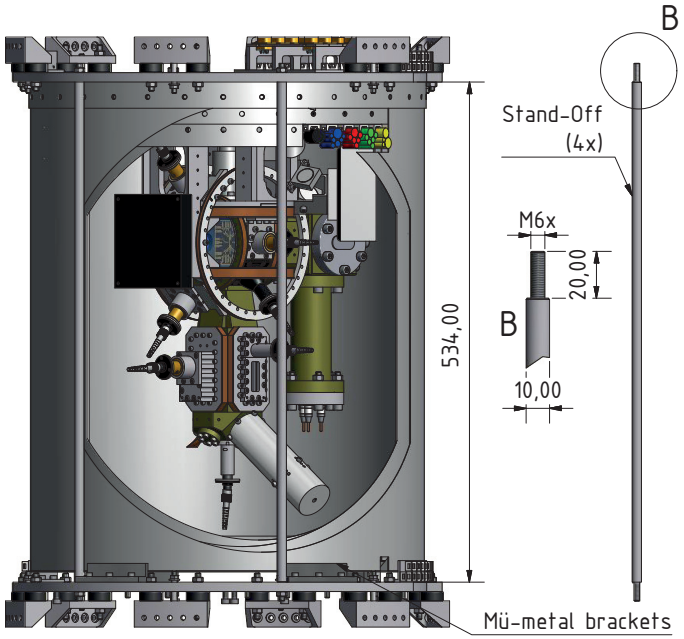


**Figure 7.20:** Physics package mounting with stand-offs needed to prevent movement of the two physics package base plates towards each other and for integration into the rocket hull.

To prevent buckling of the stand-off columns during integration of the physics package in the hull, the maximum allowable axial force has to be calculated from

$$F_{max} = \frac{\pi^2 E I_{circ,x}}{(KL)^2} \tag{7.6}$$

where E is the modulus of elasticity, $I_{circ,x}$ the area moment of inertia, defined as

$$I_{circ,x} = \frac{\pi r^4}{4} \tag{7.7}$$

and KL the effective length. The effective length is the product of the actual length of the column multiplied with a column effective length factor K, depending on the conditions of the end support of the column.

Since the columns are screwed to the instrument platforms at the top and the bottom, the column support is considered fixed on both ends. Thus the effective length factor is $K = 0.5$.

For the material properties given and the geometry presented in figure 7.20 the maximum force is calculated from equation 7.6 to be $F_{max} = 14\,271\,\mathrm{N}$ per column.

| (Sub)System | Mass [kg] |
|---|---|
| Experiment Chamber | 13.5 |
| Pumping System | 16.5 |
| Vacuum Controller | 2.0 |
| Patchpanel | 0.5 |
| Laser System | 22.3 |
| Magnetic Shielding | 35.1 |
| Instrument Platforms | 10.4 |
| Cables | $\approx 5.0$ |
| Total | 105.3 |

**Table 7.3:** Masses of physics package subsystems and lasersystem

As listed in table 7.3 the overall weight of both instrument platforms and the components mounted to them is 105.3 kg. During assembly, when gravity will be the only mechanical load, the physics package applies a maximum force to a column of $F_{c,max} = 1033\,\mathrm{N}$ if one column carries all the mass. The load per column is reduced to $F_{c,min} = 258.3\,\mathrm{N}$ if the load is distributed equally between all columns. Thus the factor of safety against buckling is

$$S_{B,min} = \frac{F_{c,max}}{F_{max}} = 13.82 \tag{7.8}$$

$$S_{B,max} = \frac{F_{c,min}}{F_{max}} = 55.25 \tag{7.9}$$

Once integration in the hull is completed, the brackets will carry most of the loads applied e.g. during launch. Nevertheless the columns would withstands accelerations of up to 55 g if the loads are distributed equally between all four columns. Thus a safe operation under mechanical loads as predicted for a regular flight in section 5.6 is guaranteed even if some of the brackets would fail.

### 7.3.1 Magnetic Shielding

The preparation of atoms for interferometry is very sensitive to fluctuations of external magnetic fields. As shown in figure 5.13 the magnetic environment will change with respect to the local experiment coordinate system due to the movement of the vehicle. To ensure variations with an intensity of $\Delta B \leq 0.4\,\text{mG}$ [KL16] as required (compare section 6.6), a shielding factor of 1000 or more is needed due to the field intensities of 400 mG to 500 mG.

The magnetic shielding of MAIUS consists of three layers. They are manufactured from MUMETALL, which is an alloy of 76.6 %Ni, 4.5 %Cu, 3.3 %Mo and 14.7 %Fe. This alloy offers high magnetic permeability $\mu_r$ between 60000 and 250000 [VAC02]. The high permeability of MUMETALL provides a low reluctance path for magnetic flux, thus external magnetic fields are guided through the metal and around the interior of the shield.

MUMETALL is produced by the German company VAC - Vacuumschmelze GmbH. Its mechanical properties are comparable to soft-annealed steal alloys. The tensile strength is specified to be $R_{p0.2} = 130\,\text{MPa}$, the yield strength $R_m = 530\,\text{MPa}$ and the elastic modulus $E = 200\,\text{GPa}$ after final annealing procedures [Dem14]. According to the manufacturer the stress within the shield should not exceed the tensile strength to maintain the magnetic properties of the material.

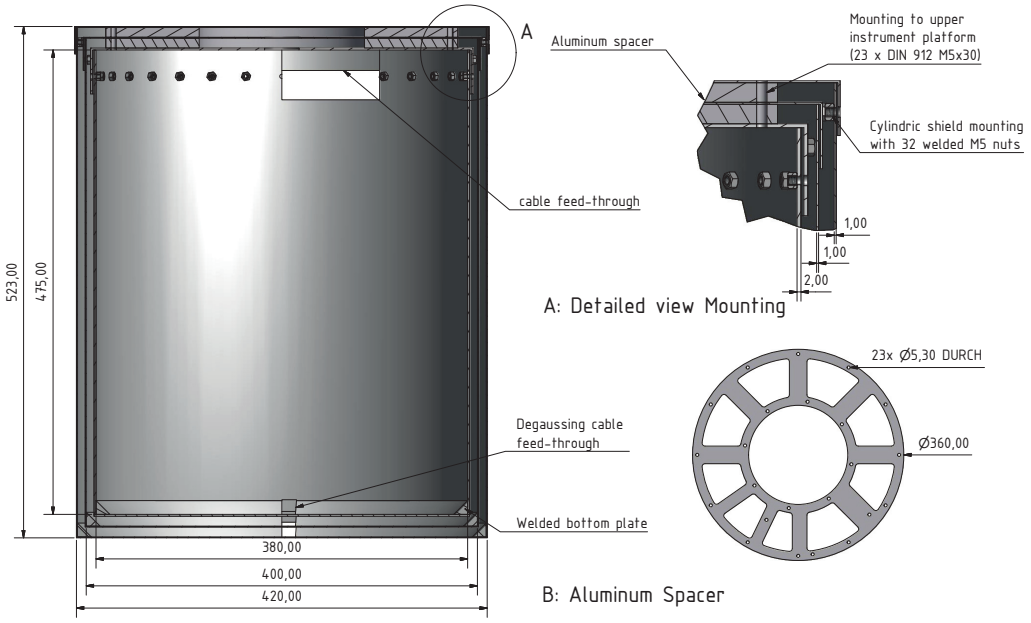


**Figure 7.21:** Detailed drawing of the MAIUS-1 MUMETALL shield giving dimensions and details of the mounting of the shield caps and cylinders (A) and a view on the aluminum spacers placed between the shield caps (B).

As shown in figure 7.21 each layer consists of an upper cap and a cylindrical mantle with welded bottom plate. A total of 32 M5 nuts are welded to the mantle of the shield. The

cap of each layer is screwed to the associated mantle by 32 M5 stainless steel screws.

The thickness of the cap and mantle of the inner layer is 2 mm, while the outer two layers only offer a wall thickness of 1 mm. The outer shield measures 420 mm in diameter and 523 mm in height at the outside. While 475 mm in height and 380 mm in diameter are available inside the shield.

The caps of the shielding are mounted to the upper instruments platform of the physics package by a total of 23 DIN ISO 4762 M5 titanium screws, which have been torqued with 5.7 N m. Moreover radial movement of the shield should be prohibited by four brackets which are clamped to the magnetic shielding.

All three shield layers exhibit three violations of a perfectly closed shield. A bore hole with a diameter of 35 mm is necessary to insert a CF16 UHV vacuum flange into the shield, which obtains a connection between the UHV chamber inside the shield an the pumping system outside. A cut-out of 100 mm $\times$ 30 mm is needed to guide cables and optical fibers into the shielding. A third feed through has been included in the shield to wrap a cable around the shield, which can be used to degauss the shield. With this technique it is possible to compensate for saturation effects of the shield material, which will occur due to external magnetic fields or smaller deformations.

A FEM simulation has been performed to predict the stress in the shield on ground and during the sounding rocket flight and thus estimate the shield performance. The simulation includes two separate load steps. In the first step the torque of the screws is simulated by applying a pretensioning force on each of the 126 screws. In the second load step an external load of 13 g along the cylinder axis is applied. This is equivilent to the loads expected during rocket ascent.

Simulation results show that the caps of the shield exhibit the areas with the highest stress. The resulting equivalent van-Miese stress intensity is presented in figure 7.22 for the pretensioning forces of the screws (load step 1) and for the rocket ascent cases (load step 2). Areas of yellow color in figure 7.22 indicate that the van-Miese stress exceeds the tensile strength of MUMETALL of 130 MPa. As illustrated in the figure the maximum van-Miese stress is present at the contact area between the screw hat and the shield bolts. At this position the van-Miese stress exceeds the tensile strength of the material. Thus it is expected that the shielding factor will decrease after assembly of the shield even if no external loads are present.

Although the affected area on the shield is comparable small, the predicted reduction of the shielding factor has been validated by measuring the residual magnetic field before and after shield assembly. A increase of the field inside the shielding from $(-8/-2/-4)\pm 5$ nT in X/Y/Z-axis (where Z is the cylinder axis) to $(-66/1/-254)\pm 5$ nT has been measured with an external field of $(9333/2498/48502)\pm 5$ nT [KL16]. This is a significant reduction of the shielding factor. Fortunately this decrease can be compensated in the full amount by the use of the degaussing cable. Thus no reduction of the torque is necessary.

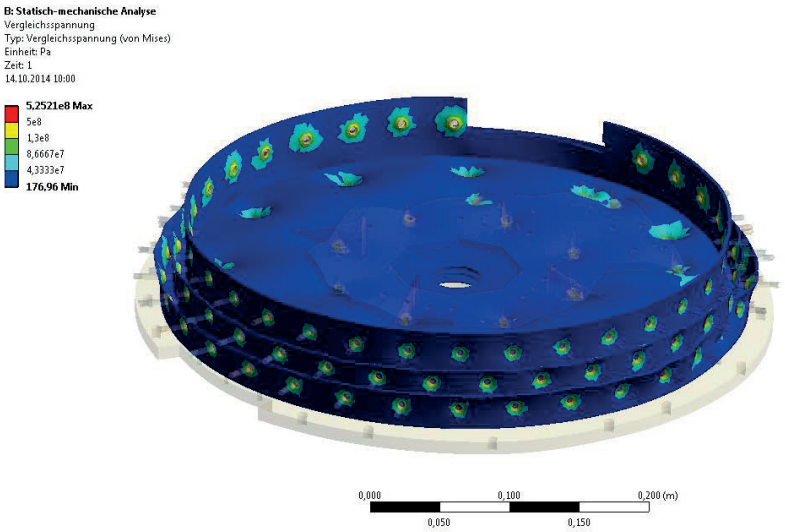


**(a)** Load step 1: Only bolt pretension forces applied

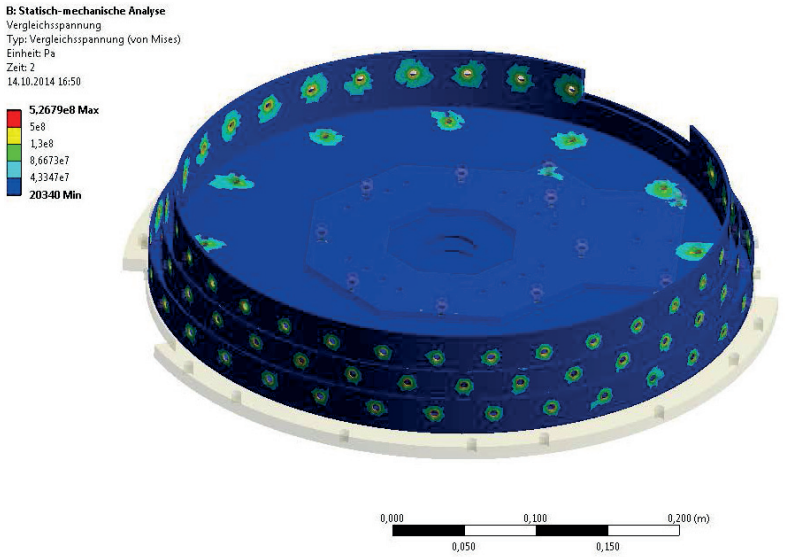


**(b)** Load step 2: 13 g acceleration applied in cylinder axis, bolt forces locked

**Figure 7.22:** Simulation results for magnetic shield with different external loads. With simulated bolt pretensioning force of 6.7 kN in M5 screws and 4.7 kN in M4 screws. Yellow color indicates that tensile strength of the material is exceeded.

According to the simulation results the additional acceleration during ascent does not cause a significant rise of the stress in the shield. For this reason no decrease of the shield performance is expected during ascent.

The vibrational test of the shield at $5.4 g_{rms}$ verified this expectation for vibrational loads. The test has been performed in all three axis and the shield, which had been degaussed prior to the test, showed no reduction in the shielding factor after the test [KL16].

### 7.3.2 Vacuum System

As stated in section 4 the objective of the mission is to achieve small expansion rates of the BECs to enable long time interferometry. Collisions of particles from the residual gas with the BEC will heat the BEC and thus fasten the expansion. A large number of particles in the background gas will enlarge the collision rate between the BEC and the background gas. For this reason an ultra high vacuum with pressures below $5 \times 10^{-10}$ hPa inside the science chamber is mandatory.

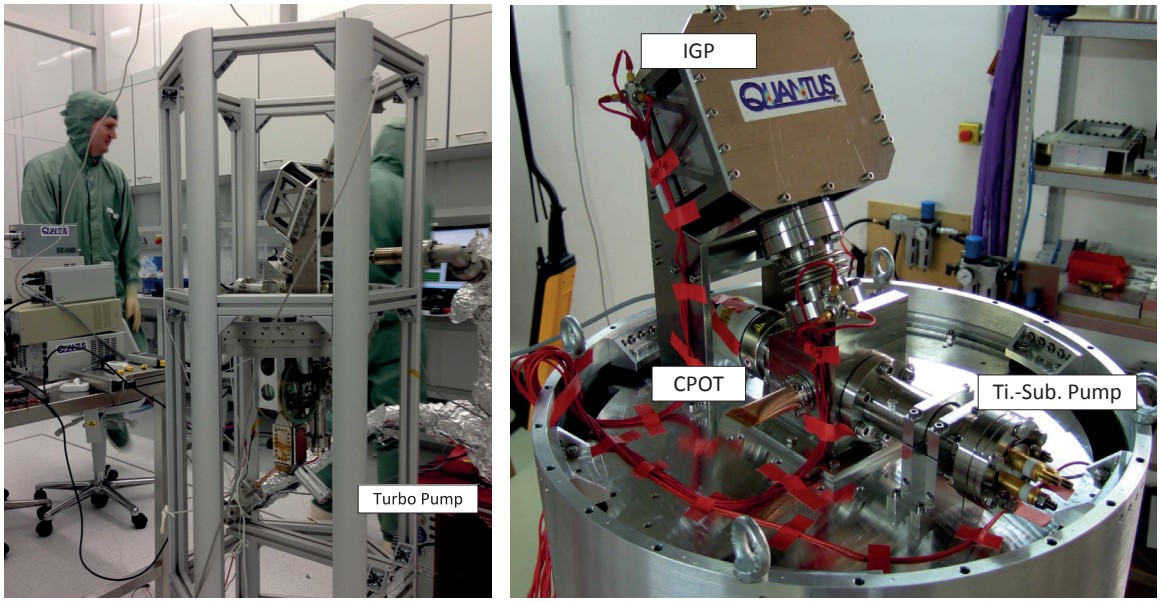


**(a)** MAIUS-1 physics package during vacuum preparation inside the ISO5 cleanroom at LNQE Hannover.

**(b)** MAIUS-1 pumping system in flight configuration during vibration test campaign

**Figure 7.23:** MAIUS-1 ultra-high vacuum system and vacuum preparation

To achieve these low pressures a combination of different pumps and an accurate cleaning and baking procedure is necessary. These procedures as well as details on the design and sizing of the UHV system will be presented in section 9.2.6. This subsection will only focus on the mechanical design and features of the vacuum system.

During vacuum preparation a turbo molecular roughening pump is used. The roughening pump is connected with one copper pinch-off tube (CPOT) each to the preparation chamber and to the pumping system. Once the base pressure of around $1 \times 10^{-9}$ hPa of the turbo pump is reached, the ion getter and titanium sublimation pump are activated and the pinch off tubes are closed using a hydraulic tool. During the pinch-off procedure the copper tube is hermetically sealed by hydraulic pinch-off jaws with a pressure of 70 MPa. This process is irreversible, thus the MAIUS pumping system has to resume pumping independently after pinch-off to compensate for residual out-gassing of components inside the vacuum or very small leaks, which can occur on each sealing.

For this reason the vacuum system is constructed from as few parts as possible. Wherever a hermetic connection between two parts was needed, the parts have been welded or brazed if possible. However some connections need to be reversible or can not be welded because of the material pairing. Those connections are sealed by indium or con-flat copper seals. The assembly procedures and the behavior of both sealing types in a (sounding) rocket environment and the impact on the vacuum pressure is one core topic of this thesis and will be discussed in chapter 9.

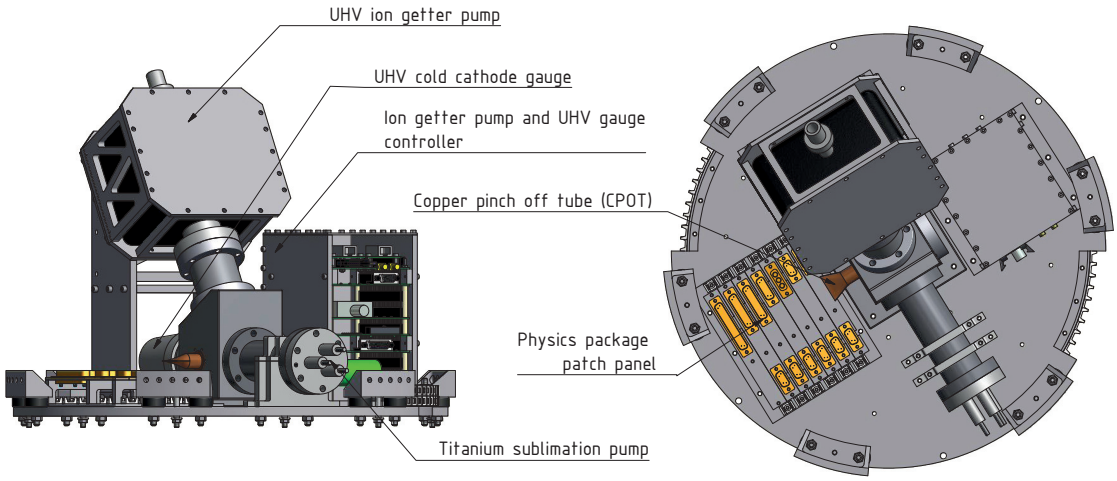


**Figure 7.24:** UHV Pumping system comprising of an ion-getter pump, a titanium sublimation pump and a cold-cathode vacuum gauge. A copper pinch off tube is used instead of valves to connect a turbo-molecular pump during vacuum preparation.

As shown in figure 7.24 the center of the MAIUS-1 pumping system is a single stainless steel cube equipped with four CF40 ports and two CF16 ports. One CF16 port is establishing the connection to the experiment chamber, while the other one is used to connect the roughening pump with a copper pinch off tube. The port for the connection to the experiment chamber is hidden below the cube. For this reason a straight pipe can be used to connect both parts, which will maximize the effective pumping speeds at the 3D chamber. Since the experiment chamber itself is rigidly mounted to the instrument platform as the center cube, a bellow has to be added to the tube to prevent mechanical stress on the seals due to the mounting situation.

The pumping rate needed to maintain the vacuum quality is generated by a commercial titanium sublimation pump ST22 manufactured by VG Sienta and a commercial ion getter pump VacIon 20Plus by Varian / Agilent. Both are connected to a CF 40 port of the center cube.

The titanium sublimation pump ST22 has been modified by the supplier to be shorter than the standard pump. Thus it measures only 105.5 mm inside the vacuum and 160.4 mm overall. This modification was necessary because of the limited space on the instrument platform. The pump is installed in a custom-made CF40 stainless steal pipe with a length

of 125 mm, which is supported by two pipe clamps with a 3 mm rubber layer between the clamps and the pipe to avoid applying loads on the seals. Moreover the pipe is equipped with a M38 $\times$ 1.5 thread at one side. This thread is used to install a mesh with 141 bore holes with a diameter of 1.5 mm. This mesh, which is installed at the sealing between the pipe and the center cube, should prevent fragments of the filaments, which get porous due to the sublimed titanium, from floating into the science chamber during microgravity phase if the filaments would break as a result of the strong accelerations during lift off. Moreover the mesh should protect the ion getter pump from titanium particles condensing inside the ion getter pump, which would reduce the pumping rate of the ion getter pump. Unfortunately the mesh will also reduce the effective pumping speed by blocking the molecular flow into the tube. A good estimation and measurement of the pumping speed of the titanium sublimation pump is given in chapter 9.

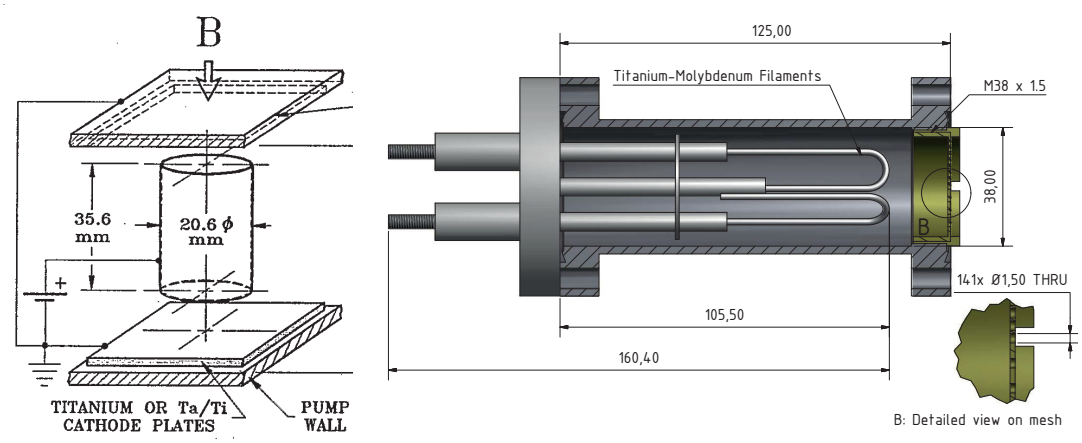


**(a)** Schematic of a single cell diode or noble diode ion-getter pump [Wel93]

**(b)** Section view through VG Sienta titanium sublimation pump mounted in a CF40 pipe with mesh installed

The ion getter pump is the only device capable of pumping inert gases, such as noble gases or methane, once the roughening pump is separated from the MAIUS vacuum system. Thus it is essential to reach pressures in the low $10^{-10}$ hPa regime. Pumping of (inert) gases is achieved by ionizing the gas molecules and employing a strong electrical potential, which will accelerate the ionized gas towards a solid cathode. At the cathode the ions will either be burried in the cathode material or are chemically or physically absorbed by the cathode material.

The noble diode pump VacIon Plus used with MAIUS-1 is equipped with cylindrical cathode elements configured as shown in figure 7.25a. Due to the high voltages applied in the ion pumps and their geometry ion pumps are sensitive to movements of the cathode, which need to be isolated electrically from the pump walls to avoid short circuits. The later constraint makes it difficult to properly support the cathode in the center of the pump. During the qualification process this fact caused a movement of the cathode at high-frequency vibrations.

The reduction of the distance between anode and cathode resulted in arching between the electrodes. Arching should be prevented because the pump is temporarily not functional if arching occurs and the arc might cause damage at the electrodes. To guarantee a reliable operation of the ion-pump the vibration damping mentioned in section 7.1 has been developed. A detailed study of this effect and the impact of the vibration damping will be described in section 9.6.

Aside from the vibrational damping of the instrument platform, the ion pump has been slightly modified to pass the qualification tests. The small gap between the pump walls and the magnets has been filled with tape to prevent a movement of the pump between the magnets. Moreover the pump has been integrated in a support structure as shown in figure 7.24. The pump with its magnets attached is placed between two 3 mm rubber mats with a hardness of 55 Shore. Thus the pump will have no direct contact to the aluminum of the support structure to reduce the vibrational loads.

The support structure will position the pump in an angle of 60° to the instruments platform. This is necessary, because of the limited space available and the constraint, that the center cube should be in the center of the instrument platform allowing a direct access to the science chamber.

Following the design approach for the cube-science chamber connection a CF40 bellow will ensure that the pump is mechanically decoupled from the center cube to avoid loads on the copper seals induced by the mounting itself.

The pressure of the vacuum is monitored by a Pfeiffer IKR270 cold cathode vacuum gauge. Cold cathode gauges are basically small ion-pumps, which ionize the residual gas and measure the current between cathode and anode caused by the ions. The higher the pressure, the more gas molecules are present, the more ions are produced, the higher is the current. Unfortunately movement of the electrodes due to vibrational loads will falsify the measurement. However the gauge is just a tool to have a fast measurement of the pressure for troubleshooting purposes. An very accurate measurement of the pressure in the science chamber can be achieved by measuring the lifetime of the BEC, which is strongly depending on the residual gas pressure in the science chamber [Sei14].

The last component of the vacuum system mounted onto the upper instruments platform of the physics package is an electronic stack, which operates the gauge and ion getter pump. It is equipped with an independent battery to keep the ion pump running, even if the main battery is disconnected, as for example during transport of the payload or arming of the motors in the launch tower.

### 7.3.3 Experiment Chamber

The experiment chamber consists of the science chamber (3D-MOT), the preparation chamber ($2D^+$-MOT) and the atom chip holder. All three parts are manufactured from Grade 5 titanium (Ti6Al4V), which is considered highly nonmagnetic and of low magnetic susceptibility. This reduces time varying residual magnetic fields within the shielding.

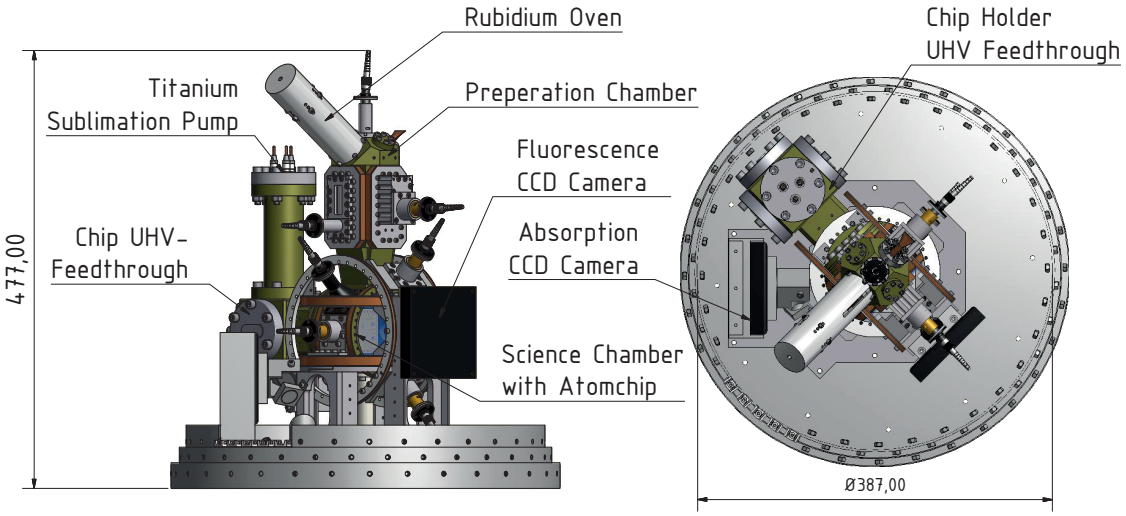


**Figure 7.26:** MAIUS-1 experiment chamber equipped with coils, telescopes, Rb-oven, two detection cameras

In both the science and the preparation chamber adhesive indium wire is used to mount the windows directly into the associated pockets in the chamber by applying pressure to the window and compressing the indium wire. Indium has been chosen instead of commercial CF optical ports to reduce the size of the chambers and allow rectangular window geometries. The connection between the science chamber and the atom chip holder is not compatible with standard con-flat sizes, thus it is sealed using the same technology.

A two-chamber system is common state-of-the-art for BEC creation and used in e.g. the experiments I.C.E or QUANTUS-2 as described in section 3.2 and 3.4. The atoms will be pre-cooled in the preparation chamber, transfered to the science chamber.

In here the atoms are cooled to an optical molasses and subsequently caught in a magneto optical trap (MOT) formed by light fields and the magnetic potentials provided by external coils and the multi-layer atomchip. From the caught atoms, the BEC is generated by evaporatively cooling the atoms below their critical temperature. Ultimately light pulse atom interferometry is performed in the science chamber.

In the following the setup of both chambers and the concept of a $2D^+$-MOT should be described in a more detailed way. For details on the cooling procedure in general refer section 1.2.

### Preparation Chamber

As mentioned above the Rubidium atoms should be pre-cooled within the preparation chamber. The gaseous Rubidium atoms are provided to the preparation chamber by an oven, which vaporizes liquid rubidium. Subsequently the rubidium vapor is caught in a two-dimensional magneto optical trap.

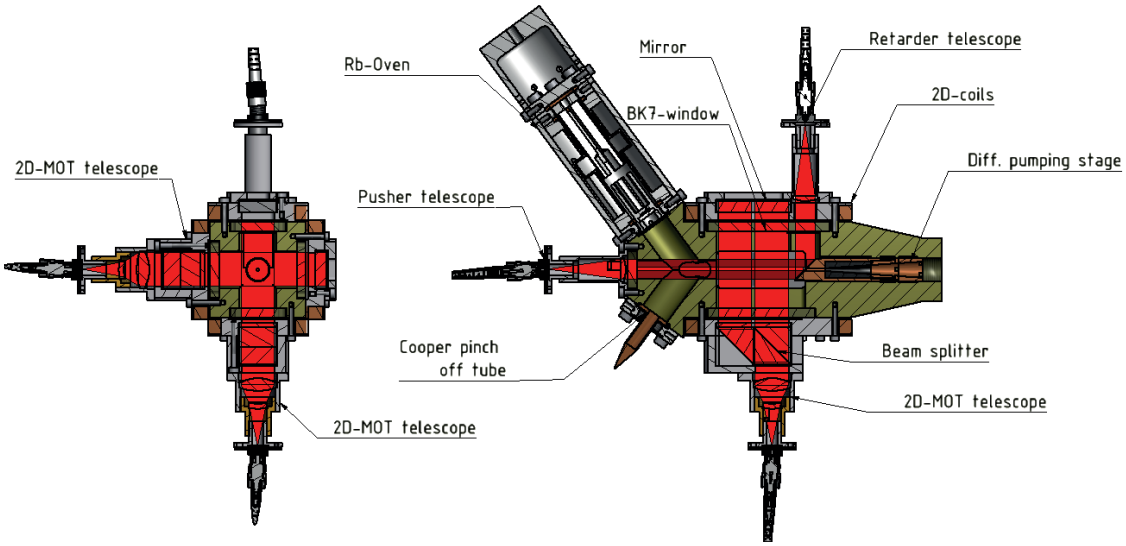


**Figure 7.27:** Assembly of preparation chamber showing the attached telescopes, coils and laser beam paths for two-dimensional trapping and pre-cooling of the atoms.

For this purpose the $2D^+$-MOT offers four rectangular optical ports. As presented in figure 7.27 the light for the MOT is shown in by two perpendicular telescopes through two windows with a size of 30 mm x 58 mm each. The light from the telescope is sent through a beam splitter and a prism forming two parallel beams with the same diameter of 18 mm. These two pairs of parallel MOT beams are reflected by a mirror mounted behind the opposite window. By the use of mirrors, a second pair of telescopes and fibres is not necessary, which reduces the size of the chamber and the laser distribution module significantly.

Each of the four optical ports is equipped with a rectangular magnetic coil, with 64 windings of 0.8 mm copper wire equally distributed on 8 layers wound onto an aluminum body. The four coils form a two-dimensional quadrupole magnetic field. The opposing coils have been wired to create a magnetic field with zero-crossing along the symmetric axis of the preparation chamber.

The aluminum coil bodies are also used to mount the two MOT-telescopes. Moreover a third telescope, used to apply a retarder beam, is attached to one of the coil bodies next to the mirror. As shown in figure 7.27 the optical port of the retarder has to increased in size (window size of 66 mm x 30 mm) to offer enough space to shine in the additional beam with a diameter of 9 mm next to the mirrored 2D-MOT beams. An additional circular window with a diameter of 22 mm is forming an optical port at the back of the chamber. This port provides access to the pusher beam completing the $2D^+$-MOT setup.

As shown in figure 7.28a a differential pumping stage (DPS) is mounted between the preparation and science chamber. A DPS is basically a baffle with small conductance, which allows high vapor pressure of Rubidium in the preparation chamber to rapidly capture high numbers of atoms but only a low vapor pressure in the science chamber to prevent atom losses because of collisions of the trapped atoms with the background gas.

This small conductance is achieved by a conical bore hole with a diameter of 1.5 mm at the inlet side with the higher pressure (preparation chamber) and 8.8 mm at the outlet facing the science chamber. Moreover a graphite inlay is mounted into the pumping stage. This material has a high surface area and absorbs a high percentage of the rubidium atoms if they get into contact with the graphite walls. The performance of the DPS has been optimized by the use of Monte-Carlo-Simulations in [Sei14].

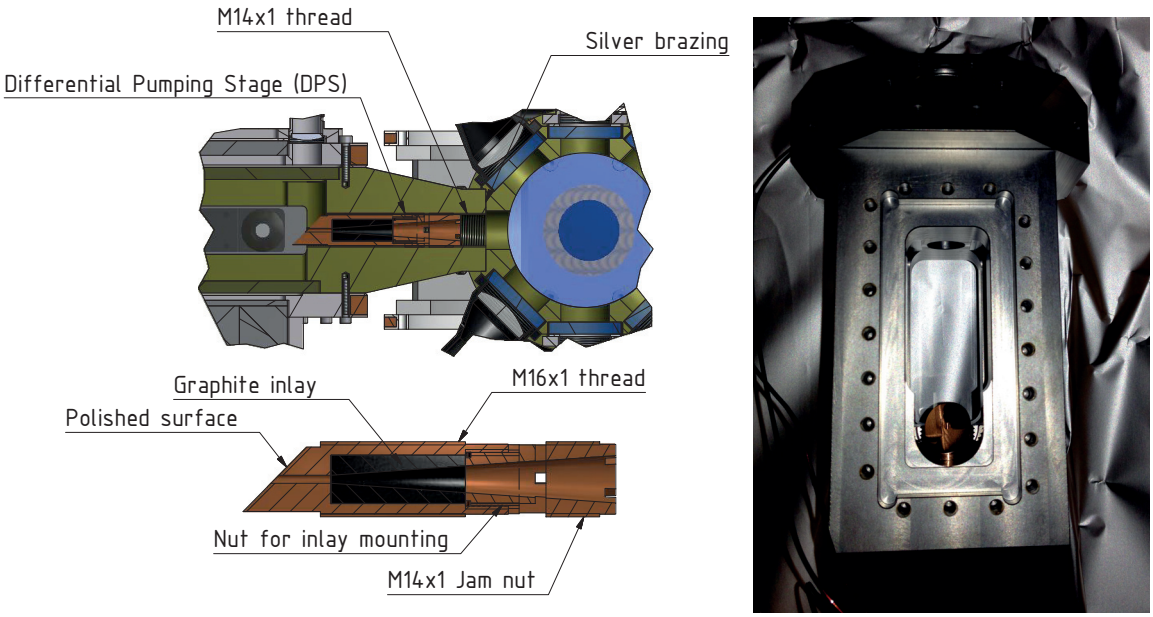


**(a)** Differential Pumping Stage (DPS) overview

**(b)** Polished DPS integrated in preparation chamber

**Figure 7.28:** MAIUS-1 differential pumping stage (DPS)

The body of the differential pumping stage is made of oxygen free copper (Luvata OFE-OK) and equipped with an external M14x1 fine thread, which is screwed into the associated thread in the preparation chamber. The end, which protrudes into the 2D-MOT forms a 45° plane which has been polished to high reflectivity (figure 7.28b). This plane is aligned to the telescope for the retarder beam. Once the mirror surface has been aligned its position is fixed with a M14 jam nut.

The retarder beam is deflected from the polished differential pumping stage to point opposite to the pusher beam. Since the hole in the center of the differential pumping stage is of low reflectivity, no light will be deflected in this region. The deflected light will retard

all atoms, but those in the cylindric region above the hole in the DPS. Thus the pusher beam will inject a concentrated beam of atoms in the differential pumping stage and along into the science chamber. This will allow to achieve loading rates of the 3D-MOT of up to $3.6 \times 10^9$ atoms/s [Sei14], which is beneficial since they will enlarge the number of experiments that can be performed in the time of micro-gravity available.

The needed circular $\sigma_+$-$\sigma_-$ polarization (refer section 1.2.2) of an opposing pair of 2D-MOT beams is achieved by a $\lambda/4$-plate placed between the telescope and the window, which will induce a circular polarization of the beam ($\sigma_+$-beam). The previously mentioned mirror is actually a $\lambda/4$-plate equipped with a anti-reflective coating at the side facing the window and with a highly reflective coating at the side facing away from the chamber. Therefore it will convert the entering $\sigma_+$-light into a linear polarized beam, being reflected at the other side and converted to a circular polarization again when passing the $\lambda/4$-plate a second time after reflection ($\sigma_-$-beam). In combination with the magnetic field of the rectangular coils, which create a quadropole field that switches its sign in the center of the chamber a suitable configuration for magneto optical trapping is achieved.

The outside of the windows of the optical ports is equipped with the same anti-reflective coating as the $\lambda$/4-mirror. At the inside the windows are not coated, because the coating might interact with rubidium [Sei14]. The coating of the windows has been carried out by Laseroptik Garbsen and will ensure that light shone in under an angle of 0° (perpendicular to the window) with wavelengths ranging from 767 nm to 1000 nm is not reflected at the windows. The wide spectrum coating will allow using not only 780 nm light for rubidium transition but also other wavelength for future experiments.

The windows themselves are made from Schott N-BK7 glass with a strength of 5 mm, which is used due to its coefficient of thermal expansion of $\alpha_{20\,^\circ\mathrm{C}/300\,^\circ\mathrm{C}} = 8.3 \times 10^{-6}\,\mathrm{K}^{-1}$ [Sch13]. This is very close to the coefficient of grade 5 titanium ($\alpha_{20\,^\circ\mathrm{C}} = 8.9 \times 10^{-6}\,\mathrm{K}^{-1}$ [Thy]). The matched coefficient of thermal expansion of the chamber and the windows will reduce stress in the windows induced by temperature fluctuations. Especially deformations such as buckling should be prevented to guarantee stable optical properties of the windows. For this reason the pockets accommodating the windows are designed to be 1 mm larger than the windows themselves. The given gap of 0.5 mm at each side is sufficient for a mismatch of the coefficient of thermal expansion of $\Delta\alpha = 0.6 \times 10^{-6}\,\mathrm{K}^{-1}$. The mismatch will lead to a negligible reduction of the gap by a maximum of 0.000 396 mm (window with $l_0 = 66\,\mathrm{mm}$) if the temperatures will stay in the requirements of $\pm 5\,\mathrm{K}$ ($\Delta T = 10\,\mathrm{K}$) as defined in section 6.5.

At the back end of the preparation chamber two CF16 ports and two CF10 ports offer additional interfaces. The rubidium oven is attached to one of the CF16 ports, while the second port is used to connect the roughening pump via a copper pinch off tube during vacuum preparation as described in section 7.3.2. The CF10 ports are not used and closed with blind flanges. They may be used in future experiments for additional atom sources.

### Science Chamber

The science chamber is used for the preparation of BECs and to perform atom interferometry. The needed magnetic and light fields ar applied by seven telescope, a set of six external coils and the printed circuits of an atomchip as described in section 7.3.4.

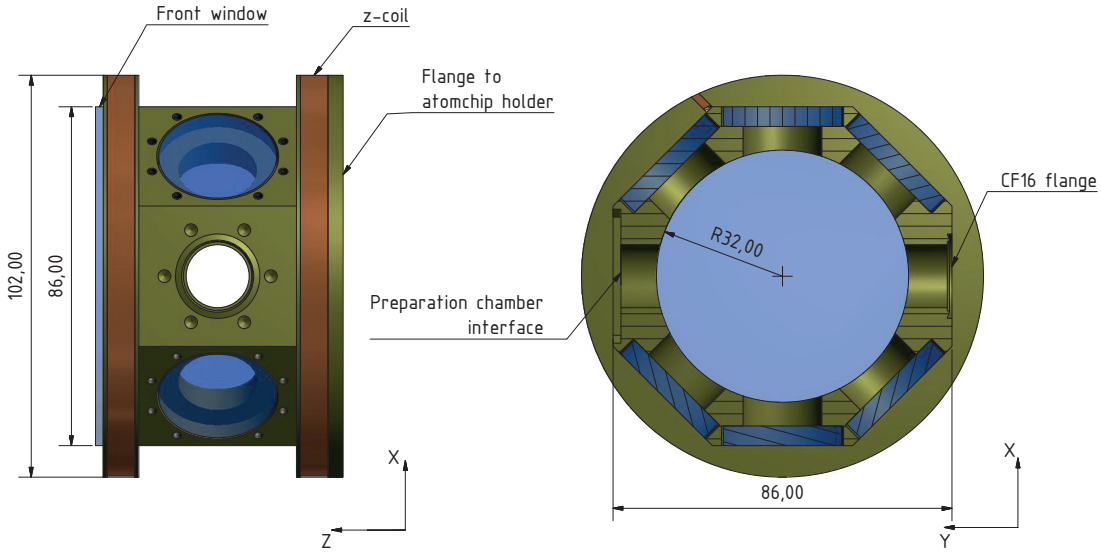


**Figure 7.29:** Science chamber geometry with a pair of magnetic coils wound onto the chamber

As shown in figure 7.29 a pair of coils (z-coils) is directly wound onto the chamber, which is requiring a cylindric shape at the front and the rear of the chamber. The maximum outer diameter of this cylindric part is 102 mm. The inside of the chamber is of cylindric shape as well measuring 64 mm in diameter. Between the coils the chamber is offering eight planar faces of the same width forming an octagon. Six of these faces are equipped with circular optical ports with a diameter of 30 mm. The two faces along the y-axis are used to establish a connection to the preparation chamber and to the pumping system outside of the magnetic shielding. At the front of the chamber a large view port with a diameter of 86 mm is installed. At the opposing side a custom made flange will establish the connection to the atom chip mount. This flange is sealed using indium wire to keep the chamber design small. Moreover commercial con-flat seals are not available in a suitable size.

All windows of the optical ports are sealed with indium as well for the same reason. As the windows of the preparation chamber, the windows of the science chamber are manufactured from Schott N-BK7 glass. While the 30 mm windows are made from glass with a thickness of 5 mm, the large window is manufactured from material with a strength of 10 mm. All preparation chamber windows have been coated from both sides with the *Laseroptik* 767 nm-1000 nm 0° coating also used in the preparation chamber.

The laser light for 3D trapping is shown in through the front window under an angle of 45° and through the two smaller ports on the side of the chamber along the x-axis. The light shown in through the front window is mirrored at the chip surface. Since the mirrored beams are perpendicular to each other, they cover two axis of freedom. The third dimension is covered by the telescopes along the x-axis. The MOT light is shown in using the same telescopes as for 2D trapping. As shown in figure 7.30B these telescopes are equipped with a $\lambda/4$-plate placed after the fiber coupler, which is causing a circular polarization of the light as needed for magneto optical trapping (refer section 1.2.2). A combination of a converging and diverging lens will produce a collimated beam with a diameter of 18 mm in a shorter telescopes compared to a single lens configuration.

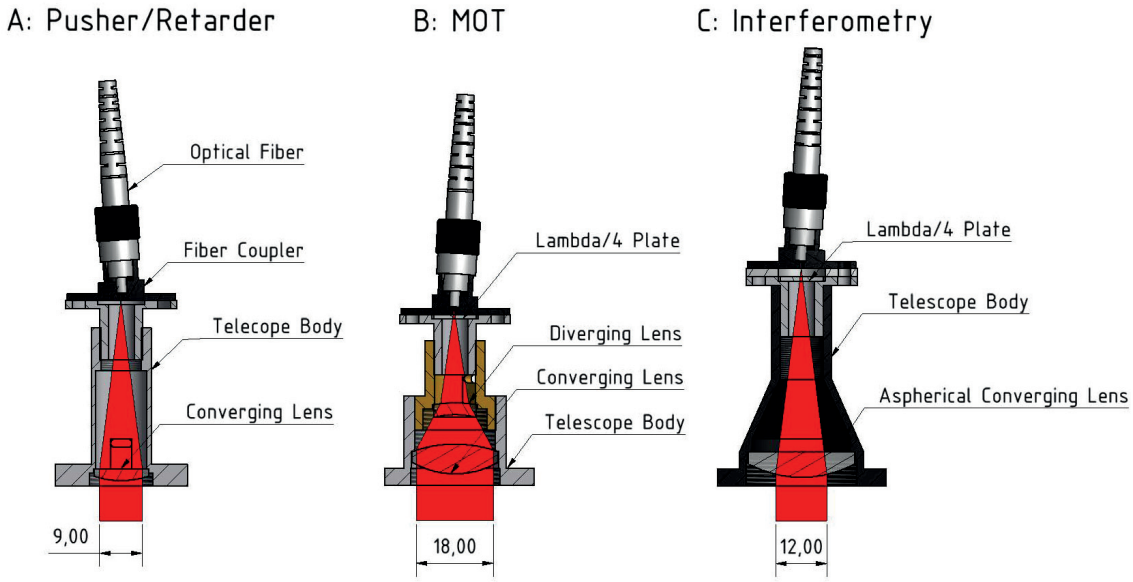


**Figure 7.30:** Three types of telescopes used in MAIUS-1 for the magneto-optical trap (MOT), the interferometry and for the pusher and retarder beam at the 2D-MOT.

Within the atom interferometry and detection telescopes (Ref. C in figure 7.30) one aspherical converging lens is used instead to reduce aberration. Thus the telescopes are longer and the collimated beam measures only 12mm in diameter. The interferometry and detection telescopes are attached to the remaining optical ports as shown in figure 7.31 forming two perpendicular axes which are rotated by 45° to the x-axis. All telescopes have been designed and qualified for sounding rocket use by the Leibniz University of Hanover [Lac12] [Sei14].

Aside from 7 telescopes and the atom chip mount, two cameras and optics for detection and two pairs of coils are mounted to the science chamber as illustrated in figure 7.31.

Two different detection techniques are used in the MAIUS-1 setup. Therefore two cameras are required. The PCO 1400 camera is used for both imaging techniques. For the absorption imaging method a light pulse is shown in through the detection telescope, this light pulse will create a shadow image of the atomic cloud on the CCD of the camera.

Since the atoms of the cloud will absorb photons of the detection light pulse, the BEC will be destroyed when taking an absorption image. The light not absorbed by the atoms is sent through the opposite viewport into a system of two lenses and two mirrors ending at the absorption camera mounted to the base plate of the chamber mounting.

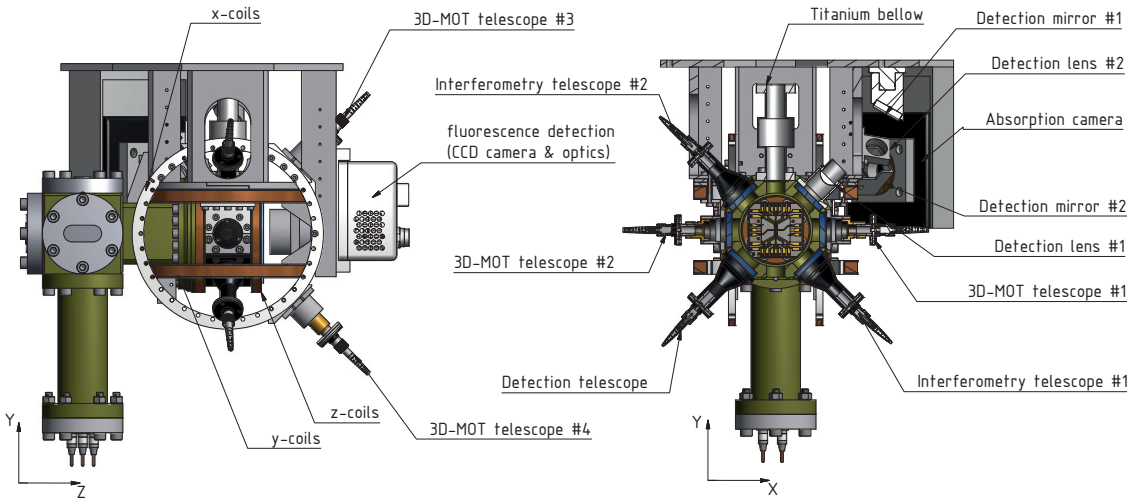


**Figure 7.31:** Fully assembled science chamber. Seven collimators, three pairs of coils and two cameras are attached to the science chamber.

The lenses used offer a focal length (f) of 60 mm. The first lens is positioned 60 mm from the center of the chamber. Thus the BEC is in the focal point of the first lens, while the CCD of the camera is in the focal point of the second lens. The distance between the first and the second lens was chosen to be 120 mm (2f). Thus the total length of the optical path is 240 mm. The beam hat to be mirrored twice to make the chamber setup compact and to fit it into the magnetic shielding.

A second camera of the same type will take fluorescence images of the atoms. This method is measuring the photons emitted by the atoms of the BEC, which are illuminated by light from either the detection or the interferometry telescopes. The camera is mounted in front of the large view port with a distance of 53 mm between the CCD and the atoms of the BEC. The light is projected by a single aspheric lens with a focal length of 26.5 mm onto the CCD of the camera.

In addition to the previously mentioned z-coils, which are wound directly onto the science chamber, two more pairs of coils are needed to trap the atoms in all three directions of space. These coils are mounted to the science chamber, the atom chip holder and the chamber mounting in a Helmholtz configuration as shown in figure 7.31.

The body of these coils is made from fiberglass (ROTEK GFK-HGW2372.4). This material is offering low density, high tensile strength and most importantly it is non-conductive. Non-conductivity will allow shorter switching times of the coils because no eddy currents will be induced in the coil body.

All three coils are wound manually using a copper wire with a diameter of 0.95 mm, which is electrically isolated by a layer of kapton coating. The diameter of the different coils, the windings, the measured and calculated resistance and the expected power consumption at the maximum output of the current driver (5 A) is given in table 7.4.

| Pair of coils | X | Y | Z | 2D |
|---|---|---|---|---|
| Inner diameter in mm | 156 | 120 | 94 | N/A |
| Inner dimension in mm | N/A | N/A | N/A | 40 x 76 |
| Windings | 21 | 102 | 30 | 64 |
| Resistance (meas.) in Ω | 0.4 | 1.0 | 0.5 | 0.53 |
| Thermal Power ($I_{max} = 5$ A) in W | 10 | 25 | 12.5 | 13.25 |

**Table 7.4:** Specifications of the science and preparation chamber coils. Resistance measured by a multimeter. Induced thermal power calculated for typical and maximum currents.

Although the calculated maximum dissipated heat is high, no active cooling is necessary to keep the chamber temperatures in the required ranges, because the typical operation currents of the coils are smaller than 5 A. Moreover the duty cycles are typically in the order of 100 ms to 1000 ms, thus no significant heating of the chamber will occur. A detailed thermal simulation of the science and preparation chamber including the heating by the atom chip and the oven has been performed in this thesis. The simulation setup and the results are presented in section 12.3.

Mechanical simulations have been performed to analyze the connection between science and preparation chamber. These two parts are brazed using a silver foil. In the predecessor experiment this connection was sealed using an indium wire as well. Unfortunately the sealing failed during the first vibration test. The mass of the preparation chamber in combination with a long lever between the center of gravity of the preparation chamber and the sealing caused high loads on the small area of indium, which resulted in a breach of the seal. However the sealing of the windows and between the atom chip holder and the science chamber was successfully qualified for sounding rocket use (refer section 9.6).

The brazing process, which was developed by the Günter-Köhler-Institut (IfW) Jena, is using a 100 µm thick brazing foil made of pure silver. The foil was cut to fit the contact area between both parts. This will create a brazed joint covering the whole contact area, which will reduce the risk of virtual leaks. Such leaks would occur if small gaps filled with air will remain at the joint and the air is slowly conducted in the vacuum chamber. The danger of virtual leaks was one reason for not using welding to establish this connection.

The mechanical properties of a silver brazed joint were studied by the IfW to ensure that the joint will withstand the mechanical loads aboard the sounding rocket. For this purpose two circular titanium tensile test probes with a diameter 4.51 mm and a length of 40 mm were prepared with the same process parameters as used for brazing the science and preparation chamber.

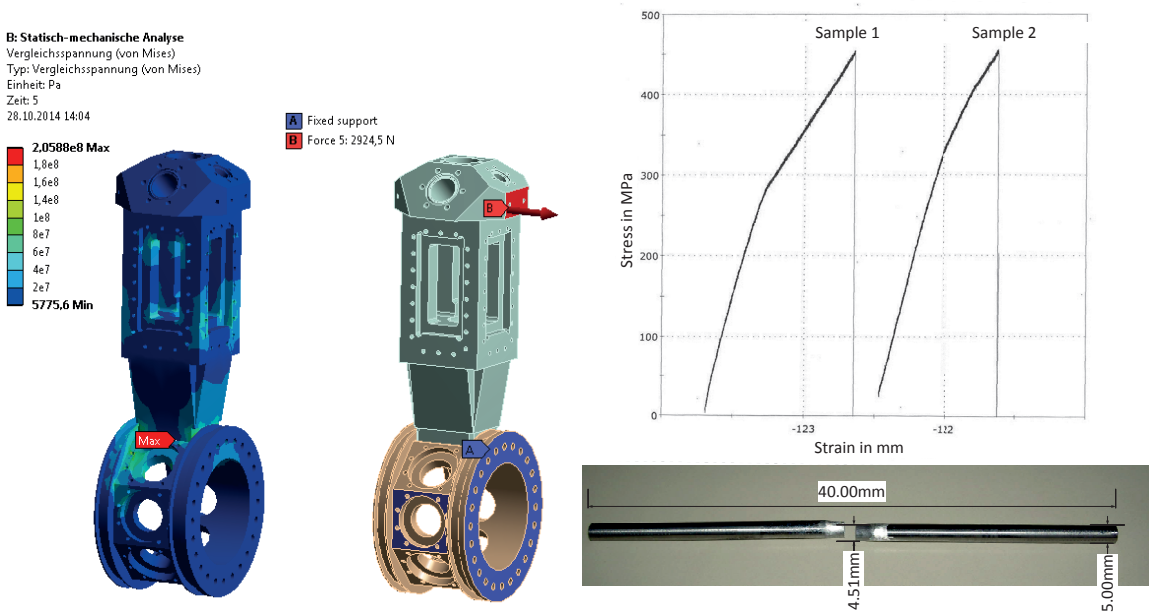


**(a)** FEM simulation setup and results of the preparation chamber at 100g

**(b)** Results of a one-dimensional tensile test of a silver-brazed circular probe performed at IfW Jena [Hor12]

**Figure 7.32:** FEM simulation and tensile test results for the brazed connection between science and preparation chamber

Figure 7.32b shows the probe after the test and the test results. An average tensile strength of $R_m = 456.25\,\text{MPa}$ was measured in two test runs [Hor12]. The yield strength is estimated to be 300 MPa from the change in the slope of the curves in diagram 7.32b.

The overall mass of the preparation chamber including telescopes, windows, oven and coils is 2.98 kg. The resulting force of this mass at an acceleration of 100 g (hard touch down) is 2924.5 N. To simulate a worst case scenario the force application point was chosen to be at the top of the preparation chamber as illustrated in figure 7.32a. Moreover a fixed support has been simulated at two telescopes and the connection to the atom chip holder. This is a simplification of the actual mounting of the experiment chamber as it is described in section 7.3.6. As expected the maximum stress is induced at the connection between preparation and science chamber. The von-Miese equivalent stress intensity is simulated to be 205 MPa, which is significantly below the tensile and yield strength of the material. Simulations at 13 g acceleration (ascent peak loads) resulted in a stress intensity of 26.8 MPa. Finally the brazed chamber has been successfully vibration tested without shock mounts at $8.1\text{g}_{\text{rms}}$. Thus a failure of the brazed joint during ascent and even during touch down is very unlikely.

### 7.3.4 Atomchip

The atomchip is a key feature for reducing the size of the experiment chamber. It is used to generate inhomogeneous magnetic fields, which are superimposed to the fields of the regular magnetic coils. Aside from its small size the advantages of an atom chip are its low power consumption and fast switching times of the generated magnetic fields compared to other methods [Ste09].

The chip is capable of forming various magnetic trap geometries by applying current to the different circuits of the chip layers. A detailed description of the chip performance and its structures is given in [Sei14].

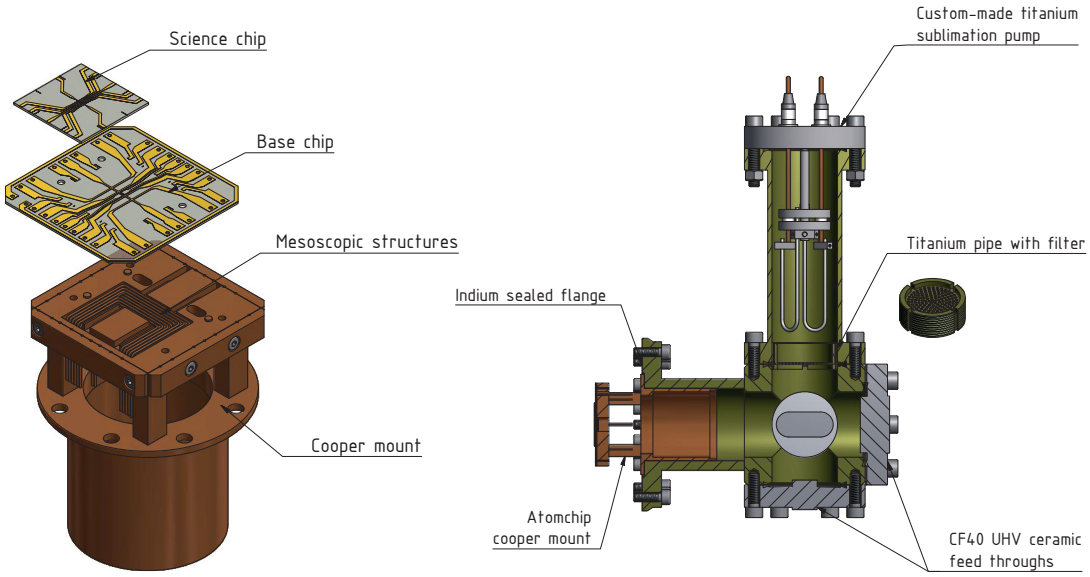


**(a)** Atomchip with its three layers and an microwave antenna integrated in the base chip layer.

**(b)** Atomchip holder with titanium sublimation pump and UHV feedthroughs

**Figure 7.33:** Atomchip assembly of MAIUS-1

As shown in figure 7.33a the chip consists of three different structures, which decrease in conductor diameter and are mounted to each other with UHV suitable glue with a high thermal conductivity (Epotek H77). While the lowest layer consist of mesoscopic structures (0.6 mm copper wire), the science and the base chip are fabricated from aluminum nitrate substrate with printed circuits made of gold. The printed circuits are of rectangular shape with a height of 0.01 mm and a width of 0.5 mm at the base chip and 0.05 mm at the science chip. Additionally three RF antennas are included in the base chip setup to apply RF signals during evaporation. The science chip is equipped with a layer of high reflectivity forming the mirror for the MOT beams as described in section 7.3.3.

The measured resistances of different structures of the chip is given in table 7.5. Moreover the thermal power generated in the chip at maximum currents is given for different circuit structures. The heat flux generated by the chip and the coils described above is part of the thermal simulation of the experiment chamber presented in section 12.3.

| Chip Structure | Resistance (mes.) in Ω | Current (max.) in A | Power (max) in W |
|---|---|---|---|
| Meso. U | 0.125 | 10 | 12.5 |
| Meso I/H | 0.070 | 10 | 7 |
| Base outer Z | 0.150 | 6 | 5.4 |
| Science outer Z | 0.700 | 2 | 2.8 |

**Table 7.5:** Resistance (measuread) and power consumption of the mesoscopic (U/I/H) and the base and science (Z) atomchip structures.

The conductors of the chip will dissipate their heat rapidly to the copper mount, because the aluminum nitrate substrate as well as the glue offers high thermal conductivity. Thus the chip itself will not heat significantly. The copper mount is made of oxygen-free copper (Luvata OFE-OK), which offers a high thermal conductivity of $391\,\mathrm{W\,m^{-1}\,K^{-1}}$ [Luv14]. To ensure that the produced heat is conducted to the titanium atom chip holder, the dimensions of the lower cylindrical part of the copper mount and the associated bore hole are designed to be a cylindrical interference fit.

Once the atomchip is fitted and screwed to the holder, the assembly is mounted to the science chamber with the atom chip protruding into the science chamber. The connection between the atom chip holder and the science chamber will be sealed using indium wire.

As shown in figure 7.33b the structure opposite to the flange is of cubic shape. This cube is equipped with a total of five CF40 ports. Four of those are reserved to highly non magnetic UHV feedthroughs (SRI SD5001-9s and D5002-2-15) to connect the atom chip structures with the current drivers. The connection between the feedthroughs and the chip is achieved using vacuum-suitable wires, which are glued to the chip circuit-ends with electro-conductive glue.

The fifth port is occupied by an additional customized titanium sublimation pump, which should especially compensate for the large surface of the cables between atom chip and feedthroughs. This surface area might lead to a rise in pressure although the cables are designed to have a low out-gassing rate.

The filaments and thus the performance of the customized pump is identical with the pump described in section 7.3.2. The feedthroughs of the commercial pump may induce magnetic fields due to small amounts of iron and brass used in the contacts. Because the pump is positioned inside the magnetic shield and close to the atoms, this feedthrough has been replaced by a non-magnetizable feedthrough.

### 7.3.5 Rubidium Oven

The alkali metal isotope Rubidium 87 is used in the MAIUS-1 atom interferometer. Natural rubidium is composed of the two isotopes 85Rb (72.2 %) and the slightly radioactive 87Rb (27.8 %). Isolating 87Rb would be very expensive, thus rubidium is usually sold in the natural compound in glas ampules. Because rubidium is very reactive, especially with water, these ampules are filled with a noble gas as helium or argon. The metal is sold in a solid form at room temperature, as its melting point is 39.31 °C [Ste03].

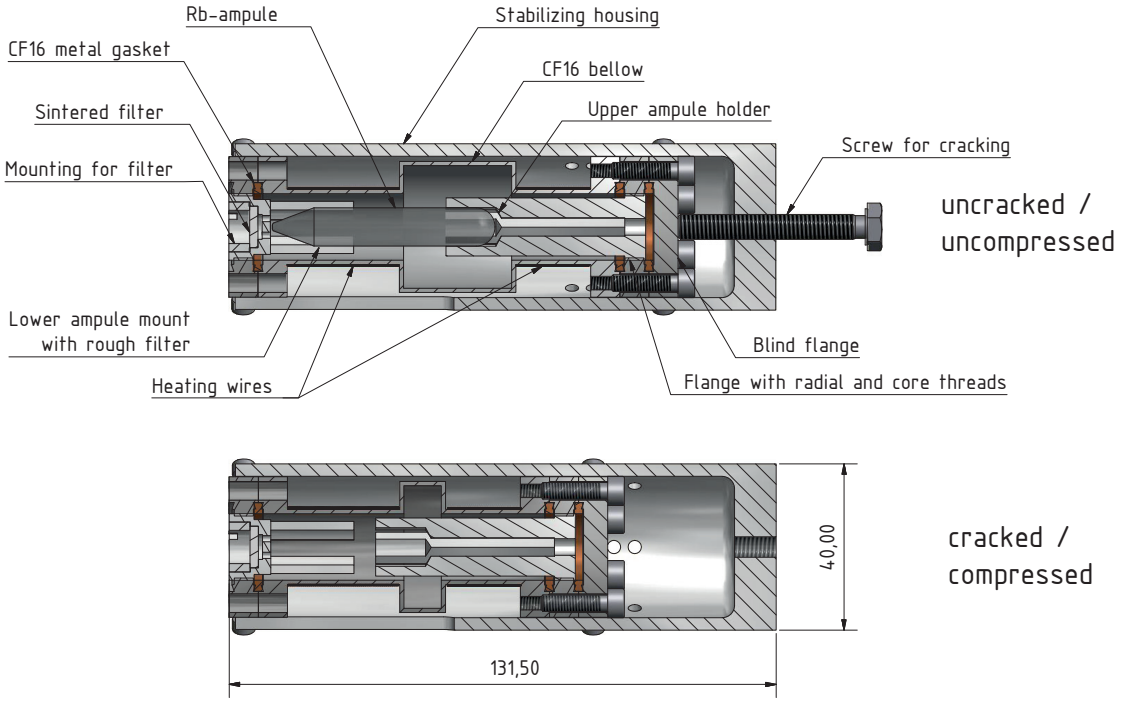


**Figure 7.34:** Rubidium oven using glass ampules filled with Rubidium, which is available of the shelf. The ampule is cracked in the vacuum by compressing the oven bellow. The figure shows the uncracked and cracked state of the oven.

To provide Rubidium for atom physics experiments, either a dispenser or an oven can be used. Dispenser dispense rubidium which is bound in chromate alloys by applying high currents, which heat the alloy. Unfortunately a lot of other atoms are dispensed along with Rubidium 87 and 85 isotopes during this procedure. These atoms will reduce the performance of the MOT and have to be removed from the system, which is especially difficult in MAIUS-1, because of the differential pumping stage reducing the conductance between the preparation chamber and the pumping system.

Due to these disadvantages a Rubidium oven has been chosen as atom source in MAIUS-1. Since no commercial solutions are available, the oven had to be designed from scratch. The most difficult part is to fill the Rubidium into the oven. Due to its high reactivity it may react with the water in the surrounding air if removed from its ampule. Filling the oven in an argon atmosphere (e.g. in a glove box) would be a possibility. This would require a

valve to hermetically seal the oven and open it once the oven is attached to the chamber and vacuum has been prepared. Obviously this is a complex and expensive procedure and the use of a valve would result in a rather bulky setup. Therefore opening the ampule in a container under vacuum, which is already attached to the preparation chamber is considered the easiest and safest way.

As shown in figure 7.34 the oven design comprises four CF16 titanium parts. The center piece is a bellow forming the oven chamber. To both sides the bellow is followed by a CF16 flange, which is equipped with a thread at its core to mount the ampoule holders. Moreover these flanges are equipped with radial blind tapped holes to mount the bellow to the stabilizing housing. The setup is closed by a blind flange to the one side and attached to the preparation chamber on the other side.

The rubidium ampule is mounted between the lower and upper ampule holder, while the system is under atmosphere. Afterwards the oven is attached to the preparation chamber and evacuated. The stabilizing housing will keep the flanges in their position and ensure that the bellow is not compressed due to the pressure difference. Once the oven should be activated the radial screws at the upper flange are removed, which will cause the bellow to compress. By turning the screw at the back of the housing clockwise additional force can be applied to crack the glass ampule. The stabilizing housing will assure that the force is only applied axially and no momentum is acting on the seals.

Once the rubidium has been released, it is heated and vaporized by a resistance heater. The heater consists of 0.25 mm copper wire, which has been wound onto the bellow in two layers. Because the second layer is wound in opposite direction with the same number of windings, the magnetic fields induced by the first layer are compensated by the second one. The measured resistance of the wire is 8.77 Ω. Thus the oven will be heated with 2.85 W if operated at a typical voltage of 5 V. This heat input has also been considered in the thermal simulation of the science chamber in section 12.3.

To prevent the liquid rubidium from floating into the preparation chamber a sintered filter (ggt Gleittechnik Ag CA200) has been included in the flange between the bellow and the preparation chamber.

To qualify the functionality of the oven the partial pressure of rubidium has been measured with a mass spectrometer prior to the installation of the oven at the chamber in a test setup. Heating the oven to 65 °C results in a rise of the partial pressure of Rubidium from $1 \times 10^{-10}$ hPa (20 °C) to $4 \times 10^{-7}$ hPa (65 °C). The performance was identical after the test chamber was tested under vibrational loads. Moreover no rubidium particles have been observed in the test chamber. Thus no liquid rubidium entered the chamber before or during the vibration test. Finally the oven was put into operation successfully in the MAIUS-1 apparatus on ground [Sei14].

### 7.3.6 Mounting of Science and Preparation Chamber

Mounting of the experiment chamber is difficult because of the complexity of the system and the large number of instruments attached to it. The mounting has to be rigid and should provide access to all sides of the experiment chamber. Moreover the chamber should only be mounted through the top caps of the magnetic shielding to the upper instruments platform, because the magnetic shield should not carry any loads (refer section 7.3.1).

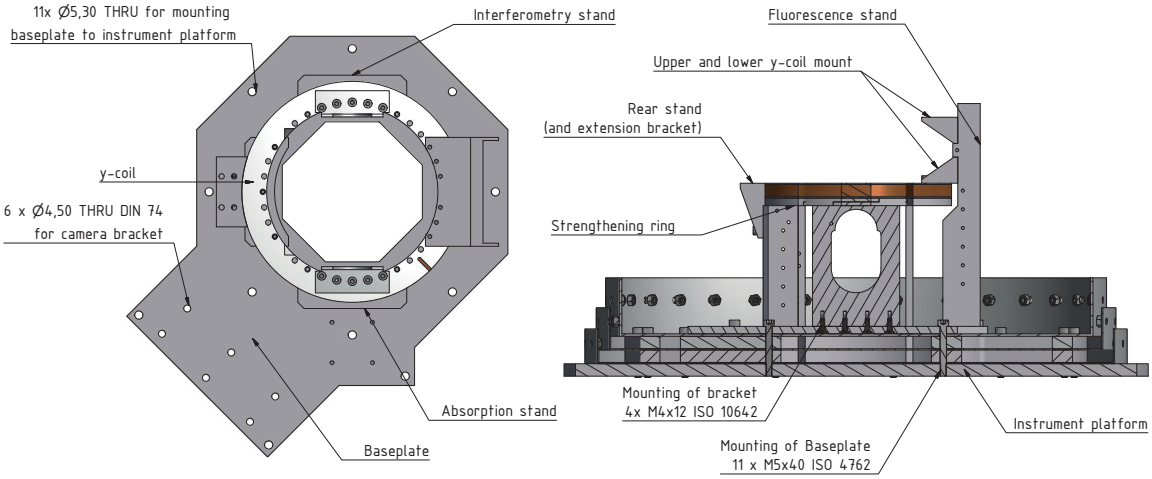


**Figure 7.35:** Support structure for mounting of experiment chamber and associate instruments to the upper instruments platform. The lower y-coil is integrated into the mounting to make the setup more compact.

To avoid additional holes in the magnetic shield 11 M5 ISO 4762 titanium screws with a length of 40 mm are used for simultaneous mounting of the shield and the baseplate of a support frame to the upper instruments platform of the physics package. As shown in figure 7.35 four stands, five brackets, a coil, a strengthening ring and a baseplate are forming this support frame for mounting the experiment chamber.

All stands and an additional bracket for mounting of the absorption detection camera (not shown) are screwed to the baseplate from below with ISO 10642 countersink screws. Moreover a mirror mount being part of the absorption detection optics is mounted directly to the baseplate.

The baseplate is made of aluminum and 6 mm strong. The strengthening ring is manufactured from aluminum as well. It consists of two parts, which have been anodized. This should prevent induction of eddy currents, which would enlarge coil switching times.

The four aluminum stands are all of similar shape. The U-profile should enlarge the bending stiffness of the stands. All of these stands have the same footprint with a width of 70 mm and a depth of 28 mm as shown in figure 7.36. Four M4 threads strengthened with Helicoils are used to mount the stand to the baseplate. The strengthening ring is fixed in its position by two M3 screws mounted from inside the stand. Subsequently the 6 M3

threaded holes at the top of the stand are used to mount the coil and the side brackets to the stands from the top. The remaining M3 threaded holes at the sides are used to mount cables of photodiodes and coils to the structure.

All but the rear stand are equipped with an oval hole as shown in figure 7.36. This hole measures 20 mm in radius and 70 mm in width. This size is sufficient to mount and adjust the telescopes even if the chamber is already integrated into the frame.

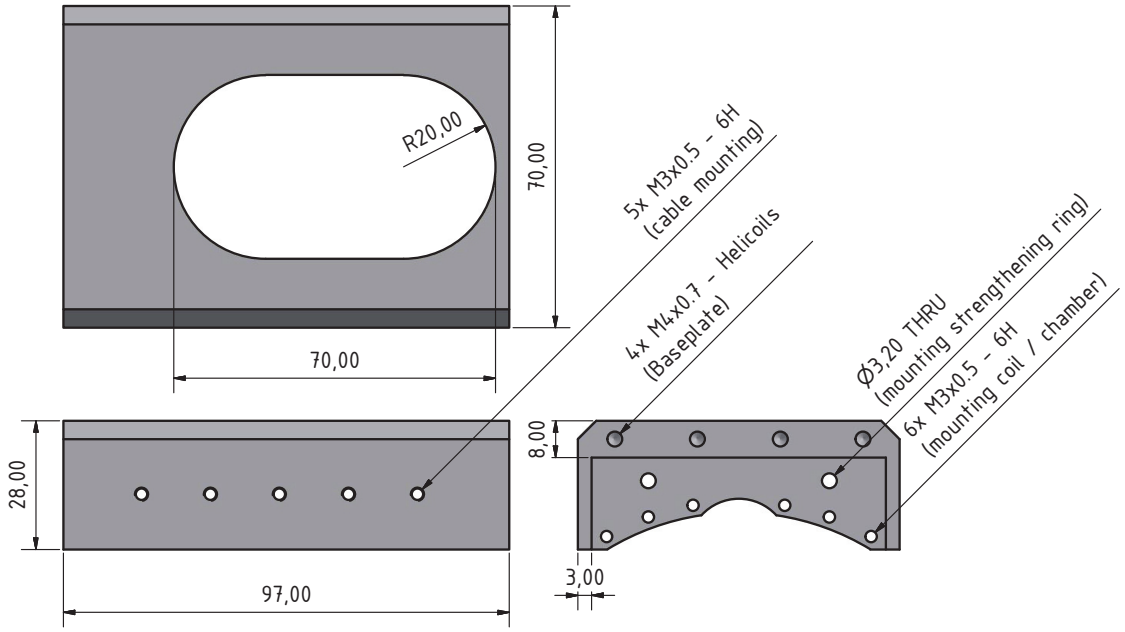


**Figure 7.36:** Detailed drawing of the interferometry stand with dimensions. The big 20 mm cut-out is to access the 3D telescopes for maintenance or adjustments

The rear stand is equipped with an extension bracket, which is used to mount the experiment chamber to the stand. The rear mounting of the experiment chamber is shown in detail in figure 7.37. The connection is achieved by a total of eight M3 ISO 4762 screws, which are mounted to threaded holes in the atom chip holder being part of the experiment chamber. Four of the screws are used for the connection of the extension bracket and the atom chip holder, while the other four are mounted through the rear stand. The remaining three screws in the rear stand are attaching the strengthening ring to the stand.

In addition to the rear mount, two side mount brackets will support the experiment chamber. These brackets are mounted to the interferometry and absorption stand through the lower y-coil and the strengthening ring by five M5 ISO 4762 screws. The connection to the chamber is achieved by four additional M3 screws, which are mounted through the telescopes as shown in figure 7.36.

The fluorescence stand is longer than the other three stands. It carries the fluorescence camera and its optics, which are positioned in front of the front window with the center of the lens aligned to be in line with the middle of the atom chip. This allows to capture good

images, since the center of the magnetic trap (and thus the atoms) will be in the middle of the chip at the beginning of the sequences as well.

Moreover the stand is equipped with two additional brackets to support the upper and lower y-coil. The lower bracket is equipped with seven 3.2 mm through holes to mount the bracket and the y-coil to the associated threads in the strengthening ring. The lower coil is mounted to all four stands in addition, since the coil and the strengthening ring will carry the mass of the experiment chamber. The upper coil is not carrying those loads. Thus it is only attached to the atom chip holder by four M3 screws (y-coil mount #2 in figure 7.37) and to the upper bracket of the fluorescence stand by seven M3 screws (y-coil mount #2).

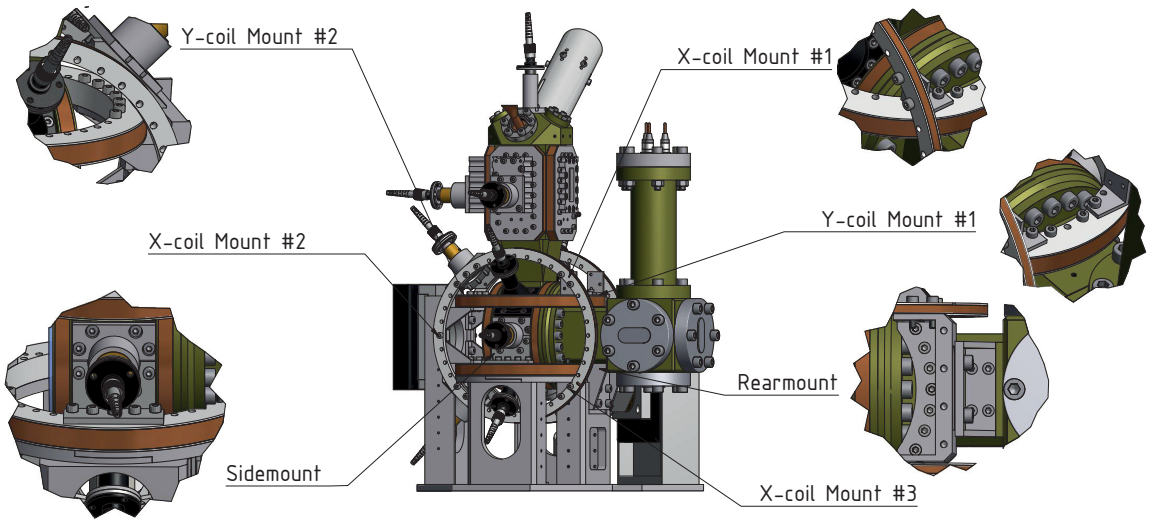


**Figure 7.37:** Details of the complex mounting of two chambers and its accessories. The science chamber is mounted at three points, the two side and rear mounts. The coils are either directly screwed to the chamber or to the support structure.

The x-coils are of lower mass and are only carrying a light aluminum structure for alignment of the 45°-MOT telescopes, thus they are only mounted by five M3 screws at three different points as shown in figure 7.37.

As mentioned in section 6.4 it is important that the position of the telescopes or coils will not change after launch to maintain a setup identical to the one on ground. This means that no plastic deformations should occur in the support frame. For this reason all aluminum parts of the frame are made from CERTAL (EN AW 7022) combining high tensile strength (555 MPa) and yield strength (495 MPa) with a low density. The frame has been designed to withstand loads of up to 50 g without plastic deformation using FEM simulations.

## 7.4 Laser System

The laser light used for laser cooling, atomic state preparation, atom interferometry and detection is generated within a diode laser based system integrated in a compact housing. Despite the limited volume the housing shelters multiple subsystems. As given in diagram 7.38 these are eight micro-integrated diode laser modules (A-C), a distribution and switching unit (D) based on free-space Zerodur optical bench technology, a Rubidium stabilization unit (E) as well as two fiber splitter systems (F-G).

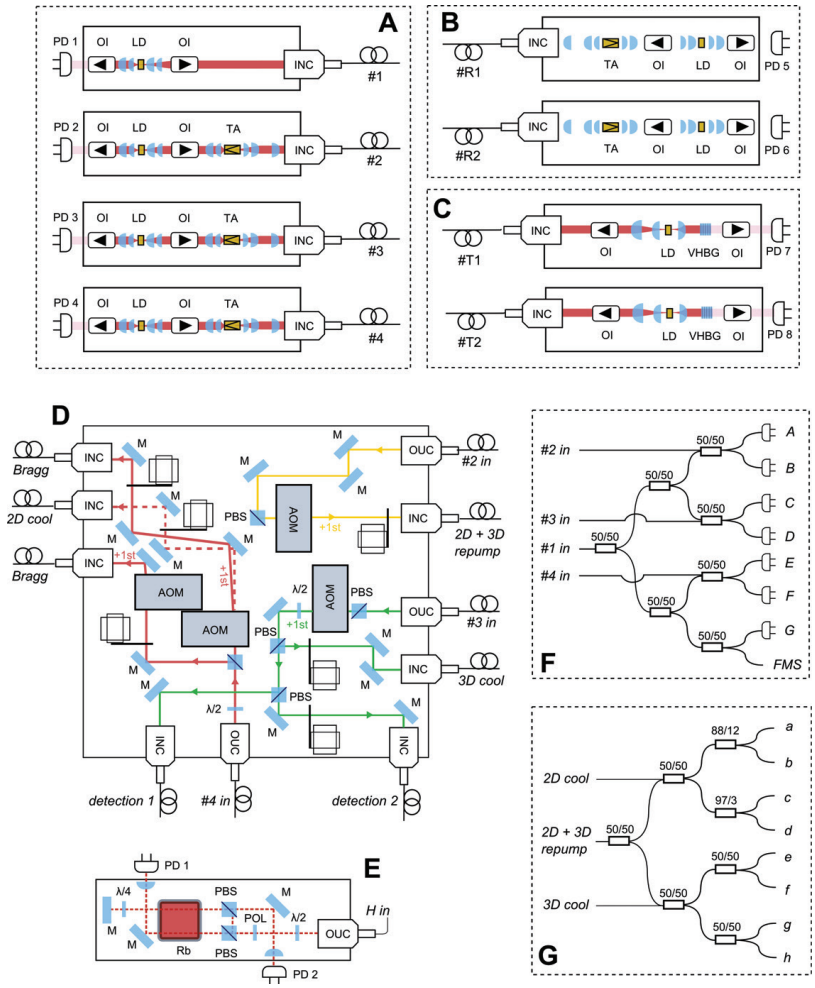


**Figure 7.38:** Functional diagram of MAIUS-1 laser system showing four science lasers (A), two (cold) redundancy lasers (B), two technology demonstration lasers (C), the free-space splitting and distribution board (D) and two fiber splitters (F&G). The connection between those components is realized with polarization maintaining fibers [Kru].

The guidance of laser light inside the laser system housing as well as to the physics package is realized with polarization maintaining optical fibers. This guarantees optimal overlapping of laser beams of each frequency as well as reliable and efficient guidance of laser light even in the harsh rocket environment.

### 7.4.1 Laser Modules

The laser modules used in MAIUS are based on a versatile platform comprising semiconductor, micro-optics and electronic interfaces altogether assembled onto very robust micro-optical benches (MIOBs). These modules are explicitly designed for rubidium BEC and atom interferometry experiments aboard sounding rockets and feature single distributed feedback (DFB) based master oscillators (MO) or master oscillator power amplifier (MOPA) setups.

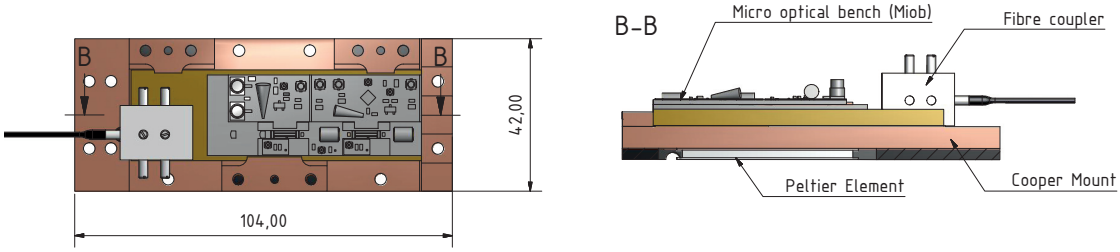


**Figure 7.39:** MAIUS laser modules consisting of a copper mount, the micro optical bench with the laser diode and a tapered amplifier as well as a fiber coupling. A peltier element stabilizes the temperature of the entire setup.

For operating the MAIUS experiment, four science laser modules are foreseen. The master laser is a DFB laser diode only, whereas the three light sources for 2D/3D MOT, Bragg interferometry and detection are DFB-based MOPA modules with a tapered amplifier section featuring free-space output powers of about 1 W at 780 nm. The remaining four modules comprise two redundancy MOPA modules and two micro-integrated extended cavity diode laser (ECDL), which have been added as technology demonstrator for future satellite-based missions targeting at high precision tests of general relativity [Agu14].

The micro-optical bench is glued onto a aluminum nitride plate which combines low thermal expansion with high thermal conductivity. The light emitted by the amplifier on the MIOB is shown into a Zerodur based fiber coupler, which is adhesively bonded onto the aluminum-nitride plate as shown in figure 7.39. The AlN plate is clamped onto a copper mount measuring 104 mm x 42 mm.

The master oscillator frequency is adjusted by modulating the current sent through the DFB laser oscillator. Additionally, the frequency strongly depends on the temperature of the oscillator. Moreover the coupling efficiency of the fiber coupler might decrease due to temperature changes of the laser module assembly. Thus the aluminum-nitride plate and the MIOB need to be temperature controlled with an accuracy of $\pm 0.1$ K. For ECDL lasers the volume holographic bragg grating (VHBG) of the laser needs to be controlled with an accuracy of $\pm 0.01$ K.

To achieve this high accuracy the copper mount and thus the aluminum-nitride plate is temperature controlled by a "TCH" peltier element provided by the German company Dr. Neumann. For the two ECDL laser modules an additional micro peltier element is added

to the setup to control the VHBG temperature. The ECDL and DFB laser modules will typically dissipate around 6 W into the payload. The efficiency of the peltier and thus the overall dissipated heat is depending on the difference between the set-point temperature on the laser chip and the heat sink temperature. This aspect will be discussed and included in the overall thermal simulation presented in section 12.4.

### 7.4.2 Distribution and switching unit

The distribution and switching unit manipulates the laser light delivered by the laser modules such that it can be efficiently used for laser cooling, manipulation and detection of atoms. This includes splitting the lasers output beams into an appropriate number of beams as well as intensity modulation and frequency shifts.

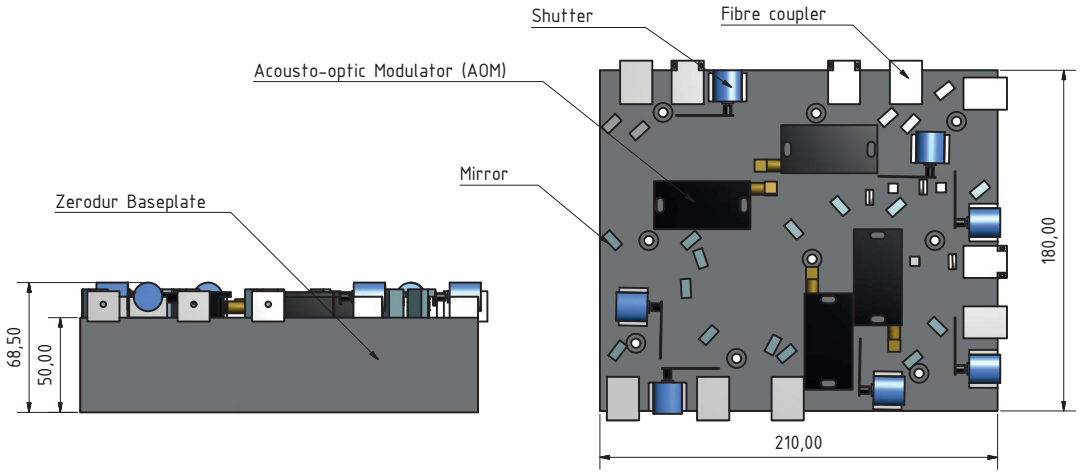


**Figure 7.40:** Zerodur-based distribution- and splitting-module of MAIUS-1

To achieve this, the module features free space polarization optics, shutters and acousto-optic modulators (AOMs) mounted on a Zerodur board. Schotts Zerodur is used because it offers a coefficient of thermal expansion close to zero ($\leq 0.020 \times 10^{-6}\,\mathrm{K}^{-1}$ [Sch13]). Thus no temperature induced change of the position of the optical components will occur, which is important to ensure that the distributed light intensities will not vary with temperature.

As shown in figure 7.40 the Zerodur base plate measures 180 mm x 210 mm x 50 mm. It is mounted to the heat sink by 11 M5 ISO 4762 screws. To compensate for unevenness or other imperfections (as e.g. burr) of the heat sink surface, a rubber mat is placed between the Zerodur board and the laser system heat sink. This will avoid high punctual loads on the glass, which might cause mechanical failure of the glass if the screws are torqued. For the same reason plastic washers are placed between the glass sink holes and the screw hats.

Due to the rubber mat and the small thermal conductivity of Zerodur of $1.46\,\mathrm{W\,m^{-1}\,K^{-1}}$

the AOMs (Crystal Technology AOMO 3080-122) and shutter (Faulhaber AM 1524-V-6-35-05) are not thermally connected to the heat sink. The dissipated heat of the AOMs (1W) and the shutters (0.9W) will be stored in the Zerodur itself.

The heat input by these components to the heat sink is negligible, because of its short operation times. However these components are also included into the thermal simulation presented in section 12.4.

### 7.4.3 Spectroscopy Unit

The components of the spectroscopy unit (Rb-Beat module) are mounted to a small Zerodur optical bench with free space optics. This module will ensure that the master laser is locked to an atomic transition of Rubidium, which is crucial for the success of the experiment, because the three slave lasers are locked with reference to the master laser.

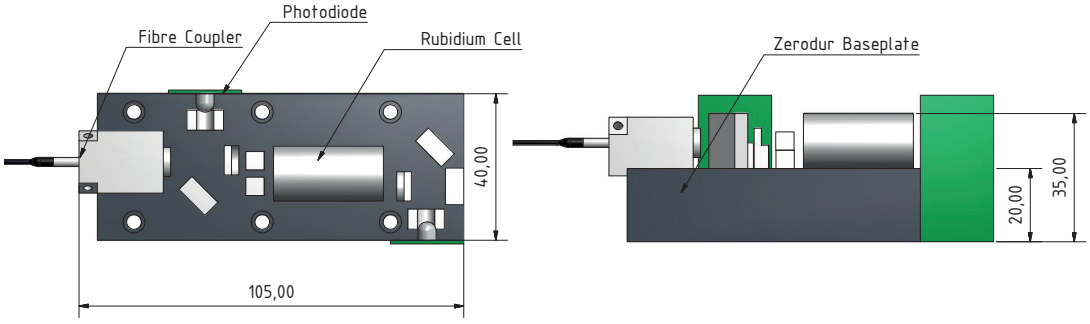


**Figure 7.41:** Zerodur-based spectroskopy module of MAIUS-1

The locking of the master laser is achieved by frequency modulation spectroscopy as described in detail in [Dun13] using a Rubidium vapor cell and two fast photodiodes. Expressed in simplified terms the laser light of the master laser is guided onto the board through the fiber coupler and sent through a glass cell filled with rubidium vapor, while the laser frequency is modulated. As soon as the transition frequency is approached light is absorbed by the rubidium atoms and a signal can be detected on the photodiodes indicating the desired laser frequency.

These photodiodes are mounted with two small printed circuits boards to the sides of the Zerodur baseplate as shown in figure 7.41. The vapor cell has to be kept at room temperature (20 °C to 30 °C) and to be protected from magnetic fields. To ensure the latter, the cell is wrapped into MUMETALL foil. No heating is necessary due to the sufficient background vapor pressure of Rubidium at room temperature.

The vapor cell, the fiber coupler and the remaining optical components are adhesively bonded to the Zerodur baseplate. This Zerodur board measures 40 mm x 105 mm x 20 mm and is mounted with six ISO 4762 M5 screws using the same technique as for the larger Zerodur board.

### 7.4.4 Laser Housing

The laser system is integrated in a compact housing measuring 274 mm x 340 mm x 226.50 mm. The housing is equipped with double walls. The air between the two aluminum parts of the walls insulates the interior of the housing from the atmosphere inside the payload and thus protects the sensitive laser modules and optics. This is necessary, because the dissipated heat of the electronic system and aerodynamic friction will heat the air inside the payload during flight (refer chapter 11).

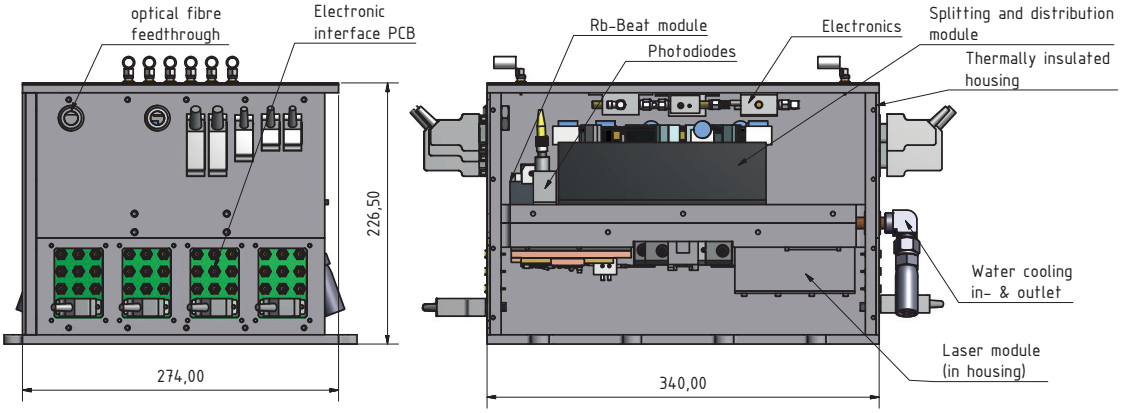


**Figure 7.42:** Laser system components integrated in housing. The components are mounted to a solid water-cooled aluminium heatsink. The walls of the housing consist of two parts with a air-filled gap in between for insulation purposes.

The two smaller walls of the housing are close to the cable ducts of the payload. For this reason all interfaces have been integrated into those walls. The electrical interface to the laser modules is formed by a printed circuit board, which is integrated in the wall behind each laser module. The electrical interface of the remaining components such as thermal sensors, photodiodes, AOMs or shutters is implemented with standard DSUB connectors. High frequency signals are fed through the walls by SMA feedthroughs, which are electrical insulated from the walls to avoid interferences. All cables connected to these interfaces are guided to the electronic system or batteries.

Moreover two holes with a diameter of 14 mm that are equipped with a rubber protection form a feedthrough for the optical fibres routed to the physical package. Last the two copper pipes of the heat sink are fed through the wall. The copper pipes are connected with a Swagelok hose by an elbow connector. The hose will establish a connection to the upper umbilical, which will provide water for cooling of the heat sink until lift-off.

The massive aluminum heat sink is forming the center of the housing. All components mentioned above are mounted to this heat sink. The heat sink consists of two parts with a total mass of 7.30 kg, which are connected by 21 ISO10642 countersink screws. As shown in figure 7.43 the copper pipe is pressed between these two parts of the heat sink, which will ensure a good thermal contact.

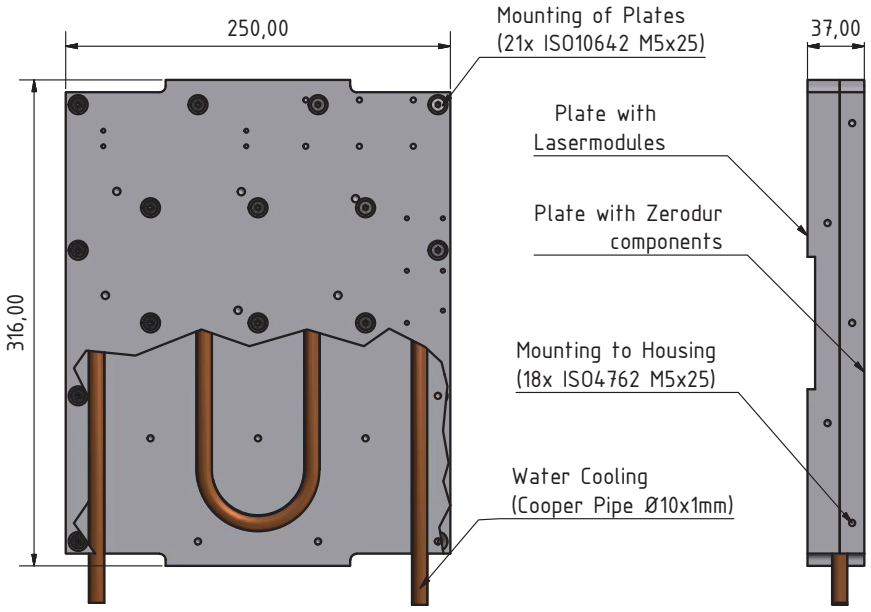


**Figure 7.43:** Heatsink design and water-cooling routing of MAIUS-1 laser system

The water cooling cycle will control the temperature of the laser heat sink to $\pm 1$ K. During flight the solid aluminium heat sink is capable of storing the heat generated by the components attached to the heat sink. The temperature of the heat sink rises by a maximum of 3 K as demonstrated in the simulation presented in section 12.4.

## 7.5 Electronics System

The purpose of the electronics is to provide power and control to all components necessary for the realization of a Bose-Einstein condensate and for performing matter-wave interferometry.

In order to reduce the size and mass of the payload most of the electronics are non-commercial components but have been developed by the Leibniz University of Hanover. A wide variety of electronic cards have been developed for the MAIUS mission and its predecessor the QUANTUS-2 drop tower experiment.

For operation of the laser system temperature controller, current drivers, shutter drivers, frequency controllers, temperature and photodiode monitoring cards and even direct digital synthesis (DDS) boards have been realized. For physics package operation a high voltage (5 kV) pump controller, a gauge monitoring card and low noise atom chip and coil current drivers have been produced. An ethernet interface card is used for communication between the hardware and the onboard computer, which is a commercial IDAN system provided by RTD Embedded Technologies, Inc.

All of these electronic boards have a uniform size of 100 mmx100 mm and a standardized bus. The electronic boards are stacked in functional groups as shown in figure 7.45. Six of these stacks with a total of 58 boards are included into the electronic system. The height of these stacks is limited to 12 cards.

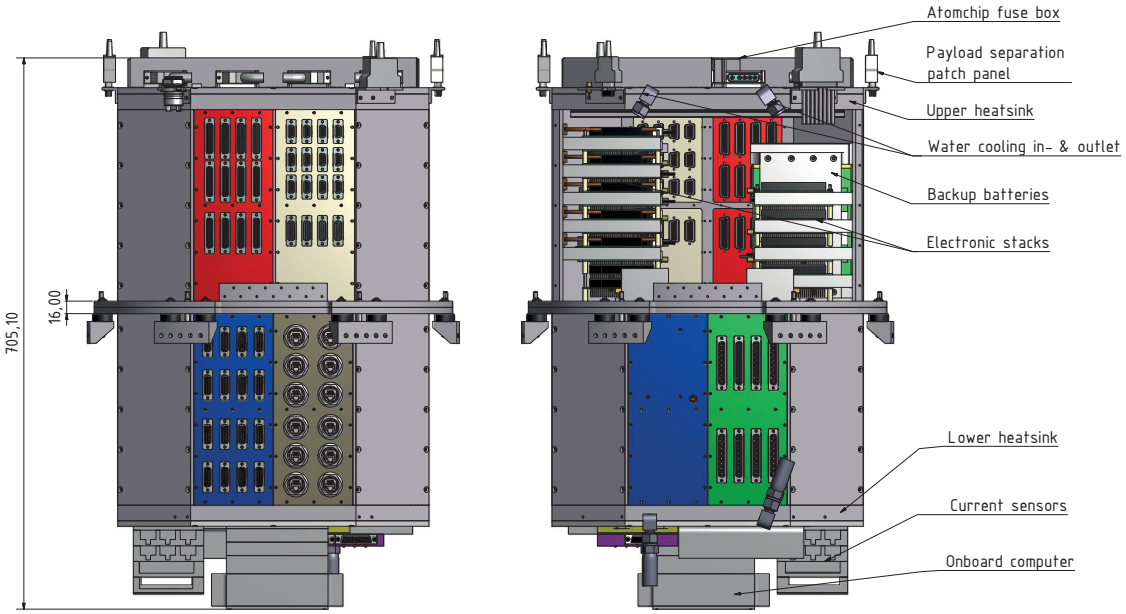


**Figure 7.44:** Overview on electronic system showing the water-cooled heat sinks at the top and bottom. Most of the electronic is in the TBUS-format developed by the University of Hanover. Those components are combined to functional stacks inside the electronic system housing.

Aside from the six electronic stacks, a modified commercial Ethernet switch, a reference oscillator card and 28 commercial radio frequency components are included in the housing. Moreover two types of batteries are placed inside the enclosure. The larger backup battery consists of three lithium iron phosphate (LiFePo4) cells of the type Headway 38120SE (3.3 V, 10 Ah). In addition to this a stack of seven boards with single-cell A123 ANR26650M1B (3.3 V, 2.5 Ah) LiFePo4 batteries, for supply of the chip and coil current drivers are part of the electronic system. These single cell batteries are electrically isolated from the remaining batteries to reduce the noise in the current driver output.

Some late modifications in the payload concept, made it necessary to add components to the system after the housing was already in production. Thus a fusebox to protect the atomchip from currents above its rating and some inline current sensors were added outside the housing enclosure to the two heatsinks as shown in figure 7.44. Originally only the on-board computer should be mounted outside of the electronic housing to establish proper thermal contact to the lower heat sink to conduct the 19.1 W of dissipated heat.

Due to the large amount of electronics needed and because of the dissipated heat, which requires a high heat sink mass for storing the heat during flight operation, the electronic system is the second largest system regarding mass and volume in the MAIUS scientific payload. The electronic system has a total mass of 66.2 kg and a length of 705.10 mm.

### 7.5.1 Mounting of Electronic Stacks

The required stacked architecture makes it difficult to find a good mounting concept for the electronic boards. Especially the accessibility for maintenance or modifications is limited compared to slot-in solutions, which are often used for electronic boards. Unfortunately a re-design of existing boards was not possible due to the limited time in the project. Thus a mounting concept was elaborated for the existing card design.

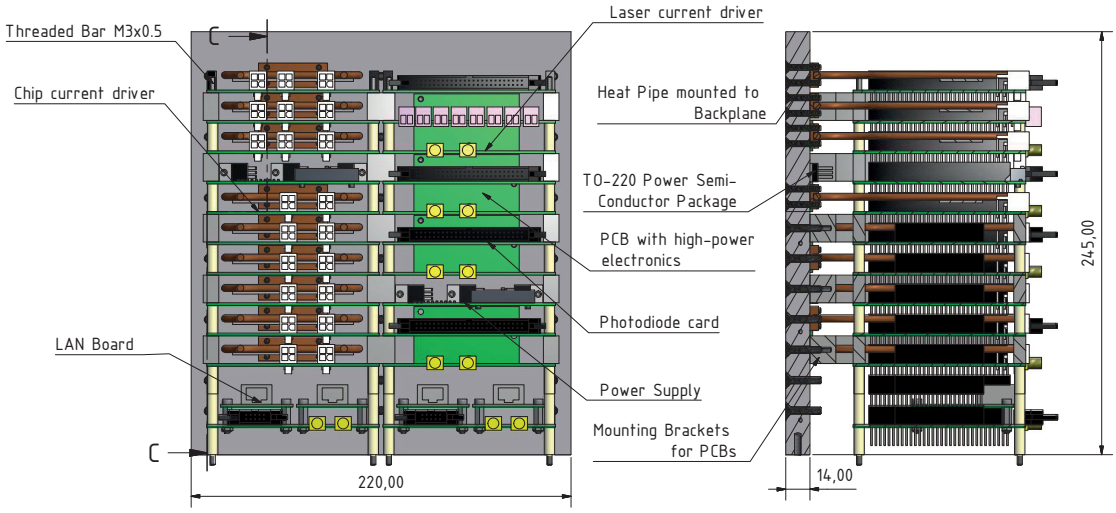


**Figure 7.45:** Mounting concept for electronic card stacks and thermal interface to high power components on the cards

Figure 7.45 shows the mounting for two stacks with the maximum height. The boards offer four holes with a diameter of 3.2 mm for mounting with M3 threaded bars to a baseplate, which has been common practice in the predecessor experiment QUANTUS-2. Spacer between the boards and a jam nut at the top prevent vertical movement of the cards.

For the MAIUS electronic system every second spacer is replaced by a printed circuit board (PCB) mounting bracket, which is mounted to a solid backplane from the outside as shown in the section view of figure 7.45. This increases the mechanical stability of the mounting significantly. The backplane also offers a good thermal interface to the remaining structure, which is serving as a heat sink for all electronic boards.

While some boards dissipate so little heat, that they do not require a heat sink at all, some need a good thermal connection to ensure that the heat is conducted into the backplane and the temperature requirements are met. The chip current drivers are equipped with copper heat pipes, which will allow a transport of the heat dissipated in the high-power components on the printed circuit board to the backplane.

Other cards use a different approach. The high-power electronics of the laser current driver and the power supply have simply been removed from the (main) PCB and have been attached directly to the backplane to ensure a good thermal connection.

### 7.5.2 Electronics Housing

The electronics system housing consists of an upper and lower part, which are almost identical with respect to the structure elements. Each part consists of a circular baseplate, four solid walls, four side covers and a heat sink.

The circular baseplate is measuring 458 mm in diameter, as the regular instrument platforms. It is also equipped with the same features as cable duct cut outs and mounting holes for rubber dampers and safety pins. Because of the large amount of cables, which will be connected to the electronic system the cable duct is spanning over 38°. Thus it is slightly bigger than the regular cable duct. The upper and lower baseplate are connected by 18 M5 ISO10642 countersink screws after mounting of the wall segments. A cable feedthrough will allow wiring between electronic components of the upper and lower part.

The four solid walls are screwed to the baseplate with a total of 16 M5 ISO10642 countersink screws. The side covers are screwed to the associated pockets in the solid walls and will close the housing.

The eight walls form an irregular octagon shape as shown in figure 7.46. All of the wall segment measure 245 mm in height and are made from aluminium EN-AW 7075.

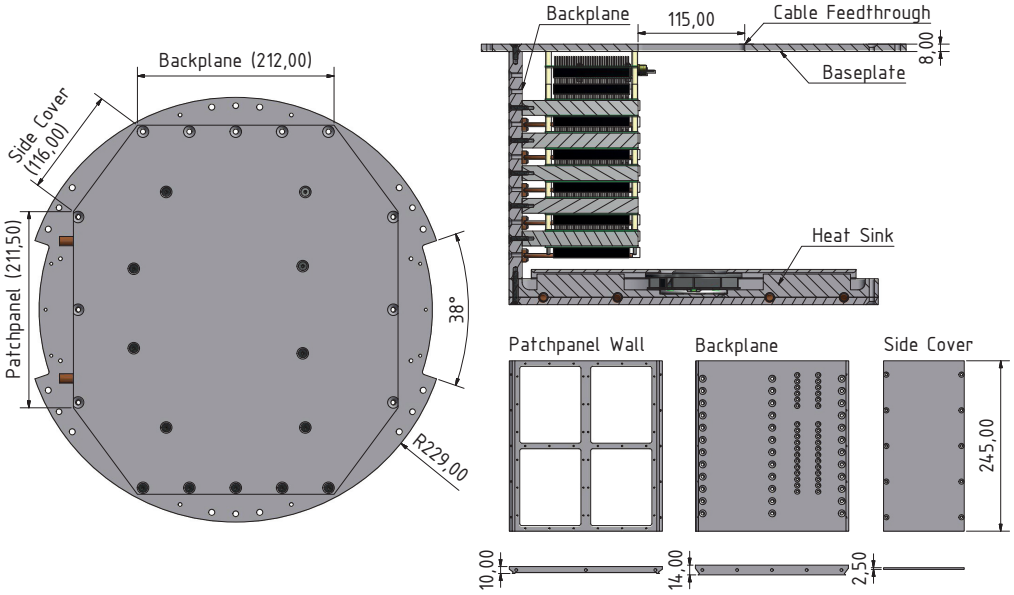


**Figure 7.46:** Top and section view on electronic system housing. Detail view on three different wall types.

Two of the solid walls are used as a patch panel for interface connectors to other payload systems. The patchpanel walls measure 211.5 mm in width and 10 mm in thickness. These walls are only frames equipped with sheet metal plates with the connector break-outs. This way all patch panel walls are identical, although the connectors differ from panel to panel. Moreover the sheet metal can be replaced easily if a connector needs to be changed.

The backplane walls are made of aluminium with an increased thickness of 14 mm. Moreover they are solid and equipped with mounting holes for the brackets holding the electronic boards. These walls measure 212 mm in width. The increased mass is beneficial, since these walls are one part of the electronic system heat sink.

The side cover walls are mounted between the patch panel and backplane wall segments. Originally they should just close the housing to prevent air heated by the electronic components getting into direct contact with sensitive instruments outside the electronic system. Due to the large number of components and the lack of space some low power commercial radio frequency components have been mounted to these walls as well.

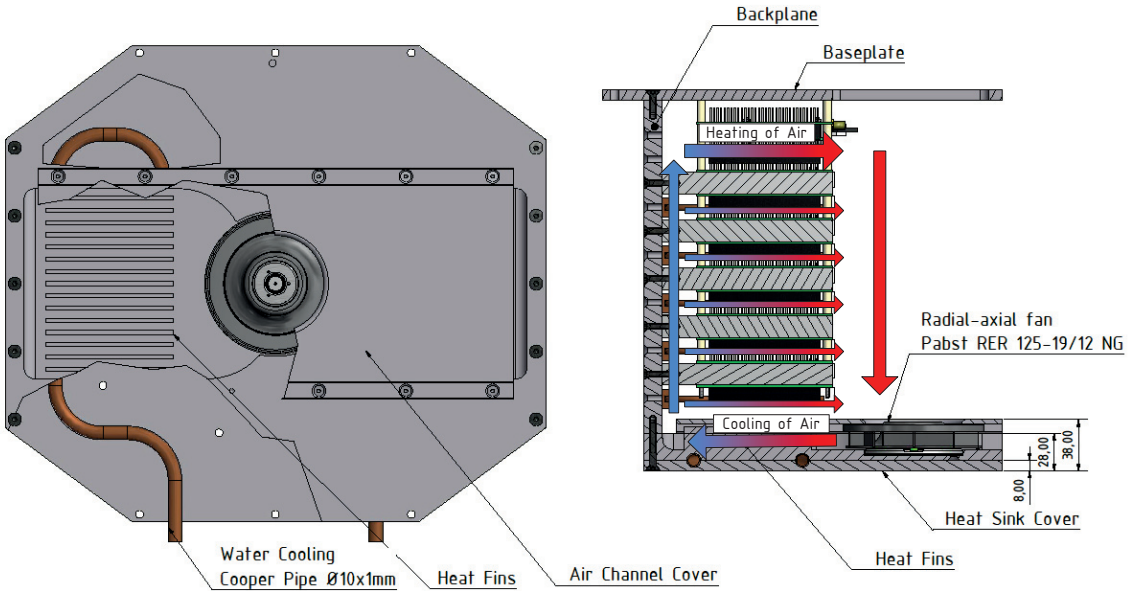


**Figure 7.47:** Heatsink and thermal control concept of electronic system. This figure shows the routing of the water cooling pipes and the expected circulating airflow caused by the fans.

As shown in figure 7.46 the heat sinks are mounted on top of the backplane and patchpanel walls with 16 ISO 10642 countersink screws. At the upper heat sink 12 brackets carrying 13 different connectors form a patch panel. This patch panel will allow a separation of the payload for transportation above the electronic system as already mentioned at the beginning of this chapter.

The heat sinks themselves consists of three aluminum parts each as shown in figure 7.47. As in the laser heat sink a copper tube with an outer diameter of 10 mm and a wall thickness of 1 mm is pressed between the heat sink cover and the heat sink body. The copper pipes of both electronic heat sinks are connected with the lower umbilical ports via Swagelok hoses. Thus the heat sink is water-cooled to 20 °C until lift-off.

In addition to this the heat sink body is equipped with a radial-axial fan EbmPabst RER 125-19/12NG. This fan is capable of transporting a maximum air flow of 110 $m^3 h^{-1}$. The

air enters the fan at its center (axial) and exits to the sides (radial). The heat sink is designed, to have an air channel with two exits and a cover, guiding the air of the fan to the side of the heat sink. The channels are equipped with heat fins, that will enlarge the surface in contact with the air. Since the whole heat sink is temperature stabilized, the air heated by the electronics will be cooled in these channels. At the side of the heat sink the air will be deflected downwards along the backplane cooling the high power electronics.

Prior to lift-off the fan has to be switched of because the rotation of the fan would cause a momentum on the payload disturbing the micro gravity environment. An active fan would result in a rotation rate of the payload of $0.024\,\mathrm{rad/s}$ for a payload mass of $280\,\mathrm{kg}$, a fan blade mass $0.32\,\mathrm{kg}$ and a nominal rotation of the fan of $2650\,\mathrm{min}^{-1}$.

Even if the fan is deactivated as stated above, the rocket spin during ascent will transfer some rotation energy in the fan. The amount of energy is depending on the quality of the roller bearing of the fan. For a coefficient of friction of the bearing of 0.01 the resulting rate of the payload at the beginning of the microgravity phase is in the order of $4.4 \times 10^{-7}\,\mathrm{rad/s}$.

While the rotation rates caused by an active fan are significantly larger than the rate control threshold or the requirements defined in section 6.2, the rates caused by a fan movement induced by the rocket spin are negligible. Thus the fan can be used for thermal control.

| Component | Mass [kg] | Quantity | Sum [kg] |
|---|---|---|---|
| Backplane | 1.95 | 4 | 7.8 |
| Heat sink (3 parts) | 8.0 | 2 | 16.0 |
| Baseplate | 3.0 | 2 | 6.0 |
| | | Total | 29.8 |

**Table 7.6:** Mass of aluminum structure elements of the entire electronic housing. This mass is used to store the dissipated heat of the electronic system during flight.

After lift-off the dissipated heat has to be stored only in the aluminum structure of the housing comprising of the two baseplates, four backplanes and the three parts of the two heat sinks. As listed in table 7.6, these parts have a total mass of 29.8 kg and thus a high overall thermal capacity. A detailed discussion and simulation of the thermal control system of the MAIUS electronics is presented in section 12.5.

## 7.6 Batteries and Power Distribution

The instrument platform situated at the bottom of the payload shelters the main batteries of the payload on the lower side and the power distribution unit (PDU) on the upper side as shown in figure 7.48.

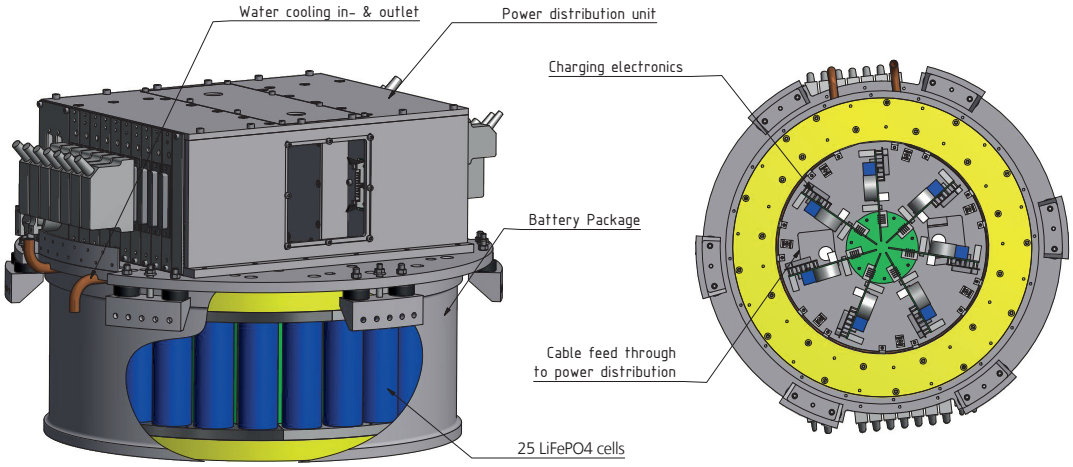


**Figure 7.48:** The MAIUS-1 power distribution unit is mounted to the top and the battery pack to the bottom of a shared instrument platform as shown on the left. A view inside the battery pack with the circular arrangement of cells and charging electronic is shown on the right

The main battery pack consists of 25 lithium iron phosphate (LiFePO4) cells of the type Headway 38120SE (3.3 V / 10 A h), which are combined to groups of 1, 2, 4 and 6 cells in series providing 7 different voltages with a capacity of 10 A h each. The voltages provided are +1C (3.0-4.2V), ±2C (6.0-8.4V), ±4C (12-16.8V) and ±6C (18-25.2V). Charge control electronics will ensure that the cell loads are balanced and will monitor the voltages and currents directly at the cells.

The battery cells and charging electronics have been integrated into a cylindric aluminum housing as shown in figure 7.49. The cylinder measures 400 mm in outer diameter and offers 20 M4 threads at the bottom and top. Using the lower threads the cylinder is mounted directly to the instruments platform, while the upper threads are used to attach the cover plate to the cylinder.

The cells are mounted between two mounting rings made from Polyoxymethylene (POM). These rings are equipped with pockets receiving the cell body, while the battery terminals are fed through the ring. The terminals are connected to a cell protection mounted to the radial face of the mounting rings as shown in detail D in figure 7.49. The threads for mounting the printed circuit boards to the mounting ring are strengthened with Helicoils to increase the bearing capacity.

The terminal may also be connected to its neighboring cell(s) with a solid bridge. The orientation of the cells is altering such that positive and negative terminal can be connected by a bridge. The number of cells bridged in series is depending on the desired voltage of the group.

A solid protection cover ring, which is also made from POM, is screwed to the mounting ring once all 25 batteries and their protection boards are assembled. This cover assures, that no short is produced by contact of the terminal or a bridge with the housing.

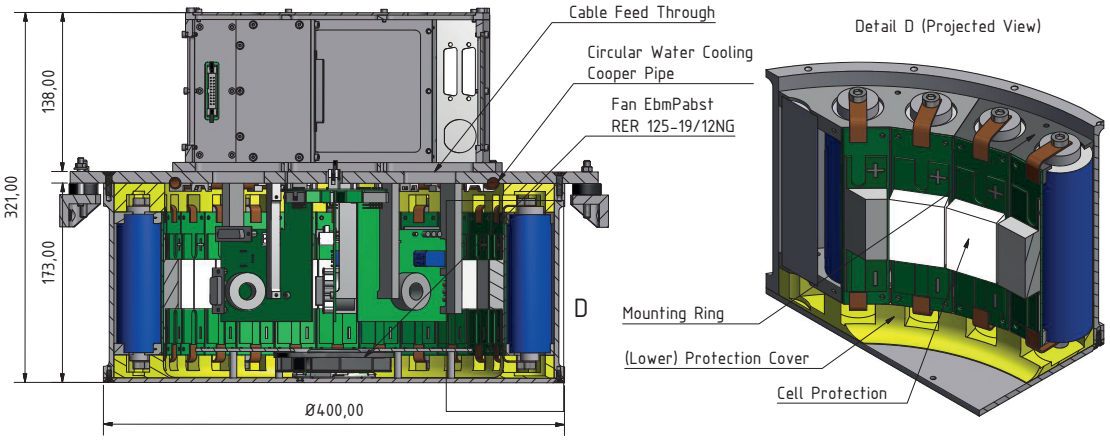


**Figure 7.49:** Batteries and power distribution unit section view with mounting of cells

The heat produced by the batteries and the associated electronics is dissipated by a water cooling pipe. The pipe, which is identically to the pipes used in the electronics or laser system (10mmx1mm) is pressed into a notch milled in the instruments platform. It is fixed in position by several clamps. As in the other water cooled systems water cooling will be provided during lab operation and until lift-off (refer chapter 12).

In addition to the water cooling a fan of identical type as used in the electronic system will cool the cell protection boards and charging electronics by convection. This fan will aspirate the air from the center of the housing and blow it through the space between the housing cover and the fan cover towards the cells. The air flow will be diverted downwards by a radius in the lower protection cover cooling the boards mounted to the cells.

The PDU is connected to the batteries by several wires routed through the internal cable feedthroughs in the center of the instruments platform. It offers 20 boards with an output providing all voltages on a single DSUB 8W8 connector. Each board can be switched individually, powering the different parts of the experiment. The boards also provide fuses for all outputs.

A micro controller powered and controlled by the MORABA service module via a RS422 interface is controlling the output boards. The service module is capable of switching the power of the entire payload except for the pump controller as mentioned above.

Contrary to the remaining boards developed for MAIUS, the PDU boards are mountable in a slot-in housing, which results in a good accessibility and compact size of the entire module. Batteries, PDU, its internal harness and its structure add up to a total mass of 32 kg and demand only 321 mm in height.

# 8
# Qualification of Systems and Components

The important difference between MAIUS-1 and other atom interferometers is the qualification for the use on a sounding rocket. The MAIUS-1 payload is the first atom interferometry experiment to be flown and operated in the harsh environment of a sounding rocket.

As presented in figure 5.9b the rocket environment is characterized by strong vibrations with an RMS value of 1.8 g and accelerations of 12.1 g along the payload cylindric axis due to the thrust of the rocket and 7.2 g in radial direction due to the spin of the rocket. In order to ensure a reliable operation of the five payload systems shown in figure 7.1 despite these environmental conditions, the used instruments and components had to be tested under similar loads. Moreover the mechanical design of all five systems developed in this thesis has been qualified in so called "system level" tests. The methodology of this qualification process and its results are described in the following sections.

## 8.1 Methodology

At an early stage of the MAIUS-1 payload design key technologies and associated commercial or custom-made components for all (sub)systems have been selected for future use on the sounding rocket mission in an technology review. Most of these were designed for the use in the laboratory, thus only few manufacturer have qualified their products for the operation under vibrational loads.

For this reason the first shaker tests in the course of the MAIUS project have been used to qualify several commercial components as fiber switches or vacuum pumps. These have been tested "hard-mounted" (with a rigid connection to the electrodynamic shaker) at the qualification level as described in table 8.1.

Once the components were successfully qualified, a proper mounting was designed for the functional group around the component. Subsequently either an additional test of a group

of components was performed or the entire system was tested. The optional test of a group of component was carried out, if one of the components is especially sensitive to vibrations or the group is complex in its architecture. This has been the case for the MAIUS-1 pumping system.

While functional groups were tested hard-mounted at qualification level, system-level tests have been performed using the acceptance test profile.

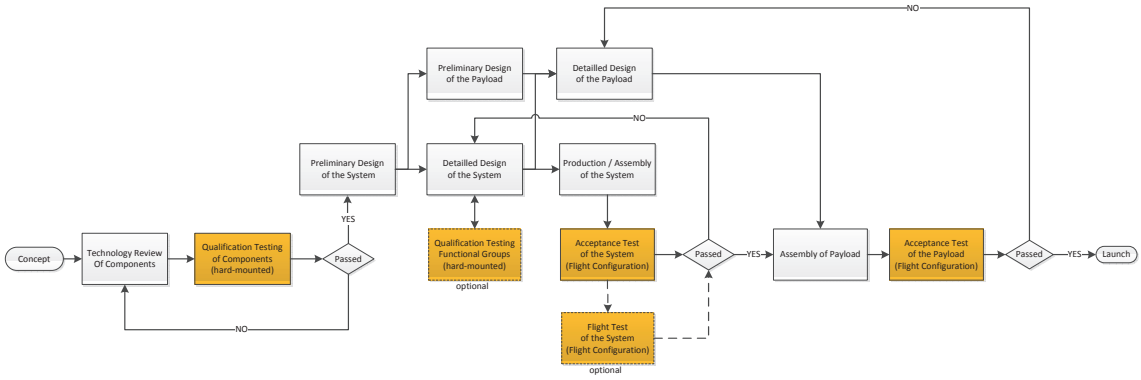


**Figure 8.1:** Qualification and design methodology in the MAIUS-1 project

In a system level tests the system is fully integrated and mounted to its instrument platform. The platform is connected to a shaker adapter using six mounting brackets including vibration damping as described in section 7.1.2. Thus the hardware is exposed to a damped load.

For these tests a shaker adapter similar to the rocket hull segments was constructed. The cylindric adapter with a length of 500 mm is designed to have the same wall thickness and the same mechanical interface to the brackets as the original hull segments.

The system level tests are the decisive tests for the qualification of the (mechanical) design of a system. If they are not passed, the design of the system has to be changed and the system level test has to be repeated as shown in the flow diagram 8.1.

Once the different systems have been qualified, the entire payload including the MORABA systems will be tested at the final environmental test campaign in Ottobrunn, Germany. This test will be carried out fully integrated at the acceptance level and will be followed by a shipment of the payload to Esrange for the launch campaign.

### 8.1.1 Test Facility and Test Profiles

The component and system level vibration tests described in this chapter have been performed at ZARM-FAB vibration test lab in Bremen using a Brüel & Kjaer LDS V875 HBT 600 vibration test facility. The data acquisition and control unit used was m+p VibRunner and the control and measuring system m+p VibControl/NT.

The test items were mounted with individually designed adapter plates to the interface of the electrodynamic shaker. The pilot accelerometer(s), fixed in the corresponding excitation direction on the adapter are used for closed loop control of the input level during all test runs. The specified excitation levels have been applied along all main axes.

| Frequency [Hz] | PSD [$g^2$/Hz] | | |
|---|---|---|---|
| | Qualification Level | Acceptance Level | Flight Level |
| 20-399 | 0.0045 | 0.002 | 0.0003 |
| 400-599 | 0.0675 | 0.03 | 0.004 |
| 600-1299 | 0.0045 | 0.002 | 0.0003 |
| 1300-2000 | 0.0675 | 0.03 | 0.004 |
| RMS Value | 8.1 g | 5.4 g | 2.0 g |
| Duration | 60 s | 60 s | 60 s |

**Table 8.1:** Vibration test level for MAIUS-1

All test runs in X- and Y- axis were carried out on the horizontal slip table. The Z-axis was tested in the vertical operation direction of the shaker. The usual test duration has been 60 seconds.

Before and after each random test run, sine resonance search tests at low level (0.25g) with a sweep rate of 2 oct/min were carried out to evaluate the significant eigenfrequencies in every excited axis. All deviations of the pre- and post-test sine resonance search test runs would indicate structural failure resulting from the vibration test.

The individual tests have been carried out as random vibration test in the frequency range between 20 Hz and 2000 Hz. The power spectral density has been set according to the values presented in table 8.1. This results in an root mean square (RMS) of the vibration level of 8.1 $gRMS$ (Qualification level), 5.4 $gRMS$ (Acceptance level) and 2.0 $gRMS$ (Flight level).

The results of the system level test shall be presented in the following subsections. To represent the results of the qualification process in a clear way it was abstained from presenting the results of the component level tests. All tests have presented herein have been carried out at acceptance level with a duration of 60 s per axis if not stated otherwise.

## 8.2 Vibration Testing of Rubber Dampers

As described in section 7.1.2 instruments of the apparatus are mounted to four platforms, attached to the payload hull by brackets and a passive vibration damping to reduce vibrational loads, especially at high frequencies. Each instrument platform is mounted to the hull segments by a total of six brackets, each equipped with two shock mounts. This suspension has been tested and the performance of the damping characterized during several system level tests.

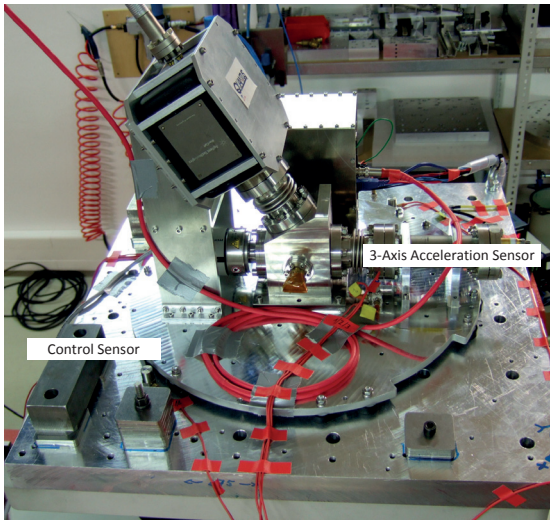


**(a)** Test setup for testing of the vibration dampers with the MAIUS-1 pumping system. The system with a mass of 17 kg is mounted onto 12 rubber dampers.

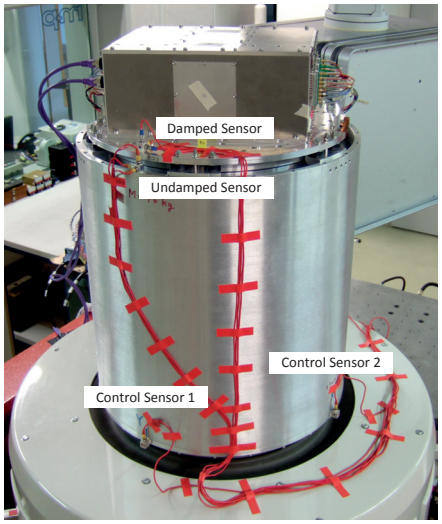


**(b)** Test setup for testing of the suspension (dampers, brackets and safety bolts) with the MAIUS-1 battery system. The system with a mass of 32 kg is mounted using six flight suspension brackets with a total of 12 dampers.

**Figure 8.2:** Test setup for vibration damper and suspension characterization

The shock mounts STS GP-TYP A 25x10 M6 SH55 by Schwingungstechnik Schuster consist of two M6 bolts, which are vulcanized into a rubber cylinder with a diameter of 25 mm and a height of 10 mm. The rubber has a shore hardness of 55 Shore A.

Figure 8.2a illustrates the setup of the MAIUS-1 pumping system test.The pumping system instrument platform is mounted to the shaker adapter plate using 12 rubber dampers. Although the main purpose of tests with this setup is to qualify the pumping system components, it also allows to test and characterize the vibration isolation performance.

As shown in figure 8.3 the main resonance frequency of the vibration is 120 Hz at a load of 1.5 kg per damper. The curve has been obtained from the z-axis sensor mounted on the damped instrument platform during the z-axis sine resonance sweep at 0.5 g. That means at resonance the recorded load was five times higher than the applied sine load.

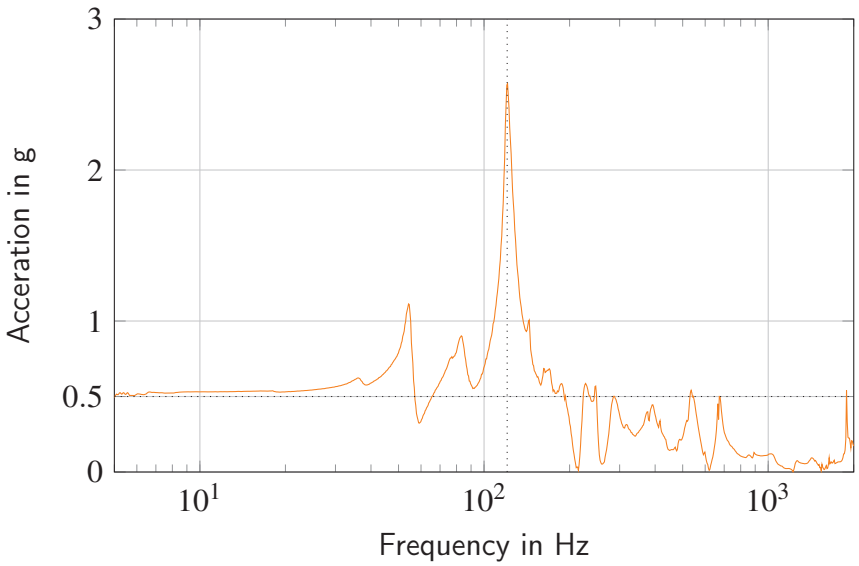


**Figure 8.3:** Acceleration level recorded at the instrument platform during a z-axis resonance sweep at 0.5 g of the pumping system. The test setup is shown in figure 8.2a. The resonance frequency of the dampers is marked as 120 Hz.

The resonance frequency of the dampers is expected to shift to lower frequencies for larger masses. Moreover the lateral resonance frequency will be below the one along the cylindric axis. Since all MAIUS-1 systems are heavier than the pumping system all resonance frequencies are expected to be below 120 Hz

The same setup depicted in figure 8.2a has been used to investigate the performance of the dampers under random vibrational loads. Tests have been performed applying all three profiles introduced in section 8.1.1.

Figure 8.4 shows the normalized acceleration level recorded by the sensors in x-, y- and z-axis during test runs in all three axes. This normalized acceleration level has been calculated by dividing the acceleration $a_{mes}$ recorded by the damped sensor on the instruments platform through the acceleration $a_{apl}$ measured from the undamped control sensor. The latter is representing the actual applied load. Thus a normalized acceleration level below 1 is representing a damping of the applied vibrations.

As expected the main resonance of the dampers along the cylindric axis is shifted to lower frequencies for x- and y-axis tests (83 Hz and 102 Hz), while the highest resonance frequency was recorded during the z-axis test at 135 Hz. The difference in x- and y-axis is most likely a result of the asymmetric load distribution on the instrument platform.

A second resonance of the dampers was found around 40 Hz, which is the lateral resonance of the dampers. Therefore the resonance is stronger in x- and y-axis tests. Despite the resonance peaks of the dampers, the vibration isolation is performing well and is especially effective above 100 Hz.

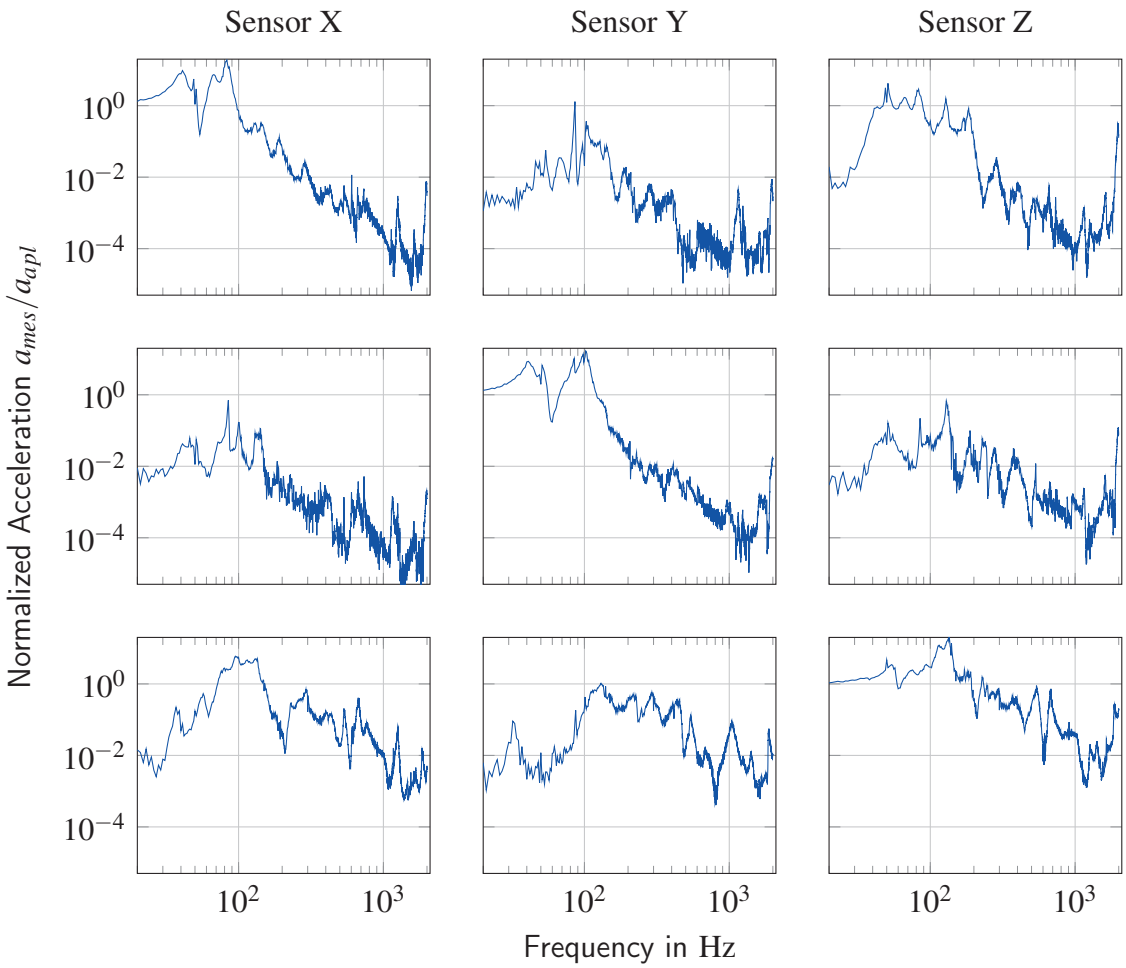


**Figure 8.4:** These figures show the quotient of the measured acceleration at the MAIUS pumping system instrument platform $a_{mes}$ and the applied acceleration $a_{apl}$. The data is depicted for the test runs in x-, y- and z-axis (top to bottom) and for sensors mounted in all three axes as labeled. In all test runs the accelerations are damped for high frequencies and show the previously mentioned rise at the eigenfrequency of the damper at around 100 Hz.

Although the recorded load at the resonance is up to 20 times higher than the load applied by the shaker the root mean square (RMS) of the vibrational load is lowered dramatically by the dampers. During tests of the pumping system at 3.03 g RMS, a value of 0.52 g was measured at the damped instruments platform. During acceptance tests the load RMS value was reduced to 0.86 g and during qualification level to 1.25 g.

These results are reproducible and have not changed unexpectedly during any of the system level tests. Exemplary the results of the battery system vibration test campaign are shown in figure 8.5. As shown in figure 8.2b the entire suspension including brackets has been used in this test, which has not effected the performance of the vibration isolation. To be able to detect also resonances caused by the cylindric shaker adapter and to get a characteristic measurement of the vibration isolation performance, a third sensor has been

placed at the top of the cylinder next to the mounting bracket as shown in figure 8.2b. The plots present the acceleration in $g^2/Hz$ with the black curve presenting the applied load by the shaker, the orange curve the measured data from undamped sensor at the top of the cylinder and the blue curve the data from the damped sensor.

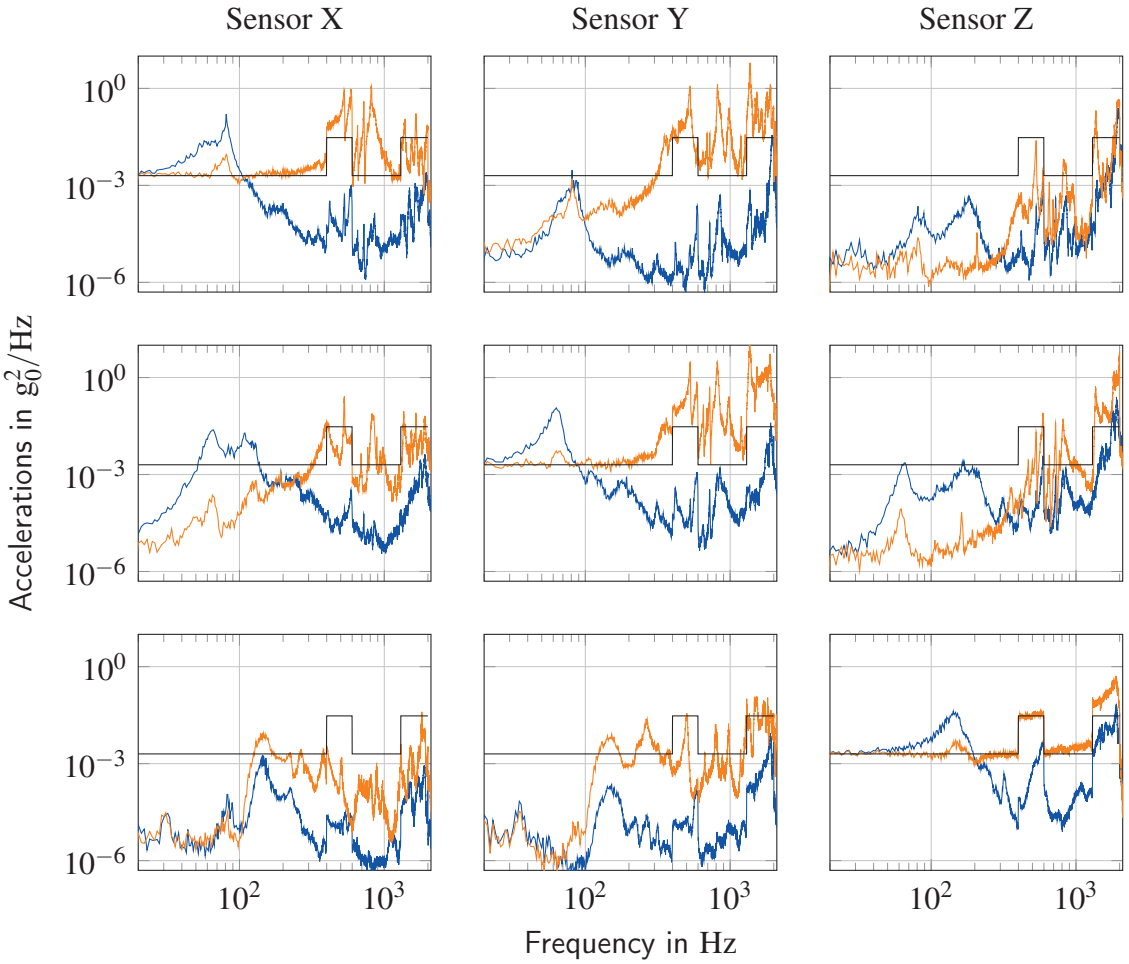


**Figure 8.5:** These figures show the results of the test of the damping system with the MAIUS battery module. The vibration response to the excited signal (black) of the sensor mounted to the damped battery module platform (blue) and the undamped cylindric shaker adapter (orange) is depicted for the test runs in x-, y- and z-axis (top to bottom) and for sensors mounted in all three axis as labeled.

The plot is showing some strong fluctuations in the upper frequency band in all test runs, which are most likely caused by resonances of thin aluminum cover plates of the tested system. These peaks do however not match with any resonances of the cylindric adapter or the battery system housing, which have been computed using FEM analysis during the design process. Nevertheless the load measured on the instruments platform is still below the excitation level, with the exception of the z-axis sensor measurement during the y- and z-axis test, which exceeded the applied level shortly at roughly 1800 Hz. The vibration isolation is performing well and is considered suitable for the use in the MAIUS-1 payload.

## 8.3 Qualification of Batteries and Power Distribution

The main battery and the central power distribution unit as described in section 7.6 has been mounted into the cylindric shaker adapter in flight configuration as shown in figure 8.6. The output voltage of four channels of the power distribution was recorded with 10 kHz, using a National Instruments data logging system. Since each card provides all voltages of the batteries at its connector, the measured data allows to detect any malfunction in the chain from the single cell to the output card connector.

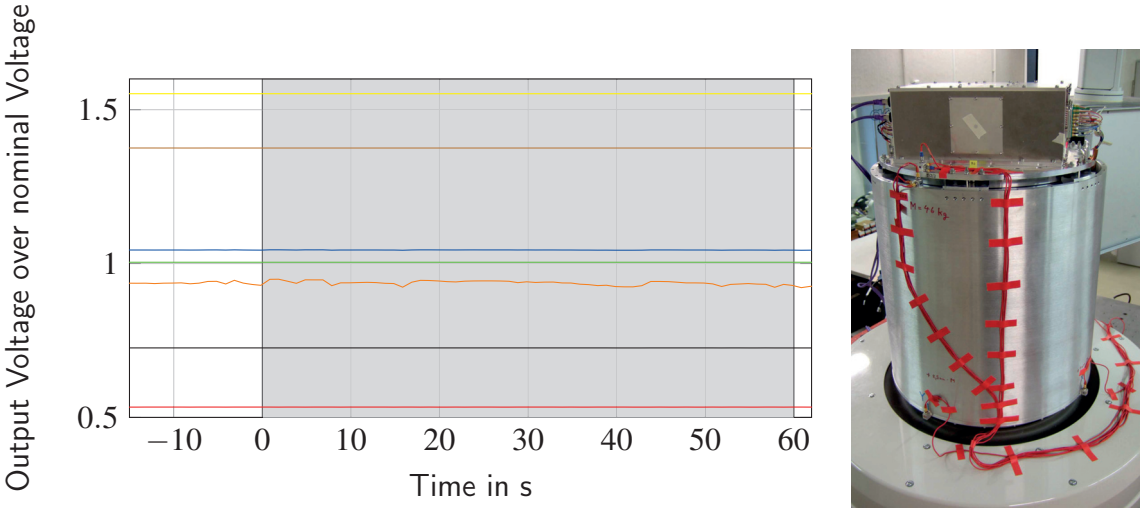


**Figure 8.6:** Voltages at the output of the card 16 of the power distribution unit during the z-axis random vibration test.The light grey area indicates the time during the random vibration test run. The data was recorded at 10 kHz and averaged over 1000 data points

Figure 8.6 displays the six voltages provided at card 16 in the PDU normalized to their nominal voltage. Depending on the battery charge status, some of the voltages deviate from their nominal value. However no fluctuations have been observed during the random vibration test run, which is indicated by the light gray area, starting at 0 s and lasting 60 s. This is in accordance with the measurements maintained from the other three cards monitored during the test run.

In addition to the direct monitoring of the voltage with a data logging system, the internal house-keeping data of the battery system was recorded from the Ethernet interface of the system. This does not only allow a direct control of the battery voltage, but includes a test of the internal house-keeping and monitoring hardware.

The internal housekeeping data did not show any abnormalities neither. Moreover visual inspection of the system revealed no damage of the electronics, batteries or the structure. Thus the system and its mechanical design, which is a part of this thesis have been qualified for the use in MAIUS-1.

## 8.4 Qualification of Electronic System

As described in section 7.5 the electronic system is very complex and consists of a high number of sensitive electronic components and even more electrical connections. For this reason a test of the fully integrated system in flight configuration is indispensable.

With the technical means given it was not possible to record all output signals of the system. The current drivers for the lasers are considered to be one of the most critical components, since a peak in the voltage or current for the laser power supply could destroy the laser. For this reason 16 output channels supplying the laser system have been monitored before, during and after the acceptance level test runs as well as during the resonance sweeps.

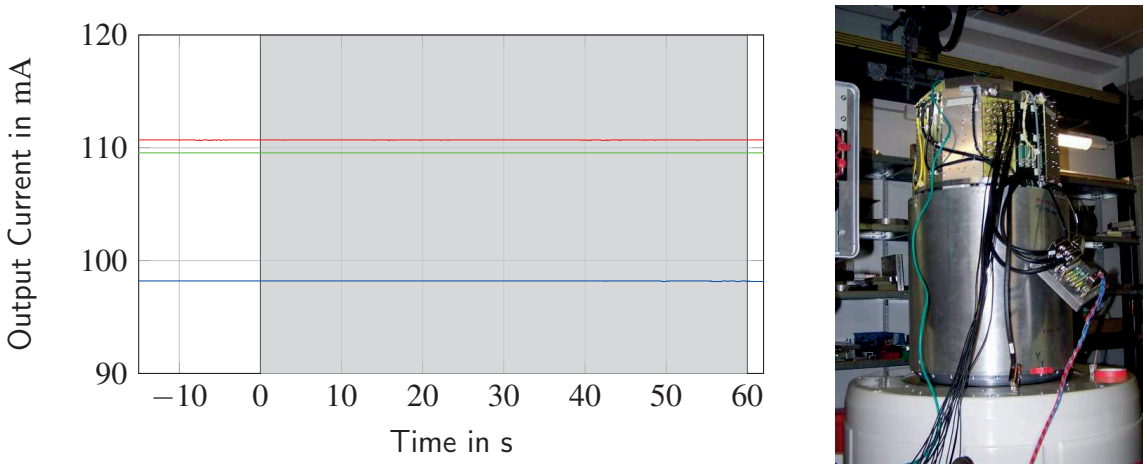


**Figure 8.7:** Current output of drivers for the master oscillator (blue), tapered amplifier (red) and rigid waveguide (green) output channels at the 22 Ohm resistors simulating the lasers during the z-axis random vibration test. The light grey area indicates the time during the random vibration test run. The data was recorded at 10 kHz and averaged over 1000 data points

During the test the lasers have been simulated with commercial 22 Ohm resistors, which have been connected to the patch panel of the electronic system. The output current of each current driver has been set to 100 mA and the voltage at the resistor has been measured with a PXI system at a sample rate of 10 kHz.
Figure 8.7 is the plot of three output channels of a current driver. These three channels are foreseen to operate one of the MOPA lasers of the experiment, as they are described in section 7.4. The channels are assigned to the master oscillator (blue), the tapered amplifier (red) and the ridge waveguide (green). Again the gray area indicates the random vibration test run at 5.4 $g_{rms}$ with a duration of 60 s.

As presented in figure 8.7 there has been no variation of the output current, during the test run. The maximum variation within 1000 recorded data points (0.1 s) over all 16 channels and three test runs was recorded at a single data point with 5 mV which equals a variation in the current of 0.227 mA (0.23 % of the output signal). This is uncritical for the

laser operation. The difference in the absolute currents might be caused by differences in the resistance of the three used resistors or unappropriated calibration of the current drivers. Moreover functional tests of the entire system as well as visual inspection showed no degradation or malfunctions. Thus the electronic system and the mechanical design, which has also been part of this thesis are also considered qualified for the use aboard the sounding rocket.

## 8.5 Qualification of Laser System

The lasers are an essential component for trapping, cooling and manipulating atoms. Those lasers need to fulfill high requirements with regards to the frequency and power stability of the light provided.

The frequency of the laser light is actively controlled by the frequency stabilization during the flight of the rocket, which has recently been demonstrated with the LASUS experiment on the TEXUS-51 sounding rocket payload. The output power of the laser system however is depending on the alignment of the optical components used in the laser system. Plastic and elastic deformation of e.g. a mirror mount during the shaker test, would thus lead to a loss in optical power.

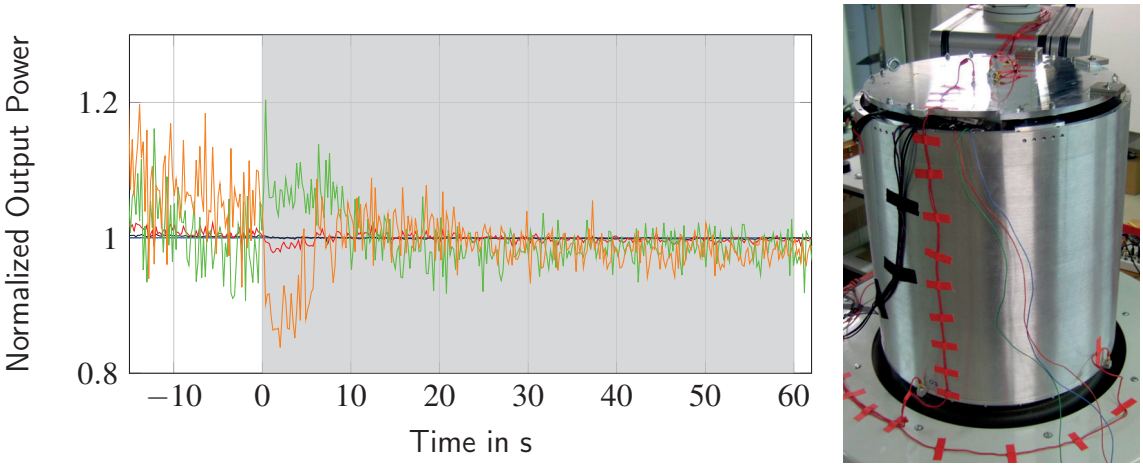


**Figure 8.8:** Normalized laser optical power at 780 nm of one laser module measured at different places in the optical path of the laser system during an acceptance level vibrational test. The power has been recorded at the laser module rear output (red), at two inline photodiodes (orange, green) and at two optical fibers (black, blue). The gray area indicates the duration of the vibrational test.

As described in section 7.4 the laser system is protected by a closed housing. This housing is mounted to the shaker adapter in flight configuration. That means, that the housing is hanging below the instrument platform inside the cylindric shaker adapter as shown in figure 8.8.

During the test the 2D MOPA laser (marked No. 4 in figure 7.38) has been in operation. The laser has been supplied via the SMA sockets at the patch panel in the housing wall.

Via a D-Sub connector the signals of three photo diodes have been fed out the housing and recorded with a PXI system. The data has been recorded with 5 kHz to ensure that short fluctuations in the light power are detected. In the post processing the data was again averaged over 1000 data points. With these photo diodes the optical power is monitored at several points along the optical path from the laser to the fibers being the interface to the experiment chamber.

Directly at the laser module a photo diode at the rear output port (red curve) is used for demonstration of the functionality of the laser diode itself, while an inline photo diode after the first isolator (green curve) ensures that the light generated on the optical bench of the laser module is coupled into the fiber successfully. Another inline photo diode (orange) is monitoring the power after exiting the switching and distribution board.

In addition to this, two of the four fibres exiting the laser system housing are connected to two power meters, monitoring the optical power that would be supplied to the collimator at the 2D MOT chamber. The power at fibre 3 (black) is measured using a Thorlabs PM100D, while a Coherent Fieldmaster GS is used to record the power in fibre 1 (blue).

Figure 8.8 shows the normalized optical power at the measurement points mentioned above. While the measurements at the fibres and the rear output of the laser module showed no abnormalities during or after the vibrational test, the signal of the inline photo diodes deviate from the other values and the set power. Anyhow the signal stabilized during the vibration test. Moreover the optical power reading at the fibers, which are located behind the inline photodiodes, did not detect these fluctuations. Thus this is expected to be a measurement artifact. In addition to that the qualification criterion has been a stable optical power at the experiment (at the fibre), which has been fulfilled.

Moreover all components of the system performed reliable before and after the test and again no damage could be found during visual inspection. Thus this system is also considered qualified including the mechanical design aspects of the housing, which have been a part of this thesis.

## 8.6 Qualification of Physics Package

The hardness of the experiment against launch loads has proven to be especially challenging for a vacuum system. A total of 18 vibration tests have been carried out, since June 2011 in the course of the project and as part of this thesis to evaluate the durability and the applicability of key vacuum technologies and to investigate the impact of vibrational loads on the vacuum quality.

During those tests several commercial vacuum components failed under the vibrational loads. Even when commercial pumps and gauges capable of surviving the loads of a sounding rocket launch were found, there was still a pressure rise observed during each vibrational test. Additional vibrational and static tests as well as intensive design effort led to the advanced vacuum system design presented in section 7.3.3 and 7.3.2. The road to this design will be presented in chapter 9.

In the following the final qualification of this system is described. As qualification criterion a pressure level below $5 \times 10^{-10}$ hPa 47 s after the vibrational tests was identified. This is the time span between $t_0$, which is the time T+44s of the MAIUS time event list (refer section 5.5) when the second stage is burned out and T+91s representing the begin of the experiment phase after the attitude acquisition is completed.

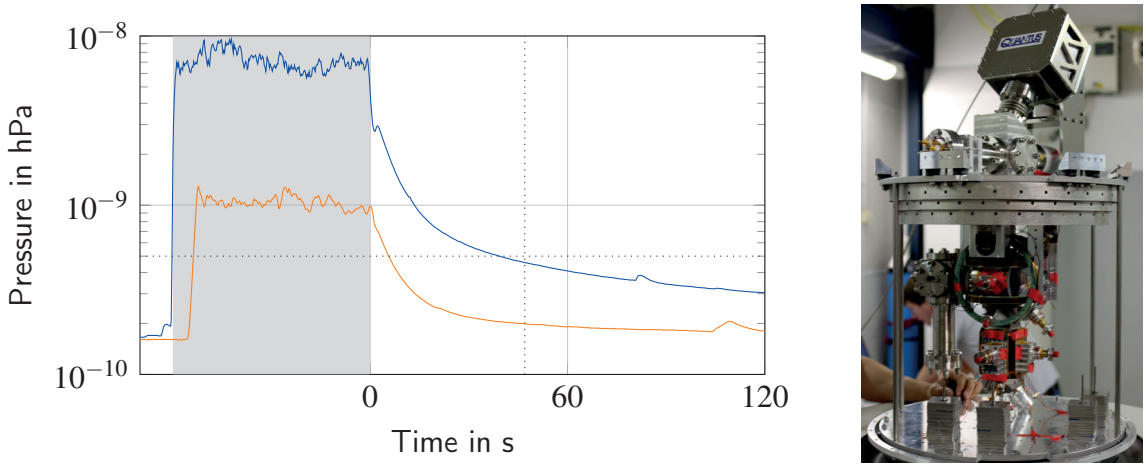


**Figure 8.9:** Pressure in the vacuum system during and after the vibration tests at acceptance (blue) and flight (orange) level. The horizontal dotted line is the desired pressure level of $5 \times 10^{-10}$ hPa and the vertical dotted line represents the time available for regaining the pressure of 47 s.

The tests were performed at the acceptance as well as the flight simulation level. During the tests the pressure is measured with the vacuum sensor located in the top of the vacuum system. During both tests the vacuum pressure showed some degradation while vibrations are present. As shown in figure 8.9 the pressure rises from initially $1.8 \times 10^{-10}$ hPa to $7 \times 10^{-9}$ hPa while vibrations are applied. Afterwards the pressure recovers quickly and drops below the critical mark of $5 \times 10^{-10}$ hPa after 40 s.

The test at flight level resulted in a pressure rise to $1.9 \times 10^{-9}$ hPa. The pressure dropped below the critical mark only 5 s after the end of the test. Since the vibration level was measured to be in this regime a comparable performance is expected during the campaign.

Although the desired pressure level was not reached within 31 s in the acceptance test, the additional 9 s are still in the extended period defined above and it would be possible to perform experiments, which require only a lower vacuum quality if the vibrational level would be higher as 2 g RMS during ascent.

Therefore the vacuum system is qualified for the use on a sounding rocket. It is the first ultra-high vacuum system operating at such low pressures to achieve this qualification. In chapter 9 the reasons for the pressure rise and ways to reduce it will be investigated.

# 9
# Design of an UHV System for the Use on a Sounding Rocket

The pressure inside the vacuum chamber is an important factor to achieve the scientific goals of the mission. As previously mentioned the pressure inside the scientific chamber has to be below $5 \times 10^{-10}$ hPa to reduce the collision rate between the residual gas and the atomic cloud to a sufficient low level [Sei14].

The design of the scientific and preparation chamber as presented in section 7.3.3 is based on the QUANTUS-II design, to ensure that experiment parameters and results obtained from drop tower experiments can be used as a baseline for the sounding rocket experiments. Thus only minor changes have been applied to this part of the vacuum system, to ensure the stability in the harsh sounding rocket environment. While the chamber geometry was set, the choice of the chamber material, sealing techniques, as well as the design of the pumping system had to be redone and reviewed to meet the pressure requirements in the given environment.

Within this chapter a design of an UHV system is elaborated to maintain the required pressure during the experimental phase of this sounding rocket mission. Contrary to other missions using vacuum for similar experiments as e.g. PHARAO [Gra04] there is no long recovery time available to regain the vacuum pressure quality. As stated in section 8.6 the mission scenario only offers 47 s to regain the desired pressure by pumping the gas that has entered the system due to the accelerations and vibrations caused by the motor burn. Thus it is important to know and to characterize the different mechanisms through which gas is released into the vacuum system.

## 9.1 Required Pumping Speed and Equilibrium Pressure Calculation

The required pumping speed to ensure that the pressure threshold is reached within these 47 s can be calculated from

$$S_{eff} = \frac{V}{\Delta t} \ln \frac{p_{init}}{p_{req}} \tag{9.1}$$

where $\Delta t = 47\,s$ is the time available to reach the required vacuum pressure $p_{req}$. Moreover the intitial pressure $p_{init}$ and the volume of the vacuum system $V$ have to be known.

The volume of the MAIUS vacuum system $V$ has been extracted from the CAD models of the design presented in section 7.3.2. The volume and surface of the different parts facing the vacuum are listed in table 9.2 and 9.3.

The initial pressure during the MAIUS flight, is the pressure at the time $T + 44s$ directly after the motor is burned out and the vibration are no longer applied. This pressure is resulting from the input into the vacuum system by desorption ($Q_{des}$), diffusion ($Q_{diff}$), permeation ($Q_{perm}$) and through leaks ($Q_{leak}$) as well as the effective pumping speed of the pumps removing gas molecules from the system. The equilibrium pressure can be calculated from the following equation [Pfe09]

$$p_{end}(t) = \frac{Q_{leak}(t)}{S_{eff}} + \frac{Q_{des}(t)}{S_{eff}} + \frac{Q_{diff}(t)}{S_{eff}} + \frac{Q_{perm}}{S_{eff}} \tag{9.2}$$

Since some parameters change with time and/or the loads applied to the system, the equilibrium pressure varies with time assuming a constant pumping speed. In the following pages the three terms responsible for the gas input will be investigated in more detail to allow for a prediction of the pressure gradient inside the chamber during the sounding rocket flight.

## 9.2 Outgassing Rates

Outgassing describes the gas flow from a material (sample) into the vacuum contributing to a pressure rise. This process is the sum of gas released by desorption, diffusion and permeation. These three mechanisms are characterized in the following.

### 9.2.1 Desorption

Desorption is the release of atoms bound at a surface facing the vacuum. These atoms oscillate with a frequency of $\nu_0 \approx 10^{13}\,\mathrm{s}^{-1}$ or their period of oscillation $\tau_0 = 10^{-13}\,\mathrm{s}$. If the kinetic energy of these particles at the wall temperature $T_w$ is larger than the desorption energy $E_{des}$ these atoms will be released into the vacuum. According to the Boltzmann equation from $n$ atoms $\Delta n$ atoms will fulfill this criteria [Jou13], where this fraction can be calculated as

$$\Delta n = n \exp\left(\frac{-E_{des}}{R T_w}\right) \tag{9.3}$$

The desorption rate per unit area can be calculated from the product of the amount of particles with sufficient energy and their oscillation frequency [Jou13]

$$q_{des} = -\nu_0 \Delta n = -\nu_0 n \exp\left(\frac{-E_{des}}{R T_w}\right) \tag{9.4}$$

The mean residence time of an atom on the chamber wall with temperature $T_w$ can be found from

$$\tau = \tau_0 \exp\left(\frac{E_{des}}{R T_w}\right) \tag{9.5}$$

Thus the time dependency of the number of particles for a surface initially covered with $n_0$ atoms per unit area can be found from integration of equation 9.4 and combination with equation 9.5

$$n(t) = n_0 \exp\left(-\frac{t}{\tau}\right) \tag{9.6}$$

For a system without re-adsorption of desorped particles, this would allow to calculate the time necessary to remove a certain amount of particles from the layer at the surface. However re-adsorption does take place and will significantly slow down this process. Hobson found a model to consider re-adsorption and solved it for a simplified vacuum system [Jou13]. He came to the important conclusion that only molecules with a desorption energy between $75\,\mathrm{kJ\,mol}^{-1}$ and $105\,\mathrm{kJ\,mol}^{-1}$ will contribute to a pressure rise on long time scales. Molecules with smaller desorption energies will be pumped very quickly and molecules with larger desorption energies will not desorp at all. Water is one of the major molecules contributing to this longterm desorption, which can require weeks. To reduce this time baking of the chamber is required as described in section 9.2.6.

During pump down the desorption rate will decrease with approximately $t^{-a}$ with $a$ varying from 0.9 to 1.3 [Dyl93]. Obviously the exact desorption energy of water is strongly

depending on the surface characteristics and varies as well. Thus the desorption rate of a certain material can only be obtained from measurements and the time dependency has to be approximated as described in section 9.2.4.

### 9.2.2 Diffusion

Gas molecules can not only be bound at the surface but also deep in the material. These molecules can exit the material by diffusion. Typically the molecules migrate along the borders of the crystalline structure of the material. Each change in the location of the adsorbed molecules will require the energy $E_{diff}$.

According to the law of Fick the outgassing by diffusion is defined as [Jou13]

$$q_{diff} = -D\frac{d\,n_l}{d\,x} \tag{9.7}$$

where $n_l$ is the amount of gas molecules solved in the material and $D$ is the diffusion coefficient. As the desorption coefficient, the diffusion coefficient is also depending on the wall temperature $T_w$

$$D = D_0\ \exp\left(\frac{-E_{diff}}{R\,T_w}\right) \tag{9.8}$$

The outgassing rate by diffusion of a vacuum chamber with thin walls of thickness $2d$, where the wall thickness is significantly smaller as the chamber length $2d << l$ and width $2d << b$ has a characteristic time constant $t_{out}$

$$t_{aus} = \frac{4d^2}{\pi^2 D} \tag{9.9}$$

If the diffusion processes is assumed to be one-dimensional and only diffusion normal to the chamber or pipe wall surface is considered the outgassing rate per unit area for $t >> 0.5t_{out}$ is defined as [Jou13]

$$q_{diff} = \frac{2D}{d}\ n_{l,0}\ \exp\left(-\frac{t}{t_{out}}\right) \tag{9.10}$$

and for $t << 0.5t_{out}$

$$q_{diff} = \frac{2D}{d}\ n_{l,0}\sqrt{\frac{\pi}{16}\,\frac{t_{out}}{t}} \tag{9.11}$$

The diffusion process is much slower than the desorption process, but the amount of gas molecules inside the material can be significantly higher than the gas stored at the surface. Due to the temperature dependency of the diffusion coefficient, baking of the chamber will also enlarge the diffusion rate. This will be discussed in section 9.2.6.

### 9.2.3 Permeation

Permeation is a combination of adsorption at the outer wall of the vacuum chamber, diffusion through the wall and desorption at the inner wall. The flow of molecules through the wall is depending on the partial pressure difference of the specific molecules from inside $p_2$ to the outside $p_1$. For a wall thickness of $2d$, the permeation rate is given as [Jou13]

$$q_{perm} = K_{perm} \frac{1}{2d} (p_1 - p_2) \tag{9.12}$$

For gas molecules that do not dissociate as for example the $N_2$ or $O_2$ in many materials, the permeation rate is given as [Jou13]

$$q_{perm} = K'_{perm} \frac{1}{2d} \left(p_1^2 - p_2^2\right) \tag{9.13}$$

where the constants $K_{perm}$ and $K'_{perm}$ is depending on the material and molecule combination. It is defined as the product of the solubility of a molecule in the material $K_s$ and the diffusion constant $D$ as defined in the previous section.

$$K_{perm} = K_s D \tag{9.14}$$

Again the solubility and the diffusion constant are both depending on the wall temperature. The dependency of $D$ has been described in the previous section. The dependency of $K_s$ is given as

$$K_s = K_{s,0} \exp\left(-\frac{E_s}{R T_w}\right) \tag{9.15}$$

with $K_{s,0}$ being the solubility of a molecule in a material for $T_w \to \infty$ and $E_s$ the enthalpy of solution, which is given in literature for a certain gas-wall material combination.

The contribution of the gas flow by diffusion to the overall gas flow is small. Even for vacuum chambers of stainless steel with a wall thickness of $2d = 2mm$ the gas flow due to permeation is three orders of magnitude below the gas flow due to diffusion of a well baked stainless steal chamber [Jou13]. Since the chamber walls in MAIUS are significantly thicker, permeation will be neglected for the sizing of the pumping system.

### 9.2.4 Outgassing of Technical Surfaces

The amount of gas, which is released from a component or sample is strongly depending on the type of material, its surface and the treatment it experienced before it was included into the vacuum chamber. For this reason it is hard to predict the outgassing rate of a material. This is why the outgassing rates are often determined experimentally.

There a several methods of determining outgassing rates [Els75]. A common and relatively easy method is to determine the outgassing rate of a material sample by measuring the pressure rise after the sample was kept under vacuum with constant pumping for a certain

time. For the measurement the sample is isolated from the pumps and the pressure rise $\Delta p$ in a time $t_m$ is recorded. It is important to use a gauge with a low pumping rate to maintain good results. The outgassing rate $q_n$ can than be calculated from [Els75]

$$q_n = \frac{\Delta pV}{t_m A_s} \tag{9.16}$$

where $V$ is the volume of the chamber the measurement is performed in and $A_s$ is the area of the sample facing the vacuum. The outgassing rate is given in $\mathrm{hPa\,l\,s^{-1}\,cm^{-2}}$. The leakage rate in the test setup is not considered in this simple approach. Its impact is discussed later.

Independent from the measurement methods the outgassing rate $q_n$ of a material at constant temperature reduces as the pumping time increases. For this reason a outgassing rate in a table should always be given with the pumping time $t_n$ at which it was measured, the treatment performed and the measuring method. The subscript $n$ is giving the pumping time in hours. In addition to this a factor $\alpha_n$ might be given indicating the slope of a double logarithmic pressure-time plot at this time $t_n$.

With a given outgassing rate $q_n$ and a known time of measurement $t_n$, the amount of gas entering the system by an outgassing process, which is dominated by desorption can be predicted for most materials as for example metals from [Pfe09]

$$Q_{des}(\mathrm{t}) = q_n \mathrm{A} \frac{t_n}{t} \tag{9.17}$$

This is in accordance with the approach presented in section 9.2.1. The characteristic outgassing rate for the material $q_n$ has to be obtained from literature or determined by experiments. The total area of this material facing the vacuum needs to be extracted from CAD models.

The amount of gas released by polymers is dominated by diffusion. The time dependency can be approximated by [Pfe09]

$$Q_{diff}(\mathrm{t}) = q_n \mathrm{A} \sqrt{\frac{t_n}{t}} \tag{9.18}$$

In section 9.2.2 it is stated that the outgassing rate is proportional to $\sqrt{\frac{1}{t}}$ and changes to $\exp(-at)$ for longer times. However it is sufficient for technical approximation to assume a constant dependency with $\frac{1}{\sqrt{t}}$ as given in equation 9.18. It has to be noticed, that the outgassing rate decreases much slower compared to metals. For this reason elastomer seals and components are considered not suitable for UHV applications.

As shown in equations 9.18 and 9.17 the gas flow into the system by desorption can be influenced by the choice of a material with a low desorption rate. Moreover minimization and treatment of the inside surface of the vacuum system and techniques as baking of the setup can reduce outgassing and thus allow to reach lower pressures.

### 9.2.5 Material Selection

As stated in the previous sections outgassing of a vacuum chamber is strongly depending on the material choice. A material for parts of a vacuum system, which is suitable for the use on a sounding rocket, needs review of multiple criteria. These are not only vacuum related, but also driven by other requirements. As such the density is of interest to minimize the mass of the chamber, which is desirable for all space missions.

The mechanical properties of the material are characterized by the yield strength $R_{p0.2}$, the youngs modulus ($E$) and the hardness according to Vickers ($H$). The material should have mechanical properties to withstand the stress as a result of the mechanical loads during launch and re-entry at the different parts of the vacuum system.

Additionally the relative magnetic permeability $\mu_r$ is important for all parts of the vacuum system inside the magnetic shielding. Permeability is the degree of magnetization that a material obtains in response to the magnetic field applied for example by the coils of the vacuum chamber. The relative permeability is the ratio of the permeability of a specific medium to the permeability of free space $\mu_0$ =1.2566 $\times 10^{-6}\,\mathrm{N\,A^{-2}}$:

$$\mu_r = \frac{\mu}{\mu_0} \tag{9.19}$$

The smaller the value of $\mu_r$ of a certain material the lower the magnetic field induced by the coils in the part manufactured from this material. This is desirable because a magnetization one of the vacuum parts would disturb the measurement. This is especially important for parts close to the atoms as the vacuum chamber walls.

| Material | $q_{10}$ [hPa L cm$^{-2}$ s$^{-1}$] | $\mu_r$ [-] | $R_{p0.2}$ [MPa] | $H$ [HV] | $\rho$ [g cm$^{-3}$] |
|---|---|---|---|---|---|
| Ti6Al4V | $4.9 - 24.5 \times 10^{-10}$ | 1.000050 | 910 | 330 - 390 | 4.45 |
| Steel (1.4404) | $18.0 \times 10^{-10}$ | 1.7 | 360 | 150 - 200 | 7.98 |
| OFHC Copper | $16.8 \times 10^{-10}$ | 0.9999936 | 220 - 380 | 85 - 115 | 8.94 |
| EN AW 7075 | $8 \times 10^{-10}$ | 1.000022 | 220 - 460 | $\leq 160$ | 2.8 |

**Table 9.1:** Material properties of candidates for vacuum chamber [Els75]

Oxygen free high conductivity copper (OFHC or C10100) should be considered for transporting high thermal loads to the chamber walls, because of its high thermal conductivity. This is the case for the chip mount, where the heat produced at the planar structures of the atomchip need to be conducted to the chamber walls. Another reasonable application are surfaces that should be polished to high reflectivity as at the differential pumping stage between preparation and science chamber. It is important to use oxygen free copper, because the solved oxygen in regular copper could only be removed by baking the part above the softening temperature of copper. Thus the oxygen would slowly diffuse out of the coper resulting in unacceptable high outgassing rates.

For the chamber itself either titanium (Ti6Al4V) or aluminum (EN AW 7075) should be used. Stainless steel (1.4404) should not be considered for the science or preparation chamber, due to its bad magnetic properties and the high density. However it could be used as a low cost alternative for vacuum components outside the magnetic shielding.

Titanium is slightly preferable to aluminum, because of its mechanical properties. The higher yield strength and hardness of the material will assure a high capacity of the chamber for carrying mechanical loads. Moreover both properties will allow a reliable use of standard CF seals at the chamber. CF knife edges made of titanium are common state of the art and have been used in several chamber designs (including QUANTUS-2). Aluminum knife edges have been presented by VACOM after completion of the MAIUS design [Ber15] but they will require aluminum or soft annealed copper gaskets and their behavior under mechanical loads is unknown. In MAIUS titanium and stainless steal have been chosen for all CF components. The allocation of the material to the different components of the MAIUS vacuum system is given in table 9.2 and 9.3.

### 9.2.6 Influence of Vacuum Preparation

As previously mentioned outgassing rates are strongly depending on the treatment of a vacuum component. In the following the influence of different preparation techniques on the vacuum quality will be summarized. Moreover the current vacuum preparation procedure for MAIUS vacuum components is described.

#### Cleaning

Lubricants from the fabrication of vacuum components on the inside will result in massive gas input, when these lubricants are vaporized. Therefore the time to reach ultra low vacuum pressures is increased. Particle contamination of the interior of the vacuum system will also extend the pump-down time for the chamber dramatically due to the large surface of these particles.

For this reason it is essential to clean the vacuum components carefully using solvents. In MAIUS-1 each vacuum component is cleaned sequentially with distilled water, isopropyl alcohol (IPA) and acetone in an ultrasonic bath. Cleaning and assembly of the pumping system and vacuum chamber is carried out inside an ISO 5 (RK100/RK1000) clean room to avoid re-contamination of the inside of the vacuum chamber with dust or other macroscopic particles from the air or the scientists assembling the system.

### Baking

As stated in section 9.2.1 to 9.2.2 all mechanisms contributing to the outgassing of a material are depending on the temperature. A rise in temperature will reduce the time necessary to remove a certain amount of gas bound in the material or at its surface. In the temperature regime below 400 °C it can be stated, that it is advisable to use temperatures as high as possible for baking, since the time for the removal of an amount of gas scales with the wall temperature. Moreover temperatures above 90 °C will ensure a fast removal of water from the chamber walls. In any case it should be taken care, that the wall temperature is equivalent at all walls of the vacuum system. Otherwise the gas molecules removed from the hot surface will stick to the cold ones, where their mean residence time (compare section 9.2.1) is higher, which will reduce the efficiency of the baking process significantly [O'H04].

For most technical metals the dependency of the outgassing rate on the baking temperature is well documented. The most measurements and experiments have been performed for stainless steel, as it is commonly used in vacuum chambers. The outgassing rates for different metals with different preparation methods have been summarized by Elsey in 1975 [Els75]. Herein a reduction of the outgassing rate of Ul5C stainless steel by more than three orders of magnitude to $2.133 \times 10^{-14}\,\mathrm{hPa\,L\,s^{-1}\,cm^{-2}}$ has been reported. This has been achieved by baking the sample for 3 h in a vacuum furnace followed by 25 h of in-situ baking at 360°. Unfortunately the indium seals in the assembled MAIUS apparatus limit the maximum baking temperature to 100 °C. Although the melting point of indium is 156.6 °C the baking temperature limit has been set to the 100 °C to avoid local melting of the seals due to hot spots, which might occur next to the heating bands used for baking.

Each part of the MAIUS vacuum system is baked at 250 °C or at the maximum baking temperature in a vacuum oven for at least 24 hours prior to assembly. Subsequently the entire vacuum chamber is baked in-situ at 100 °C once more. By permanent baking and pumping with the turbo pump for 3-4 weeks the outgassing rate can be reduced sufficiently to reach a pressure of $5 \times 10^{-10}$ hPa. At this point the pressure is limited by the back stream through the turbo pump. After switching to the internal pumps from MAIUS the lowest pressure demonstrated in the system has been $6.7 \times 10^{-11}$ hPa. An estimation of the outgassing rates for the MAIUS components will be given in 9.2.7.

### Surface Treatment

In general a reduction of $q_{10}$ outgassing rates has been reported in [Els75] for polished or plated surfaces. For a mechanically polished OFHC copper surface the outgassing rate after 10 h in vacuum reduces from $5.53 \times 10^{-9}$ to $4.75 \times 10^{-10}\,\mathrm{hPa\,L\,s^{-1}\,cm^{-2}}$.

Similar dependencies have been recorded for mechanical polished or sanded stainless steel probes [Els75], where the outgassing rate decreases from $1.96 \times 10^{-9}$ (fresh) to $1.39 \times 10^{-9}$ (sanded) and finally to $6.13 \times 10^{-10}\,\mathrm{hPa\,L\,s^{-1}\,cm^{-2}}$ for a mechanically polished sample. The outgassing rate could even be reduced to $5.71 \times 10^{-10}\,\mathrm{hPa\,L\,s^{-1}\,cm^{-2}}$ if the stainless steel probe was electro polished.

For stainless steel and titanium chemical polishing has been proposed [Kur08] to reduce the surface roughness of the inner vacuum chamber walls. In combination with baking at 393 K for 20 h this treatment resulted in an outgassing rate of $1 \times 10^{-13}\,\mathrm{hPa\,L\,s^{-1}\,cm^{-2}}$ for stainless steel and rates smaller than $7 \times 10^{-16}\,\mathrm{hPa\,L\,s^{-1}\,cm^{-2}}$ (detection limit) for titanium.

Although this results look promising it has to bes considered, that electro polishing or chemical polishing is an expensive procedure and most likely the overall outgassing rate will be dominated by the gas released from the chip surface and the surfaces of the chip cables. For this reason it has not been applied within MAIUS-1. However it should be considered for future missions to reduce pump-down times and residual outgassing rates.

### 9.2.7 Outgassing Rates of the MAIUS Setup

To calculate the gas flow due to outgassing of the MAIUS chamber walls from equation 9.17 or 9.18, the area $A$ of a certain surface facing the vacuum and the material outgassing rate $q_n$ has to be known.

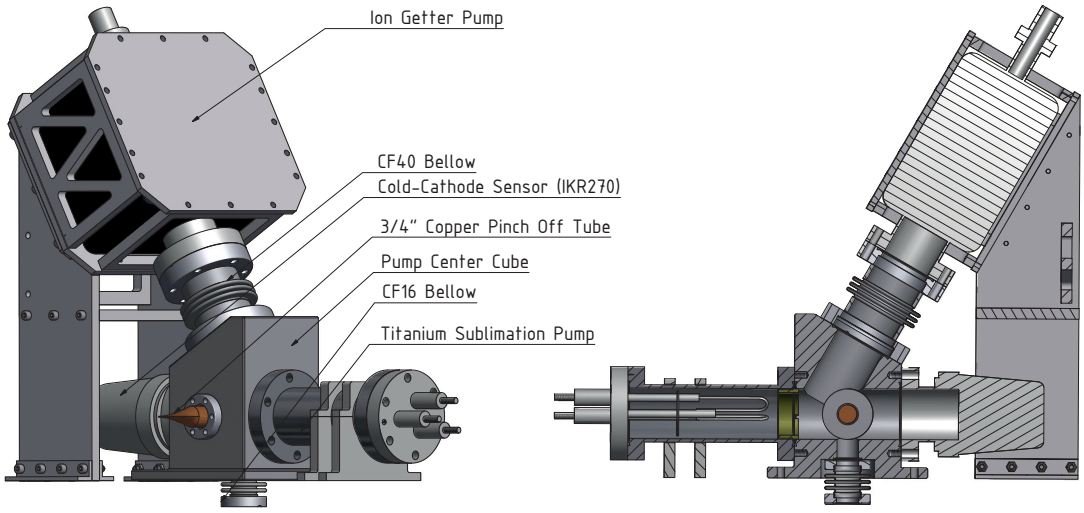


**Figure 9.1:** Overview on the vacuum system setup outside the magnetic shielding

The area of complex parts as they are used in the MAIUS vacuum system setup can be determined from the CAD models of the parts with high accuracy. The same can be done to obtain the enclosed volume of these parts contributing to the overall volume of the MAIUS vacuum system. Moreover a specific material is assigned to each part, to determine a material specific outgassing rate. If a part or group of parts consists of multiple materials, the area sum of the material exposed to vacuum is used.

| Component | Material | Surface [$cm^2$] | Volume [$cm^3$] |
|---|---|---|---|
| Center Cube | 1.4404 | 149.9447 | 0.2266 |
| Bellow CF40 | 1.4404 | 146.7535 | 0.0816 |
| Bellow CF16 | 1.4404 | 12.0637 | 0.0048 |
| Blind flange | 1.4404 | 13.5026 | - |
| 3/4" CPOT pinched | OFHC | 27.1277 | 0.0024 |

**Table 9.2:** Components of the pumping system (above magnetic shielding), their assigned materials, their surface area in direct contact with the vacuum and the volume of vacuum enclosed

For the sake of clarity the assigned materials and the area exposed to vacuum are summarized separately for the portion of the vacuum system inside the magnetic shielding and for the pumping system outside the magnetic shielding.

The area sum of a certain material for each component obtained from CAD is presented in table 9.2. Figure 9.1 gives an overview and section view of the vacuum system setup outside the magnetic shielding to illustrate the geometries of this portion of the MAIUS vacuum system and to visualize the components listed in table 9.2.

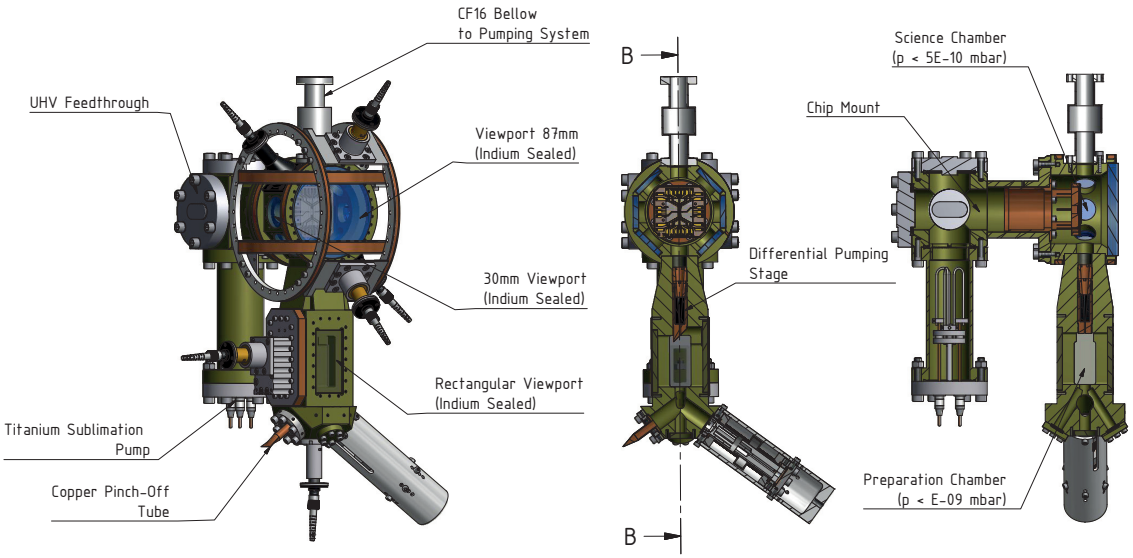


**Figure 9.2:** Vacuum system setup inside the magnetic shielding

The same applies for figure 9.2 showing the experiment chamber setup in an overview and two perpendicular section views, to give an insight in the interior of this two-chamber system as it has been described in section 7.3.3. Table 9.3 is presenting the associated results of the virtual measurements.

The ion-getter pump, both titanium sublimation pumps and the cold cathode gauge are intentionally not listed in these tables, because the measured pumping speed of these pumps

is a net pumping speed at the connecting flange of the pump. Thus it already accounts for potential outgassing of the pump (compare section 9.4). As the cold-cathode gauge is in principal a small ion-pump with an unknown (small) net pumping speed, its area should also be neglected.

The length of the pinched cooper pinch off tube was defined to be 50 mm, which is an reasonable assumption for the MAIUS setup. The cables used to connect the atom chip with the vacuum feedthroughs are Kapton insulated wires of the type Allectra 311-KAP2 with 0.6 mm conductor diameter [Sei14]. The outer diameter is roughly 1 mm (measured) and the length of the 36 cables connecting the chip structures with the feed throughs is 180 mm. In addition to this 8 loops of cables with a length of 140 mm have been used for the mesoscopic structures. So the overall length of the cable is 7600 mm resulting in an surface area of 238.76 $cm^2$.

The chip itself is difficult to model, due to the different layers (base chip, science chip and mirror), which are clued to each other. Especially the glue will contribute to the outgassing, but the area of the glue in contact with the vacuum and its outgassing rate is unknown. Measurement of the chip outgassing rates is planned for following setups. As a simple model the base chip aluminum nitride (AlN) surface and the base chip conductor surface (Gold) have been extracted from the CAD model and are given in table 9.3.

| Component | Material | Surface [$cm^2$] | Volume [L] |
|---|---|---|---|
| Science Chamber | Ti6Al4V | 106.6346 | 0.1853 |
| Preparation Chamber | Ti6Al4V | 112.6153 | 0.1069 |
| DPS | OFHC | 10.7982 | 0.0011 |
| DPS Insert | Graphite | 2.5573 | 0.0002 |
| View Ports | BK7 | 91.8049 | - |
| Chip Cube | Ti6Al4V | 180.3707 | 0.3052 |
| Chip Mount | OFHC | 136.1015 | - |
| Chip Cables | Kapton | 238.7610 | - |
| Chip | AlN | 1247.84 | - |
| | Gold | 975.80 | - |
| CF16 Tube | Ti6Al4V | 27.1277 | 0.0210 |
| 3/4" CPOT pinched | OFHC | 27.1277 | 0.0117 |
| Oven | Ti6Al4V | 36.6901 | 0.0183 |
| | Aluminum | 60.8275 | - |

**Table 9.3:** Components of the science chamber system (inside the magnetic shielding), their assigned materials, their surface area in direct contact with the vacuum and the volume of vacuum enclosed

Estimation of the outgassing rate of the materials used in MAIUS is difficult, because these do not only depend on the treatment the material experienced in the laboratory, but also on the initial states of the sample. And these depend on manufacture, pre-treatment and

storage conditions. This is also the reason for large variations of the measured outgassing rates for a single material in literature [Els75].

However outgassing rate measurements for each material or each vacuum component could not be realized in the tight schedule of the MAIUS project. For this reason the rates will be estimated using literature values taking into account the treatment of the overall apparatus as described in section 9.2.6.

The CERN performed outgassing measurements of material probes for the PHARAO project [Gra04], which have been baked under vacuum at 140 °C for 24 h. After cooling the outgassing rate of the samples was measured using an accumulative technique. The accumulation time was 3 h resulting in an detection limit of $2.6 \times 10^{-13}\,\mathrm{hPa\,L\,s^{-1}\,cm^{-2}}$. The in-situ baking temperature is close to the one used in MAIUS. Thus the values measured for graphite ($6.6 \times 10^{-13}\,\mathrm{hPa\,L\,s^{-1}\,cm^{-2}}$, stainless steel ($2.6 \times 10^{-12}\,\mathrm{hPaL/s/c^2m}$) and titanium ($2.6 \times 10^{-13}\,\mathrm{hPa\,L\,s^{-1}\,cm^{-2}}$ / below detection limit) should give a good approximation. Indeed this rate might be conservative, since the bakeout performed in MAIUS was at a lower temperature, but significantly longer (4 weeks).

For aluminum and copper outgassing rates have been given in the outgassing summary by Elsey [Els75] for a heat treatment at 100 °C for 20 h. These are $5.33 \times 10^{-14}\,\mathrm{hPa\,L\,s^{-1}\,cm^{-2}}$ for aluminum and $1.47 \times 10^{-12}\,\mathrm{hPa\,L\,s^{-1}\,cm^{-2}}$ for OFHC copper.

| Material | $q_n$ [$\mathrm{hPa\,L\,s^{-1}\,cm^2}$] | $\sum A_{3D}$ [$\mathrm{cm^2}$] | $Q_{out,3D}$ [$\mathrm{hPa\,L\,s^{-1}}$] | $\sum A_{2D}$ [$\mathrm{cm^2}$] | $Q_{out,2D}$ [$\mathrm{hPa\,L\,s^{-1}}$] |
|---|---|---|---|---|---|
| Ti6Al4V | $2.6 \times 10^{-13}$ | 393.54 | $1.02 \times 10^{-10}$ | 149.31 | $3.88 \times 10^{-11}$ |
| 1.4404 | $2.6 \times 10^{-12}$ | 322.26 | $8.38 \times 10^{-10}$ | - | - |
| OFHC | $1.47 \times 10^{-12}$ | 174.03 | $2.56 \times 10^{-10}$ | 12.15 | $1.7 \times 10^{-11}$ |
| Graphite | $6.6 \times 10^{-13}$ | 2.56 | $1.69 \times 10^{-12}$ | - | - |
| BK7 | $2.13 \times 10^{-10}$ | 51.02 | $1.09 \times 10^{-8}$ | 40.79 | $8.69 \times 10^{-9}$ |
| Kapton | $1.1 \times 10^{-10}$ | 238.76 | $2.63 \times 10^{-8}$ | - | - |
| AlN | $2.6 \times 10^{-13}$ | 12.48 | $3.24 \times 10^{-12}$ | - | - |
| Gold | $6.80 \times 10^{-10}$ | 9.76 | $6.64 \times 10^{-9}$ | - | - |
| Aluminum | $5.33 \times 10^{-14}$ | - | - | 60.83 | $1.79 \times 10^{-11}$ |
| Sum | | 1204.41 | $4.50 \times 10^{-8}$ | 263.08 | $8.75 \times 10^{-9}$ |

**Table 9.4:** Gasflow due to outgassing of the different materials used in the MAIUS vacuum system

For the VIRGO interferometer in Italy measurements of the outgassing of 30 m Kapton insulated cable with a surface of $490\,\mathrm{cm^2}$ have been performed [Ber96]. The outgassing rates varied strongly from initially $4.08 \times 10^{-7}$ to $1.5 \times 10^{-9}\,\mathrm{hPa\,L\,s^{-1}\,cm^{-2}}$ after 72 h in vacuum. Baking at 120 °C for approximately 30 h could decrease the outgassing rate to $1.1 \times 10^{-10}\,\mathrm{hPa\,L\,s^{-1}\,cm^{-2}}$. The lowest rate recorded in the study was $4.9 \times 10^{-11}\,\mathrm{hPa\,L\,s^{-1}\,cm^{-2}}$ after 251 h of pumping without baking.

For Schott BK7 glass and aluminum nitride no outgassing rates could be obtained from the literature. For gold no outgassing rates could be obtained for baked materials. For gold the outgassing rate after 10 h of pumping has been measured to be$6.80 \times 10^{-10}\,\mathrm{hPa\,L\,s^{-1}\,cm^{-2}}$ [Els75]. The rate for Pyrex glass is the material most similar to Schott BK7 glass. Its outgassing rate after 10 h is given as $2.13 \times 10^{-10}\,\mathrm{hPa\,L\,s^{-1}\,cm^{-2}}$. For aluminum nitride (AlN) no data was found in the literature. In the PHARAO measurement campaign a measurement was carried out for silicon carbide reinforced aluminum (AlSiC). This should be used as a first estimation. The measured rate has been below the detection limit, thus it has been set to $2.6 \times 10^{-13}\,\mathrm{hPa\,L\,s^{-1}\,cm^{-2}}$.

## 9.3 Leakage Rates

Aside from outgassing of the chamber walls and components inside the vacuum, leaks are a possible cause for a pressure rise in the chamber. One will have to differentiate between internal and external leaks.

Internal leaks are trapped volumes of gas, which are only pumped with very bad conductance, which will result in a small long-term gas flow from the trapped volume into the chamber. Virtual leaks can be avoided by good engineering according to vacuum chamber design guidelines. For example threads inside the vacuum should always be equipped with slits or bore holes, to ensure that trapped air can be sufficiently pumped. This has successfully been done in MAIUS as part of this thesis and resulted in a good ultimate pressure of $6.4 \times 10^{-11}$ hPa.

Leaks to the exterior are typically detected by tests with acetone or helium. While acetone is injected into the gap between two flanges with a micro-liter syringe and a leak is detected by a rise in the chamber pressure, helium is sprayed onto the flange and the helium partial pressure is measured inside the chamber. This allows to detect even very small leaks.

### 9.3.1 Leakage rates of sealing methods for UHV vacuum

In the past years a high number of sealing techniques has been developed and been used in UHV experiments. In MAIUS the commercial Conflat copper seals and indium wire seals are used. Both sealing techniques are suitable for vacuum pressures of $1 \times 10^{-11}$ hPa.

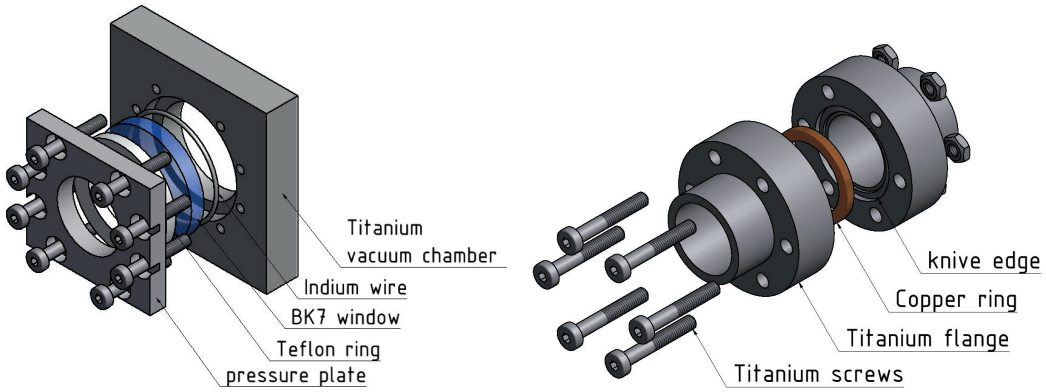


**(a)** MAIUS indium sealing principle

**(b)** Commercial con-flat (CF) sealing principle

**Figure 9.3:** Sealing techniques used in MAIUS-1 [Gro11]

The commercial Conflat seals consist of a OFHC copper gasket, which is pressed between two knife edges by fastening the flange screws as illustrated in figure 9.3b. In MAIUS the flange connections have been prepared with a minimum torque of 10 N m for M6 screws used for DN40 flanges and 3 N m for M4 screws used for connecting DN16 flanges. The bolts are fastened in a star pattern slowly increasing the torque in multiple steps to avoid tilting of the flange. This guarantees a uniform minimum sealing force at all flange connections, which creates a hermetic seal. This seal reaches a leakage rate smaller than $1 \times 10^{-11}$ hPa L s$^{-1}$ at temperatures of up to 450 °C [Vac15]. Conflat seals are commonly used in industry and research applications for diameters up to 250 mm. However a use in an sounding rocket environment with pressures below $5 \times 10^{-10}$ hPa has not been reported so far.
Indium seals are made from pure (99.995 %) indium wire, which is compressed between the two surfaces to be sealed. The soft metal will compensate imperfections in the material surface. Moreover its ductility allows to compensate for thermal expansion rate mismatches between the two materials to be sealed. Indium is often used for cryogenic vacuum seals, because it remains malleable at cryogenic temperatures. The operating temperature for indium seals ranges from 50 mK to 100 °C [Ste10]. The leakage rates at room temperature are below $1.97 \times 10^{-11}$ hPa L s$^{-1}$ [Kup10].

In MAIUS the indium seals are used to seal the viewports and the connection between chip mount and science chamber as described in section 7.3.3. For preparation of the seal the indium wire is cleaned with acetone and subsequently centered in the small flange area of the pocket as shown in figure 9.4b. The overlap of the ends will complete the seal, which is formed by cold welding of the indium wire to itself and to the surfaces under pressure.

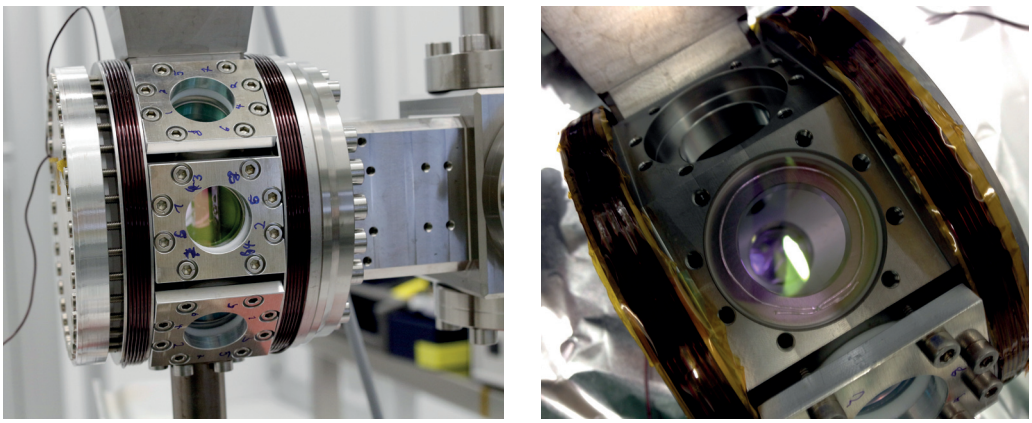

**(a)** Science chamber with pressure plates

**(b)** Indium wire at one of the circular view ports prior to compression

**Figure 9.4:** MAIUS science chamber during preparation of the indium seals

The pressure breaks the oxide layer of the indium to allow the cold welding process.

The pressure is applied by a pressure plate which is pressed against the window by tightening the M3 screws next to the seal as shown in figure 9.4a. The window is protected from damage by a Teflon ring between the pressure plate and the window. The screws are fastened diagonal in a specific order as indicated by the numbers in figure 9.4a. The torque is raised in 0.1 N m steps to reach the maximum of 0.8 N m after a round has been completed. Again this will guarantee a uniform pressure along the seal for an accurate hermetic seal.

Although both sealing methods are commonly used in experiments, no data is available for the performance of the seals under static or vibrational loads as expected aboard the sounding rocket. For this reason intensive testing of the seals has been performed as part of this thesis and will be presented in section 9.5.2 and 9.6.

## 9.4 MAIUS-1 Pump Concept and Effective Pumping Speed

The MAIUS setup uses four different pumps to prepare the vacuum and to maintain the pressure. In this section the different kinds of pumps shall be characterized in terms of pumping speed and lifetime.

Moreover the local distribution of the effective pumping speed over the vacuum system should be determined by calculation of the conductance of tubes and other components alomg the path of the area of interest to the pump(s).

For the determination of the conductance it is important to specify the type of flow in the vacuum vessel. One has to differentiate between continuum flow, Knudsen flow and molecular flow. The type of flow is depending on the pressure inside the vessel $p$, the medium and the characteristic width of the vessel $d$ and is determined by the Knudsen Number $Kn$

$$Kn = \frac{\pi}{4} \frac{\bar{c}\,\eta}{p\,d} \tag{9.20}$$

For air at 20 °C the viscosity $\eta$ is given as $18.2 \times 10^{-6}$ Pa s and the mean velocity $\bar{c}$ as $463\,\mathrm{m\,s^{-1}}$ [Jou13]. For a given geometry and pressure the flow can be determined by the Knudsen number as follows

$$Kn > 0.5 \qquad \text{Molecular flow}$$

$$0.5 > Kn > 0.01 \qquad \text{Knudsen flow}$$

$$0.01 < Kn \qquad \text{Continuum flow}$$

To avoid calculating a Knudsen number for each component inside the vacuum chamber, a critical characteristic width $d_c$ at which the flow turns from molecular flow into a Knudsen flow can be calculated from

$$d_c = \frac{\pi}{2} \frac{\bar{c}\,\eta}{p} \tag{9.21}$$

The critical width for a pressure of $1 \times 10^{-6}$ hPa is 132.3 m. This pressure is typically reached within minutes during the initial pump down. The region of interest for normal laboratory operation of the MAIUS apperatus is $5 \times 10^{-10}$ hPa and below. For this reason molecular flow is assumed for every calculation herein.

### 9.4.1 Roughening Pump

During vacuum preparation a turbo pumping station Pfeiffer HiCube 80 Classic is used as a roughening pump. The station combines a turbo molecular pump Pfeiffer HiPace 80 and a rotary vane pump Pfeiffer DUO5. This combination offers a pumping speed of $67\,\mathrm{L\,s^{-1}}$. The ultimate pressure is given as $5 \times 10^{-10}$ hPa.

The pumping station is equipped with a CF63 flange. As shown in figure 9.5 a CF 63 pipe and cross with a total length of 410 mm is mounted to the pump during vacuum preparation of the MAIUS setup. Two CF40 corrugated hoses with a length of 1 m and a sensor Pfeiffer PKR251 are connected to the cross at the pump. The end of the hoses is

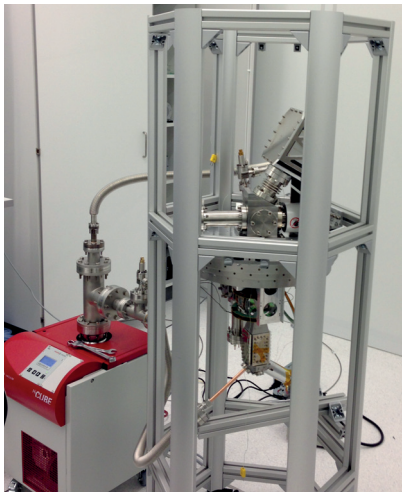

(a) Pfeiffer Vacuum turbo pump station during first pump down of the MAIUS-1 physics package

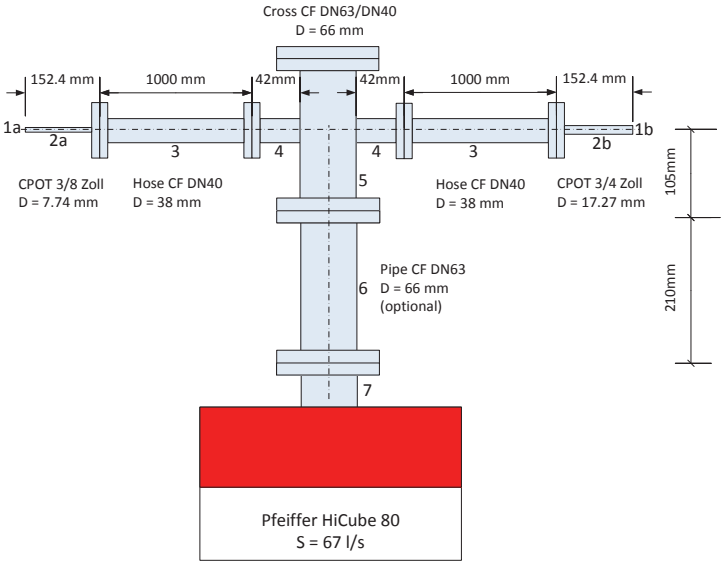


(b) Shematic showing all components between pump inlet and MAIUS vacuum chamber

**Figure 9.5:** Turbo pumping station and components used in MAIUS-1 during vacuum preparation

connected with one copper pinch-off tube (CPOT) each to the 2D MOT chamber and to the pumping system center cube. This way both sides of the differential pumping stage are pumped, which will reduce the time needed for evacuation of the 2D-MOT dramatically. Otherwise the 2D-MOT would be pumped down only through the differential pumping stage, which is designed to have only a small conductance for gases. Which would be an inefficient method.

The conductance of a single tube of arbitrary length can be calculated from the product of the conductance of a orifice with the tube diameter $C_o$ with the transmission probability through the pipe for a molecule $P_p$ [Jou13].

$$C_t = C_o P_p \tag{9.22}$$

where

$$C_0 = \frac{1}{4}\bar{c}A \tag{9.23}$$

$$P_p = \frac{14+4\frac{l}{d}}{14+18\frac{l}{d}+3\left(\frac{l}{d}\right)^2} \tag{9.24}$$

For a series of $n$ vacuum components the overall conductivity $C_{1n}$ between component 1 and $n$ is given as [Jou13]

$$\left(\frac{1}{C_{1n}}-\frac{4}{\bar{c}\,A_1}\right)=\sum_{i=1}^{n}\left(\frac{1}{C_i}-\frac{4}{\bar{c}\,A_i}\right)+\frac{4}{\bar{c}}\sum_{i=1}^{n-1}\left(\frac{1}{A_{i+1}}-\frac{4}{\bar{c}\,A_i}\right)\delta_{i,i+1} \tag{9.25}$$

The overall conductivity is depending on the change in the cross section $A$ between the components. If the cross section between the component $i$ and $i+1$ is reduced the losses at the entrance of the flow into the component with the smaller cross section have to be included in the calculation. This is done by setting the factor $\delta_{i,i+1}$ in equation 9.25 to 1. This will include the last term of the equation into the calculation. If cross section of component $i+1$ is increasing with respect to the previous component or does not change the effects at the entrance into the next component are neglected by setting $\delta_{i,i+1}$ to 0.

| Component | Index | d [mm] | l [mm] | A [$m^2$] | C [$L\,s^{-1}$] |
|---|---|---|---|---|---|
| 2D inlet | 1a | 7.74 | - | 0.0000471 | $S_{eff,2D}$ |
| Cube inlet | 1b | 17.27 | - | 0.000234 | $S_{eff,cube}$ |
| CPOT 3/8 | 2a | 7.74 | 152.4 | 0.000047 | 0.33 |
| CPOT 3/4 | 2b | 17.27 | 152.4 | 0.000234 | 3.29 |
| VAT Series57 CF16 | 3 | 16 | - | 0.00020 | 5 |
| VAT Series57 CF40 | 3’ | 38 | - | 0.0011 | 50 |
| CF40 hose | 4 | 38 | 1000 | 0.0011 | 6.10 |
| CF16 hose | 4’ | 16 | 1000 | 0.00020 | 0.48 |
| Cross CF40 part | 5 | 38 | 42 | 0.0011 | 64.38 |
| Cross CF63 part | 6 | 66 | 105 | 0.0034 | 160.54 |
| Pipe CF63 | 7 | 66 | 210 | 0.0034 | 104.13 |
| Pump | 8 | 66 | - | 0.0034 | $S = 67$ |

**Table 9.5:** Geometry and conductivity of the different components between the roughening pump and the MAIUS chambers

Table 9.5 summarizes all important data to solve equation 9.25. For the inlet into the preparation (2D MOT) chamber it is assumed that the chamber is a large vacuum tank which is true compared with the small diameter of the CPOT. The pump is modeled as a pipe with the diameter of the pump flange (CF DN63). It is assumed that the pressure inside the pump is 0 (perfect vacuum) and the conductivity of the pipe equals the pumping speed ($C = S$) [Jou13].

Transformation of equation 9.25 will result an equation for calculation of the effective pumping speed $S_{eff}$

$$S_{eff} = \left[ \sum_{i=2}^{6} \left( \frac{1}{C_i} - \frac{4}{\bar{c} A_i} \right) + \frac{4}{\bar{c}} \sum_{i=2}^{5} \left( \frac{1}{A_{i+1}} - \frac{4}{\bar{c} A_i} \right) \delta_{i,i+1} + \left( \frac{1}{S} - \frac{4}{\bar{c} A_7} \right) + \frac{4}{\bar{c} A_1} \right]^{-1} \quad (9.26)$$

This calculation has to be carried out for the two paths to the 2D-MOT chamber and the pumping system central cube as illustrated in figure 9.5. Each path consists of 6 pipe components ($i$= 2- 7, as listed in table 9.5), the pump ($i$ = 8) and the target chamber ($i$ = 1).

| Setup | 2D MOT | | Pump Cube | |
|---|---|---|---|---|
| | $S_{eff}$ [L s$^{-1}$] | $t_{pd}$ [s] | $S_{eff}$ [L s$^{-1}$] | $t_{pd}$ [s] |
| CF16 hose /w CF63 pipe | 0.1882 | 478 d | 0.3868 | 93 d |
| CF40 hose /w CF63 pipe | 0.2924 | 307 d | 1.4463 | 60 d |
| CF40 hose $l$ = 500 mm | 0.2991 | 300 d | 1.6243 | 58 d |
| CF40 hose CPOT $l$ = 75 mm | 0.5134 | 175 d | 2.0558 | 34 d |
| CF40 hose CPOT $l$ = 75 mm / CF40 valve | 0.5657 | 159 d | 3.2636 | 30 d |
| CF40 hose CPOT $d$=25.4 mm / CF40 valve | 5.1767 | 17 d | - | - |

**Table 9.6:** Pumping rates at different positions of the roughening pump

Pump down times to the desired pressure $p_{end}$ of $5 \times 10^{-10}$ hPa are in the order of weeks. The pump down time is dominated by the gas flow into the chamber by outgassing as defined in section 9.2. Thus the pumpdown time (without bake-out) can be estimated from

$$t_{pd} = \frac{Q_{des}\, t_0}{S_{eff}\, p_{end}} \quad (9.27)$$

During vacuum preparation of the MAIUS-1 physics package, the used corrugated hoses have been changed from CF16 to CF40, to reduce the pump down time. Moreover it was proposed to remove one of the CF63 pipes and to shorten the copper pinch off tubes. In table 9.6 these modifications and their effect on the effective pumping speed and pump down time are listed.

Since the copper pinch off tubes offer the lowest conductance, they are limiting the effective pumping speed. Thus it is advisable to shorten the tubes or increase the diameter of the smaller (3/8") copper pinch off tube. As shown in table 9.6 this will improve the pump performance significantly. A possibility to improve the conductance even more is to chose a larger diameter CPOT and a larger valve. However these CPOTs can not be pinched by the tool purchased for MAIUS-1. Moreover section 9.4.4 will show that the vacuum system geometry will limit the pumping speed in the science chamber anyway.

The copper pinch off tubes are closed once a pressure of at least $5 \times 10^{-10}$ hPa is reached

by a hydraulic toll as described in section 7.3.2. Before the pinch off process is initiated, the CF16 valves are closed to protect the turbo pump, if the pinch off process is not successful and gas will enter the system. At this point the internal pumps of the MAIUS-1 vacuum system have to maintain the pressure autonomously. Their pump characteristics should be discussed in the following.

### 9.4.2 Titanium Sublimation Pump

As mentioned in section 7.3.2, two titanium sublimation pumps VG Sienta ST22 have been installed in the MAIUS vacuum system setup. While the pump outside of the magnetic shielding has been modified by the supplier to be shorter than the standard version, the pump inside the shielding has been rebuild completely with the aim of reducing the magnetic permeability. For this reason a different high current feed-through have been used and a new mounting of the filaments has been designed. However the outer dimensions of the pump tube as shown in figure 9.6a and the used titanium-molybdenum filaments are identical with the commercial pump. Both pumps carry three filaments with 6 g of usable titanium.

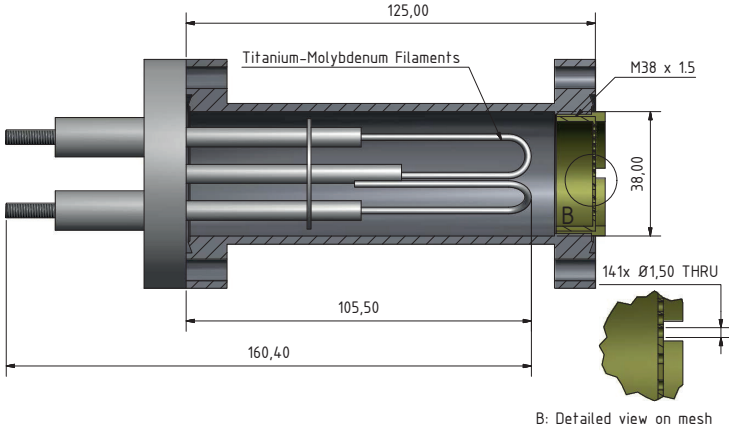


(a) Section view through VG Sienta titanium sublimation pump mounted in a CF40 pipe with mesh installed

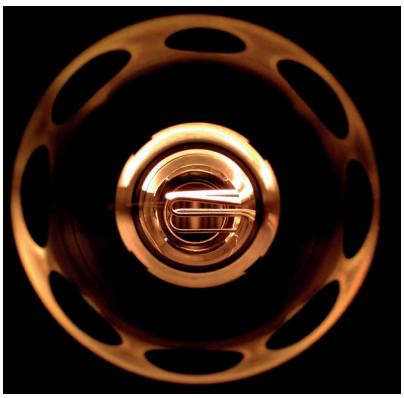

(b) View on the titanium pump filaments during activation process in a test setup

**Figure 9.6:** Titanium sublimation pump VG Sienta ST22

Both pumps have successfully been qualified according to the test profile described in section 8.1 at loads of up to 8.1 $g_{rms}$. A total of 7 test runs in a hard mounted setup in all three-axis have been carried out with the pump in vacuum at a pressure $5 \times 10^{-10}$ hPa. The filaments have been degassed and activated at least 10 times prior testing. Visual inspection after the tests showed no damage at the filaments and no dust inside the vacuum tube.

The pumps are activated by sending a current of 48 A through the filaments of the pump. These filaments with a diameter of 2 mm consist of an alloy of Molybdenum and Titanium.

The high current will heat the filaments as shown in figure 9.6b. The heat will cause the titanium to sublime and condense on the cold chamber walls afterwards.

The condensed Titanium is pumping all but noble gases and methane by chemical absorption. The pumping rates attainable for different types of gases are mainly depending on the area of the condensing surface and the temperature of this surface [VG 09].

Table 9.7 is giving the theoretical pumping speed $S_t$ for different gases, assuming the tube wall being the condensing surface with an area of $149.22\,\mathrm{cm}^2$ and the room and wall temperature being constant at 293 K.

| Gas | Rate per area $[\mathrm{L\,s^{-1}\,cm^{-2}}]$ | Tube $[\mathrm{L\,s^{-1}}]$ | After Sieve $[\mathrm{L\,s^{-1}}]$ |
|---|---|---|---|
| Hydrogen ($H_2$) | 3 | 447.66 | 18.28 |
| Water ($H_2O$) | 3 | 447.66 | 18.28 |
| Carbonoxide ( CO ) | 9 | 1342.98 | 18.79 |
| Nitrogen ($N_2$) | 4 | 596.88 | 18.47 |
| Oxygen ($O_2$) | 2 | 298.44 | 17.91 |
| Carbondioxide ($CO_2$) | 8 | 1193.76 | 18.76 |
| Methane ($CH_4$) | 0 | 0 | 0 |

**Table 9.7:** Pumping rates of condensed titanium per area [VG 09] and in MAIUS-1 for different gases

However it has to be noted, that the mesh installed at the tube inlet as shown in figure 9.6a is lowering the effective pumping speed significantly. This mesh should prevent fragments of the filaments from floating into the science chamber during microgravity phase if the filaments would break as a result of the strong accelerations during lift off. This could happen despite the successful qualification of the pump, because the filaments get porous over time due to the sublimed titanium. Moreover the mesh should serve as a baffle to protect the ion getter pump from condensation of titanium particles, which would reduce the pumping rate of the ion getter pump.

The mesh holes measure 1.5 mm in diameter and 0.8 mm in length. From this geometry the conductivity of a single hole can be calculated from

$$C_{hole} = \frac{\pi}{16}\bar{c}d^2\frac{14+4\frac{l}{d}}{14+18\frac{l}{d}+3\left(\frac{l}{d}\right)^2} \tag{9.28}$$

to be $0.1351\,\mathrm{L\,s^{-1}}$ if the mean velocity of air at 20 °C is $\bar{c} = 463\,\mathrm{L\,s^{-1}}$ [Jou13]. The total conductivity of the mesh can be found from

$$C_{mesh} = 141 C_{hole} \tag{9.29}$$

Because the mesh comprises from 141 parallel bore holes with identical dimension. Thus the total conductivity of the mesh is $19.06\,\mathrm{L\,s^{-1}}$. This is 85.17 % below the conductivity

of a straight CF40 tube with a inner diameter of 38 mm and an identical length of 0.8 mm.

With the calculated conductivity of the mesh the effective pumping speed $S_{eff}$ after the mesh can be calculated from

$$S_{eff} = \frac{S_t}{1 + \frac{S_t}{C_{mesh}}} \tag{9.30}$$

Results of this calculation are given in table 9.7. In addition to this significant reduction of the pumping speed due to the poor conductance of the mesh, the degradation of the titanium layer has to be considered.

The pumping speed reduces due to saturation effects of the reactive titanium layer. This effect is depending on the number of atoms in the vacuum chamber (the residual pressure) and the type of molecules, since this is determining how many titanium atoms are needed to pump a gas molecule.

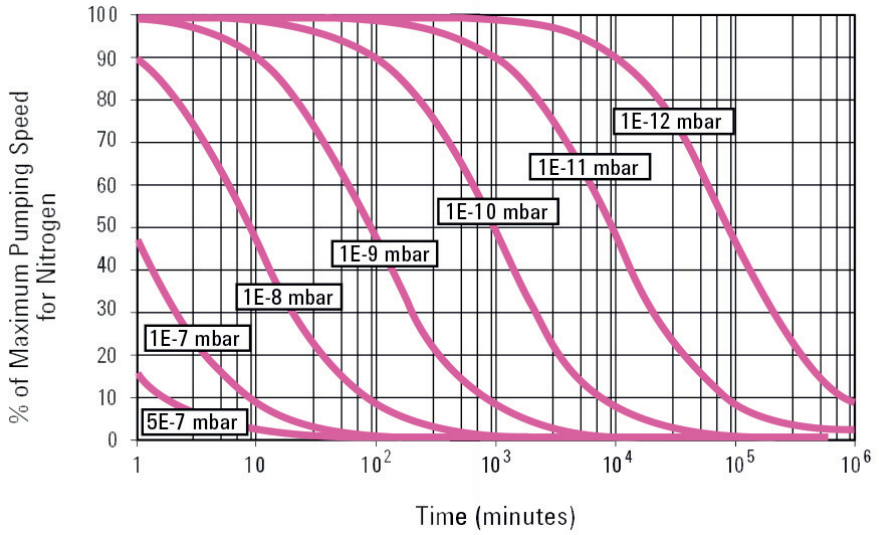


**Figure 9.7:** Degradation of the pumping speed of titanium layers at different pressures for nitrogen [Agi14]. Pressure is given by Agilent in mbar = hPa.

For nitrogen as the main constituent of air, the chemical reaction at the titanium surface is

$$2Ti + N_2 \rightleftharpoons 2TiN \tag{9.31}$$

thus two titanium atoms are needed to getter one nitrogen molecule. Figure 9.7 illustrates the degradation effect of the pumping speed for nitrogen molecules for different pressures inside the vacuum chamber. In MAIUS the titanium sublimation pumps are usually activated and operated at pressures between $5 \times 10^{-10}$ hPa to $1 \times 10^{-11}$ hPa. In this regime the pumping speed in the tube would be reduced by 50 % after approximately 1000 min at $1 \times 10^{-10}$ hPa and respectively after 10000 min at $1 \times 10^{-11}$ hPa. After this a reactivation of the pump would be advisable. This will renew the titanium layer and provide the initial pumping speed again.

Although a reduction of 50 % seems dramatic, it has to be stated that the effect of the mesh is still dominant. Thus a reduction of the pumping speed for nitrogen by 50 % from 596.88 $\mathrm{L\,s^{-1}}$ to 298.44 $\mathrm{L\,s^{-1}}$ results in a reduction by only 3.03 % (18.47 $\mathrm{L\,s^{-1}}$ to 17.91 $\mathrm{L\,s^{-1}}$) behind the mesh.

Assuming that the pump is reactivated after the pumping rated dropped below 50 % and that this time interval between the activations is constant amd assuming a constant activation time $t_{act}$ of 60 s, the lifetime of the filaments can be calculated from

$$t_{fil} = \frac{m_{ti}}{R_{evap}\, t_{act}} \tag{9.32}$$

VG Sienta states in the pump manual, that the maximum evaporation rate of titanium $R_{evap}$ is 10 $\mathrm{mg\,min^{-1}}$. With a given amount of usable titanium per filament $m_{ti}$ of 6 g the maximum number of activation cycles per filament is 600. The theoretical lifetime of a pump with three filaments is approximately 3.5 years if operated at $1 \times 10^{-10}$ hPa or approximately 34 years if operated at $1 \times 10^{-11}$ hPa.

### 9.4.3 Ion Getter Pump

In MAIUS-1 a noble diode pump VacIon 20 Plus is used as ion-getter pump, which should be characterized in the following.

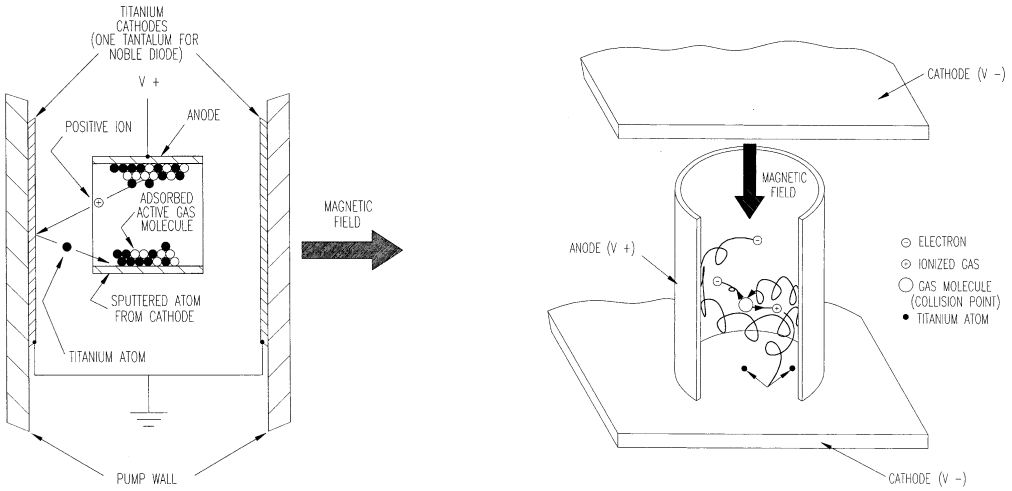


**(a)** Section view through a single cell pump showing the principle of ion-getter pumping. The positive ions are accelerated to the pump walls, where they will remove titanium or tantalum from the wall, which will bind the molecules at the pump surfaces.

**(b)** Section view through a single cell pump showing the principle of ionization of gas molecules in a circular pump anode.

**Figure 9.8:** Principle of ion-getter pumping. Figures from [Agi14]

As already stated before, the ion getter pump is the only device in MAIUS-1 capable of

pumping noble gases. Thus it is essential to be able to remove those gases from the system. Noble and active gases (as nitrogen, Oxygen, etc.) are removed by ionization of gas molecules.

As shown in figure 9.8b the pump consists of an anode in the center of the pump and two cathodes at the pump walls. Between anode an cathode a strong electrical potential between 3000 V and 7000 V is generated. The high voltage will produce a cloud of high-energy electrons inside the circular cells of the anode. Permanent magnets at the outside of the pump will form a magnetic field along the center axis of the anode elements as shown in figure 9.8b. This will cause the electrons to move on a oscillating cylindric path, which enlarges the probability of an electron striking an molecule of the residual gas.

If a molecule is hit, it loses one or more of its own electrons and is transformed into a positive ion. This ion is accelerated towards the cathode, where it will impact and removes material from the cathode. This material will then deposit on the surfaces of the pump and will capture the absorbed molecules as shown in figure 9.8a.

The pump cathodes consist of titanium, which is chemically reactive and will thus absorb the ionized gas molecules forming stable compounds. In noble diode pumps the second cathodes is made from tantalum which serves as a high-inertia crystal lattice structure burying especially particles that are not chemically reactive. Adding tantalum to the cathode material will increase pumping rates for noble gases [Wel93].

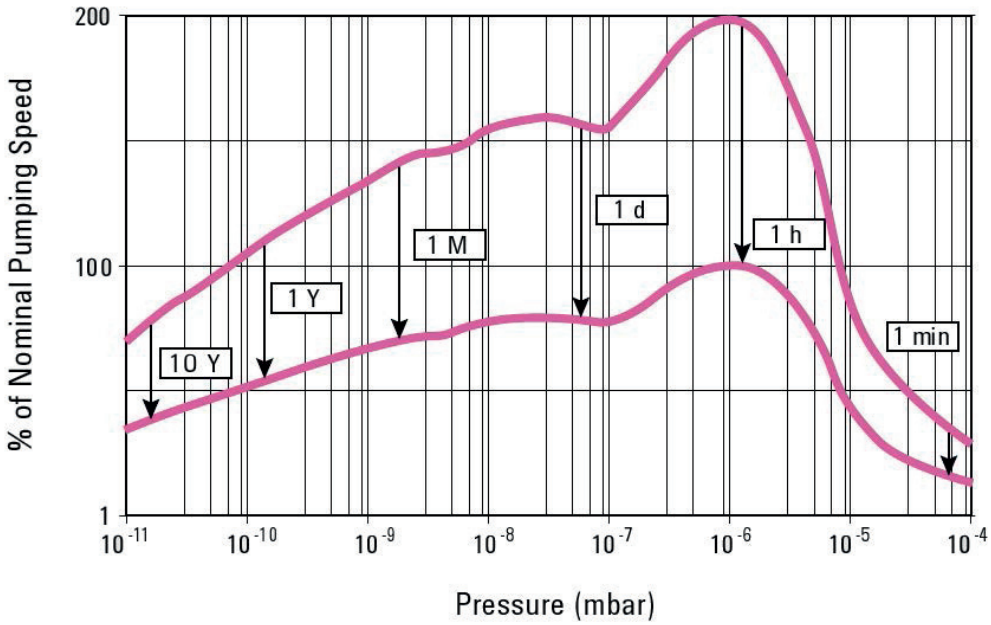


**Figure 9.9:** Time for saturation of Agilent VacIon Plus 20 in dependency of chamber pressure [Agi14]. Pressure is given by Agilent in mbar = hPa.

As more and more gas molecules are bound at the cathode, the probability of an ion hitting

a bound molecule and causing its re-emission increases. This increase of the re-emission rate will cause a decrease in the pumping rate. As shown in figure 9.9 a equilibrium condition between pumping and re-emission is reached after a certain time. This time is depending on the pressure in the chamber. The equilibrium pumping rate in a saturated state will be around 50 % of the nominal rate. It will take approximately one year for the pump to saturate in the MAIUS-1 vacuum system with a nominal operation pressure of $1 \times 10^{-10}$ hPa.

However if the pump is started at a pressure of $1 \times 10^{-9}$ hPa and operated at this level for one month, as during bake-out, it will already be saturated once the operation pressure is reached. Thus it is advisable to activate the ion-getter pump at the lowest pressure achievable with the turbo and titanium sublimation pump alone.

Even though this procedure will postpone the saturation, a lifetime of one year is not sufficient, since it will take longer to optimize the experiment parameter, which is necessary to achieve the scientific goals. A operation at a pressure of $1 \times 10^{-11}$ hPa is not realistic, because of the large outgassing rate of the Kapton used at the atom chip.

To regenerate the pump, the pump has to be baked between 150 °C and 220 °C for at least 24 h while connected to a roughening pump to remove the molecules from the vacuum system, which are released from the pump walls. Since the roughening pump can not be re-connected to the MAIUS-1 vacuum system, a pump regeneration is not feasible in MAIUS-1. For this reason the saturated pumping speed shall be used for the sizing of the pump and the design of the vacuum system.

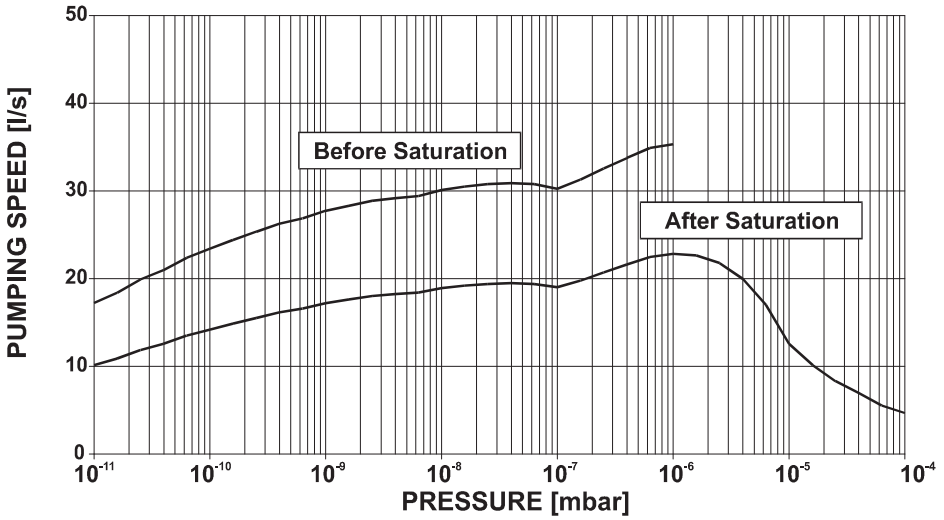


**Figure 9.10:** Pumping rates for Nitrogen with Agilent VacIon Plus 20 in dependency of chamber pressure [Agi11]. Pressure is given by Agilent in mbar = hPa.

As shown in figure 9.10 the pumping speed of the ion getter pump is depending on the pressure and on the saturation state of the pump cathodes. The pumping rate will increase

to higher pressures, because of the higher probability of molecules to be ionized. While saturated cathodes will decrease the pumping rate as explained above.

In MAIUS the pressure in the usual operation is expected to be around $2 \times 10^{-10}$ hPa, which results in a pumping rate for nitrogen of $25\,\mathrm{L\,s^{-1}}$ in the unsaturated state and $15\,\mathrm{L\,s^{-1}}$ in the saturated state as depicted in figure 9.10. If the pressure in the system rises as observed if external loads are present (refer section 9.5.2), the pumping rate assumptions have to be adapted accordingly.

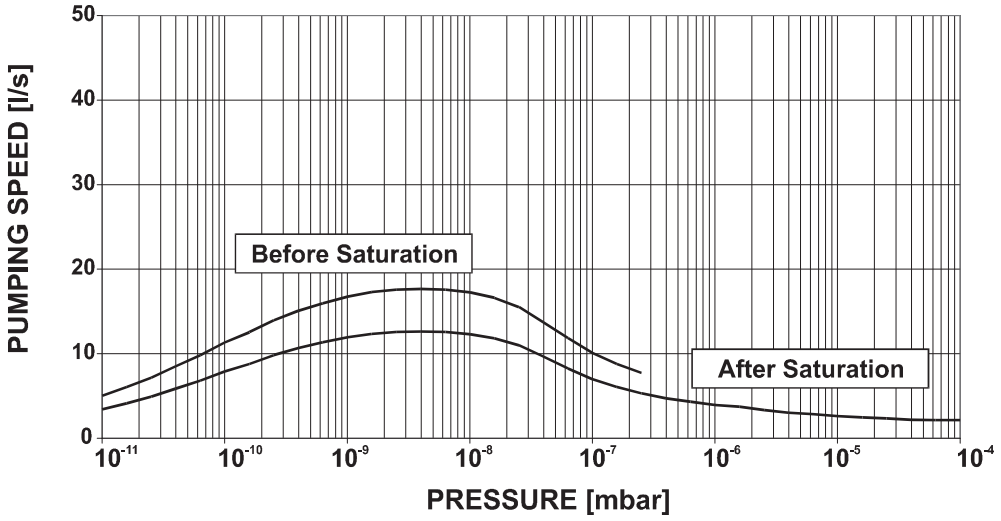


**Figure 9.11:** Pumping rates for Argon with Agilent VacIon Plus 20 in dependency of chamber pressure [Agi11]. Pressure is given by Agilent in mbar = hPa.

The pumping rates for noble gases as Argon are generally smaller than those for Nitrogen. As shown in figure 9.11 they subject to the same dependencies as the nitrogen pumping rates. At a pressure of $2 \times 10^{-10}$ hPa the pumping rate for Argon is $13\,\mathrm{L\,s^{-1}}$ in the unsaturated state and $9\,\mathrm{L\,s^{-1}}$ in the saturated state.

### 9.4.4 Local Distribution of the Effective Pumping Speed

Although a uniform pressure will establish in the entire vacuum system in isothermal conditions, the pumping speed will vary over the system. For this reason some regions might require a longer time to reach the equilibrium pressure. The effective pumping speed is depending on the conductance of the components betwenn the pump and e.g. the experiment chamber and is calculated as described in section 9.4.1.

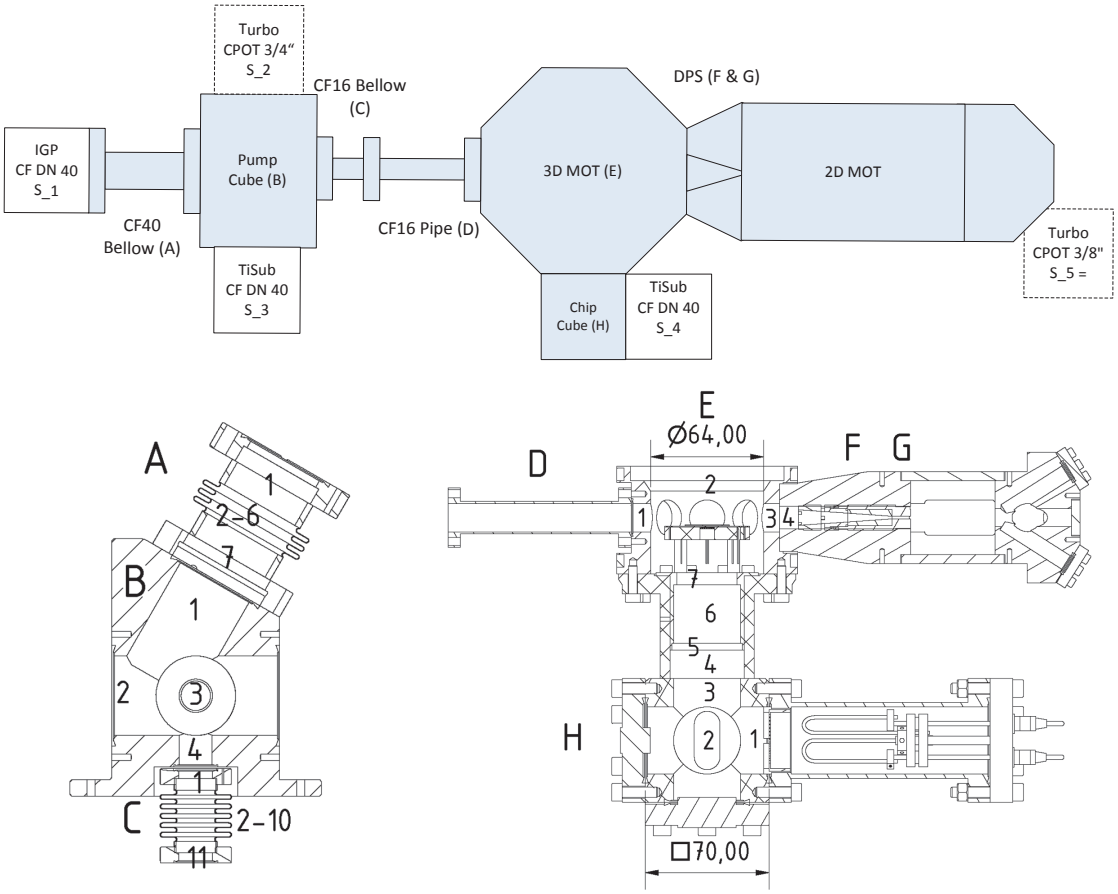


**Figure 9.12:** Schematic showing all components between pump inlets and MAIUS vacuum chamber. The section view at the bottom assigns letters to each component. The numbers reflect sections with different geometries. The relevant dimensions are given in table 9.9.

Figure 9.12 illustrates the line of components in the MAIUS-1 vacuum system and the pumps attached. The pumps have been characterized in the previous sections. Their pumping rates are summarized in table 9.8. A saturated ion getter pump and a titanium sublimation pump that degraded by 50 % has been assumed.

The components of the MAIUS-1 have been labeled with the letters A to H, while the different sections relavant for a calculation of the conductance have been marked with numbered indexes. The order of the indexes does not reflect the direction of the molecules passing the component.

| Pump | Index | Pumping Rate Nitrogen [$\mathrm{L\,s^{-1}}$] | Pumping Rate Argon [$\mathrm{L\,s^{-1}}$] |
|---|---|---|---|
| Turbo Cube | $S_2$ | 1.45 | 1.45 |
| Turbo 2D | $S_5$ | 0.29 | 0.29 |
| Titanium Sublimation Pumps | $S_3$ & $S_4$ | 17.91 | 0 |
| Ion getter Pump | $S_1$ | 15 | 9 |

**Table 9.8:** Pumping rates at the MAIUS-1 chamber of different pumps

For the calculation of a conical pipe as in the differential pumping stage (DPS) a solution for the transmission probability $P_{cone}$ is proposed in literature [Jou13] for transmission from the larger cross-section to the smaller ($1 \rightarrow 2$) and vice versa

$$\frac{1}{P_{cone,12}} = \frac{r_2^2}{r_1^2} + \frac{r_1 + r_2}{4\,r_1^2}\,l \tag{9.33}$$

$$\frac{1}{P_{cone,21}} = 1 + \frac{r_1 + r_2}{4\,r_2^2}\,l \tag{9.34}$$

This results in $P_{cone12} = 0.0082$ and $P_{cone21} = 0.2715$, however the product of the probability with the inlet cross section is identical

$$A_{cone2}\,P_{cone21} = A_{cone1}\,P_{cone12} \tag{9.35}$$

thus the transmission probability and the conductance is not depending on the direction the molecule passes the cone. It can be found from [Jou13]

$$C_{cone} = \frac{1}{4}\,\bar{c}\,A_{cone2}\,P_{cone21} \tag{9.36}$$

to be $0.055\,\mathrm{L\,s^{-1}}$ for the geometry given in table 9.9.

While the conductance of usual pipe components can be calculated with formulas given in the literature, more complex geometries need to be approximated by reasonable assumptions. As such the two bellows, the pump cube, the chip cube and the science chamber (3D MOT) will be approximated as a series of pipes with different diameters. The diameter and the associated length are listed in table 9.9.

At intersections of pipes as in the pump cube, the diameter was chosen to be the length of the pipe crossing. At the pump cube it affects section 3, where the width of the cube of 80 mm was chosen as diameter. Accordingly the diameter was set to the width of the chip cube (70 mm) at section 2 of this component. At the science chamber (3D MOT) the diameter was chosen to be the chamber diameter.

Although the results will not be accurate and will produce higher conductivities of the three

affected sections above, this will take into account the outlet and inlet effects at the crossing and the resulting reduce transmission probability for gas molecules at an intersection. Since this effect is dominant and scales with the change in cross section, this approach is a reasonable estimation.

| Component | Index | d [mm] | l [mm] | A [$mm^2$] | P [-] | C [$L\,s^{-1}$] |
|---|---|---|---|---|---|---|
| CF40 Bellow (A) | 1,7 | 40.5 | 24.5 | 1288.2 | 0.6319 | 38.80 |
| | 2,4,6 | 57 | 2.5 | 2551.8 | 0.9581 | |
| | 3,5 | 40.5 | 2.5 | 1288.2 | 0.9421 | |
| Pump Cube (B) | 1 | 38 | 50 ($S_1$) | 1134.1 | 0.4493 | 58.98 |
| | 2 | 38 | 21 ($S_3$) | 1134.1 | 0.6520 | 85.59 |
| | 3 | 80 | 38 | 5026.6 | 0.6846 | 398.28 |
| | 4 | 16 | 15 | 201.1 | 0.5297 | 12.33 |
| CF16 Bellow (C) | 1,11 | 16 | 11.25 | 201.1 | 0.5974 | 3.10 |
| | 2,4,6,8,10 | 37.7 | 2.5 | 1116.3 | 0.9381 | |
| | 3,5,7,9 | 16 | 2.5 | 201.1 | 0.8661 | |
| CF16 Pipe (D) | 1 | 16 | 103.5 | 201.1 | 0.1558 | 3.63 |
| 3D MOT (E) | 1 | 16 | 11.3 | 201.1 | 0.5964 | 13.88 |
| | 2 | 64 | 64 | 3217.0 | 0.5143 | 191.5 |
| | 3 | 16 | 9 | 201.1 | 0.6481 | 15.08 |
| | 4 | 12.92 | 10.5 | 131.1 | 0.5636 | 8.55 |
| DPS Cone (F) | 1 | 8.8 | 53 | 60.8 | 0.2715($P_{12}$) | 0.055 |
| | 2 | 1.5 | | 1.77 | 0.0082($P_{21}$) | |
| DPS Straight (G) | 1 | 1.5 | 9.8 | 1.77 | 0.1546 | 0.03 |
| Chip Cube (H) | 1 | 38 | 16 | 1134.1 | 0.7093 | 93.12 |
| | 2 | 70 | 70 | 3848.4 | 0.5143 | 229.1 |
| | 3 | 38 | 16 | 11341 | 0.7093 | 93.12 |
| | 4 | 42 | 16 | 1385.4 | 0.7291 | 116.92 |
| | 5 | 40 | 4 | 1256.6 | 0.9097 | 132.31 |
| | 6 | 38 | 33 | 1134.1 | 0.5479 | 71.92 |
| | 7 | 34 | 7 | 907.9 | 0.8312 | 87.36 |

**Table 9.9:** Geometry and conductivity of the different components in the MAIUS-1 vacuum system

For more accurate computation of the conductivity a Monte-Carlo-Simulation would be a suitable but time-consuming approach. However the estimations made herein still allow to identify the components limiting the overall conductivity.

In addition to the results presented in table 9.9 the conductance for passing the chamber cube from after the IGP bellow (1) to the CF16 flange (4) has been calculated from

equation 9.25 as $C_{B,134} = 7.14\,\mathrm{L\,s^{-1}}$. Accordingly the conductance for passing the science chamber from the CF16 flange (1) to the DPS (4) is $C_{E,14} = 4.31\,\mathrm{L\,s^{-1}}$ and the conductance for passing the chip cube from the titanium sublimation pump (1) to the chip (7) $C_{H,17} = 27.89$.

Comparing those numbers to the conductances in table 9.9, shows that the CF16 bellow and the CF16 pipe are limiting the overall conductivity between the pumps of the pumping system and the science chamber. An increase of the diameter of these components to CF25 or CF40 would improve the conductance and thus significantly, especially because all interface ports would also increase in diameter.

However such an design change would require to enlarge the feed through in the magnetic shielding, which would reduce the shielding factor as mentioned in section 7.3.1. For this reason a smaller pipe diameter was chosen in MAIUS-1. As shown in table 9.10

| Pumping Rates | Nominal [$\mathrm{L\,s^{-1}}$] | Pump Cube [$\mathrm{L\,s^{-1}}$] | 3D MOT [$\mathrm{L\,s^{-1}}$] | 2D MOT [$\mathrm{L\,s^{-1}}$] |
|---|---|---|---|---|
| $S_1$ | 15 | 11.67 | 1.43 | 0.02 |
| $S_2$ | 1.45 | 1.45 | 0.05 | 0.02 |
| $S_3$ | 17.91 | 17.91 | 1.5 | 0.02 |
| $S_4$ | 17.91 | 1.45 | 11.9 | 0.02 |
| $S_5$ | 0.29 | - | 0.02 | 0.29 |
| Sum Flight | | 29.58 | 13.44 | 0.03 |
| Sum Prep. | | 1.45 | 0.05 | 0.29 |

**Table 9.10:** Effective pumping rates of MAIUS-1 pumps at different locations in the vacuum system and overall pumping rate at these locations in flight configuration ($S_1, S_3 \& S_4$ activated) and in preparation configuration with only the roughening pump activated ($S_2 \& S_5$)

the conductance is also limiting the effective pumping rates, which are calculated at the three reference spots for each individual pump in a stand-alone mode. Especially the high pumping rates at the pump cube, have only a small effect down at the science chamber, due to the small conductance.

Luckily the second titanium sublimation pump will compensate for that, with a pumping rate of $11.9\,\mathrm{L\,s^{-1}}$ at the back of the chip. However it has to be stated, that the actual pumping speed might be lower, because the wires connecting the atom chip and the feedthroughs are not considered in these calculations and will reduce the conductance of this path.

At the bottom of table 9.10 the sum of the pumping rates of the system in flight and in preparation configuration are given. In flight configuration the roughening pump has been disconnected and only the internal pumps are operating, while in preparation configuration only the roughening pump is activated.

Both sums are already taking into account limiting conductances, thus the sum of the pumping speed of e.g. the titanium sublimation pump ($S_3$) and the ion getter pump $S_1$ at the 3D MOT is not $2.93\,\mathrm{L\,s^{-1}}$ but $1.54\,\mathrm{L\,s^{-1}}$, since the bad conductance of the CF16 pipe and bellow is limiting the effective pumping speed.

While in flight configuration the overall pumping rates are satisfactorily high at the pump cube and the science chamber, a very small pumping rate is calculated for the science chamber in preparation configuration. Thus it is advisable to activate the lower titanium sublimation pump even during vacuum preparation to speed up the preparation process.

Moreover the numbers prove that pumping through the differential pumping stage (DPS) is not feasible, as the DPS is designed to have a bad conductance to separate both chambers (compare section 7.3.3). As already explained above the conductance of the pump is equivalent in both directions, which is also reflected by the numbers. This results in an ultra low effective pumping speed of $0.05\,\mathrm{L\,s^{-1}}$ in flight configuration.

## 9.5 UHV Testbed Setup

As stated in section 9.3 the leakage rate of seals under loads needs to be investigated as part of this thesis. For this purpose a test stand was developed, which allows to apply a static and vibrational force on a test specimen and simultaneously measure not only the pressure in the test setup, but also the composition of the residual gas. Moreover the testbed is capable of performing outgassing rate and pumping rate measurements.

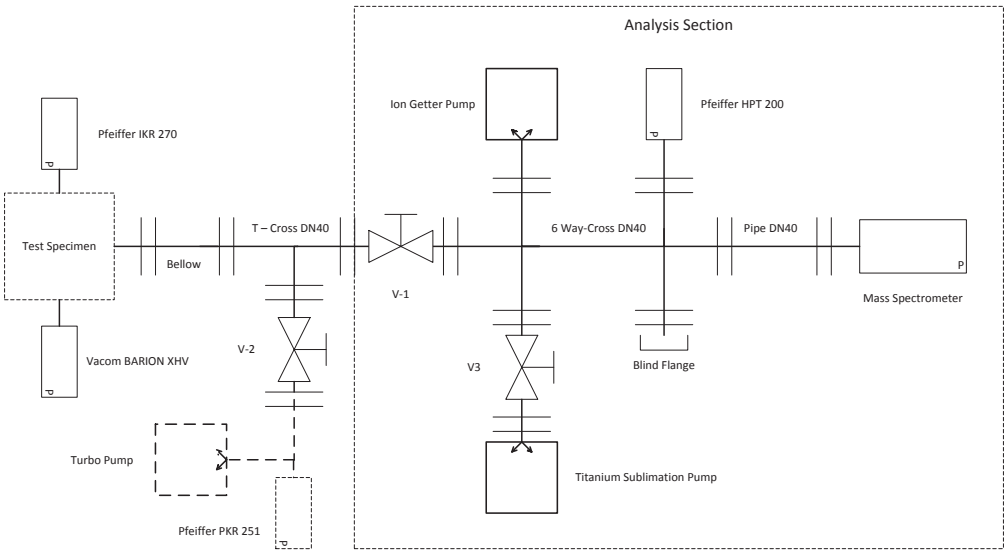


**Figure 9.13:** Schematic of the UHV testbed

Figure 9.13 shows a shematic of the testbed with all components used. For reaching ultra high vacuum pressures of $5 \times 10^{-10}$ hPa and below the system is equipped with three

pumps, which are also used in the MAIUS setup.

A ion-getter pump Agilent VacIon 20 Plus and a titanium sublimation pump VG Sienta ST-22 as specified in section 9.4.3 and 9.4.2 are used in the analysis unit of the testbed for maintaining the pressure. These pumps are currently mounted to a cross between the test specimen and the mass spectrometer, which is not ideal because the pumps reduce the probability for molecules to be detected by the mass spectrometer. Thus the measured quantity of a gas detected at the mass spectrometer might be lower than its actual value. However this will not effect the general detection of gases or the leak detection. For future measurements the assembly should be rearranged accordingly to improve the performance.

In addition to those two pumps a turbo-molecular pumping station Pfeiffer HiCube 80 Classic as described in section 9.4.1 is used as a roughening pump. It is connected to a T-cross equipped with two valves. Once the vacuum in the testbed reached the desired level, valve *V-1* is closed and the test specimen can be pumped and baked separately without breaking the vacuum in the analysis section, which reduces the vacuum preparation time and test cycle time significantly.

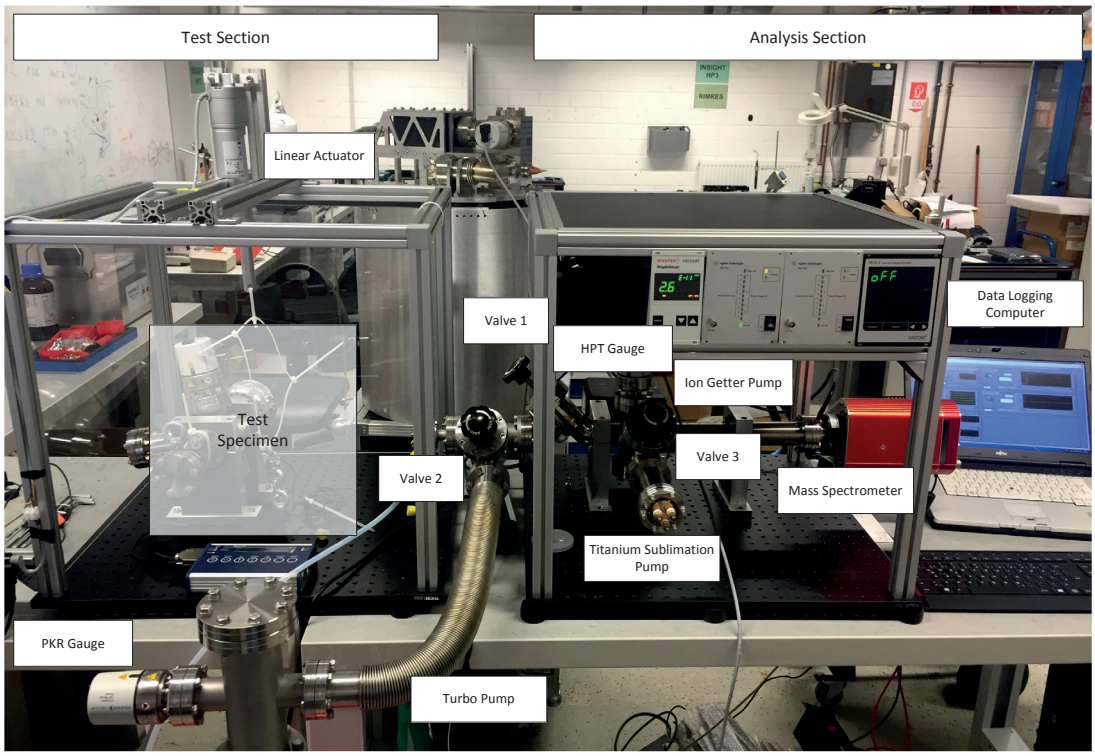


**Figure 9.14:** UHV testbed for static and vibrational load testing of the sealing techniques used in MAIUS-1. Leak tests and analysis of the residual gas are possible during testing of the seals.

Once the vacuum in the test specimen reached the desired pressure level, valve *V-2* is closed and the turbo-molecular pumping station is shut down. Subsequently the connection to the analysis section is re-established by opening valve *V-1* again.

The centerpiece of the analysis section is an Pfeiffer Prisma QMG 220 M2 mass spectrometer capable of detecting masses 1 - 200. The device is equipped with an open ion source and thus designed for residual gas analyses in high and ultra-high vacuum. The analysis software QUADERA allows to do scans of the residual gas in a specified mass range and to monitor the ion current or partial pressure of specific masses over time. Moreover it is possible to monitor the ion current of mass 4 to perform helium leak detection. The device is connected to the data logging computer shown via ethernet. The software allows exportation of the raw data in an ASCII file format for post processing.

The pressure in the setup is monitored with up to four gauges. In the analysis section the pressure is monitored by a Pfeiffer HPT-200 gauge. This combined digital Pirani and Bayard-Alpert gauge is connected to the mass spectrometer via an RS-485 interface. The measurement range of the sensor is $5 \times 10^{-10}$ hPa to 1000 hPa. The pressure reading is logged directly with the ion currents of the different masses in the previously mentioned ASCII file.

A second full range process gauge of the type Pfeiffer PKR 251 is placed closed to the roughening pump. This gauge is a combined Pirani and cold cathode gauge with a measurement range from $1 \times 10^{-9}$ hPa to 1000 hPa. In addition to these two process gauges up to two gauges can be mounted directly to the test specimen. These are a Pfeiffer IKR 270 cold cathode gauge and a Vacom Barion extended Bayard-Alpert gauge. The latter is more accurate and capable of measuring ultra low pressures down to $5 \times 10^{-12}$ hPa, while the cold cathode gauge is used for comparative measurements.

The test section of the testbed is equipped with a linear actuator to apply static loads of up to 1200 N on a test specimen. The applied force is measured with a membrane load cell KM26z made by ME Systeme. There are two sensor available for tests in this setup with two measurement ranges with an accuracy of 1 % from the measured value and a maximum deviation of 0.1 % of the maximum force. One sensor is capable of measuring compressive and traction forces from 1 kN to 5 kN and the other from 1 N to 500 N, where the latter is more accurate.

The analysis section was also designed to be connected to a test specimen mounted to a shaker as described in section 8. For this application it is possible to measure the vibrational loads with an sensor provided by the ZARM facility. This sensor will provide a voltage proportional to the loads, which can be logged by the testbed data acquisition to exactly trigger the start and the end of a test run. The exact level of the applied vibrations is obtained and logged by the shaker test facility.

Pressure, temperature and force readings as well as the trigger signal for vibrational loads are logged by a Labview program running on the testbed computer. This data can be synchronized with the data logged by the QUADERA software via a system time stamp written to both files. This will result in a full dataset providing not only the total pressure, external forces and temperature of the test specimen but also the composition of the residual gas.

For leak tests under external loads its necessary to know the signal response time of the setup during a leak test to ensure that the load is applied long enough to detect a leak and determine its size. The signal response time $\tau_{63\%}$ is defined as the time which elapses until a volume is filled with the tracer gas to 63 % of its equilibrium level [Pfe13].

For a given volume $V$ of the test setup including the test specimen and $S_{eff}$ the effective pumping speed at the position of the leak this can be calculated from

$$\tau_{63\%} = \frac{V}{S_{eff}} \tag{9.37}$$

The effective pumping speed can be estimated from [Pfe13]

$$\frac{1}{S_{eff}} = \frac{1}{C_{tot}} + \frac{1}{S} \tag{9.38}$$

with $S$ being the nominal pumping speed of the setup and $C_{tot}$ the total conductance for vacuum components in series.

$$\frac{1}{C_{tot}} = \sum_{i=1}^{n} \frac{1}{C_i} \tag{9.39}$$

giving a good estimation for the total conductance of the components between the mass spectrometer and the test specimen. Table 9.11 summarizes the geometry, transmission probability $P_p$ and conductance $C_t$ of these components. The last two parameters are calculated using equation 9.22 to 9.24 as specified in section 9.4.

| Component | l [mm] | d [mm] | V [L] | $P_p$ [-] | $C_t$ [$\mathrm{L\,s^{-1}}$] |
|---|---|---|---|---|---|
| Bellow | 175 | 38 | 0.1985 | 0.2020 | 26.51 |
| T-Cross | 126 | 38 | 0.2143 | 0.2556 | 33.55 |
| Pipe | 126 | 38 | 0.1429 | 0.2556 | 33.55 |
| CF40 6-way cross | 126 | 38 | 0.3425 | 0.2556 | 33.55 |
| Valve | 133 | 38 | 0.1508 | 0.2462 | 50 |
| Ion Getter Pump | - | 38 | 0.9 | - | - |
| Sum | | | 1.9491 | | 6.80 |

**Table 9.11:** Geometry and conductivity of the different components in the analysis section of the testbed

From the given parameters and assuming a scenario, where the pumping speed of the devices in the analysis section is $20\,\mathrm{L\,s^{-1}}$, the effective pumping speed after the bellow is calculated to be $5.07\,\mathrm{L\,s^{-1}}$. The signal response time $\tau_{63\%}$ for a leak at the bellow would be 0.38 s. Thus a immediate detection of a leak is possible. However it has to be noted that the actual signal response time is also depending on the volume of the test specimen.

### 9.5.1 Verification with Calibration Leak

To verify the functionality of the testbed and to determine the actual response time a test has been performed with a gas line calibration leak fabricated by Pfeiffer vacuum (Part Number: 803922) with a leakage rate of $5.0 \times 10^{-9}\,\mathrm{hPa\,L\,s^{-1}}$.

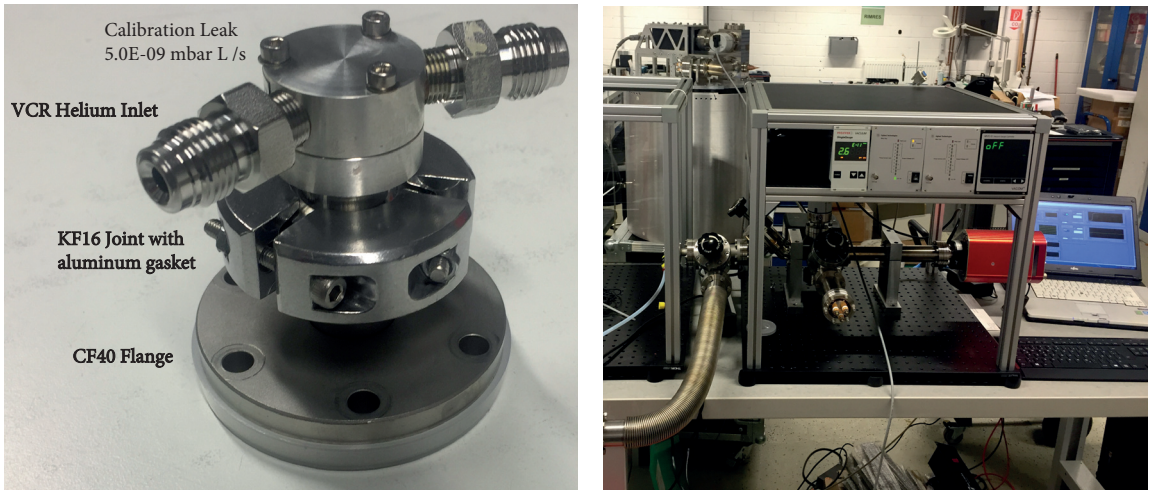


**(a)** Pfeiffer test leak with customized CF flange connection

**(b)** Test leak (hidden behind aluminum profile) attached to testbed with hose connected to helium gas bottle

**Figure 9.15:** Proof-of-concept setup with modified calibration leak

The leak is equipped with a ISO-KF flange and not available as CF component. Unfortunately rubber seals are not suitable for leak detection measurements, because of their permeability for gases, which will give false signals. For this reason a sharp edged aluminum gasket and a solid clamping ring is used to seal the connection between the calibration leak and a ISO-KF16 to CF40 adapter. This assembly as shown in figure 9.15a can now easily be mounted to any CF40 flange with a standard copper gasket.

The calibration leak is also equipped with two 1/4" VCR connectors, where one is used to connect the leak to a helium gas bottle and the other one is used as exhaust as shown in figure 9.15b. The flow of helium is controlled to be $10\,\mathrm{L\,min^{-1}}$ by a flow meter at the gas bottle. For this test run the valve V-3 to the titanium sublimation pump was closed and the ion getter pump was deactivated. Thus no pumping occurred during the test run. This should proof the concept in a worst case scenario.

The flow of helium was started at t = 624 s resulting in an immediate rise of the ion current for helium as shown in figure9.16. The background ion current has been constant at $1.1 \times 10^{-11}$ A prior to this rise. The current saturated at an equilibrium of $9.7 \times 10^{-9}$ A after 200 s at t = 800 s. It took 51 s to reach 63 % of the helium equilibrium pressure.
These results demonstrate, that a leak with a leakage rate as small as $5.0 \times 10^{-9}\,\mathrm{hPa\,L\,s^{-1}}$ is reliably detected by the testbed setup. Moreover it was demonstrated, that the ion current will rise immediately indicating the leak. The signal response time $\tau_{63\%}$ without active

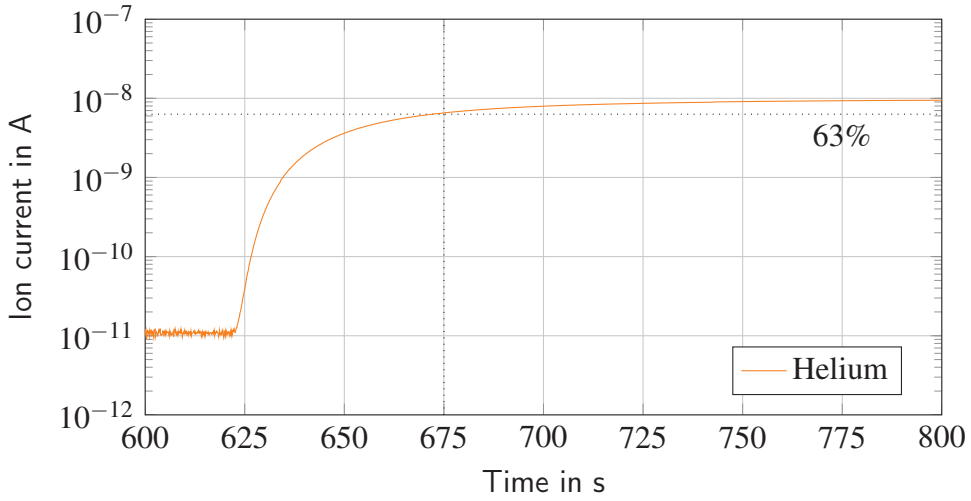


**Figure 9.16:** Ion current reading for mass 4 (Helium) during test measurement of a calibration leak with a leakage rate of $5.0 \times 10^{-9}\,\mathrm{hPa\,L\,s^{-1}}$. The horizontal dotted line indicates the 63 % of the equilibrium ion current / concentration of helium.

pumps was measured to be 51 s. Since the pumping rate in the usual test setup is unknown, the minimum duration for applied loads is set to 60 s to ensure a proper detection of leaks regardless of the effective pumping speed.

### 9.5.2 Static Load Testing of UHV Sealings

As part of this thesis static load tests have been performed for both sealing techniques used in MAIUS-1 to identify the forces necessary to cause a leak at one of the seals. These information help to find suitable designs for UHV vacuum system operated in harsh environments. The results and the test setup is described in the following.

### 9.5.3 Static Load Test of Conflat Seals

For testing of the Conflat sealing, a DN40 pipe was equipped with a clamp to connect it to the linear actuator. The clamp was positioned 95 mm away from the seal to be tested as shown in figure 9.17b.
The flange joint has been prepared using a regular OFHC copper gasket provided by Pfeiffer Vacuum (Part Number: 490DFL040-S10). The bolts of the flange connection have been fastened with 10 N m using Pfeiffer Duo-nuts (Part Number:420BMD040), which connect two neighboring bolts.

As shown in figure 9.17a two hoses have been positioned close to the tested flange to ensure a constant flow of helium. The flow has been set to $10\,\mathrm{L\,min^{-1}}$ using a flowmeter at the gas bottle. To minimize disturbances by the air flow of the air condition and to guarantee a high concentration of helium around the flange the test section of the testbed was equipped with windshields made of transparent plastic walls.

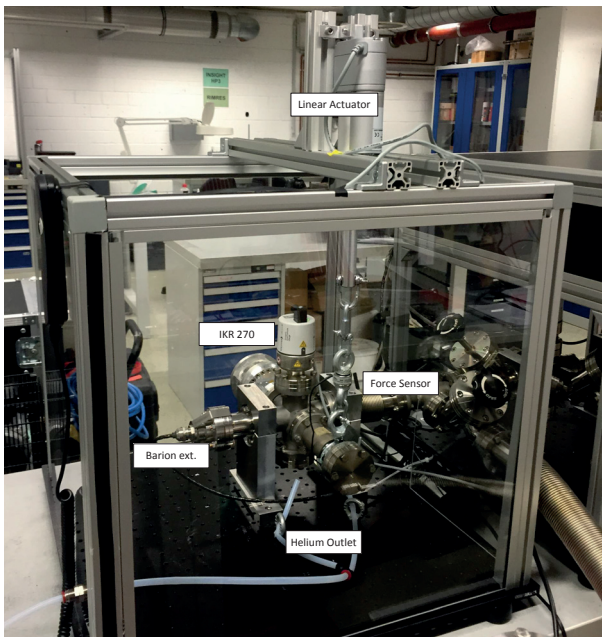


**(a)** Test specimen setup for static load tests of the CF seals

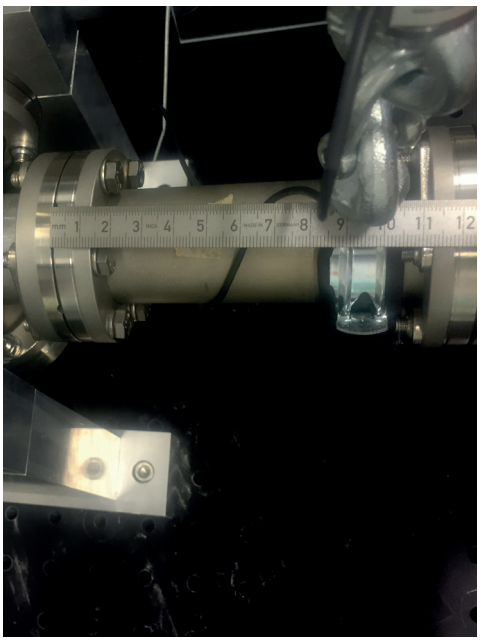

**(b)** Detailed view on the standard CF40 tube tested with the clamp for load application shown on the right. The lever from the point of load application to the seal is 95 mm.

**Figure 9.17:** Test setup for static load test of Conflat seals

The applied load has been monitored with the 5 kN force sensor, while the pressure was monitored using the Pfeiffer IKR 270 cold cathode gauge. The initial absolute pressure was set to $1.16 \times 10^{-8}$ hPa. The valve to the turbo pump was closed and the ion getter pump was deactivated during the measurement.
The static load was applied by a Transmotec DC linear actuator DLA DLA-12-40-A-100-POT with a gear ratio of 40:1 and a maximum load force of 1200 N, which is mounted to the frame carrying the windshields as shown in figure 9.17a. The load was set manually to the desired value according to the force sensor measurement, because an active control loop is not implemented in the test setup. This procedure makes it difficult to set the applied load exactly to the desired value as the peaks an variations in the load level measurements in figure 9.18 indicates.

During the measurement the load was varied between 0 N and 1100 N. The load was raised in steps of 100 N with an accuracy limited by the load adjustment procedure. Each raise in the load was followed by a measurement sequence of at least 90 s. During this time the load was not changed.

Figure 9.18 shows the ion current measurement for mass 4 (Helium) recorded with the mass spectrometer. The background signal noise ranges between $5.2 \times 10^{-13}$ A and $5.6 \times 10^{-13}$ A. A first rise in the ion current could be observed after the raise from 800 N to 900 N. After

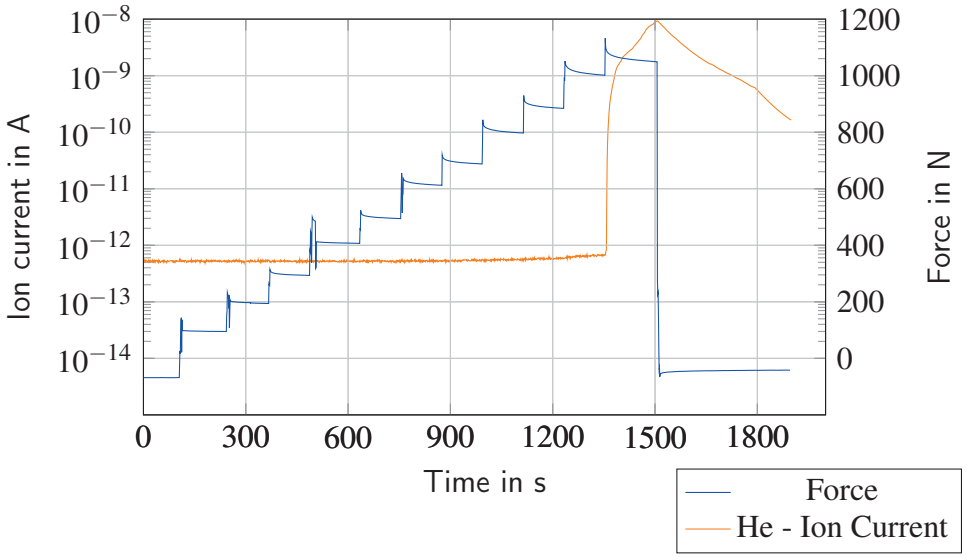


**Figure 9.18:** Ion current reading for mass 4 (Helium) during static load test of a CF40 pipe. The force has been varied between 0 N and 1050 N and applied for at least 90 s

the load was raise at 1115 s the ion current slowly raised to values around $5.8 \times 10^{-13}$ A at 1234 s. Unfortunately the signal is still very noisy, thus it is hard to tell . As shown in figure 9.19 the absolute pressure only rose by $1 \times 10^{-10}$ hPa in this time. Thus it is assumed, that the leak (if present) might be to small to be detected.

During the next rise, the load peaked at 1050 N, which caused a rise in absolute pressure from $1.18 \times 10^{-8}$ hPa to $1.28 \times 10^{-8}$ hPa and ion current rise from $5.8 \times 10^{-13}$ A to $6.2 \times 10^{-13}$ A. After the load was stabilized at 1010 N the pressure also stabilized at $1.20 \times 10^{-8}$ hPa. While still a slow rise in ion current could be observed. This is indicating that there has been a detectable leak at 1050 N, while the leak at 1010 N is barely detectable at this pressure level.
Setting the load to 1100 N resulted in a strong rise in ion current and pressure as shown in figures 9.18 and 9.19. At this load level some plastic deformation occurred in the clamp transferring the load to the pipe. This deformation resulted in a decrease of the load to 1060 N. The pressure raised from $1.20 \times 10^{-8}$ hPa to $6.02 \times 10^{-8}$ hPa rapidly. At 1500 s the valve was closed and the pressured dropped to its initial value after 450 s. This proofs that the leak was only temporal and that it closed completely after the load disappeared.

It is difficult to determine the actual leakage rate from the data obtained, since the effective pumping rate is not known. The equilibrium pressure without loads is defined as

$$p_{end,1} = \frac{Q_{L,1}}{S_{eff}} + \frac{Q_{in}}{S_{eff}} \tag{9.40}$$

where $Q_{L,1}$ is the leakage rate of the tested seal without loads applied and $Q_{in}$ should represent the sum of the remaining gas input by leaking of the other seals or outgassing.

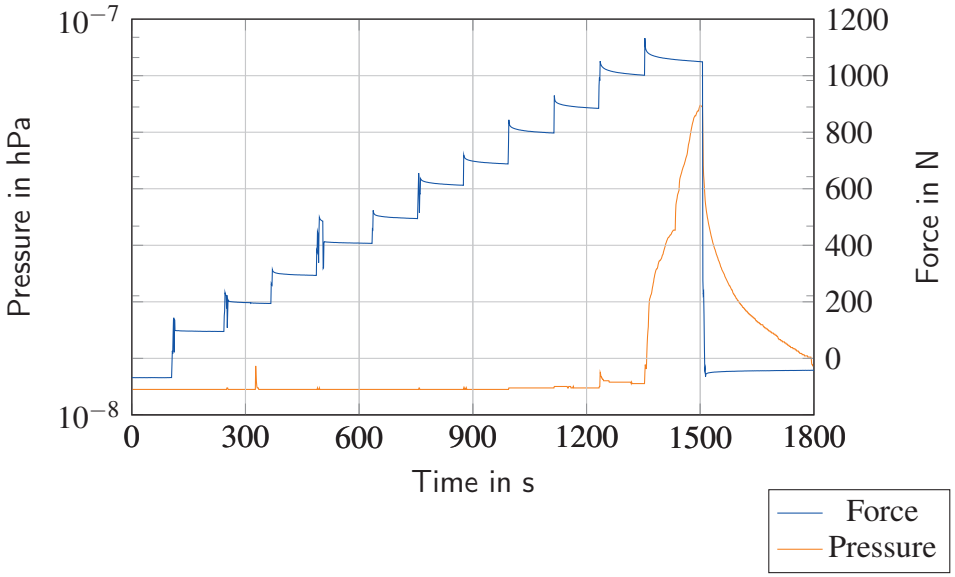


**Figure 9.19:** Pressure reading during static load test of a CF40 pipe. The force has been varied between 0 N and 1050 N and applied for at least 90 s

The same equation is valid if loads are applied.

$$p_{end,2} = \frac{Q_{L,2}}{S_{eff}} + \frac{Q_{in}}{S_{eff}} \tag{9.41}$$

While the summarized gas flow $Q_{in}$ is constant, the leakage rate of the tested seal will change to $Q_{L,2}$, where $Q_{L,2} >> Q_{L,1}$. Neglecting the initial leakage rate of the seal, which should be below $1 \times 10^{-11}$ hPa L s$^{-1}$ combination of equation 9.41 and 9.40 will yield:

$$Q_{L,2} = \left(p_{end,2} - p_{end,1}\right) S_{eff} \tag{9.42}$$

For the rise in equilibrium pressure of $2 \times 10^{-10}$ hPa at a load of 1000 N, this would result in an leakage rate of $1 \times 10^{-9}$ hPa L s$^{-1}$ assuming an effective pumping speed of roughly 5 L s$^{-1}$ as calculated in section 9.5.1. For the pressure rise at 1060 N the leakage rate can not be determined, because the load was reduced before the equilibrium pressure was reached. Thus it can only be stated that it has to be higher than $2.41 \times 10^{-7}$ hPa L s$^{-1}$ assuming the same pumping rate.

### 9.5.4 Static Load Test of Indium Seals

The indium seals have been tested using a similar setup. As shown in figure 9.20a the linear actuator has been moved to allow mounting it to the MAIUS breadboard chamber opposite to the CF pipe tested before. In MAIUS the indium seals have mainly been used to seal the viewports. For this reason the loads should not been applied as a momentum, but as a direct pulling force on the seal as it will also occur during flight. The test should be performed perpendicular to the glass surface to allow a exact evaluation of the force applied. Applying sheer forces is more difficult and might be investigated in the future using a different force sensor.

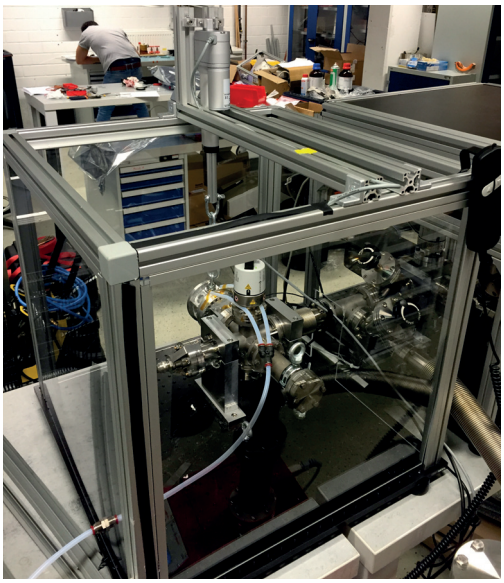

**(a)** Test specimen setup for static load tests of the indium seals

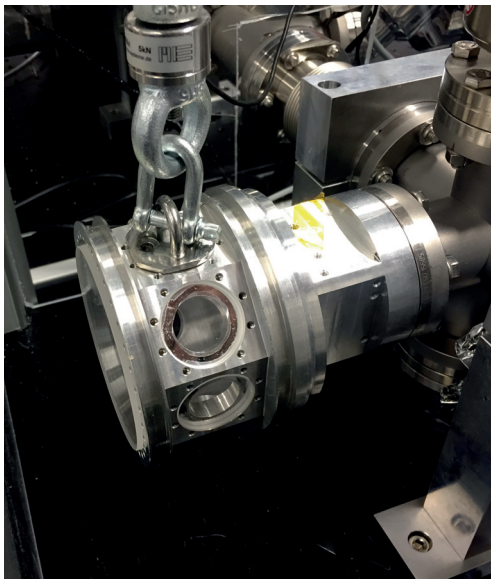

**(b)** Detailed view on the indium seal test setup. Showing the MAIUS breadboard chamber, with the force sensor mounted to the attachment ring glued to one of the 30 mm view ports.

**Figure 9.20:** Test setup for static load test of indium seals

To perform this test the load has to be applied perpendicular to the glass surface. To allow this a attachment eye equipped with a mounting plate was glued to one of the small windows as shown in figure 9.20b. To allow application of loads as high as in the Conflat seal tests, the glue Loctite 319 in combination with an activator 7649 was used. This combination was especially developed for gluing glass to metal and achieves a strength of up to $10\,\mathrm{N\,mm^{-2}}$. The contact area was limited to 25 mm in diameter to ensure that no glue will get in contact with the chamber. This still allows to apply a load of approximately 4900 N, which is sufficient for this application.
As in the previous test, the load has been raised in steps of 100 N. Again it was difficult to set the load to the right level. Therefore the load level deviates from the desired value in some steps as plotted in figure 9.21 and 9.22.

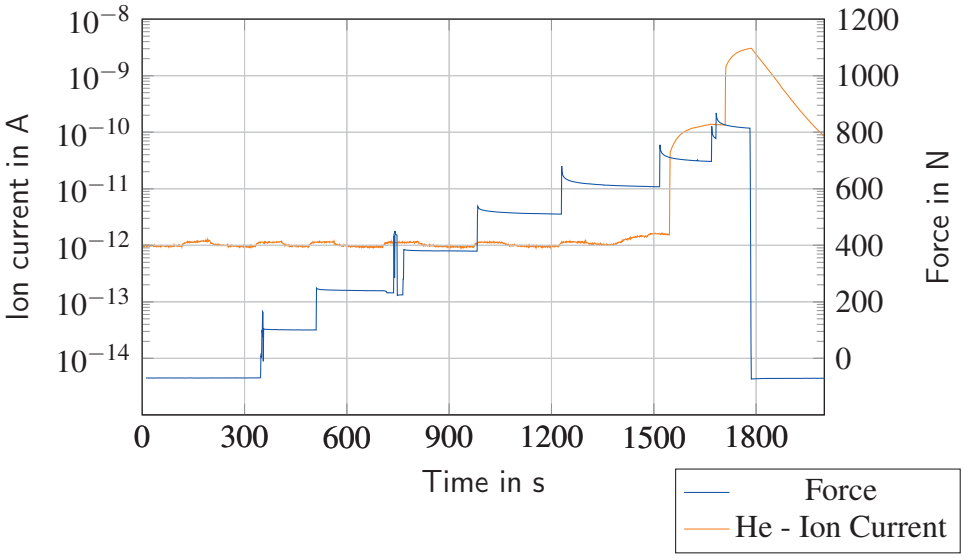


**Figure 9.21:** Ion current reading for mass 4 (Helium) during static load test of a indium sealed view port. The force has been varied between 0 N and 800 N and has been applied for at least 120 s

Although Indium seals should withstand sheer loads of up to 700 N [Kup10], it is not known how and under which load the indium seals prepared for MAIUS will fail. For this reason the valve V-1 connecting the analysis and the test section was closed before each new load was applied. This was done to protect the mass spectrometer, which could get damaged if operated at pressures above $1 \times 10^{-4}$ hPa. The valve was re-opened after 30 s allowing to perform the helium partial pressure measurement to detect possible leaks. In total a certain load level was held for at least 120 s

Closing the valve caused a pressure rise in the analysis section from initially $1.9 \times 10^{-8}$ hPa to values around $2.25 \times 10^{-8}$ hPa after 110 s. This rise is cause by the separation from the titanium sublimation pump. Moreover a peak was observed when the re-opening the valve as shown in figure 9.22. Moreover some small variations in the ion current can be observed in figure 9.21 when the valve is opened and closed, even if no force is present as done between 0 s and 280 s. Thus these signals do not indicate a leak.

The first leak was detected at 600 N, where the ion current rises considerably to values around $2 \times 10^{-12}$ A after the valve was opened. The pressure reading is not that definite, because of the pressure fluctuations caused by the opening and closing of the valve. However the pressure level after closing and even after re-opening the valve was slightly above the level of previous tests.
Raising the applied load to 700 N resulted in a strong rise in the ion current to $2 \times 10^{-10}$ A. The impact on the pressure was also stronger. The equilibrium pressure after re-opening the valve measured $2.3 \times 10^{-8}$ hPa.

A load of 800 N increased the leak size once more. This was indicated by a drastic rise of the pressure to $1 \times 10^{-6}$ hPa, while the valve was closed. After re-opening the valve

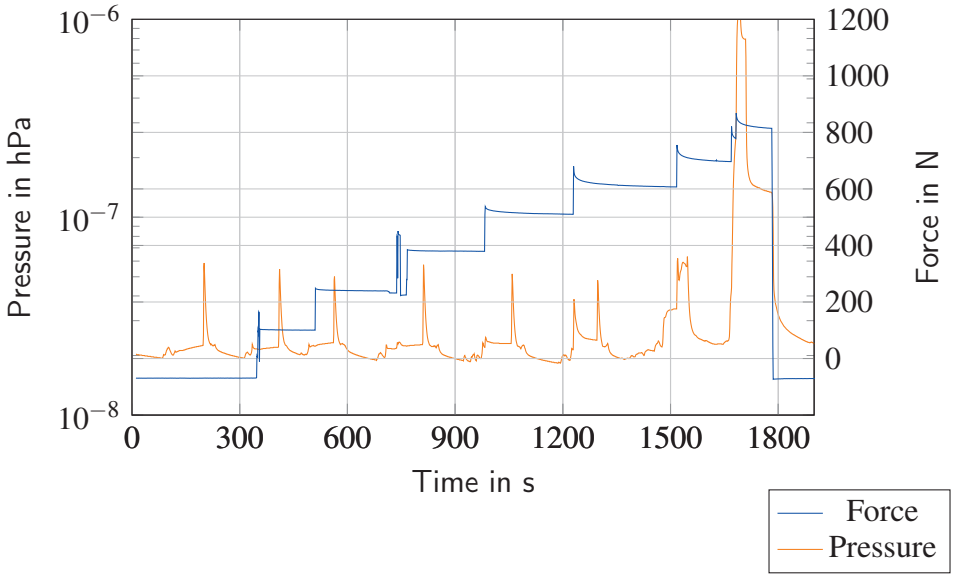


**Figure 9.22:** Pressure reading during static load test of a indium sealed view port. The force has been varied between 0 N and 800 N and has been applied for at least 120 s

the pressure dropped to $2 \times 10^{-7}$ hPa quickly. Unfortunately the pressure was still droping when the load was removed. Thus the equilibrium pressure is expected to be below the last recorded value of $1.4 \times 10^{-7}$ hPa. Removing the load caused a fast recovery of the pressure below $3 \times 10^{-8}$ hPa. A full recovery to the initial pressure of $1.9 \times 10^{-8}$ hPa was achieved after 303 s. This proves that the leak in the indium seal was also closed completely after the load was removed.

The leakage rates calculated from the pressure readings are $2 \times 10^{-8}\,\mathrm{hPa\,L\,s^{-1}}$ at 700 N and $6.1 \times 10^{-7}\,\mathrm{hPa\,L\,s^{-1}}$ at 800 N. However the ion current only rose to a maximum of $3 \times 10^{-9}$ A, which is below the current of the leak detected at the CF seal under a load of 1050 N, which should indicate a smaller leak, while the pressure development indicates the opposite. This may be caused by the fact, that the equilibrium pressure did not fully develop during the CF test or the opening and closing of the valve might falsify the pressure measurement in the indium test. In general the absolute leakage rates should be handled with care, since the ion current saturated at a value of $1 \times 10^{-8}$ A when the calibration leak with a leakage rate of $3 \times 10^{-9}\,\mathrm{hPa\,L\,s^{-1}}$ was tested. A calculated higher leakage rate e.g. during the indium tests at a smaller ion current indicates that the assumed effective pumping speed is too high or the pump is falsifying the measurement, because it is located in front of the mass spectrometer.

The important outcome of the measurements is, that leaks have been detected at CF seals under loads of 900 N applied as a side load with a lever of 95 mm resulting in a bending momentum of 85.5 N m and at indium seals under loads of 600 N pulling on a view port. Although the leaks are only temporary and close completely once the load is removed, these load levels should be avoided in the construction of future UHV systems.

## 9.6 Vibrational & Shock Testing of the MAIUS Pumping System

Aside from static load test, 17 vibrational tests and one shock test have been performed to test multiple vacuum components in different setups. These tests resulted in the vacuum system design presented in section 7.3. In the following the test results for the final pumping system setup shall be presented and the influence of load level, test duration and vacuum pressure level shall be discussed discussed.

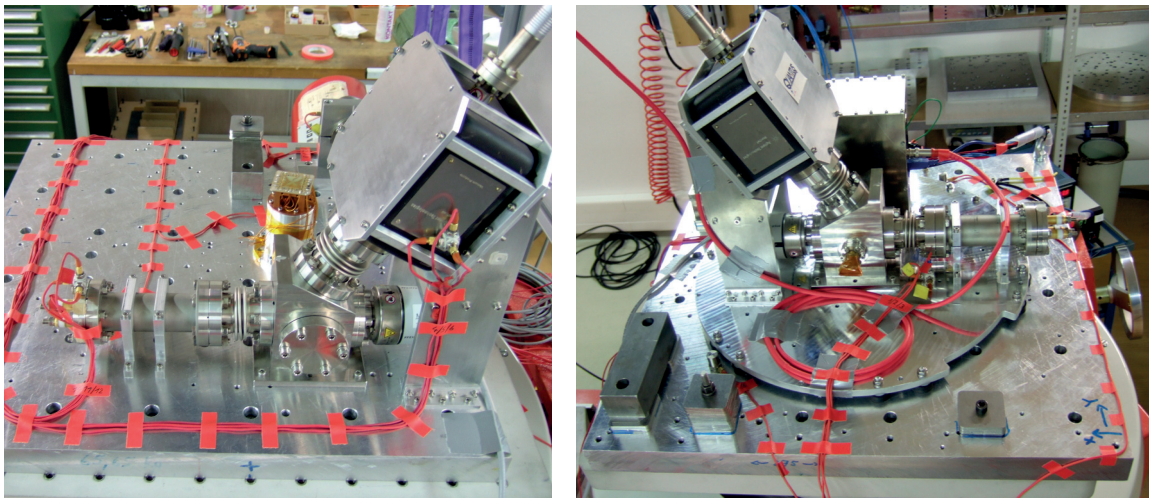

**(a)** MAIUS-1 pumping system mounted directly to the shaker adapter plate. The mounting of the components is realized as it will be done during flight.

**(b)** Mounting of the MAIUS-1 pumping system including instruments platform and passive vibration isolation. This configuration is similar to the flight configuration.

**Figure 9.23:** Test setup for vibrational and shock tests of MAIUS-1 pumping system

In total five tests have been performed with the MAIUS-1 pumping system in its flight configuration. Three tests have been carried out "hard-mounted" as shown in figure 9.23a. In these tests the components of the pumping system have been mounted directly to the rectangular shaker adapter plate, which has been mounted to the shaker using the head expander or the slip table of the shaker as described in section 8.

Two additional tests have been done with the pumping system mounted using the vibration isolation and an instruments platform as introduced in section 7.1.2. The components have been mounted to the instruments platform, which is mounted to the shaker adapter plate using passive vibration isolation as shown in figure 9.23b.

While the hard-mounted tests are used to qualify and test the components of the setup and their mounting under various pressures and test conditions, the damped tests simulate the flight environment and allow investigations of the pumping system performance during flight. The combination of both setups demonstrates the impact of the vibration insulation on the pumping system performance.

In the hard mounted tests all components could be qualified for the use on a sounding rocket. The ion getter pump and the titanium sublimation pump have even been qualified before hand, since a visual inspection was necessary after the tests, which requires to break the vacuum. The visual inspection showed no degradation or failure of the pump anode or the titanium filaments. Moreover no dust was found in the vacuum chamber, which would indicate abrasion from the titanium filaments.

The data of the ion getter pump current showed no variations during the vibrational tests. This rules out arching between pump anode and cathode, because this would result in a peak in the pump current. A stable pump current will also guarantee a reliable operation of the pump at a constant pumping speed.

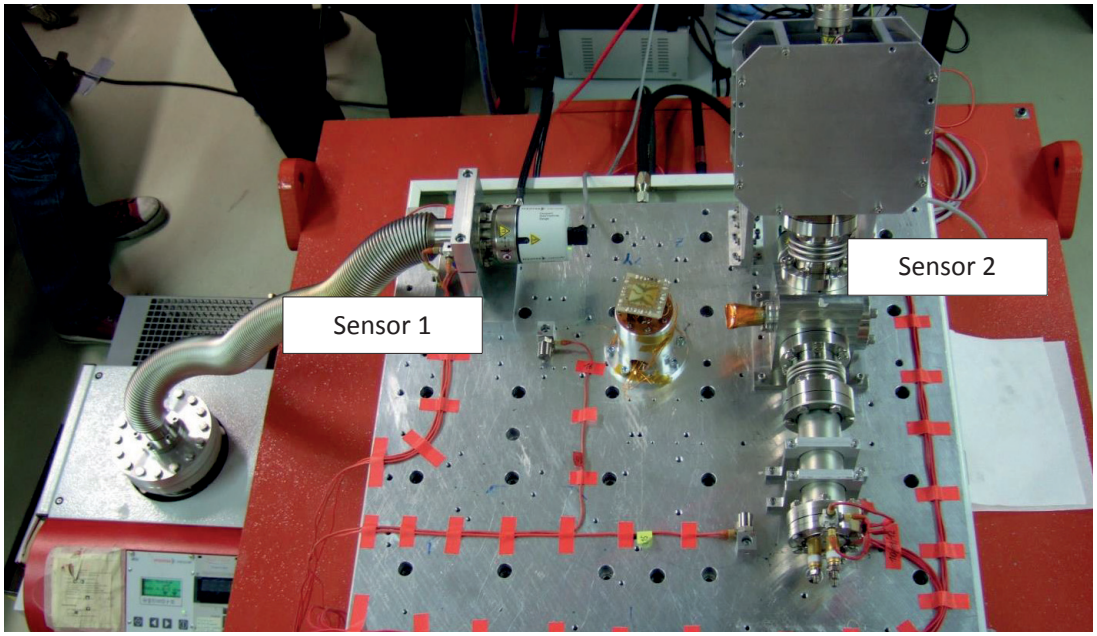


**Figure 9.24:** Pfeiffer IKR 270 sensor qualification setup using two cold cathode sensors of the same type at different pressure levels. Sensor 1 at a pressure of $1 \times 10^{-8}$ hPa and Sensor 2 (hidden under the ion-getter pump) at a pressure of $4 \times 10^{-11}$ hPa.

At tests with a pressures below $1 \times 10^{-10}$ hPa, the cold cathode sensor switched to "under-range" as soon as the test run was started. When the test run was completed it took up to 12 s until the sensor recovered. The pressure reading started at $1 \times 10^{-2}$ hPa and dropped to lower values almost immediately undershooting the actual pressure before returning to a reliable operation. The same behavior is observed, if the sensor is re-started at low pressures and is considered to be an electronic artifakt. I will take approximately 30 s to return to a reliable operation of the sensor.

To investigate this behavior and to rule out that the sensor generally malfunctions under vibrations, a second sensor was mounted to the shaker during one of the test runs as shown in figure 9.24. While this sensor (Sensor 1) was operated at $1 \times 10^{-8}$ hPa, the second sensor (Sensor 2) at the pumping system was operated at the usual pressure of $4 \times 10^{-11}$ hPa.

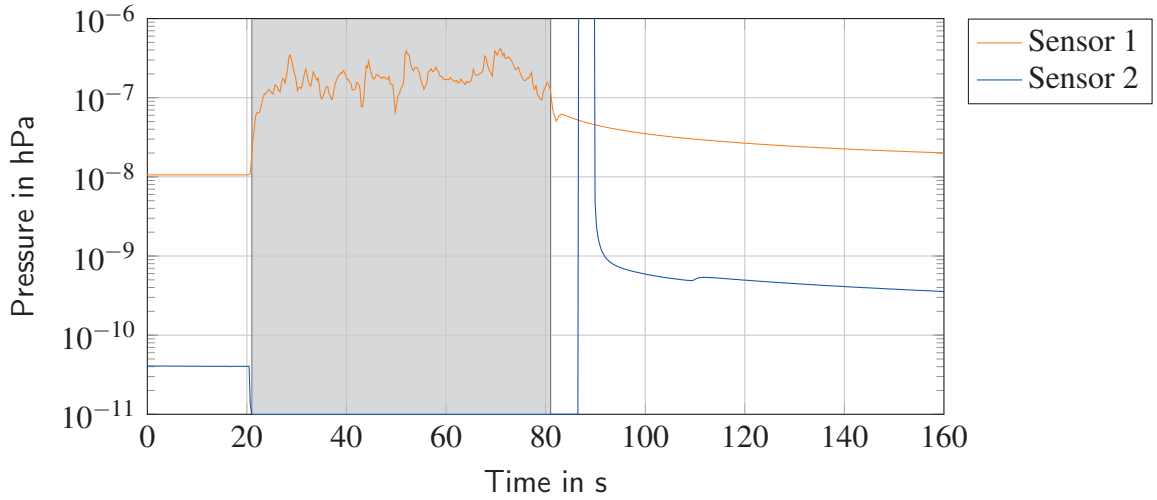


**Figure 9.25:** Pressure reading during vibrational test at 8.1 $g_{rms}$ with a duration of 60 s of two hard-mounted Pfeiffer IKR 270 cold-cathode sensors at different pressure levels. The light gray area indicates the test run.

As shown in figure 9.25 sensor 1 showed a reliable pressure reading and recorded a pressure rise to $2 \times 10^{-7}$ hPa, while the second sensor showed the malfunction described above. In a later test it was proven, that the sensor also performs reliable at a starting pressure of $2.7 \times 10^{-10}$ hPa at a level of 5.4 $g_{rms}$ or if the vibration isolation is used.

For this reason the sensor is considered qualified to a vibration level of 5.4 $g_{rms}$ for pressures above $2.7 \times 10^{-10}$ hPa. In any case the sensor will operate reliable after the test with the restriction of a long recovery time as also shown in figure 9.27.

During the sine resonance sweep carried out before and after the test runs it was observed, that the pressure rises rapidly after roughly 120 s. This indicates a frequency dependency of the intensity of the pressure rise and thus also of the leak size. Figure 9.26 shows the pressure in the hard-mounted MAIUS-1 pumping system plotted over the frequency of the sine vibrations applied during a z-axis sine resonance sweep. The frequency was sweep from 5 Hz to 2000 Hz with a sweep rate of 2 oct/min and a load level of 0.5 g. Since the start of the resonance sweep $t = 0$ is known from the trigger signal, the frequency at the time $t$ can be calculated from

$$f(t) = f_0 \, 2^R \tag{9.43}$$

This has been done in this case with the start frequency $f_0 = 5$ Hz and the sweep rate $R = t/30s$. Figure 9.26 shows, that the impact of the vibrations is stronger between 95 Hz and 2000 Hz with a strong peak at 100 Hz. Avoiding or reducing loads at these high frequencies would thus reduce the leakage rate, which has been one reason to design the vibration isolation as described in section 7.1.2.

Figure 9.27 demonstrates a dependency between the pressure rise and not only the fre-

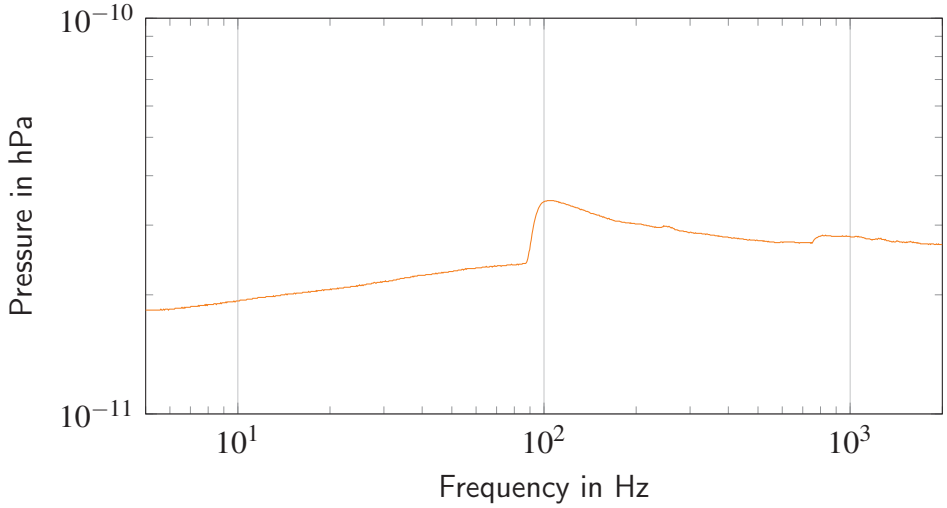


**Figure 9.26:** Frequency dependency of the pressure rise in the hard mounted MAIUS-1 pumping system. The data was obtained by logging the pressure and simultaneously the applied vibrations during a sine resonance sweep at $0.5\,\mathrm{g}$ with a sweeping rate of $2\,\mathrm{oct/min}$

quency but also the RMS load level over the complete frequency band. The measured value after recovery of the sensor ranges from $2.3 \times 10^{-11}$ hPa (no pressure loss) at $2.04\,\mathrm{g_{rms}}$ to $5.4 \times 10^{-10}$ hPa at $8.10\,\mathrm{g_{rms}}$.

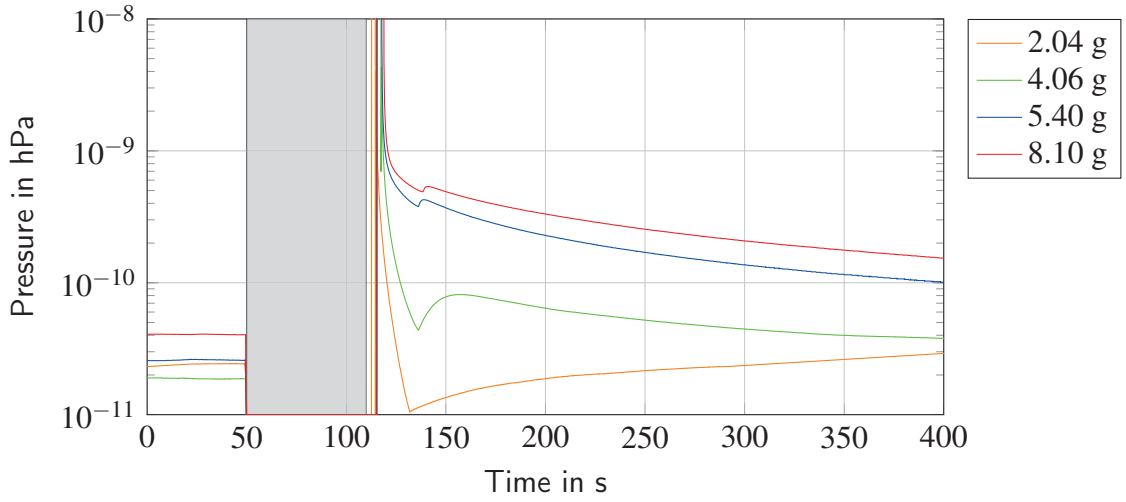


**Figure 9.27:** Pressure in the MAIUS Pumping System during z-axis random vibration tests on four different levels. The test was carried out without shock mounts. During all four tests the sensor went to "underrange" which is indicated by a pressure of $1 \times 10^{-11}$ hPa. The undershooting of the actual value is an electronic artifact as it can also be observed when re-starting the sensor.

Based on the results of the static load tests this is an expected behavior, if the pressure rise is caused by an external leak. As demonstrated in section 9.5.2 the leak size depends on the applied load. Thus a rise in the vibrational load will also cause a larger leakage rate resulting in a higher (equilibrium) pressure during vibration.

The leak should be closed once the test run is completed as it has been observed during the static tests. The exponential drop of the pressure and the fact, that the initial pressure is regained after the tests proves that this is also the case if the load is applied in the form of vibration.

As already mentioned in section 8.2 the vibration isolation will reduce the RMS value by damping in particular high level vibrations. For this reason it is expected, that the pressure rise will be smaller, when the pumping system is mounted on the dampers.

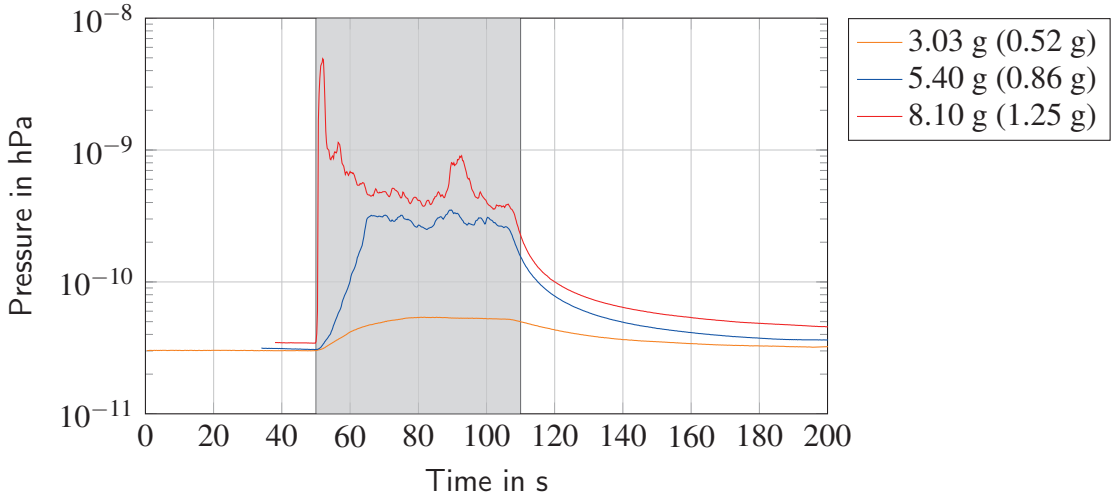


**Figure 9.28:** Pressure in the MAIUS pumping system during z-axis random vibration tests on three different levels. The test was carried out with shock mounts. The values in brackets indicate the actual load level on the pumping system platform.

As shown in figure 9.28 this is in accordance with the measurements performed. Either due to the low level of vibrations or the isolation of the high frequencies the sensor also shows a constant pressure reading. This allows to analyze the course of the pressure during the test run. It shows that a equilibrium pressure is reached, which is also depending on the load level.

The load level on the instruments platform has been measured by two different vibration sensors. The RMS values are given in the legend of figure 9.28 in brackets behind the load level applied by the shaker.

To compare those pressure curves with the ones obtained from the hard mounted tests it is important to consider the "dead-time" of the sensor of roughly 30 s. During this time the pumping system was still operating and thus reducing the pressure in the system, although the sensor did not support proper data. Since the test run starts at 50 s in both tests it is possible to compare pressures at times larger than 150 s of both tests as done in table 9.12.

In analogy to the calculations performed in section 9.5.3 the leakage rate $Q_{L,2}$ can be found from the equilibrium pressure before the test run p(t=45) and during the test run

p(t=110). The effective pumping speed at the pump cube was calculated in section 9.4.4 as $29.58\,\mathrm{L\,s^{-1}}$.

In addition to the leakage rate $Q_{l,2}$ a residual pumping rate shall be obtained from the course of the pressure after the end of the test as

$$S_{res} = \frac{V}{t_2 - t_1} \ln\left(\frac{p(t_1)}{p(t_2)}\right) \tag{9.44}$$

where $V$ is the pumping system volume of 0.4 L and $t_1$ and $t_2$ have uniformly been chosen to be 160 s and 200 s to get comparable results for the residual pumping rate.

At such low pressures outgassing of the chamber walls is dominant and the actual pumping rate will compensate for all kinds of gas inputs simultaneously. Thus the calculated pumping rate is very low.

This pumping rate characterizing the pump down from the raised equilibrium pressure during the test to the initial level shall be defined as a the residual pumping rate.

| Load Level $[g_{rms}]$ | p(t=45) | p(t=110) | p(t=160) | p(t=200) | $Q_{L,2}$ | $S_{res}$ |
|---|---|---|---|---|---|---|
| | | [ $10^{-11}$ hPa ] | | | [hPa L s$^{-1}$] | [L s$^{-1}$] |
| 0.52 | 3.01 | 5.23 | 3.52 | 3.2 | $6.57 \times 10^{-10}$ | $6.06 \times 10^{-4}$ |
| 0.86 | 3.10 | 25.8 | 4.13 | 3.64 | $6.71 \times 10^{-9}$ | $1.26 \times 10^{-3}$ |
| 1.25 | 3.45 | 37.7 | 5.36 | 4.57 | $1.01 \times 10^{-8}$ | $1.59 \times 10^{-3}$ |
| 4.06 | 1.87 | - | 8.13 | 6.41 | $> 1.85 \times 10^{-9}$ | $2.37 \times 10^{-3}$ |
| 5.40 | 2.62 | - | 32.7 | 22.91 | $> 8.90 \times 10^{-9}$ | $3.56 \times 10^{-3}$ |
| 8.10 | 4.08 | - | 44.3 | 33.2 | $> 1.19 \times 10^{-8}$ | $2.88 \times 10^{-3}$ |

**Table 9.12:** Evaluation of vibrational tests performed with the MAIUS pumping system. The additional leakage rate $Q_{L,2}$ during the tests and the residual pumping speed $S_{res}$ while regaining the initial pressure have been calculated for each test run.

As shown in table 9.12 the leakage rates and the equilibrium pressure increase with the RMS value of the vibration applied. Unfortunately the sensor malfunction does not allow to calculate the leakage rate for the hard mounted tests from the equilibrium pressure, thus the leakage rate has been calculated using the pressure at t = 150 s. The actual pressure during the test will be higher, thus the actual leakage rate will be larger than the calculate values.

The residual pumping rate also increases with the pressure at which it is calculated. The residual pumping rate after the 5.4 $g_{rms}$ test (initial pressure $4.67 \times 10^{-10}$ hPa) is twice as high as after the 1.25 $g_{rms}$ test (initial pressure $5.77 \times 10^{-11}$ hPa).

This is also an expected behavior, since the pumping speed of the ion-getter pump is depending on the pressure in the system. Therefore the pumping rate of the ion getter pump

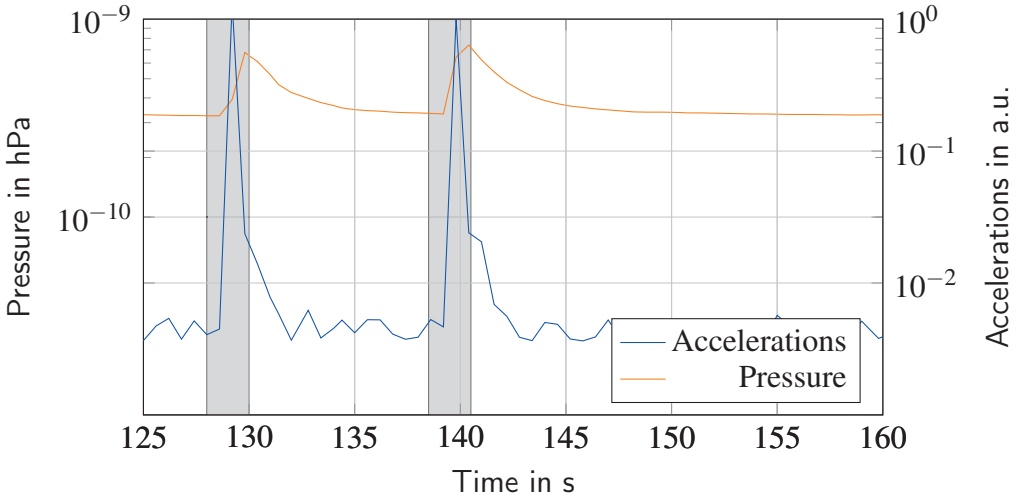


**Figure 9.29:** Pressure in the hard-mounted MAIUS Pumping System during 15 g half-sine z-axis shock test.

will increase if the pressure in the chamber rises. Only the rate calculated from the 8.1 $g_{rms}$ test deviates from this rule.
The duration of the test also influences the pressure rise. Very short tests, will not allow the leak to open completely and the leakage rate will be smaller. As part of the MAIUS-1 pumping system a hard-mounted half-sine shock test at 15 g with a duration of 15 ms has been carried out. In figure 9.29 the results of the two shock tests are depicted.

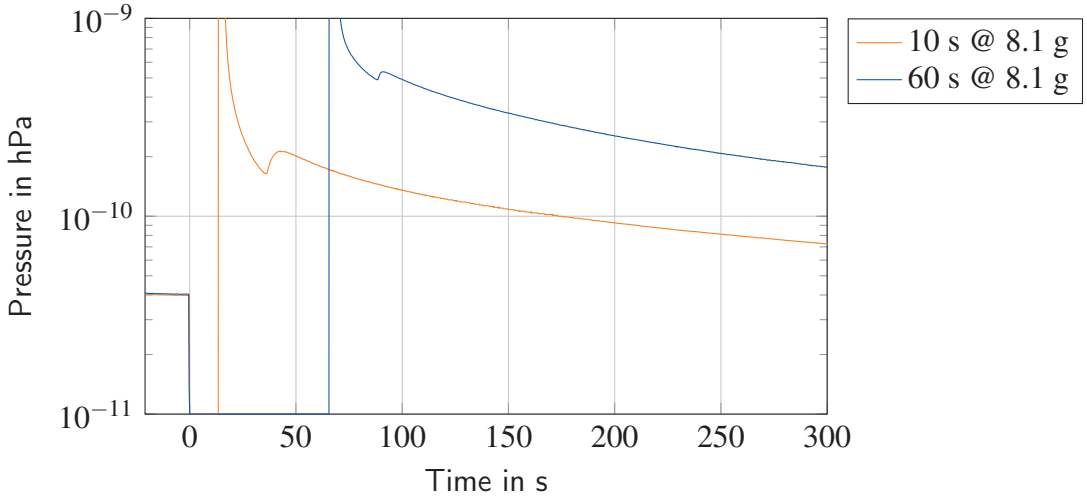


**Figure 9.30:** Impact of test durations on vacuum pressure in the MAIUS-1 pumping system. The test was performed hard-mounted at qualification level.

The pressure rises from $3.25 \times 10^{-10}$ hPa to $6.79 \times 10^{-10}$ hPa as a result of the shock. This is much lower than expected, when compared to the load levels and associated pressures in table 9.12. Thus the MAIUS-1 pumping system will not only survive shock loads of 15 g, but these will have no significant influence on the vacuum pressure.

A similar effect is observed at random vibrations. Very short test durations of 10 s will allow fast recovery of the pressure to its initial value, while durations of 60 s will require longer pump times to recover the pressure as shown in figure 9.30. Both tests have been performed hard-mounted at qualification level with the same initial pressure but different test durations.

The increase in test duration will result in an rise in the amount of gas entering the system. Although it will be pumped this gas will cause a degradation of the titanium sublimation pump. Moreover the gas has more time to spread in the system. These might be reasons for the dependency on the test duration.

In addition to variation of the test parameters and the test setup, one vibrational test was performed with the analysis section of the vacuum testbed described in section 9.5 attached to the MAIUS-1 pumping system.

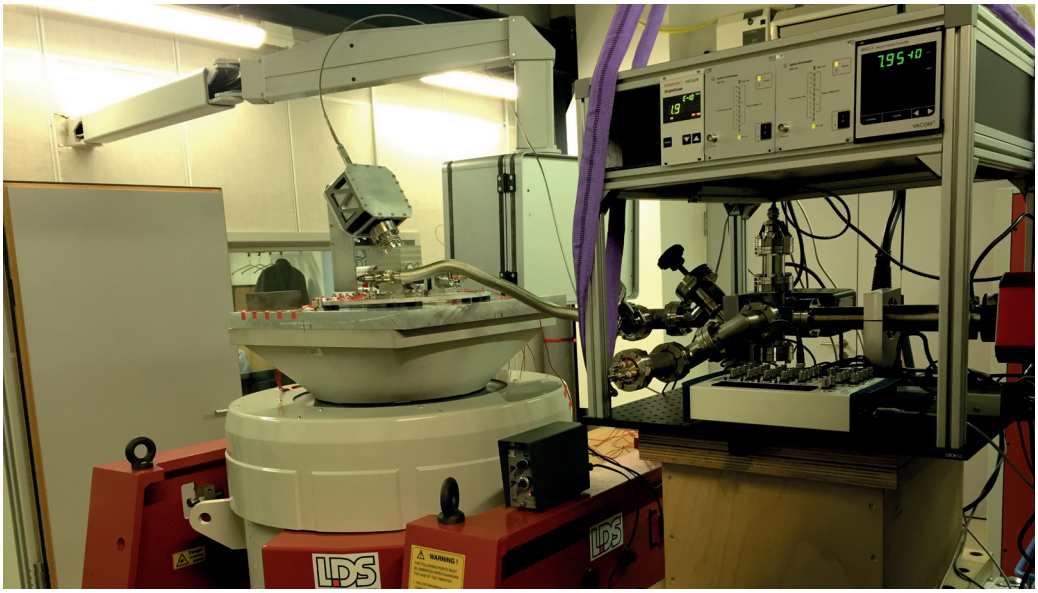


**Figure 9.31:** MAIUS-1 Pumping system mounted to the shaker in the ZARM facility. The analysis section of the UHV testbed including a mass spectrometer is connected to the test specimen with a CF16 bellow.

As shown in figure 9.31 the analysis section and the pumping system are connected with a 500 mm CF16 bellow. It was necessary to decouple the mass spectrometer from the shaker, because the spectrometer is very sensitive and expensive and it should not be damaged by the vibrational loads applied during the test. The pressure at the pumping system was $1.9 \times 10^{-10}$ hPa. The test duration was 60 s at acceptance level.

During the test the ion currents of the masses 14, 16, 17, 18, 20, 28, 32, 40 and 44 have been monitored. These represent the characteristic masses of the main components of air. As shown in figure 9.32 a rise in the ion currents for masses 28, 14 and 16 was observed. This indicates that the main component of the gas entering the system is nitrogen with the

characteristic masses 28 and 14. This would support the assumption that the pressure rise is caused by temporary external leak.

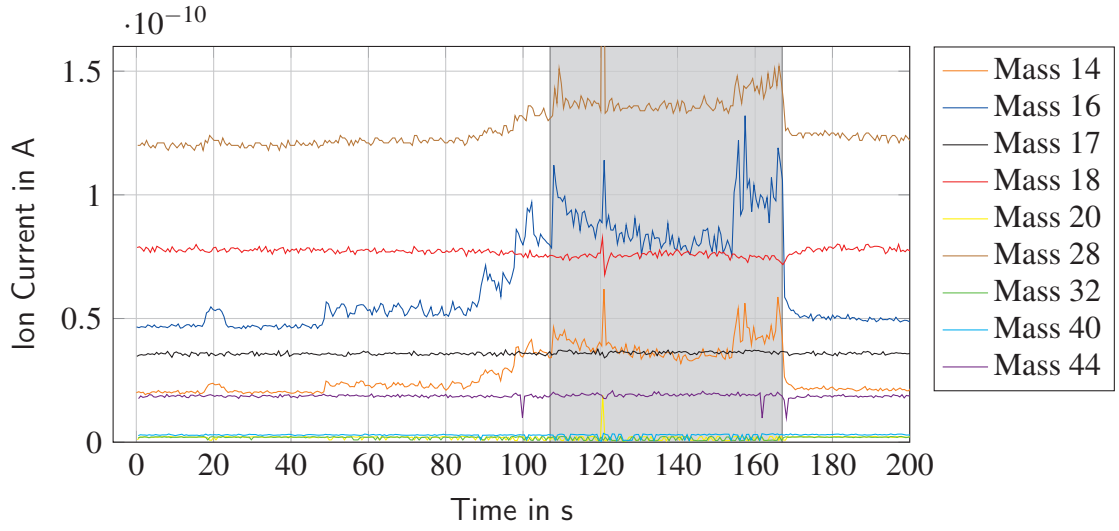


**Figure 9.32:** Ion current reading of characteristic masses for air during vibration test of the MAIUS-1 pumping system at acceptance level for 60 s

However, there is no good explanation for the rise in the ion current of mass 16. Mass 16 could indicate an gas input of oxygen. However if this was caused by oxygen a rise in mass 32 should also be observed. Unfortunately the ion current of mass 32 is only showing noise. One reason for these inconclusive results might be the two ion pumps and the two titanium sublimation pumps that have been operated during the test. As already stated in section 9.5 it is not ideal to have these pumps operating while measuring. The pumps will falsify the test results, because they will remove molecules from the residual gas. A test run under a dome filled with a test gas as helium would clearly prove that the pressure rise is caused by external leaks.

## 9.7 Estimation and Improvement of the Equilibrium Pressure in MAIUS

The intensive investigations carried out in this chapter helped to design an vacuum system suitable for the use on a sounding rocket. The vacuum system as described in section 7.3.2 and 7.3.3 has demonstrated Bose-Einstein condensation [Sei14] and was successfully qualified for the use on the VSB30 sounding rocket as reported in section 8.6.

As stated in section 8.1 the maximum vibration level at the structure of the payload is expected to be 1.8 g RMS during motor burn. The motor will burn for 44 s as shown in the time event list (table 5.2). For this reason the pressure coarse obtained from the flight level test at 2 g RMS for 60 s is a reasonable prediction for the pressure during the flight of MAIUS-1. Indeed the pressure might even recover quicker, because of the shorter duration of the vibration and the dependency of the pump down time from the duration presented in section 9.6.

For an estimation of the pressure coarse during the ascent of the rocket all loads have to be considered. Aside from the vibrational loads a shock of 20 g with a duration of 15 ms and accelerations of up to 13 g are expected as characterized in section 5.6. Although the shock level during motor ignition is slightly above the one in the performed tests, the impact on the vacuum quality should be comparable to the one observed during the tests.

The acceleration will result in quasi static loads on the seals. The windows are to light (max. 130 g), thus the indium seals will experience static loads of 17 N, which is not sufficient to cause a leak. To cause a leak at CF-flanges, the bending momentum on the seal would have to exceed 80 N m as described in section 9.5.3. At 13 g this would be equivalent to 0.627 kg m. To reach this momentum a component of 6.27 kg has to be mounted to a CF flange with a distance of 100 mm between the flange and the center of gravity of the component. Consequently it would require a heavy component or a long lever to cause a leak at one of the CF flanges. Since all heavy components are supported properly this value will not be exceeded at any CF seal. Thus no impact on the pressure is expected from the static acceleration.

A proper mounting of the (vacuum) components and the use of vibration dampers to reduce the loads on the seals and thus the leakage rates has already been implemented in MAIUS-1. To improve the vacuum quality further the effective pumping speed has to be enlarged or the outgassing rate has to be reduced. Both methods would increase the net pumping rate available to compensate for the increased leakage rates while (vibrational loads) are applied.

Enlarging the effective pumping speed could be achieved by increasing the conductance between the different sections of the vacuum system or by using pumps with a larger pumping capacity. Unfortunately the pumping speed of e.g. ion-getter pump always scales with the weight of the pump. Thus the mass of the vacuum system would increase significantly.

The conductance could especially be improved at the connection between the pumping system and the science chamber. This could be achieved by enlarging the pipe diameter to 25 mm, which would result in a decrease of the magnetic shielding factor. If this decrease in shielding factor is affordable for future missions without risking to miss the scientific goals would have to be investigated by the scientists.

One important lesson learned from the laboratory operation of MAIUS-1 is, that not all structures of the chip are needed for operation of the experiment. Thus the number of cables connecting the atom chip with the feed-throughs could be minimized by connecting only the structures that are used. This would decrease the outgassing rate of the Kapton isolation, which is dominating the overall outgassing rate of the experiment chamber.

Moreover the atom chip itself could be simplified to fewer layers and it could be abstained from using glue to connect the different layers of the chip, which would also contribute to the reduction of the outgassing rate. To decrease the outgassing rate electro-chemical polishing of titanium as described in section 9.2.6 might reduce the outgassing rate of titanium by three orders of magnitude.

A combination of those methods is promising a strong increase in the performance of the vacuum system. Therefore all methods mentioned above are currently under investigation for the use in future vacuum systems for quantum optic experiments.

# Part IV

# Thermal Design, Simulation and Testing

# 10
# Simulation of Aerothermal Heating

For designing a thermal control system it is essential to know all thermal loads in interaction with the studied system. While the power consumption of the instruments aboard a sounding rocket are generally well known, the heat input due to aerodynamic friction is depending on the trajectory and geometry of the rocket.

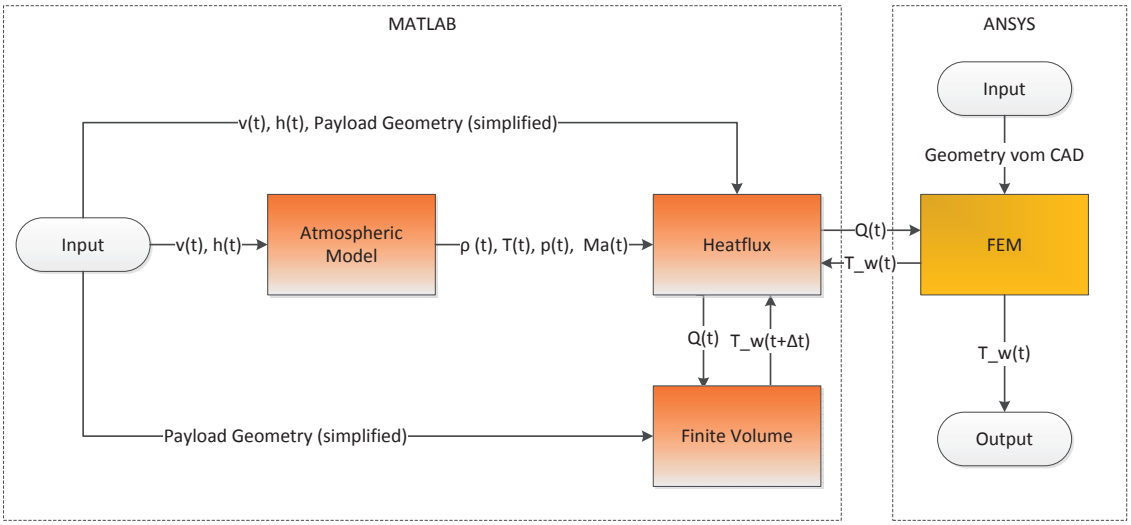


**Figure 10.1:** Schematic of the computation approach for the heat input into the rocket structure due to thermo-fluid dynamics

Thus it may differ depending on the rocket geometry, trajectory and hull thickness. Unfortunately no data of the hull temperatures along the payload modules is available for blunted nose cone payloads with similar mass, hull geometry and trajectory as MAIUS-1. The only temperature measurements accessible have been performed at the service or recovery module of the rocket for Ogive nose cones. These results are shown in figure 10.10 for comparison. However these are not representative for the hull temperatures at the scientific payload, which are located downstream of the service module.

In the following a method for an estimation of the heat flux into the rocket structure due to aerodynamic friction shall be presented, which has been developed within this thesis.

In the first step a MATLAB script is used to compute the properties of the air surrounding the payload based on a DIN ISO 2533 standard atmosphere model. As shown in the schematic 10.1, the flight parameters altitude and velocity are used as an input to compute the atmospheric parameters as well as the actual heat flux.

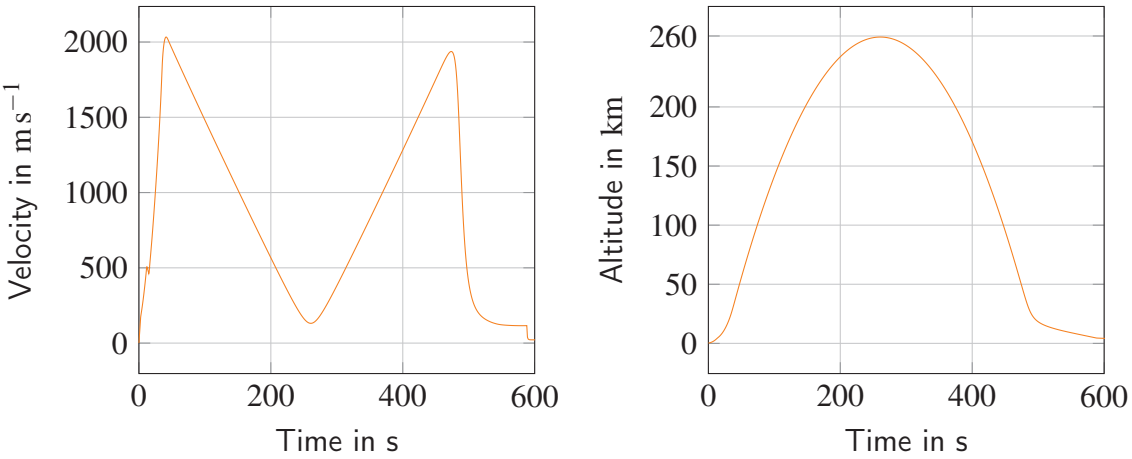


**(a)** Predicted velocity of MAIUS-1 **(b)** Predicted altitude of MAIUS-1

**Figure 10.2:** MAIUS flight parameter for heat flux computation

These parameters are provided by DLR MORABA, where the trajectory of the rocket is simulated using the rocket simulator software ROSI. This has to be done to ensure that the altitude does not exceed the limits of ESRANGE for unguided rockets and to be able to compute the aerodynamic behaviour of the rocket during ascent and descent. The ROSI output for the MAIUS-1 flight is plotted in figure 10.2.

In the next step a MATLAB script computes the heat flux into the structure by aerodynamic heating based on the parameters of the atmosphere and the relative velocity of the rocket as plotted in figure 10.2a. Wind speeds and the attitude of the rocket are not considered in this simulation. The script is using an numeric approach in combination with a simplified finite volume model of the payload to compute the heat fluxes as presented in section 10.3.

The computed heat flux for each volume element is finally fed in a transient-thermal FEM simulation to obtain the temperature field along the hull segments with a good spacial resolution and with consideration of all details of design. The temperature field will be used to compute the heat flux from the hull into the different systems of the payload as described in chapter 11.1.

## 10.1 Atmospheric Model

With increasing altitude the physical properties of the air change significantly. These changes have a strong impact on the (thermo)fluid dynamics of the MAIUS sounding rocket. Thus these changes have to be considered for computation of the aerodynamic heating.

Based on the altitude information provided in figure 10.2b the essential parameters of the atmosphere such as density $\rho_{air}$, pressure $p_{air}$ and temperature $T_{air}$ will be computed according to DIN ISO 2533 in dependency of the altitude corresponding to the respective flight time. The international standard atmosphere (ISA) model is valid for altitudes up to 88 km and shall be described in the following. At higher altitudes the aerodynamic friction is negligible.

The atmosphere between 0 km and 88 km is idealized as a model with 8 layers, 3 of which are isothermal layers. For isothermal layers the three basic parameters are computed as

$$T_{air} = T_a = const \tag{10.1}$$

$$p_{air} = p_a \exp\left[-\left(\frac{g_0}{R\,T_{air}}\right)(h-h_a)\right] \tag{10.2}$$

$$\rho_{air} = \rho_a \exp\left[-\left(\frac{g_0}{R\,T_{air}}\right)(h-h_a)\right] \tag{10.3}$$

and respectively for the other layers

$$T_{air} = T_a + a\,(h-h_a) \tag{10.4}$$

$$p_{air} = p_a \left(\frac{T_{air}}{T_a}\right)^{-\left(\frac{g_0}{aR}\right)} \tag{10.5}$$

$$\rho_{air} = \rho_a \left(\frac{T_{air}}{T_a}\right)^{-\left(\frac{g_0}{aR}+1\right)} \tag{10.6}$$

where $R = 287.05\,\mathrm{J\,kg^{-1}\,K^{-1}}$ is the specific gas constant for air and $g_0 = 9.81\,\mathrm{m\,s^{-2}}$ is the gravitational acceleration. The altitude of the rocket $h$ is an input parameter, the start altitude of an layer $h_a$ and the remaining coefficients have to be chosen from table 10.1.

In addition to these basic parameters, the dynamic $\mu_{air}$ and kinematic viscosity $\eta_{air}$ in $\mathrm{Pa\,s^{-1}}$ and $\mathrm{m^2\,s^{-1}}$ are approximated by an approach presented by *Sutherland* [Sut93] as

$$\mu_{air} = 1.458 \times 10^{-6}\,\frac{T_{air}^{1.5}}{T_{air} + 110.4} \tag{10.7}$$

$$\eta_{air} = \frac{\mu_{air}}{\rho_{air}} \tag{10.8}$$

Moreover the speed of sound and thus the Mach number $Ma = \frac{v}{c}$ are depending on the air temperature as well. Thus the speed of sound $c$ needs to be calculated in dependency of the altitude from

$$c = \sqrt{\kappa R T_{air}} \tag{10.9}$$

where $\kappa = 1.4$ is a good approximation for air in this altitude regime. The change in $c$ will directly influence the Mach number. With this all parameters for computation of the aerodynamic heating are defined for altitudes of up to 88 km.

| Layer # | $h$ km | $h_a$ km | $T_a$ K | $a$ $\mathrm{K\,m^{-1}}$ | $p_a$ Pa | $\rho_a$ $\mathrm{kg\,m^{-3}}$ |
|---|---|---|---|---|---|---|
| 1 | -0.5 - 11 | 0 | 288.15 | $-6.5 \times 10^{-3}$ | 101325 | 1.2250 |
| 2 | 11 - 20 | 11 | 216.65 | 0.0 | 22632 | 0.3639 |
| 3 | 20 - 32 | 20 | 216.65 | $+1.0 \times 10^{-3}$ | 5475 | 0.0880 |
| 4 | 33 - 47 | 32 | 228.65 | $+2.8 \times 10^{-3}$ | 868 | 0.0132 |
| 5 | 47 - 52 | 47 | 270.65 | 0.0 | 111 | 0.0014 |
| 6 | 52 - 61 | 52 | 270.65 | $-2.0 \times 10^{-3}$ | 59 | 0.0008 |
| 7 | 61 - 79 | 61 | 252.65 | $-4.0 \times 10^{-3}$ | 18 | 0.0002 |
| 8 | 79 - 88 | 79 | 180.65 | 0.0 | 1 | $1.9 \times 10^{-5}$ |

**Table 10.1:** Parameters for calculation of density, pressure and temperature of the standard atmosphere according to DIN ISO 2533

Above 88 km the atmosphere is already very thin ($\rho(88\,\mathrm{km}) = 3.463 \times 10^{-6}\,\mathrm{kg\,m^{-3}}$), which reduces the aerodynamic heating rate to less than 1 % of its maximum value during ascent. For MAIUS-1 this portion of the heat flux is neglected. For more accurate thermal simulation an implementation of look-up-tables from other atmospheric models as e.g. NASA MSIS-E-90 is possible, however less handy.

Figure 10.3 illustrates the course of the six most important atmosphere properties for the first 70 s of flight. For completeness and clarity the altitude and the velocity of the rocket are also plotted in the first line of this figure.

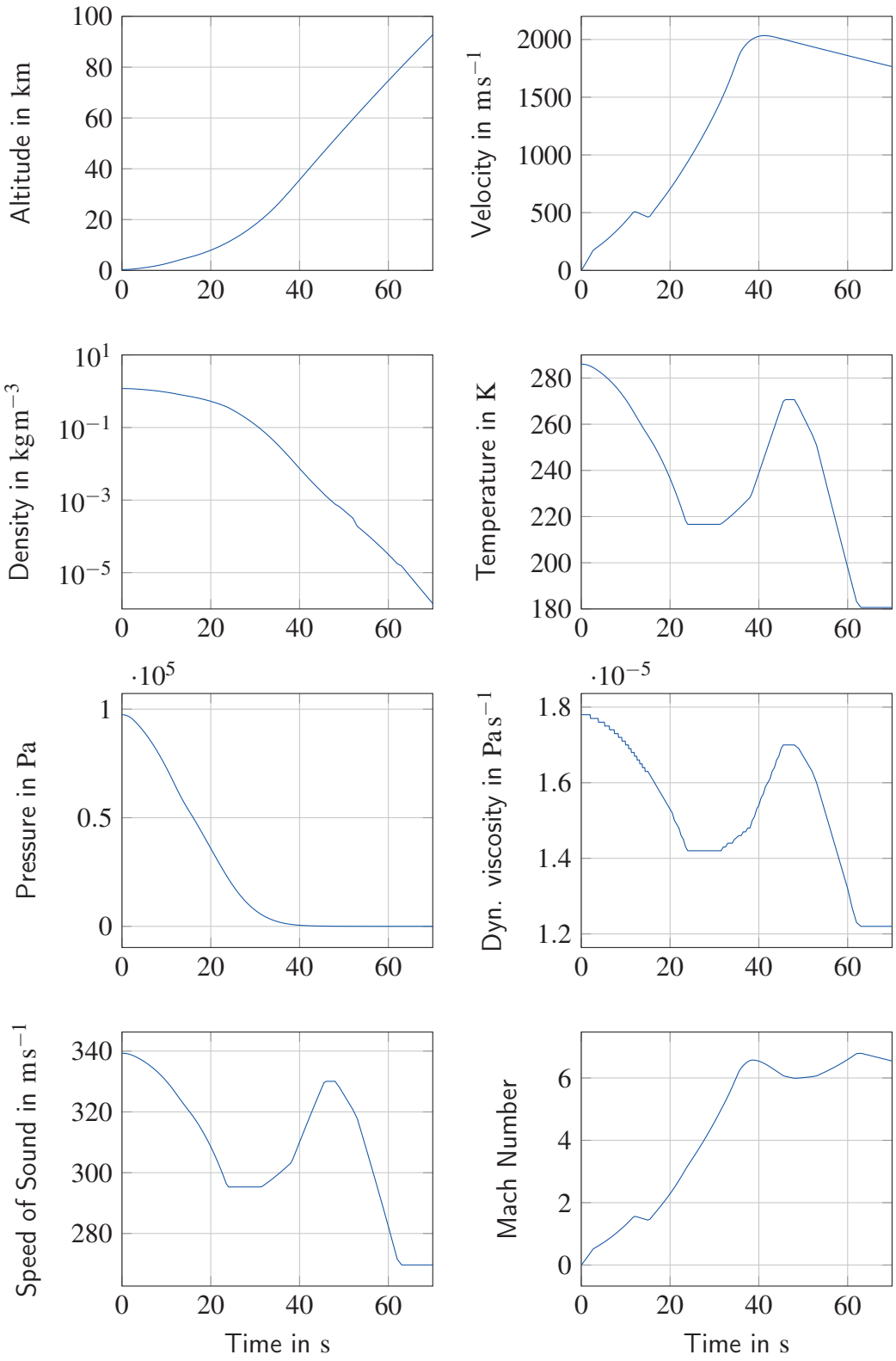


**Figure 10.3:** Output of the atmosphere model for the first 70 s of the MAIUS-1 flight

## 10.2 Geometric Model and the Finite Volume Method

The heat flux into the structure is depending on the wall temperature of the rocket. Thus it is not possible to completely decouple the heating of the wall and the conduction in the wall from the computation of the heat flux. For this reason a finite volume approach was used to consider those effects. For simplicity the geometry of the rocket hull has been simplified and is considered radially symmetric.

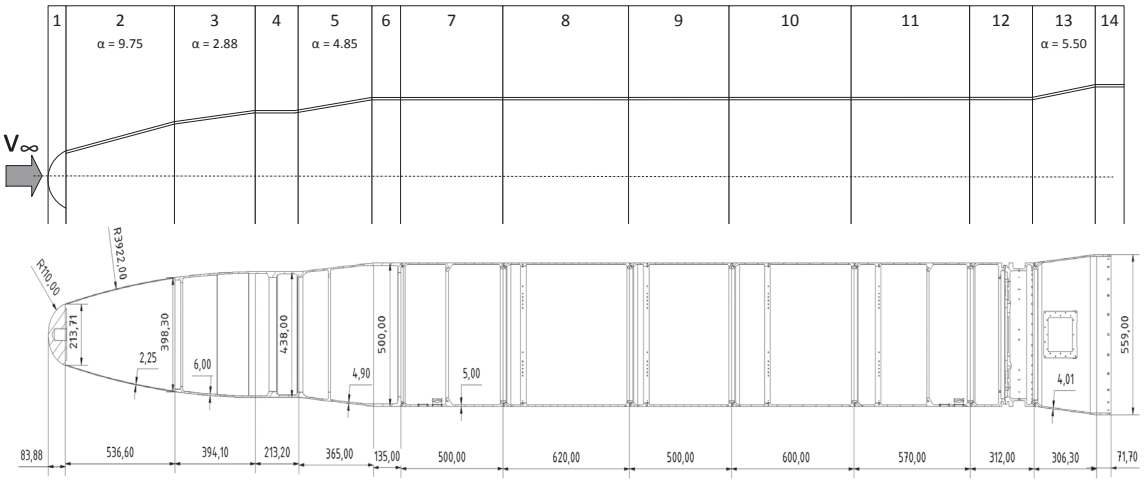


**Figure 10.4:** Finite volume model of the MAIUS-1 payload including MORABA systems

This results in a model consisting of 14 volume elements, which are all of cylindrical or conical shape, with the nose tip being the only exception. Figure 10.4 gives an overview on the model and a good comparison to the detailed model.

In the simplified model all flanges with increased wall thickness for mounting of the e.g. instrument platforms as well as the hatches have been neglected. Moreover the curved path of the nose (elements 2 and 3) was approximated by a simple conical shape, with a slope of $\alpha_2 = 9.75°$ of $\alpha_3 = 2.88°$. This allows to describe the geometry of all elements but element 1 using a truncated cone or cylinder model without changes in the wall thickness within a single element.

This simplification is especially important to be able to cover the nose section with the approach described in section 10.3 to calculate the heat flux by aerodynamic heating. The same simplification can also be used to model tangent ogive noses, by dividing them in multiple cone elements to approximate the radius of the nose.

Figure 10.5 illustrates the nomenclature for the geometric properties and heat fluxes of the volume elements. The right boundary of the element is referred to as "east" (index $e$) and the left boundary is referred to as "west" (index $w$). Although one volume element is characterized by a total of four radii, only the eastern radius is stored with the index of the element. The western radius is defined by the previous element $r_w(j) = r_e(j-1)$.

| Element # | $r$ [m] | $r_i$ [m] | $L$ [m] | $\alpha$ [°] | $m$ [kg] |
|---|---|---|---|---|---|
| 1 | 0.1069 | 0.1048 | 0.0839 | - | 4.21 |
| 2 | 0.1992 | 0.1969 | 0.5366 | 9.75 | 3.23 |
| 3 | 0.219 | 0.213 | 0.3941 | 2.88 | 5.96 |
| 4 | 0.219 | 0.213 | 0.2132 | 0 | 4.86 |
| 5 | 0.250 | 0.2451 | 0.365 | 4.85 | 8.09 |
| 6 | 0.250 | 0.2451 | 0.135 | 0 | 2.88 |
| 7 | 0.250 | 0.2450 | 0.500 | 0 | 10.89 |
| 8 | 0.250 | 0.245 | 0.620 | 0 | 13.50 |
| 9 | 0.250 | 0.245 | 0.500 | 0 | 10.89 |
| 10 | 0.250 | 0.245 | 0.600 | 0 | 13.06 |
| 11 | 0.250 | 0.245 | 0.570 | 0 | 12.41 |
| 12 | 0.250 | 0.245 | 0.312 | 0 | 6.79 |
| 13 | 0.2795 | 0.2755 | 0.3063 | 5.50 | 6.35 |
| 14 | 0.2795 | 0.2755 | 0.0717 | 0 | 1.40 |

**Table 10.2:** Geometric parameters of the 14 volume elements of the payload model

The same applies to the contact surface between Element j and its neighboring surfaces, which are computed as

$$A_e(j) = \pi \left[ r^2(j) - r_i^2(j) \right] = A_w(j+1) \tag{10.10}$$

The reference cone envelope line $L_m$ is calculated as

$$L_m(j) = \sqrt{[r(j) - r(j-1)]^2 + l^2(j)} \tag{10.11}$$

This includes the special case of cylindric elements, where $r(j) = r(j-1)$ and therefore $L_m(j) = L(j)$. The outer surface of element $j$ is given as

$$A(j) = \pi L_m(j) \left( r(j) + r(j-1) \right) \tag{10.12}$$

and the volume respectively as

$$V(j) = \frac{\pi L}{3} \left[ \left[ r^2(j) + r(j)\, r(j-1) + r^2(j-1) \right] - \left[ r_i^2(j) + r_i(j)\, r_i(j-1) + r_i^2(j-1) \right] \right] \tag{10.13}$$

As shown at the top of figure 10.4, there are 13 cone/cylinder shell elements and one nose tip element, which is hemispherical with a nose radius $r_n = 0.110$. The geometric properties of all elements of the model of the MAIUS-1 payload are given in the lower drawing of figure 10.4. Moreover the properties needed as an input for calculation of the areas and volumes mentioned above are summarized in table 10.2.

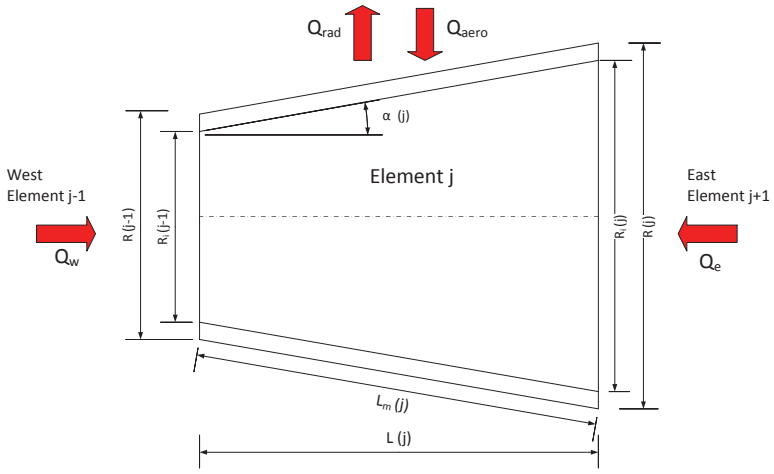


**Figure 10.5:** Finite volume elements for conduction computation

Wherever possible the mass is extracted from the CAD files or from actual measurements to allow a accurate calculation of the element hull temperature $T(j)$. As initially stated and as given in section 10.3 this temperature is directly influencing the heat flux due to aerodynamic heating. To compute the temperature of each element, the heat flux by conduction between an element $j$ and its neighbouring elements $j+1$ ($\dot{Q}_e$) and $j-1$ ($\dot{Q}_w$), as well as the heat flux by radiation ($\dot{Q}_{rad}$) and aerodynamic friction ($\dot{Q}_{aero}$) has to be considered as also illustrated in figure 10.5.

In order to solve this problem an additional discretization in time using the finite difference method as proposed in [Pol05] will be carried out. Considering all heat fluxes interacting with the element, the balance of energy will provide a discretized solution for the change of the stored heat $Q$ in element $j$

$$\frac{\Delta Q(j)}{\Delta t} = \dot{Q}_e(j) + \dot{Q}_w(j) + \dot{Q}_{rad}(j) + \dot{Q}_{aero}(j) \tag{10.14}$$

where the heat $Q(j)$ is linked to the element temperature $T(j)$ by

$$Q(j) = c(j)\,m(j)\,T(j) \tag{10.15}$$

with $m$ being the mass of the element and $c$ being the specific heat capacity for the wall material. This leads to a discrete formula for explicit computation of the element temperature

$$T(j,t+\Delta t) = T(j,t) + \frac{\Delta t}{c(j)\,m(j)}\left[\dot{Q}_e(j,t) + \dot{Q}_w(j,t) + \dot{Q}_{rad}(j,t) + \dot{Q}_{aero}(j,t)\right] \tag{10.16}$$

Such an explicit approach is not naturally stable. Large steps in time $\Delta t$ or space $L$ can lead to instabilities. For this reason a stability criterion has to be met to ensure proper

performance. For thermal simulations this is given as [Pol05]

$$\frac{\lambda}{c\rho}\frac{\Delta t}{L^2} \leq 0.5 \tag{10.17}$$

This has to be checked for each element and each time step with $\lambda$ being the thermal conductivity and $\rho$ the density of the wall material. For the MAIUS simulation it has been implemented in the MATLAB script as an abort function.

If this criteria is met, the heat fluxes at the time $t$ have to be known to solve equation 10.16. For the conduction to or from the neighboring elements, the heat fluxes $\dot{Q}_e(j,t)$ and $\dot{Q}_w(j,t)$ can also be approximated using the finite difference method, which leads to [Pol05]

$$\dot{Q}_e(j,t) = -2\lambda A_e \left[\frac{T(j+1,t)-T(j,t)}{L(j)+L(j+1)}\right] \tag{10.18}$$

and respectively

$$\dot{Q}_w(j,t) = -2\lambda A_w \left[\frac{T(j,t)-T(j-1,t)}{L(j)+L(j-1)}\right] \tag{10.19}$$

The radiation into the surrounding of a wall element with the outer area $A(j)$ and a emissivity $\varepsilon$ and the Boltzmann constant $\sigma = 1.380\,65 \times 10^{-23}\,\mathrm{J\,K^{-1}}$ can be approximated by the Stefan-Boltzmann law

$$\dot{Q}_{rad}(j,t) = \varepsilon\,\sigma\,A(j)\,T^4(j,t) \tag{10.20}$$

In MAIUS-1 the scientific payload hull segments were made of aluminum EN-AW-7075. The material properties of the hull segments have been set according to the values given in the material datasheet [Gle15] to $\lambda = 145\,\mathrm{W\,m^{-1}\,K^{-1}}$, $\rho = 2800\,\mathrm{kg\,m^{-3}}$, $c = 960\,\mathrm{J\,kg^{-1}\,K^{-1}}$ and $\varepsilon = 0.11$. The time step $\Delta t$ is defined by the input data from the ROSI software, which varies between 0.05 s at the beginning and 1 s towards the end of the flight. Use of smaller time steps is however possible by interpolation between two points of the input data. By default the software will use the timestep generated by the ROSI software.

## 10.3 Computation of the Heat Flux at the Rocket Hull

The only heat flux, which has not yet been determined is the heat input by aerodynamic heating. For its determination an approach presented by Professor Steven P. Schneider in a script on Preliminary Spacecraft Designs [Sch03] of the Purdue University has been adapted. Although the script is aiming at designing a thermal protection system (TPS) for re-entry, the equations used in here are based on approaches published by Tauber et al [Tau87] and White [Whi91], which are also valid for ascent of (re-entry) vehicles.

As discussed in the following the approach will use a number of simplifications, however the simulation returns reasonable data for the nose cone and payload module temperatures.

Thus the approach will be used with care and a sufficient margin as a design tool to approximate the heat input into the systems by aerodynamic heating.

The approach differentiates between two different calculation methods: stagnation point heating applicable on the nose tip only and flat plate heating, which will be used for the remaining elements. This implies that the cone element will be treated as an angled plate with equivalent surface area and length, which is a reasonable and common approximation in fluid dynamics. Moreover the angle-of-attack is assumed to be $0^\circ$ as indicated in figure 10.4 neglecting wind and the rocket altitude.

### 10.3.1 Stagnation Point Heating

The stagnation point heating rate will be approximated using a approach presented by Tauber et. al. [Tau87]. The heating rate will be applicable at the nose tip only. The heating rate per unit area is generally given as

$$\dot{q}_{sp}(t) = C\,100^2 \rho_{air}(t)^N\, v(t)^M \tag{10.21}$$

Here $\rho_{air}$ is the freestream air density in $\mathrm{kg\,m^{-3}}$ as computed for each time of flight $t$ in the atmosphere script and $v$ is the rocket speed in $\mathrm{m\,s^{-1}}$, which is the input data originally computed by the ROSI software. The coefficients $C$, $N$ and $M$ will be discussed in the following. The equation will return the heating rate in $\mathrm{W\,m^{-2}}$ with the constants defined herein.

The constants for stagnation point heating are defined as $M = 3$, $N = 0.5$ and

$$C = \left(1.83 \times 10^{-8}\right) r_n^{-0.5}\,(1 - g_w(t)) \tag{10.22}$$

where $r_n$ is the nose tip radius in m, which is 0.110 m for the MAIUS-1 blunted nose (compare figure 10.4). Moreover $g_w$ is defined as the ratio between wall enthalpy $h_w$ and atmosphere enthalpy $h_o$. With the wall enthalpy defined as

$$h_w(t) = T_w(t)\,c \tag{10.23}$$

with $c = 960\,\mathrm{J\,kg^{-1}\,K^{-1}}$ being the wall specific heat capacity of the MAIUS hull segments and respectively $T_w$ being the wall temperature of the hull. The total enthalpy $h_0$ of the atmosphere at a given altitude is found from

$$h_0(t) = h_{air}(t) + 0.5\,v^2(t) \tag{10.24}$$

where the local enthalpy $h_{air}$ has to be calculated from

$$h_{air}(t) = T_{air}(t)\,c_{p,a} \tag{10.25}$$

where $c_{p,a} = 1006\,\mathrm{J\,kg^{-1}\,K^{-1}}$ is the assumed specific heat of air. Changes in $c_{p,a}$ are neglected. This leads to a definition of $g_w$

$$g_w(t) = \frac{c_{p,w}\,T_w(t)}{T_{air}(t)\,c_{p,a} + 0.5\,v^2(t)} \tag{10.26}$$

This will allow computation of the heating rate per unit area for the nose tip element of the rocket model as defined in section 10.2. Multiplication with the nose area will return the heat input into the volume element

$$\dot{Q}_{aero}(j=1,t) = A(1)\,\dot{q}_{sp}(t) \tag{10.27}$$

### 10.3.2 Large Angle of Attack Flat-plate Heating

As initially stated the heating rate of the remaining elements will be computed by treating the cylinder wall as a flat plate. For computation of the heating rate the calculation approach will differ depending on the angle between the free flow and the plate. The critical angle is also depending on the free stream velocity or in this case the rocket velocity. As such the criterion

$$\sin\alpha\, Ma_\infty > 1 \tag{10.28}$$

defines a large angle of attack [Sch03]. If this is the case the method for the heating rate calculation is similar to the one for the stagnation point heating. Thus the heating rate of the wall elements is defined as

$$\dot{q}_s(j,t) = C(j,t)\,\rho_{air}(t)^{N(j,t)}\,v(t)^{M(j,t)} \tag{10.29}$$

As indicated in equation 10.29 the coefficients $C$, $N$ and $M$ may differ from element to element and even over time. Therefore one will have to differentiate between laminar and turbulent flow at every time step to determine the correct coefficients.

The criterion for the turbulence of the flow is given by the Reynolds number. To avoid the complex computation of the local densities, viscosities and velocities at the hull, the Reynolds number is computed using free stream parameters.

$$Re(j,t) = \frac{v(t)\,\rho_{air}(t)\,\sum_{n=1}^{j} L_m(n)}{\eta_{air}(t)} \tag{10.30}$$

The atmospheric parameters $\rho_{air}$ and $\eta_{air}$ will change with $t$ (time of flight) and are provided by the atmospheric simulation. The velocity $v$ equals the rocket velocity.

The characteristic length of the element $j$ was chosen to be the sum of the element reference cone line length (as defined in section 10.2) from 1 to $j$, which considers the boundary layer development over the previous elements. Possible detachments of the boundary layer due to changes in the diameter are neglected.

This method will produce higher Reynolds numbers especially for the rear volume elements, than computation of the element Reynolds number by considering only the element length $L_m(j)$. The difference ranges from factor 1 to 26.3 as shown in figure 10.6 and 10.7. Logically it will differ the most for small volume elements, which are located at the rear of the rocket.

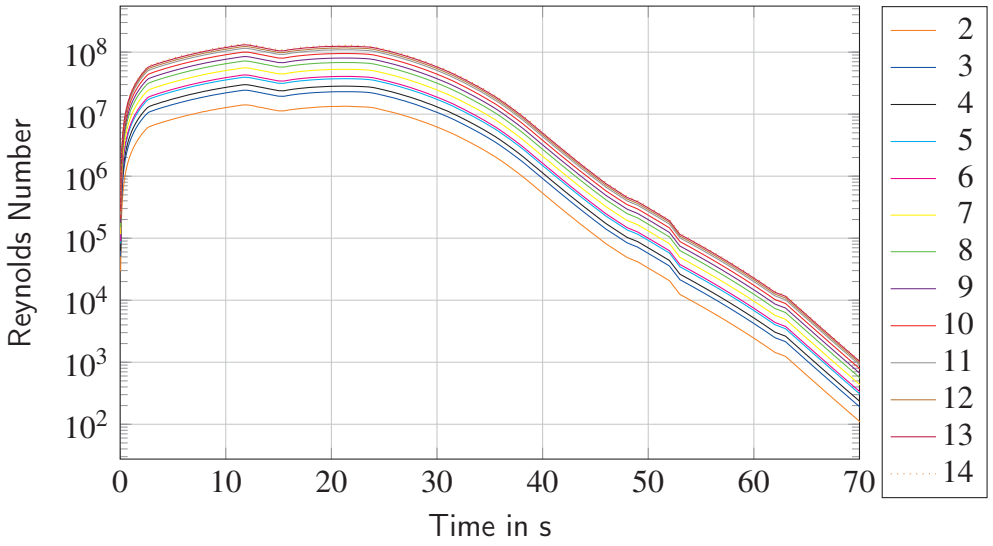


**Figure 10.6:** Reynolds numbers for the different volume elements along the hull computed from the sum of the element lengths and the free-stream conditions as described in the text. This approach was used in the computation for the heat flux presented herein.

Unfortunately it is difficult to determine a criterion for the change from laminar to turbulent flow based on free stream Reynolds numbers. Generally the transition will occur at higher Reynolds numbers, because e.g. the velocities at the wall will be smaller than the free-stream velocities. At HIFiRE-1 [Kim15] the transition Reynolds number was reported to be $1.51 \times 10^7$. In this case a different criterion was used for laminar flow

$$\log(Re(t)) <= 6.6 + 0.2\,,Ma(t) \tag{10.31}$$

this approach is based on an aerodynamic heating program from the NASA [Qui90], which is also based on free stream conditions. The factor at the left of the equation was originally $5.3 + 0.2Ma(t)$. The first factor of the left site of the equation was raised stepwise, until the results for the hull temperatures are matching the available data from other VSB-30 flights. Ultimately this factor has to be configured using data from temperature measurements performed during the MAIUS-1 flight. For this purpose MAIUS-1 is equipped with numerous temperature sensors.

Since the Reynolds number changes over time as shown in figure 10.6, a check for turbulence is performed at each time step. Based on this check one of the following approaches will be used to calculate the heat flux for large body angles. For simplicity the laminar-turbulent transition will be neglected and a "switch" between laminar and turbulent flow is assumed.

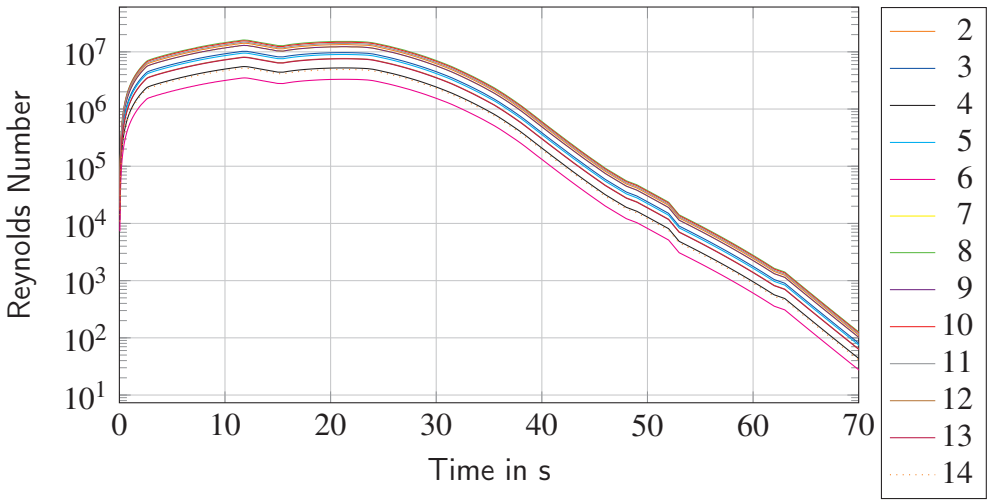


**Figure 10.7:** Alternative Reynolds number for the different volume elements along the hull computed from the respective element length only. Again free stream parameters are used for Reynolds number calculation. This numbers are given for comparison only.

### Laminar Flow

For laminar flow at large angles of attack, the approach from equation 10.21 is used. The constants are $M = 3.2$, $N = 0.5$ and

$$C(j,t) = \left(2.53 \times 10^{-9}\right) \left(\cos\alpha(j)\right)^{0.5} \left(\sin\alpha(j)\right) \left(x^{-0.5}(j)\right) \left(1 - g_w(j,t)\right) \tag{10.32}$$

here $g_w$ is defined as in equation 10.26. The body angle $\alpha$ is defined as illustrated in figure 10.4. The variable $x$ defines the distance between the stagnation point and the element end. Thus $x(j) = \sum_{n=1}^{j} L(n)$ referring to the geometric model again.

### Turbulent Flow

For turbulent flow the value of the constant $N$ is 0.8. For the other constants further distinctions have to be made based on the free stream velocity $v(t)$.

For $v(t) \leq 3962\,\mathrm{m\,s^{-1}}$ these are $M = 3.37$ and

$$\begin{aligned} C(j,t) = &\left(3.35 \times 10^{-8}\right) \left(\cos\alpha(j)\right)^{1.78} \left(\sin\alpha(j)\right)^{1.6} \left(x^{-0.2}(j)\right) \\ &\times \left(\frac{T_w(j,t)}{556}\right)^{-0.25} \left(1 - 1.11\, g_w(j,t)\right) \end{aligned} \tag{10.33}$$

For larger velocities, the constants shall be chosen as $M = 3.7$ and

$$\begin{aligned} C(j,t) = &\left(2.20 \times 10^{-9}\right) \left(\cos\alpha(j)\right)^{2.08} \left(\sin\alpha(j)\right)^{1.6} \left(x^{-0.2}(j)\right) \\ &\times \left(1 - 1.11\, g_w(j,t)\right) \end{aligned} \tag{10.34}$$

Again the check for the current velocity will be performed at every time step and the right coefficients will be chosen respectively.

### 10.3.3 Small Angle of Attack Flat-plate Heating

For small angles of attack ($\sin\alpha Ma_\infty \leq 1$) the heat flux calculated with the approach above will be zero. It is known from experience and experiments, that this is not correct. Thus a different approach is presented by the Prof. Schneider. The heat flux into the hull shall be approximated using an approach for flat plates at zero angle of attack originally proposed by White [Whi91]. This approach will use the Stanton number to calculate the heat flux into the wall in $\mathrm{W\,m^{-2}}$:

$$\dot{q}_{aero} = C_{he}\,\rho_{air}(t)\,v(t)\,c_{p,a}\,(T_{aw} - T_w) \tag{10.35}$$

with $\rho_{air}$, $v$ and $c_{p,a}$ defined as above. These parameters are thus evaluated for the free stream, although usually demanded for the edge of the boundary layer. However assuming the edge conditions to be equal to those of the free stream is a reasonable approximation.

The dimensionless heat transfer coefficient $C_{he}$, needs to be evaluated depending on the flow conditions again. For laminar and turbulent flow this coefficient is found by using the reference temperature concept. This concept evaluates all fluid/air properties at a reference temperature $T^*$, which is depending on the Mach number and wall temperature. A good correlation for computation of the reference temperature is

$$T^*(j,t) = 0.5\,T_{air} + 0.039\,Ma_\infty^2(t)\,T_{air} + 0.5T_w(j,t) \tag{10.36}$$

This will allow to use a series of simplified expressions for evaluation of the skin friction coefficient $C_{fe}$ and heat transfer coefficient $C_{he}$. It has to be noted, that this concept will produce good results for an adiabatic wall, but rather poor results for a constant hot or cold wall.

The heat transfer coefficient $C_{he}$ can be computed as

$$C_{he} = \frac{0.5\,C_{fe}}{(Pr^*)^{2/3}} \tag{10.37}$$

with a proposed constant value for $Pr^*$ for air of 0.72. To find the skin friction coefficient $C_{fe}$ and the adiabatic wall temperature $T_{aw}$ it has to de differentiated between laminar and turbulent flow.

### Laminar flow

For laminar flow conditions the skin friction coefficient is defined as

$$C_{fe}(j,t) = \frac{2\,\tau_w}{\rho_{air}(t)\,v^2(t)} = \frac{0.664\,\sqrt{C^*}}{\sqrt{Re(j,t)}} \tag{10.38}$$

with the Reynolds number as defined in equation 10.30. The Chapman-Rubesin parameter $C^*$ is giving the similarity relation between the edge or free stream properties and those at reference temperature. In this case it is defined as

$$C^*(j,t) = \left(\frac{T^*(j,t)}{T_{air}(t)}\right)^{-1/3} \tag{10.39}$$

This will allow computation of the skin friction coefficient. However to be able to find the heat flux into the wall, the adiabatic wall temperature is the last missing property, which is given as

$$T_{aw}(t) = T_{air}\left[1 + \sqrt{Pr^*}\left(\frac{\gamma-1}{2}\right)Ma_\infty^2\right] \tag{10.40}$$

where $\gamma$ is 1.4 and $Pr^*$ is again assumed to be constant equal 0.72.

### Turbulent Flow

For turbulent flow the skin friction coefficient is found from

$$C_{fe}(j,t) = \frac{0.027}{Re^{1/7}(j,t)} \tag{10.41}$$

and the adiabatic wall temperature shall be computed from

$$T_{aw}(t) = T_{air}\left[1 + (Pr^*)^{1/3}\left(\frac{\gamma-1}{2}\right)Ma_\infty^2\right] \tag{10.42}$$

With this the heat flux per unit area into the wall is defined for all possible scenarios (large/small angle of attack and laminar or turbulent flow). The absolute heat flux in Watts will require multiplication with the element surface area

$$\dot{Q}_{aero}(j,t) = A(j)\,\dot{q}_{aero}(j,t) \tag{10.43}$$

The resulting heat flux density of this computation is shown in figure 10.8. As expected the heat flux density peak is found in the stagnation point. The remaining heat flux densities are in total significantly smaller. All heat flux densities show a strong increase with a transition from laminar to turbulent flow in the first 2 seconds of flight. This first transition is barely notable in figure 10.8, because it happens very early in the flight. This first transition starts at the rear modules of the rocket and moves upstream to the front.

Due to the decrease in the density of air and a rise in viscosity after passing the first

isothermal layer of atmosphere (refer figure 10.3), the Reynolds number will start to decrease before the velocity has reached its peak. For this reason the type of flow changes again from turbulent to laminar between 25 s and 35 s, which results in a sudden decrease of the heat flux density as shown in figure 10.8. This time the transition will start at the front elements and move downstream towards the rear of the rocket.

As mentioned earlier, it is difficult to determine the exact point in time when these transition occurs. Obviously especially an early second transition (higher $Re_c$) will lead to an significantly lower heat input into the rocket walls and to lower hull temperatures.

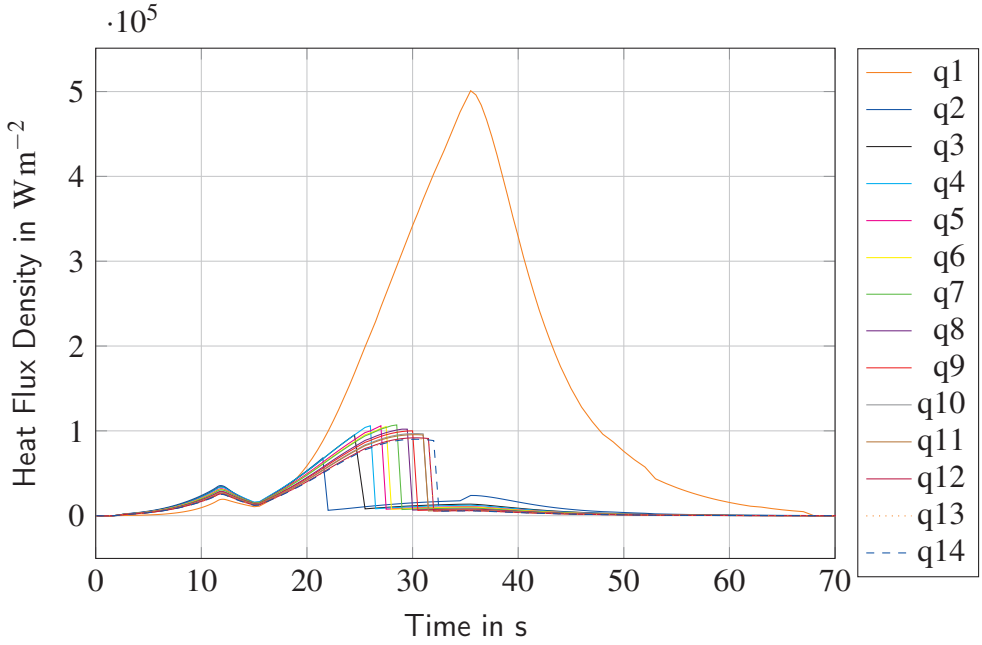


**Figure 10.8:** Heat flux densities into hull segments due to aerothermal heating

The transition criterion described earlier in the text produced reasonable results matching with the few hull temperature measurements available, however it is not necessarily the best choice. Indeed the transition might even occur earlier in the flight resulting in lower hull temperatures. Thus the values presented in figure 10.8 is considered an worst case scenario.

The code presented in this section produces good results for both laminar and turbulent flows. The uncertainties with the time of transition will result in inaccuracies in the heat flux density, anyhow the code is still suitable for an engineers approximation of the heat flux into the rocket during ascent.

## 10.4 Coupling with FEM Simulations

The rocket model as shown in figure 10.4 only uses 14 elements, which are simplified in their geometry. This will result in low accuracy of the hull temperatures computed. Thus the temperature distribution along the hull shall be solved using a transient thermal finite element simulation in ANSYS.

Making use of the axis symmetry of the rocket hull, a wedge of 36° will be simulated, which results in a resonable number of $1.5 \times 10^5$ elements. The quick changes of the heat-flux require 640 load steps to cover the 446 s from launch to beginning of re-entry. The time steps between the load steps are varied from 0.05 s at the beginning to 1 s during micro-gravity to cover the quick changes in the heat flux shortly after launch and optimize computation time during micro-gravity, where the heat flux due to aerodynamic heating is negligible. The sub-step number is controlled by ANSYS with a maximum sub-step number of 4.


**Figure 10.9:** Finite elements model of the MAIUS-1 payload including MORABA systems. The figure is showing a 36° slice with exemplary applied heat flux densities at flight time T+30s and the applied radiation into the surrounding atmosphere. The radiation is simulated using a emissivity of 0.11 and a space node temperature obtained from the atmosphere simulation. After crossing the Karman line at 100 km altitude the space node temperature is assumed to to be 3 K

A component is created covering all surfaces of the detailed model, which match the equivalent element in the volume model. The heat flux density as plotted in 10.8 is applied as thermal load in 640 load steps onto the surfaces of the component. Thus 14 loads are applied on the model as shown in figure 10.9.

Solving the simulation will return the temperature along the hull with high spacial accuracy. The results of the FEM simulation are discussed in the following chapter.

## 10.5 Expected Temperatures at Rocket Hull

Figure 10.11 shows the temperature distribution at the hull of the MAIUS-1 payload at some important events during the flight. Especially at the beginning, there are hot spots at the nose tip and the European Recovery System (ERS) as well as at the motor adapter at the rear of the rocket.

Areas with larger wall thickness, as the e.g. the RADAX flanges or the flanges for mounting the instrument platforms, are colder than regions with low wall thickness, because of the higher heat capacity in these regions. The same applies for the lower region of the ERS, where the wall thickness is 6 mm.

Above 88 km altitude, when the heat flux due to aerodynamic heating is negligible, the temperature in the hull segments equalizes, which is notable by the increasing minimum temperature and the decreasing maximum temperature in the temperature chart in figure 10.11

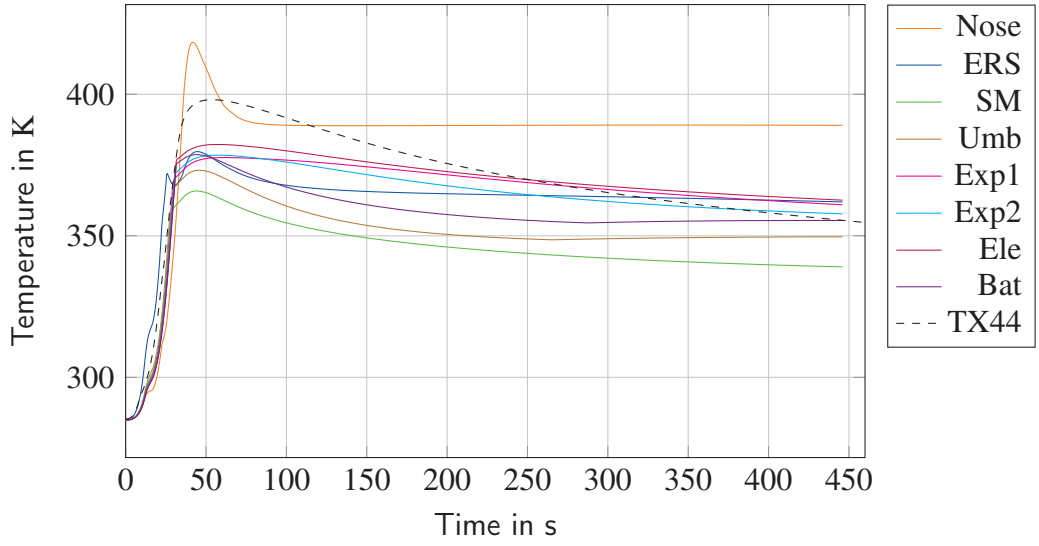


**Figure 10.10:** Maximum temperatures of the hull segments of the different MAIUS-1 systems. The systems are sorted from top to bottom. For comparison the measured temperature at the european recovery system (ERS) during the TEXUS 44 flight is given as well.

The maximum temperatures of the hull segments of the MAIUS-1 systems are plotted in figure 10.10 from the launch to the begin of the re-entry. Again the highest temperatures are found at the stagnation point at the nose tip. The lower part of the european recovery system (ERS) is slightly colder. During the Texus-44 mission the skin temperature has been measured at the ERS. Although Texus-44 was using an Ogive nose cone, these temperatures are also plotted in figure 10.10 (TX44) for comparison. Although the curves are not matching perfectly the results presented are a reasonable approximation. Unfortunately no data from blunted nose cones is available, which would help to improve the simulation and to find a better criterion for laminar-turbulent transition.

In MAIUS-1 a total of 6 temperature sensors will be placed along the scientific payload hull. The measurements obtained from the MAIUS-1 flight will help to optimize the simulation.

For the thermal design of the MAIUS-1 scientific payload systems, the inner temperatures of the hull segments and the temperatures at the instrument platform flanges are of interest. Those will have an impact on the heat input of the scientific payload systems by conduction and convection as described in the following sections. For clarity these temperature courses will be given directly in these sections.

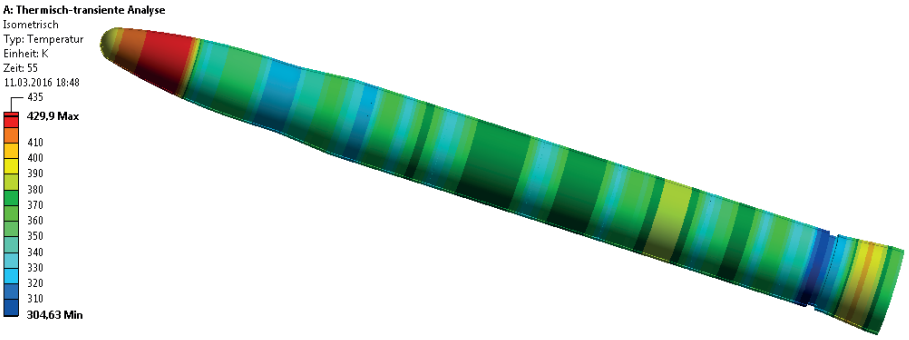


**(a)** Temperatures at t=55 s (Peak of Temperature)

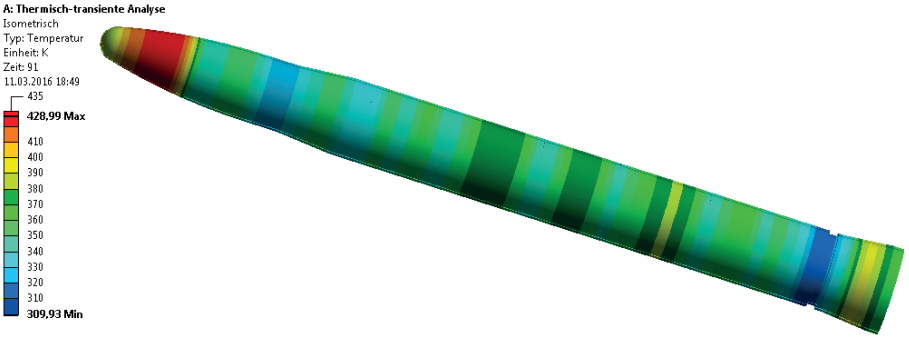


**(b)** Temperatures at t=91 s (Beginn of Microgravity)

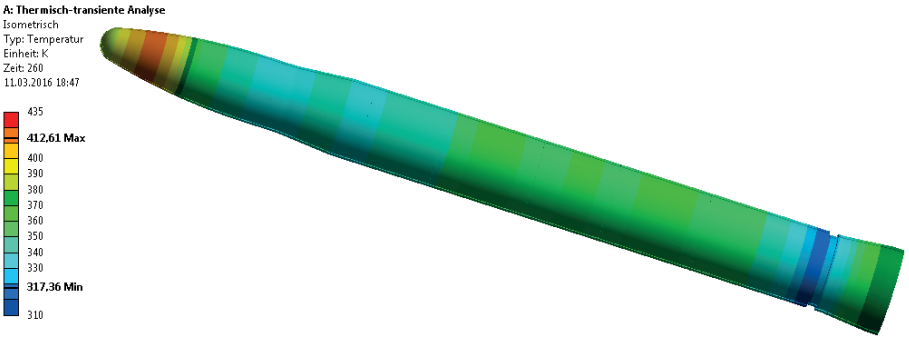


**(c)** Temperatures at t=260 s (Apogee)

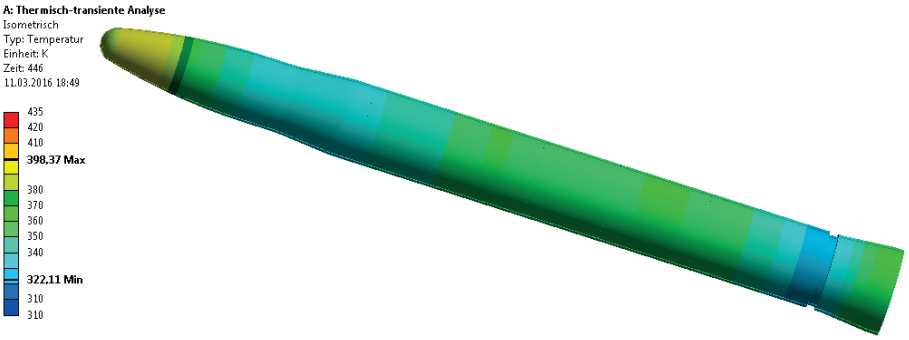


**(d)** Temperatures at t=440 s (Begin of re-entry)

**Figure 10.11:** Temperature distribution along the hull of MAIUS-1 payload during ascent and microgravity phase. In the early phase of the flight regions with larger wall thickness are colder due to their higher heat capacity.

# 11
# Heating of Payload Interior

With a known temperature distribution along the scientific payload hull, the impact of these temperatures on the payload systems and the enclosed air will be estimated in this chapter.

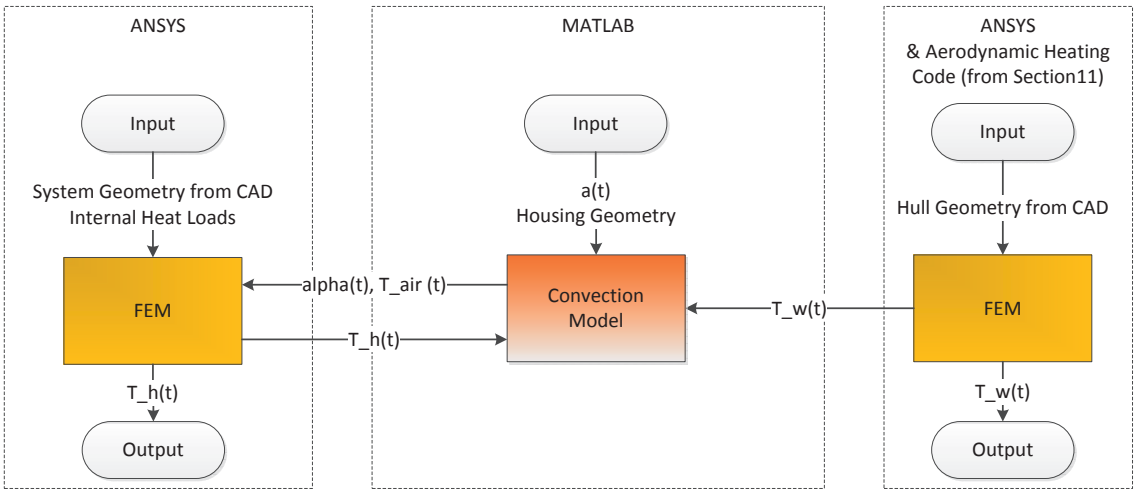


**Figure 11.1:** Schematic of the computation approach for the heating of the internal air and the heat transfer coefficient of natural convection. Both parameters are ultimately determined by iterating between the MATLAB code and a FEM analysis of the effected MAIUS system.

In general heat from the rocket hull can be transported to the housing of the payload systems by conduction, convection or radiation. While conduction and radiation are present during the entire flight, convection will only have a considerable contribution to the overall transfered heat on ground and during ascent of the rocket. All three transfer mechanisms and their integration into the system simulations presented in chapter 12 are discussed in the following.

## 11.1 Thermal Convection to MAIUS-1 systems

Since the air volume inside the scientific payload is capsuled from the exterior only natural convection will occur inside the payload. During ascent this effect will cause the air to be heated at the outer hull of the rocket as discussed later in this section.

The flow or current of natural convection is caused by density inhomogeneities due to e.g. local temperature differences. The flow of natural convection is characterized by the dimensionless Grashof number $Gr$, which puts the buoyancy force in relation to shear forces caused by the fluids viscosity [Pol05].

$$Gr = \frac{g\,\beta\,(T_w - T_\infty)\,L^3}{\nu^2} \tag{11.1}$$

As equation 11.1 illustrates, natural convection is negligible in micro-gravity, because the previously mentioned currents will not establish. Thus in micro-gravity the enclosed air will transport heat only by conduction form the rocket hull to the wall of the system housing.

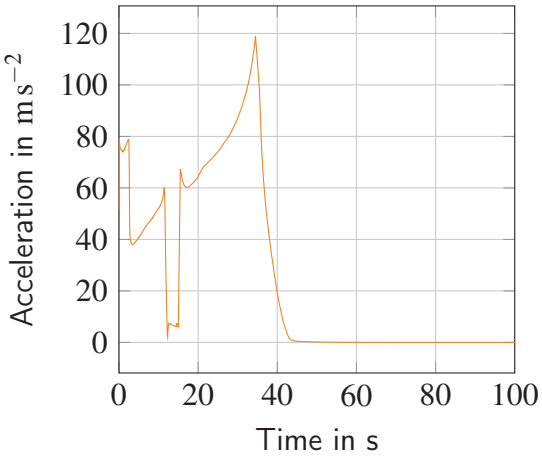


**(a)** Predicted acceleration of MAIUS-1

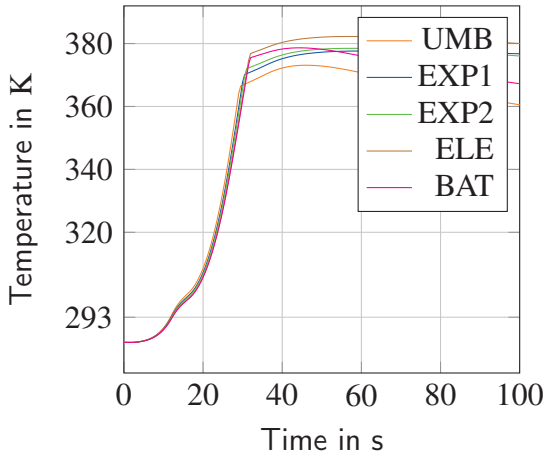


**(b)** Temperature at the inside of the rocket hull of MAIUS-1 payload modules obtained from the code presented in section 10

**Figure 11.2:** Input data for natural convection computation during ascent of MAIUS-1

In the laboratory and during ascent the previously mentioned currents will establish and the heat transfered from the hull walls to the air is given as

$$Q_{air} = \alpha A_{w,r}\,(T_w - T_{air}) \tag{11.2}$$

where $T_w$ is the wall temperature at the inside of the hull modules as obtained from the code described in section 10 and plotted in figure 11.2b. The heat transfer coefficient of

the natural convection $\alpha$ is defined through the Nusselt number as

$$\alpha = \frac{Nu\,\lambda_{air}}{L} \tag{11.3}$$

where $L$ is the length of the cylindric wall and $Nu$ the Nusselt number. To determine the Nusselt number for natural convection, the Rayleight number has to be calculated first, from

$$Ra = GrPr = \frac{g\beta(T_w - T_\infty)L^3}{\nu a} \tag{11.4}$$

where the characteristic length is the cylinder length $L$. Assuming the enclosed air to be an ideal gas, the coefficient of thermal expansion $\beta = 1/T_\infty$. The kinematic viscosity of air at 20 °C is $18.3 \times 10^{-6}\,\mathrm{m^2\,s^{-1}}$. For simplicity changes in viscosity due to temperature changes shall be neglected. The thermal diffusivity is $20.06 \times 10^{-6}\,\mathrm{m^2\,s^{-1}}$. In the laboratory the acceleration $g$ is equal to the earth gravitational acceleration $g_0 = 9.81\,\mathrm{m\,s^{-2}}$, however during motor burn the acceleration will be significantly larger, measuring up to $13 \times g_0$ as shown in figure 11.2a. The resulting Rayleight and Grashof number are plotted in figure 11.3a for the wall temperatures presented in section 10.5.

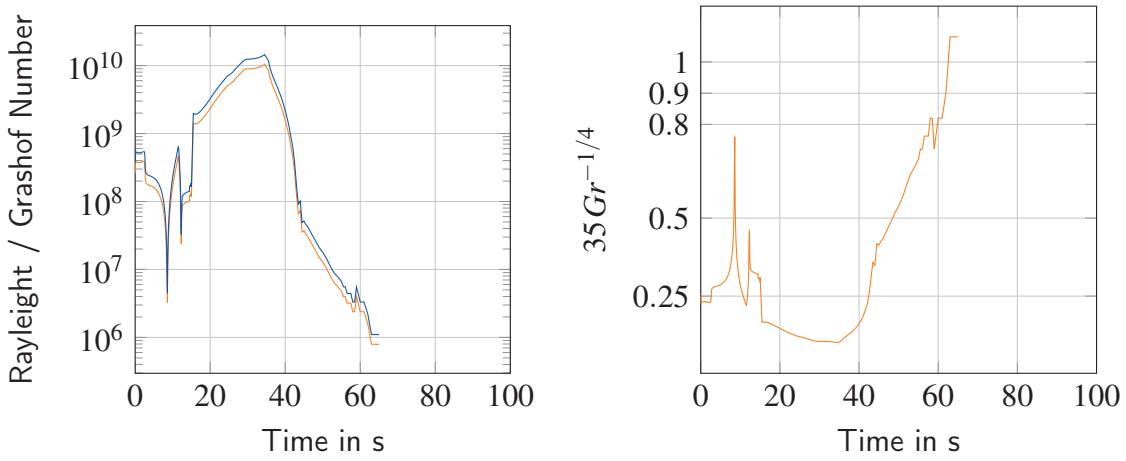


**(a)** Rayleight (orange) and Grashof (blue) number for heat flux computation from outer hull to system housing due to natural convection

**(b)** Criterion to check if the vertical cylinder can be treated as a vertical wall. The ratio between $D$ and $H$ is 0.98 for the module EXP 2. Thus the equations are valid until $t = 52\,\mathrm{s}$

**Figure 11.3:** Exemplary Rayleight and Grashof number and flat plate criterion for the module EXP 2 with a length of 500 mm

To determine the Nusselt number, a vertical cylinder can be treated as a vertical wall, if the following constraint is met [Pol05]

$$\frac{D}{H} \geq 35\,Gr^{-1/4} \tag{11.5}$$

Moreover it has to be differentiated between laminar and turbulent flow. The correlation for laminar flow is given as

$$Nu = 0.68 + 0.668\, f(Pr)\, Ra^{1/4} \tag{11.6}$$

and is only valid for vertical plates and characteristic Rayleight numbers between $10^4$ and $10^9$ [Pol05]. For larger Rayleight numbers a turbulent flow is present and the Nusselt number has to be computed from [Pol05]

$$Nu = 0.15\, [f(Pr)]^{4/3}\, Ra^{1/3} \tag{11.7}$$

The Prandtl number is assumed to be 0.72 for air. Respectively the correction term $f(Pr)$ is given as

$$f(Pr) = \left[1 + (2\,Pr)^{-9/16}\right]^{-4/9} = 0.7673 \tag{11.8}$$

If the criterion of equation 11.5 is not met or the Rayleight number drops below $1 \times 10^4$, the equations mentioned above are not valid and it is assumed that heat is only transported by conduction, because of the low gravitational acceleration and the leak of temperature gradient induced currents. The heat flux by conduction is significantly lower than the one by natural convection, it reduces from 100 W to 200 W transfered by natural convection to values between 20 W to 30 W.

For the calculation of the heat transfer by conduction the finite volume method will be used as it has been done in section 10.2. Here the hull segments, the air and the system housing will be modeled as one element each. For simplicity it shall be assumed, that the system housings are of cylindric shape with diameter $r_h$ as well. Cylinder Radius and length shall be representative for the actual system housing geometry. Especially the gap between system housing wall and rocket hull shall match. The radial heat flux through the cylindric wall and the rapid change in heat conductivity between the rocket hull or system housing made of aluminum ($\lambda_w = 145\,\mathrm{W\,m^{-2}\,K^{-1}}$) and the air ($\lambda_w = 0.0262\,\mathrm{W\,m^{-2}\,K^{-1}}$) has to be considered in the heat flux equation. Thus equation 10.18 will change to

$$\dot{Q}_{air}(j,t) = A_{w,r} \left[ \frac{0.5\,(r_i + r_a)\,\ln\left(\frac{r_a}{r_i}\right)}{\lambda_{w,r}} + \frac{0.5\,(r_i + r_h)\,\ln\left(\frac{r_i}{r_h}\right)}{\lambda_{air}} \right]^{-1} (T_{w,r}(j,t) - T_{air}(t)) \tag{11.9}$$

where $T_w(j,t)$ is the wall temperature of the scientific payload hull segments, $r_i$ is the inner radius and $r_a$ the outer radius of the hull segment.

While a convective boundary condition is easy to implement into an ANSYS simulation, implementation of a (virtual) air body to consider the heat flux is requiring more effort and usage of APDL code. Thus the heat conduction will be considered as a convective heat transfer as well. This is done by determining a virtual heat transfer coefficient $\alpha$.

Comparison of equation 11.2 and 11.9 will show that

$$\alpha(j,t) = \left[ \frac{0.5\,(r_i + r_a)\,\ln\left(\frac{r_a}{r_i}\right)}{\lambda_{w,r}} + \frac{0.5\,(r_i + r_h)\,\ln\left(\frac{r_i}{r_h}\right)}{\lambda_{air}} \right]^{-1} \tag{11.10}$$

if natural convection can be neglected. Since the system housing wall thicknesses are similar to those of the rocket hull, $\alpha$ is assumed to be identical at the system housing. With this the heat transfer coefficient $\alpha$ is defined for the entire time of flight of the rocket. However to determine the heat flux from the hull segments to the air and onwards to the walls of the MAIUS-1 system housing, the air temperature has to be known. Moreover the air temperature is needed to apply a convective heat flux onto the system housing walls in the system thermal simulation performed in ANSYS (compare 12.3 to 12.6). Thus the air temperature will also be computed with the script described in this section.

The gas inside the payload is a mixture of 80 % nitrogen and 20 % oxygen. Both molecules are linear two-atomic molecules, thus they have 5 degrees of freedom ($f = 5$). Since the payload is hermetically sealed as described in section 7.1.3, the gas volume will not change over time and the heating of the enclosed air can be considered an isochore process.

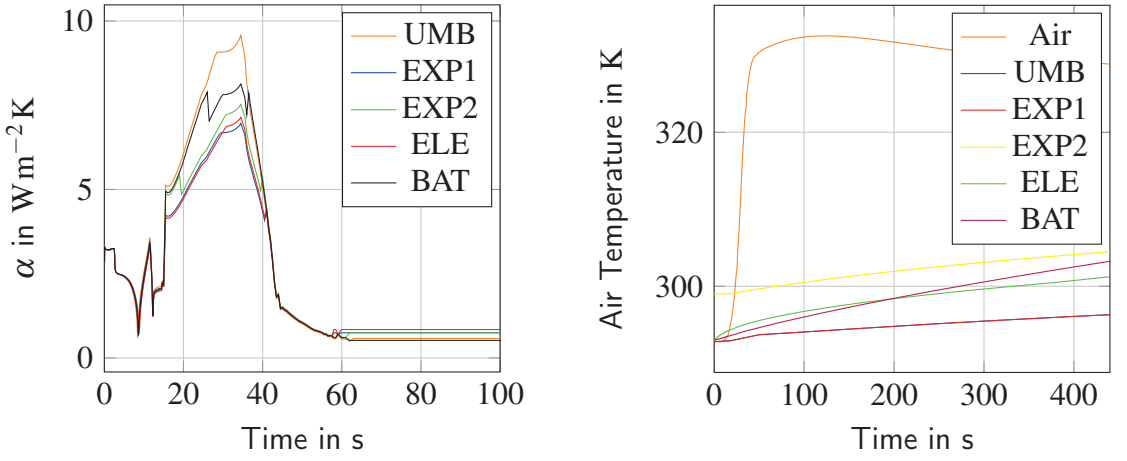


**(a)** Heat transfer coefficient for the 5 modules of the scientific payload

**(b)** Housing and predicted air temperature inside scientific payload during ascent

**Figure 11.4:** Heat transfer coefficient and air temperature of the scientific payload of MAIUS-1

The gas shall be treated as ideal gas, thus the isochore specific heat capacity $c_v$ is defined as

$$c_v = \frac{1}{2} f R = 20.785\,\mathrm{J\,mol^{-1}\,K^{-1}} \tag{11.11}$$

where $R = 8.314\,\mathrm{J\,mol^{-1}\,K^{-1}}$ is the universal gas constant. Moreover the amount of air in mol $n$ in the payload can be calculated from the ideal gas law as

$$n = \frac{p_0 V}{R T_0} \tag{11.12}$$

where $p_0 = 1100\,\text{hPa}$ is the initial pressure and $T_0$ the initial temperature of the gas in the payload. The volume $V$ is given from the geometry. With a known amount of gas $n$, the heating of the gas inside the payload can be found from

$$T_{air}(t+\Delta t) = \frac{\left(Q_{air} + Q_{housing}\right)\Delta t}{n\,c_v} \tag{11.13}$$

with $Q_{housing}$ being the amount of heat transfered between the system housing and the air. It is defined by the heat transfer coefficient $\alpha$, the area of the system housing facing the gas $A_{w,s}$ and the system housing wall temperature $T_{w,s}$

$$Q_{housing} = \alpha A_{w,s}\left(T_{w,s} - T_{air}\right) \tag{11.14}$$

The air temperature influences the heat fluxes $Q_{housing}$ and $Q_{air}$, thus these equations have to be solved iteratively. This will result in an air temperature course as presented in figure 11.4b. The air temperature is assumed to be homogeneous in the payload volume, spacial changes in temperature are neglected.

A similar calculation is necessary for the estimation of the heat transfer coefficient on ground in the laboratory. While the geometry will not change with respect to the previously performed calculation, the gravitational acceleration in this setup is constant $g = 9.81\,\text{m}\,\text{s}^{-2}$. Moreover the hull temperature is expected to be constant at ambient temperature, since the outside area as well as the heat transfer coefficient at the outside of the hull, are significantly larger than the parameters inside the payload. In the laboratory the ambient temperature is typically controlled to be 293 K.

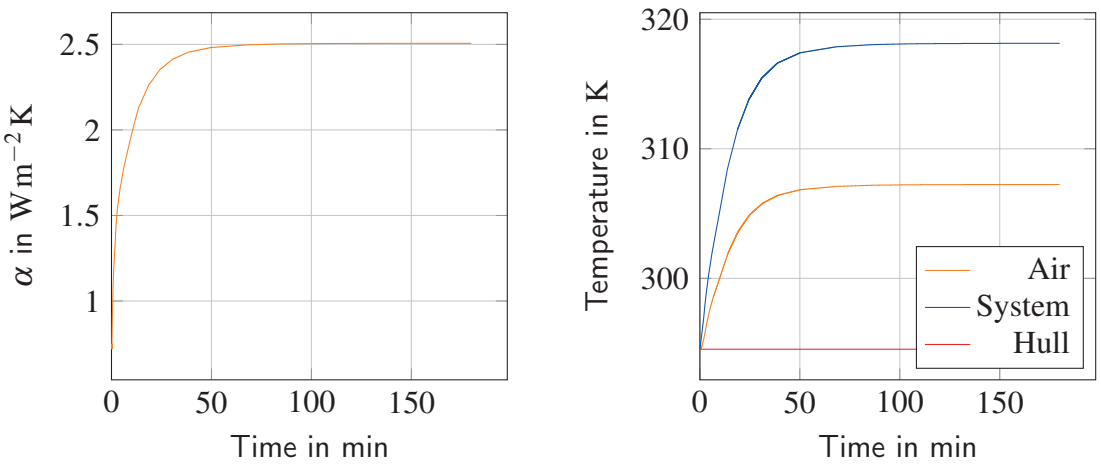


**(a)** Heat transfer coefficient for the 5 modules of the scientific payload

**(b)** Housing temperatures and the predicted air temperature inside scientific payload

**Figure 11.5:** Heat transfer coefficient and air temperature of the scientific payload of MAIUS-1 in the laboratory for a worst case system housing temperature

The system housing however will heat up over time to an equilibrium temperature. This

temperature course is simulated using an initial guess for $\alpha$. With these temperatures another run of the calculations defined above is performed.

As shown in figure 11.5b a equilibrium air temperature will establish after 3600 s of operation. For a temperature gradient between hull and system housing of 20 K, the air temperature inside the payload will rise by 11 K. Once the equilibrium temperatures have developed the heat transfer coefficient is also constant as shown in figure 11.5a.

For a precise computation of the air temperature and heat transfer coefficient, the calculations and FEM simulations have to be performed iteratively until the change in the solutions for the heat transfer coefficient is below 1 %.

## 11.2 Thermal Conduction to MAIUS-1 systems

In micro-gravity usually the biggest part of the heat is transported from the outer rocket hull to the instrument platforms by conduction. The instrument platforms are connected to the outer hull by six brackets and 12 rubber dampers as described in section 7.1.2.

By nature rubber as an isolation material is a bad conductor. In literature the thermal conductivity of rubber is ranging from $\lambda_{rub} = 0.045\,\mathrm{W\,m^{-1}\,K}$ to $\lambda_{rub} = 2.5\,\mathrm{W\,m^{-1}\,K}$ depending on the type of rubber, its hardness and whether it has been vulcanized or not. Since two steel plates with threads are vulcanized into the rubber and the type of rubber of the mounting is unknown, the actual conductance of the mounts has been determined experimentally.

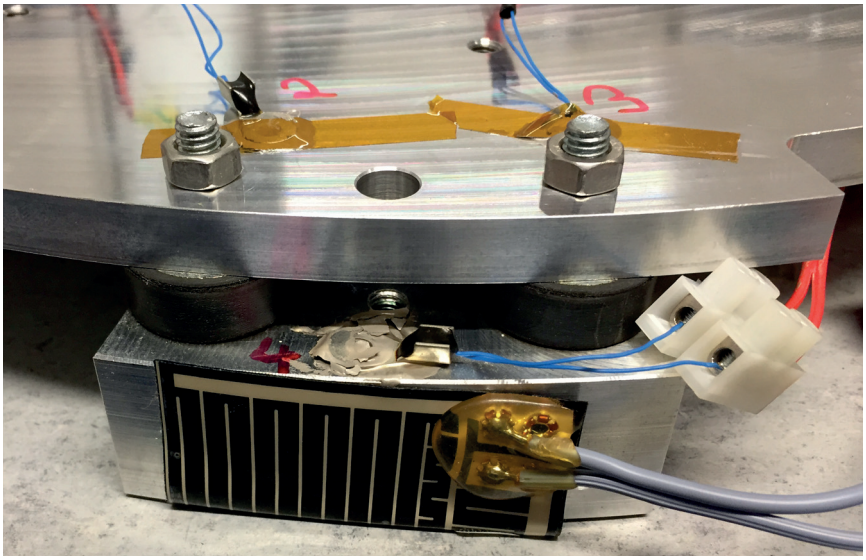

**Figure 11.6:** Test setup to measure thermal conductivity of instrument platform suspension

This has been done with the simple test setup shown in figure 11.6. A bracket has been mounted to a instruments platform with a defined torque of 10 N m. The bracket is heated

with a foil resistance heater on the face which will be in contact with the hot rocket hull. To minimize the effect of convection the instruments platform and the bracket have been wrapped into aluminum foil during the test.

The heater is powered with 20 V for 2 hours. This results in a meassured power consumption of 6.8 W, which reduces to 5.8 W after 1200 s, because of the increasing resistance of the heater. After 2400 s the measured power reaches its minimum of 5.4 W which is maintained until the end of the test.

The temperatures are monitored using 10 kΩ NTCs. The sensors are mounted using thermal glue at the top of the bracket (Sensor 4) and at the top of the instrument platform close to the two mounting points (Sensor 2 and 3). A fourth sensor is used to measure the ambient temperature as a reference.

The results are presented in figure 11.7. The temperature of the bracket reaches 332.20 K after 7834 s, while the plate temperature rises only from 294.0 K (ambient temperature) to 298.5 K. Thus the temperature gradient between plate and bracket are 33.7 K. This indicates a bad conductance from the bracket to the plate as expected.

To guarantee a proper simulation of the conductance, the test case was simulated using a transient-thermal FEM analysis in ANSYS. Usage of the thermal conductivity for rubber proposed in literature $\lambda_{rub} = 0.16\,\mathrm{W\,m^{-1}\,K}$ results in a significantly higher absolute temperature of the bracket of 473.4 K and a temperature gradient between plate and bracket of 175.2 K. Therefore the actual conductivity has to be significantly higher.

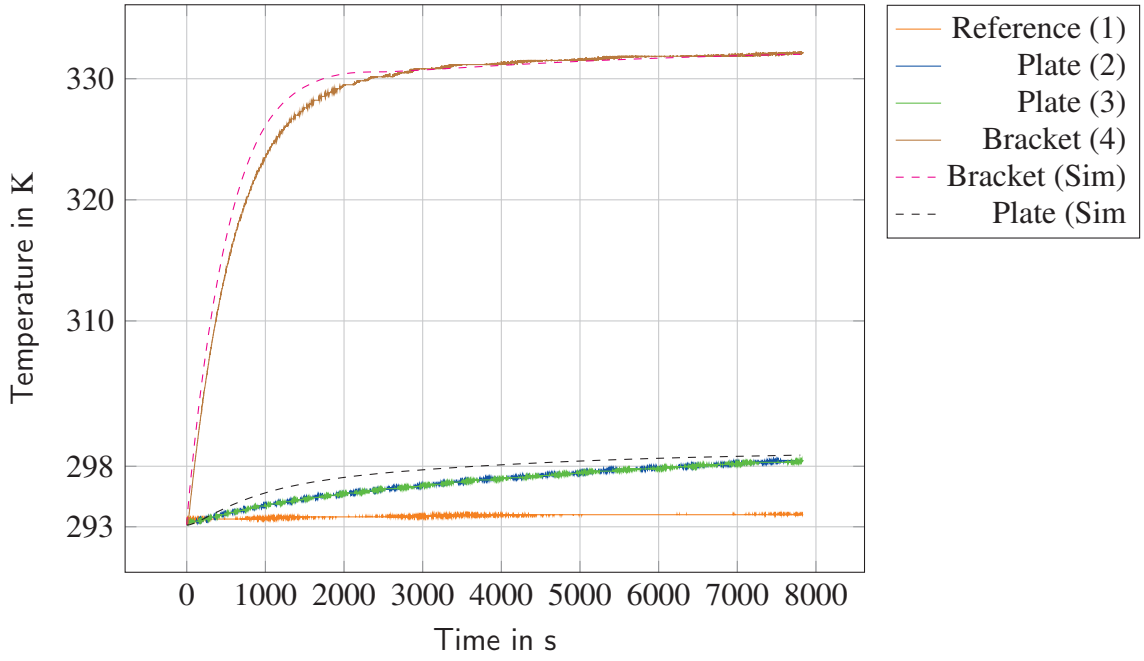


**Figure 11.7:** Measured and simulated instrument platform and bracket temperatures. Measured data for sensors position 1 to 4 according to figure 11.6. Simulated values (Sim) for $\lambda_{rub} = 1.6\,\mathrm{W\,m^{-1}\,K^{-1}}$.

A stepwise increase of the thermal conductivity in the material properties of the rubber in ANSYS was used to find a suitable approximation. For $\lambda_{rub} = 2\,\mathrm{W\,m^{-1}\,K}$ a good correlation is found for the bracket temperature ($T_{max} = 333\,\mathrm{K}$). However the plate temperature is simulated to be 307 K, which is 9 K above the measured value. This is most likely caused by convection or conductance into the surrounding air and/or the table.

For this reason a convective heat flux to the surrounding air is added to the simulation with an air temperature of 293.15 K and a heat transfer coefficient of $4.3\,\mathrm{W\,m^{-2}\,K^{-1}}$.This gives a good correlation for the plate temperature. Additionally the thermal conductivity of the rubber mounts has to be reduced to $1.6\,\mathrm{W\,m^{-1}\,K^{-1}}$ to achieve a good match between measurement and simulation for both the plate and bracket temperature as shown in figure 11.7.

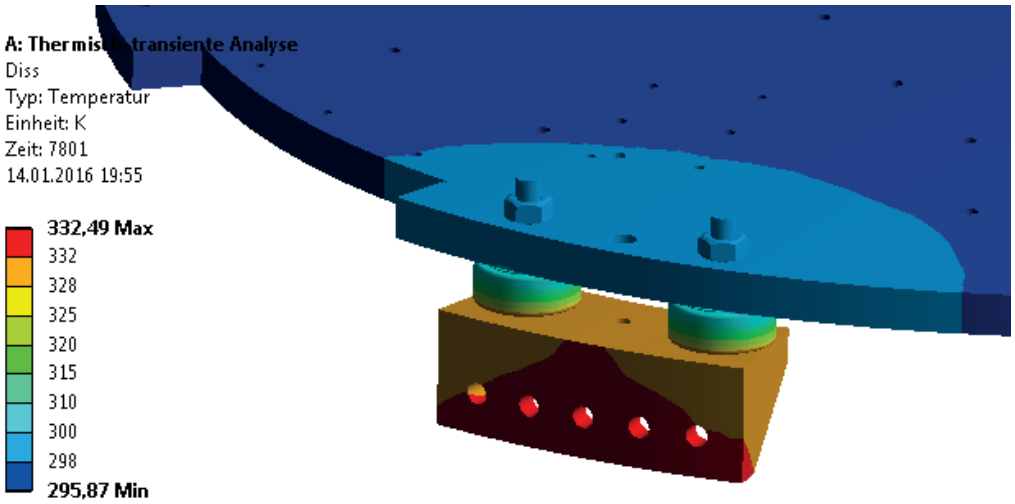


**Figure 11.8:** Spatial temperature distribution for simulation of bracket test setup

The determined conductivity is used to simulate the heat transport by conduction between the rocket hull and the instruments platform in the simulations for the design of the thermal control system.

## 11.3 Thermal Radiation to MAIUS-1 systems

The last missing method to transport heat from the rocket hull to the system housings is radiation. Calculation of the heat flux by radiation usually requires the determination of view factors between the planes of the system housing and the rocket hull.

Assuming that the system housing is of cylindric shape and concentric with the surrounding rocket hull segment, a much simpler approach for radiation heat transfer between a convex body and its enclosing walls can be used to approximate the heat flux [Pol05].

$$\dot{Q} = A_h\, s_{rh} \left(T_r^4 - T_h^4\right) \tag{11.15}$$

where $A_h$ and $T_h$ corresponds to the system housing and $A_r$ and $T_r$ to the rocket hull segments. The mutual exchange coefficient $s_{rh}$ for this special case is defined as

$$s_{rh} = \frac{\sigma}{\frac{1}{\varepsilon_h} + \left(\frac{1}{\varepsilon_r} - 1\right) \frac{A_h}{A_r}} \tag{11.16}$$

Setting the Stephan Boltzmann constant to $\sigma = 5.669 \times 10^{-8}\,\mathrm{W\,m^{-2}\,K^{-4}}$ and the emissivity of both aluminum bodies to $\varepsilon_h = \varepsilon_r = 0.11$ will allow to get a good approximation of the heat input into the MAIUS-1 system housings by radiation.

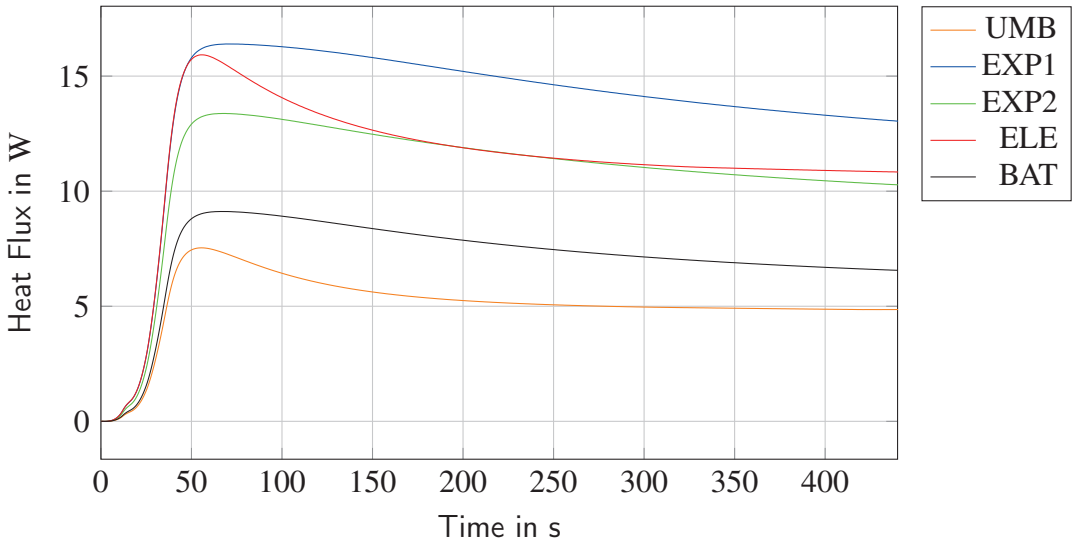


**Figure 11.9:** Radiation heat flux into the system housings sorted by hull segment names. The umbilical hull segment (UMB) will radiate onto the pumping system, the EXP1 module onto the magnetic shielding, the EXP2 module onto the laser system, the ELE hull onto the electronics system and the BAT module onto the battery system and power distribution.

As shown in figure 11.9 the total heat fluxes into the system housing for hull temperatures as shown in figure 11.2b are below 17 W, thus this portion of the overall heat input will be neglected.

# 12
# Thermal Design and Control System

## 12.1 Thermal Control System Concept of the MAIUS-1 Payload

The MAIUS1 thermal control system is designed for two operation modes of the payload: laboratory and flight operation. During lab operation the payload is temperature controlled by two separate water cooling circuit regulating the heat sink temperature as shown in the functional diagram 12.2. Moreover three fans are used to cool the components inside the electronics and battery enclosure.

The upper circuit keeps the temperature of the laser heat sink stable to $299 \pm 1$K, to ensure a reliable operation of the peltier elements, which control the micro optical bench and thus the laser diode temperature. The lower circuit controls the temperatures of the two electronic system heatsinks and the battery heatsink. In this circuit the equilibrium temperature of the heat sinks is required to be below 323 K to ensure a sufficient temperature gradient between the circulated air and the heatsink to guarantee that the dissipated heat of the PCBs is deducted. Since both water cooling circuits are designed to keep the temperatures constant, a continuous operation of the payload systems is possible as long as water cooling is provided.

During flight operation the heat is stored in the aluminum heatsinks of the systems. The heatsinks are designed to guarantee a time of operation of at least 447 s within the required temperature range as defined in section 6.5. The threshold of 447 s equals the estimated overall flight time from lift-off to re-entry as shown in the time event list in section 5.5. The detailed design of the system heatsinks and thermal control systems of the laser, battery and electronic system is presented in chapter III. A thermal simulation of these systems and its results are presented in section 12.3 to 12.6 of this chapter.

The water cooling is not only used in the laboratory, but also prior to the launch, while the payload is in the launch tower. This allows continuous operation within the tower to make final adjustments and to react on possible countdown holds. Moreover the heat sink temperature at the beginning of the flight can be adjusted very precisely.

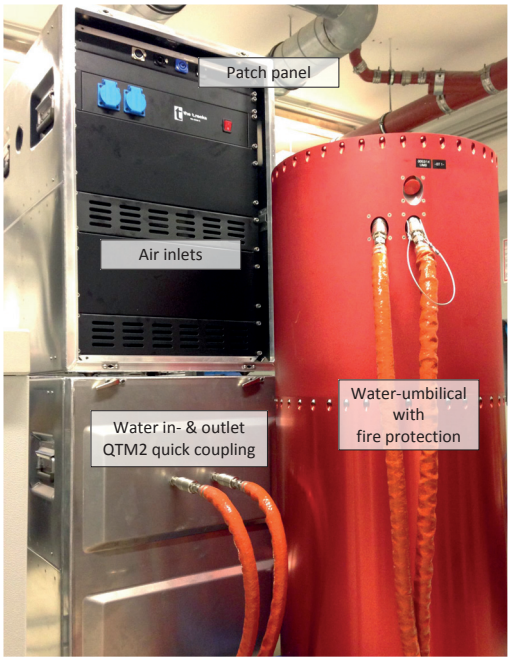


(a) Two thermostats in cases with water umbilical connected to a payload module

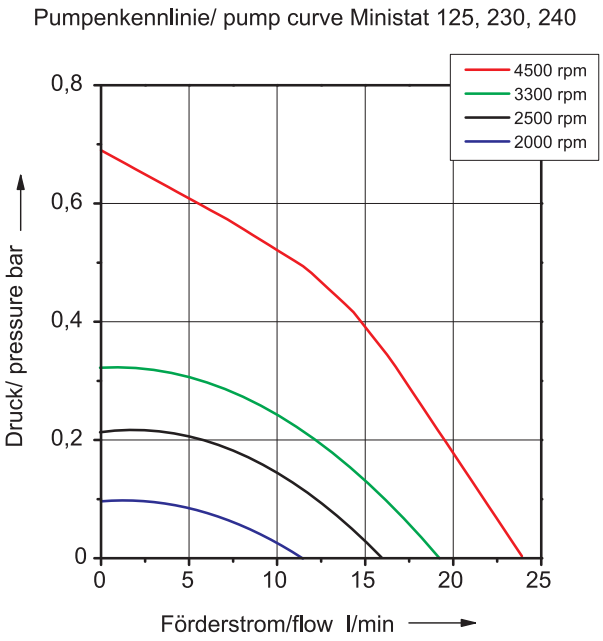


(b) Delivery pressure depending on flow in l per min and speed of pump in Rpm [Hub14]

**Figure 12.1:** MAIUS water cooling ground support equipment

As described in section 7.2.1 the water for cooling will be provided by a total of four umbilicals until lift-off. These umbilicals are connected to two compact cooling bath circulation thermostats integrated into two 19" flight case. The thermostats are equipped with a bath with a fixed volume of water. An air-cooled refrigeration machine controls the temperature of the water inside the bath.

For temperature control of the laser system a Huber Ministat-125 is used. This device offers a bath volume of 2.75 L, a heating capacity of 1 kW and a cooling capacity of 300 W at temperatures between 20 °C and 100 °C. The electronic system is cooled by a Huber Ministat 240, a larger device of the same series, offering a bath volume of 4.9 L, a heating capacity of 2 kW and a cooling capacity of 600 W temperatures between 20 °C and 100 °C.

Both devices are using the same pumps. They are equipped with a suction pump with a maximum delivery rate of 20 L $\text{min}^{-1}$ at a delivery rate pressure of 400 hPa and a pressure pump with a maximum delivery of 27 L $\text{min}^{-1}$ and a delivery pressure of 700 hPa. The actual delivery rate and delivery pressure depends on the rotational speed of the pump which can be adjusted in a range between 1500 and 4500 Rpm. The pump characteristics are shown in diagram 12.1b.

As illustrated in figure 12.1a the flightcase is made of aluminum and is designed to withstand the rough environment inside the launch tower. The Umbilical is connected to the chiller flight case with a quick coupling connector (Swagelok QTM) as used on the rocket side. The quick coupling stem is directly integrated in the aluminum cover of the case.

This protects the chiller itself from the rocket exhaust, since this side of the case will directly face the rocket.

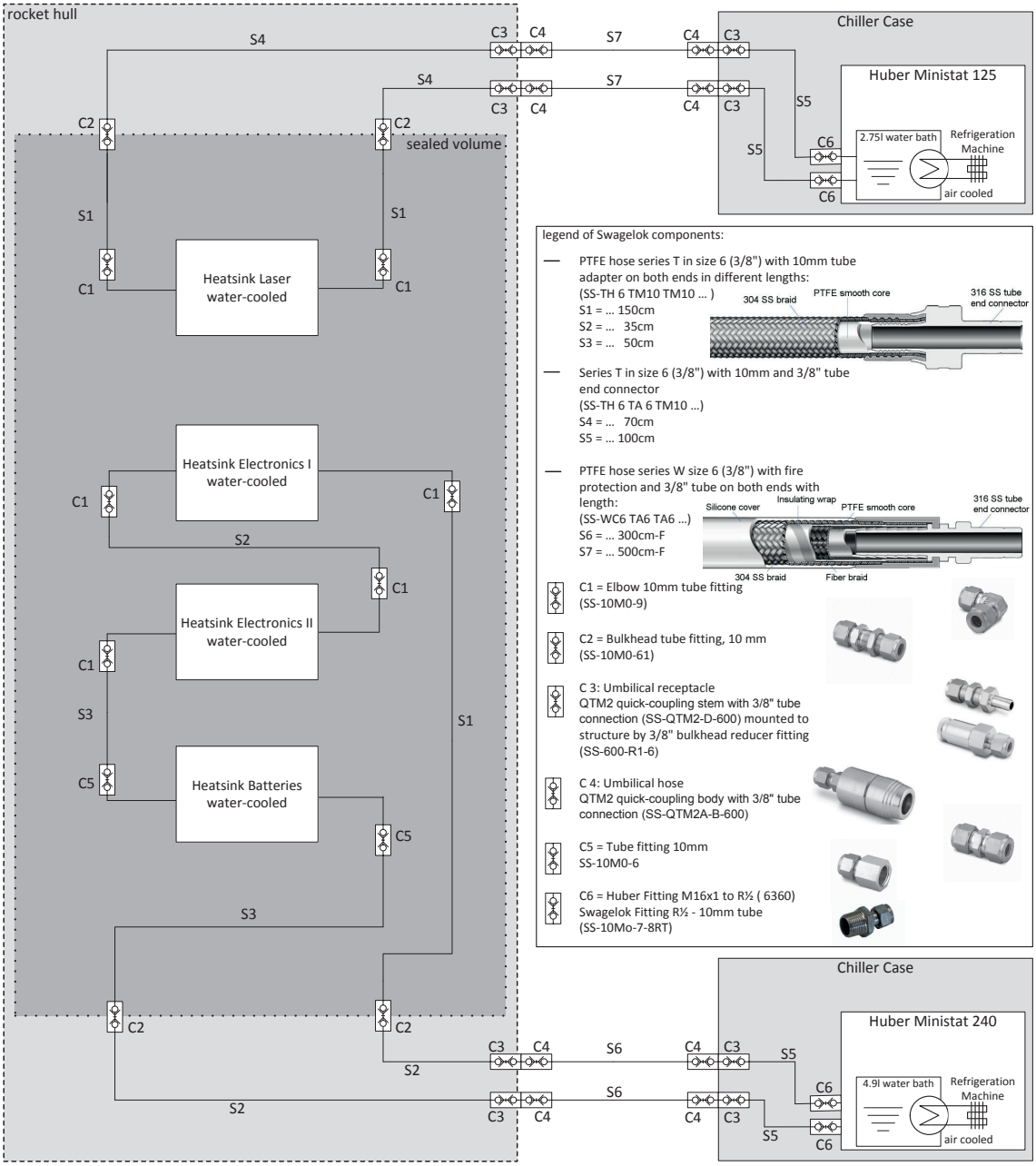


**Figure 12.2:** Functional diagram of the two MAIUS water cooling circuits naming each component. The dark gray area indicates the pressurized volume of the payload, while the light gray box represents the payload itself. The two chiller cases will be positioned next to the payload on the launch tower.

The electrical connections are situated on the opposite side of the case at an 19" patch panel. This patch panel is equipped with an ethernet port for remote control of the chiller, an XLR 4pin connector to connect with the remote PT100 temperature sensors at the elec-

tronic system and laser system heat sink and a PowerCon connector for 240 V power supply. This will allow full operation of the chiller from the block house, including setting new temperatures and disabling the pump.

## 12.2 Effective Flow and Heat Transfer Coefficient of the Water Cooling Circuits

The heat transfer coefficient and thus the amount of heat, that can be transfered by the cooling fluid is strongly depending on the mass flow through the cooling circuits. This flow is limited by the pressure losses in the circuit caused by wall friction in the tubes and hoses as well as pressure losses in the different fittings of the cooling circuit.

Due to the high number of fittings in both water circuits, a simulation of the water losses is time consuming and rather inaccurate. Thus the losses have been minimized in the design process by minimizing the hose and pipe length and the number of fittings used and performing simple numeric simulations. Subsequently measurements have been performed before and after the installation of the cooling circuit into the payload to ensure a sufficient mass flow for cooling of the systems. The measurement methods and results as well as the resulting heat transfer coefficient are given in this section and shall be used as an input to the system level thermal simulations and designs.

### 12.2.1 Flow Measurement Device

A water flow meter sensor BIO TECH FCH-C-Ms-N has been used to measure the effective flow in the cooling circuit. The measurement is based on a small turbine in the sensor, rotated by the fluid passing the sensor.

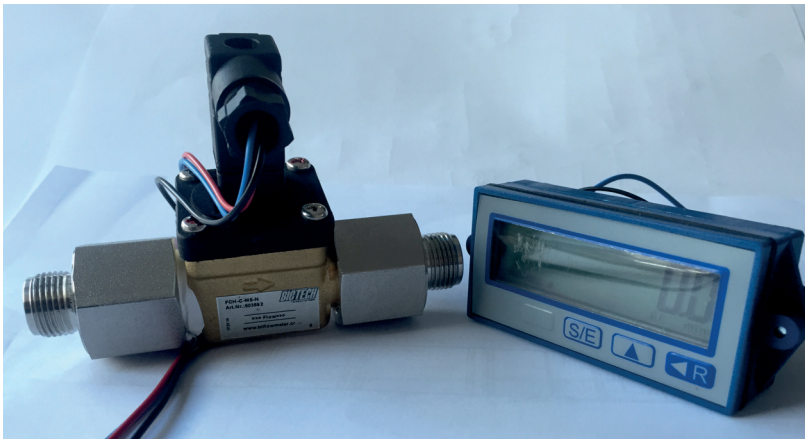


**Figure 12.3:** Modified flow meter (left) and counter (right) for measurement of the flow rate in the MAIUS cooling circuits.

Making use of the hall effect, the sensor will return a rectangular signal for each passing of

a turbine blade. Since the geometry of the sensor pipe and the turbine is given, the signal can be converted into a flow. According to the sensor data sheet the conversion factor is 450 Impulses/L for water at 20 °C.

This conversion rate can directly be set in the counter shown in figure 12.3. After setting the conversion rate the counter directly displays the flow in $\mathrm{L\,min^{-1}}$. This setup is capable of measuring flow rate ranging from $0.5\,\mathrm{L\,min^{-1}}$ to $30\,\mathrm{L\,min^{-1}}$. The accuracy is given as $\pm 2\,\%$ for constant flows in the sensor data sheet. Data logging is not possible with this device, thus the data has to be protocoled manually.

For integration in the MAIUS-1 cooling circuit, the sensor was equipped with two fittings reducing the two G1/2" male thread ports to two Swagelok 10 mm tube ports as shown in figure 12.3. This is compatible with all hoses inside the payload and allows measurements at every position in the cooling circuit.

### 12.2.2 Cooling Circuit Flow Measurement

The flow of water in the two cooling circuits of the MAIUS-1 payload was measured using the flow meter described in section 12.2.1. The device has been mounted in the cooling circuit backflow between the water feed-through in the sealing plate and the umbilical shoe as shown in figure 12.4a.

**(a)** Flow sensor mounted between the sealing plate feedthrough and the backflow umbilical shoe.

**(b)** Setup for flow measurement of the laser system cooling circuit. The chiller case shown in the front, with the sensor display on top. In the back the assembeled payload with attached water umbilicals.

**Figure 12.4:** Setup for flow measurement of the laser system cooling circuit

The measurement has been performed with a fully assembled scientific payload as shown

in figure 12.4b for both colling circuits. In addition to this a measurement has been performed with the sensor mounted between an 1.5 m and 0.5 m Swagelok hose, directly attached to the chiller to determine the flow directly at the chiller.

| Pump Speed in $\mathrm{min}^{-1}$ | Flow in $\mathrm{L\,min}^{-1}$ | | |
|---|---|---|---|
| | Laser | Electronic | Chiller |
| 1500 | 0 | 0 | 3.1 |
| 1750 | 0 | 0 | 3.7 |
| 2000 | 0 | 1.60 | 4.3 |
| 2250 | 0 | 1.86 | 4.9 |
| 2500 | 2.1 | 1.98 | 5.5 |
| 2750 | 2.61 | 2.18 | 6.2 |
| 3000 | 2.97 | 2.53 | 6.9 |
| 3250 | 3.22 | 3.38 | 7.6 |
| 3260 | 3.42 | 3.34 | N/A |
| 3270 | 3.50 | 3.40 | N/A |
| 3280 | 3.47 | 3.35 | N/A |
| 3300 | 3.4 | 3.11 | N/A |
| 3500 | 3.1 | 2.9 | 8.2 |
| 3750 | 2.64 | 2.45 | 8.9 |
| 4000 | 2.67 | 2.53 | 9.6 |
| 4250 | 2.84 | 2.79 | 10.2 |
| 4500 | 3.05 | 3.00 | 10.7 |

**Table 12.1:** Flow measurements of the cooling circuits and directly at the chiller. The refinement in the step size has not been necessary at the chiller, therefore these values are marked N/A.

In all test runs the rotational speed of the pump has been increased stepwise from $1500\,\mathrm{min}^{-1}$ to $4500\,\mathrm{min}^{-1}$. As shown in table 12.1 a pump speed of $2500\,\mathrm{L\,min}^{-1}$ is required, until the flow establishes. This is explained by the vertical height of the umbilical shoes and the resulting pump pressure necessary to overcome this height.

The flow increases with the rotational speed of the pump as expected. At the payload the flow starts to decrease at $3270\,\mathrm{min}^{-1}$, which might indicate a transition in the type of flow.

It has to be noted that the measured flow directly at the chiller is also lower than expected. According to the pump curve in figure 12.1b a flow of $10.7\,\mathrm{L\,min}^{-1}$ would indicate a pressure loss of 500 hPa. This is a high loss for a setup with a 1.5 m hose. Thus the accuracy of the flow measurement is unknown. It might be possible, that the measured flow is to lower than the actual value. The pumps will be operated at the determined optimum and a cooling water flow of $3.5\,\mathrm{L\,min}^{-1}$ will be assumed for the thermal simulations in section 12.4 and 12.5.

### 12.2.3 Heat Transfer Coefficient for the Water Cooling Circuits

With the determined flow and the geometry of the water cooling pipes mounted into the heat sinks, it is possible to approximate the heat transfer coefficient of the water at the inside of the pipe walls. For this purpose a MATLAB code has been developed.

As already given in section 11.1 during the discussion of the natural convection, the heat transfer coefficient $\alpha$ is defined as

$$\alpha = \frac{Nu\,\lambda_{water}}{L} \tag{12.1}$$

where $Nu$ is the Nusselt number, $\lambda_{water}$ the thermal conductivity of water and $L$ the characteristic length, which is in this case the inner diameter of the pipe $d_i$. The Nusselt numbers for forced convection in circular pipes are well defined in the literature [Wet11]. The applicable formulas change with the type of flow, which is determined by the Reynolds number.

The Reynolds number for a flow through a pipe is defined as

$$Re = \frac{u\,d_i}{\nu} \tag{12.2}$$

with a flow of $\dot{V} = 3\,\mathrm{lmin}^{-1}$ and a flow velocity $u = \dot{V}/A = 0.9947\,\mathrm{m\,s}^{-1}$ and the kinematic viscosity $\nu$ according to table 12.2. The properties of the fluid are determined at the mean fluid temperature $T_m = (T_{in} + T_{out})/2$. Unfortunately neither $T_{out}$ nor $T_{in}$ are known at the start of the calculation. The input temperature is actively controlled by the chiller to maintain a constant temperature of the heat sink $T_{HS}$. This is achieved by a sensor mounted to the heatsink, which will fed back the temperature to the chiller.

In the code presented here, this is simulated by varying the input temperature of the water to maintain a constant temperature at the heatsink despite the dissipated heat of the components. As initial guess the measured temperature of the water in the chiller bath is used. The output temperature is also guessed and will be calculated iteratively as well as described below.

With those initial guesses the fluid properties and the Reynolds number can be determined. Subsequently the Nusselt number is computed. For Reynolds numbers between $10^4$ and $10^6$ a turbulent flow is assumed. For pipes with $l/d_i > 1$ the Nusselt number is given as [Wet11]

$$Nu_{turb} = \frac{(\zeta/8)\,Re\,Pr}{1 + 12.7\sqrt{\zeta/8}\,(Pr^{2/3} - 1)}\,f_1\,f_2 \tag{12.3}$$

While the Praandtl number for the water flow is given in table 12.2, the friction factor $\zeta$ needs to be calculated from [Wet11]

$$\zeta = [1.8\log(Re) - 1.5]^{-2} \tag{12.4}$$

| T in K | $\rho$ in $\mathrm{kg\,m^{-3}}$ | $c_p$ in $\mathrm{J\,kg^{-1}\,K^{-1}}$ | $\lambda$ in $\mathrm{W\,m^{-1}\,K}$ | $\nu$ in $10^{-6}\,\mathrm{m^2\,s^{-1}}$ |
|---|---|---|---|---|
| 293 | 998.2 | 4184 | 0.598 | 1.003 |
| 303 | 995.7 | 4180 | 0.616 | 0.801 |
| 313 | 992.3 | 4178 | 0.631 | 0.658 |

**Table 12.2:** Basic properties of water in dependency of the temperature in the range of interest for this application. In between the given values the properties are found by linear interpolation [Wet11].

The same applies $f_1$, a factor depending on the pipe length and the factor $f_2$, which takes into account the direction of the heat flow. The pipe length factor is defined as [Wet11]

$$f_1 = 1 + \left(\frac{d_i}{l}\right)^{2/3} \tag{12.5}$$

The second factor is defined by the Prandtl numbers of the stream $Pr$ and at the pipe wall $Pr_w$ [Wet11]

$$f_2 = \left(\frac{Pr}{Pr_w}\right)^{0.11} \tag{12.6}$$

The Prandtl number at the pipe wall is initially determined with the fluid parameters at the heatsink temperature. This implies that the temperature gradient across the pipe wall is not considered. The actual wall temperature is calculated later in the code. The properties are given in table 12.2, which is also implemented in the code to compute the heat transfer coefficient. In between the given values linear interpolation is used to determine the parameters.

For Reynolds numbers below 2300 laminar flow is assumed. In this regime the Nusselt number is given as [Wet11]

$$Nu_{lam} = \left[3.66^3 + 0.644^3\, Pr \left(Re\,\frac{d_i}{l}\right)^{3/2}\right]^{1/3} \tag{12.7}$$

As stated before the turbulent Nusselt number is valid starting from $Re = 10^4$, thus a valid formula is needed for the transition regime $2300 < Re < 10^4$. The Nusselt number in this regime is interpolated between the two given formulas as [Wet11]

$$Nu = (1-\gamma)\left[Nu_{lam}(Re = 2300) + Nu_{turb}(Re = 10^4)\right] \tag{12.8}$$

where

$$\gamma = \frac{Re - 2300}{7700} \tag{12.9}$$

With this the Nusselt number is defined for Reynolds Numbers up to $Re = 10^6$. The heat transfer coefficient found from the Nusselt number allows a computation of the heat tran-

sition coefficient $k$ corresponding to the inside wall area $A_i$ is calculated as

$$k = \left[\frac{1}{\alpha} + \frac{d_i}{\lambda_{pipe}} \ln \frac{d_a}{d_i}\right] \tag{12.10}$$

All pipes used in MAIUS-1 are made of copper with a conductivity of $\lambda_{pipe} = 380\,\mathrm{W\,m^{-1}\,K^{-1}}$, an inner diameter of $d_i = 8\,\mathrm{mm}$ and an outer diameter $d_a = 10\,\mathrm{mm}$. Since the pipe is in good thermal contact with the heat sink, the outside temperature of the pipe is assumed to be equal to the heatsink temperature. With given $k$ and a mean temperature difference

$$\Delta T_m = \frac{T_{out} - T_{in}}{\ln\left(\frac{T_{HS}-T_{in}}{T_{HS}-T_{out}}\right)} \tag{12.11}$$

the actual temperature of the inner pipe wall is calculated as

$$T_{pipe} = T_m + \Delta T m \frac{k\,d_i}{\alpha d_a} \tag{12.12}$$

with this temperature the variables $Pr_w$, $Nu$ and $\alpha$ need to be computed once more as described above. With the newly determined values the cooling power can be calculated as

$$Q_{water} = k\,\pi\,d_i\,l\,\Delta T_m \tag{12.13}$$

Subsequently the actual output temperature is calculated with the specific heat of water $c_p$ and the mass flow of water through the pipe $\dot{m}$ as

$$T_{out} = T_{in} + \frac{Q_{water}}{\dot{m}\,c_p} \tag{12.14}$$

with the new outlet temperature the whole code is restarted. This process is repeated until the change in the outlet temperature is smaller than 0.2 %. Ultimately a check is performed, whether $Q_{diss} \leq Q_{water}$. This ensures that the cooling power is sufficient to compensate the dissipated heat of the system components and the heat sink temperature is constant. If this is not the case the code is restarted with a lower input temperature. The resulting parameters are listed in table 12.3.

| System | $Q_{diss}$ in W | $l$ in m | $T_{HS}$ in K | $T_{in}$ in K | $T_{out}$ in K | $T_m$ in K | $\alpha$ in $\mathrm{W\,m^{-2}\,K^{-1}}$ |
|---|---|---|---|---|---|---|---|
| Laser | 60.73 | 1.167 | 299.0 | 298.2 | 298.5 | 298.4 | 3308.5 |
| Electronic I | 160.5 | 1.254 | 297.8 | 295.7 | 296.5 | 296.1 | 3107.7 |
| Electronic II | 182.85 | 1.254 | 297.2 | 294.8 | 295.7 | 295.3 | 3038.2 |
| Battery | 378.6 | 0.989 | 299.0 | 293.0 | 294.8 | 293.9 | 2975.6 |

**Table 12.3:** Applicable heat transfer coefficient $\alpha$ and mean temperature $T_m$ of water cooling circuits for given pipe length $l$, heat sink temperature $T_{HS}$ and dissipate heat $Q_{diss}$.

## 12.3 Physics Package

In the physics package multiple components dissipate heat into the vacuum chamber walls and the surrounding structure. Aside from the magnetic coils and the chip structures, two cameras and the rubidium oven will produce an significant amount of heat. The physics package is the only MAIUS-1 system without an active thermal control system during lab operation. Thus the entire heat will be stored in the system structure.

In this section the dissipated heat and the duty cycle for all of these components is characterized for a typical experiment sequence. Moreover the impact of the three-layer magnetic shielding on natural convection will be investigated. Finally thermal simulations of the physics package during lab and flight operation are carried out.

### 12.3.1 Dissipated Heat and Duty Cycle

The amount of heat dissipated at the physics package varies depending on the experiment sequence performed. While in other systems most components are operated continuously, in the physics package especially the coils and the chip structures are switched often and with short duty cycles.

In order to find realistic parameters for a simulation a typical sequence as it is performed in the laboratory was analyzed. The currents applied to the different coils and chip structures are summarized in table 12.4 for the different steps of the sequence.

As shown in figure 12.4 the cameras and the oven are operated continuously, the dissipated heat of the coils and chip add to the heat generated by those components. The maximum overall dissipated heat of 35.56 W is applied to the structure in the MOT loading phase typically lasting 1500 ms.

Once the magneto-optical trap in the science chamber is loaded, it is stepwise cooled below the critical temperature as described in section 1.2 in the steps 2 - 10. In step 11 the BEC is transfered into an non-magnetic state to make it insensitive to external magnetic fields. This procedure has already been mentioned in section 3.3 and 3.4, as well as the delta kick-cooling, which is applied in step 13 to reduce the expansion velocity of the BEC. Finally the BEC is released and the time of flight (TOF) is measured or atom interferometry is performed in step 13, followed by the detection in step 14. The time of flight and the interferometer times will be increased in the course of the mission aiming at times in the order of seconds.

Depending on the length of the sequences up to 100 sequences could be performed during the 355 s long period of microgravity in the MAIUS-1 flight. To model these sequences exactly 1400 load steps would be required, resulting in an high computation afford and long simulation times. For simulation of the laboratory operation, where 2-3 hours are simulated the load step number scales accordingly.

| Power Consumption BEC 100 ms ToF | | | | | | | | | | | | | | | | | |
|---|---|---|---|---|---|---|---|---|---|---|---|---|---|---|---|---|---|
| Step # | Duration | Starting Time | Phase | Average Sum | 2D-MOT-Coils | Chip: Meso-U | Chip: Meso-H | Chip: Meso-I | Chip: Basis-Z | Chip: Science-Z | X-coil | Y-coil | Z-coil | Camera 1 | Camera 2 | Oven |
| | | | | | Resistance [Ohm] | | | | | | | | | | | |
| | | | | | 2.12 | 0.13 | 0.07 | 0.07 | 0.15 | 0.70 | 0.71 | 2.02 | 1.00 | - | - | - |
| | | | | | Current [A] | | | | | | | | | | | |
| | [ms] | [ms] | | [W] | Power [W] | | | | | | | | | | | |
| 1 | 1500 | 0 | MOT-Loading | | 2.80 | 6.90 | 0.00 | 0.00 | 0.00 | 0.00 | -0.13 | -0.81 | 1.08 | | | |
| | | | | **35.56** | 16.62 | 5.95 | 0.00 | 0.00 | 0.00 | 0.00 | 0.01 | 1.31 | 1.17 | 4.00 | 4.00 | 2.50 |
| 2 | 37 | 1500 | C-MOT | | 0.00 | 5.00 | 0.00 | 0.00 | 0.00 | 0.00 | -0.45 | -0.84 | 1.10 | | | |
| | | | | **16.41** | 0.00 | 3.13 | 0.00 | 0.00 | 0.00 | 0.00 | 0.15 | 1.43 | 1.21 | 4.00 | 4.00 | 2.50 |
| 3 | 5 | 1537 | Molasses | | 0.00 | 0.00 | 0.00 | 0.00 | 0.00 | 0.00 | -0.01 | -0.04 | -0.01 | | | |
| | | | | **10.50** | 0.00 | 0.00 | 0.00 | 0.00 | 0.00 | 0.00 | 0.00 | 0.00 | 0.00 | 4.00 | 4.00 | 2.50 |
| 4 | 5 | 1542 | Optical Pumping | | 0.00 | 0.00 | 0.00 | 0.00 | 0.00 | 0.00 | 1.26 | 0.20 | 0.00 | | | |
| | | | | **11.72** | 0.00 | 0.00 | 0.00 | 0.00 | 0.00 | 0.00 | 1.14 | 0.08 | 0.00 | 4.00 | 4.00 | 2.50 |
| 5 | 20 | 1547 | Transfer Meso -> BC | | 0.00 | 0.00 | 10.00 | 10.00 | 5.00 | 0.00 | 0.31 | -1.22 | 0.68 | | | |
| | | | | **31.77** | 0.00 | 0.00 | 7.00 | 7.00 | 3.75 | 0.00 | 0.07 | 2.99 | 0.46 | 4.00 | 4.00 | 2.50 |
| 6 | 20 | 1567 | Transfer BC -> SC | | 0.00 | 0.00 | 0.50 | 0.00 | 5.00 | 2.00 | -0.18 | -1.40 | -0.35 | | | |
| | | | | **21.19** | 0.00 | 0.00 | 0.02 | 0.00 | 3.75 | 2.80 | 0.02 | 3.98 | 0.12 | 4.00 | 4.00 | 2.50 |
| 7 | 650 | 1587 | Compress & Evaporation I | | 0.00 | 0.00 | 0.00 | 0.00 | 5.00 | 2.00 | -0.27 | -2.34 | 0.00 | | | |
| | | | | **28.16** | 0.00 | 0.00 | 0.00 | 0.00 | 3.75 | 2.80 | 0.05 | 11.06 | 0.00 | 4.00 | 4.00 | 2.50 |
| 8 | 350 | 2237 | De-Compress & Evaporation II | | 0.00 | 0.00 | 0.00 | 0.00 | 5.00 | 2.00 | -0.15 | -1.90 | 0.00 | | | |
| | | | | **24.36** | 0.00 | 0.00 | 0.00 | 0.00 | 3.75 | 2.80 | 0.02 | 7.29 | 0.00 | 4.00 | 4.00 | 2.50 |
| 9 | 500 | 2587 | De-Compress & Evaporation III | | 0.00 | 0.00 | 0.00 | 0.00 | 5.00 | 2.00 | -0.06 | -1.60 | 0.00 | | | |
| | | | | **22.22** | 0.00 | 0.00 | 0.00 | 0.00 | 3.75 | 2.80 | 0.00 | 5.17 | 0.00 | 4.00 | 4.00 | 2.50 |
| 10 | 160 | 3087 | Decompression & Transfer | | 0.00 | 0.00 | 0.00 | 0.00 | 5.00 | 2.00 | 0.00 | -0.53 | -0.15 | | | |
| | | | | **17.65** | 0.00 | 0.00 | 0.00 | 0.00 | 3.75 | 2.80 | 0.00 | 0.58 | 0.02 | 4.00 | 4.00 | 2.50 |
| 11 | 2 | 3247 | ARP | | 0.00 | 0.00 | 0.00 | 0.00 | 0.00 | 0.00 | 0.00 | 0.00 | 0.00 | | | |
| | | | | **10.50** | 0.00 | 0.00 | 0.00 | 0.00 | 0.00 | 0.00 | 0.00 | 0.00 | 0.00 | 4.00 | 4.00 | 2.50 |
| 12 | 6 | 3249 | DKC | | 0.00 | 0.00 | 0.00 | 0.00 | 0.00 | 0.00 | 0.10 | -0.45 | -0.17 | | | |
| | | | | **10.95** | 0.00 | 0.00 | 0.00 | 0.00 | 0.00 | 0.00 | 0.01 | 0.41 | 0.03 | 4.00 | 4.00 | 2.50 |
| 13 | 100 | 3255 | Bragg or TOF | | 0.00 | 0.00 | 0.00 | 0.00 | 0.00 | 0.00 | 1.26 | 0.20 | 0.00 | | | |
| | | | | **11.72** | 0.00 | 0.00 | 0.00 | 0.00 | 0.00 | 0.00 | 1.13 | 0.08 | 0.00 | 4.00 | 4.00 | 2.50 |
| 14 | 20 | 3355 | Detection | | 0.00 | 0.00 | 0.00 | 0.00 | 0.00 | 0.00 | 1.26 | 0.20 | 0.00 | | | |
| | | | | **11.72** | 0.00 | 0.00 | 0.00 | 0.00 | 0.00 | 0.00 | 1.14 | 0.08 | 0.00 | 4.00 | 4.00 | 2.50 |
| Average Sum Total | | | | **28.85** | 7.39 | 2.68 | 0.04 | 0.04 | 1.89 | 1.39 | 0.06 | 4.32 | 0.54 | 4.00 | 4.00 | 2.50 |

**Table 12.4:** Physics package duty cycle and dissipated heat during Bose-Einstein Condensate creation with 100 ms time of flight.

For this reason the average power for each component was calculated from

$$Q_{avg} = \frac{\sum_1^{14} Q_{seq} t_{seq}}{\sum_1^{14} t_{seq}} \tag{12.15}$$

where $Q_{seq}$ is the dissipated heat of one sequence and $t_{seq}$ is the associated duration of the sequence. The averaged powers for each component are given in the last column of figure 12.4. This load is then continuously applied to the structure for the specified time in which experiments will be performed. A detailed description of the applied loads is given in section 12.3.4 for the laboratory operation and section 12.3.3 for the operation during flight.

### 12.3.2 Impact of Magnetic Shielding on Natural Convection

As described in section 11.1 the air inside the payload will heat up during the ascent of the rocket. The air is heating the different payload systems by natural convection or conduction as described in section 11.1. However the sensitive experiment and science chamber is surrounded by a three-layer magnetic shielding made of Mumetall as mentioned in section 7.3.1. The impact of these three layers of Mumetall and the enclosed air between the shield layers is discussed in the following.

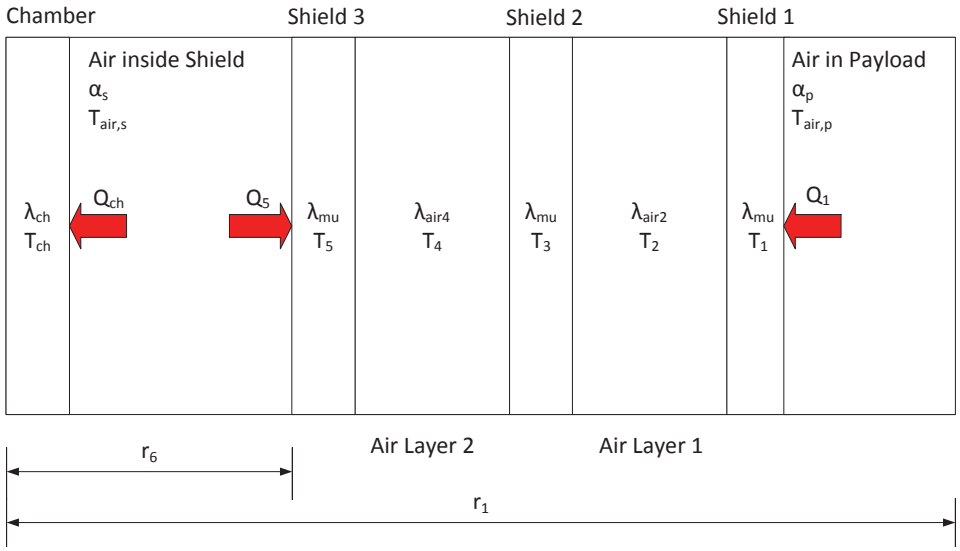


**Figure 12.5:** Thermal model of the three-layer magnetic shielding. The heat transfer coefficient $\alpha_p$ and the air temperature in the payload $T_{air,p}$ are obtained from the simulation presented in section 11.1.

As shown in figure 12.5 the shield will be modeled as heat conduction through five cylindric walls. A convective boundary condition is set at the outside wall of the inner and outer layer of the shield. At the outer layer the heat transfer coefficient $\alpha_p$ and the air temperature in the payload $T_{air,p}$ are obtained from the simulation presented in section 11.1.

The heat transfer coefficient $\alpha_s$ and the air temperature inside the shielding $T_{air,s}$ are going to be computed using the approach presented in 11.1. To do so the wall temperature of the inner layer has to be known.

To obtain this temperature the heat flow through the three shield layers and the two enclosed air layers is computed using a finite volume approach as described in section 10.2. Contrary to the approach presented therein, the flow will be radial in this case and the thermal conductivity will change significantly. Thus the equations for heat conduction will change to

$$Q_w(j,t) = \left[ \frac{[r(j)+r(j+1)]\ln\left(\frac{r(j)}{r(j+1)}\right)}{2\lambda(j,t)} + \frac{[r(j+1)+r(j+2)]\ln\left(\frac{r(j+1)}{r(j+2)}\right)}{2\lambda(j+1,t)} \right]^{-1} \times A_w(j)\,(T(j+1,t)-T(j,t)) \tag{12.16}$$

the heat fluxes to the west are calculated for $j = 1-4$. The heat flux to the east is found from

$$Q_e j,t = -Q_w(j-1) \tag{12.17}$$

for $j = 2-5$. The conductive heat fluxes of the boundary elements 1 and 5 are zero ($Q_e(1,t) = 0$ and $Q_w(5,t) = 0$). Instead a convective heat flux is applied to these elements.

The conductance of the air in the enclosures is a virtual thermal conductance, which considers also the effect of the natural convection in these gaps. This virtual conductance as well as the heat transfer coefficient are hanging with acceleration and temperature difference as already described in section 11.1.

| Element | Type | Radius in m | Height in m | Thermal Conductivity in $\mathrm{W\,m^{-1}\,K^{-1}}$ |
|---|---|---|---|---|
| 1 | MUMETALL | 0.210<br>0.209 | 0.523<br>0.521 | 19 |
| 2 | Air | 0.209<br>0.201 | 0.521<br>0.501 | to be calculated |
| 3 | MUMETALL | 0.201<br>0.200 | 0.501<br>0.499 | 19 |
| 4 | Air | 0.200<br>0.192 | 0.499<br>0.479 | to be calculated |
| 5 | MUMETALL | 0.192<br>0.190 | 0.479<br>0.475 | 19 |

**Table 12.5:** Geometric parameters and thermal conductivity of the five cylindric shell volume elements modeling the magnetic shielding. The thermal conductivity of the air layers has to be calculated for each time step as described below.

The virtual conductance can be calculated for the cylindric gap in dependency of the Rayleigh number

$$Ra = GrPr = \frac{g\beta(T_w - T_\infty)s^3}{\nu a} \tag{12.18}$$

where the characteristic length is the gap width $s$. For a cylindric gap with a radial heat flow and a characteristic Rayleigh number $Ra < 10^8$, the virtual conductance $\lambda_s$ can be found from [Pol05]

$$\lambda_s = \lambda_{air}\left(1 + \frac{0.119\,Ra^{1.270}}{Ra + 1.45\times 10^4}\right) \tag{12.19}$$

To calculate the virtual conductance the Rayleigh number $Ra$ has to be determined first. Assuming the enclosed air to be an ideal gas, the coefficient of thermal expansion is defined as $\beta = 1/T_\infty$. The kinematic viscosity $\nu$ of air at 20 °C is $18.3\times 10^{-6}\,\mathrm{m^2\,s^{-1}}$. The kinematic viscosity is depending on the air temperature. The thermal diffusivity $a$ is $20.06\times 10^{-6}\,\mathrm{m^2\,s^{-1}}$.

The heat transfer coefficient for the convection at the inside of the innermost layer and the air temperature is computed using the approach presented in section 11.1. Where the characteristic length is the height of the inner layer. With the geometric parameters given in table 12.5, the heat transfer equations can be solved. The resulting temperatures of the different shield layers and the air enclosed in the shield are given in figure 12.6.

Although the air temperature in the payload reaches 330 K the inner layers are thermally isolated especially by the air enclosures in between the shield layers. Thus the temperature of the innermost layer rises by only 0.1 K. Due to this small temperature difference between the shield layer and the air inside the shield, there is no relevant heating of the air inside the shield due to the air temperature change in the payload.

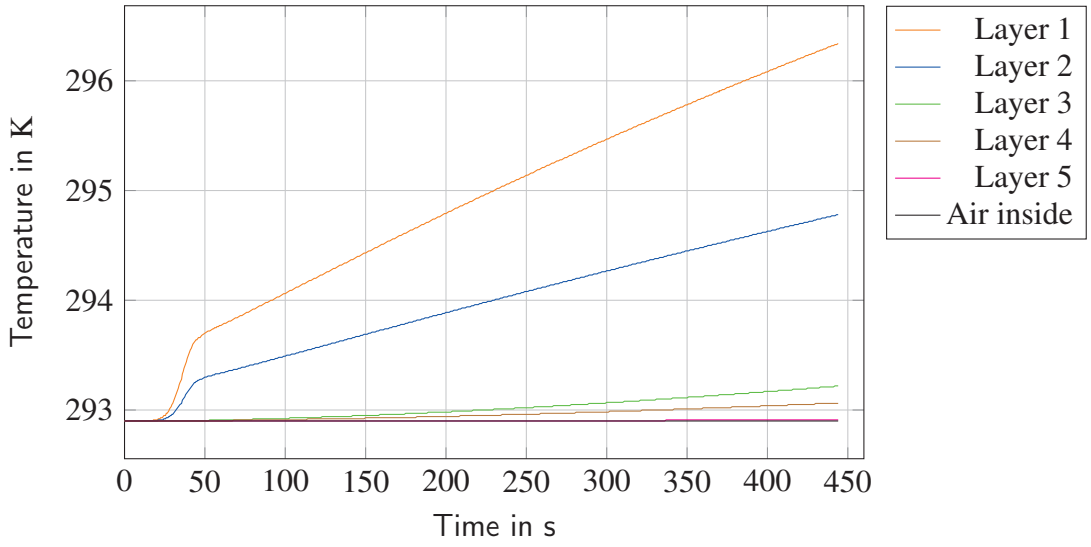


**Figure 12.6:** Predicted temperatures of the magnetic shield layers and the enclosed air during the ascent and microgravity phase of the rocket.

However the components of the physics package will transfer their dissipated heat partly into the air due to natural convection. For the simulation of the flight operation in section 12.3.3 the effect of convection shall be neglected as a worst case assumption.

For the lab operation the virtual conductivity and the heat transfer coefficient differ, thus they have to be determined individually. The heat transfer coefficient at the components inside the shield at a constant gravitational acceleration of 9.81 $\mathrm{m\,s^{-2}}$ is mainly driven by the temperature difference between the chamber and instruments and the surrounding air.For this reason the temperature of the chamber has to be known to find the heat transfer coefficient. With an initial guess for an time invariant heat transfer coefficient of 5 $\mathrm{W\,m^{-2}\,K^{-1}}$ a FEM simulation is run with all loads applied as described in section 12.3.4. Hereby the wall temperature is mainly influenced by the dissipated heat of the components and not by convection. The results for the chamber wall temperature are fed in the code to determine the heat transfer coefficient. The chamber is treated as a vertical flat plate with an area of 0.004 $\mathrm{m^2}$ and a characteristic length of 0.420 m.

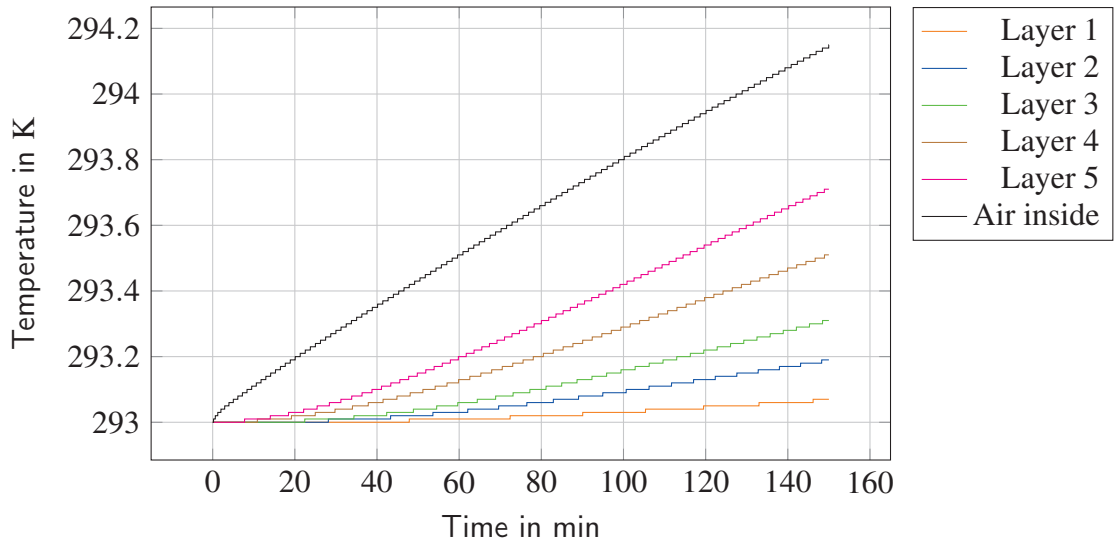


**Figure 12.7:** Predicted temperatures of the magnetic shield layers and the enclosed air during laboratory operation of the experiment.

As shown in figure 12.7 the air is heated only slowly and the heat transfer coefficient rises with the increasing temperature difference as shown in figure 12.8. The heat transfer coefficient found in this simulation run is subsequently used in a new FEM simulation. Iteratively repeating this process will result in a more accurate solution for the heat transfer coefficient. For the simulation of the laboratory operation, the values plotted in figure 12.8 will be used.

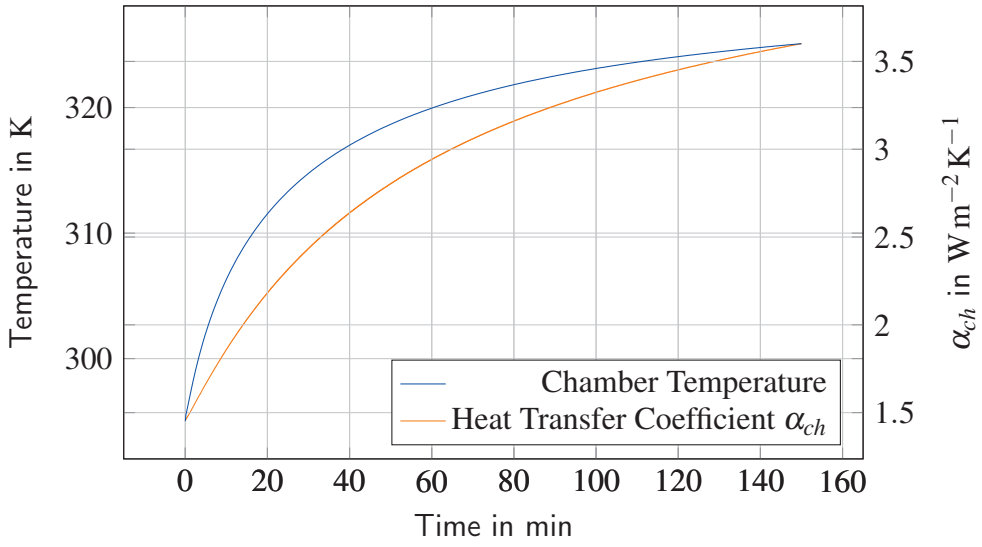


**Figure 12.8:** Predicted temperatures of the vacuum chamber walls and the resulting heat transfer coefficient during laboratory operation of the scientific payload.

### 12.3.3 Flight Operation Simulation

The physics package as described in section 7.3 is a complex and sensitive part of the scientific payload. For this reason it is essential to be able to predict the temperatures at the physics package during the flight.

In the simulation of the flight operation of this system the dissipated heat of the components as given in table 12.4 is modeled either as a heat flux applied to a surface or as internal heat generation. The latter is used for the four sets of coils and the two cameras, which are represented by solid models.

The heat generated in the structures of the atom chip are applied as a heat flux onto the copper chip mount. The titanium oven is heated by a resistance heater. The heat generated by the wire heater is applied to the two circular sections of the oven in direct contact with the heater. The last load applied is the representative heat flux generated by the electronic stack controlling the ion getter pump and the UHV sensor. Its power consumption of the stack has been measured to be 6 W. An equivalent heat flux is applied to the inner walls of the pump stack housing.

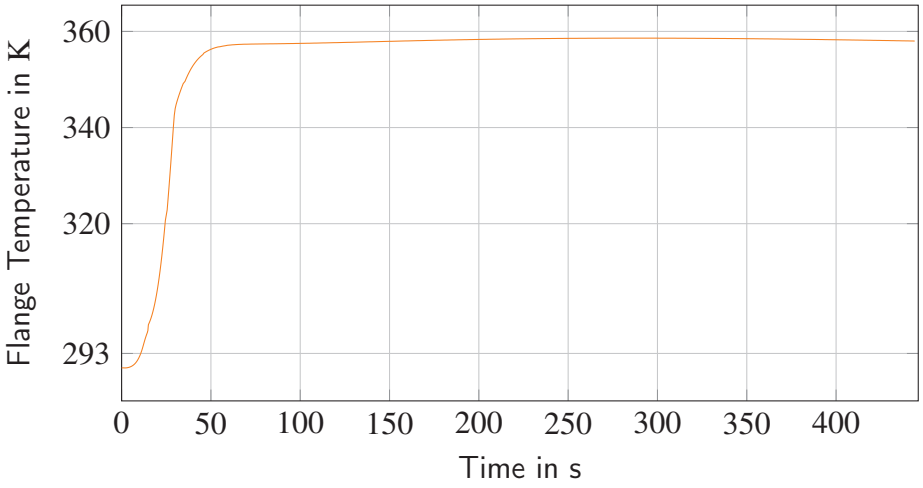


**Figure 12.9:** Temperature at the flange to the brackets of the upper physics package instruments platform.

While the pump stack, the cameras and the oven will be operated continuously and will be started prior to the launch of the rocket, the coils and the atom chip will start their operation with the begin of the microgravity phase at T=91s. As initially stated all loads will be applied as continuous loads with the average values given in table 12.4.

In addition to the internal heat loads, the impact of the aerodynamic heating of the hull needs to be considered. A temperature boundary conditions applied to the face of the brackets in contact with the hull in 33 load steps.

The temperature distribution as presented in figure 12.9 is obtained from the simulation described in section 10.5. As a result of the discussion in the previous section a convective heat flux will not be included in the flight simulation of the physics package because of the thermal isolation by the magnetic shielding.

The maximum temperatures at different components of the physics package are shown in figure 12.11. The temperature of the oven rise quickly to a temperature of 328 K, which is desired to ensure a sufficient Rubidium partial pressure in the 2D chamber.

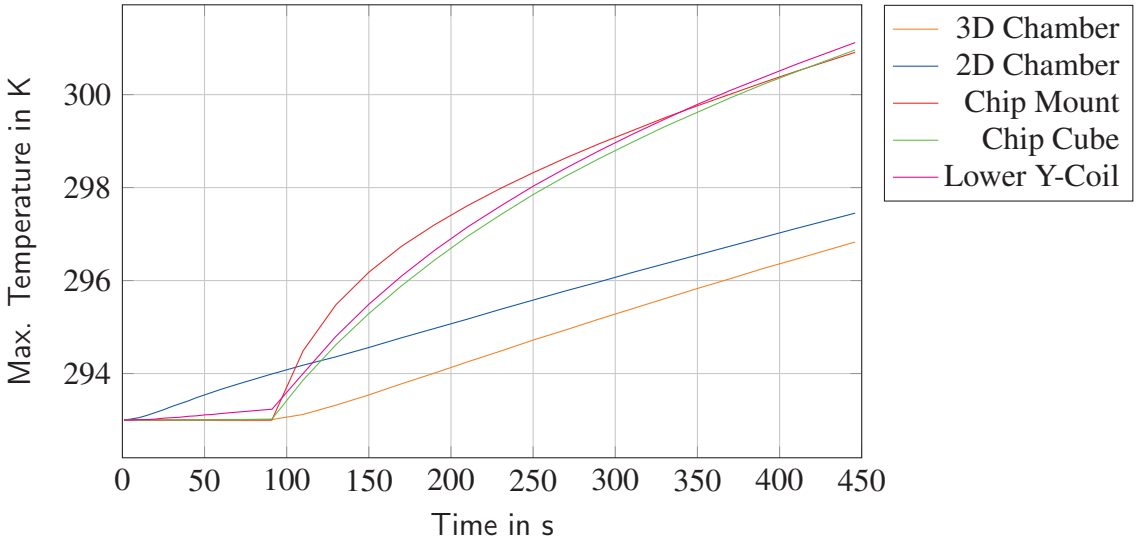


**Figure 12.10:** Simulated maximum temperatures of important components of the physics package during ascent.

Actually the oven will be heated prior to lift-off. The temperature at the contact area between the 2D chamber and the oven is slowly following this temperature. Due to the low conductance of the oven flanges, this region is only heated by 5 K to 300 K, which is still within the requirements. Due to the low conductance of the 2D chamber the other regions are not affected.

The 3D chamber has its hot spot on the plane in contact with the chip cube. Here the temperature rises by 4 K, while the opposite side with the large window is only affected by the z-coil dissipated heat of 0.25 W and keeps its initial temperature. The chip mount and the chip cube temperature illustrate that the copper mount conducts the heat generated by the chip itself very well to the walls of the chip cube resulting in an small temperature gradient between the maximum temperatures of those two parts. The chip mount is heated by 9 K, which is in the expected range.

As shown in the temperature distribution in figure 12.10, the lower y-coil is getting warmer than the upper coil. Both are dissipating the identical amount of heat, thus the lower coil is not sufficiently contacted to the structure to ensure a proper conduction of the heat into the structure.

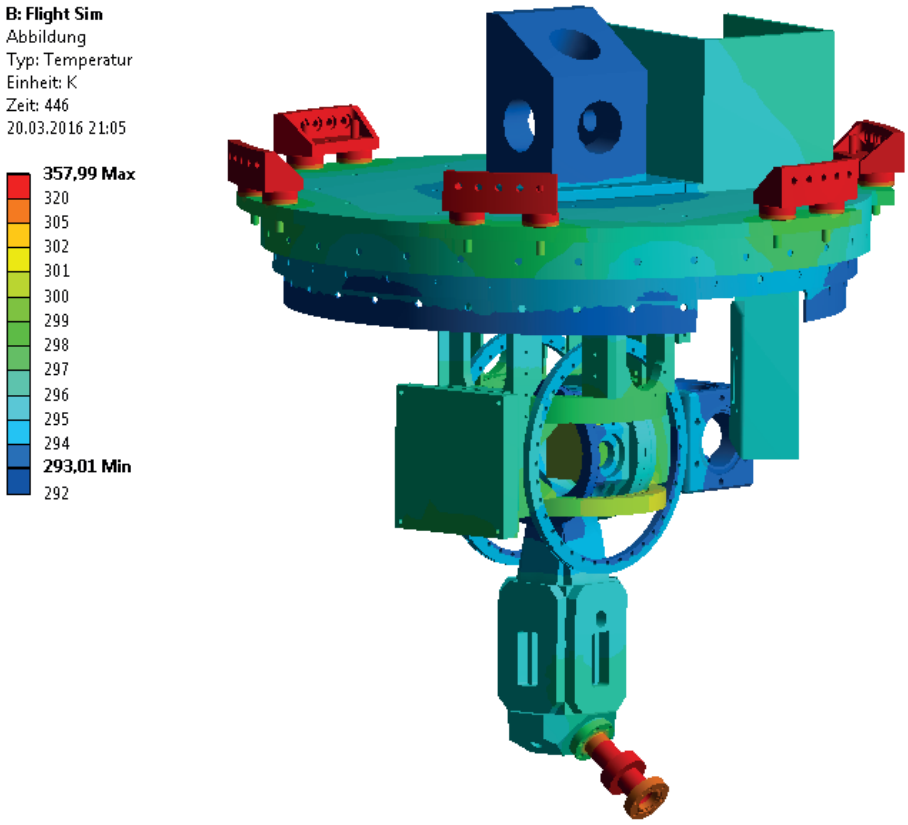


**Figure 12.11:** Spatial temperature distribution at the physics package at end of microgravity phase (T=446s). The temperatures of the chambers are within the requirements. The impact of the low conductance of the rubber dampers is clearly visible.

While the upper coil is in direct contact with the strengthening ring and the four columns holding the chamber assembly, the lower coil is only contacted at two points. This results in the higher temperatures, especially at longer operation times (compare section 12.3.4). This is not problematic for MAIUS-1 but should be addressed for future missions.

### 12.3.4 Laboratory Operation Simulation

For the simulation of the operation in the laboratory a typical lab sequence had to be defined. This is difficult, because the sequences vary depending on the scientific objectives. For this reason a continuous operation with the average loads defined in the table 9.3 is simulated for a duration of 120 min, which is considered a worst-case scenario.

A longer continuous operation is unlikely and therefore not considered. After 120 min another load step with a duration of 30 min will simulate a experiment standy-by, where only the oven and the two cameras are active. This is the typical state, while the data from the previous experiment runs is evaluated.

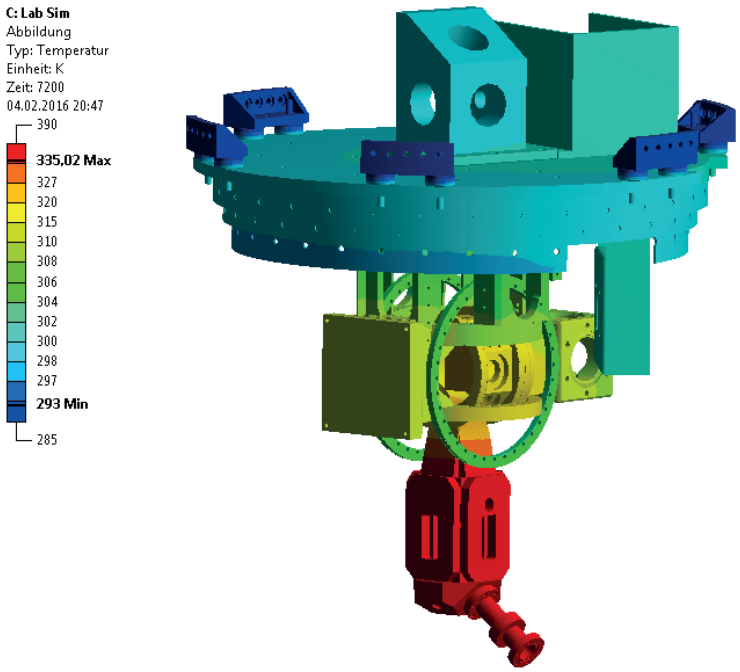


**Figure 12.12:** Spatial temperature distribution at the physics package in the laboratory after 120 min of continuous operation

In this simulation setup a convective heat flux has to be included as discussed in the previous section. It is applied on all surfaces of the physics package components inside the magnetic shielding. The heat transfer coefficient increases stepwise from 2.5 $\mathrm{W\,m^{-2}\,K^{-1}}$ to 3.5 $\mathrm{W\,m^{-2}\,K^{-1}}$ as plotted in figure 12.7. The air temperature inside the magnetic shielding is modeled to rise from 293 K to 293.9 K within 120 min as plotted in figure 12.7.

The temperature of the hull in contact with the brackets is set to 293 K, which is a common air temperature in a laboratory with an appropriate air condition. The air temperature outside the magnetic shielding and the heat transfer coefficient is modeled as given in section 11.1.

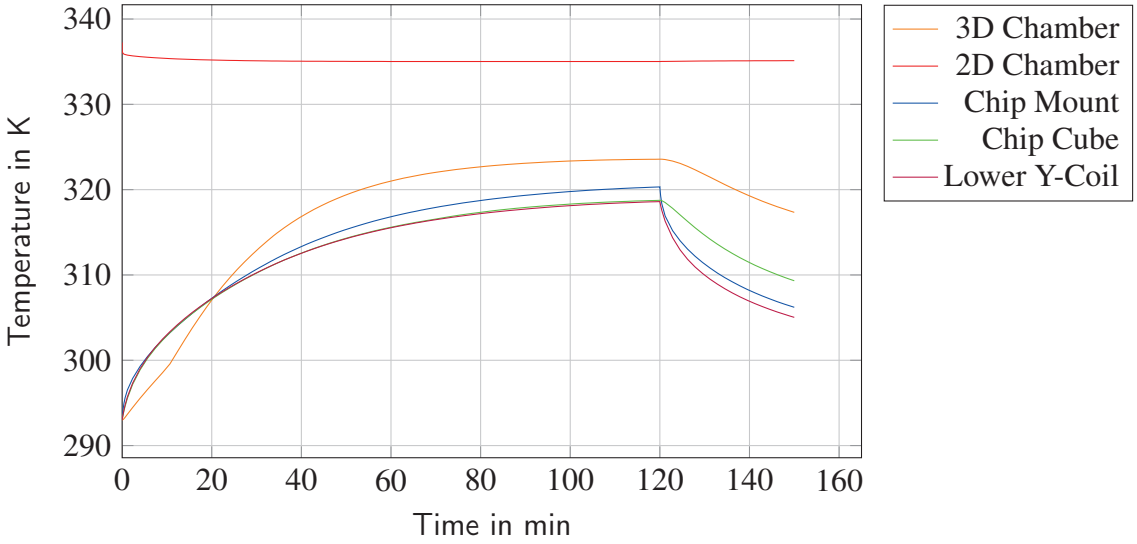


**Figure 12.13:** Simulated maximum temperatures of important components of the physics package in the laboratory. The simulation covers 120 min of continuous experiment operation followed by 30 min of stand-by for data analysis. As the oven temperature is set to be constant at 335 K the maximum preparation chamber temperature is close to this value because both bodies are in direct contact.

As shown in figure 12.13 the temperature of the components inside the magnetic shield rises slowly towards an equilibrium temperature. This temperature is approximately 320 K for the science (3D) and 330 K for the preparation (2D) chamber walls. This is a temperature rise of 27 K at the science chamber, which is considerably above the requirements specified for in flight operation.

Although an temperature of 320 K will not harm the indium seals or any other component attached to the chamber, it results in a pressure rise in the chamber due to outgassing (refer section 9.2), which might affect the quality of the measurements. However until today no measurement was corrupted due to a temperature or pressure rise. As stated at the beginning this is a worst-case scenario. Typically one experimental sequence as defined in section 12.3.1 followed by approximately 5 min of data analysis, which reduces the thermal loads dramatically resulting in a temperature rise of only 9 K.

In the design phase active cooling of the components has been discarded, because the needed feedthroughs would have had reduced the magnetic shielding efficiency. Moreover realization of an active cooling without the use of magnetic materials has been considered difficult. Thus the temperature in the laboratory shall be controlled operational by e.g. pauses between long experiment sequences. Nevertheless an active control will be advantageous for future experiments.

## 12.4 Laser System

The laser system as described in section 7.4 is housing the microintegrated diode laser modules. These are the instruments, which are most sensitive to temperature changes of the entire payload.

To protect its interior from the heated air inside the scientific payload, the laser system housing is equipped with double walls. These walls are filled with air, which reduces the conductivity through the wall. Because the enclosed volume of air is small, the enclosed air is modeled as a solid body with a conductivity $\lambda_{air} = 0.0262\,\mathrm{W\,m^{-2}\,K^{-1}}$. Usually the increased virtual conductivity would have to be considered as described in section 12.3.2. The Rayleight number for a worst case scenario with gap width $s = 0.01\,\mathrm{m}$, a gravitational acceleration $g = 9.81\,\mathrm{m\,s^{-2}}$ and a temperature difference between enclosed air and wall temperature of 10 K is calculated as $Ra \approx 939$. This will result in an increase of the conductivity in the order of $1.2 \times 10^{-3}\,\mathrm{W\,m^{-2}\,K^{-1}}$. The maximal conductivity will be present during the flight when the peak acceleration is reached. Here the change in conductivity is approximately $1.8 \times 10^{-2}\,\mathrm{W\,m^{-2}\,K^{-1}}$, which is a increase by 69 %. However this is still a worst case assumption and the peak acceleration only affects the rocket for a short period of time. Thus the impact of natural convection inside the walls will be neglected in the simulation presented herein. Accordingly the conductivity of the air volumes is set to $\lambda_{air} = 0.0262\,\mathrm{W\,m^{-2}\,K^{-1}}$ and will not change with time.

In addition to the isolated walls the massive aluminum heat sink is water cooled until lift-off, which will allow to adjust the heat sink temperature in the laboratory and set an initial temperature of the heatsink just prior to the flight. According to the considerations in section 12.2.3 the mean fluid temperature in the FEM simulation is set to 298.35 K and the heat transfer coefficient between the water and the pipe walls is set to $3308.5\,\mathrm{W\,m^{-2}\,K^{-1}}$ as given in table 12.3. The water cooling is keeping the heat sink temperature constant at 299 K. In reality the chiller is actively controlling the heatsink temperature in a closed loop. For this purpose a PT100 temperature sensor has been applied on the laser heatsink, which feeds the temperature signal back to the chiller via the data umbilical.

### 12.4.1 Dissipated heat and duty cycle

To determine the temperature rise at the heat sink, the heat dissipation of the laser system components has to be characterized. Although the laser system is packed with components only a very limited number of these components is actually powered and dissipates a reasonable amount of heat into the structure. These are listed in table 12.6. While all other components are operated continuously, the shutter driver motors will only be activated if their state is changed from open to close or vis versa. The activation time is only in the order of milliseconds, thus the dissipated heat is comparably low and this portion will be neglected.

As described in section 7.4.1 the temperature of the laser modules is controlled by Peltier

| Component | Location | Quantity | Power [W] | Duty Cycle |
|---|---|---|---|---|
| Lasermodule(MOPA) & Peltier | Heatsink | 3 | 6.60 | Always on |
| Lasermodule(ECDL) & Peltier | Heatsink | 3 | 0.495 | Always on |
| AOMs | Zerodur Board | 5 | 1.00 | Always on |
| Shutter Motor | Zerodur Board | 12 | 0.9 | only if changed |
| Amp ZFL-1000LN+ | Top Cover | 2 | 1.02 | Always on |
| Amp ZJL-6G | Top Cover | 3 | 0.6 | Always on |
| Bias-Tee ZFBT-6G+ | Top Cover | 5 | 6.0 | Always on |

**Table 12.6:** Power dissipation, location and duty cycle of laser system components

elements. These elements conduct the dissipated heat into the heatsink. The energy consumption of these devises is depending on the temperature difference between their hot and cold side as well as from the amount of heat they have to transport. In MAIUS the heat sink temperature has been chosen to be 299 K. The desired temperature of the laser modules is approximately 309 K. Thus the temperature difference across the Peltier element is around 10 K.

The laser modules with powered amplifier have a nominal power consumption of 2.4 A at 2.3 V. The ECDL technology demonstration modules and the master laser only consume 0.2 A at the same voltage. The amplified modules provide 500 mW and the other modules 10 mW, which results in an dissipated heat of $Q_{diss} = 5.02\,\mathrm{W}$ and $Q_{diss} = 0.45\,\mathrm{W}$.

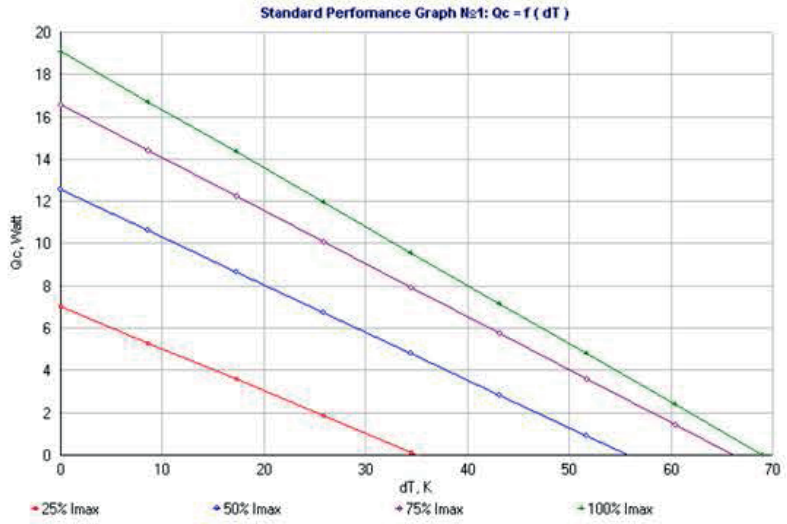


**Figure 12.14:** Performance curve of the Dr. Neumann TCH peltier element used in MAIUS-1 laser system.

From the peltier element performance data presented in figure 12.14 the operation current at the modules with amplification can be determined precisely. It is given as $0.25\,I_{max}$ with

a maximum operation current of 2 A given in the data sheet the typical operation current is 0.5 A. The operation current of the peltier elements at the laser modules, which are not amplified is estimated to be 0.15 A. The loss in the peltier is found from $P = R_{peltier} I^2$ with the resistance of the peltier given in the data sheet as 6.4 Ω.

This results in a overall dissipated heat of the two laser types as given in table 12.6. The heat generated at the peltier element reduces during the flight of the rocket as the temperature of the heatsink increases slowly, which results in a lower temperature difference across the peltier and thus a lower operation current. Since the temperature change in the heatsink is expected to be small, this effect is neglected.

### 12.4.2 Flight Operation Simulation

The laser modules need to be stabilized to their required temperature prior to the start to ensure that the laser light is emitted at the right frequency. To ensure a reliable operation of the peltier elements, the heat sink is heated to 299 K prior to the start. For the flight simulation an uniform initial temperature of 299 K is assumed for all components.

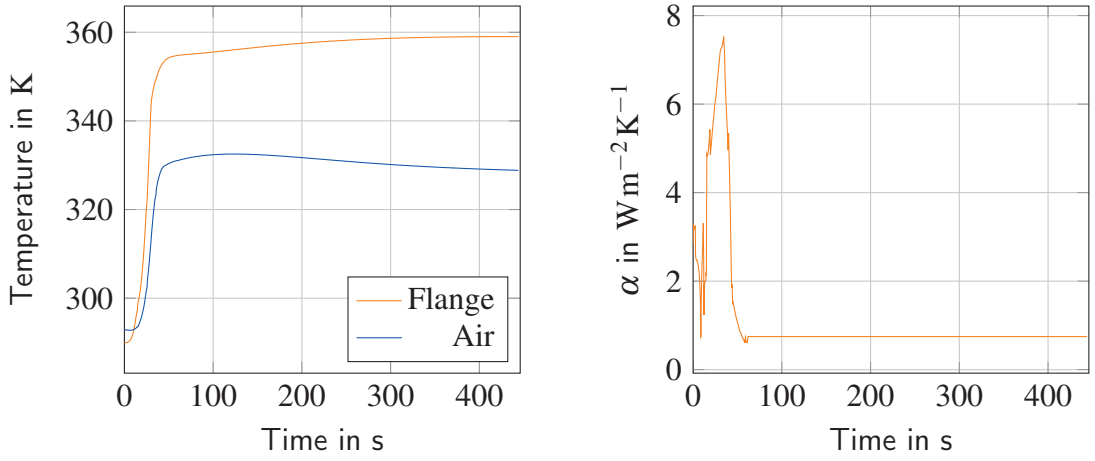


**(a)** Predicted air and flange temperature at the laser system

**(b)** Heat transfer coefficient at the laser system housing

**Figure 12.15:** Input parameters for the simulation of the flight operation of the laser system. Obtained from the simulations presented in section 11.1 and 10.

A convective heat flux is applied to the outside of the housing walls with the parameters presented in figure 12.15. Moreover the temperature boundary condition at the contact area between instrument platform brackets and the flange at the rocket hull is set according to figure 12.15a. Convection inside the laser system housing is neglected.

The dissipated heat from the components inside the system as given in table 12.6 is modeled as internally generated heat in the respective component. The laser modules themselves are not included in the simulation, as their temperature is actively controlled by the peltiers and will not change. Instead the heat generation is modeled to occur inside the

peltier element. The heat loads of six of the peltier elements is chosen according to table 12.6. The two redundancy lasers will not be active during the flight. Thus no thermal load is expected here.

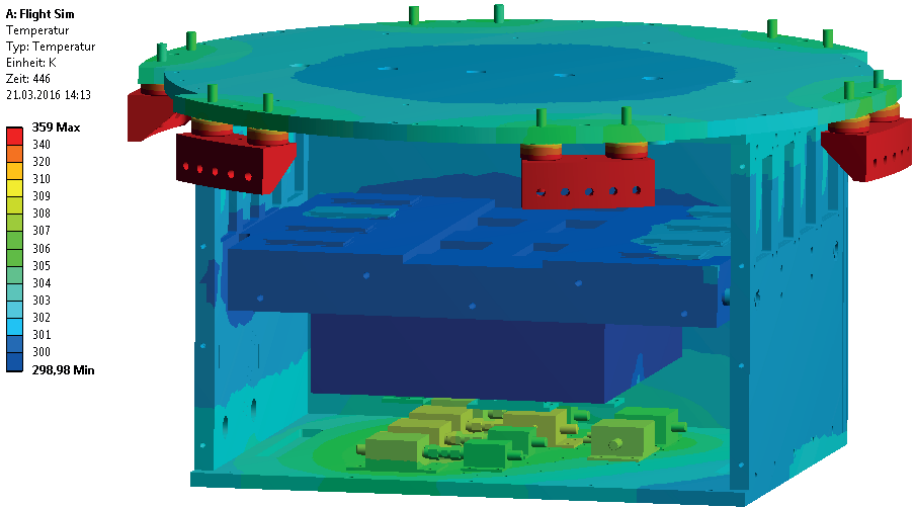


**Figure 12.16:** Spatial temperature distribution in the laser system at the end of the microgravity phase at T+446s.

Contrary to the components of physics package, all laser system components are operational prior to the launch. Thus the respective loads are applied from the beginning of the simulation. As shown in figure 12.16 the MiniCircuits components at the top cover of the housing experience a temperature rise of 10 K. However their absolute temperature of 309 K is well below the maximum operation temperature of 344 K given in the data sheet. The acusto-optical modulators (AOMs) on the Zerodur board will heat to 305 K, which is also in the required range.

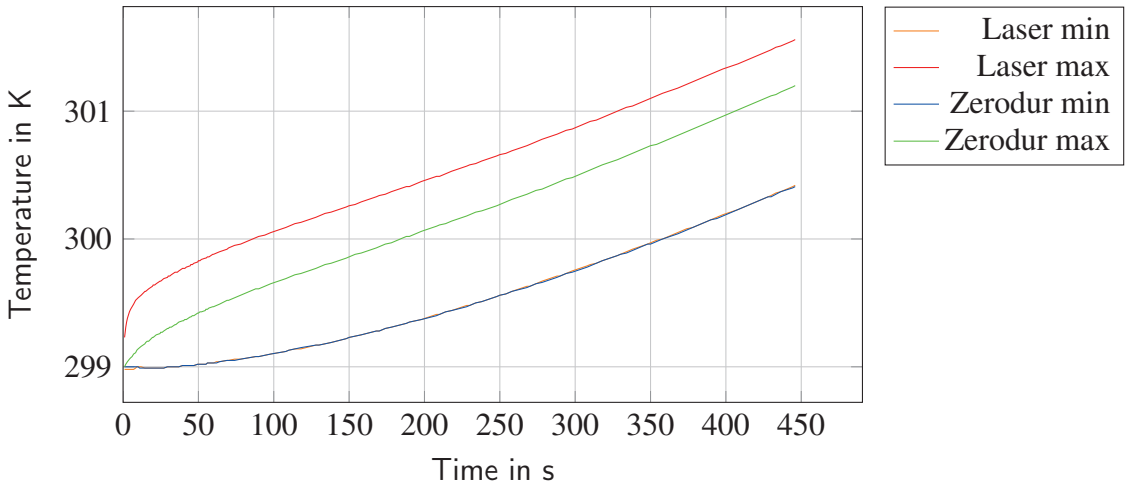


**Figure 12.17:** Minimum and maximum temperatures of the laser module and Zerodur side of the laser system heatsink during flight.

Figure 12.18 depicts that the heatsink shows a small temperature gradient between the right and left side. The temperature of the right side of the heatsink equipped with the master laser and two of the amplified lasers rises by up to 2.56 K, while the left side with only one amplified laser and a technology demonstrators rises only by 2.2 K. The applied heat is well distributed across the heatsink.

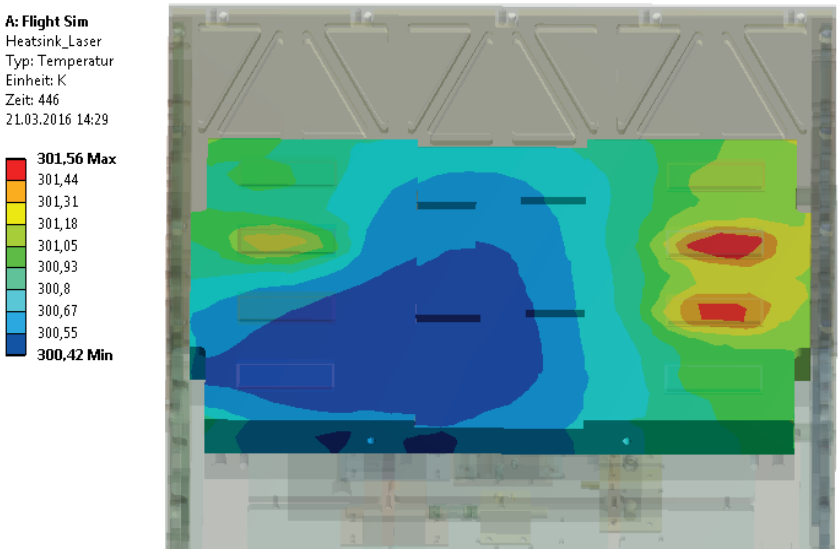


**Figure 12.18:** Spatial temperature distribution at the laser system heatsink at the end of the micro gravity phase after 446 s of continuous operation. A hot spot is located beneath the high-power lasers, while the lower left corner with the inactive lasers is the coldest spot at the heatsink.

Moreover a small gradient of approximately 0.5 K is observed at the right side of the heatsink between the lower half carrying the Zerodur components and the upper side sheltering the lasers. These are the maximum temperatures plotted in figure 12.17. The minimum temperatures are assigned to the left side, where almost no temperature gradient is observed between the upper and lower half of the heatsink. In total all temperatures are within the requirements.

### 12.4.3 Laboratory Operation Simulation

The setup for simulation of the operation in the laboratory is identical for the internal components. However the water cooling needs to be included. This is done by implementing a convective heat flux onto the inner wall of the pipe with a heat transfer coefficient of $3308.5\,\mathrm{W\,m^{-2}\,K^{-1}}$ and a constant mean fluid temperature of 298.35 K as calculated from the code described in section 12.2.3.

Moreover a convective heat flux simulates natural convection on the outside walls of the laser system housing with a heat transfer coefficient and an air temperature, that changes with time as shown in figure 11.5a and 11.5b in section 11.1. Figure 12.19 depicts that the water cooling is successfully removing most of the heat from the system resulting in moderate housing and stable heatsink temperatures.

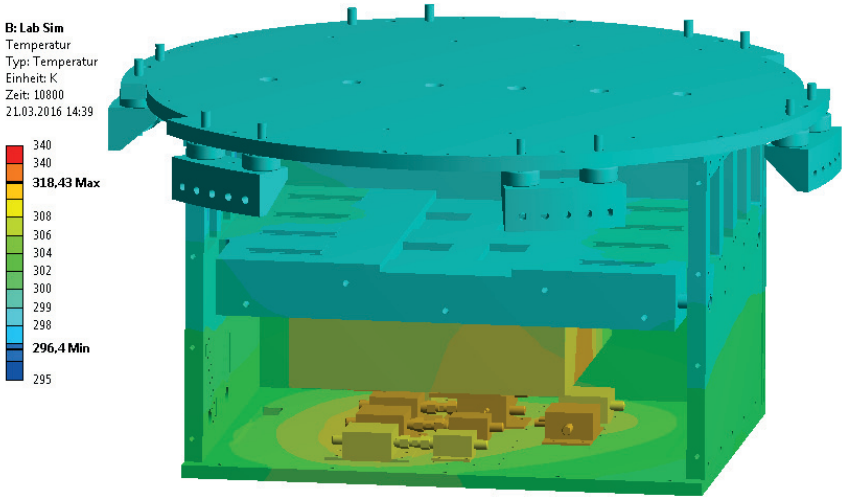


**Figure 12.19:** Spatial temperature distribution at the laser system housing after 180 min of of continuous operation.

The MiniCircuits components at the upper cover and the AOMs are the elements with the highest equilibrium temperature.They heat up to 318 K, which is still within the temperature ratings. The Zerodur board and the lower part of the system housing heats up to temperatures around 308 K. Due to the low coefficient of thermal expansion of Zerodur this is uncritical for the alignment of the optical components of the splitting an distribution board.

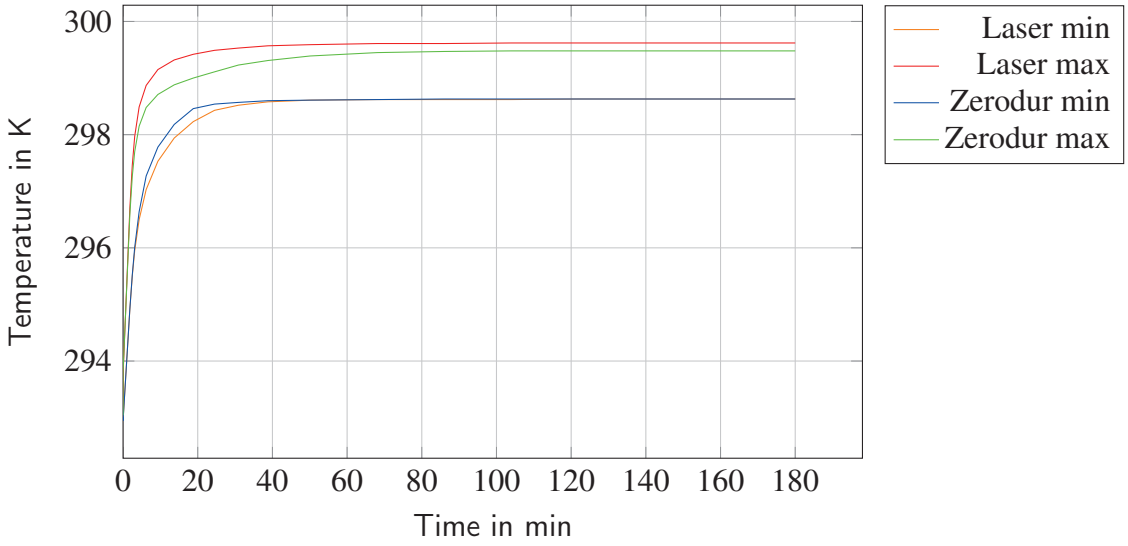


**Figure 12.20:** Minimum and maximum temperatures of the laser module and Zerodur side of the laser system heatsink during 180 min of continuous operation.

Again the heatsink temperature is of interest to ensure a reliable longtime operation of the lasers. As shown in figure 12.21 and 12.20 the temperature gradient across the heatsink is approximately 1 K. While the hot spots are located below the high power lasers as shown

in figure 12.21, the center region of the heatsink is even cooled below 299 K. Such a small gradient is tolerable and will not cause problems with the stabilization of the laser modules.

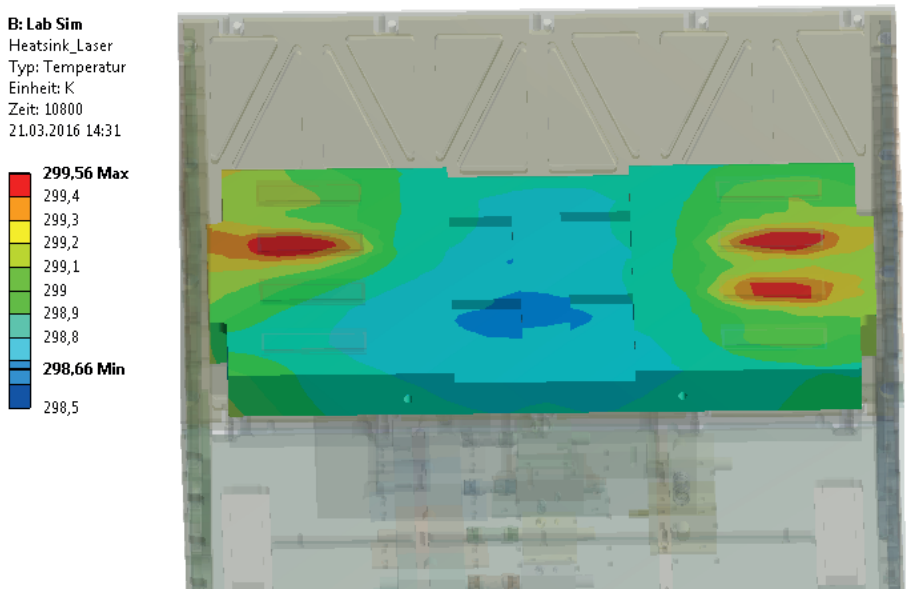


**Figure 12.21:** Temperature distribution at the laser system heatsink after 180 min of continuous operation in the laboratory showing hot spots below the high-power lasers.

Another important information obtained from figure 12.20 is, that it will take up to 20 min to heat the heatsink to 299 K when starting at 293 K even if all components are operated. This is especially important in the launch tower, because it influences the time-event list of the countdown. It has to be assured that this time is available.

## 12.5 Electronic System

The electronic system assembly as it is described in section 7.5 is the most complex system in the MAIUS-1 scientific payload. A total of 147 components heat the system with an average total power of 343 W. The characterization of these loads is presented in this section. The large amount of dissipated heat requires a massive heatsink and a powerful water cooling.

During the flight the heat will be stored in eight aluminum parts of the housing with a total mass of 29.8 kg, which function as the electronic system heatsink. The detailed design of the electronic system housing and its thermal control system is given in 7.5.2.

During the operation in the laboratory the large octagonal heatsink at the top and the bottom of the electronic system is water cooled by a copper pipe integrated into those two plates. The two pipes are part of the lower cooling water circuit. Before the water enters the lower heatsink it has already passed the battery heatsink, thus the inlet temperature is

defined by the outlet temperature of the battery heatsink given as 294.8 K in table 12.3. The mean temperature of the water flow is calculated as 295.25 K and the heat transfer coefficient as 3038.2 $\mathrm{W\,m^{-2}\,K^{-1}}$ in section 12.2.3. This results in an output temperature of 295.7 K, which is equivalent to the input temperature of the second heatsink. The fluid mean temperature at this part of electronic system is determined as 296.1 K and the heat transfer coefficient as 3107.7 $\mathrm{W\,m^{-2}\,K^{-1}}$.

### 12.5.1 Forced Convection in the Electronic System

In addition to the water cooling the electronic system heatsink is equipped with two radial fans Ebm Pabst RER 125-19/12NG. The exact mounting of those fans has been described in detail in section 7.5.2. The fans cool the high power components mounted to the backplane and the regular cards as shown in figure 12.22. Subsequently the heated air is cooled in the heatsink air channel. In this section the heat transfer coefficient for the forced convection in the heatsink air channel and at the electronic components shall be estimated.

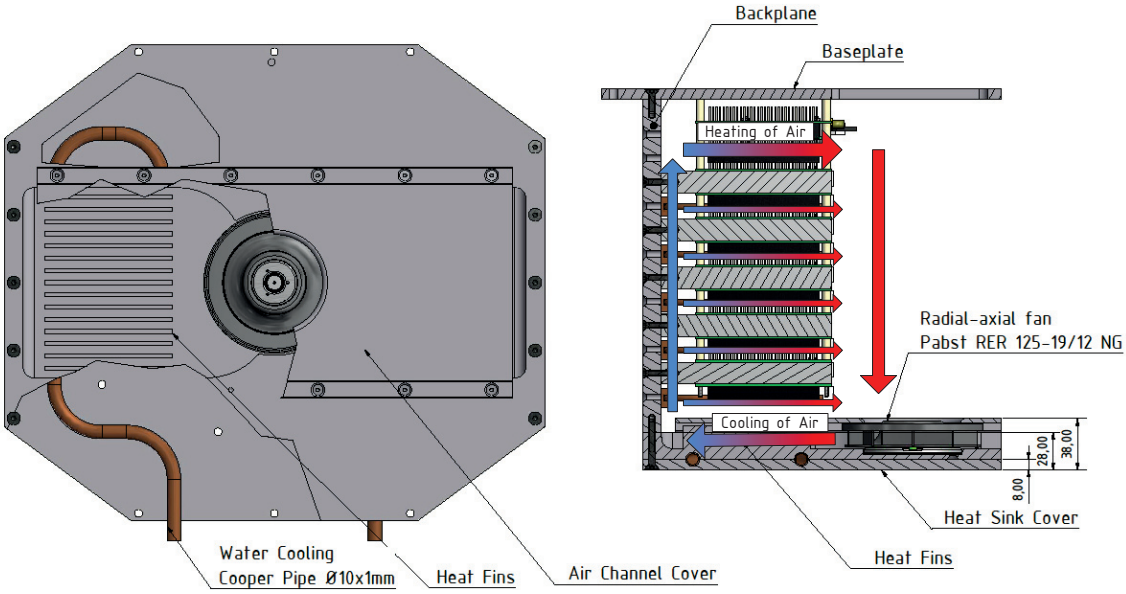


**Figure 12.22:** Heat sink and active cooling of electronic system. This figure shows the routing of the water cooling pipes and the expected circulating airflow caused by the fans.

The fan has been chosen to according to the manufacturers catalog. Ebm Pabst states [ebm16] that the required air flow $q_v$ for a given amount of dissipated heat $Q_{diss}$ and a maximum temperature rise of the of the air $\Delta T$ is given as

$$q_v = \frac{Q_{diss}}{c_{p,air}\,\rho_{air}\,\Delta T} \tag{12.20}$$

For the given power dissipation of 182.85 W at the upper half and 160.5 W at the lower half of the electronic system and a temperature rise of 10 K in the airflow, the required

flow is $0.026\,\mathrm{m^3\,s^{-1}}$. This equals $47.9\,\mathrm{m^3\,h^{-1}}$. The chosen fan has an unblocked air flow of $110\,\mathrm{m^3\,h^{-1}}$. Thus the airflow is sufficient, especially because some portion of the dissipated heat will also be transfered into the heatsink by conduction. However it has also to be considered, that the air circulates in the electronic system. For this reason it has to be assured, that the air is properly cooled. For this purpose a heat transfer coefficient has to be estimated.

Forced convection of an fluid stream has already been discussed in section 12.2.3. As stated there, the Nusselt number needs to be determined first to calculate the heat transfer coefficient. For this purpose the velocity of the flow has to be known. The outlet velocity $c_{out}$ of the fan is depending on th air flow and the outlet area $A_{out}$.

$$c_{out} = \frac{q_v}{A_{out}} \tag{12.21}$$

the outlet area of the fan used in MAIUS is $A_{out} = 0.0137\,\mathrm{m^2}$, which results in an maximum outlet velocity of $2.23\,\mathrm{m\,s^{-1}}$. The actual air flow is depending on the pressure losses due to friction with the walls and components blocking the flow. For this purpose the Reynolds number has to be found first from

$$Re = \frac{c_{out}\,d_h}{\nu} \tag{12.22}$$

with $d_h$ being the hydraulic diameter of non circular channels, that is defined by the ratio between the cross section and circumference of the channel

$$d_h = 4\frac{A}{U} = \frac{2\,d\,h}{d+h} \tag{12.23}$$

The cross section of the 2 x 12 channels in the heatsink is characterized by the depth $d = 6\,\mathrm{mm}$ and the height $h = 18.5\,\mathrm{mm}$. This results in an hydraulic diameter of 9.06 mm. With an kinematic viscousity $\nu = 18.3 \times 10^{-6}\,\mathrm{m^2\,s^{-1}}$ the Reynolds number in the channel is 1104 and the flow is fully laminar. The pressure loss for a single channel is given as

$$\delta p = \lambda \frac{l}{d_h} \frac{\rho_{air}}{2} c_{out}^2 \tag{12.24}$$

where $\lambda = 64/Re$ is the friction factor for laminar flow in a pipe. With a channel length $l = 100\,\mathrm{mm}$ the pressure loss in the 24 channels sums up to 45.82 Pa. The flow over the printed circuit boards and along the backplane is difficult to calculate, since it is not a closed channel and the air is inlet by the fan forming a closed circuit. The pressure loss was thus increased to 65 Pa, which is considered a worstcase assumption. The actual output flow at a pressure loss of 65 Pa according to the fan data sheet is $55\,\mathrm{m^3\,h^{-1}}$.

With an resulting air speed of $1.1\,\mathrm{m\,s^{-1}}$ the Reynolds number reduced to 544.6. The Nusselt number for a laminar flow is given in section 12.2.3 as

$$Nu_{lam} = \left[3.66^3 + 0.644^3\, Pr \left(Re \frac{d_h}{l}\right)^{3/2}\right]^{1/3} = 4.846 \tag{12.25}$$

This results in an heat transfer coefficient in the air channels of $\alpha = 14.92\,\mathrm{W\,m^{-2}\,K^{-1}}$.

The heat transfer coefficient at the printed circuit boards and the high-power components mounted to the backplane is more difficult to calculate. For the lack of a better solution, the coefficient is determined using the model of a flow along a flat plate with the height of the backplane $l_{BP} = 245\,\mathrm{mm}$. The Reynolds number with the $l_{BP}$ being the characteristic length is 14726.77. The Nusselt number for a flat plate with $Re < 10^5$ (laminar flow) is defined as [Wet11]

$$Nu = 0.664\, Pr^{1/3}\, Re^{1/2} \tag{12.26}$$

The Nusselt number for the flow over the electronic components is consequently 71.55 and the heat transfer coefficient $8.15\,\mathrm{W\,m^{-2}\,K^{-1}}$. Now both heat transfer coefficients have been successfully estimated. For the use in ANSYS the air temperature is also needed. As initially stated the air temperature will rise by more than 5 K, because the air circulates in the housing and is constantly heated. Thus the air temperature has to be determined, at which the amount of heat dissipated by the components to the air is fully transferred to the heatsink. With the contact area in the air channels being $A = 0.2\,\mathrm{m^2}$ the needed temperature difference between air and heatsink is calculated as

$$\Delta T = \frac{Q_{diss,\alpha}}{\alpha A} \tag{12.27}$$

Unfortunately the amount $Q_{diss,\alpha}$ of the total dissipated heat, that is transfered to the air by convection is unknown. Due to the low heat transfer coefficient and the good thermal contact of the high-power components with the heat sinks it seems reasonable to crudely estimate $Q_{diss,\alpha}$ to be one third of the overall dissipated heat. For $Q_{diss,\alpha} = 60\,\mathrm{W}$ a temperature difference of 20.10 K is needed to transfer the full amount of heat. With an heat sink temperature of 293.7 K the air temperature for the ANSYS input is 313.8 K for the convective heatflux at the heatsink. The output temperature of the air channel is calculated using equation 12.14 resulting in 310.5 K. This temperature is used for the convective heat fluxes at the electronic components.

### 12.5.2 Dissipated Heat and Duty Cycle

With known parameters for simulation of the water cooling and the fans, the characterization of the internally dissipated heat needs to be addressed. As described in section 7.5 the electronic system is divided into the upper and the lower part. Both are assembled from the same structural components, but are equipped with different electronic components.

The standardized 100 mm x 100 mm TBUS electronic boards developed at the University Hanover are stacked in functional groups of maximum 12 cards, which are connected to the two backplanes using brackets. High-power components are either thermally connected to the backplane using copper pipes or are directly mounted to the backplane as shown in figure 12.23 and 12.24.

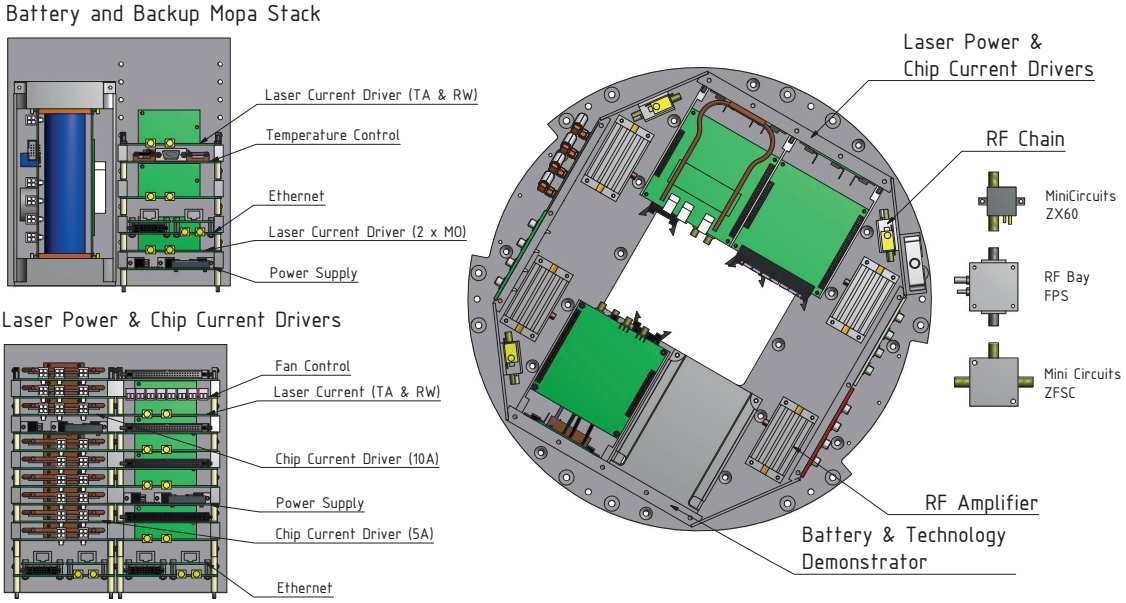


**Figure 12.23:** Mounting position of the upper electronic section components. Shown are three stacks of TBUS electronic cards, a large battery pack with three cells and several commercial non-TBUS components.

At the lower part of the electronic system, the laser power driver and the chip current driver functional stacks share one backplane as shown in figure 12.24. The back plane directly opposite is equipped with a three-cell battery pack and the laser stack powering the redundancy lasers. As stated in section 12.4 these lasers are a cold redundancy, thus this stack will not be active and is not considered in these simulations.

The cards in a stack are enumerated in table 12.8. They are numbered from 1 to 12, where 1 is the card at the bottom to give the location of the card in the stack. The dissipated heat of the cards has been defined by the scientists in Hanover. The laser current drivers as most of the cards are constantly running to ensure a stable operation of the lasers. The same applies for the ethernet, fan control and temperature (NTC) or photodiode (PD) monitoring cards.

The dissipated power of the current drivers for the chip and the coils will vary significantly with the switching of the corresponding structures. For a sequences as defined in section 12.3.1 the average and maximum dissipated power is given in table 12.7. In the simulation the average power will be used to model a continuous operation of these cards.

| Card Name | Comment or Position | Card # or Quantity | Avg. Power in W | Max. Power in W |
|---|---|---|---|---|
| Chip Current Driver Stack | | | | |
| Current Driver (10 A) | 2D-3/4 | 11 | 5.69 | 20.18 |
| Current Driver (10 A) | Meso H | 10 | 0.22 | 0.80 |
| Current Driver (10 A) | Meso U | 9 | 18.23 | 64.70 |
| Current Driver (5 A) | z - coil | 7 | 0.15 | 0.53 |
| Current Driver (5 A) | y - coil | 6 | 3.15 | 11.16 |
| Current Driver (5 A) | x - coil | 5 | 0.99 | 3.51 |
| Current Driver (5 A) | Science Chip | 4 | 3.59 | 12.75 |
| Current Driver (5 A) | Ba. & Sc. Chip | 3 | | |
| Current Driver (5 A) | Base Chip | 2 | 10.59 | 37.59 |
| Power supply | | 8 | 5.00 | - |
| Ethernet | | 1 | 2.00 | - |
| Sum | | | 48.61 | 157.22 |
| Laser Power Stack | | | | |
| NTC / PD Monitor | | 11,8,6,3 | 0.50 | - |
| Fan Control | | 10 | 5.00 | - |
| Laser Current Driver | RW & TA | 9,7,5,2 | 10.00 | - |
| Power supply | | 4 | 5.00 | - |
| Ethernet | | 1 | 2.00 | - |
| Sum | | | 54.00 | - |
| Non T-Bus components | | | | |
| Opto Electronic RF Amp. | Base plate | 4 pcs. | 10.00 | - |
| MiniCircuits ZX 60 | RF Chain | 3 pcs. | 0.65 | - |
| RFBay FPS Devider | RF Chain | 3 pcs. | 0.83 | - |
| MiniCircuits ZFSC Splitter | RF Chain | 3 pcs. | 0.13 | - |
| Headway 38120SE Cell | Backplane | 3 pcs. | 5.40 | 15.00 |
| Chip Safety Box | Top Heatsink | 4 pcs. | 5.00 | - |
| Sum | | | 80.25 | - |
| Sum Total | | | 182.86 | 320.27 |

**Table 12.7:** Power dissipation of the components of the upper part of the electronic system.

| Card Name | Comment or Position | Card # or Quantity | Avg. Power in W | Max. Power in W |
|---|---|---|---|---|
| Signal Generator Stack | | | | |
| Current Sensor Monitor | | 11 | 0.20 | |
| Current Driver (10 A) | 2D-1 | 10 | 5.54 | 19.66 |
| Current Driver (10 A) | 2D-2 | 9 | 5.61 | 19.91 |
| Signal Generator | | 5-8 | 2.00 | |
| Shutter Driver | | 2,3 | 0.20 | |
| Power supply | | 4 | 5.00 | |
| Ethernet | | 1 | 2.00 | |
| Sum | | | 26.75 | 55.17 |
| Laser Control Stack | | | | |
| Laser Current Driver | 2 x MO each | 7,9 | 2.00 | - |
| NTC Monitor | | 8 | 0.50 | - |
| Temperature Control | | 2,3,6 | - | 6.00 |
| Frequency Control | | 4 | 2.00 | - |
| Power supply | | 5 | 5.00 | - |
| Ethernet | | 1 | 2.00 | - |
| Sum | | | 31.5 | - |
| Technology Demonstrator Stack | | | | |
| Computer | Tot. power | 7-9 | 6.00 | - |
| Frequency Controller | | 5,6 | 2.00 | - |
| Laser Current Driver | | 4 | 2.00 | - |
| Temperature Controller | | 2,3 | 5.00 | - |
| Power supply | | 1 | 5.00 | - |
| Sum | | | 22.00 | - |
| Non T-Bus components | | | | |
| Opto Electronic RF Amp. | Base plate | 4 pcs. | 10.00 | - |
| MiniCircuits ZX 60 | RF Chain | 4 pcs. | 0.65 | - |
| RFBay FPS Devider | RF Chain | 4 pcs. | 0.83 | - |
| A123 Battery | Backplane | 7x2 pcs. | 0.6 | - |
| Switch | Backplane | 1 pc. | 2.00 | - |
| Clock | Backplane | 1 pc. | 2.00 | - |
| IDAN Computer | Heatsink | 1 pc. | 19.1 | - |
| Sum | | | 80.25 | - |
| Sum Total | | | 160.5 | 188.92 |

**Table 12.8:** Power dissipation of the components of the lower part of the electronic system.

The dissipated heat of the radio frequency components is given in the related datasheets. The four large radio frequency amplifiers from Opto Electronic are mounted directly onto the base plate as shown in figure 12.23. The smaller components are forming one RF chain, which is mounted to three of the diagonal walls of the housings. All RF components are operated constantly.

The large battery pack consists of three cells of the type Headway 38120SE with an inner resistance of 6 mΩ. The maximum discharge current is given as $5C = 50\,\mathrm{A}$ and the maximum charging current as $4C = 40\,\mathrm{A}$. The typical discharge current is expected to be below 30 A. The dissipated heat of a single cell is calculated as $Q_{diss} = RI^2$. The maximum heat loss at the cell is 15 W, while the dissipated heat at 30 A is 5.4 W.

As shown in figure 12.24 the lower part of the electronics system is housing three active TBUS stacks and some non-TBUs components. The cards in the stacks are enumerated in table 12.8.

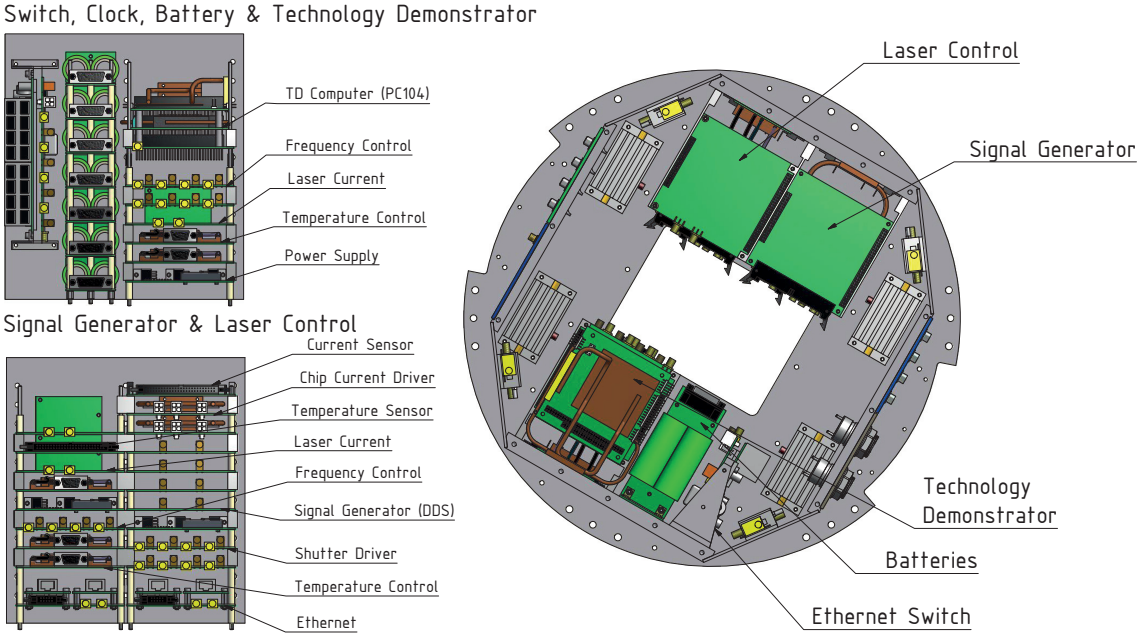


**Figure 12.24:** Mounting position of the lower electronic section components. Shown are three stacks of TBUS electronic cards, seven small battery packs with two cells each, an master clock timing board and several commercial non-TBUS components.

The laser control stack and the signal generator stack share one backplane in this assembly. The four temperature controllers are part of this stack. The heat load of the temperature controllers, which are powering the peltier elements of the lasers is strongly depending on the temperature difference across the peltier and the transported heat as described in section 12.4. The 6 W assumed in the simulation is a worst case assumption considering the maximum output power of the controller.

The technology demonstrator stack located on the opposing backplane is designed to be

a self-sustaining system. Therefore it is equipped with its own computer at the top of the stack. The computer spans over three boards and dissipates 6 W. The remaining cards are well specified in table 12.8.

The radio frequency components are similar to the ones used in the upper section of the electronic system. However the RF chains are shorter, because the MiniCircuits splitter ZFSC is not needed in these chains. The chains are mounted to the four diagonal walls of the housing. At the technology demonstrator heatsink a timing module and a commercial ethernet hub are mounted on a common baseplate. The seven battery packs are neighboring this assembly. One battery pack consists of two A123 ANR26650M1B 2500 mA h cells with an internal resistance below 6 mΩ. At the recommended charge and the expected discharge current of 10 A the cells dissipate 0.6 W.

The IDAN on-board computer is the last component listed in table 12.8. It is mounted to the outside of the heatsink to ensure a optimal cooling of the computer.

### 12.5.3 Flight Operation

In the flight simulation, the water cooling and the fans are not considered. The dissipated heat is only passively stored in the heat sink.

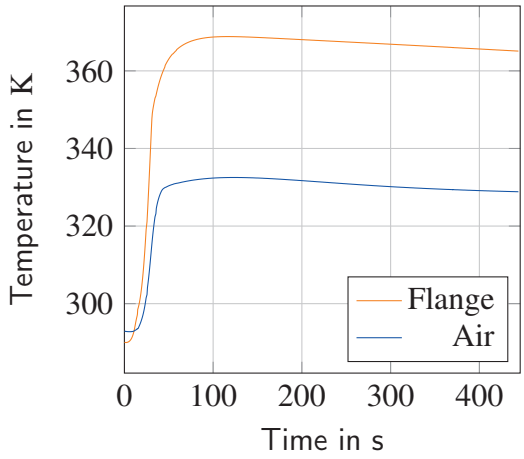


**(a)** Predicted air and flange temperature at the electronic system

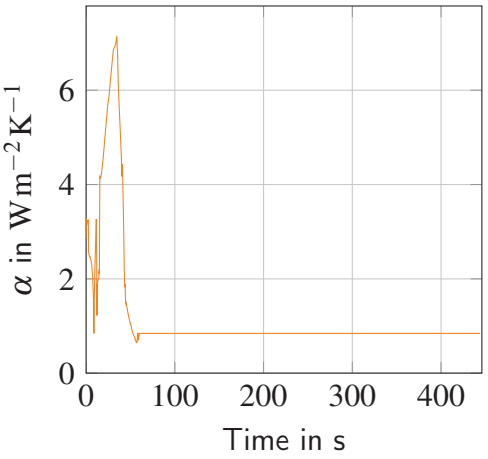


**(b)** Heat transfer coefficient at the electronic system housing

**Figure 12.25:** Input parameters for the simulation of the flight operation of the electronic system. Obtained from the simulations presented in section 11.1 and 10.

As in the other system simulation a convective heat flux is applied to the outside of the housing walls with the time depending parameters presented in figure 12.25. The temperature boundary condition at the instrument platform brackets is set according to figure 12.25a. Convection inside the electronic system housing is neglected, representing an worst case estimation during the flight.

The loads of printed circuit board components is modeled as a heat flux applied directly on the boards. The different parts on the boards are not included in the simulation. The board made of FR-4 composite is model as a single body. This allows to consider the heat capacity of the boards in the simulation, which is important because the low-power boards are designed to store the heat internally and are barely in contact with the heat sink. With this approach it is possible to identify boards that are getting to hot, because their thermal mass is to low.

An exception from this approach are the high power boards with copper heat pipes as e.g. the chip or coil current driver. Here the load is applied on the copper pipe assuming a good thermal contact between the pipes and the high power components. As stated earlier the loads are applied continuously from T=0s.

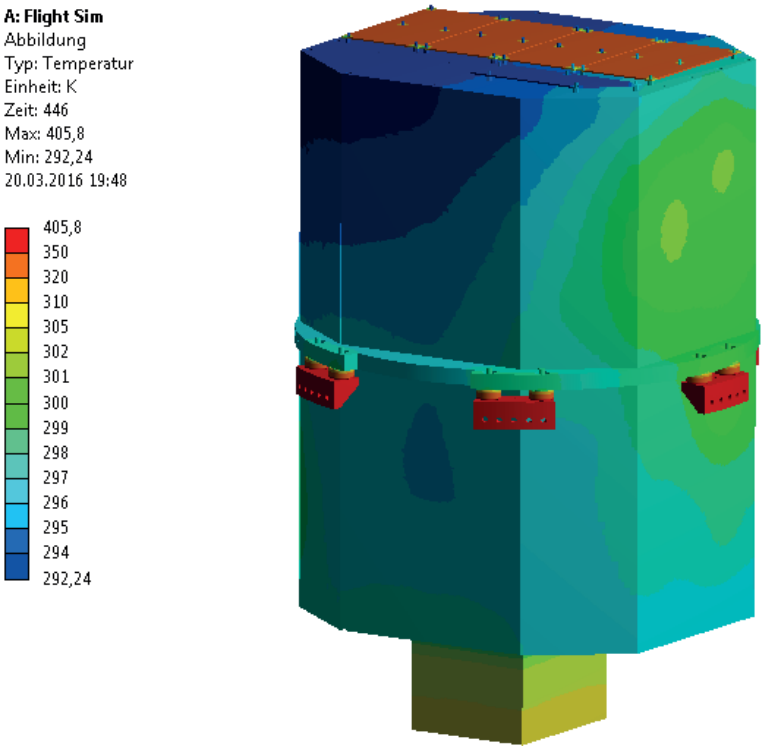


**Figure 12.26:** Spatial temperature distribution at the electronic system housing after 446 s at the end of the microgravity phase. The coldest spot is located at the upper left backplane.

As shown in figure 12.26 the backplanes in contact with the high-power boards of the laser and chip current drivers (located at the upper right backplane) are heating up the most. As expected the backplane of the large battery pack and redundancy laser stack is the coldest spot of the housing, as only little heat is dissipated at this point. Figure 12.27 quantifies this statement. While the other three backplane temperatures increase by approximately 9 K, the battery backplane increases by only 4 K. The maximum temperature rise across all backplanes is 9 K, which is still within the required ranges of the coil and chip current drivers, which require a rise below 10 K. The temperature rise is far from the maximum heatsink temperature of 323 K defined in section 6.5. Although the primary goal of these

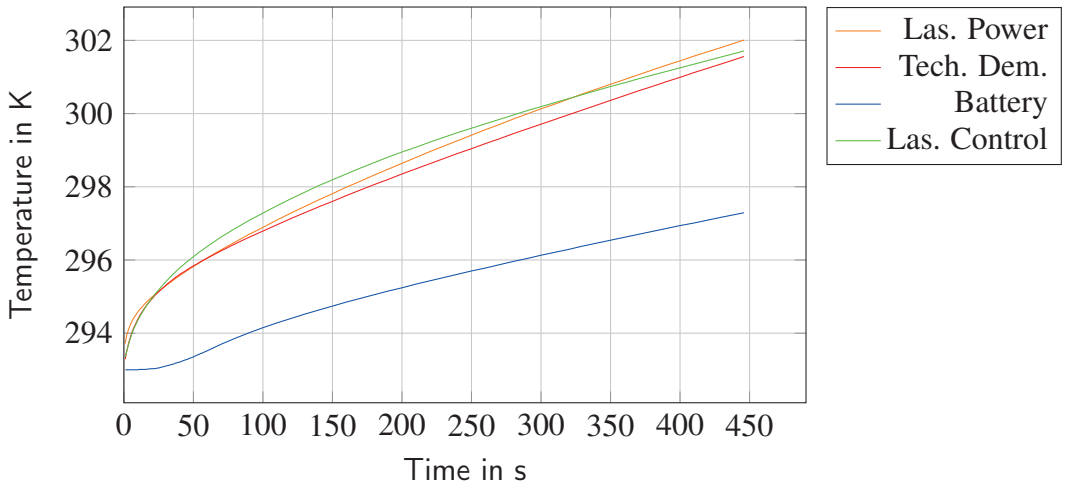


**Figure 12.27:** Maximum temperatures of the four backplanes of the electronic system housing during the flight of the MAIUS-1 payload.

simulation is the sizing of the heatsinks, some board temperatures shall be discussed in the following. The board temperatures of high-power components as e.g. the laser and chip current drivers in figure 12.28a is underestimated in this simulation, because the heat is applied to the part of the card in contact with the backplane and the contact and conduction of the component with the board is neglected.

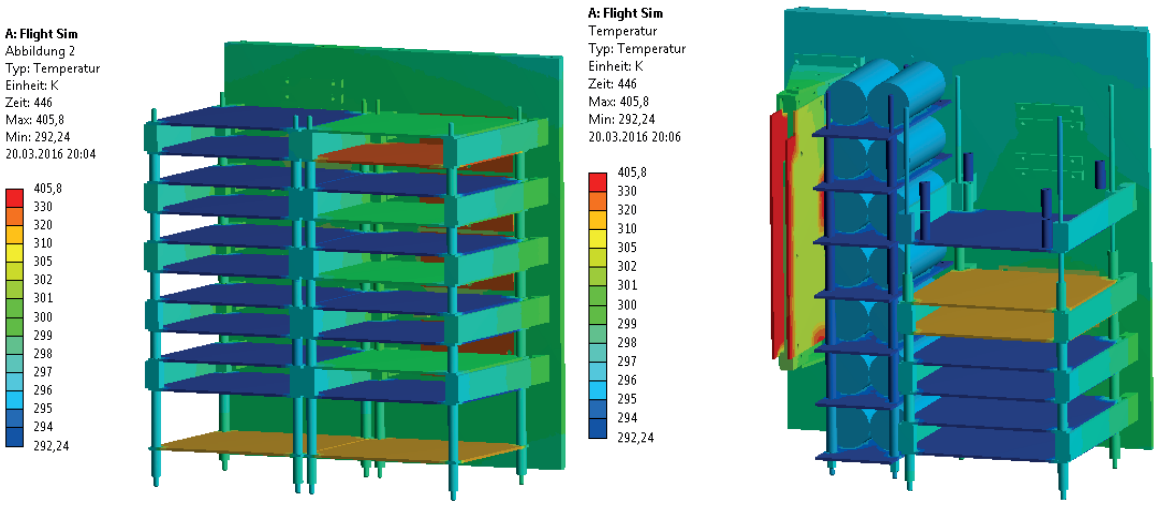


**(a)** At the laser power and chip current driver stack the ethernet card at the bottom and the high-power laser electronics show a significant temperature rise to 320 K and 330 K.

**(b)** At the technology demonstrator and battery stack the ethernet hub is close to its maximum operation temperature of 340 K and the frequency driver cards show a temperature rise to 320 K

**Figure 12.28:** Detail view on backplane and stack temperatures at the electronic system after 446 s.

However, the temperature of those boards that are supposed to store the dissipated heat in

the printed circuit board or conduct the heat from there into the structure are representative. As shown in figure 12.28 the ethernet cards in the laser power and chip current driver stack as well as the frequency controller cards in the technology demonstrator heat up to 320 K under their load of 2 W. This is not critical, since the tolerable board temperature is defined as 343 K. Comparable temperatures are reached at the high-power components of the laser current drivers attached to the backplane as shown in figure 12.28a.

The temperature is exceeded at the ethernet and timing board shown in figure 12.28b, which reaches 335 K. Moreover similar temperatures are reached at the chip safety boards at the upper heatsink shown in figure 12.26. In both cases the actual dissipated heat is not available and a worst-case assumption is used instead. Moreover both boards have poor thermal contact to the structure. For this reason an improvement of the contacting is proposed.

In conclusion the electronic system heatsink temperature and the board temperatures are within the requirements. Nevertheless it has to be considered, that the chip current driver backplane temperature is at the upper edge of the required range. However it has to be considered, that all assumptions made herein are rather conservative, thus the actual temperature during flight is expected to be below the simulated one.

### 12.5.4 Laboratory Operation Simulation

In the simulation of the laboratory operation the internal loads will not change. The simulation aims at finding the equilibrium temperatures of the electronic system heatsinks and to identify potential hot spots. For this reason an operation time of 180 min is chosen to allow the equilibrium temperatures to develop.

As in the simulation of the laser system, the water cooling needs to be included. This is done by implementing a convective heat flux onto the inner wall of the copper pipe in both heatsinks. As given in table 12.3 the mean fluid temperature is set to 295.25 K and the heat transfer coefficient to $3038.2\,\mathrm{W\,m^{-2}\,K^{-1}}$. In addition to this natural convection on the outside walls of the electronic system housing is considered by applying a convective heat flux with a heat transfer coefficient and an air temperature, that will change with time as shown in figure 11.5a and 11.5b in section 11.1.

Moreover the forced convection by the fans has to be included. This is done with a convective heat flux, that is applied on all components attached directly to the backplane and the backplane itself. Moreover the heat flux is applied onto the stacked TBUS boards. The heat transfer coefficient is set to $8.15\,\mathrm{W\,m^{-2}\,K^{-1}}$ and the mean air temperature as 310.5 K as defined in section 12.5.1. The impact of the hot air cooled in the air channels of the heatsink is taken into account by another convective heat flux apllied on the surfaces in the air channels with a air temperature of 313.8 K and a heat transfer coefficient of $14.92\,\mathrm{W\,m^{-2}\,K^{-1}}$.

Figure 12.29 shows, that the water cooling succeeds in removing the applied heat from

the electronic system housing. A temperature gradient of up to 14 K develops between the stabilized heatsinks at the top and bottom and the four backplanes. Again the battery backplane is significantly colder than the others.

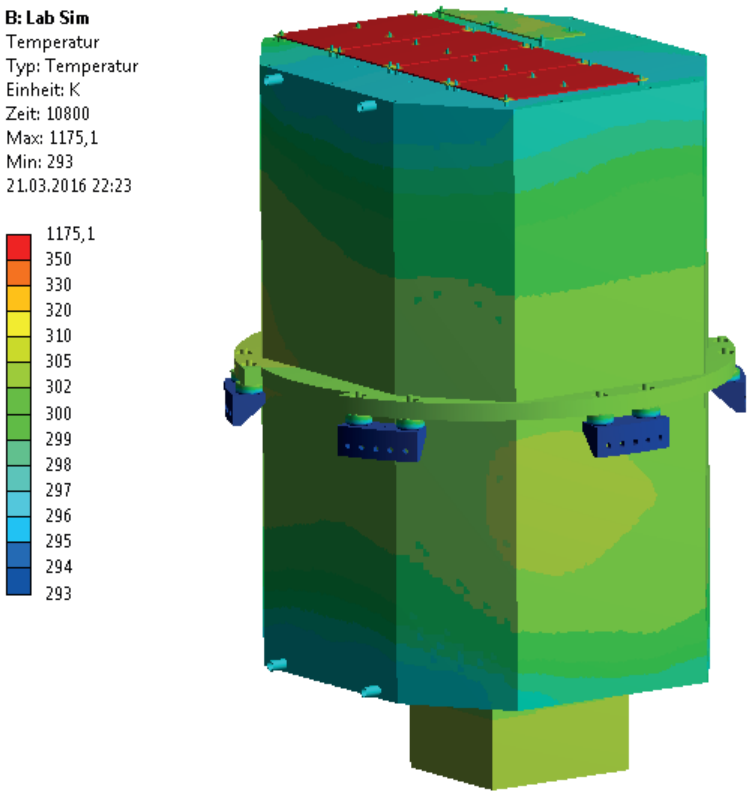


**Figure 12.29:** Spatial temperature distribution at the electronic system housing after 180 min of continuous operation. The water cooled heatsinks at the top and bottom are successfully kept at 298 K.

As shown in figure 12.30 the equilibrium temperature at the backplanes is reached after approximately 120 min. As expected the backplane with the laser and chip current drivers heats up the most reaching temperatures of 311 K. Because of the convective cooling of the fans the cards not directly connected to the backplane are showing moderate temperatures between 308.9 K and 320.7 K.

The laser power and chip current driver stack heatsink is exceeding the limit for the temperature rise of 10 K only 16 min after the begin of operation. Since these temperatures are maximum temperatures, the mean temperature is lower than this, however this might cause a drift in the current driver outputs. A solution to this problem is lowering the heatsink temperature using the water cooling by 9 K. The additional cooling by convection will limit the temperature rise to 9.5 K.

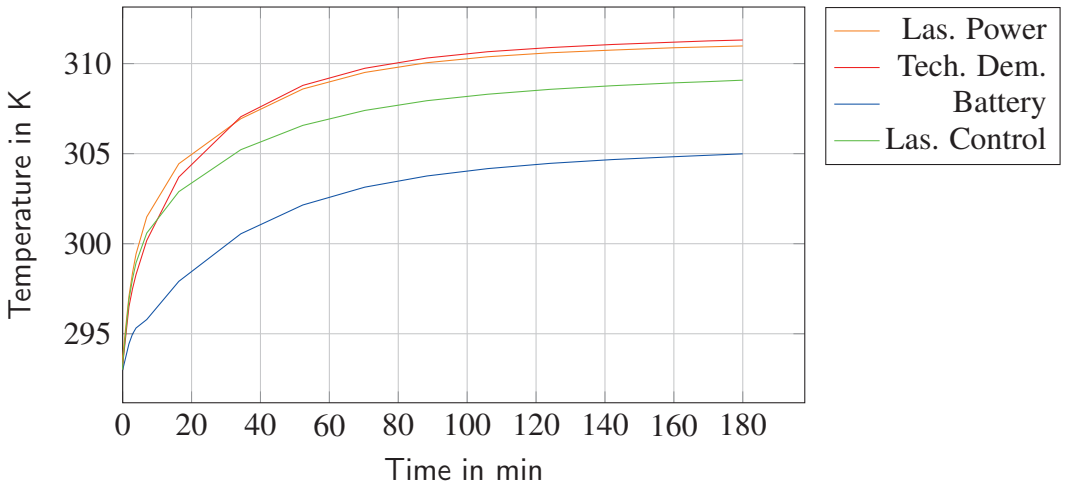


**Figure 12.30:** Maximum temperatures of the four backplanes of the electronic system housing during 180 min of continuous operation in the laboratory.

The board temperature of the chip safety boxes also exceeds its maximum rating significantly. The boards reach temperatures of 439 K, despute the fact that convection is already considered. These high temperatures are caused by the low conduction of the mounting pins. Heatstraps connecting the boards with the heatsink will ensure that the generated heat is dissipated properly.

## 12.6 Battery System

The battery system consists of the power distribution unit and the battery pack itself as described in section 7.6. The system is equipped with a copper pipe cooling the platform separating both parts of the system. As stated in section 12.5 this system is the first in the flow of the lower cooling circuit. The inlet temperature is chosen to be 293 K. With the given flow of $3\,\mathrm{L\,min^{-1}}$ the mean fluid temperature was determined in section 12.2.3 as $T_m = 293.9\,\mathrm{K}$ and the heat transfer coefficient as $2975.6\,\mathrm{W\,m^{-2}\,K^{-1}}$. These parameters will be used to simulate the water cooling as a convective heat flux at the inside of the pipe. The outlet temperature $T_{out} = 294.8\,\mathrm{K}$ has been used as the input temperature for the water cooling calculations of the lower electronic system in section 12.5.

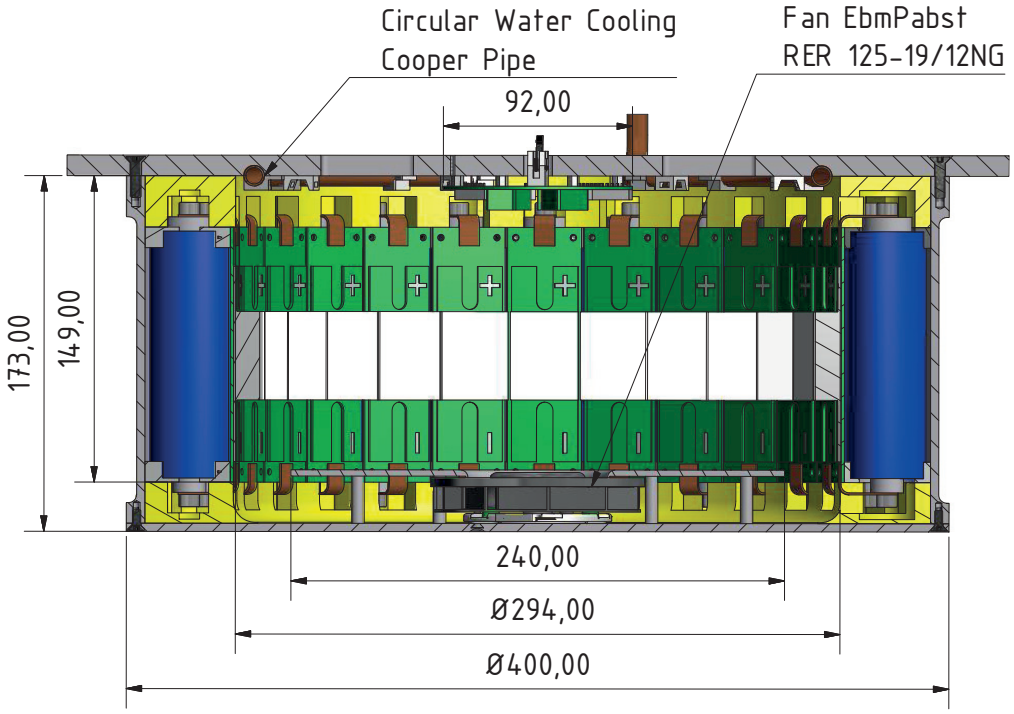


**Figure 12.31:** Thermal control system in the battery pack showing the radial fan in the center and the battery cells and the cell protection arranged as a ring at the battery pack walls. In the center the charging electronics are mounted on a circular PCB.

A fan identical with the one examined in section 12.5.1 is mounted the top cover of the battery pack. The fan absorbs the air in the center of the cylindric housing and blows it towards the housing walls, where the cells and the charging fuses are located. Similar to the calculations performed in section 12.5.1 the cooling of those components is modeled as a stream across a flat plate with a length $l = 149\,\mathrm{mm}$, which is equivalent to the cell assembly height. The stream is significantly blocked, thus it is assumed, that the air circulates with a velocity of $2\,\mathrm{m\,s^{-1}}$, which is reasonable based on the outlet velocity of the fan of $2.23\,\mathrm{m\,s^{-1}}$ as calculated in section 12.5.1. This results in an Reynolds number of 16284, a Nusselt number of 72.96 and ultimately in an heat transfer coefficient of $13.66\,\mathrm{W\,m^{-2}\,K^{-1}}$.

The air heated at the cell assemblies is cooled on the base plate of the battery pack. The characteristic length of the area not covered by the charging electronics board is 101 mm as shown in figure 12.31. This result in an heat transfer coefficient of $16.67\,\mathrm{W\,m^{-2}\,K^{-1}}$ for forced convection at a flat plate as discussed in section 12.5.1.

For the implementation of the air cooling in the simulation the air temperature is needed. Again following the procedure given in section 12.5.1 the temperature difference between the air and the baseplate to transfer one third of the average dissipated power of $Q_{diss} = 93.75\,\mathrm{W}$ is 30.63 K. With a heatsink temperature of 293 K this results in an equilibrium air temperature of 323.63 K. The temperature of the air after being cooled at the base plate is 322.78 K.

The air temperature is relatively high and the setup will not allow to compensate for the dissipated heat at maximum charge/discharge currents. An increase of the cool plate area is desirable, however the charging electronic and cables not shown in figure 12.31 do not allow to enlarge the surfaces. An implementation of the water cooling in the top cover of the battery pack has been proposed and could be implemented as an upgrade, if the measured average discharge currents during operation exceed 25 A.

### 12.6.1 Dissipated Heat and Duty Cycle

The batteries used in the battery pack are Headway 38120SE an thus identical with the ones used in the large battery pack inside the electronic system. As discussed in the electronic system section, the maximum discharge current is given as $5C = 50\,\mathrm{A}$ and the maximum charging current as $4C = 40\,\mathrm{A}$. This results in an maximum heat loss of 15 W at each cell. The average discharge current across all cells is expected to be below 25 A resulting in 3.75 W of dissipated heat.

| Component | Quantity | Avg. Power | Max. Power [W] | Duty Cycle |
|---|---|---|---|---|
| Headway 38120SE | 25 | 3.75 | 15.00 | Always on |
| Cell Protection | 25 | - | 7.50 | if cell is overcharged |
| Charging Electronics | 1 | 3.6 | - | Always on |

**Table 12.9:** Power dissipation and duty cycle of battery system components

Each cell is equipped with a charge limiter and load balancer, that prevents the cells from being overcharged. Once the cell voltage reaches its maximum, the charging current is sent through the limiter, which protects the cell. The limiter sends the current through resistors, where it is converted into approximately 7.5 W of heat. The cell protection is only active if the cell ultimate voltage is reached, thus the heat load should not be constantly applied on the battery pack structure.

Moreover a number of current sensors and monitoring electronics is part of the charging electronics at the center of the battery package. The circular board will dissipate 3.6 W in total.

### 12.6.2 Flight Operation

The flight simulation is performed without considering the water cooling and the forced convection caused by the fans as both are not active during the flight. However as in all previous flight simulations a convective heat flux is applied to the outside of the housing walls with the air temperature and heat transfer coefficient presented in figure 12.32.

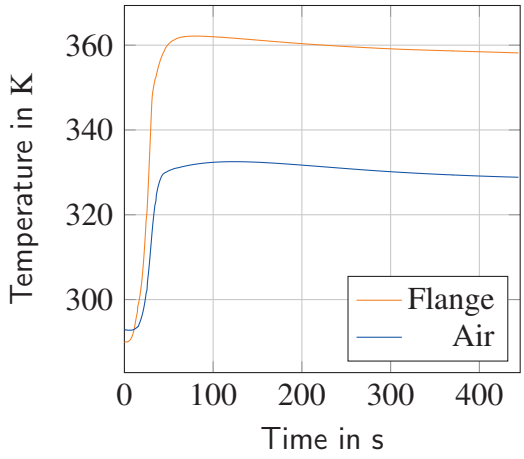


**(a)** Predicted air and flange temperature at the battery system

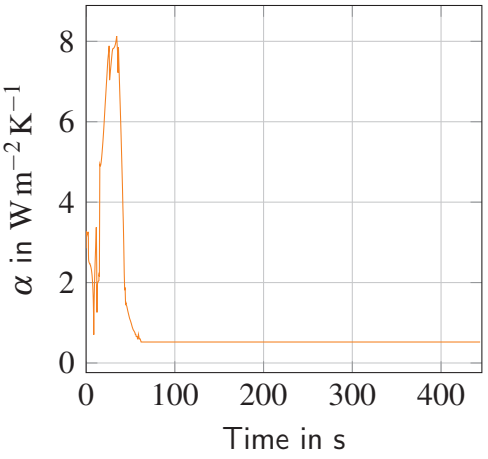


**(b)** Heat transfer coefficient at the battery system housing

**Figure 12.32:** Input parameters for the simulation of the flight operation of the battery system obtained from the simulations presented in section 11.1 and 10.

The temperature boundary condition at the instrument platform brackets is set according to figure 12.32a. Convection inside the battery pack is neglected, which is considered a worst case scenario.

The discharge current is assumed to be at the maximum of 50 A, which is modeled with internal heat generation in the cell body of 15 W. This is a worst case assumption. The load of the charging electronic center board is applied as a constant heat flux of 3.6 W.

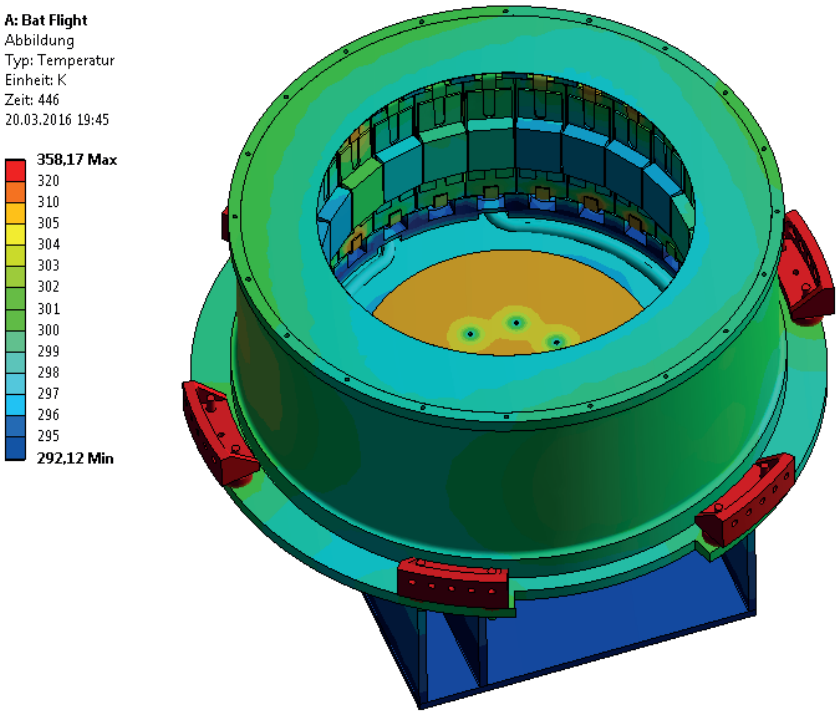


**Figure 12.33:** Spatial temperature distribution at the battery system after 446 s at the end of the microgravity phase.

As shown in figure 12.33 the housing temperature rises from 293 K to 302 K. No particular hot spots could be identified at the housing or the components of the battery system. For the temperature analysis four different cells with an angular distance of approximately 90° have been chosen.

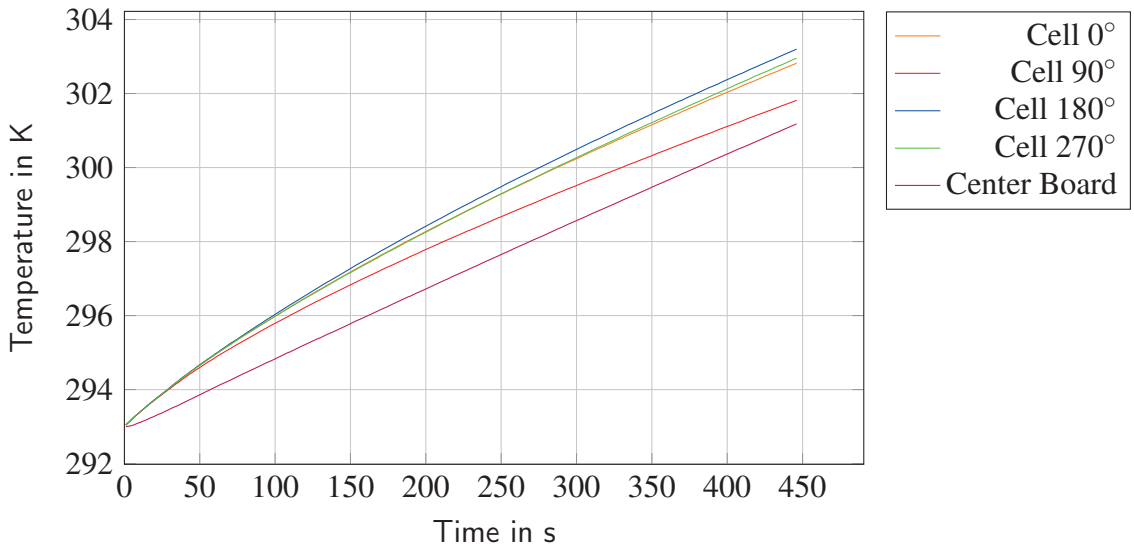


**Figure 12.34:** Temperature of the battery cells and charging electronics center board during ascent and microgravity phase.

The rise of the cell temperature plotted in figure 12.34 changes in the same range as the housing. The cell at 90° is located in the middle between two brackets, while all other cells are in close proximity to one of the brackets. This results in a temperature difference of approximately 2 K. Overall the cell temperatures are within the required range of 283 K to 323 K.

### 12.6.3 Laboratory Operation

As discussed in the beginning of this section the simulation of the laboratory operation requires the implementation of the water cooling and forced convection by the fans. These are realized just as in the previous simulations. The convective heat flux on the inner wall of the copper pipe uses a mean fluid temperature of 293.9 K and a heat transfer coefficient of 2975.6 $\mathrm{W\,m^{-2}\,K^{-1}}$ as given in table 12.3.

In addition to this natural convection is considered by applying another convective heat flux on the outside walls. As in the previous systems the heat transfer coefficient and an air temperature are set in accordance with the data plotted in figure 11.5a and 11.5b

Moreover the forced convection by the fans has to be included as done in the electronic system simulation. For the convective heat flux on the cell protection the heat transfer coefficient is set to 13.66 $\mathrm{W\,m^{-2}\,K^{-1}}$ and the mean air temperature to 322.78 K as discussed at the beginning of this section. The cells themselves are shielded by the protection boards, therefore no convective heat flux is applied on their surfaces.

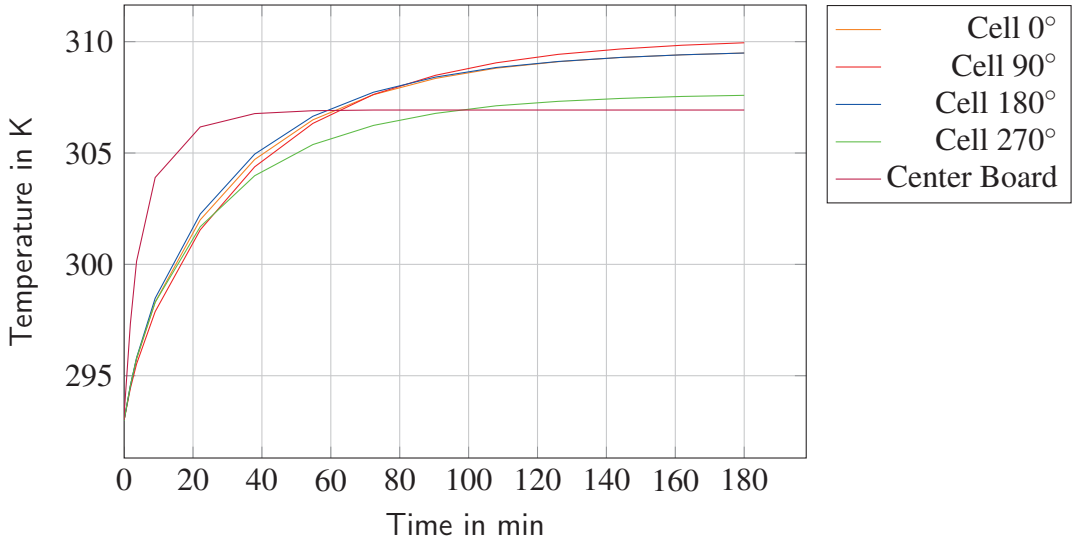


**Figure 12.35:** Temperature of the battery cells and charging electronics center board during 180 min of continuous discharge/charge with 25 A

The cooling of the hot air at the baseplate is modeled with a second convective heatflux with an air temperature of 323.6 K and a heat transfer coefficient of 16.67 $\mathrm{W\,m^{-2}\,K^{-1}}$ as determined at the beginning of this section.

The charge or discharge current is assumed to be 25 A, which is supposed to be the average load as defined in table 12.9. The discharge load is modeled with internal heat generation in the cell body of 3.75 W. The load of the charging electronic center board is applied as a constant heat flux of 3.6 W.

As shown in figure 12.35 the simulated time of 180 min is sufficient to reach an equilibrium temperature at the cells, the center board and the housing. his temperature is reached after 140 min. The equilibrium temperature of the center board is reached after 40 min.

The temperature at the center board rises only by 13 K. The maximum cell equilibrium temperature is 310 K. This corresponds to a rise in temperature by 17 K. The cell temperatures are within the required range of 283 K to 323 K, but it has to be noted, that the margin to the maximum temperature is only 13 K. For this reason an increase of the discharge current by a factor 4 to the maximal load of 15 W, will result in temperatures above the rating and might cause damage at the cells. For this reason high discharge current should be avoided.

# 13
# Thermal Testing of MAIUS-1 payload

It is common practice in space projects to perform not only vibrational tests, but also thermal tests on system level as well as with the entire payload. This was originally also planned for MAIUS. The different systems should be tested individually in their rocket hull segments. In this tests the influence of convection should be minimized by closing the segments at top and bottom. Thermal vacuum test were not considered due to the limited budget and because the payload is pressurized during the entire flight.

In the end all system level tests were canceled due to delayed delivery of the systems or because other test as e.g. the optimization of the experiment sequence were prioritized. Instead several thermal tests shall be performed with the entire scientific payload.

After the complete assembly of the payload the water cooling system and the fans will are tested in the laboratory to ensure that no component or system will exceed the temperature range. In addition to the usual laboratory operation, two bench tests with the scientific payload and the MORABA systems are planned.

In these tests the scientific payload will be operated via the ground support equipment and via the MORABA service module. As part of the second bench test a flight simulation will be performed, where the water cooling and the fans are deactivated and the experiment sequences planned for the flight are performed. Although this test is performed under gravity, it will be a representative test for the MAIUS thermal control system.

## 13.1 Test Setup and Parameters

As the experiment is still not performing perfectly, the long term test in the laboratory have not yet been performed, because the payload is typically disassembled to allow full access to the instruments for debugging.

Nevertheless a first bench test has been performed with the MORABA systems at the German Aerospace Center (DLR) Oberpfaffenhofen. In this test all systems were activated via the ground support equipment and a sequence to generate a MOT was successfully executed via the ground support equipment.

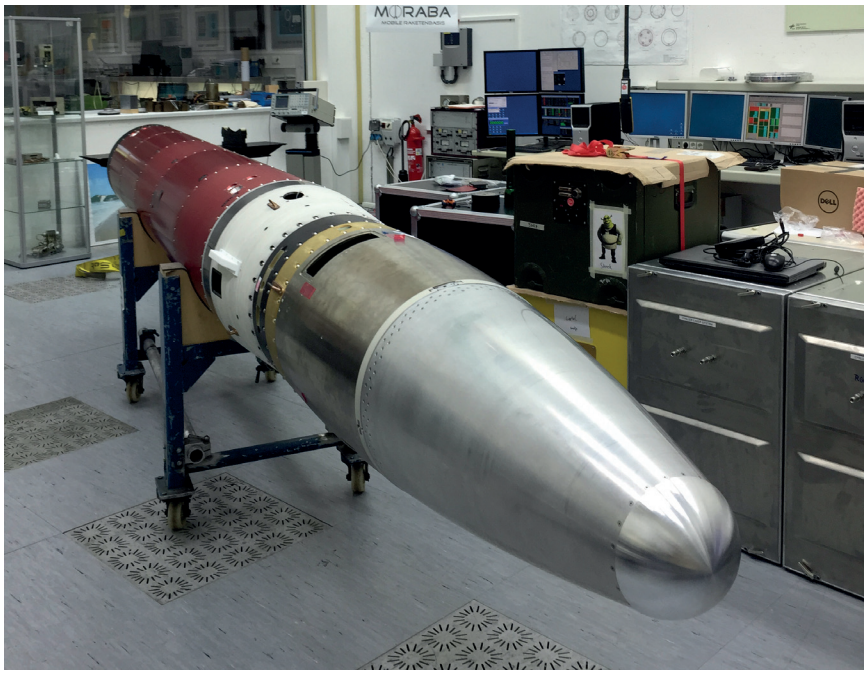


**Figure 13.1:** MAIUS-1 scientific payload assembled with the MORABA systems after the first bench test in Oberpfaffenhofen

During the test the temperatures of different components and structural parts of the laser system, physics package and electronic system as well as the hull temperatures have been measured by the payload housekeeping system.

The temperatures are measured using 10 kΩ negative temperature coefficient (NTC) thermistors. It has to be noticed, that the thermistors are not calibrated, thus the measured absolute temperature may be inaccurate.

In the following the sensor data gathered during the bench test shall be analyzed and compared with the simulations. Furthermore the functionally of the thermal control system shall be discussed wherever possible. Unfortunately no thermistors were placed at the battery system, thus neither a comparison between the measured and simulated data nor a validation of the functionality of the thermal control system is possible.

## 13.2 Physics Package

The data logging at this test was performed for the first time with the flight software and the ground support equipment. Due to software issues some of the logging hardware was activated to late (110 min in the test), which resulted in a massive loss of data. Unfortunately this affected all 12 temperature channels recording the temperatures at the physics package.

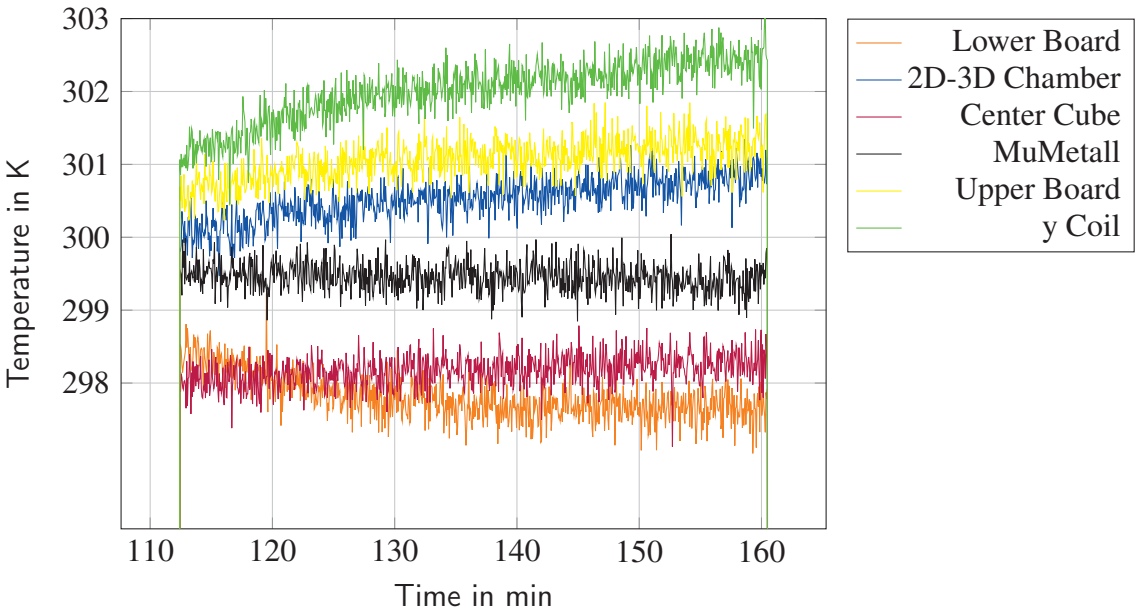


**Figure 13.2:** Temperature of some physics package parts during a three hour bench test. The two instrument platforms, the Mumetall and the center cube of the vacuum system are at an stable temperature, while the chamber and y-coil temperatures are still rising.

Figure 13.2 shows the recorded data of from minute 110 until the end of the test at 160 s. The temperatures seem to have stabilized in the first 110 min of the test. The center cube and the lower instruments platform are stable at 298 K. The Mumetall temperature is also stable at 299.5 K.

The y coil is the component with the highest temperature. This is in good accordance with the result of the laboratory operation simulations performed in 12.3. The y-coil temperatur rises by 1.5 K in the ploted 45 min of the test. The sensor at the connection between the preparation and science chamber is also still rising, which is caused by the heating of the preparation chamber by the 2D-coils. This is also expected and has been simulated in section 12.3.

After 160 min of operation all sensors of the physics package show small or no temperature gradients. Therefore the system is assumed to be in a thermal equilibrium and only minor temperature changes are expected if the system is operated longer. All temperatures are within the requirements with a significant margin.

In comparison with the simulations the temperature gradient is significantly smaller. In the simulation the temperature at the connection between 2D and 3D chamber has risen by 20 K as shown in figure 12.12, while the temperature rise is below 5 K assuming an initial temperature of 298 K.

This has been expected, since the simulations represent a worst case scenario with roughly 2100 experiments performed in the simulated time. In the bench test only around 30 MOT sequences were run in the same amount of time. In summary the test demonstrated, that a long time operation of the physics package without active thermal control is possible. However automated optimization sequences might cause a severe temperature rise as simulated in section 12.3.

## 13.3 Laser System

At the laser system only one of the two temperature logging cards was activated late in the test. This affected the log of the AOM, Splitter and Zerodur board temperatures as shown in figure 13.3.

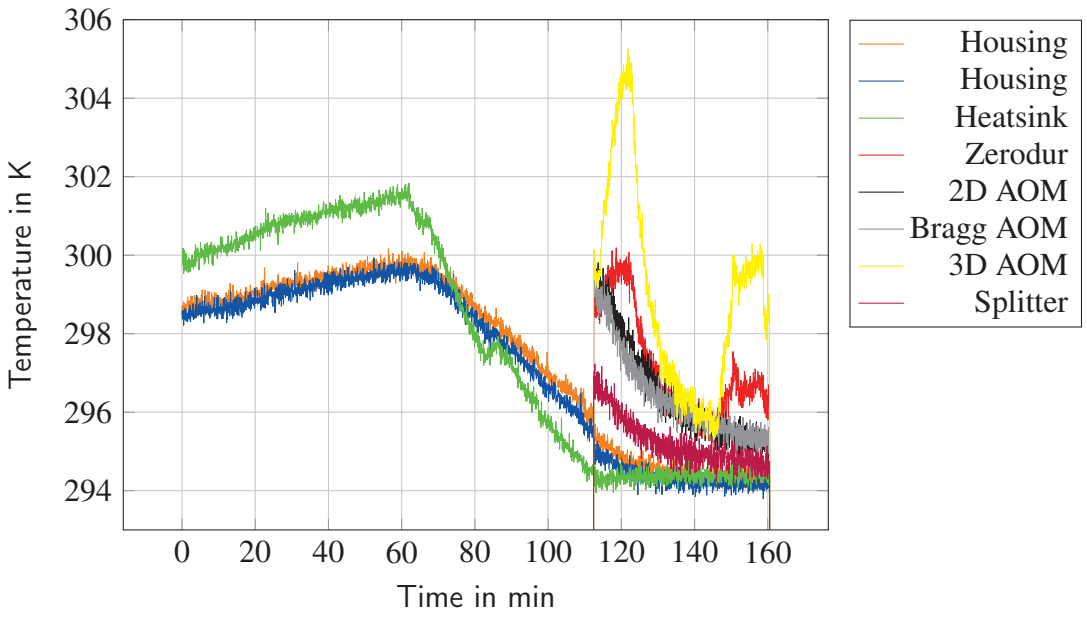


**Figure 13.3:** Temperature of the laser system housing walls, the heatsink close to the redundancy lasers and the Zerodur board close to the acusto-optical modulators (AOMs).

During the test the system was operated without water cooling until $t = 60\,\mathrm{s}$, after this the water cooling was activated. Prior to the activation the temperature of the housing walls and the heatsink close to the redundancy lasers are rising linearly with a gradient of 2 K in 3600 s this is a gradient of $5.5 \times 10^{-4}\,\mathrm{K\,s^{-1}}$. In the simulation of the flight performance shown in figure 12.17 the heatsink temperature rises 1.2 K in 446 s, which is a gradient of $2.5 \times 10^{-3}\,\mathrm{K\,s^{-1}}$. The higher gradient is explained by the additional thermal load due

to aerothermal heating in the flight simulation and the neglected natural convection in the laser system housing.

When the water cooling is activated the heatsink temperature reaches the set point of 294 K is reached after 40 minute. The temperatures of the housing walls and all components are significantly reduced after activation of the water cooling, which indicates a sufficient thermal contact between the components and the heatsink.

The AOMs mounted to the Zerodur board and the board itself are following slowly the heatsink temperature, die to their bad conductance. The Zerodur board temperature fluctuates with the AOM for the cooling light of the 3D chamber, which is intensively powered during the MOT sequences.

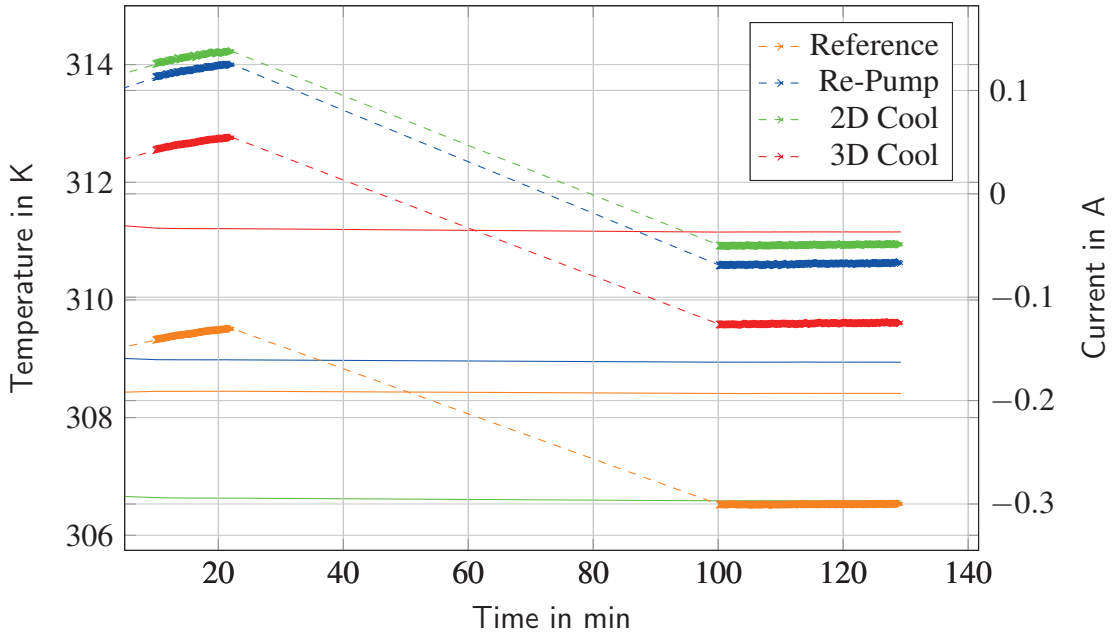


**Figure 13.4:** Solid lines indicate the temperatures of the reference, re-pumping, preparation (2D) cooling and science chamber (3D) cooling laser modules. Each laser diode is stabilized to a unique temperature. The dashed lines represent the operation current of the associated peltier element. No data is available for the current from 24 to 100 min.

The laser temperature is not affected by the change in the heatsink temperature. The peltier elements succeed in keeping the temperature of the laser modules stable to $\pm 0.1\,\mathrm{K}$ as required. However the current of the peltier element changes as depicted in figure 13.4. The reference laser peltier element is constantly operated at negative current (heating mode), because the dissipated heat of the components of the laser module is not sufficient to maintain the desired temperature. Due to the change in the heatsink temperature more heating is required and the current is increased.

The other three modules are initially cooled by the peltier. At the new heatsink temperature the current changes its sign and the peltier elements switches in heating mode. Unfortunately the data logging was deactivated during the transition between 24 min and 100 min

for unknown reasons.

Nevertheless it has been demonstrated, that the water cooling removes the generated heat efficiently. No component temperature exceeded the requirements during 120 min of operation. The laser were successfully stabilized at their nominal temperature despite a change by 8 K in the heat sink temperature.

## 13.4 Electronic System

The electronic temperature has been logged during the entire test. At this system the water cooling was activated from the beginning, but the fans have been activated at $t = 60$ min. Some of the hardware has already been active before data logging was started.

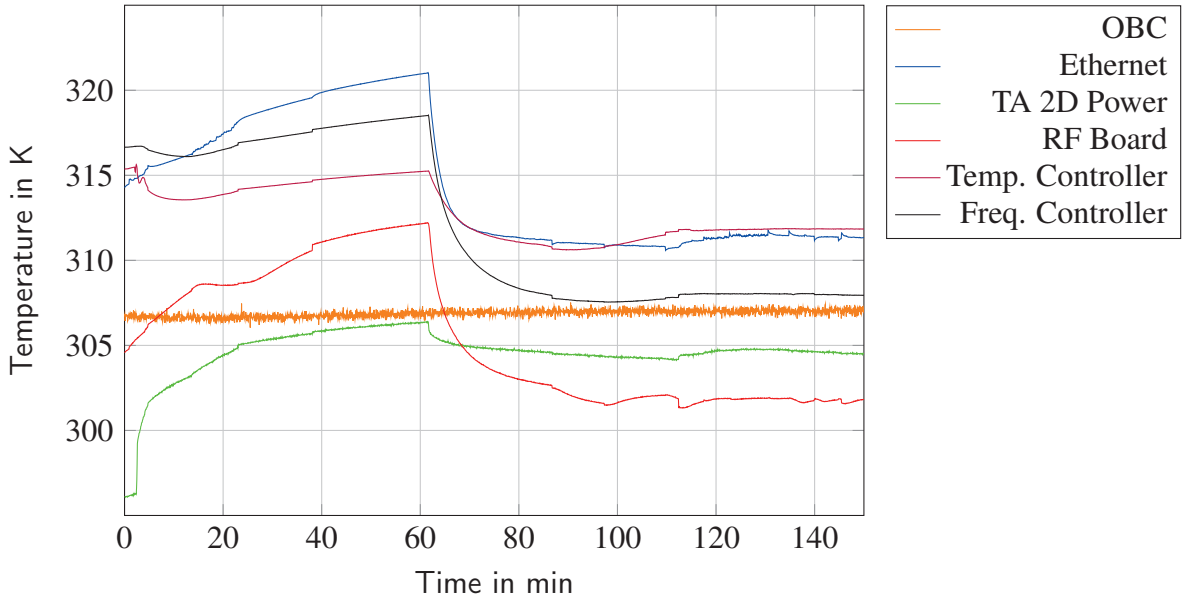


**Figure 13.5:** Temperature of five selected cards of the electronic system with high power consumption and of the on-board computer (OBC) during bench test. The activation of the fans at t = 60 min causes a drop in the card temperatures.

The temperature reading of five selected cards with high power consumption and the on-board computer are shown in figure 13.5. The on board computer and the high-power PCB of the 2D colling laser tampered amplifier (TA) driver are in direct contact with the heatsink. For this reason these components are cooled from the beginning. The constant temperature of the computer indicates a heat sink temperature of below 305 K. This is in accordance with the simulated values shown in figure 12.29. The temperature of the ethernet card also matches very well with the simulation as shown in figure 12.29.

The temperature of the four stacked cards is reduced by 10° by the activation of the fan. In total even the high power cards are kept at moderate temperatures, which have been stabilzed after the activation of the fans. This proves the concept of the thermal control system and allows long time operation of the electronic system.

# Part V

# Conclusion

# 14
# Summary

This thesis gives a detailed description of the mechanical and thermal design of the first BEC-based atom interferometer payload, that has been qualified for the use on a sounding rocket. The payload presented in this thesis measure 2.79 m in length and 0.5 m in diameter. The mass has been measured to be 327.5 kg.

The payload hull consists of 5 segments, which are sealed in between the modules and at the top and bottom to form a pressurized volume of 0.422 $m^3$. A stable pressure between 800 hPa and 1100 hPa is required by the laser system and optics during the entire flight. A sealing method for the hull elements is presented in this thesis. The sealing is achieved by rubber o-ring seals and the data and power connections are realized with hermetic feedthroughs. The hull assembly including sealing and feedthroughs has been tested at an absolute pressure of 2000 hPa for 40 h showing a degradation of 55 hPa in pressure.

The hull segments shelter four systems needed to perform atom interferometry. At the bottom of the payload a battery and power distribution system provides 7 voltages ranging from 3.0 V to 25.2 V with a capacity of 10 A h per voltage.

The electronic system located above the battery system is the most complex system in the MAIUS-1 payload. A total of 147 mostly custom-made components are packed in a octagonal housing. Among these components are e.g. low noise current drivers, frequency controllers and direct digital synthesis (DDS) boards. The high number of components results in an average power of 343 W requiring a complex thermal control system.

The fibre-based laser system houses eight laser modules and a free-space splitting and spectroscopy module, which are mounted on an Zerodur base plate, in an ultra compact housing with a volume of 0.021 $m^3$ and a mass of 23 kg. The four science lasers provide light at a wavelength of 780 nm with a measured in-fiber power of approximately 200 mW.

The laser light is guided to the physics package located above the laser system with polarization maintaining optical fibers, which have proven to be insensitive to variations of the environment. The physics package is divided into two parts. At the very top of the sealed volume the UHV pumping system is autonomously maintaining a pressure below $1 \times 10^{-10}$ hPa in the two titanium vacuum chambers of the physics package. These chambers with a total of 13 viewports, three pairs of coils and planar magnetic structures form a setup to magneto-optical trap and cool atoms. This setup is integrated into a three-layer magnetic shield, which reduces the residual magnetic fields to below 100 nT.

The mechanical design of these systems is an important part of this thesis. All structural components of these systems have been designed to withstand shock loads of 100 g and vibrational loads of up to 8.1 $g\,RMS$. All payload systems have successfully been qualified in a random vibration test at a level of at least 5.4 $g\,RMS$.

The instruments of the systems described above are mounted to four platforms, attached to the payload hull by brackets equipped with passive vibration isolation devices developed in the scope of this thesis. The mounting is designed to withstand loads of 100 g and damps vibrations repeatably by a factor 5.8 to 6.5 for frequencies between 100 Hz and 2000 Hz.

Furthermore the in-depth design of the first UHV vacuum system for pressures below $5 \times 10^{-11}$ hPa, which has been qualified for the operation on a sounding rocket is presented in this thesis. This system fulfills the requirements of quantum optic experiments regarding magnetic permeability by using only titanium and oxygen free copper in the area of interest. The design makes use of an advanced brazing-technique to connect the two vacuum chambers.

The impact of outgassing of vacuum materials is discussed intensively and the outgassing rate of the MAIUS setup is approximated. The effective pumping rate of a commercial ion-getter pump and two titanium sublimation pumps is calculated at different locations of the vacuum system considering the conductance of all parts of the vacuum system. Ultimately the leakage rate of all metal con-flat seals and indium seals under static and vibrational loads has been determined.

The tested vacuum system showed a pressure rise in both the static and the vibrational tests, which is caused by temporal external leaks. The pressure rise is depending on the static or vibrational load level. If the vacuum system is vibration tested in flight configuration with an initial pressure of $1.61 \times 10^{-10}$ hPa, a rise to $7.9 \times 10^{-9}$ hPa was observed at 5.4 g RMS, while the rise is limited to $1.03 \times 10^{-9}$ hPa at 2.0 g RMS. This corresponds to a leakage rate of $2.28 \times 10^{-7}$ hPa L s$^{-1}$ at acceptance level and $2.5 \times 10^{-8}$ hPa L s$^{-1}$. Although the time to regain the desired pressure level for experiments is long (40 s) it will not reduce the available time for experiments.

In the last part of this thesis a thermal control system has been developed for every payload system. For operation on ground two water cooling circuits will control the system heatsink temperature. These circuits are fed from two thermostats outside the payload via

a water cooling umbilical especially designed for this purpose. Moreover fans are used to cool electronic components by forced convection inside the electronic and battery system housing.

During the flight the dissipated heat of the system components is entirely stored in the system heatsinks. For the sizing of the heatsinks multiple codes have been developed in this thesis to estimate the heat flux into the rocket hull by aerodynamic heating as well as the heat transfer from the rocket hull to the system housing walls by natural convection. For the simulation of natural convection, the heat transfer coefficient and air temperature inside the pressurized volume of the payload are determined for the operation on ground, during ascent and during the microgravity phase. These codes can easily be adapted for the use with other (pressurized) payloads.

For validation of the thermal control system design, temperature data obtained from a bench test performed with the fully integrated payload has been analyzed and is discussed in this thesis. The data does not indicate any thermal problems during the 3-day test.

# 15
# Outlook

The MAIUS-1 experiment recently demonstrated a BECs of $1 \times 10^5$ Rubidium-87 atoms in the laboratory, which was produced in less then 2 s. The performance of the system is currently optimized.

Subsequently thermal tests and flight simulation tests will be performed with the fully assembled payload. Finally the entire payload will be vibration tested at acceptance level during the environmental test campaign. Within this campaign the quality of the BEC will be investigated directly after applying vibrations to learn about the impact on the BEC quality. The results of this test will end in a go or no-go for a launch in October 2016.

During the MAIUS-1 flight temperature data will be gathered at several points along the hull of the scientific payload. This data will help to improve the simulation of aerodynamic heating during ascent. The code and the obtained data will be published after the flight to allow the use by other payload engineers. The tool will also help to improve the thermal control system of future MAIUS payloads.

In the next three years two follow-up missions MAIUS-2 and MAIUS-3 are planned with the objective of demonstrating all necessary techniques for testing the universality of free fall. Therefore a new apparatus design capable of creating BECs with potassium and rubidium atoms has recently been carried to the critical design review (CDR). With this system it will be possible to demonstrate dual species atom interferometry in space for the first time.

A successful sounding rocket flight will be an important step towards future missions with cold-atoms in space. For these missions new technologies need to be investigated to improve the system performance or to reduce the payload mass and volume.

To decrease the system mass, the magnetic shielding typically made of steel with a high material density, could be replaced by active real-time compensation of external fields with coils. This is especially interesting for setups with large interferometer chambers.

In the field of vacuum technology electro-chemical polishing is an interesting process with the potential of decreasing the outgassing rates of the chamber walls. This would allow to use smaller and lighter pumps. Outgassing rates could also be decreased for the atomchip technology by avoiding gluing of the chip layers. Both topics are currently addressed in different studies of the QUANTUS consortium. The vacuum test stand, which has been developed as part of this thesis will be used to measure outgassing rates of different material probes.

In the course of this thesis chemical reactions between the indium seals and rubidium were experienced at high rubidium partial pressures. Within 6-12 months these lead to destruction of the indium seals, which makes this sealing technique a potential single-point-of-failure for long-term satellite missions. Moreover the indium is limiting the bake-out temperature to below 100 °C. To speed up the bake-out procedure and to allow further reduction of the outgassing of the chamber walls higher temperatures are desirable. To address this issues a technique has been developed in parallel to this thesis to braze BK7 viewports directly into a titanium chamber. This connection is chemically inert and will allow to use bakeout temperatures of up to 200 °C. A chamber prototype is currently in production. In the near future this prototype shall be tested mechanically and optically.

Moreover, a new generation of rubidium and potassium ovens has been developed in parallel to this thesis. The size and mass of the oven has been reduced by approximately 50 % in this new design. The second generation ovens have successfully been tested and will be used in the MAIUS-2 and MAIUS-3 sounding rocket missions.

A future oven design is currently in development and should include a valve to remotely close the oven to be able to control the rubidium partial pressure instantaneously. The valve will also allow to fill the oven with pure rubidium or potassium. This will avoid the use of glass ampules, which cause a massive input of gaseous argon into the vacuum system, when the ampule is cracked. Furthermore the glass fragments could potentially block the flow of rubidium or potassium into the chamber. Both issues are solved with the new design approach.

The technology development and the understanding of atom interferometry in microgravity from drop tower and sounding rocket experiments, pave the way for the next generation of atom interferometer experiments to be launched on a satellite. These future payloads will allow to perform fascinating experiments as a test of the weak equivalence principle, measurements of earth's gravity gradient field or detection of the recently revealed gravitational waves, each with the potential to have a huge impact on the world of physics.

# List of Figures

# List of Tables

# Bibliography


[Ada97] C. Adams and E. Riis: Laser cooling and trapping of neutral atoms. *Progress in Quantum Electronics* (1997), Bd. 21(1):S. 1 – 79 7

[Agi11] Agilent Technologies: VacIon Plus 20 Pumps - User Manual (2011) 182, 183

[Agi14] Agilent Technologies: Ion Pumps - Catalogue and Technical Notes (2014) 179, 180, 181

[Agu14] D. N. Aguilera, H. Ahlers, B. Battelier, A. Bawamia, A. Bertoldi, et al.: STE-QUEST - Test of the Universality of Free Fall Using Cold Atom Interferometry. *Classical and Quantum Gravity* (2014), Bd. 31(11):S. 115010 77, 129

[Air09] Airbus S.A.S France: *A300B2 - Airplane Characteristics for Airport Planning Revision 22* (2009) 17

[Ari11] Arianespace: *Ariane 5 Users Manual Issue 5 Revision 1* (2011) 26, 27

[Ari12] Arianespace: *Soyuz CSG Users Manual Issue 2* (2012) 24, 26

[Bar12] A. N. Barbosa and L. N. F. Guimarães: Multidisciplinary Design Optimization of Sounding Rocket Fins Shape Using a Tool Called MDO-SONDA. *Journal of Aerospace Technology and Management* (2012), Bd. 4(4):S. 431–442 22

[Bar13] B. Barrett, P. A. Gominet, E. Cantin, L. Antoni-Micollier, A. Bertoldi, et al.: Mobile and Remote Inertial Sensing with Atom Interferometers. *Phys. Rev. Lett.* (2013), Bd. 100:S. 041101 14

[Ber96] M. Bernardini, C. Bradaschia, H. Pan, A. Pasqualetti, R. Poggiani, et al.: Outgassing Measurements of Kapton Insulated Cables (1996) 169

[Ber15] U. Bergner, S. Wolfgramm, S. Gottschall, and M. Flämmich: Vakuumkomponenten für UHV und XHV aus Aluminium. *Vakuum in Forschung und Praxis* (2015), Bd. 27(1):S. 33–35 164

[Bos24] Bose: Plancks Gesetz und Lichtquantenhypothese. *Zeitschrift für Physik* (1924), Bd. 26(1):S. 178–181 3

[Bra97] A. Bradford and E. Hedqvist: Mechanical Testing of Teamsat, in: T.D. Guyenne (Herausgeber) *Environmental Testing for Space Programs*, Bd. 408 von *ESA Special Publication*, S. 217 26

[Bro10] P. Brozynski: Demonstration eines Chip-Gravimeters in QUANTUS-I (2010) 42

[Ceg05] E. Ceglia: *European Users Guide to Low Gravity Platforms - Issue 2 Revision 0* (2005) 22, 23, 24, 25, 26

[Dal89] J. Dalibard and C. Cohen-Tannoudji: Laser cooling below the Doppler limit by polarization gradients: simple theoretical models. *J. Opt. Soc. Am. B* (1989), Bd. 6(11):S. 2023–2045 8

[Dem14] M. Demper: E-Mail Correspondence (2014) 105

[Deu08] Deutsche Edelstahlwerke GMBH: Werkstoffdatenblatt 1.4404 (2008) 103

[Dic13a] Dichtomatik GMBH: O-Rings catalogue, Techn. Ber. (2013) 89

[Dic13b] S. Dickerson, J. Hogan, A. Sugarbaker, D. Johnson, and M. Kasevich: Multiaxis Inertial Sensing with Long-Time Point Source Atom Interferometry. *Phys. Rev. Lett.* (2013), Bd. 111:S. 083001 32, 33

[Din04] R. Dinter: *Aufbau und Charakterisierung einer Magnetfalle zur simultanen Speicherung von 40K und 87Rb*, Dissertation, Universität Hamburg, Hamburg, Germany (2004) 9

[Dro12] Drop Tower Operation and Service Company (ZARM FABmbH): *Drop Tower Bremen User Manual* (2012) 19, 20

[Dun13] H. Duncker: *Ultrastable Laser Technologies and Atom-Light Interactions in Hollow Fibers*, Phd. thesis, Universität Hamburg (2013) 131

[Dyl93] H. F. Dylla, D. M. Manos, and P. H. LaMarche: Correlation of outgassing of stainless steel and aluminum with various surface treatments. *Journal of Vacuum Science and Technology* (1993), Bd. 11(5):S. 2623–2636 159

[ebm16] ebm-papst Landshut GmbH: Kompaktlüfter für Gleich- und Wechselspannung (2016) 270

[Ein07] A. Einstein: Über das Relativitätsprinzip und die aus demselben gezogenen Folgerungen. *Jahrbuch der Radioaktivität* (1907), Bd. 4:S. 411–462 11

[Ein24] A. Einstein: Quantentheorie des einatomigen idealen Gases. *Sitzungsberichte Der Preussichen Akademie Der Wissenschaften* (1924):S. 261–267 3

[Els75] R. Elsey: Outgassing of vacuum materials-II. *Vacuum* (1975), Bd. 25(8):S. 347 – 361 161, 162, 163, 165, 169, 170

[Ett06a] J. Ettl: Post Flight Report TEXUS 42 DLR-MR-TEXUS 42-0002, Techn. Ber., German Aerospace Center - Mobile Rocket Base (2006) 22

[Ett06b] J. Ettl: Post Flight Report: TEXUS 42 (PRELIMINARY VERSION), Techn. Ber. DLR-MR-TEXUS 42-0002, MORABA, German Aerospace Center (2006) 23, 68

[Gei11] R. Geiger, V. Menoret, G. Stern, N. Zahzam, P. Cheinet, et al.: Detecting inertial effects with airborne matter-wave interferometry. *Nature Communications* (2011) 36, 38

[Gle15] Gleich Aluminium GmbH und Co KG: EN AW 7075: Technisches Datenblatt (2015) 221

[Gra04] F. Grangeon, C. Monnin, M. Mangeard, and D. Paulin: Development of an ultra-high vacuum system for space application. *Vacuum* (2004), Bd. 73(2):S. 243 – 248, Proceedings of the European Vacuum Congress Berlin 2003, 23-26 June 2003, featuring the 8th European Vacuum Conference, 2nd Annual Conference of the German Vacuum Society 157, 169

[Gro11] J. Grosse, M. Scharringhausen, S. Stephan, M. Krutzik, T. Wendrich, et al.: QUANTUS/MAIUS Preliminary Design Report, Technical report, QUANTUS III Consortium (2011) 171

[Hau13] M. Hauth, C. Freier, V. Schkolnik, A. Senger, M. Schmidt, et al.: First gravity measurements using the mobile atom interferometer GAIN. *Applied Physics B* (2013), Bd. 113(1):S. 49–55 32, 33

[Her13a] W. Herr: *Eine kompakte Quelle quantenentarteter Gase hohen Flusses für die Atominterferometrie unter Schwerelosigkeit*, Dissertation, Gottfried Wilhelm Leibniz Universität Hannover, Hannover, Germany (2013) 4, 43, 44, 46

[Her13b] W. Herr: QUEST lecture: Atom interferometry in free fall (2013) 45, 46, 47

[Hof14] S. Hoffmann: *TEXUS - Sounding Rockets for Microgravity Research*, German Aerospace Center (2014) 22

[Hog14] J. Hogan: Precision atom interferometry in a 10 meter tower (2014) 32

[Hor12] G. Horn: Zugversuch nach DIN ISO 6892-1 (B) Rundprobe, Testreport Auftragsnummer 12235, Günther-Köhler-Institut für Fügetechnik und Werkstoffprüfung GmbH (2012) 120

[Hub14] Huber GmbH: Catalogue 2014/2015 (2014) 244

[Jou13] K. Jousten: *Wutz Handbuch Vakuumtechnik: Theorie und Praxis; 11. Aufl.*, Springer Vieweg, Wiesbaden (2013) 159, 160, 161, 173, 174, 175, 178, 185

[Kas13] M. Kasevich: Long interrogation time precision atom interferometry (2013) 32, 34, 35

[Kim15] R. L. Kimmel, D. Adamczak, A. Paull, R. Paull, J. Shannon, et al.: HIFiRE-1 Ascent-Phase Boundary-Layer Transition. *Journal of Spacecraft and Rockets* (2015), Bd. 52(1):S. 217–230 224

[KL16] A. Kubelka-Lange, S. Hermann, J. Grosse, C. Lämmerzahl, E. M. Rasel, et al.: A three-layer magnetic shielding for the MAIUS-1 mission on a sounding rocket. *Review of Scientific Instruments* (2016) 77, 105, 106, 107

[Kri08] J. Krieger: *Zeeman-Slower und Experimentsteuerung für das NaLi-Experiment*, Diploma Thesis, Kirchhoff-Institut für Physik (2008) 5, 6

[Kru] M. Krutzik: *Space qualified laser system (unpublished)*, Phd. thesis, Universität Bremen 128

[Kup10] M. E. Kupfer: *Analysis Of Low-Temperature Indium Seals For Hermetic Packaging Of Large-Area Photodetectors*, Master Thesis, University of Illinois at Chicago (2010) 171, 198

[Kur08] H. Kurisu, K. Ishizawa, S. Yamamoto, M. Hesaka, and Y. Saito: Application of titanium materials to vacuum chambers and components. *Journal of Physics: Conference Series* (2008), Bd. 100(9):S. 092002 166

[Lac12] M. D. Lachmann: *Realisierung, Charakterisierung und Weltraumqualifizierung von Strahlformungsoptiken*, Bachelor thesis, Gottfried Wilhelm Leibniz Universität Hannover (2012) 117

[Lei13] Leibniz University Hannover: Cosmic Vision Mission: STE-QUEST ATI Performance Analysis (2013) 11, 15, 35, 51

[Luv14] Luvata: Alloy OFE-OK - Data Sheet (2014) 122

[Maw14] S. Mawn: *REXUS User Manual*, EuroLaunch (2014) 22

[Men11] V. Menoret, R. Geiger, G. Stern, N. Zahzam, B. Battelier, et al.: Dual-wavelength laser source for onboard atom interferometry. *Opt. Lett.* (2011), Bd. 36(21):S. 4128–4130 38

[Met99] H. J. Metcalf and P. van der Straten: *Laser Cooling and Trapping*, Springer-Verlag, New York (1999) 7

[Mun13] H. Muntinga, H. Ahlers, M. Krutzik, A. Wenzlawski, S. Arnold, et al.: Interferometry with Bose-Einstein Condensates in Microgravity. *Phys. Rev. Lett.* (2013), Bd. 110:S. 093602 39, 42, 43, 47

[NAS] NASA: *International Space Station Users Guide - Release 2.0* 25

[Nym06] R. Nyman, G. Varoquaux, F. Lienhart, D. Chambon, S. Boussen, et al.: I.C.E.: a transportable atomic inertial sensor for test in microgravity. *Applied Physics B* (2006), Bd. 84(4):S. 673–681 36

[O'H04] J. F. O'Hanlon: *A User's Guide to Vacuum Technology*, John Wiley and Sons, Inc. (2004) 165

[Ols81] R. Olsen and J. Mockovciak: Operational Factors Affecting Microgravity Levels in Orbit. *Journal of Spacecraft and Rockets* (1981), Bd. 18(2):S. 141–144 26, 28

[Pet01] A. Peters, K. Chung, and S. Chu: High-precision gravity measurements using atom interferometry. *Metrologia* (2001), Bd. 38(1):S. 25 11

[Pet02] C. Pethick and H. Smith: Bose-Einstein Condensation in Dilute Gases. *Cambridge University Press* (2002) 3

[Pfe09] *Vacuum Technology Know How*, Pfeiffer Vacuum GmbH, Asslar (2009) 158, 162

[Pfe13] *Leak Detection - Compendium*, Pfeiffer Vacuum GmbH, Asslar (2013) 191

[Pol05] W. Polifke and J. Kopitz: *Wärmeübertragung : Grundlagen, analytische und numerische Methoden*, Pearson, München (2005) 220, 221, 234, 235, 236, 241, 255

[Qui90] R. D. Quinn and L. Gong: Real-Time Aerodynamic Heating and Surface Temperature Calculations for Hypersonic Flight Simulation (1990) 224

[Ric08] H. Rice and V. Benischek: Submarine navigation applications of atom interferometry, in: *Position, Location and Navigation Symposium, 2008 IEEE/ION*, S. 933–939 11

[Ros09] P. Rosier: *NOVESPACE A300 ZERO-G RULES AND GUIDELINES*, NOVESPACE (2009) 17, 18

[Rud11] J. Rudolph, N. Gaaloul, Y. Singh, H. Ahlers, W. Herr, et al.: Degenerate Quantum Gases in Microgravity. *Microgravity Science and Technology* (2011), Bd. 23(3):S. 287–292 39, 43

[Sch] A. Schütte: Template for a TEXUS Experiment Hardware/Software Interface Control Document, Techn. Ber. TX-RIBRE-ICD-TBD, EADS 55, 63, 65

[Sch03] S. P. Schneider: Methods for Analysis of Preliminary Spacecraft Designs (2003) 221, 223

[Sch08] S. Schlamminger, K.-Y. Choi, T. Wagner, J. Gundlach, and E. Adelberger: Test of the Equivalence Principle Using a Rotating Torsion Balance. *Phys. Rev. Lett.* (2008), Bd. 100:S. 041101 11

[Sch13] Schott AG: Optische Gläser Datenblätter (2013) 115, 130

[Sei14] S. Seidel: *Eine Quelle für die Interferometrie mit Bose-Einstein-Kondensaten auf Höhenforschungsraketen*, Phd. thesis, Gottfried Wilhelm Leibniz Universität Hannover (2014) 9, 72, 111, 114, 115, 117, 121, 124, 157, 168, 209

[Sta12] A. Stamminger: *MAIUS User Manual Version 1.1*, German Aerospace Center - Mobile Rocket Base (2012) 22, 54, 55, 56, 59

[Sta13] A. Stamminger, L. Altenbuchner, J. Ettl, M. Horschgen-Eggers, W. Jung, et al.: DLR's Mobile Rocket Base - Flight Tickets For Your Microgravity Experiments, in: *64th International Astronautical Congress* 21

[Ste03] D. A. Steck: Rubidium 87 D Line Data, Data reference, Los Alamos National Laboratory (2003) 123

[Ste09] G. Stern, B. Battelier, R. Geiger, G. Varoquaux, A. Villing, et al.: Light-pulse atom interferometry in microgravity. *The European Physical Journal D* (2009), Bd. 53(3):S. 353–357 36, 121

[Ste10] M. Stewart, G. Koutroulakis, N. Kalechofsky, and V. Mitrovic: A reusable, low-profile, cryogenic wire seal. *Cryogenics* (2010), Bd. 50(1):S. 50 – 51 171

[Sut93] W. Sutherland: LII. The viscosity of gases and molecular force. *Philosophical Magazine Series 5* (1893), Bd. 36(223):S. 507–531 215

[Swa11] Swagelok: Swagelok Produkt-Katalog (2011), mS-01-300G4 99

[Tau87] M. E. Tauber, G. P. Menees, and H. G. Adelman: Aerothermodynamics of transatmospheric vehicles. *Journal of Aircraft* (1987), Bd. 24(9):S. 594–602 221, 222

[Thy] ThyssenKrupp Materials Schweiz: Titan Grade 5 Werkstoffdatenblatt 115

[VAC02] VAC Vacuumschmelze Hanau: Weichmagnetische Werkstoffe und Halbzeuge (2002) 105

[Vac15] Vacom GmbH: *Vacom Produktkatalog* (2015) 171

[VG 09] VG Scienta: *Operating and Maintenance Handbook ST22 Titanium Sublimation Pump Cartridge Issue B (Doc. Numb. UI62494B)* (2009) 178

[vZ10] T. van Zoest, N. Gaaloul, Y. Singh, H. Ahlers, W. Herr, et al.: Bose-Einstein Condensation in Microgravity. *Science* (2010), Bd. 328(5985):S. 1540–1543 39, 40, 52

[Wel93] K. M. Welch, D. Pate, and R. J. Todd: The pumping of helium and hydrogen by sputter-ion pumps part II (1993) 110, 181

[Wet11] T. Wetzel and P. Böckhaus: *Wärmeübertragung : Grundlagen und Praxis*, Springer (2011) 249, 250, 272

[Whi91] F. White: *Viscous Fluid Flow - 2nd Edition*, McGraw-Hill series in mechanical engineering, McGraw-Hill (1991) 221, 226

[Wil04] J. G. Williams, S. G. Turyshev, and D. H. Boggs: Progress in lunar laser ranging tests of relativistic gravity. *Phys. Rev. Lett.* (2004), Bd. 93:S. p. 261101 11

[Zho11] L. Zhou, Z. Xiong, W. Yang, B. Tang, W. Peng, et al.: Development of an atom gravimeter and status of the 10 meter atom interferometer for precision gravity measurement. *General Relativity and Gravitation* (2011), Bd. 43(7):S. 1931–1942 35